N. Ramesh Babu
Santosh Kumar
P. R. Thyla
K. Sripriyan   *Editors*

Advances in Additive Manufacturing and Metal Joining

Proceedings of AIMTDR 2021

Springer

Lecture Notes in Mechanical Engineering

N. Ramesh Babu · Santosh Kumar · P. R. Thyla ·
K. Sripriyan
Editors

Advances in Additive Manufacturing and Metal Joining

Proceedings of AIMTDR 2021

Springer

Editors
N. Ramesh Babu
Department of Mechanical Engineering
Indian Institute of Technology Madras
Chennai, India

P. R. Thyla
Department of Mechanical Engineering
PSG College of Technology
Coimbatore, India

Santosh Kumar
Department of Mechanical Engineering
Indian Institute of Technology (BHU)
Uttar Pradesh, India

K. Sripriyan
Department of Mechanical Engineering
PSG College of Technology
Coimbatore, India

Foreword

8th International and 29th All India Manufacturing Technology, Design and Research Conference Proceedings (Volumes 1–5)

(Edited by Different Professors and Researchers)

First, I would like to congratulate the editors of five different volumes of proceedings of the 8th International and 29th All India Manufacturing Technology, Design and Research Conference (AIMTDR) proceedings being published by Springer. These volumes are a very good collection of the research and review papers on the manufacturing processes like Modern Machining Processes (Volume-1), Additive Manufacturing and Metal Joining (Volume-2), Simulation, Product Design and Development (Volume-3), Forming, Machining and Automation (Volume-4) and Micro and Nano Manufacturing and Surface Engineering (Volume-5). These five volumes are a comprehensive collection of the research papers focusing on the most recent research and developments in the area of manufacturing processes. These subject areas continue to be dominant manufacturing technologies, say, the *technologies of future*, namely 3D printing (additive manufacturing) which generally lacks speed, surface finish and dimensional accuracy. To compensate these weaknesses of 3D printing in the real-life production, I could also see good papers on micro-/ nano-manufacturing and nano-finishing. Theoretical analysis, optimization and simulation of manufacturing processes would definitely provide the necessary insights into the physics and mechanisms of these processes, as well as their basic understanding. These five volumes would be invaluable to the researchers working in research laboratories and engineers in industrial organizations working on shop floors for learning, consulting and applying some of the findings deliberated in the conference by the authors of different research papers.

Such conferences encourage the interaction between the research scholars, faculty members and user industries' representatives from different parts of the world. Unfortunately, this could not happen in this hybrid conference to the desired extent due to the pandemic effects across the globe. Apart from these contributed papers, there were many online and offline keynote lectures delivered by the researchers from different countries including India. I am sure that these papers should be of great help to the readers of these proceedings. These proceedings/collections of the papers should be of great help to the academia and industries as well as reference books in different sub-fields of manufacturing processes.

I would like to congratulate the authors for their contributions to all these five volumes of the proceedings and the editorial committee members for their untiring efforts made in bringing out these research papers' collections in five volumes. I would also like to thank the technical committee members in general and the ex-vice-president of NAC, Prof. Uday S. Dixit for inviting me to write this foreword.

Kanpur, India   Dr. V. K. Jain
                                                              Professor (Retired) IIT Kanpur
                                                                Member, National Advisory
                                                                Committee, AIMTDR 2021

Preface

All India Manufacturing Technology, Design and Research (AIMTDR) is a reputed international conference series focused in the domain of manufacturing. The first All India Machine Tool Design and Research conference, also abbreviated as AIMTDR, was organized by Jadavpur University, Kolkata, in the year 1967. Those were the days when main focus of manufacturing was toward efficient design and utilization of machine tools. PSG College of Technology, Coimbatore, organized 7th and 15th AIMTDR conferences in 1976 and 1992, respectively. Other institutes who organized this conference before the 15th AIMTDR conference are Central Machine Tool Institute (CMTI), Indian Institute of Technology (IIT) Bombay, IIT Madras, University of Roorkee, IIT Kanpur, Central Mechanical Engineering Research Institute and IIT Delhi, some of them multiple times. After the 15th AIMTDR conference, the necessity of widening the scope of the conference arose. It was decided to encompass entire manufacturing technologies in its fold, rather than just focusing on the technologies related to machine tools. Accordingly, the phrase "machine tool design" was replaced by "manufacturing technology, design". Thus, the conference series was rechristened as All India Manufacturing Technology, Design and Research, without making any alteration to acronym AIMTDR. Thus, the 16th AIMTDR conference with new unabridged title was organized at CMTI, Bangalore, in 1994. It is interesting to note that CMTI had renamed itself from Central Machine Tool Institute to Central Manufacturing Technology Institute in 1992, adapting with the current trends in manufacturing.

AIMTDR received its international status in the year 2006, when the first International and 22nd National AIMTDR was organized at IIT Roorkee. Subsequent conferences were held at IIT Madras, Andhra University, Jadavpur University, IIT Guwahati, College of Engineering Pune and Anna University. The recent edition of the conference, viz., the 8th international and 29th national conference was jointly organized by the Departments of Mechanical Engineering of *PSG College of Technology*, Coimbatore, and *PSG Institute of Technology and Applied Research*, Coimbatore, during *December 9–11, 2021* in virtual mode. The theme of AIMTDR 2021 was "*Transformational Changes in Manufacturing*".

After a rigorous review process, about *250 technical papers* from academia and industry were accepted for the presentation at the conference. In addition, *eight keynote talks* on advanced technologies such as the development of high precision machine tools, simulation of material flow, nanostructured surfaces, additively controlled material mechanics, product development platforms, next-generation milling, diamond turning and hybrid machining were delivered by experts. Further, *two case studies* from the industry highlighting the innovation practices and challenges in machine tool structure design were presented.

Select papers from the conference are being published by *Springer in the series—Lecture Notes in Mechanical Engineering*, in five volumes—*Volume 1*: *Advances in Modern Machining Processes*, *Volume 2*: *Advances in Additive Manufacturing and Metal Joining*, *Volume 3*: *Advances in Simulation, Product Design and Development*, *Volume 4*: *Advances in Forming, Machining and Automation* and *Volume 5*: *Advances in Micro and Nano Manufacturing and Surface Engineering.*

Volume 2 entitled *Advances in Additive Manufacturing and Metal Joining* covers a wide variety of technical papers related to fused deposition modeling, PolyJet 3D printing, metal 3D printing, weld deposition-based technology and solid-state joining process for various applications. We hope that researchers as well as practicing engineers will find this volume useful.

We sincerely thank members of National Advisory Committee members of AIMTDR, organizers, reviewers, authors and participants. Special thanks go to Springer for publishing the select papers of AIMTDR since AIMTDR 2014. Readers are requested to send us the feedback about this volume.

Coimbatore, India   P. R. Thyla
March 2022   K. Sripriyan
                                                                                                 N. Ramesh Babu
                                                                                                 Santosh Kumar

Contents

Metal Joining

About the Editors

Dr. N. Ramesh Babu is V. Balaraman Institute Chair Professor in the Department of Mechanical Engineering, IIT Madras, Chennai. He is Secretary, Advanced Manufacturing Technology Development Centre, IIT Madras Research Park, Chennai. He is Honorary Professor, College of Engineering at Swansea University, UK. He has received his Master's in Mechanical Engineering from IISc Bangalore and Ph.D. from IIT Madras. His research interests include manufacturing technology, grinding, abrasive waterjet machining, sheet metal fabrication, laser beam machining, robotics, precision machine tool development, process modelling and simulation of manufacturing systems. He has published nearly 85 peer-reviewed international journal and national journal papers and 104 international and national conferences papers. He is Member of American Society of Mechanical Engineers, Society of Manufacturing Engineers, Indian Institution of Plant Engineers and Fluid Power Society of India. He is Visiting Fellow in Texas A&M University, USA, and Honorary Member in Romanian Society of Mechanical Engineers.

Dr. Santosh Kumar is Professor in the Department of Mechanical Engineering, Indian Institute of Technology (BHU), Varanasi. He is Fellow IE (India) and presently Chairman and Coordinator of Teaching-Learning Cell at IIT (BHU). He has received his Master's and Ph.D. degrees from IIT Kanpur. He has published nearly 70 international and national journal papers. He has completed eight sponsored research projects, and four projects are in progress. He has developed four new machines from scratch for government organizations out of which three are patented.

Dr. P. R. Thyla is Professor and Head in the Department of Mechanical Engineering, PSG College of Technology, Coimbatore. She has completed her M.Tech. in Machine Design from IIT Madras, Chennai, and Ph.D. degree in Mechanical Engineering from Bharathiar University, Coimbatore. Her research interests include composite materials, alternate materials for machine tools and metal joining. She has published nearly 50 peer-reviewed international journal and national journal papers. She has been involved in research projects sponsored by DST, AICTE, BRNS, office of PSA and IGCAR. She has also completed more than 20 industrial consultancy projects.

Dr. K. Sripriyan is Assistant Professor (Sr. Gr.) in the Department of Mechanical Engineering, PSG College of Technology, Coimbatore. He has completed his Master's in Manufacturing Engineering from Alagappa Chettiar Government College of Engineering and Technology, Karaikudi, and Ph.D. degree in Welding Technology from Anna University, Chennai. He has published 12 peer-reviewed international journal and national journal papers and 11 international and national conference papers and holds two patents. He is a member of Institution of Engineers (India) and life member in Indian Society of Systems for Science and Engineering (ISSE).

Additive Manufacturing

A Review on Fused Deposition Modeling of Thermoplastics

Kriti Srivastava and **Yogesh Kumar**

1 Introduction

The 3D printing or additive manufacturing is a thoughtfully designed manufacturing technique that involves layering materials to produce three-dimensional components straight from CAD models by Charles Hull in 1986. The major benefit of AM over subtractive manufacturing techniques is the ability to deal with material and geometric challenges that subtractive manufacturing techniques cannot produce [1]. This modeling method applies to mathematical principles that aid in guiding the production process toward predetermined functionality goals. This information is presented in the form of a computational system (finite element method) that estimates the desired features. Modeling approaches associated with 3D printing can be easily converted into finite element models in this sense [2].

It enables the production of printed parts as well as prototypes. The ability to produce virtually any shape that would be impossible to machine is one of the main benefits that this approach brought to product production. Other benefits include reduced time and expense, increased human involvement, and, as a result, a shorter product development period. For the making of dies and molds, there is a requirement for a longer lead time. Tooling may be fabricated in less time due to AM technology. These speed up the time it is taking to get items to market. Because AM machines do not require expensive setups, they are cost-effective in small batch manufacturing. The quality of the components is determined by the process rather than operator competency. As a result, production can easily be synchronized with consumer demand [3].

K. Srivastava (✉) · Y. Kumar
National Institute of Technology Patna, Patna, Bihar 800005, India
e-mail: kritis.phd20.me@nitp.ac.in; kritisrivastava.17@gmail.com

Y. Kumar
e-mail: yogesh.me@nitp.ac.in

3

Each operation on these devices is likely to have a limited number of options and entail minimum effort. However, this means that there are limited options, such as a small range of materials and other factors in which to explore. Larger, more powerful computers are more likely of being modified to meet consumer needs, making them more difficult to control, while still providing a broader range of potential outcomes and effects that an advanced operator can bring to good use. In addition, such printing machines typically necessitate more cautious implementation in workspace conditions.

There was a plethora of facts to back up additive manufacturing's promises in these areas such as (i) personalized healthcare goods to enhance population health, wellbeing, and quality of life; (ii) decreased environmental footprint for manufacturing resilience; and (iii) a streamlined distribution network to improve demand fulfillment reliability and responsiveness [4].

1.1 Process Chain of Additive Manufacturing

The process chain of the additive manufacturing technology is as shown in Fig. 1.

The process starts with creating a CAD model and then its conversion into STL file.

After that the STL file is transferred on AM machine, and finally, the build process starts that results in 3D printed parts.
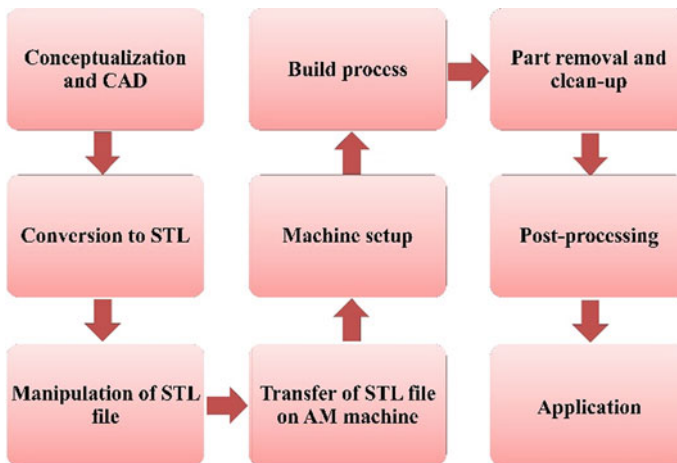
Fig. 1 Process chain of additive manufacturing [5]

Fig. 2 AM process selection criteria [6]
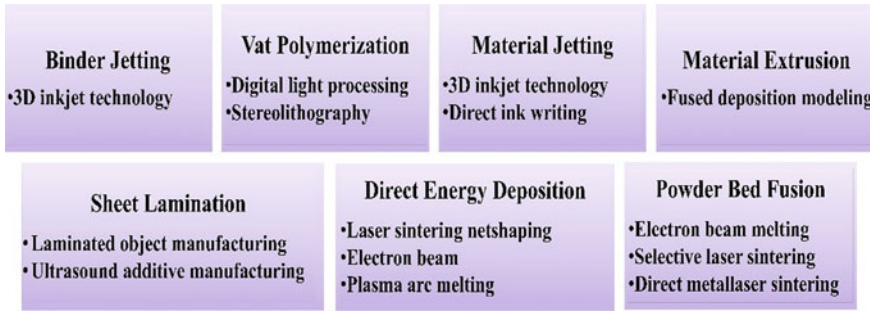
Fig. 3 Classification of AM processes

1.2 Classification of Additive Manufacturing

Selection of AM process requires the following criteria as given in Fig. 2. It basically involves the availability of materials and technology, requirement of quality, their characteristics, and post-processing techniques involved.

Additive manufacturing process is classified into seven processes according to "The International Organization for Standardization (ISO)/ American Society for Testing and Materials (ASTM) 52,900:2015" [7] as shown in Fig. 3.

Comparison among various AM technologies based on the form of feed, principle, and typical resolution is shown in Table 1.

1.3 Advantages of Additive Manufacturing [18]

1. Shortening of the time that it takes to get a product to market by speeding up prototyping.
2. Decrease the cost of development of product.
3. Increasing the efficiency and competitiveness of businesses in terms of innovation.
4. Produce extremely complicated work at a reasonable cost.

Table 1 Comparison among various AM technologies [8–10]

Process	Form of feed material	Principle	Typical resolution
Binder jetting	Powders and binder	Selectively depositing a liquid bonding agent to combine powder components to form the 3D component [11]	100 μm
Powder bed fusion	Powders	An infrared energy source fuses powder particles layer by layer [12]	50–100 μm
Metal extrusion	Rods or wire	Material is melted and then extruded through a nozzle [13]	100 μm–1 cm
Sheet lamination	Sheet	Sheets of material are melted together in this procedure, with the required form engraved into each form [14]	200–300 μm
Direct energy deposition	Wire	Laser is used to melt substrate material and then wire is fed in the melt pool [15]	100 μm–1 cm
Vat polymerization	Photosensitive resin	Depositing focused energy onto the surface of a liquid photopolymer [16]	0.1–100 μm
Material jetting	Molten wax as filler or liquid photosensitive resin	Deposition of drops of photopolymers in liquid form by utilization of piezoprinting heads and curing it by using UV lamps [17]	10–25 μm

1.4 Issue Related to AM

The materials, process parameters, contact to emissions created during the engineering process, and supply chain distribution are the main challenges addressed to enhance the sustainability of AM systems [19]. Requirement of development of integrated system is robust, user-friendly, and safe so that it may provide desired speed, good resolution, dimensional accuracy, and less energy consumption. Stair stepping, build-up volume, and voids formation are some of the common issues related to AM that should be avoided [8].

2   Fused Deposition Modeling

Reason: The methods accessible to small enterprises, organizations, and private consumers are typically mentioned to as 3D printing technologies, with most of them relying on molten material deposition frequently called as fused filament fabrication (FFF) or fused deposition modeling (FDM). The cheap cost, wide variety of processable material, and scalability of this technology have permitted a large expansion of small system based on it, giving it a growing presence in a wide range of productive sectors and creating a large potential for the current and future growth of the industry. By extruding melted or semi-melted material through a nozzle, metal extrusion additive manufacturing is the most commonly used 3D printing method for producing products. The most significant benefit of extrusion-based AM process is the reduced operating costs [20]. The basic steps involved in FDM are shown in Fig. 4.

The first step in the FDM process is to create a model of the part to be created in a suitable computer-aided design program that can show the object's detailed structure. The 3D scanners may also be used to scan an actual object or a concept that has already been developed. This file is then transformed to an.stl format using program known as a slicer. This program divides the model template into layers that can be printed. In order to print the design correctly, the printer follows the design's led course.

The material is rolled on a spool and is fed into a heater that heats the material to a certain temperature in order for it to bond with the previously applied layer. With the support of the nozzle, the outflow can be heated and controlled [21]. The arm that

Fig. 4 Basic steps in FDM
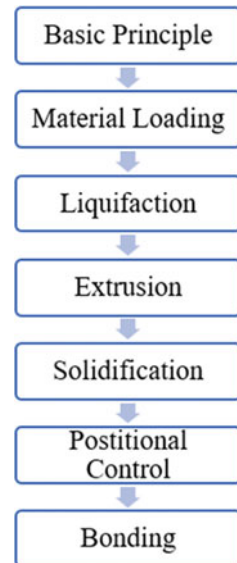
Fig. 5 Schematic working of FDM
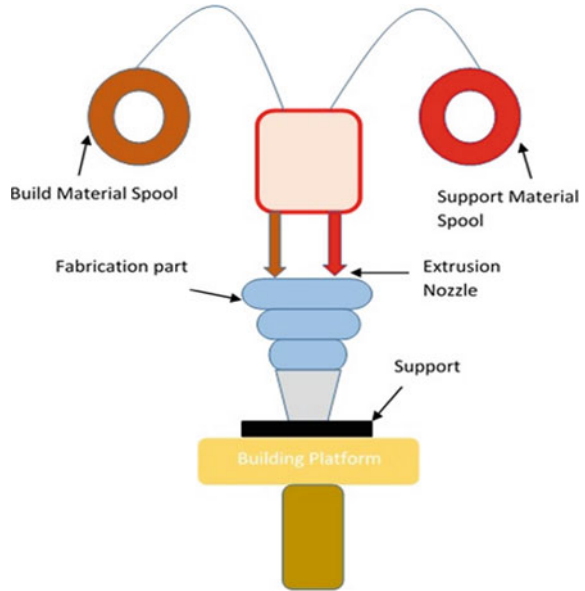
positioned the material on the surface controls the x-axis and y-axis motion for 3D printing, while the table upon which printing is to be performed shifts in the z-axis direction in the FDM process as shown in Fig. 5 [22].

2.1 History

Scott Crump, Stratasys's co-founder, invented an AM technique in 1988 that formed layers by physically extruding molten thermoplastics (such as acrylonitrile butadiene styrene or polylactic acid) onto a surface. Fused deposition modeling (FDM) is a trademarked technology that demands high working temperatures and produces prints with extreme porosities [23, 24]. Extrusion systems, on the other hand, are becoming increasingly popular among DIY enthusiasts because of their low cost and flexibility. While thermoplastic materials are processed by most of the extrusion systems, efforts have been made to process metal pastes and ceramics [25].

2.2 Filament Manufacturing

Based on the design of the nozzle of the extruder and the fused deposition modeling 3D printing device employed, a filament manufacturing method employs an extruder with either one screw or two screws to extrude a filament with required dimensional

tolerance. In light of this, the controllable speed of the screw, temperature, and pressure were discovered to be the most important parameters to manage during filament manufacturing in order to attain the desired diameter of the filament of polymer that had been created before [26]. These provide a path to attaining the best values of extrusion for the filament manufacturing process.

More precisely, the 3D printing filaments should be capable of delivering and maintaining the pressure required for a complete extrusion operation. Unsuccessful to do so, however, cause filament buckling, which happens when the pressure of extrusion is lower or greater than the filament's critical buckling load that it can handle? In such instances, the elastic modulus is determined by the filament's load-bearing capabilities, while the melt viscosity is used to determine the extrusion pressure. Selecting the ideal material for filament for method effectiveness and efficiency would entail employing materials with advantageous and manageable structural, rheological, physical, chemical, and mechanical characteristics, as well as taking into account their impacts on their ability to be printed, application, and done at a stage after processing [24].

2.3   FDM Process Parameter

Wettability: It is defined as the polymer's capability to damp other solid surfaces with which it comes into touch, and it is one of the important rheological, physical, and chemical properties listed above. The wetting angle is used to describe this, with angles more than $150°$ indicating super-hydrophobicity and angles smaller than $5°$ indicating super-hydrophilicity [27]. In essence, a polymer's ability to wet other surfaces increases its bonding capability, which is critical for ME3DP bonding among layers of polymer paths.

Viscosity: The resistance to flow of a specific substance, in this case, a polymeric substance, is termed as viscosity, which is another important element in ME3DP [28]. The capability of a polymer to sustain a required flow behavior while being transported from the heating zone to the nozzle and onto the build plate is defined by its governing characteristics in mechanical-based manufacturing. The durability of the intermolecular links between separate polymeric chains greatly determines this property; higher viscosities result from stronger bonds and vice versa [29].

Isoelectric point: The pH at which the polymer has a net neutral charge of 0 is termed as isoelectric point (pI) at a certain pH in additional case of polymeric characteristics [30]. The pI of acidic polymers is higher, while the pI of simple polymers is lower. This element would also influence the polymer's electrostatic behavior during the ME3DP process, as well as its adhesion and segregation characteristics with the surfaces and materials it comes into contact with.

Flowability: It is a resultant property that is closely linked to the polymeric material's viscosity [31]. More viscous the materials that are more viscous have a lower flow ability than less viscous materials, which would impair the polymer's capability to flow from the heated nozzle zone to the build plate.

Glass Transition Temperature: It is the temperature at which amorphous polymer's spontaneous molecular form starts to flow as a result of heat energy supply [30]. It will relate to the effect of thermal stress on the adhesion of the bed that is evolved at the time of printing.

Melting Temperature: It is based on the similar idea as of glass transition temperature, but it refers to the initiation of flow of a polymer's ordered molecules (crystalline). It has the effect on the printing temperature at which the polymer is to be printed by the extruder.

Speed at Which Printing is Done: It may be defined as the build nozzle's traverse speed when depositing material on the printer's bed in the XY plane. The printing speed has a direct impact on the printing time of part. The distortion of the construction component is also influenced by the printing speed [32]. This is due to the high amount of residual tension generated during material deposition as a result of the quicker extrusion process.

Rastor Angle: "It specifies the x-axis material deposition direction in the used FDM machine along the build area." The raster angle might range from 0 to 90 degrees in general. The maximum ultimate and yield strength is found in the 0^0 orientation, where molecules are aligned parallel to the stress axis, and the weakest orientation is found in the $45^°$–$90^°$ range, where interlayer bonding is weak [33].

Air Gap: It denotes the space between two adjacent depositions of bead. If the air gap is zero, that means materials are in touch with each other after deposition. If it is positive, it indicates loose structure, and negative air gap indicated highly dense structure [8].

Diameter of Nozzle: The diameter of the nozzle has a major impact on the width of the raster. This is because the nozzle diameter has a direct effect on the pressure decrease along the liquefier. The selection of an optimal nozzle diameter is critical for maintaining a good, steady flow of the extruding material [8].

Specific Energy Equation: The specific energy equation for incompressible melted material flows in the FDM process differs from those of other processes and may be stated as follows [9]:

$$\rho c_p \left(\frac{dT}{dt} + (\vec{v}.\nabla)T \right) = -\nabla\vec{q} - (\vec{\tau} : \nabla\vec{v}) + \emptyset, \qquad (1)$$

where ∇q is the energy change per unit time and volume due to conduction of heat, ρ is the density, p is the pressure applied, velocity is denoted by v, temperature is given by T, heat source increases the internal energy which is represented by φ, τ is the force on the surface, and c_p is specific heat of the melt.

3   Materials for FDM

Table 2 shows some of the materials used in FDM along with its properties and application. Table 3 shows salient features of general fused deposition modeling printer.

Table 2   FDM materials and its application

FDM materials [34]	Properties and applications
Acrylonitrile butadiene styrene (ABS) plus thermoplastic	Stable in the environment and have strength higher than basic ABS (approximately 40%)
M30-ABS thermoplastic	They have good tensile as well as flexural strength and are 25–75% stronger than standard ABS. Its application includes end-use components, concept modeling, etc.
ABS-M30i thermoplastic	They are biocompatible, high-strength thermoplastic material and finds their application in the medical and food-packaging industries
ABSi thermoplastic	They are translucent material and beneficial for observing transmission of light and flow of materials and frequently used for aero, automotive, and medical devices
Polycarbonate (PC)-ABS thermoplastic	They possess favorable characteristics of both PC and ABS such as flexibility, refractiveness, and strength. They are used in electronics and telecommunication engineering and the automotive industry
ABS-ESD7 (electrostatic dissipative)	They possess the durability and strength of ABS combined with carbon which gives electrostatic dissipative properties (ESD). They find application in electronics components assembly
PC thermoplastic (polycarbonate)	It possesses good stability and durability for creating functional models. It is highly used in industries such as automobile, medical, and tooling due to its mechanical properties and high refractiveness
PC-ISO thermoplastic	They are also considered as biocompatible material in their raw form. They are widely used in the medical, drug, and food industries
PPSF/PPSU thermoplastic (polyphenylsulfone)	It is a high-strength, technically excellent material that is ideal for caustic and high-temperature applications PPSF/PPSU may be sterilized using ethylene oxide, autoclaving, or radiation, making it appropriate for the production of medical equipment. They are also employed in the tooling and automotive sectors

Table 2 (continued)

FDM materials [34]	Properties and applications
ULTEM 9085	It is a thermoplastic designed primarily for aeronautical applications. It is a tough, light, flame-resistant thermoplastic that is commonly used in airplane interiors. ULTEM is suited for quick prototyping and specialized tooling applications in aerospace, automobile, pharmaceutical, and food manufacturers because of its "high strength-to-weight ratio" and current certification
Nylon 12	It is considered as one of the toughest FDM materials. It provides durability and high resolution of surface and possesses good resistant to chemicals. They frequently find applications in housings and enclosures, ductwork, impellers, connectors, complex plastic parts, etc
PLA	Polylactic acid is ecofriendly material that is used for esthetic purposes for both home and office
TPU thermoplastic polyurethane	Extraordinary elongation at break and resistance to corrosion to a wide range of industrial chemicals and lubricants. For a range of industrial applications, this highly adaptable material combines rubber and plastic qualities
PEEK (poly-ether-ether-ketone)	It has good dimensional stability, semi-crystalline in nature, highly refractive, and resistant to chemicals. It is used in automotive, electrical, and medical sectors. It has very high compressive and bending strength (approximately 114–115% higher than ABS)
Novel material	
Hydrogels [9]	Hydrogels, a three-dimensional system of molecules made up of hydrophilic polymer chains, may be shaped, sized, and formed into any figure, magnitude, or form and may absorb up to 1000 times their dry weight when placed in a water-rich atmosphere. Hydrogel-based systems can be used as cell carriers in tissue engineering, as well as chemical or drug distribution media in stem cell and cancer research [35]
Functional inks	They find application in optoelectronics, cardiac micro-physiological devices, super-capacitors, sensors, etc. [36]
CB/PCL	They are used in sensors
Polybutylene succinate (PBS)	They produce safe degradation by-products, biocompatible, good tissue biomimicry, good mechanical properties, and biodegradable [10]
Polyhydroxyalkanoates (PHA)	
Cellulose	

Table 2 (continued)

FDM materials [34]	Properties and applications
Lignin	

Table 3 Salient features of fused deposition modeling printer

Features	Values
Dimension of FDM 3D printer	x ≤ 900, y ≤ 600, z ≤ 900
Resolution	100 μm–1 cm
Fabrication speed	0.5 cmh^{-1}
Company	Stratasys

Fig. 6 Comparison between tensile strengths of some FDM materials [10]
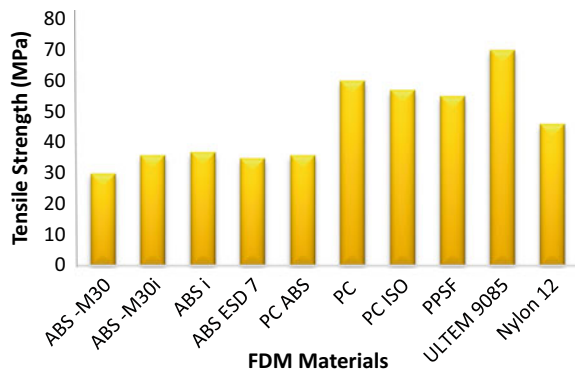
Development of the latest 3D printers can withstand the temperature up to 520 °C.

Figure 6 shows the comparison between tensile strengths of some of the FDM materials taken in XZ orientation.

The mechanical characteristics of any material govern its application in any given field of industry or study [37].

4 Advantages and Limitation

Some advantages and limitation of FDM are shown in Table 4 [38].

Table 4 Advantages and limitation of FDM

Advantages	Limitation
Expenditure of machine at entry level is low	Requires long printing time
Availability of different types of raw materials	Precision is low
Customization is easy	Sharp external corners are difficult to make
It is versatile in nature	Printed part shows anisotropic property

5 Major Challenges and Future Prospective—Conclusion

In FDM, a widespread range of materials may be utilized, and part precision can approach 0.08 mm. The FDM machine is small and needs little maintenance. The materials, functionality, process parameters (speed, resolution), exposure to emissions created during the manufacturing process, and supply chain distribution are the main challenges addressed to enhance the sustainability of FDM systems. More concentration should be given on the development of biocompatible and environment-friendly materials.

In order to further enhance the mechanical properties of the printed part, the actual printable scenario of FDM process should be considered to get the optimal choice of process parameters. Researchers are concentrating their efforts on important parameters and their optimization; nevertheless, there are still many unknown aspects that need to be investigated since they may have a significant impact on component quality and efficiency of process. Apart from that, there is a lot of room to expand the spectrum of materials that may be utilized as filaments because most literary works use polymer-based materials. Since there is a greater focus on using metals as filament materials in research, FDM may witness an upswing trend, as this may broaden the range of materials utilized, making this method suitable to maintain numerous levels of competitiveness. It was also discovered that the impact of environmental variables such as dampness, temperature, and noise was not well supported by the literature, indicating that further research is needed in this area.

References

1. Hegab, H.A.: Design for additive manufacturing of composite materials and potential alloys: a review. Manuf. Rev. **3**(11) (2016)
2. Chaunier, L., Guessasma, S., Belhabib, S., Della Valle, G., Lourdin, D., Leroy, E.: Material extrusion of plant biopolymers: opportunities and challenges for 3D printing. Additive Manuf. 220–233 (2018)
3. Prakash, K.S., Nancharaih, T., Rao, V.S.: Additive manufacturing techniques in manufacturing-an overview. Mater. Today: Proc. **5**(2), 3873–3882 (2018)

4. Huang, S.H., Liu, P., Mokasdar, A., Hou, L.: Additive manufacturing and its societal impact: a literature review. Int. J. Adv. Manuf. Technol. **67**(5–8), 1191–1203 (2013)
5. Gibson, I., Rosen, D.W., Stucker, B.: Additive Manufacturing Technologies. Springer, New York (2010)
6. Gokuldoss, P.K., Kolla, S., Eckert, J.: Additive manufacturing processes: selective laser melting, electron beam melting and binder jetting-selection guidelines. Materials **10**(6) (2017)
7. Tofail, S.A.M., Koumoulos, E.P., Bandyopadhyay, A., Bose, S., O'Donoghue, L., Charitidis, C.: Additive manufacturing: scientific and technological challenges, market uptake and opportunities. Mater. Today **21**(1), 22–37 (2018)
8. Solomon, I.J., Sevvel, P., Gunasekaran, J.: A review on the various processing parameters in FDM. Mater. Today: Proc. **37**(Part 2), 509–514 (2020)
9. Lee, J.Y., An, J., Chua, C.K.: Fundamentals and applications of 3D printing for novel materials. Appl. Mater. Today **7**, 120–133 (2017)
10. Stratasys homepage (2021). https://www.stratasysdirect.com/technologies/fused-deposition-modeling. Last Accessed 28 June 2021
11. Cordero, Z.C., Siddel, D.H., Peter, W.H., Elliott, A.M.: Strengthening of ferrous binder jet 3D printed components through bronze infiltration. Addit. Manuf. **15**, 87–92 (2017)
12. Chatham, C.A., Long, T.E., Williams, C.B.: A review of the process physics and material screening methods for polymer powder bed fusion additive manufacturing. Prog. Polym. Sci. **93**, 68–95 (2019)
13. Barocio, E., Brenken, B., Favaloro, A., Bogdanor, M., Pipes, R.B.: Extrusion deposition additive manufacturing with fiber-reinforced thermoplastic polymers. In: Structure and Properties of Additive Manufactured Polymer Components. Elsevier Inc (2020)
14. Molitch-Hou, M.: Overview of additive manufacturing process. In: Additive Manufacturing: Materials, Processes, Quantifications and Applications. Elsevier Inc. (2018)
15. Kareem, M.A., Harshitha, V.: A direct metal deposition 3d printer: review on future prospects. In: AIP Conference Proceedings, pp. 2200. (2019)
16. Ligon, S.C., Liska, R., Stampfl, J., Gurr, M., Mülhaupt, R.: Polymers for 3D printing and customized additive manufacturing. Chem. Rev. **117**, 10212–10290 (2017)
17. Yap, Y.L., Wang, C., Sing, S.L., Dikshit, V., Yeong, W.Y., Wei, J.: Material jetting additive manufacturing: an experimental study using designed metrological benchmarks. Precis. Eng. **50**, 275–285 (2017)
18. Attaran, M.: The rise of 3-D printing: the advantages of additive manufacturing over traditional manufacturing. Bus. Horiz. **60**(5), 677–688 (2017)
19. Ford, S., Despeisse, M.: Additive manufacturing and sustainability: an exploratory study of the advantages and challenges. J. Clean. Prod. **137**, 1573–1587 (2016)
20. Kuipers, T., Wu, J., Wang, C.C.L.: CrossFill: foam structures with graded density for continuous material extrusion. CAD Comput. Aided Design **114**, 37–50 (2019)
21. Galantucci, L.M., Bodi, I., Kacani, J., Lavecchia, F.: Analysis of dimensional performance for a 3D open-source printer based on fused deposition modeling technique. Proc. CIRP **28**, 82–87 (2015)
22. Gokhare, V.G., Raut, D.N., Shinde, D.K.: A review paper on 3D-printing aspects and various processes used in the 3D-printing. Int. J. Eng. Res. Technol. **6**(06), 953–958 (2017)
23. Morissette, S.L., Lewis, J.A., Cesarano, J., Dimos, D.B., Baer T (2000) Solid freeform fabrication of aqueous alumina-poly(vinyl alcohol) gelcasting suspensions. J. Am. Ceram. Soc. **83**(10), 2409–16 (2000)
24. Pandey, M., Reddy, V.N., Dhande, S.G.: Slicing procedures in layered manufacturing: a review. Rapid Prototyp. J. **9**(5), 274–288 (2003)
25. Agarwala, M.K., Jamalabad, V.R., Langrana, N.A., Safari, A., Whalen, P.J., Danforth, S.C.: Structural quality of parts processed by fused deposition. Rapid Prototyp. J. **2**(4), 4–19 (1996)
26. Li, X., Jiang, Y., Jiang, Z., Li, Y., Wen, C., Lian, J.: Reversible wettability transition between superhydrophilicity and superhydrophobicity through alternate heating-reheating cycle on laser-ablated brass surface. Appl. Surf. Sci. **492**, 349–361 (2019)

27. Prescott, J.K., Barnum, R.A.: On powder flowability: part I. Pharmaceutical Technol. Eur. **13**(1), 37–39 (2001)
28. Balani, K., Verma, V., Agarwal, A., Narayan, N.: In: Physical, Thermal, and Mechanical Properties of Polymers, Biosurfaces. pp. 329—344. Wiley, Inc (2015)
29. Polymer engineering science and viscoelasticity, characteristics, applications and properties of polymers. In: Polymer engineering science and viscoelasticity, pp. 55–57. Springer US
30. Righetti, P.G.: Determination of the isoelectric point of proteins by capillary isoelectric focusing. J. Chromatogr. A **1037**, 491–499 (2004)
31. Dudek, P.: FDM 3D printing technology in manufacturing composite elements. Arch. Metall. Mater. **58**(4), 1415–1418 (2013)
32. Kacergis, L., Mitkus, R., Sinapius, M.: Influence of fused deposition modeling process parameters on the transformation of 4D printed morphing structures. Smart Mater. Struct. **28,** 105042:9 (2019)
33. Es-Said, O.S., Foyos, J., Noorani, R., Mendelson, M., Marloth, R., Pregger, B.A.: Effect of layer orientation on mechanical properties of rapid prototyped samples. Mater. Manuf. Processes **15**(1), 107–122 (2000)
34. Barna, J., Torok, J.: In: INES 2012 : IEEE 16th International Conference on Intelligent Engineering Systems: Proceedings : Lisbon, Portugal, June 13–15, vol. 578 (2012)
35. Unagolla, J.M., Jayasuriya, A.C.: Hydrogel-based 3D bioprinting: a comprehensive review on cell-laden hydrogels, bioink formulations, and future perspectives (2020)
36. Hassan, K., Nine, M.J., Tung, T.T., Stanley, N., Yap, P.L., Rastin, H., Yu, L., Losic, D.: Functional inks and extrusion-based 3D printing of 2D materials: a review of current research and applications. Nanoscale **12**(37), 19007–19042 (2020)
37. Srivastava, K., Sinha, A.A., Sahani, R.: Effect of heat treatment on hardness and toughness of EN8 steel. Mater. Today: Proc. **42**, 1297–1303 (2021)
38. Daminabo, S.C., Goel, S., Grammatikos, S.A., Nezhad, H.Y., Thakur, V.K.: Fused deposition modeling-based additive manufacturing (3D printing): techniques for polymer material systems. Mater. Today Chem. **16**, 100248 (2020)

Analysis of Density of Laser Powder Bed Fusion Fabricated Part Using Decision Tree Algorithm

Abhishek Agnihotri , **B. Hemanth Vinay** , **and Radha Raman Mishra**

1 Introduction

Additive manufacturing (AM) is a process of fabricating materials using layer-by-layer approach from 3D model data [1]. In the earlier stages, additive manufacturing was limited to only making prototypes, but now this technology is gaining interest in manufacturing because of its ability to produce complex parts with customized properties. It is a low-cost process because it reduces the wastage of material and finds applicability in many fields such as aerospace, medical, automotive, fashion, and food industries. There are many additive manufacturing processes that are used to build 3D parts using different process parameters. Each process parameter plays a crucial role in fabricating a quality part. The quality of additively fabricated parts can be improved by optimizing the process parameters. In recent years, the laser powder bed fusion (LPBF) process has emerged as a potential additive manufacturing process for the processing of metallic parts by fusing powder particles layer by layer [2]. The LPBF process uses a high-power laser that follows a certain path that is determined by a selected laser scanning strategy and a numerical model of the part. The parts fabricated by the LPBF process usually offer improved density, properties, and surface finish [3]. The major problem in the LPBF process is the formation of defects in the fabricated parts. The quality of manufactured parts by the LPBF process depends on many process parameters such as power, scan speed, hatching space, etc. The detection of process parameters that influences product

A. Agnihotri · B. Hemanth Vinay · R. R. Mishra (✉)
Department of Mechanical Engineering, Birla Institute of Technology and Science, Pilani 333031, India
e-mail: rraman.mishra@pilani.bits-pilani.ac.in

A. Agnihotri
e-mail: h20200200@pilani.bits-pilani.ac.in

B. Hemanth Vinay
e-mail: h20200202@pilani.bits-pilani.ac.in

quality is a challenging task using the experimental approach as it is a very costly and time-consuming affair. Alternatively, modelling and simulation tools can be used for optimizing the process parameters and achieving the desired quality using the finite element method; however, it is computationally expensive. In recent years, the machine learning approach has been used to optimize process parameters and to predict the quality of the product. In the present work, the decision tree algorithm has been utilized for the prediction of the density of the LPBF-processed parts. It required experimental data to make a model, optimize, and predict the quality of the product. Therefore, the main aim of the present work is to optimize the process parameter of the LPBF process by using a decision tree algorithm to get desired density of the as-built parts.

2 Methodology

In this study, the experimental data (Table 1) has been collected from the previously published work [4]. First, the calibration coupons IN625, Ti64, and Fe powders were built with LPBF process. Then, the densities were measured using conventional material characterization techniques.

The quality of a manufactured part depends on process parameters; therefore, parametric optimization was the main objective of the present work to predict density using the decision tree algorithm. Process parameters—laser power, scan speed, and hatching space—were selected as an input feature and density as an output feature. The decision tree algorithm was used to make a model as shown in Fig. 1.

The relationship between the process parameters with density was identified; subsequently, the model was trained and tested. The mean absolute error, mean square error, and root mean square are calculated to find the accuracy of the model. A comparative study was carried out to analyse the actual density and the predicted density. The optimum process parameters were achieved for developing the highest possible density parts.

3 Machine Learning

Machine learning is a subset of artificial intelligence (AI) techniques that allow a machine to learn from past data and make decisions or predictions. The fourth industrial revolution is the modern movement on intelligent automation technologies, and additive manufacturing is one of the important components [5]. The additive manufacturing processes can be optimized using machine learning approach. Machine learning is mainly divided into two types: supervised learning and unsupervised learning (Fig. 2). Supervised learning enables a machine to learn from a set of labelled data in the training set; subsequently, tested using the testing set and the accuracy of the model is calculated [6]. Whereas, an unsupervised learning model is

Table 1 Process parameters and density of the parts developed using LPBF process [4]

Power (Watt)	Scan speed (m/s)	Hatching space (mm)	Energy density (J/mm^2)	Build rate (cm^3/h)	Density (%)
160	2.8	0.092	15.6	37	78.3
160	2.8	0.061	23.3	24.7	87.6
160	2.8	0.052	27.4	21	91.6
160	2.8	0.046	31.1	18.5	95.6
160	2.8	0.037	38.9	14.8	95.6
160	2.8	0.031	46.7	12.3	97.7
225	1.94	0.265	10.9	74.1	79.03
225	1.94	0.133	21.9	37.1	92.5
225	1.94	0.088	32.8	24.7	97.3
225	1.94	0.075	38.5	21.1	98.7
225	1.94	0.066	43.7	18.5	99.5
225	1.94	0.053	54.6	14.8	99.6
225	1.94	0.044	65.6	12.4	99.6
350	1.68	0.347	15	83.9	85
350	1.68	0.173	30	42	96.4
350	1.68	0.116	45	28	99.1
350	1.68	0.099	52.8	23.8	99.4
350	1.68	0.087	60	21	99.6
350	1.68	0.069	75.1	16.8	99.4
350	1.68	0.058	90.1	14	99.6
350	1.18	0.388	19.1	65.9	93
350	1.18	0.194	38.2	32.9	98.9
350	1.18	0.129	57.4	22	99.3
350	1.18	0.11	67.3	18.7	99.5
350	1.18	0.097	76.5	16.5	99.4
350	1.18	0.078	95.6	13.2	99.6
350	1.18	0.065	114.7	11	99.7
345	1.06	0.429	19	65.4	93.3
345	1.06	0.214	38	32.7	98.7
345	1.06	0.143	57	21.8	99.3
345	1.06	0.122	66.8	18.6	99.4
345	1.06	0.107	75.9	16.4	99.4
345	1.06	0.086	94.9	13.1	99.5
345	1.06	0.071	113.9	10.9	99.7
350	0.8	0.469	23.3	54.1	94.3

(continued)

Table 1 (continued)

Power (Watt)	Scan speed (m/s)	Hatching space (mm)	Energy density (J/mm^2)	Build rate (cm^3/h)	Density (%)
350	0.8	0.235	46.6	27	99.1
350	0.8	0.156	69.9	18	99.5
350	0.8	0.133	82	15.4	99.5
350	0.8	0.117	93.2	13.5	99.7
350	0.8	0.094	116.5	10.8	99.4
340	0.56	0.551	27.5	44.4	96.3
340	0.56	0.276	55.1	22.2	99.4
340	0.56	0.184	82.6	14.8	99.4
340	0.56	0.157	97	12.6	99.5
340	0.56	0.138	110.2	11.1	99.2

Fig. 1 Flowchart of the ML process
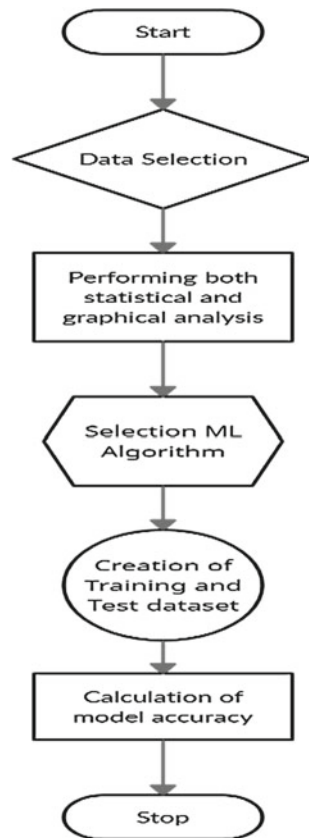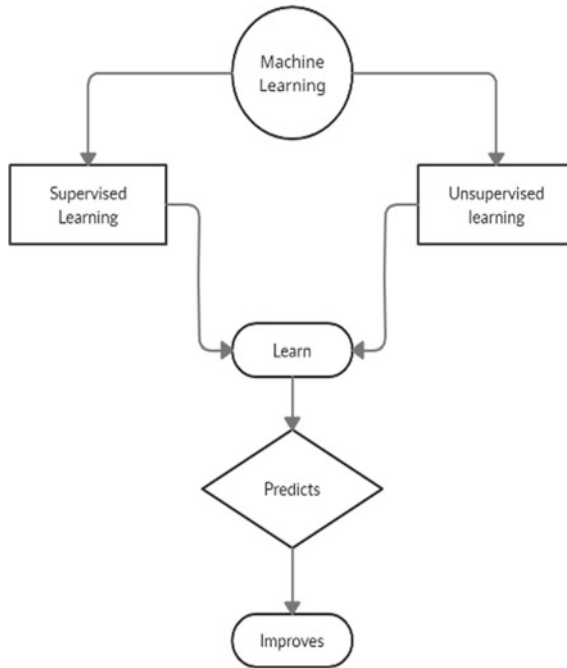
Fig. 2 Machine learning model

used to find hidden patterns from unlabelled data. In the present work, a decision tree regression algorithm which is a supervised learning model was used to develop the model. A decision tree is one of the most versatile supervised learning algorithms in machine learning capabilities for both classification and regression problems. The decision tree algorithm divides the whole dataset into a tree-like structure based on some rules and conditions (Fig. 3).

Further, it predicts the targeted property based on the conditions using the random number of nodes and branches at each node. This algorithm helps to find the optimal decision tree by minimizing the fitness function [7]. A regression model is fit to the output feature using each of the input features. The complex decision tree models can be easily understood just by visualizing the dataset [8, 9].

4 Results and Discussion

4.1 Process Parameters and Their Relation with Density

The parameters that were taken as input features for the decision tree algorithm are laser power, scan speed, hatching space, energy density, and built rate [10–12]. Each
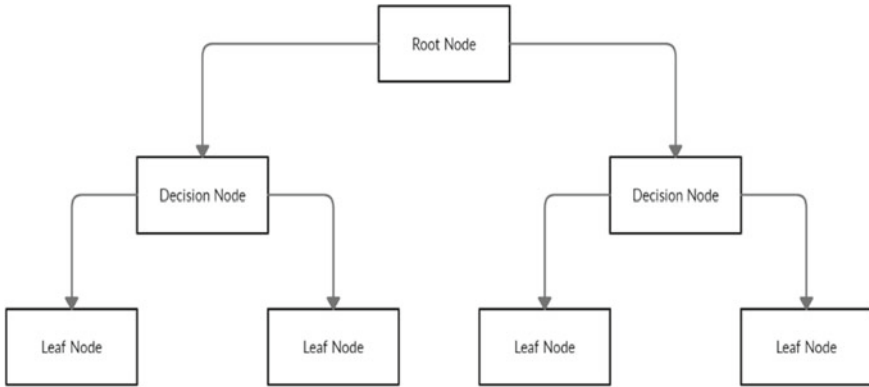
Fig. 3 Decision tree model

parameter has a significant relationship with the density of the manufactured part. The correlation of each parameter with the part density has been shown in Fig. 4.

It was observed that the density of the part increases with increasing laser power. The energy density is a function of power, scan speed, and layer thickness. The energy density increases with increasing power and decreases with an increase in scan speed, hatching space, and layer thickness. On the other hand, the build rate depends on power, scan speed, and layer thickness. Variation of the part density with processing parameters has been shown in Fig. 5.

It was observed that when scan speed increases beyond 2 m/s, the density of manufactured part decreases. When the hatching space increases above 0.3 mm, the density of the part decreases. Increase in the power from 225 to 350W increases the density of the fabricated part. The density of manufactured parts increases with variation in the energy density from 60 to 120 J/mm^3. The density of part decreases
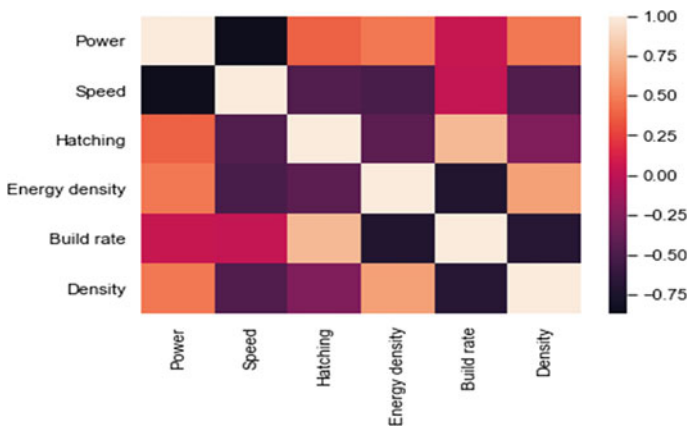
Fig. 4 Correlation chart for input parameters with the part density
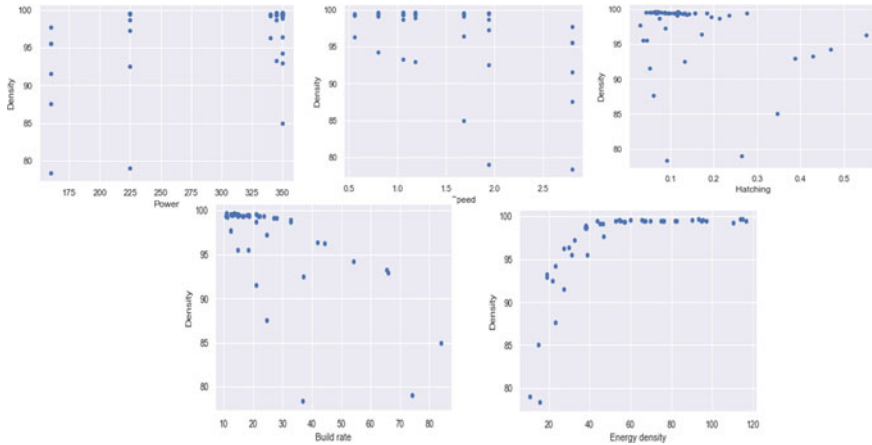
Fig. 5 Relationship between process parameters and density

Table 2 Optimum values of the process parameters

Sl. No	Process parameters	Optimum values
1	Power	225–350 W
2	Scan speed	0.5–2.0 m/s
3	Hatching space	0.5–0.3 mm
4	Energy density	50–120 J/mm^3
5	Build rate	10–20 cm^3/h

with an increase of build rate beyond 30 cm^3/h. The optimum values of the powder bed fusion are mentioned in Table 2.

Figure 6 shows the plots between input features like power, scan speed, hatching, energy density, and output feature which is the part density. It has been observed that the input features are highly correlated with density. Variation in the power (from 250 to 300 W) and scan speed (between 0.5 and 1.5 m/s) improves the density of the fabricated parts. On the other hand, increase in the scan speed above 2 m/s decreases the density. Moreover, while increasing in the hatching beyond 0.3 mm, the density of the part decreases. The higher density was observed when the build rate was in between the range 10 and 20 cm^3/h, and energy density was between the range 50 and 120 J/mm^3.

4.2 Model Testing and Prediction

The model was trained with a 50% dataset, and the remaining 50% data was used for testing. The parameters that were used to calculate model accuracy are R-squared (R^2), adjusted R^2, mean absolute error (MEA), mean square error (MSE), and root
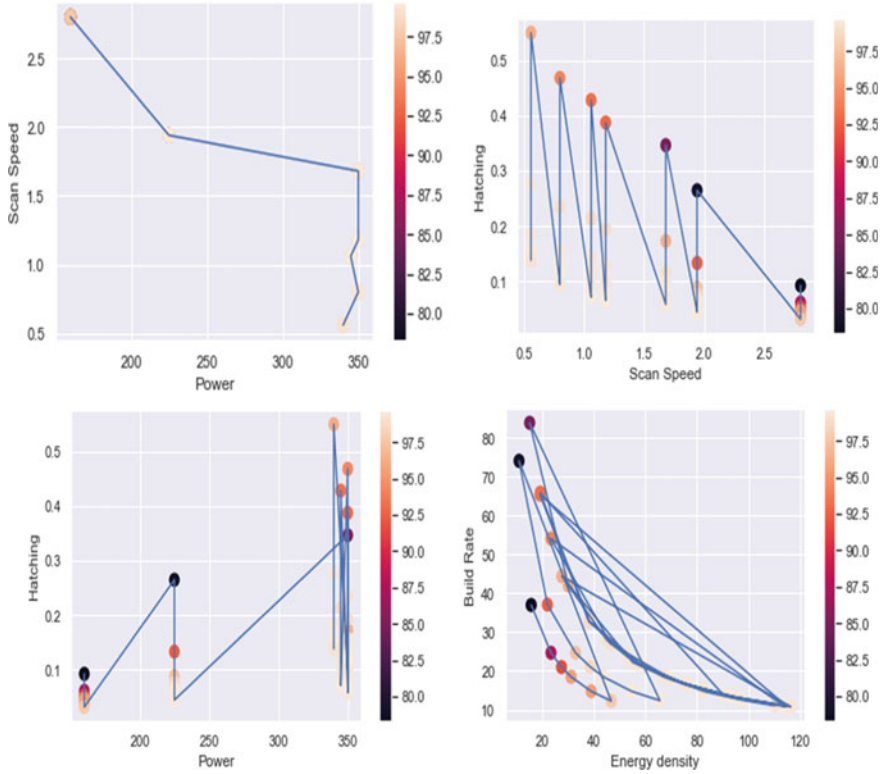
Fig. 6 Relationship between process parameters and density

mean square error (RMSE). RMSE is used for assessing the accuracy of prediction obtained by a model. It measures the differences or residuals between actual and predicted values using

$$\mathbf{RMSE} = \sqrt{\frac{\sum_{i=1}^{N} (x_i - \hat{x}_i)^2}{N}}$$

where N is the total number of observations, x_i is the actual value, whereas $\hat{x}_i$ is the predicted value. The main benefit of using RMSE is that it penalizes large errors. It also scales the scores in the same units as the predicted values. MAE is the simplest measure of prediction accuracy. It provides the absolute value of the difference between the predicted value and the actual value and indicates how big of an error will be from the prediction on average. It is calculated using the formula

$$\mathbf{MAE} = \frac{\sum_{i=1}^{N} |\hat{x}_i - x_i|}{N}$$

Table 3 Statistical analysis

Sl. No.	Dataset (%)	Details of testing				
		R^2	Adj.R^2	MAE	MSE	RMSE
1	50–50	0.75	0.70	0.93	3	1.73
2	60–40	0.80	0.74	0.61	1.34	1.15
3	70–30	0.73	0.62	0.73	2.1	1.45
4	75–25	0.89	0.83	0.45	0.61	0.78
5	80–20	0.88	0.77	0.53	0.73	0.77

MSE is the average squared distance between the actual and the predicted values. It is the measure of the quality of an estimator, and it is always positive. The error decreases as the value approaches zero. It is estimated using the formula

$$\mathbf{MSE} = \frac{\sum_{i=1}^{N}(x_i - \hat{x}_i)^2}{N}$$

R-squared (R^2) measures the proportion of variation of the dependent variable that can be assigned to the independent variable. It provides the goodness of fit and ranges from 0 to 1. It represents the accuracy of the model and is calculated using the formula

$$\mathbf{R}^2 = 1 - \frac{\text{RSS}}{\text{TSS}}$$

where residual sum of square (RSS) is the difference between actual and predicted values, and total sum of square (TSS) differentiates between the average predicted value and the predicted values.

The detailed results of the training and testing datasets are presented in Table 3. An increase in the training size of the dataset increases the R^2 value and approaches the highest at 75–25% train–test split. Further, the overfitting of the model decreased with the increase in the training dataset. The highest accuracy was achieved at 75% training and 25% testing datasets. It is evident from Fig. 7 that the graph between actual and predicted density becomes linear.

5 Conclusion

In the present study, the optimal process parameters for LPBF were identified using the decision tree algorithm by reducing time and cost significantly as compared to other approaches such as modelling and simulation or conducting a large number of experiments. It also enables the prediction of the quality of manufactured parts. A decision tree algorithm was used to build a model with reasonable accuracy of

Fig. 7 Actual versus
predicted density
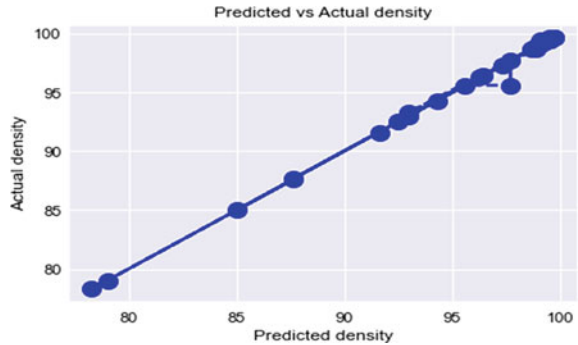
approximately 90%. The relationship between process parameters like laser power,
scan speed, hatching space, energy density, and build rate was identified, and optimal
process parameters for LPBF were obtained for achieving higher density of the
developed parts.

References

1. Baturynska, I., Semeniuta, O., Martinsen, K.: Optimization of process parameters for powder bed fusion additive manufacturing by combination of machine learning and finite element method: a conceptual framework. Proc. CIRP **67**, 227–232 (2018)
2. Brailovski, V., Kalinicheva, V., Letenneur, M., Lukashevich, K., Sheremetyev, V., Prokoshkin, S.: Control of density and grain structure of a laser powder bed-fused superelastic Ti-18Zr-14Nb alloy: simulation-driven process mapping metals **10**(12), 1697 (2020)
3. Zhang, Y., Wu, L., Guo, X., Kane, S., Deng, Y., Jung, Y.-G., Lee, J.-H., Zhang, J.: Additive manufacturing of metallic materials: a review. J. Mater. Eng. Perform. **27**(1), 1–13 (2017)
4. Letenneur, M., Kreitcberg, A., Brailovski, V.: Optimization of laser powder bed fusion processing using a combination of melt pool modeling and design of experiment approaches: density control. J. Manuf. Mater. Process **3**(1), 21 (2019)
5. Dilberoglu, U.M., Gharehpapagh, B., Yaman, U., Dolen, M.: The role of additive manufacturing in the era of industry 4.0. Proc. Manuf. **11**, 545–554 (2017)
6. Wang, C., Tan, X.P., Tor, S.B., Lim, C.S.: Machine learning in additive manufacturing: state-of-the-art and perspectives. Additive Manuf. **36**, 101538 (2020)
7. Pekel, E.: Estimation of soil moisture using decision tree regression. Theoret. Appl. Climatol. **139**(3–4), 1111–1119 (2019)
8. Acharya, R., Sharon, J.A., Staroselsky, A.: Prediction of microstructure in laser powder bed fusion process. Acta Mater. **124**, 360–371 (2017)
9. Ahmed, A., Wahab, M.S., Raus, A.A., Kamarudin, K., Bakhsh, Q., Ali, D.: Effects of selective laser melting parameters on relative density of alsi10mg. Int. J. Eng. Technol. **8**(6), 2552–2557 (2016)
10. Delgado, J., Ciurana, J., Rodríguez, C.A.: Influence of process parameters on part quality and mechanical properties for DMLS and SLM with iron-based materials. Int. J. Adv. Manuf. Technol. **60**(5–8), 601–610. 5 (2011)
11. Gao, W., Zhang, Y., Ramanujan, D., et al.: The status, challenges, and future of additive manufacturing in engineering. Comput. Aided Des. **69**, 65–89 (2015)

12. Gorsse, S., Hutchinson, C., Gouné, M., Banerjee, R.: Additive manufacturing of metals: a brief review of the characteristic microstructures and properties of steels, ti-6al-4v and high-entropy alloys. Sci. Technol. Adv. Mater. **18**, 584–610 (2017)

ANP–MOORA-Based Approach for Selection of FDM 3D Printer Filament

M. Maity (ORCID)**, J. K. Mondal** (ORCID)**, S. Das** (ORCID)**, and S. Das**

1 Introduction

A three-dimensional (3D) printer is now an advanced technology among several technologies. In the field of production, 3D printing is commonly known as additive manufacturing (AM) which is used to create three-dimensional layers by layers from 3D models to rapid prototyping (RP), and it is a different method to a subtractive manufacturing process that includes cutting of three-dimensional objects layer by layer. Nowadays, the manufacturing industry is growing rapidly, and more varieties of FDM 3D printers and filament are available in the market. For this reason, the manufacturer cannot choose the desired quality filament for the right FDM 3D printer within a short time period. The multi-criteria decision analysis process is the only solution to find the best alternative within different product criteria. MCDA is a benchmark-based decision-making analytical process that is classified as an important research infrastructure.

The rapid prototyping process is a developing region in the manufacturing sector to produce products rapidly, accurately. The demand for customization in the global market has multiplied because nowadays the volume production is less than the quantity expected to provide innovative designs to the industry [1, 2], and engineering has become a powerful tool in the field of 3D printing prototyping. According to a report published by Allied Marketing Research, 3D printing is one of the fastest-growing processes in the world today [3]. According to another report published by Gartner [4], the global rate of 3D printers has increased by 75% by 2014 and will double every year. Hideo Kodama of the Noyoga Municipal Industrial Research Institute

M. Maity (✉) · J. K. Mondal
Department of Mechanical Engineering, Swami Vivekananda University, Kolkata 700121, India
e-mail: mriganka141998maity@gmail.com

S. Das · S. Das
Department of Mechanical Engineering, Swami Vivekananda Institute of Science and Technology, Kolkata 700145, India

is mostly believed to have printed the first solid objects from CAD design [5]. The technology has evolved since 1984 when Charles W. Hull of 3D Systems Corporation first conceived and realized 3D printers, and these processes have become more usable, as they have become less cost-effective and more affordable [6].

In today's competitive industrial situation, it is important to build a consistent and long-term relationship between customers and manufacturers. For this reason, multiple-criteria decision-making (MCDM) supports decision-makers with a wide range of solutions to complex problems with multiple and consistent criteria. MCDM is usually a decision based on the presence of multiple and contradictory criteria. It may have different units of measurement in different scales, quality properties, and relative weight [7]. It is possible that some criteria can be measured numerically and other criteria can only be described thematically. Multi-criterion decision-making (MCDM) or multi-criterion decision analysis (MCDA) is usually a sub-discipline of operational research that evaluates different types of criteria for explicit decision-making. When the stakes are high, it is important to create the problem correctly and clearly evaluate several criteria [8].

In this research work, we are choosing analytical network process and multi-objective optimization by ratio analysis procedures for selecting FDM 3D printer filament in the market. A large number of scholars have chosen the ANP–MOORA method for solving simple or complex problems in different areas and have generally used the ANP–MOORA method for solving a variety of problems [9, 10].

2 Methodology

2.1 Overview of MCDA/MCDM

Multi-criterion decision-making (MCDM) or multi-criterion decision analysis (MCDA) is usually a sub-discipline of operational research that evaluates different types of criteria for explicit decision-making in both everyday use and business settings, such as medicine and car. MCDM uses a variety of methods in the literature, such as analytic hierarchy process, analytic network process, inner product of vectors, best worst method, choosing by advantages, evaluation based on distance from average solution, dominance-based rough set approach, evidential reasoning approach, goal programming, gray relational analysis, simple multi-attribute rating technique, multi-attribute global inference of quality, multi-objective optimization by ratio analysis, non-structural fuzzy decision support system, stochastic multi-criteria acceptability analysis, and technique for the order of prioritization by similarity to ideal solution. Although the literature mentions a variety of MCDM strategies that can be used to help decision-makers make better judgments, in all of these methods, the ranking of options is determined by the weight of the criteria. However, some of these methods are very complex to understand and apply because they require a
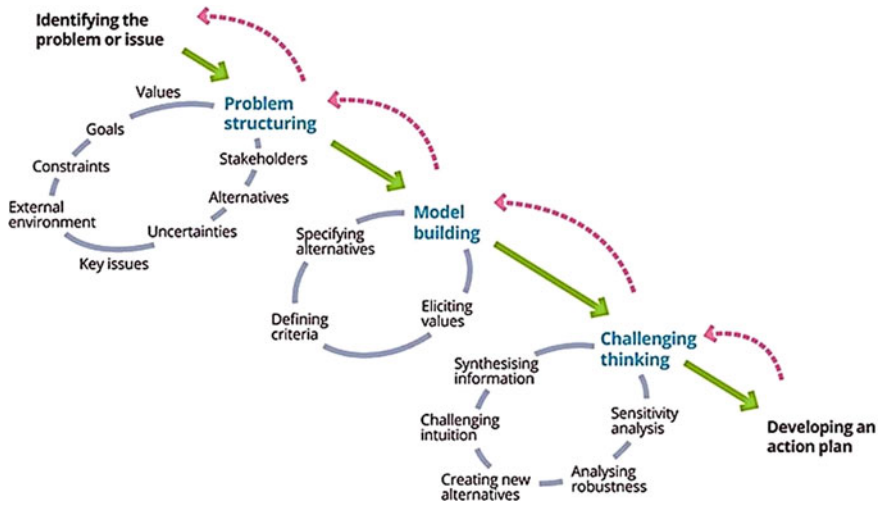
Fig. 1 Overview of MCDA workflow

great deal of mathematical knowledge. All the steps of the ANP–MOORA method are given below. Figure 1 provides an overview of the MCDA workflow.

2.2 Overview of ANP Method

Many decision-making problems cannot be solved immediately because they involve the dependence of the higher-level elements of a sequence on the lower-level elements. In this case, the ANP allows for a complex interrelationship between the decision and the features. The ANP system consists of four basic steps. Figure 2 exhibits the stepwise procedure for performing the ANP method.

2.3 Overview of MOORA Method

Multi-objective optimization or programming, also known as multi-criteria or multi-attribute optimization, is the process of optimizing two or more conflicting objectives simultaneously, subject to certain limiting features. The MOORA method was first introduced in 2009 by Brauers and Zavadskas as a multi-purpose optimization strategy to solve a variety of complex problems in the production environment. The MOORA method begins with a decision matrix that succeeds in showing different types of performance depending on different characteristics:

Step 1: The first step in the MOORA approach is to create a problem-solving matrix. The criteria and alternatives are listed in columns and rows of the decision

Step-1: Model construction and problem structuring
The problem should be stated clearly and decomposed into a rational system like a network.

Step-2: Pairwise comparisons and priority vectors
In ANP, like AHP, pairs of decision elements at each cluster are compared with respect to their importance toward their control criteria. In addition, interdependencies among criteria of a cluster must also be examined pairwise; the influence of each element on other elements can be represented by an eigenvector. The relative importance values are determined with Saaty's scale.
The problem should be stated clearly and decomposed into a rational system like a network.

Step-3: Supermatrix formation
the supermatrix concept is similar to the Markov chain process. To obtain global priorities in a system with interdependent influences, the local priority vectors are entered in the appropriate columns of a matrix. As a result, a supermatrix is actually a partitioned matrix, where each matrix segment represents a relationship between two clusters in a system.

Step-4: Synthesis of the criteria and alternatives' priorities and selection of the best alternative.

Fig. 2 Stepwise procedure for performing ANP method

matrix, respectively. The decision matrix shows the work of different alternatives subject to different criteria.

Here, x_{ij} is the performance value of ith number of alternatives on jth number of criteria, and m and n are the numbers of alternatives and criteria, correspondingly.

$$X = [x_{ij}]_{m \times n} = \begin{bmatrix} X_{11} & X_{12} & \dots & X_n \\ X_{21} & X_{22} & \dots & X_{2n} \\ \vdots & \vdots & \ddots & \vdots \\ X_{m1} & X_{m2} & \dots & X_{mn} \end{bmatrix} \tag{1}$$

Step 2: The performance of an alternative to a standard is calculated against the performance of other alternatives to that standard:
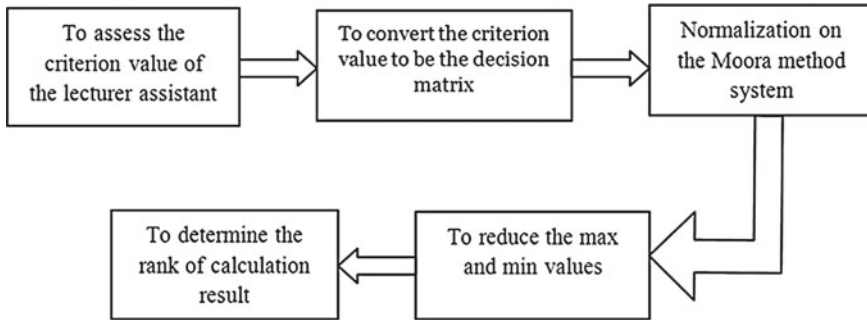
Fig. 3 Block diagram of MOORA technique

$$x_{ij}^* = \frac{x_{ij}}{\sqrt{\sum_{i=1}^{m} x_{ij}^2}} \quad i = 1, 2, \ldots, m \quad \text{and} \quad j = 1, 2, \ldots, n \tag{2}$$

where x_{ij}^* is a dimensionless number between [0, 1] and the normalized performance of ith number of alternatives on jth number of criteria.

Step 3: For multi-objective optimization, these normalized performances are added in the case of beneficial attributes and subtracted in the case of non-beneficial attributes. Then, the optimization problem is

$$Y_i = \sum_{j=1}^{g} X_{ij}^* - \sum_{j=g+1}^{n} X_{ij}^* \tag{3}$$

Step 4: The Y_i value can be positive or negative dependent on the totals of its beneficial attributes and non-beneficial attributes in the decision matrix. A general ranking of Y_i shows the final choice. Thus, the best option has the highest Y_i value, while the worst option has the lowest Y_i value. Figure 3 shows that the block diagram of the MOORA method.

3 Result and Discussion

Figure 4 shows the first level of the hierarchy for the choice of a good FDM 3D printer filament. The second level of the hierarchy is formed by the criteria used for the purchase. In this research work, the selecting five criteria are density (g/cm^3), printing temperature (0C), elongation at break (%), tensile strength (MPa), and flexural strength (MPa) for choosing a good FDM 3D printer filament. The third level is made up of the necessary options among the various filaments available in the market. In this research work, selecting six alternatives are shown in Table 1.
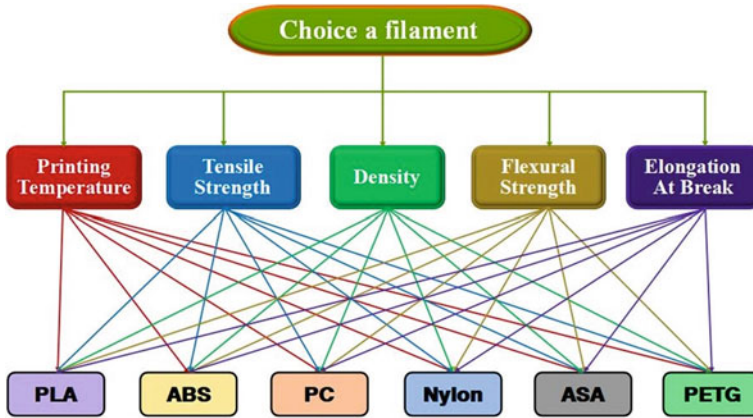
Fig. 4 Decision hierarchy for choice a good FDM 3D printer filament

Table 1 Selective different types of alternatives

Sl. No.	Name of the filament
01	Polylactic acid (PLA)
02	Acrylonitrile butadiene styrene (ABS)
03	Polycarbonate (PC)
04	Nylon
05	Acrylonitrile styrene acrylate (ASA)
06	Polyethylene terephthalate glycol (PETG)

Criteria required for the process of multi-objective optimization based on the ratio analysis that influences their calculation options. Selective different types of alternatives and their various criteria can be seen in Table 2 and Fig. 5 shows that selected different alternatives and their various criteria data chart in this research work.

Table 2 Selective different types of alternatives and their various criteria

Criteria	Criteria name	Alternative	Alternative name
C1	Density	A1	Polylactic acid (PLA)
C2	Printing temperature	A2	Acrylonitrile butadiene styrene (ABS)
C3	Tensile strength	A3	Polycarbonate (PC)
C4	Elongation at break	A4	Nylon
C5	Flexural strength	A5	Acrylonitrile styrene acrylate (ASA)
		A6	Polyethylene terephthalate glycol (PETG)

	A1	A2	A3	A4	A5	A6
■C1	1.24	1.04	1.2	1.14	1.07	1.23
■C2	230	250	285	260	260	250
■C3	64.4	46.4	62.7	40.2	50.5	50
■C4	4	75	12.4	4	40	25
■C5	94.7	65	100.4	67	78.6	77
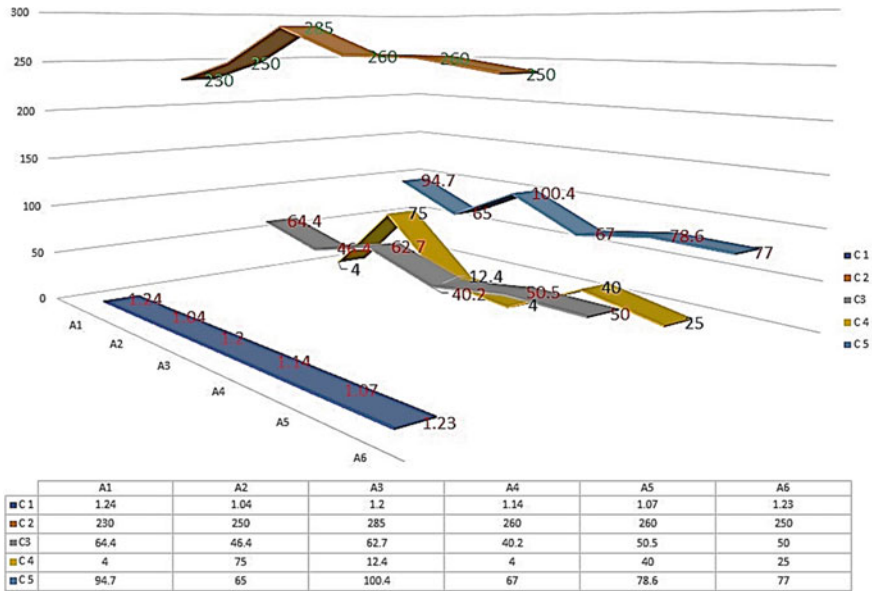
Fig. 5 Different types of alternatives and their various criteria data chart

3.1 Calculation of ANP Method

The first step in AHP analysis is to create a hierarchy for decision-making. It is also called decision modeling and is used only to create a hierarchy to analyze the choice.

Step 1: Model construction and problem constructing**:** This is called intensity judgment or simply judgment in each of the comparative pairs to reflect the relative preference. It is considered that C1 is more strongly important than C2; C1-C2 comparison cell (i.e., the intersection of row 'C2' and column 'C1'). Mathematically, this means that the ratio of the importance of C1 to the importance of C2 is two.

For this reason, inverse comparisons, the importance of C1 with the importance of C1, the comparison of Table 3, as shown in cell C1-C2 in the matrix, gives the result of the relative value of 1/2 of this value. The approximation method requires normalization of the comparison matrix; that is, values must be added to each column shown in Table 4.

Step 2: Pairwise comparisons and priority vectors: But, keep in mind that this method offers a valid estimate of the overall weight only when very few variations in the comparison matrix are observed. Then divide each cell by the total of the columns shown in Table 5. From this normal matrix, only the average value of each row has to be calculated as shown in Table 6.

Step 3: Supermatrix creation**:** The concept of the supermatrix is similar to the Markov chain process. To get a global priority in a system with interdependent effects, the priority vectors are inserted into the appropriate column of a matrix

Table 3 Pair-based comparison matrix with intensity finding

	C1	C2	C3	C4	C5
C1	1	1/2	1/3	1/4	1/3
C2	2	1	1/2	1/3	2
C3	3	2	1	1/4	1/3
C4	4	3	4	1	2
C5	3	1/2	3	1/2	1

Table 4 Column adding matrix

	C1	C2	C3	C4	C5
C1	1	0.5	0.333	0.25	0.333
C2	2	1	0.5	0.333	2
C3	3	2	1	0.25	0.333
C4	4	3	4	1	2
C5	3	0.5	3	0.5	1
SUM	13	7	8.833	2.333	5.666

Table 5 Normalized matrix

	C1	C2	C3	C4	C5
C1	0.077	0.071	0.038	0.107	0.059
C2	0.154	0.143	0.057	0.143	0.353
C3	0.231	0.286	0.113	0.107	0.059
C4	0.308	0.429	0.453	0.429	0.353
C5	0.231	0.071	0.340	0.214	0.176

Table 6 Calculation of priorities weight

	C1	C2	C3	C4	C5	Weight
C1	0.077	0.071	0.038	0.107	0.059	0.070
C2	0.154	0.143	0.057	0.143	0.353	0.170
C3	0.231	0.286	0.113	0.107	0.059	0.159
C4	0.308	0.429	0.453	0.429	0.353	0.394
C5	0.231	0.071	0.340	0.214	0.176	0.207

shown in Table 7. The result is a supermatrix commonly known as a split matrix, where each matrix segment represents the relationship of two clusters in a system. The supermatrix is a fragment-based on factors and sub-factors. The corresponding results are shown in Table 8. Weighted supermatrix drives a supermatrix multiplied by the collection weight.

Table 7 Arrangement of results: unique judgments and priorities

	C1	C2	C3	C4	C5	Weight
C1	1	0.5	0.333	0.25	0.333	0.070
C2	2	1	0.5	0.333	2	0.170
C3	3	2	1	0.25	0.333	0.159
C4	4	3	4	1	2	0.394
C5	3	0.5	3	0.5	1	0.207

Table 8 Design of supermatrix

	Value of supermatrix	Rank
C1	0.375	5
C2	0.935	3
C3	0.876	4
C4	2.234	1
C5	1.159	2

3.2 Result and Discussion of ANP Method

In this research work, ANP method is used to get the average value of supermatrix and put this value for plotting graph between supermatrix and criteria as publicized in Fig. 6. The bar graph illustrations that C4 is preferable then C1, C2, C3, and C5, so C5 is the most important criteria in this research work.

From the Fig. 7, it is clearly shown that the final result. From the result, A2 is ranked as best and appropriate alternative which has extremely good % of elongation at break (C4) then A1, A3, A4, A5, and A6.
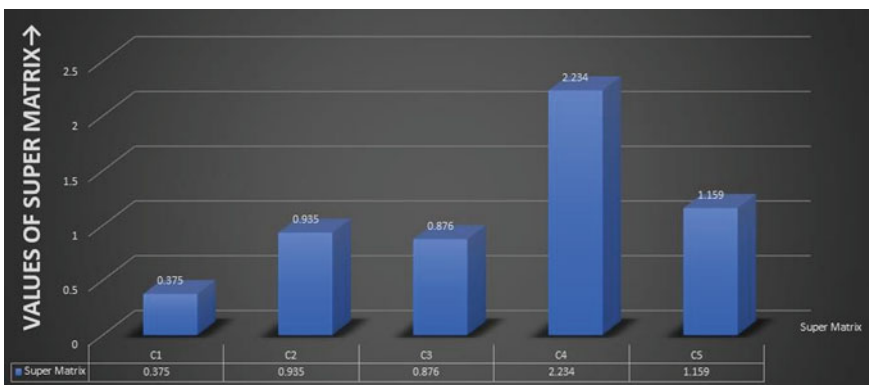
Fig. 6 Criteria versus supermatrix bar chart for ANP method
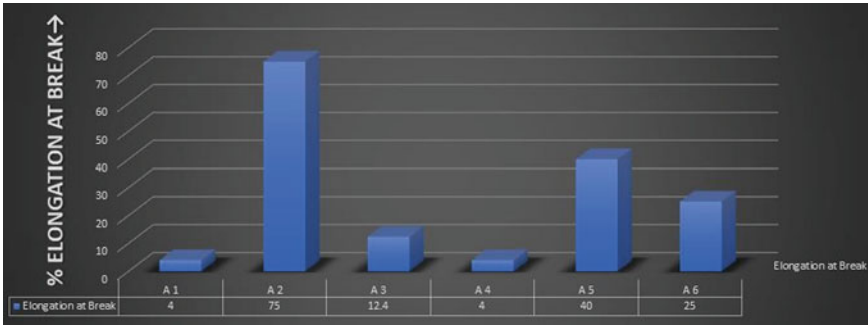
Fig. 7 % of elongation at break versus alternatives bar chart for ANP method

3.3 Calculation of MOORA Method

Multi-objective optimization through ratio analysis is the most imperative selection technique strategy for this problem. In this research work, MOORA method is used to compare the ANP method and verify the result of the ANP method. Table 9 shows that selected different alternatives and their various criteria in this research work.

Step 1: The strategy of the decision matrix: The first and foremost step in the TOPSIS algorithm is to create a decision matrix that determines the weight of a criterion. In this case, relative weights are determined quantitatively and qualitatively not only on the basis of each criterion but also on their importance. Since defining the weight of a criterion is a main step in the decision-making process, in this case, a high degree of accuracy is important for defining the weight for each criterion and value.

Step 2: Normalized decision matrix: The normalized value is determined by the normalized decision matrix, which represents the relative performance of the alternatives created. Typically, MCDM problems have both a benefit attribute and a cost feature. From equation-1, calculating the value X_{ij} is shown in Tables 10 and 11 shows the construct normalized decision matrix in this research work.

Step 3: All selection criteria may or may not be of equal importance, and so the introduction of weights from the MOORA strategy has been suggested to measure the

Table 9 Different alternatives and their various criteria

	C1	C2	C3	C4	C5
A1	1.24	230	64.4	4	94.7
A2	1.04	250	46.4	75	65
A3	1.20	285	62.7	12.4	100.4
A4	1.14	260	40.2	4	67
A5	1.07	260	50.5	40	78.6
A6	1.23	250	50	25	77

Table 10 Establish the decision matrix

	C1	C2	C3	C4	C5
A1	1.24	230	64.4	4	94.7
A2	1.04	250	46.4	75	65
A3	1.20	285	62.7	12.4	100.4
A4	1.14	260	40.2	4	67
A5	1.07	260	50.5	40	78.6
A6	1.23	250	50	25	77
$\sqrt{\sum_{i=1}^{m} X_{ij}^2}$	2.83136	627.953	129.9919	89.6424	199.67276

Table 11 Determine a normalized decision matrix

	C1	C2	C3	C4	C5
A1	0.438	0.366	0.495	0.045	0.074
A2	0.367	0.398	0.357	0.837	0.326
A3	0.424	0.454	0.482	0.138	0.503
A4	0.403	0.414	0.309	0.045	0.336
A5	0.378	0.414	0.388	0.446	0.394
A6	0.434	0.398	0385	0.279	0.386

relative importance of different selection criteria. The weight determination decision matrix is made by multiplying the table of each element in each column of the generalized decision matrix by the random weights shown in Tables 12, and 13 shows the weighted normal decision matrix of this research work (Table 14).

Step 4: Estimation of assessment values (Y_i): The Y_i value can be positive or negative depending on the sum of its beneficial properties and non-beneficial properties in the decision matrix.

A general ranking of Yi is shown in the final. Thus, the highest Yi value of the best option is determined, while the lowest Yi value is shown in Table 11.

Table 12 Determine a weighted matrix

	C1	C2	C3	C4	C5
A1	0.438	0.366	0.495	0.045	0.074
A2	0.367	0.398	0.357	0.837	0.326
A3	0.424	0.454	0.482	0.138	0.503
A4	0.403	0.414	0.309	0.045	0.336
A5	0.378	0.414	0.388	0.446	0.394
A6	0.434	0.398	0385	0.279	0.386
Weight	0.2	0.2	0.2	0.2	0.2

Table 13 Determine a weighted normalized choice matrix

	C1	C2	C3	C4	C5
A1	0.088	0.073	0.099	0.009	0.095
A2	0.073	0.080	0.071	0.167	0.065
A3	0.085	0.091	0.096	0.028	0.101
A4	0.081	0.083	0.062	0.009	0.067
A5	0.076	0.083	0.078	0.089	0.079
A6	0.087	0.080	0.077	0.056	0.077

Table 14 Calculate the performance value

	Yi
A1	0.364
A2	0.457
A3	0.400
A4	0.301
A5	0.404
A6	0.376

3.4 Result and Discussion of MOORA Method

In this research work, MOORA method is used to get the relative closeness value and put this value is plotting between % of elongation at break versus alternatives shown in Fig. 8. From the Fig. 8, it is shown that % of elongation at break is the major and best criteria and plotting the graph between % of elongation at break versus criteria. From this graph, it is shown that the result that A2 is ranked as best and appropriate alternative which has extremely good % of elongation at break than A1, A3, A4, A5, and A6.

3.5 Comparison of ANP and MOORA Results

In this research work, applying ANP and MOORA technique for selecting an FDM 3D printer filament with a high % of elongation at break. Table 15 shows the comparison between ANP and MOORA methods. From this table, it is shown that the result that A2 is ranked as best and appropriate alternative which has extremely good % of elongation at break than A1, A3, A4, A5, and A6.
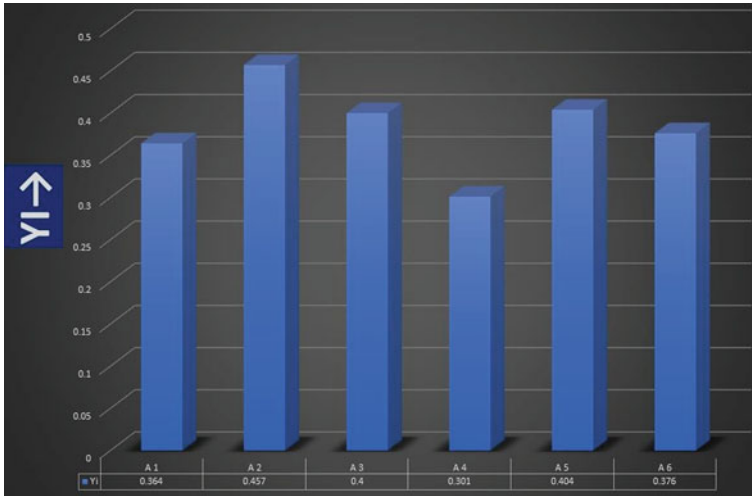
Fig. 8 % of elongation at break versus alternatives bar chart for MOORA method

Table 15 Comparison between ANP and MOORA results

Rank	ANP method (% of elongation at break)	MOORA method (% of elongation at break)
1	A2	A2
2	A5	A5
3	A6	A3
4	A3	A6
5	A1	A1
6	A4	A4

4 Conclusions

This research work provides a multi-criteria decision analysis and solves a selection problem of different models of a car based on the ANP and MOORA methods. As the number of options and their selection criteria increases, so does the complexity of choosing them. To solve this problem, ANP–MOORA methods are chosen to solve supply chain problems so that the best option can be selected from a variety of options. It is therefore believed that the use of the MCDM method is unparalleled in the decision-making of an ANP-based structure and in the development and selection of the best supply chain. The problems and sub-issues mentioned in this study will help decision-makers to analyze them by visualizing the impact on different types of supply chains. There may be some inconsistencies in the ranking of options due to the different opinions of the decision-makers so the weight of the issues may vary depending on the method used and the dependence or interdependence of the issues. The results obtained from this study will help to select an FDM 3D printer filament

with high % elongation during the break. The application of the ANP–MOORA approach to an extensive variety of problems in the choice of dissimilar types of supply chains will guide upcoming research work.

From the calculations, it is proved that acrylonitrile butadiene styrene (ABS) is ranked as best and appropriate alternative which has extremely good % of elongation at break than polylactic acid, nylon, polyethylene terephthalate glycol, acrylonitrile styrene acrylate, and polycarbonate. Thus, it is clear that existing research work on multi-criteria decision analysis is the only solution to find the best option within different product criteria. And the ANP and MOORA method are a very much efficient technique for alternative selection under multiple criteria.

References

1. Wang, X., Jiang, M., Zhou, Z., Gou, J., Hui, D.: 3d printing of polymer matrix composites: a review and prospective. Compos. B Eng. **110**, 442–458 (2017)
2. Zeltmann, S.E., Gupta, N., Tsoutsos, N.G., Maniatakos, M., Rajendran, J., Karri, R.: Manufacturing and security challenges in 3d printing. Jom **68**(7), 1872–1881 (2016)
3. Person, L.: Global 3d printing market (2019). https://www.alliedmarketresearch.com/3d-printing-market. Feb (2019)
4. Umair, M., Kim, W.S.: An online 3d printing portal for general and medical fields. In: 2015 International conference on computational intelligence and communication networks (CICN). 2015, pp. 278–282. IEEE (2009)
5. Agarwal, G., Vijayvargy, L.: An application of supplier selection in supply chain for modeling of intangibles: a case study of multinational food coffee industry. Afr. J. Bus. Manage. **5**(28), 11505–11520 (2011)
6. Brauers, W.K.M., Zavadskas, E.K.: Robustness of the multi-objective MOORA method with a test for the facilities sector, technological and economic development of economy. Baltic J. Sustain. **15**(2), 352–375 (2009)
7. Brauers, W.K.M., Zavadskas, E.K., Peldschus, F., Turskis, Z.: Multi-objective decision-making for road design. Transport **23**(3), 183–193 (2008)
8. Buyukozkan, G.: An integrated fuzzy multi-criteria group decision-making approach for green supplier evaluation. Int. J. Prod. Res. **50**(4), 2892–2909 (2012)
9. Chung, S., Lee, A.H.I., Pearn, W.L.: Analytic network process (ANP) approach for product mix planning in semiconductor fabricator. Int. J. Prod. Econ. **96**(1), 15–36 (2005)
10. Deng, X.Y., Hu, Y., Deng, Y., Mahadevan, S.: Supplier selection using AHP methodology extended by D numbers. Expert Syst. Appl. **41**(1), 156–167 (2014)

Applications of Laser Beam Welding in Automotive Sector-A Review

A. R. Biswas , **N. Banerjee** , **A. Sen** , **and S. R. Maity**

1 Introduction

Day-by-day automotive industry is adopting laser beam welding widely for various applications such as welding of body structures, door frames, auto hoods, chassis, and trunks [1–3]. It is also used for welding of different sub-components such as airbag initiators, electrical interconnection, motor coil windings, engine parts, transmission components, solenoids, air-conditioning equipment, fuel injectors, fuel filters, and alternators [4–7]. Electrification of motors is a new trend nowadays because of the increased demand for hybrid and electric vehicles. Fabrication of electric motor parts, including stator hairpins and power train connections, is the key requirements. Other additional applications in vehicle electrification are battery welding and connections. Laser beam welding is adopted to make the battery cell and join cells for creating a module. Besides, LBW helps to connect these modules to make a complete battery assembly. It is suited for the connections in the battery pack and electric motor [6–8].

Laser welding is also trending to fasten electronic components within vehicles at present. Laser welding of electronic connections gained a high safety record. These include the increase in vehicle safety equipment namely connecting sensor-based safety equipment and advanced driver-assistance system. Laser beam welding technology is also preferable for fast production lines like fiber lasers having no power degradation and no consumables [9]. Before the introduction of laser beam welding, industrial applications were running using conventional welding processes despite having several disadvantages.

A. R. Biswas (✉) · N. Banerjee · A. Sen
Department of Mechanical Engineering, Calcutta Institute of Technology, Howrah, India
e-mail: arbamit.mech@gmail.com

S. R. Maity
Department of Mechanical Engineering, National Institute of Technology, Tiruchirappalli, India
e-mail: srmaity@mech.nits.ac.in

The first problem with such welding processes is the production of excessive toxic smoke and fumes which is not environment friendly. Again control of heat generated during welding is a big problem for those outdated processes. Welding quality and surface appearance may hamper due to spatter formation; thus, precision in weld dimension is under scanner. In the case of arc welding, high heat generated during operation may affect the grain size; thus, mechanical properties may change. Improper distribution of heat sometimes distorts the product shape. Larger HAZ is also responsible for the failure of the welded joint [10–14].

Laser beam welding eliminates most of the drawbacks of the traditional welding processes and is thus adopted by almost all industries nowadays. It is an environment-friendly process with less generation of fumes and gasses. Heat is pointed on a very narrow zone, which does not affect mechanical properties due to changes in grain size. Laser beam direction and position can be altered using a lens attached to the laser system. The process is suitable for welding pre-machined parts with minimal distortion and restricted heat. Laser welding imparts localized heat with a smaller HAZ, design flexibility, better accessibility, enabling approaches that are impossible with other processes [15, 16]. Different laser technologies have been adopted by the automotive sector, which includes pulsed ND: YAG for small components, blue direct diode lasers, pulsed disk lasers, and fiber lasers [9, 17]. A doping element ytterbium provides good conversion efficiency that matches well with existing laser delivery components. But fiber lasers have overtaken almost all applications in the automotive industry at present. Fiber laser offers ease of use, handling, and longevity. Fibers are economical and relatively cheap draws less electricity compared to YAG or pulsed disk lasers [18].

Researchers untiringly working hard to develop the process more advanced and effective from the application point of view by coupling this with other fabrication processes like gas metal arc welding, gas tungsten arc welding, and plasma arc welding. When laser welding is coupled with any arc welding process, then the system of welding is termed as hybrid laser welding. It improves weld bead pattern along with penetration as seen in Fig. 1. A start of art review has been done by Acherjee [19] about hybrid laser welding. The study indicates that hybridization has several advantages over individual arc welding and laser welding. These benefits are higher speed of welding, increased productivity, deeper penetration, higher process efficiency, better process stability, excellent gap bridging capability, etc. Sebestova et al. [20] have utilized TIG-assisted laser welding to join a 3 mm low-alloy and high-strength thick S460MC steel plate with DC01 to examine the effect of arc current rate on weld cooling rate, microstructure, and mechanical properties. A defect-free fully penetrated joint was the result. Also, it was found that during the increase in welding current, HAZ width increased strongly over FM dimensions. The weld microstructure was formed mainly of fine acicular ferrite and bainite. Casalino et al. [21] fabricated AISI 410 with AISI 304 stainless steel sheets using a fiber laser-assisted TIG welding. The FZ microstructure formed was predominantly martensitic with an increase of micro-hardness of about 350 HV. The crack was initiated near the weld root and distributed along the heat affected zone in the martensitic stainless steel. Song et al. [22] utilized TIG and laser-assisted TIG welding of cast magnesium alloy AZ80

Fig. 1 Weld bead pattern and penetration for **a** arc welding, **b** laser welding, and **c** hybrid laser welding
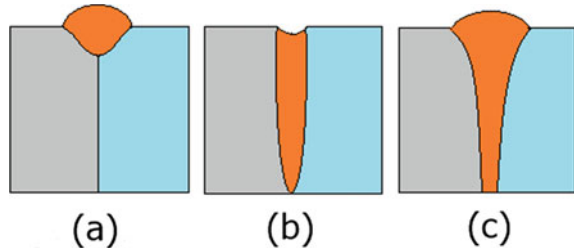
with wrought magnesium alloy AZ31B. Results showed good weld formation with good tensile strength in both welding methods but hybrid welding possessed wider parameters than TIG welding, which makes it more reliable and flexible in industrial applications. Song et al. [23] joined a 1.6 mm AZ31 B sheet of Mg alloy with 1.0 mm Q235 steel using laser-assisted GTAW hybrid butt welding using AZ61 filler metal to determine the effect of welding heat on the interface bonding, morphology, fracture modes, and mechanical properties of the welded joints.

The maximum average tensile load (fracture) of the joints was 3265 Xue et al. [24] used laser-assisted MIG welding-brazing to join 6061-T6 aluminum alloy with 304 stainless steel to study the mechanical properties and microstructure of the welded joint. An excellent joint with good wettability was achieved on both sides of the stainless steel. Scanning electron microscopy, X-ray diffractometry, and energy-dispersive spectroscopy indicated an IMC layer at the 6061-T6/304 interface. Casalino et al. [25] joined DP/AISI316 with TWIP/AISI316 using fiber laser-MAG hybrid welding with austenitic steel filler. The heat affected zone at the TWIP side was austenitic in nature and showed a grain coarsening at the DP side. New martensitic grains were formed near the fusion zone. TWIP/AISI316 showed greater tensile strength than DP/AISI316. Zongtao Zhu et al. [26] butt welded AA6061 aluminum alloy with Ti-6Al-4 V titanium alloy of 3 mm thickness adapting laser-assisted MIG hybrid welding-brazing without a level. Cracks formed with a 0.2 mm laser-arc offset and an insufficient interfacial reaction occurred with the 1.2 mm offset in the lower region of the butt plane.

The present study shows the impact of LBW in the automotive industry, its recent development, its adaptation over traditional fastening processes, various processes of LBW used in the automotive sector, future aspects of the process, and a detailed survey of various applications of LBW in the automotive sector. As the study is strictly focused on automotive applications of LBW, thus it would be helpful for the budding researchers who are planning to work in this research domain in future.
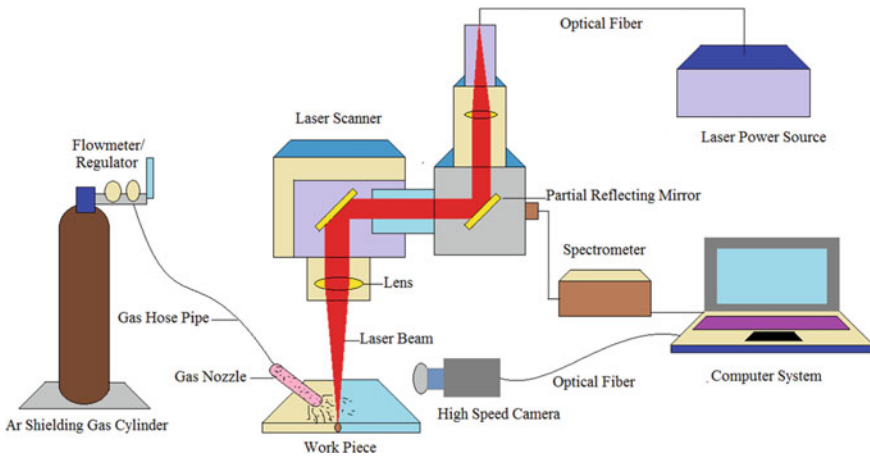
Fig. 2 Block diagram of laser beam welding setup

2 Laser Beam Welding

2.1 Experimental Setup

Figure 2 indicates a block diagram of the laser welding setup. Here, the laser beam can be controlled by the use of a focusing lens. Focal length, focal position, and even beam diameter before striking on the work pieces to be welded can be controlled. The shielding gas with various chemical compositions, flow rate, and density is used to make a defect-free welded joint. Most importantly, a wide range of parameters can be varied or analyzed in this process for a specific desired required output or response. A high-speed camera has been installed to take images and videos during the welding operation. Using a computer system with specific software, the whole system can be monitored and controlled. A spectrometer is installed to measure the property of light such as its wavelength, frequency, and energy.

2.2 Process Parameter

Figure 3 shows a fishbone diagram of laser beam welding parameters and responses. The process parameters of LBW are classified based on laser source and laser processing system. Parameters based on laser source are pulse wave mode, continuous wave mode, pulse frequency, spot size, pulse shape, laser power, etc. Now, parameters based on the laser processing system are welding speed, angle of ray inclination, focus depth, stand-off distance, focal length, focal position, beam diameter, etc. These parameters can be varied as per the requirement for a certain
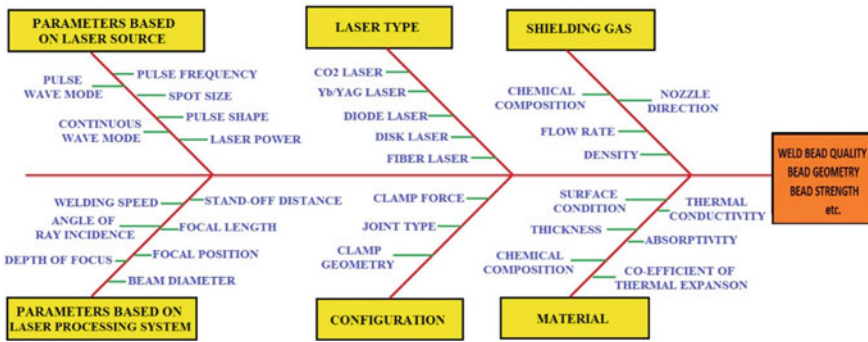
Fig. 3 Fish bone diagram of laser beam welding parameters and responses

response factor. The responses for LBW may be as follows: micro-hardness, residual stress, joint strength, grain size, penetration, etc. Researchers perform parametric optimization using different optimization techniques to see changes in these responses.

2.3 Shielding Gas

Shielding gas is useful in LBW for many purposes such as prevention of oxidation of molten weld pool, protection from atmospheric impurities, and stabilization of weld pool by creating a gaseous envelope. According to requirements, e.g., oxidation prevention capability, cost-effectiveness, penetration needed, plasma suppression, and limitations, shielding gas is selected. Table 1 shows different shielding gasses with specific features for LBW applications [27].

2.4 Types of Materials

LBW is suitable for a wide range of materials except for certain reactive materials, even some materials which are not weldable using conventional welding processes, easily weldable by LBW. It is a versatile process for welding both metals and non-metals. Some metals which are welded by LBM are stainless steel, carbon steels, HSLA steel, aluminum, and titanium [9, 28–31]. However, the high cooling rate is responsible for the problem of cracking during welding of high-carbon steels. Non-metals such as plastics and polymers are also using LBW technology [4, 5]. But at present, a wide variety of composites are laser welded for various applications in all fields of engineering. Before welding operation, certain material conditions must be considered such as surface condition, thickness, absorptivity, chemical composition, thermal conductivity, and coefficient of thermal expansion.

Table 1 Shielding gases used in LBW [27]

Shielding gas	Plasma suppression	Oxidation prevention	Relative cost	Flow rate (liter/min)	Penetration	Limitation
He	Excellent	Good	High	30–40	Deepest	None
Ar	Lower	Excellent	Medium	20–25	Wide	Plasma cloud reduces power density
N_2	Lower	Good	Low	20–25	Deep	Embrittlement of certain alloys (e.g., Ti)
CO_2	Lower	Poor	Lowest	30–45	Nominal	Not useful for reactive materials
Ar 80% He 20%	Good	Very good	Medium	30–35	Nominal	None

3 Applications of LBW in Automotive Sector

There are several applications of laser beam welding in the field of automotive sector which includes multi-thickness welded blanks, car assembly components, body in white applications, and mechanical fastening of different components [1–3, 6, 28]. The automotive applications are divided into a few categories as shown in Fig. 4.

3.1 Tailor Blank Applications

Tailor blanks are used to reduce material consumption and cost. Some applications are inner door panels, floor panels, cross rail bumpers, inner panel tailgates, wheel housings, etc. [1]. For the reduction of car costs and fuel consumption, innovative

Fig. 4 Automotive applications of LBW
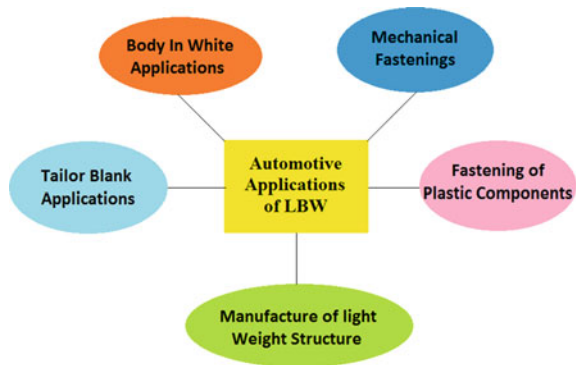
design is the only solution. In this regard, Assunção et al. [2] made a comparative study to show the effectiveness of fiber laser over Nd: YAG and CO_2 laser. According to the study, welding speed was higher in the case of the thicker plate. The study result also showed the failure of the thin section outside the weld and cracks initiated in the case of the thin plate. A study has been made for the development of tailor blank for Nissan automobile company by Shibata [3]. The author addressed various issues of tailor blank application during vehicle production.

3.2 Body in White Applications

Body in white applications is the welding of various components for making final structure such as welding of car roof to the body side. To make a lightweight as well as a good strength car body, laser welding of DC 04 low carbon steel to a 6016 aluminum alloy was done using a fiber laser. Qianqianet et al. [32] showed optimal parameter values such as 0 mm defocusing value, 1400 W laser power, 40 mm/s welding velocity, and 35 L/min shielding gas flow for sound welding performance. High welding power and slow welding speed resulted in the formation of island solute which leads to internal crack formation. Higher weld strength was achieved with shorter Fe-Al reaction time and faster welding speed. A model has been developed by Franciosa et al. [33] for the selection of process parameters to control the volume of the molten weld pool and achieved the gap bridging with the application of remote laser welding of aluminum components. The model reduces the process parameter selection time which leads to a reduction of the number of physical experiments. The author suggested further development of the model by investigating the effect of welding speed on weld quality loop. Using remote laser welding, joining of selective laser melting (SLM) steels (made of 316L and 18-Ni 300) with conventional cold-rolled steels has been done for automotive application by Fieger et al. [34]. The result showed that the combination of boron steel and maraging steel should be considered only when 22MnB5 was on the top to ensure a high-quality assembly. A study has been done by Ribolla et al. [17] on laser beam welding of steel roof and side panels for an automobile body. For large-scale production of the car body, a continuous 4 KW power was ideal.

Steels have a property like high strength which is desirable for a car not only for the body but also for the main structure. Agarwal et al. [35] welded advanced high-strength automotive steel for automotive application to study solidification cracking. The result indicated the transverse strain near the fusion boundary to predict the cracking behavior as shown in Fig. 5. With the decrease in heat input, susceptibility to solidification cracking decreased. Both for the passengers' safety and fuel consumption, high-strength and low-alloy steel HC340LA, dual-phase steel HCT600X, and multi-phase austenitic steel RAK40/70 were laser welded by Evin et al. [36] for making car structures. The high-quality joint is produced with high strength without porosity.
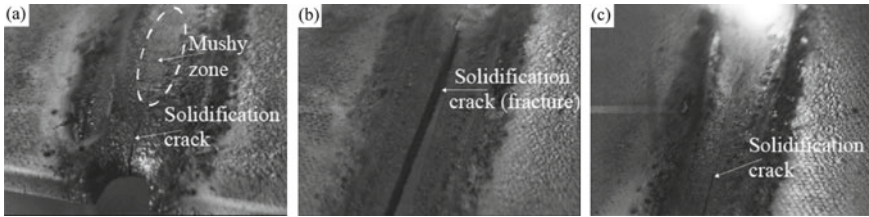
Fig. 5 High-speed camera images showing solidification cracking during welding. **a** solidification crack initiating at the trailing edge of the mushy zone (5 mm); **b** full fracture observed (5 mm); **c** the solidification crack ceases propagating beyond (7 mm) [35]

The result also indicated the highest work hardening for multi-phase steel RAK40/70 because of the formation of austenite to martensite structure as shown in Fig. 6. For the same purpose, a dual-phase advanced high-strength steel (DP600) was welded by Fernandes et al. [15] using laser welding. The hardness at the weld zone HAZ dropped significantly after the heat treatment. Due to the automotive applications, 304 L steel and carbon steel st37 of 1.4 mm thickness were welded by Kumar et al. [37] in butt-joint configuration.

At the fusion zone, coarse recrystallized grains were found. The change of heat affected zone width was negligible in austenitic stainless steel and in case of st37 decreased with an increase in pulse width. Passengers' safety is the priority for car manufacturers; thus, they promote researches to gain a new domain of knowledge. For making a strong and safe car structure, a high-strength galvanized steel sheet was joined by Mei et al. [38] using laser welding. The high-quality joint was made without porosity and cracks.

The hardness was achieved due to high welding speed and recrystallized fine grain structure. Laser welding has been performed on DP980 dual-phase and high-strength and low-alloy steels by Westerbaan et al. [9] for automotive applications.

Fig. 6 Fusion zone microstructure of laser welded steel HC34OLA-HC34OLA [36]
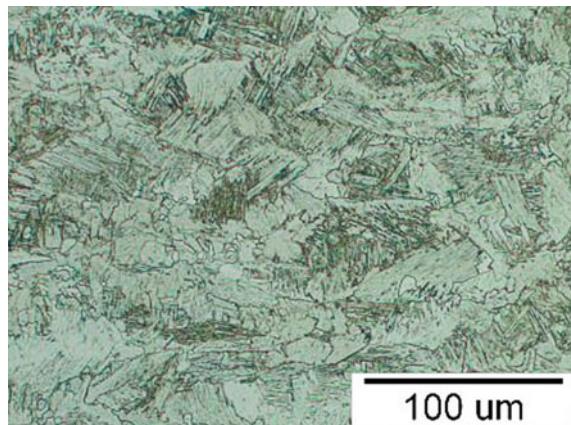
The weld concavity of DP980 and HSLA steels was due to reduced power and increased welding speed. The result indicated higher concavity while reduction of tensile strength of the DP980 welds without affecting the HSLA welds.

3.3 Manufacture of Lightweight Structure

As the price of fossil fuel is increasing day-by-day so it is essential for car manufacturers to cut down the overall weight of the car to reduce fuel draining. The most popular combination of materials for this purpose is steel and aluminum. Steel possesses high strength, and aluminum is corrosion resistant with lightweight. A 1.5 mm thick aluminum 5182 sheet and a 590DP steel sheet with Zn coating were remote laser welded by Kotadia et al. [28] to form a lightweight structure. The research pointed out that for a thin sheet dissimilar welding keyhole formation was undesirable due to uncontrolled mixing in the weld pool, formation of porosity, and defects. Due to their lightweight, aluminum and its alloys are trending in the automotive sector for the lightweight vehicle. Using laser welding, 5754 (AlMg3) alloys were fabricated by Çevik et al. [29], and the experiment showed that tensile strength was unaffected by welding speed. Another experiment was done by AlShaer et al. [39] to weld AC-170PX (AA6014) aluminum for lightweight automobile vehicles. The study showed that the filler with higher Mn and Mg content leads to a significant decrease in porosity compared to 80% porosity with the silicon rich wire. A 6 mm thick AA5754 aluminum alloy sheet was welded by Casalino et al. [40] in butt welding configuration with varied speed and shielding gas to get a high-quality weld bead. An ANN optimization technique was adapted to establish the relationship between process parameters and bead characteristics.

To have a lightweight automobile structure, Al alloy and Zn coated steel were welded by Chen et al. [41] adapting laser welding. The experimental result showed that nitrogen acted as the shielding gas. The corrosion resistance and the surface finish could be improved during double pass welding with argon as the shielding gas. Another investigation was done by Kim et al. [42] to have a lightweight car body by welding of aluminum (AA5182) alloy with AA5356 filler wire. The authors found optimal welding conditions with laser power of 4 Kw, filler wire feed rate of 2.7 m/min, and welding speed of 7.95 m/min. For manufacturing car body, zinc-coated steel sheets with aluminum sheets have been joined by Liedl et al. [43] in a butt-joint as well as in a lap joint configuration. The experimental results indicated that the laser welding of aluminum and steel samples produced narrow and well-defined IMPs with 10 μm thicknesses. Lap joint as well as butt-joint weld configurations showed good reproducibility.

Laser welding was adopted by Long et al. [44] to join 6016 aluminum alloy to DC04 steel with pre-placed metal powders in a lap joint configuration to reduce the weight of the car structure. The combined Taguchi-response surface method optimized process parameters for good quality weld as shown in Fig. 7 as 30 mm/s welding speed, 1344.73 W laser power, defocus distance −2 mm, and shielding gas

flow rate of 30 L/min. For the same purpose, AA5182 aluminum alloy with AA5356 filler wire was welded by Park et al. [45] with wire feed rate, laser power, and welding speed as control parameters. A genetic algorithm tool was used for parametric optimization which showed optimal process variables as 2.3871 m/min wire feed rate, 4 kW laser power, and 8.4762 m/min welding speed. Aluminum welding is challenging because of pore formation which weakens the joint. An investigation was done by Pastor et al. [46] to weld 5182 and 5754 automotive aluminum alloys using Nd: YAG laser welding. The researchers concluded that an unstable keyhole was responsible for pore formation in an aluminum structure.

Even Mg alloy in combination with Al alloy can create a lightweight car body but is tough to weld because of brittle intermetallic phases. Laser welding of Mg alloy to Al alloy has been done by Scherm et al. [30] using ZnAl as filler material which showed that strength was affected by Al content of filler. Due to lightweight and good mechanical properties, Mg alloys are also adopted by car manufacturers. Abderrazaka et al. [31] determined the bead width and the penetration depth as a function of both the welding speed and the incident laser power.
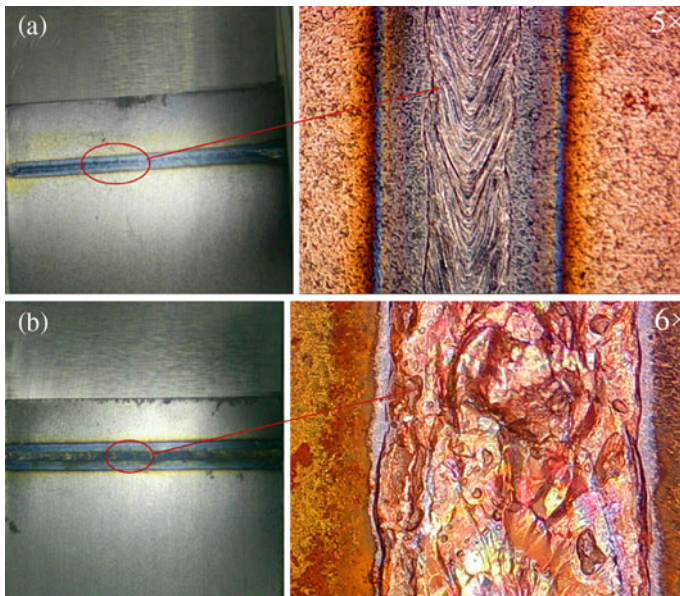
Fig. 7 **a** Bead appearance of aluminum alloy to steel with metal powder and **b** without metal powder [44]

3.4 Fastening of Plastic Components

The use of molded plastics has been adopted by the automotive industry for different car components. Most of them are simple components such as headlights and taillights [4]. But for welding of complex geometrical shapes, laser welding is suitable over traditional welding processes. Another popular application of laser beam welding is car keys [5]. Other applications are sensor housings, under hood components, instrument panels, etc.

3.5 Mechanical Fastenings

For the manufacturing of distributed windings of electrical drives with high-power density for battery-operated electric vehicles, an element called hairpins is assembled by the use of the laser to the stator lamination and contacted afterward to produce the winding [6]. Aluminum alloys such as AA6060-T6, AA6063-T6, and AA6008-T7 have been used for the construction of the battery tray. Sun et al. [7] used filet lap joint coupled with power modulation and beam oscillation to avoid centerline cracks. For making a low resistance battery module connection, aluminum Al 99.5 and copper Cu-ETP were laser welded by Hollatz et al. [8]. For aluminum on top of the copper, the oscillation leads to a wider connection width. Due to the growing demand for electric vehicles, lithium-ion battery cells are being increasingly used as energy storage devices. Fabrication of CuSn6 sheet with a battery, which consists of nickel-plated DC04 steel in an overlapping welding configuration were done by Mehlmann et al. [47]. The copper sheet was effectively connected with the steel sheet of the battery by the laser beam micro-welding. During laser welding of copper, small spot size along with keyhole welding leads to a small contact area between the two joining components which has been rectified using additional parameters such as amplitude and oscillation frequency, in conjunction with spatial power modulation. Haeusler et al. [48] showed that the maximum penetration depth decreased while using higher oscillation amplitudes compared to a conventional laser weld. The reduction of the surface roughness was indicated a more stable behavior of the weld pool and the solidification. No spattering was detected during the process with the use of spatial power modulation. A 99.5% aluminum ribbon (Al H11) with a cross-section of 300 $\times$ 2000 μm^2 was welded by Helm et al. [49] with a 2 mm AlMgSi1 plate designed to minimize the contact resistance of the connection area. The metallographic study showed a correlation between the width of the connecting zone and the number of lines. The batteries having limited terminal thickness would not be penetrated during welding to avoid damage to the cell.

The investigation of the influence of spatial power modulation on the weld seam geometry and intermetallic mixing of copper and aluminum was done by Hollatz et al. [50]. Stainless steel was selected to study the behavior and the stability of developed data processing strategy and the resulting depth values. Low melting

point and high thermal conductivity of copper make poor weld which leads to low-energy utilization. A 1064 nm wavelength Nd: YAG laser to improve weld efficiency and welding quality was proposed by Maina et al. [51] for good surface quality and deep penetration enhancing absorption rate. The study showed good surface quality and deep penetration achieved for transitional processing conditions between keyhole and heat conduction welding with enhanced rate of absorption. For safety, it is important to seal the battery can as many failures occurred in recent years. The weld area of aluminum and copper was investigated by Mian et al. [16] via SEM and energy-dispersive spectroscope to understand the microstructural and physical characteristics. The scanning speed did not affect heat affected zone as the samples were observed from the aluminum side as the laser power and spot size were same for both of the scanning speeds.

For joining of pressure sensors and battery cells, the small processing time is economical; thus, thin metal sheets like nickel, stainless steel, titanium, and aluminum of thickness below 100 μm are worthy. Seiler et al. [52] studied the humping effect during LBW of thin metal sheets. The author showed the way to avoid the generation of the humping effect, and the indicator was the ratio of laser power to weld seam cross-sectional area for the materials.

4 Conclusions

In the present research work, the advantages of the laser beam welding over other welding processes have been discussed along with various applications in the automotive sector. Discussions on the making of the fuel-efficient lightweight car body, multi-thickness weld blank, car assembly components, body in white elements, mechanical fastening in case of electrical, and electronic elements have been zeroed in this paper. In most cases, for making a lightweight structure, aluminum and its alloys have been utilized. But the most used dissimilar material combination, i.e., aluminum and steel have been adopted as aluminum makes the car body light and steel adds strength.

Mechanical fastening of electrical lighting elements and electronic sensors has been increased nowadays as the automotive sector is keeping eye on electric and hybrid vehicles. The ultimate target is to make a good quality welded joint with desired mechanical properties and fatigue strength with a low overall cost; thus, further study in this field must go on.

5 Future Scope

Parametric optimization has been done based on few parameters; thus, a vast study can be done in this domain using several newly developed optimization techniques such as MACONT, Pythagorean fuzzy DNMA method, and ant colony optimization.

Even study can be done with variation of shielding gasses or mixture of two or more shielding gasses with right proportion and a comparative study then may be done on weld quality, weld strength, micro-hardness, etc. For example, Corgon is used in arc welding applications for its numerous advantages. Though a number of papers have been published on identifying various welding defects but for future prospective, further study is required to find ways to reduce pores, various forms of cracks, and other welding defects as quality matters. For making the overall process cost effective, research must be done to design and develop new setup.

References

1. Couso, E.V., Gómez, J.V.: Laser beam welding and automotive engineering. Adv. Struct. Mater. **8**, 59–84 (2012)
2. EuricoAssunção, L.Q.: Rosa Miranda, Comparative study of laser welding in tailor blanks for the automotive industry. Int. J. Adv. Manuf. Technol. **49**, 123–131 (2010)
3. Shibata, K.: Laser welding of tailored blanks at Nissan. In: International Congress on Applications of Lasers and Electro-Optics, vol. 1996(2), pp. 11–20. Laser Institute of America (1996)
4. Chang, I.S.: Plastic laser welding for automotive lamps at Hyundai. In: European Automotive Laser Applications, EALA 2011, Bad Nauheim, 9–10 Feb (2011)
5. Flowers, S.T.: The growth of laser welding of plastics. Indus. Laser. Solut. (2011)
6. Glaessel, T., Seefried, J., Masuch, M., Riedel, A., Mayr, A., Kuehl, A., Franke, J.: Process reliable laser welding of hairpin windings for automotive traction drives. In: Research Supported by German Federal Ministry for Economic Affairs and Energy (BMWi) (2019)
7. Sun, T., Franciosa, P., Sokolov, M., Ceglarek, D.: Challenges and opportunities in laser welding of 6xxx high strength aluminium extrusions in automotive battery tray construction. Proc. CIRP **94**, 565–570 (2020)
8. Hollatz, S., Heinen, P., Limpert, E., Olowinsky, A., Gillner, A.: Overlap joining of aluminium and copper using laser micro welding with spatial power modulation. Welding in the World **64**(3), 513–522 (2020)
9. Westerbaan, D., Parkes, D., Nayak, S.S., Chen, D.L., Biro, E., Goodwin, F., Zhou, Y.: Effects of concavity on tensile and fatigue properties in fibre laser welding of automotive steels. Sci. Technol. Weld Joining **19**(1), 60–68 (2014)
10. Pires, I., Quintino, L., Miranda, R.M., Gomes, J.F.P.: Fume emissions during gas metal arc welding. Toxicol. Environ. Chem. **88**(3), 385–394 (2006)
11. Popovic, O., Prokic-Cvetkovic, R., Burzic, M., Lukic, U., Beljic, B.: Fume and gas emission during arc welding: hazards and recommendation. Renew. Sustain. Energy Rev. **37**, 509–516 (2014)
12. Ghosh, A., Chattopadhyaya, S., Das, R.K., Sarkar, P.K.: Assessment of heat affected zone of submerged arc welding process through digital image processing. Phys. Eng. **10**, 2782–2785 (2011)
13. Zhu, M.-L., Xuan, F.-Z.: Correlation between microstructure, hardness and strength in HAZ of dissimilar welds of rotor steels. Mater. Sci. Eng. **527**, 4035–4042 (2010)
14. Baune, E., Bonnet, C., Liu, S.: Assessing metal transfer stability and spatter severity in flux cored arc welding. Sci. Technol. Weld Joining **6**(3), 139–148 (2001)
15. Fernandes, F.A.O., Oliveira, D.F., Pereira, A.B.: Optimal parameters for laser welding of advanced high-strength steels used in the automotive industry. Proc. Manuf. **13**, 219–226 (2017)

16. Mian, A., Taylor, C., Vijwani, H., Hartke, K., Mukhopadhyay, S., Dosser, L.: Microstructural analysis of laser micro-welds between electrode materials for Li-Ion battery applications. In: ASME international mechanical engineering congress and exposition, vol. 56390, pp. V010T11A011. American Society of Mechanical Engineers (2013)

17. Ribolla, A., Damoulis, G.L., Batalha, G.F.: The use of Nd: YAG laser weld for large scale volume assembly of automotive body in white. J. Mater. Process Technol. **164**, 1120–1127 (2005)

18. https://fastenerengineering.com/how-is-laser-welding-used-in-the-automotive-industry/

19. Acherjee, B.: Hybrid laser arc welding: State-of-art review. Opt. Laser Technol. **99**, 60–71 (2018)

20. Sebestova, H., Hornik, P., Mrna, L., Dolezal, P.: Microstructure and mechanical properties of hybrid LasTIG welds of HSLA steel. Proc. CIRP **74**, 743–747 (2018)

21. Casalino, G., Angelastro, A., Perulli, P., Casavola, C., Moramarco, V.: Study on the fiber laser/TIG weldability of AISI 304 and AISI 410 dissimilar weld. J. Manuf. Process. **35**, 216–225 (2018)

22. Song, G., Diao, Z., Lv, X., Liu, L.: TIG and laser–TIG hybrid filler wire welding of casting and wrought dissimilar magnesium alloy. J. Manuf. Process. **34**, 204–214 (2018)

23. Song, G., Jingwei, Y., Li, T., Wang, J., Liu, L.: Effect of laser-GTAW hybrid welding heat input on the performance of Mg/Steel butt joint. J. Manuf. Process **31**, 131–138 (2018)

24. Jun-yu, X.U.E., Yuan-xing, L.I., Hui, C.H.E.N., Zong-tao, Z.H.U.: Wettability, microstructure and properties of 6061 aluminum alloy/304 stainless steel butt joint achieved by laser−metal inert-gas hybrid welding−brazing. Trans. Nonferrous Met. Soc. China **28**, 1938–1946 (2018)

25. Casalino, G., Angelastro, A., Perulli, P., Casavola, C., Moramarco, V.: Study on the fiber laser/TIG weldability of AISI 304 and AISI 410 dissimilar weld. J. Manuf. Process **35**, 216–225 (2018)

26. Zhu, Z., Wang, W., Li, Y., Chen, H.: Effect of laser-arc offset and laser-deviation angle on the control of a Ti-Al Interlayer. J. Mater. Process. Tech **271**, 336–345 (2019)

27. https://www.primapowerlaserdyne.com/selecting-and-delivering-shield-gas-in-laser-welding/

28. Kotadia, H.R., Franciosa, P., Ceglarek, D.: Challenges and opportunities in remote laser welding of steel to aluminium. In: MATEC Web of Conferences, vol. 269, pp. 02012. (2019)

29. Çevik, B., Gülenç, B.: The effect of welding speed on mechanical and microstructural properties of 5754 Al (AlMg3) alloy joined by laser welding. Mater. Res. Expr. **5**, 086520 (2018)

30. Scherm, F., Bezold, J., Glatzel, U.: Laser welding of Mg alloy MgAl$_3$Zn$_1$ (AZ31) to Al alloy AlMg$_3$ (AA5754) using ZnAl filler material. Sci. Technol. Weld Joining **17**(5), 364–367 (2012)

31. KamelAbderrazaka, W.B., Salem, H.M., Lepalec, G., Autric, M.: Modelling of CO$_2$ laser welding of magnesium alloys. Opt. Laser Technol. **40**, 581–588 (2008)

32. Qianqian, G., Long Jiangqi, Y., Ping, J.S., Wenhao, H., Jianxi, Z.: Effect of steel to aluminum laser welding parameters on mechanical properties of weld beads. Opt. Laser Technol. **111**, 387–394 (2019)

33. Franciosa, P., Serino, A., Al Botros, R., Ceglarek, D.: Closed-loop gap bridging control for remote laser welding of aluminum components based on first principle energy and mass balance, Laser Institute of America. J. Laser Appl. **31**, 022416 (2019)

34. Fieger, T.V., Sattler, M.F., Witt, G.: Developing laser beam welding parameters for the assembly of steel SLM parts for the automotive industry. Rapid Prototyping J. **24**(8), 288–1295 (2018)

35. Agarwal, G., Gao, H., Amirthalingam, M., Hermans, M.: Study of solidification cracking susceptibility during LaserWelding in an advanced high strength automotive steel. Metals **8**, 673 (2018)

36. Evin, E., Tomáš, M.: The influence of LaserWelding on the mechanical properties of dual phase and trip steels. Metals **7**, 239 (2017)

37. Kumar, P., Sinha, A.N.: Effect of pulse width in pulsed Nd:YAG dissimilar laser welding of austenitic stainless steel (304 L) and carbon steel (st37). Lasers in Manuf. Mater. Process. (2018)

38. Mei, L., Chen, G., Jin, X., Zhang, Y., Qiang, W.: Research on laser welding of high-strength galvanized automobile steel sheets. Opt. Lasers Eng. **47**, 1117–1124 (2009)

39. AlShaer, A.W., Li, L., Mistry, A.: Effect of filler wire properties on porosity formation in laser welding of AC-170PX aluminium alloy for lightweight automotive component manufacture. ProcIMechE Part B: J. Eng. Manuf. 1–13 (2015)
40. Casalino, G., Facchini, F., Mortello, M., Mummolo, G.: ANN modelling to optimize manufacturing processes: the case of laser welding. IFAC-PapersOnLine **49**, 378–383 (2016)
41. Chen, H.-C., Pinkerton, A.J., Li, L., Liu, Z., Mistry, A.T.: Gap-free fibre laser welding of Zn-coated steel on Al alloy for light-weight automotive applications. Mater. Des. **32**, 495–504 (2011)
42. Kim, T.W., Park, Y.W.: Parameter optimization using a regression model and fitness function in laser welding of aluminum alloys for car bodies. Int. J. Precis. Eng. Manuf. **12**(2), 313—320 (2011)
43. Liedl, G., Bielak, R., Ivanova, J., Enzinger, N., Figner, G., Bruckner, J., Pasic, H., Pudar, M., Hampel, S.: Joining of aluminum and steel in car body manufacturing. Phys. Proc. **12**, 150–156 (2011)
44. Long, J., Huang, W., Xiang, J., Guan, Q., Ma, Z.: Parameter optimization of laser welding of steel to Al with pre-placed metal powders using the Taguchi-response surface method. Opt. Laser Technol. **108**, 97–106 (2018)
45. Park, Y.W., Rhee, S.: Process modeling and parameter optimization using neural network and genetic algorithms for aluminum laser welding automation. Int. J. Adv. Manuf. Technol. **37**, 1014–1021 (2008)
46. Pastor, M., Zhao, H., Debroy, T.: Pore formation during continuous wave Nd:YAG laser welding of aluminium for automotive applications. Welding Int. **15**(4), 275–281 (2001)
47. Mehlmann, B., Olowinsky, A., Thuilot, M., Gillner, A.: Spatially modulated laser beam micro welding of CuSn6 and nickel-plated DC04 steel for battery applications. JLMN-J. Laser Micro/Nano Eng. **9**(3) (2014)
48. Haeusler, A., Mehlmann, B., Olowinsky, A., Gillner, A.: Efficient copper microwelding with fibre lasers using spatial power modulation. Lasers in Eng. (Old City Publishing) **36** (2017)
49. Helm, J., Haeusler, A., Schwetlick, M., Olowinsky, A., Gillner, A., Poprawe, R.: Connecting battery cells by aluminium ribbon bonding using laser micro welding. J. Laser Appl. (2014)
50. Hollatz, S., Hummel, M., Jaklen, L., Lipnicki, W., Olowinsky, A., Gillner, A.: Processing of keyhole depth measurement data during laser beam micro welding. J. Mater.: Design Appl. **234**(5), 722–731 (2020)
51. Maina, M.R., Okamoto, Y., Inoue, R., Nakashiba, S.-I., Okada, A., Sakagawa, T.K.: Influence of surface state in micro-welding of copper by Nd:YAG laser. Appl. Sci. **8**, 2364 (2018)
52. Seiler, M., Patschger, A., Tianis, L., Rochholz, C., Bliedtner, J.: Experimental determination of influencing factors on the humping phenomenon during laser micro welding of thin metal sheets. J. Laser Appl. **29**(2):022413 (2017). 1938–1387/2017/5

Application of S-LCA Principles to Additive Manufacturing

Rohit Agrawal and **S. Vinodh**

1 Introduction

The manufacturing sector has been witnessing a digital revolution, and additive manufacturing (AM) has brought tremendous changes in manufacturing patterns [1]. Several AM technologies emerged with the application ranging from prototyping to near net shape manufacturing. As AM technologies are revolutionizing manufacturing industries, research in several aspects has been progressing from materials, product, process, life cycle impacts, and so on [2]. In line with studies on environmental impact analysis, societal aspects of these technologies are also to be analyzed. In this regard, this study starts with the fabrication of a case product named bevel gear. Fused deposition modeling (FDM) was used to fabricate the bevel gear. FDM is an extrusion-based AM technology that uses polymer filament to fabricate the parts. It prints the part in a layered manner which is supported by support material. Once the part is fabricated, the support material can be removed either manually or by keeping the part in a chemical solution. Acrylonitrile butadiene styrene (ABS) material was considered to fabricate the bevel gear. This study presents the societal life cycle assessment (LCA) of AM technology. In this study, we aimed to calculate the social impact generated due to the fabrication of bevel gear. The assessment model was developed to analyze the social impact of bevel gear. The evaluation model includes two levels. 17 impact indicators are analyzed. The inferences are highlighted.

R. Agrawal · S. Vinodh (✉)

Department of Production Engineering, National Institute of Technology, Tiruchirappalli 620 015, India

e-mail: vinodh_sekar82@yahoo.com

R. Agrawal

Operations Management & Quantitative Techniques, Indian Institute of Management, BodhGaya, Bihar, India

2 Literature Review

Ruben et al. [3] aimed to provide a framework for social LCA, which can be implemented in manufacturing organizations to evaluate social sustainability. A two-level framework was developed by them, which includes three stakeholders at the first level and nine subcategories at the second level. They validated the framework by performing a case study in a manufacturing firm. For the case study, they selected a case product and collected data from two workers and two managers for the case product. They analyzed the results and derived inferences based on performance assessment scores. The limitations of their study are they considered limited indicators which can be explored further.

Traverso et al. [4] aimed to analyze the feasibility of quantitative assessment methods for product social impact. They presented a case study involving the social impact assessment of a tire in its complete life cycle. The authors involved 13 companies in developing two methodologies (one is qualitative, and the other one is quantitative) for assessing the social impact of the product. They presented a case study of a BWM car tire by including 26 indicators in three groups. The distance to target method was used for quantification of social impact. For the assessment, they identified the scope of improvement. Future work which can be identified from this study was the integration of social LCA with environmental LCA and life cycle costing (LCC) for enhancing decision-making.

Parent et al. [5] explored the importance of S-LCA in sustainable production. They analyzed the applications of S-LCA so that it can be effectively implemented for sustainable production. They discussed the S-LCA in the entire supply chain cycle of the product. They gave a theoretical overview of S-LCA and how it will help in sustainable production and consumption.

Ma et al. [6] presented an LCA-based framework for assessing the sustainability of 3D printed components and analyzed the performance of 3D printed components. They also did a case study to validate the applicability of the developed framework. They inferred that 3D printed parts have a significant impact on environmental and economic sustainability. They suggested that implementing AM technologies for mass production can reduce the sustainability impacts.

Matos and Jacinto [7] discussed AM process and its impact on social sustainability. They also discussed significant AM challenges pertaining to the social impact associated with the additively manufactured product. They suggested that future works need to be the focus on analyzing and quantifying the social impact associated with additively manufactured products.

Chen et al. [8] analyzed direct digital manufacturing from various manufacturing perspectives. They compared direct digital manufacturing with craft and mass production. They also analyzed the sustainability aspect of the direct digital manufacturing process considering all three aspects of sustainability. They analyzed energy consumption in mass production of the considered process to get better insights. Finally, they concluded that direct digital manufacturing has a positive impact on sustainability.

Machado et al. [9] aimed to develop a checklist for analyzing the sustainable performance of AM process. They highlighted the importance of different phases of LCA in AM process. A detailed list of performance indicators for assessing sustainable performance was presented and grouped into three aspects of sustainability. The developed checklist helped the firm to analyze the sustainable benefits in line with sustainable development goals by implementing AM technologies. Finally, they presented a case study that showed that the implementation of AM technologies might result in more sustainable benefits.

3 Methodology

S-LCA is a social impact assessment method that aims to analyze the social impact of a product or a process and identify the positive and negative impact on different phases of the life cycle. An LCIA method includes characterization, normalization, and weighting as suggested by ISO 14040. S-LCA method also follows ISO 14040 and has characterization normalization and weighting stage.

In S-LCA, characterization includes the conversion of social information into a list of impact indicators. Normalization includes rescaling of characterization value of all impacts into a comparable scale. Weightage is to assign weights to the impacts based on their importance for the specific study.

For impact assessment, characterization includes providing ratings to the impact indicators. After providing the ratings to all the impact indicators, normalization is done. Normalization is done by converting all impact indicators into a $-1, 0, 1$ value so that all impact lies in the -1 to 1 range. Further, the weighted average score is being calculated by adding all normalized scores under a category divided by the total number of impact indicators.

The calculation process for S-LCA is as follows [10]:

Step 1: Development of conceptual model linking stakeholders, subcategories, and impact indicators. For a different study, different models can be developed. Usually, a 2-level or a 3-level model is preferred.

Step 2: Characterization of categories into impact indicators and providing rank to impact indicators. Equation 1 is used for characterization [3, 10].

$$CHi = Ini \tag{1}$$

where CHi and Ini are the characterization result and indicator value pertaining to ith indicator

Step 3: Normalization of impact indicators into a comparable score. Equation 2 is used for normalization [3].

$$NRi = CHi \times Ni \tag{2}$$

where NRi is the normalized score of impact indicator

Ni is the normalization factor that varies between −1 and 1.

Step 4: Weighted normalized score calculation for each stakeholder.

A weighted score is calculated by adding all normalized scores under a category divided by the total number of impact indicators.

Step 5: Calculation of single impact score.

The single score is calculated as the summation of the weighted score of all stakeholders.

Finally, inferences need to be derived based on a single score, and future recommendations need to be derived to enhance the social aspect of sustainability.

4 Case Study

The bevel gear has been taken for life cycle assessment. The bevel gear is a conical-shaped gear designed to transmit power between two intersection shafts. Bevel gears are used in lots of areas like automobiles, power plants, locomotives, marine applications, etc.; the bevel gear has been modeled in Autodesk Inventor.

4.1 Social Life Cycle Assessment

The aim of the present study is to conduct social LCA. For conducting S-LCA, a conceptual model consisting of two levels is developed. Level one consists of stakeholders, and level two consists of impact indicators. In level one, four stakeholders have been considered, namely workers, consumers, society, and products. A total of 17 impact indicators have been identified from the literature survey pertaining to AM and are categorized into four stakeholders categories. Table 1 presents the conceptual model consisting of stakeholders and corresponding impact categories.

After identifying impact categories, data have been collected from four experts. A Likert's scale of five-point is used for collecting data. On the scale, 5 stands for most important, and 1 stands for least important. After collecting inputs, the data are then normalized by providing a normalized factor. The normalization factor lies in the range of 1 to −1, where 1 stands for best performance and −1 stands for worst performance. The collected data are shown in Table 2.

After collecting input data, basic statistics have been used to calculate the mean of each impact indicator for identifying the importance of each indicator. Table 3 presents the mean of each indicator. Using the normalization equation, the normalized impact score has been calculated and is presented in Table 4.

Table 1 A conceptual model for S-LCA

Stakeholders	Impact indicator	References
Workers	Health and safety	[4, 10]
	Physical working conditions	[11]
	Training and education of employees	[4, 11, 12]
	Social benefit	[4, 13]
Consumer	Health and safety	[11, 14]
	End of life responsibility	[14]
Society	Technology development	[3, 14, 15]
	Supplier relation	[14, 15]
	Access to material resources	[13, 15]
	Access to non-material resources	[13, 14, 16]
	Transparency on social/environmental issues	[13]
	Contribution to local employment	[3, 14]
	Contribution to economic development	[3, 11, 14]
	Transfer of technology and knowledge	[13]
Product	Product safety	[3]
	Orientation	[3]
	Secured operating condition	[3]

Table 2 Collected data from the expert panel

Stakeholders	Impact indicator	Importance of categories by Expert			Normalization value
		E1	E2	E3	
Workers	Health and safety	4	4	3	1
	Physical working conditions	4	5	4	1
	Training and education of employees	5	5	4	1
	Social benefit	4	3	4	1
Consumer	Health and safety	3	3	4	0
	End of life responsibility	5	4	5	1
Society	Technology development	4	5	4	1
	Supplier relation	3	3	4	0
	Access to material resources	4	4	5	1
	Access to non-material resources	3	3	4	0
	Transparency on social/environmental issues	4	3	4	1
	Contribution to local employment	3	4	4	1

Table 2 (continued)

Stakeholders	Impact indicator	Importance of categories by Expert			Normalization value
		E1	E2	E3	
	Contribution to economic development	4	5	4	1
	Transfer of technology and knowledge	4	4	5	1
Product	Product safety	3	3	4	0
	Orientation	4	4	4	1
	Secured operating condition	4	4	3	1

Table 3 Calculation of mean value of indicators

Stakeholders	Impact indicator	Importance of categories by Expert			Mean
		E1	E2	E3	
Workers	Health and safety	4	4	3	3.667
	Physical working conditions	4	5	4	4.333
	Training and education of employees	5	5	4	4.667
	Social benefit	4	3	4	3.667
Consumer	Health and safety	3	3	4	3.333
	End of life responsibility	5	4	5	4.667
Society	Technology development	4	5	4	4.333
	Supplier relation	3	3	4	3.333
	Access to material resources	4	4	5	4.333
	Access to non-material resources	3	3	4	3.333
	Transparency on Social/environmental issues	4	3	4	3.667
	Contribution to local employment	3	4	4	3.667
	Contribution to economic development	4	5	4	4.333
	Transfer of technology and knowledge	4	4	5	4.333
Product	Product safety	3	3	4	3.333
	Orientation	4	4	4	4.000
	Secured operating condition	4	4	3	3.667

5 Result

After calculating the normalized score, the next step is calculating the weighted score and single score. Table 5 presents the weighted score for each impact indicator and total impact score.

Table 4 Normalized score of the impact indicator

Stakeholders	Impact indicator	Mean	Normalization value	Indicator normalized score
Workers	Health and safety	3.667	1	3.66667
	Physical working conditions	4.333	1	4.33333
	Training and education of employees	4.667	1	4.66667
	Social benefit	3.667	1	3.66667
Consumer	Health and safety	3.333	0	0
	End of life responsibility	4.667	1	4.66667
Society	Technology development	4.333	1	4.33333
	Supplier relation	3.333	0	0
	Access to material resources	4.333	1	4.33333
	Access to non-material resources	3.333	0	0
	Transparency on social/environmental issues	3.667	1	3.66667
	Contribution to local employment	3.667	1	3.66667
	Contribution to economic development	4.333	1	4.33333
	Transfer of technology and knowledge	4.333	1	4.33333
Product	Product safety	3.333	0	0
	Orientation	4.000	1	4
	Secured operating condition	3.667	1	3.66667

From Table 5, it can be inferred that the total impact score of the process is 3.33. The weighted score of different stakeholders is identified, and the total impact score has been calculated. The weighted score of worker, consumer, society, and product is 1.021, 0.292, 1.542, and 0.479, respectively. Societal LCA has been conducted on the present study, and the total societal impact is a 3.33 score.

Table 5 Weighted score and single impact score

Stakeholders	Impact indicator	Impact category normalization score	Impact category weighted normalization score	Total score
Workers	Health and safety	16.333	1.021	3. 333
	Physical working conditions			
	Training and education of employees			
	Social benefit			
Consumer	Health and safety	4.667	0.292	
	End of life responsibility			
Society	Technology development	24.667	1.542	
	Supplier relation			
	Access to material resources			
	Access to non-material resources			
	Transparency on Social/environmental issues			
	Contribution to local employment			
	Contribution to economic development			
	Transfer of technology and knowledge			
Product	Product safety	7.667	0.479	
	Orientation			
	Secured operating condition			

6   Conclusions

As need exists to analyze societal aspects of emerging technologies, this article presents the societal LCA of AM technology. To analyze the social impact of FDM-based AM technology, a two-level evaluation model with appropriate stakeholder dimensions and indicators was developed. The developed model consists of 17 social

impact indicators which were further grouped into four different stakeholders of a social aspect. To analyze the social impact, the inputs have been obtained from industrial and academic experts. The normalized and weighted scores for different stakeholder dimensions are derived. The weighted score of worker, consumer, society, and product is found, and the total score for societal impact is calculated as 3.33. The study has contributed toward the analysis of societal impacts of AM from the viewpoint of different stakeholder dimensions. In future studies, additional indicators could be included. The present study will help the industrial practitioners, government officials, and policymakers to analyze the social impact generated from the production phase.

References

1. Majeed, A., Zhang, Y., Ren, S., Lv, J., Peng, T., Waqar, S., Yin, E.: A big data-driven framework for sustainable and smart additive manufacturing. Robot. Comput. Integr. Manuf. **67**, (2021). https://doi.org/10.1016/j.rcim.2020.102026
2. Agrawal, R., Vinodh, S.: Sustainability evaluation of additive manufacturing processes using grey-based approach. Grey Syst. Theory Appl. **10**, 393–412 (2020)
3. Ruben, R.B., Menon, P., Sreedharan, R.: Development of a social life cycle Assessment framework for manufacturing organizations. In: 2018 International Conference on Production and Operations Management Society, POMS 2018 (2019). https://doi.org/10.1109/POMS.2018.8629496
4. Traverso, M., Bell, L., Saling, P., Fontes, J.: Towards social life cycle assessment: a quantitative product social impact assessment. Int. J. Life Cycle Assess **23**, 597–606 (2018). https://doi.org/10.1007/s11367-016-1168-8
5. Parent, J., Cucuzzella, C., Revéret, J.-P.: Revisiting the role of LCA and SLCA in the transition towards sustainable production and consumption. Int. J. Life Cycle Assess **18**, 1642–1652 (2013). https://doi.org/10.1007/s11367-012-0485-9
6. Ma, J., Harstvedt, J.D., Dunaway, D., Bian, L., Jaradat, R.: An exploratory investigation of additively manufactured product life cycle sustainability assessment. J. Clean Prod. **192**, 55–70 (2018). https://doi.org/10.1016/j.jclepro.2018.04.249
7. Matos, F., Jacinto, C.: Additive manufacturing technology: mapping social impacts. J. Manuf. Technol. Manag. **30**, 70–97 (2019). https://doi.org/10.1108/JMTM-12-2017-0263
8. Chen, D., Heyer, S., Ibbotson, S., Salonitis, K., Steingrímsson, J.G., Thiede, S.: Direct digital manufacturing: definition, evolution, and sustainability implications. J. Clean Prod. **107**, 615–625 (2015). https://doi.org/10.1016/j.jclepro.2015.05.009
9. Machado, C.G., Despeisse, M., Winroth, M., Ribeiro da Silva, E.H.D.: Additive manufacturing from the sustainability perspective: Proposal for a self-assessment tool. In: Procedia CIRP. pp. 482–487. (2019). https://doi.org/10.1016/j.procir.2019.03.123
10. Dong, Y.H., Ng, S.T.: A social life cycle assessment model for building construction in Hong Kong. Int. J. Life Cycle Assess **20**, 1166–1180 (2015). https://doi.org/10.1007/s11367-015-0908-5
11. Jørgensen, A., Le Bocq, A., Nazarkina, L., Hauschild, M.: Methodologies for social life cycle assessment. Int. J. Life Cycle Assess **13**, 96–103 (2008). https://doi.org/10.1065/lca2007.11.367
12. Siebert, A., Bezama, A., O'Keeffe, S., Thrän, D.: Social life cycle assessment indices and indicators to monitor the social implications of wood-based products. J. Clean Prod. **172**, 4074–4084 (2018). https://doi.org/10.1016/j.jclepro.2017.02.146

13. Manik, Y., Leahy, J., Halog, A.: Social life cycle assessment of palm oil biodiesel: a case study in Jambi Province of Indonesia. Int. J. Life Cycle Assess **18**, 1386–1392 (2013). https://doi.org/10.1007/s11367-013-0581-5

14. Benoît, C., Norris, G.A., Valdivia, S., Ciroth, A., Moberg, A., Bos, U., Prakash, S., Ugaya, C., Beck, T.: The guidelines for social life cycle assessment of products: just in time! Int. J. Life Cycle Assess **15**, 156–163 (2010). https://doi.org/10.1007/s11367-009-0147-8

15. Hosseinijou, S.A., Mansour, S., Shirazi, M.A.: Social life cycle assessment for material selection: a case study of building materials. Int. J. Life Cycle Assess **19**, 620–645 (2014). https://doi.org/10.1007/s11367-013-0658-1

16. Lehmann, A., Zschieschang, E., Traverso, M., Finkbeiner, M., Schebek, L.: Social aspects for sustainability assessment of technologies—challenges for social life cycle assessment (SLCA). Int. J. Life Cycle Assess **18**, 1581–1592 (2013). https://doi.org/10.1007/s11367-013-0594-0

Areal Surface Texture Characterization Methods for Selective Laser-Sintered Parts

Shrijay V. Mahajan

1 Introduction

Recent development trends in additive manufacturing technology have made it popular in many industries. Additive manufacturing (AM) has the capability of producing parts without any shape limitation. The surface texture of AM parts is significantly different from that of the parts produced by conventional manufacturing processes and has a significant impact on the performance of parts function. Surface texture characterization refers to the evaluation of surface texture features that can have a significant impact on a part's performance. Loss in performance of horn antennas printed with EBM with an increase in surface roughness [1]. Characterization methods are developed to investigate the relation between SLM surface texture and its performance. Choice of surface measurement technology for the particular surface is an important factor in characterization and is influenced by the manufacturing process. Surface roughness measurements can be done either by stylus tip-based instruments or optical instruments. SLM produces surfaces by selectively sintering the layer of powder particles. Layer-by-layer sintering involves complex physical phenomena like balling and melt pool formation which results imparts a specific texture to the SLM part's surface [2]. This surface texture is significantly rough and difficult to measure by stylus-based instruments due to the risk of tip damage [3]. The recent trend toward the uses of areal roughness parameters for the characterization of AM surfaces increased the use of optical measurement technologies. Optical measurement techniques such as coherence scanning microscopy successfully captured surface data from PBF surfaces without any significant error [4]. SLS part surface roughness measurement obtained by contact profilometer (VeecoDektak 150) was compared with a non-contact optical microscope (Leica

S. V. Mahajan (✉)
Department of Mechanical Engineering, National Institute of Technology, Calicut, India
e-mail: mahajan_m190590me@nitc.ac.in

DCM 3D microscope). An optical microscope was found to capture more information than a contact profilometer [5].

Surface texture characterization is a step-by-step procedure that starts with the acquisition of surface data with suitable measuring instruments. The measured dataset is then processed to remove the presence of anomalies that may influence the values of computed parameters. Data processing was followed by filtering operations performed to separate roughness and waviness components from the surface at a specified cut-off length. Current published works claimed a variety of cut-off lengths for filtering. SLM coupons with a 2.5-mm by 2.5-mm area of the evaluation were found to be sufficient to capture surface height data with 2.5-mm cut-off length [6]. Cut-off length is also referred to as nesting index in ISO 25178-2 [7]. Gaussian high-pass filter was used with a 0.2-mm cut-off length to separate the large-scale waviness that arises due to weld tracks on the laser powder bed fusion (LBPF) surface. The selection of cut-off length was based on visual inspection to obtain the local shape of weld tracks along with surface features like weld ripples, partially melted particles, etc. Spatial filters were used for removing fictitious points. Cut-off lengths of 5 mm were used to remove longwave components while 1 mm was used to suppress short-wave components [8]. Gaussian filtering was performed as per ISO 4287 standard with cut-offs of 25 μm and 0.8 mm for short- and long-wavelength components, respectively [9, 10]. The question of selecting cut-off is remaining due to a lack of standards in AM surface metrology. It is unclear whether the currently developed ISO standards are suitable for AM surfaces. Most of the current work is focused on the Gaussian filtering of profile data. Gaussian filter was explored to separate waviness components with cut-off lengths $\lambda c = 0.25$ mm and $\lambda f = 4$ mm from the SLM surface. The profile generated with standard Gaussian filter and robust Gaussian regression filter was compared. Robust Gaussian regression filter was found to be superior in suppressing fake dimples on residual profiles. Morphological filter was explored as an alternative method to suppress globules and pores on SLM surfaces. Both filters were found suitable for the extraction of surface features. However, more work is needed to validate the suitability of these filters for SLM surfaces which is an objective of this work.

Filtering operation is followed by roughness parameters evaluation to quantify the surface texture characteristics. Profile roughness parameters such as R_a (Average roughness) and R_q (RMS roughness) are more common in academic research as well industrial practice. R_a was used to obtain surface roughness of top and side surfaces of Inconel 625 parts processed with SLM. However, R_a did not provide comprehensive information about high peaks and deep valleys present on the surface [11]. R_a provides little knowledge about surface roughness characteristics of vertical and upward facing L-PBF surfaces. Profile roughness parameters gain popularity due to simple measurement procedures. Areal roughness parameters are still gaining acceptance due to the advantages of optical measuring techniques over stylus-based techniques for AM surfaces. Recent advancements in surface texture measurement made it possible to extract high-quality information. The surface texture of electron beam melted Ti6Al4V parts oriented at different angles (0°, 55°, 90°) was characterized with areal roughness parameters. Correlation between surface roughness

in terms S_a (average roughness of the surface over the selected area) and powder particle size as well as layer thickness was observed. EBM surface valley depth was expressed in terms of S_v (minimum height of the surface from the mean plane) which was found to be minimum for surfaces with a complete melting of powder particles. A high value of S_p (maximum height of the surface from the mean plane) was observed for surfaces with a high density of nonmelted powder particles [12]. S_a and S_q (average roughness of the surface over the selected area) were correlated to quantify the amplitude of waviness obtained after filtering. S_{sk} (skewness) and S_{ku} (kurtosis) provided insights on peaks and sharpness of height distribution generated on the residual surface after being obtained after filtering [13]. Hybrid parameters such as S_{dq} represent the root mean square slope of the surface whereas S_{dr} represents developed interferential area ratio. S_{dq} and S_{dr} parameters were found to be suitable for the classification of the laser-sintered surface having different inclinations. S_{dr} and S_{dq} showed 93.1 and 91.5% correlation to the surface angles [8]. The selection of a particular surface texture parameter should be based on its linkage with AM process and functionality requirements. Hence, current work is carried out with another objective to identify the roughness parameters that can be used to investigate the functionality requirement of SLM surfaces.

2 Methodology

To develop sophisticated characterization methods for SLM surface texture, methodology used as shown in Fig. 1.

Major steps adopted in Fig. 1 are explained in detail as follows.

2.1 Sample Manufacturing and Measurement

In this work, the cylindrical and flat-shaped samples are manufactured on an EOS M290 machine. Following are the process parameters used to manufacture these samples as shown in Table 1.

After manufacturing, sample surfaces were scanned with a Bruker Alicona 3D profilometer with $10\times$ magnification. The sampling areas from both flat and cylindrical samples are 1.42 mm × 1.08 mm and 2.8 mm × 2.8 mm, respectively. Figure 2 shows the 3D images of sample surfaces rendered in Mountainsmap software by Digital Surf. The cylindrical and flat sample surfaces shown in Fig. 2a, b will be further referred to as case 1 and case 2, respectively.
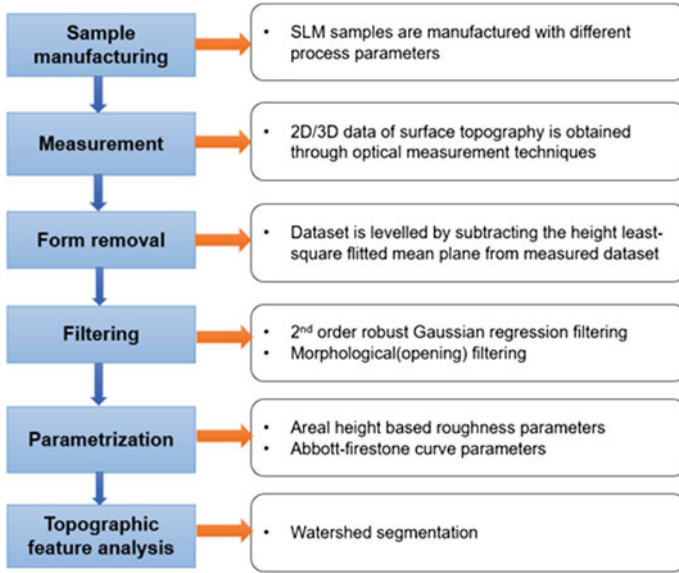
Fig. 1 Methodology for characterization of SLM surface texture

Table 1 Process parameters for SLM sample manufacturing

Process parameters	Cylindrical sample (case 1)	Flat sample (case 2)
Laser power (W)	370	100
Scan speed (mm/s)	1500	5000
Hatch spacing (μm)	130	110
Layer thickness (μm)	40	50

Fig. 2 Sample surfaces after measurement from the cylindrical surface (**a**) and from a flat surface (**b**)

(a)   (b)
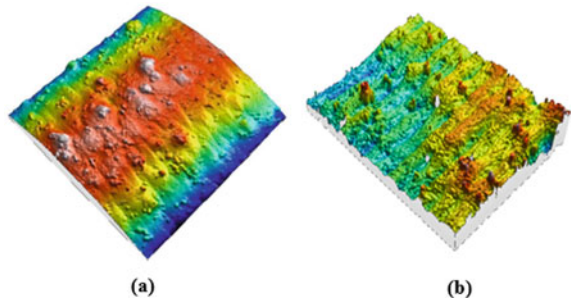
2.2 Form Removal, Filtering, and Parameterization

Surface roughness parameters are usually evaluated on planer are nearly planer surfaces. In this work, both the surfaces taken for characterization contain the form. To remove this form from surfaces, F-operator in Mountainsmap software was used which works on the 'Total least-square approximation' technique. This technique generates a reference plane by fitting a polynomial and subtracts this reference plane $\text{TLS}(x)$ from measured surface $f(x)$ to give residual surface $z(x)$ as given in Eq. 1. The residual surface obtained is used in further operations such as filtering and roughness parameter calculations.

$$z(x) = f(x) - \text{TLS}(x) \tag{1}$$

For the surfaces shown in Fig. 2, F-operator has calculated 3rd and 2nd-degree polynomials given by Eqs. 2 and 3, respectively. The surfaces obtained after the form removal as shown in Fig. 3 are the SLM surface topographies. These topographies are used to depict the surface texture features in SLM samples.

$$
\begin{aligned}
z(x, y) = {}& 20.2 + 0.7641 - 0.0004739x^2 - 1.1444x^3 e^{-8} \\
& - 0.0370 - 4.962xy e^{-6} + 3.58x^2 y e^{-8} - 2.415y^2 e^{-5} \\
& + 2.646y^2 x e^{-8} - 1.179y^3 e^{-9}
\end{aligned}
\tag{2}
$$

$$
\begin{aligned}
z(x, y) = {}& 1.518 + 0.06175x + 1.4741x^2 e^{-5} + 0.1553y \\
& - 0.0001601xy + 5.571y^2 e^{-5}
\end{aligned}
\tag{3}
$$

To obtain the surface texture features in SLM samples, filtering operations are performed on the topographies obtained after the form removal operation. In this work, two filters 2nd-order robust Gaussian regression filter and a morphological filter have been used to separate the waviness components from SLM surfaces. Each of the filtering operation is performed for three different cut-off lengths for the surfaces in each cases. For 2nd-order robust Gaussian regression filtering, cut-off lengths used are 0.25, 0.45, and 0.75 mm for case 1 and 0.025, 0.055, and 0.075 for case 2. At

Fig. 3 Topographies obtained after form removal from the surfaces in case 1 (**a**) and case 2 (**b**)
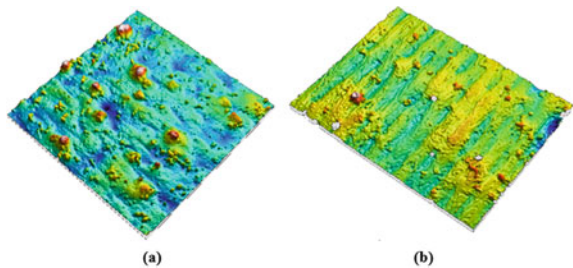
0.25-mm cut-off value, 2nd-order Gaussian regression filter started the separation of waviness components from the topographies shown in Fig. 3. With a further increase in cut-off values, more waviness can be observed on samples. Beyond 0.75-mm cut-off value, no changes were observed in the waviness components; hence, the range for cut-off lengths is chosen in between 0.25 and 0.75 mm. In the case of morphological filter, at 0.25-mm cut-off length, peaks are observed in the surface texture.

The height of these peaks gets reduced with a further increase in cut-off values. So, the 0.75 mm is taken as the maximum cut-off length. In morphological filtering, diameter of the structuring element is equivalent to the cut-off length. In the 0.25–0.75 mm range of cut-off values, significant changes in the surface texture characteristics of the SLM samples were obtained. Therefore, to observe the changes in surface texture with the application of 2nd-order robust Gaussian filter and morphological filter, three different cut-off lengths are chosen in the range of 0.25–0.75 mm. Figures 4 and 5 show topographies obtained after performing 2nd-order robust Gaussian regression filtering and morphological filtering for case 1 and case 2, respectively. Surface texture parameters after applying filtering techniques are evaluated to compare the effect of 2nd-order regression filtering and morphological filtering on surfaces taken in case studies 1 and 2. In this work, areal texture parameters defined by ISO 25178-2 are used. Areal roughness parameters describe surface roughness over an area whereas profile roughness parameters give roughness measured over a profile. Therefore, areal height-based roughness parameters S_a, S_p, S_v as well as Abbott-Firestone curve parameters such as S_{pk} (reduced peak height) and S_{vk} (reduced valley depth) are evaluated for each surface after filtering operation. For the SLM surface, profile-based roughness parameters are not suitable because many different profiles can be obtained from the same area, and it will give different values of roughness parameters for each of the profiles, so it is a more accurate approach to areal roughness parameters which gives surface roughness over an area.

3 Result and Discussion

3.1 Areal Roughness Parameter

As shown in Fig. 6a, b, decrement in average surface roughness S_a after morphological filtering is less as compared to the 2nd-order robust Gaussian regression filtering. It shows that 2nd-order Gaussian regression filter removes more spatial components from surface topographies as compared to the morphological filter. S_p values are plotted after each filtering operation as shown in Fig. 6c, d. Decrease in S_p value is more for morphological filtering as compared to 2nd-order robust Gaussian filtering for case 1. It shows that morphological filters are more suitable for peak filtration whereas 2nd-order robust Gaussian regression filter suits more for filtering out waviness components. This behavior of the filter can be observed from topographies shown in Fig. 4. In Fig. 4a, waviness components can be seen whereas

Fig. 4 Topographies obtained after 2nd-order robust Gaussian filtering at 0.25-mm cut-off length (**a**), morphological filtering filtering at 0.025-mm cut-off length (**b**), 2nd-order robust Gaussian filtering at 0.45-mm cut-off length (**c**), morphological filtering at 0.055-mm cut-off length (**d**), 2nd-order robust Gaussian filtering at 0.75-mm cut-off length (**e**), morphological filtering at 0.075-mm cut-off length (**f**) for the surfaces in case 1
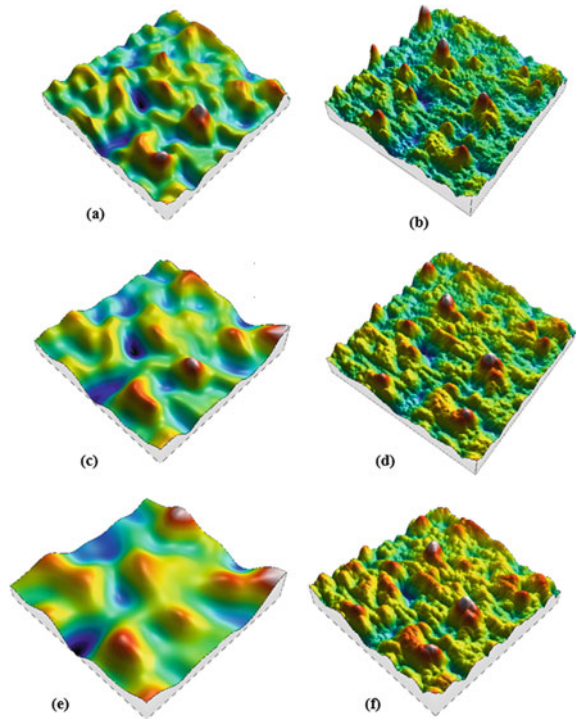
peaks can be seen in Fig. 4b. With an increase in cut-off length of 2nd-order robust Gaussian regression more, waviness components are filtered out as shown in Fig. 4c, e. In the case of the morphological filter, peak height reduces with an increase in cut-off length as seen in Fig. 4d, f. Figure 6d shows that the difference between the S_p values is small for both filters. The surface topographies in case 2 have texture dominated with waviness due to weld tracks with no high peaks. Comparing the topographies in Fig. 5e, f, clear and smooth waviness pattern due to weld tracks is obtained with 2nd-order Gaussian regression filter than the morphological filter. This effect of filtering can be quantified in terms of the S_v parameter shown in Fig. 6f. For the 2nd-order Gaussian regression filter, S_v decreases whereas for the morphological filter little changes in values are observed. With the increase in cut-off length, 2nd-order Gaussian regression filter separates micro-roughness components from the surface resulting in the reduction of valley depth.

3.2 Abbott-Firestone Curve Parameters

Abbott-Firestone (AF) curve (Bearing area ratio curve) shows its importance in contact mechanics. Parameters drawn from the AF curve can be used to predict

Fig. 5 Topographies
obtained after 2nd-order
robust Gaussian filtering at
0.25-mm cut-off length (**a**),
morphological filtering
filtering at 0.025-mm cut-off
length (**b**), 2nd-order robust
Gaussian filtering at
0.45-mm cut-off length (**c**),
morphological filtering at
0.055-mm cut-off length (**d**),
2nd-order robust Gaussian
filtering at 0.75-mm cut-off
length (**e**), morphological
filtering at 0.075-mm cut-off
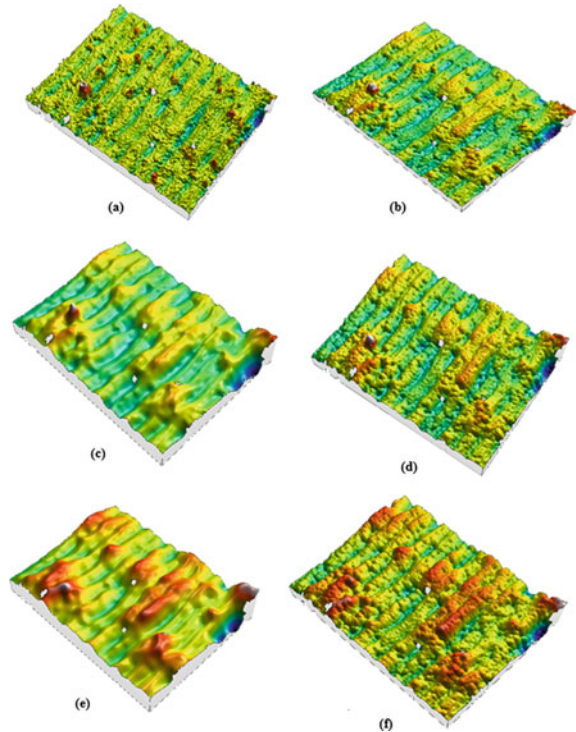length (**f**) for the surfaces in
case 2

surface tribological performance. Figure 7 shows the AF curve obtained for case 1 surface after 2nd-order robust Gaussian filtering with 0.25-mm cut-offs. Values of parameters like S_k and S_{pk} were evaluated after obtaining similar curves for all filtered surfaces and plotted for different cut-off lengths as shown in Fig. 8. S_{pk} and S_{vk} parameters are calculated from Abbott-Firestone curves for different values of cut-off lengths. As a result of an increase in cut-off length, the decrease in S_{pk} values is more for morphological filter as compared to robust Gaussian regression filter as shown in Fig. 8a. The decrease in S_{pk} values is due to a decrease in the maximum peak height above the core roughness of the surface. It proves that morphological filters are more suitable for the extraction of peak information as compared to robust Gaussian regression filters.

The S_{vk} values are decreasing with increase in cut-off lengths for robust Gaussian regression filter, whereas they are almost constant for morphological filter as shown in Fig. 8b. This indicates that robust Gaussian regression filters are more suitable for computing the maximum valley depth below the core roughness of the surface.
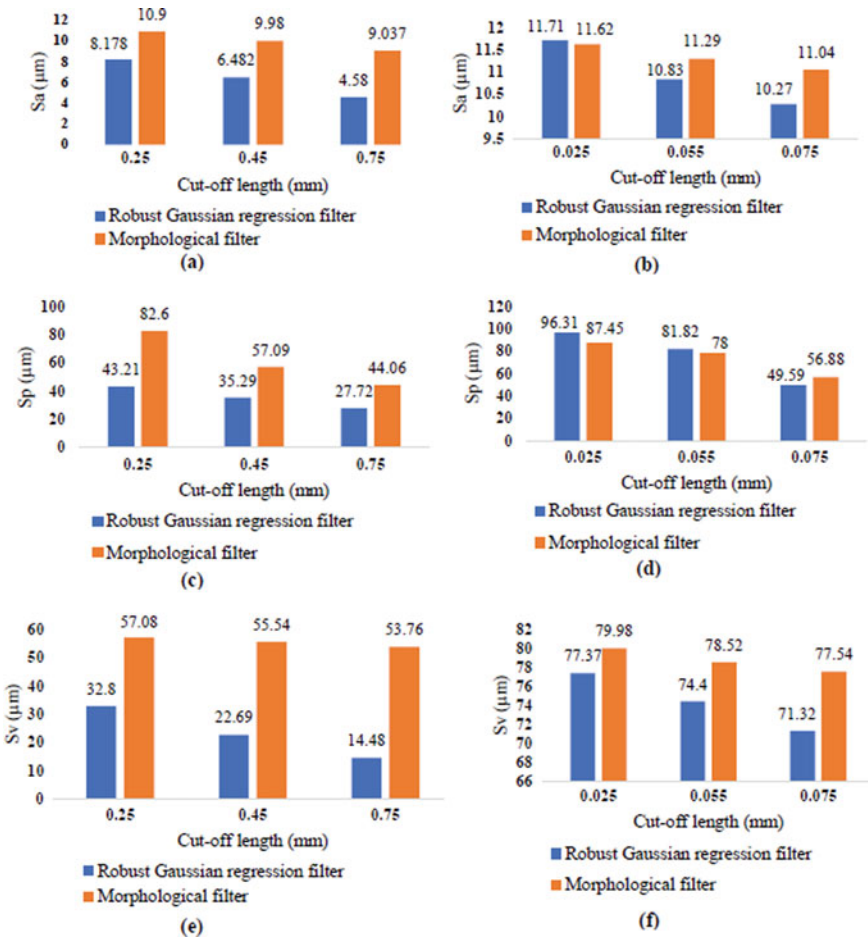
Fig. 6 S_a for the surface in case 1 (**a**), S_a for the surface in case 2 (**b**), S_P for the surface in case 1 (**c**), S_P for the surface in case 2 (**d**), S_V for the surface in case 1 (**e**), S_V for the surface in case 2 (**f**)

4 Conclusion

Selective laser melting (SLM) is the powder-based additive manufacturing process. It produces surfaces by selectively melting the powder layers. A 3D optical profilometer was used to capture surface texture from cylinder surface (case 1) and flat surface (case 2). With the optical method, surfaces with denser data points (1600 × 1600) were obtained. After measurement, high peaks and waviness were observed on cylindrical surfaces whereas flat surface texture was found to be dominant with waviness due to weld tracks. For filtering of these topographies, 2nd-order robust Gaussian regression filter and morphological filters were used. Waviness from the surfaces in case 1 was successfully extracted with 2nd-order Gaussian regression filter whereas

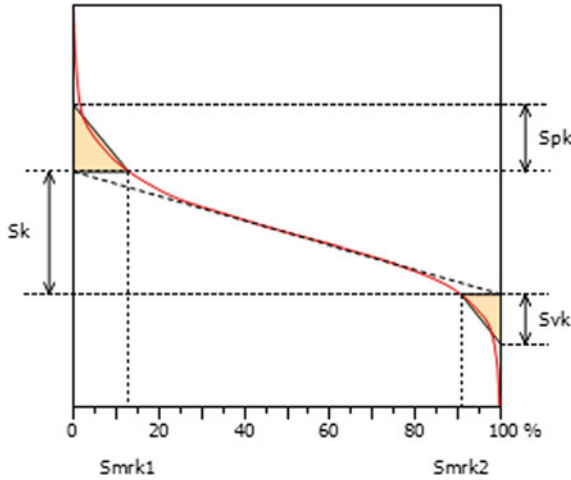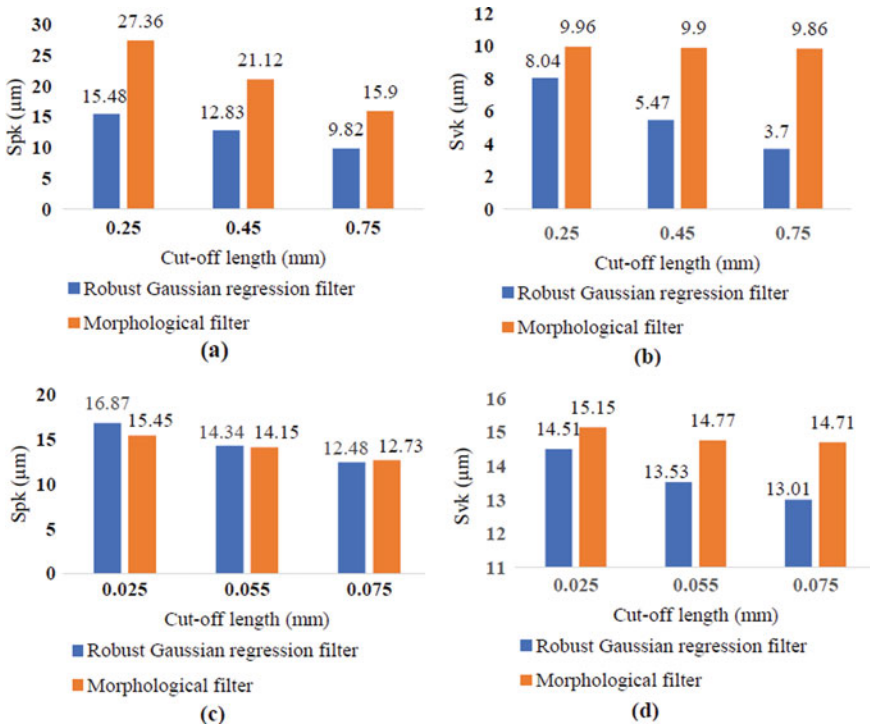**Fig. 7** Abbott-firestone curve

Fig. 8 S_{Pk} for the surface in case 1 (**a**), S_{vk} for the surface in case 1 (**b**), S_{Pk} for the surface in case 2 (**a**), S_{vk} for the surface in case 2 (**b**)

a morphological filter extracted the peaks present in the surface. For extracting the waviness due to weld tracks on the surface in case 2, the 2-order Gaussian regression filter was found to be more useful than a morphological filter. Areal roughness parameters such as S_a, S_{sk}, S_{ku}, S_p, and S_v, and Abbott-Firestone curve parameters such as S_{pk} and S_{pv} were computed to quantify and compare the results of filtering. This work has identified the parameters S_p, S_v, S_{pk}, and S_{vk} which are related to the SLM surface texture characteristics such as peaks, valleys, and waviness.

5 Future Scope

Surface texture plays a very important role in various functionalities such as wear, lubrication, surface contact behavior, and biocompatibility. The values of surface texture parameters identified in this work are influenced by the characteristic features such as peaks and waviness generated on the SLM surface due to weld tracks, weld ripples, and partially melted powder particles. The formation of these features is linked with many process parameters such as laser scan speed, hatching distance, and layer thickness. Further work is needed to develop the relationship between the roughness parameters and SLM process parameters to satisfy the functional requirement of the SLM parts.

References

1. Garcia, C.R., Rumpf, R.C., Tsang, H.H., Barton, J.H.: Effects of extreme surface roughness on 3D printedhornantenna. ElectronLett **49**, 734–736 (2013)
2. Gu, D., Shen, Y.: Balling phenomena in direct laser sintering of stainless-steel powder: metallurgical mechanisms and control methods. Mater. Des. **30**(8), 2903–2910 (2009)
3. Townsend, A., Senin, N., Blunt, L., Leach, R.K., Taylor, J.S.: Surface texture metrology for metal additive manufacturing: a review. Precis. Eng. **46**, 34–47 (2016)
4. Senin, N., Thompson, A., Leach, R.: Feature-based characterization of signature topography in laser powder bed fusion of metals. Meas. Sci. Technol. **29**, 045009 (2018)
5. Vetterli, M., Schmid, M., Wegener, K.: Comprehensive investigation of surface characterization methods for laser sintered parts. In: Fraunhofer Direct Digital Manufacturing Conference (2014)
6. Triantaphyllou, A., Giusca, C.L., Macaulay, G.D., Roerig, F., Hoebel, M., Leach, R.K., Tomita, B., Milne, K.A.: Surface texture measurement for additive manufacturing. SurfTopogr: Metrol. Prop. **3**, 024002 (2015)
7. ISO 25178-2.: Geometrical Product Specifications (GPS)—Surface Texture: Areal—Part 2: Terms, Definitions, and Surface Texture Parameters. International Organization of Standardization, Geneva (2012)
8. Grimm, T., Wiora, G., Witt, G.: Characterization of typical surface effects in additive manufacturing with confocal microscopy. Surf. Topogr. Metrol. Prop. **3**, 014001 (2015)
9. Fox, J., Moylan, S., Lane, B.: Preliminary study toward surface texture as a process signature in laser powder bed fusion additive manufacturing. In: Proceedings of the 2016 ASPE Summer Topical Meeting: Dimensional Accuracy and Surface Finish in Additive Manufacturing, Raleigh, NC [online] (2016)

10. ISO 4287:1997.: Geometrical Product Specifications (GPS)—Surface Texture: Profile Method—Terms, Definitions, and Surface Texture Parameters. ISO, Geneva (1997)
11. Mumtaz, K., Hopkinson, N.: Top surface and side roughness of Inconel 625 parts processed using selective laser melting. Rapid Prototyp. J. **15**(2), 96–103 (2009)
12. Sidambe, A.T.: Three-dimensional surface topography characterization of the electron beam melted Ti6Al4V. Metal Powder Report 72(3), 200–205 (2017)
13. Lou, S., Jiang, X., Sun, W., Zenga, W., Pagania, L., Scotta, P.J.: Characterisation methods for powder bed fusion processed surface topography. Precis. Eng. **57**, 1–15 (2019)

Controlling Waviness in Additive Manufacturing of Thin Walls by Laser-Directed Energy Deposition Process

Srinath Gudur [ID], **Shivam Shukla** [ID]**, J. John Rozario Jegaraj** [ID]**, P. Mastanaiah** [ID]**, Muvvala Gopinath** [ID]**, and Suryakumar Simhambhatla** [ID]

1 Introduction

Laser-based directed energy deposition (LDED) is an additive manufacturing process where the feedstock and laser beam are simultaneously delivered treating a localized zone [1]. The process is gaining wide popularity in industrial applications spurred on by the advantages of geometrical flexibility, resolution and dimensional accuracy, the capability of multi-material deposition, localized treatment, low heat input, thermal distortion, and lead time compared to conventional or competitive manufacturing processes like powder bed fusion process, wire-arc additive manufacturing process, etc. [2]. The LDED process is widely exploited for various processes like laser surface engineering, i.e., laser cladding, alloying, etc., and direct generation of 3D metal components from the CAD model [3, 4].

LDED is well established for 2D surface coatings. However, in the case of depositing 3D components, the process encounters a large range and variety of problems. This includes a dynamic molten pool whose shape and size vary with layer number due to heat accumulation. This becomes more predominant when depositing

S. Gudur · S. Shukla · M. Gopinath · S. Simhambhatla (✉)
Department of Mechanical and Aerospace Engineering, Indian Institute of Technology
Hyderabad, Hyderabad, India
e-mail: ssurya@mae.iith.ac.in

S. Gudur
e-mail: me17resch01002@iith.ac.in

M. Gopinath
e-mail: mgopinath@mae.iith.ac.in

J. John Rozario Jegaraj · P. Mastanaiah
Defence Research and Development Laboratory (DRDL), Hyderabad, India
e-mail: johnmfrg@drdl.drdo.in

P. Mastanaiah
e-mail: mastanaiah@drdl.drdo.in

thin walls. In the case of a multi-layer thin wall deposition process, the initial few layers close to substrate cool or solidify fast by dissipating the heat to substrate maintaining the molten pool stability. However, with an increase in layer number, the distance between the molten pool or processing zone and the substrate increases decreasing the heat dissipation capacity through conduction [5]. Further, due to the thin nature of the wall, i.e., single layer depositions, the lateral conduction will also be insignificant. This leads to an increase in molten pool lifetime, leading to the spreading of molten pool losing the dimensional accuracy [6]. Further, the catchment efficiency under optimized conditions for thin walls is typical of the order of ~ 50%. Therefore, this leaves a chance for an increase in catchment efficiency with any additional energy or heat being provided [7, 8]. Also, the laser absorptivity in metals increases with an increase in substrate temperature [9]. Thus, the heat accumulation results in the availability of additional energy as well as an increase in laser absorptivity. This results in variation in molten pool size with layer number causing geometrical inaccuracy or waviness. Further, Apratim et al. [10] reported stress distribution in thin walls also leads to distortion and consequent failure, making it difficult to add layers for continued fabrication. Jinoop et al. [11] investigated the effect of laser energy per unit powder feed, and variation in wall height was reported to increase with it. Apart from the heat input and layer number, the scan strategy greatly affects the build quality. A bidirectional scanning was reported to give a relatively uniform wall height compared to unidirectional deposition [6]. Further, the combination of laser energy and powder mass flow rate was also reported to influence the geometrical aspects of the multi-layer deposition. In addition to all the process parameters discussed above, effective shielding also plays a major role in dictating the quality and geometrical accuracy of the thins walls. As the deposition height increases, in addition to heat accumulation, the shielding becomes relatively weak as shrouding gas cloud may not cover the molten pool as it does in initial layers which are close to substrate surface [12].

From the above discussion, it can be observed that maintaining the geometrical integrity in the case of multi-layered thin walls is a challenging task involving a large number of process parameters and processing conditions. Therefore, a deep understanding of the spatiotemporal variations of the molten pool thermal history throughout the build, individual tracks, and layers is critical to the control of undesired deposition profiles in the LDED process. There are several studies that reported a positive role of interpass delay during the deposition process [13, 14]. However, these lack the spatiotemporal thermal data of the molten pool. Therefore, the present study focuses on monitoring molten pool thermal history and its variation in real-time with layer number and systematic variation of energy input to overcome the issue of heat accumulation. Further, the study also investigates and reports the possibility of mitigating the existing/generated waviness through judicious selection of relative position between the powder focusing point and the peak and valley position of the undulating surface.

2   Experimental Setup

In the present study, a 2 kW Yb-fiber laser (Coherent FL 02 FFS) operating at 1.07 μm wavelength and integrated with a co-axial laser cladding head with motorized optics (Precitec: YC52) was used for the LDED process. The motorized optics facilitate the independent control on the spot diameter with respect to the stand-off distance (SOD). A 5-axis CNC workstation was used as a kinematic system. Figure 1a shows the experimental setup used. A monochromatic IR pyrometer (Micro-Epsilon, Model: CTLM-2HCF3–C3H) operating at 1.6 μm wavelength was used to monitor the molten pool thermal history. The operating frequency, measuring temperature range and zone at 200-mm focal length, set emissivity, and accuracy of the IR pyrometers are 1 kHz, 385–1600 °C, 0.7 mm, 0.7 and ± (0.3% of reading + 2 °C), respectively. To prevent the effect of reflected laser light on the IR pyrometer, a 1064 ± 25 nm notch filter was mounted in front of the pyrometer [15]. During the deposition process, the pyrometer and the substrate were kept stationary, and linear motion was provided to the laser cladding head. The pyrometer was focused on the line of deposition using the dual guide diode lasers provided on the pyrometer.

For the deposition process, an inert gas atomized Inconel 718 powder (Make: Oerlikon Metco, MetoClad 718) with spherical morphology as shown in Fig. 1b was used as the feedstock and EN-8 steel as the substrate. The nominal range of the powder was −90 + 44 μm with D90 distribution. The powder was fed to the cladding head by a pressurized twin hopper powder feeder. The images of the powder stream from the co-axial laser cladding head were captured using a Nikon D5200 DSLR camera fitted with a 55–200-mm lens. The shutter speed of the camera was set at 1/2000s. Further, the powder stream was illuminated with 15 W rectangular array LED lights from the bottom as well as sides while imaging. In case of continuous deposition without any interpass delay, the laser power, scanning speed, spot diameter, SOD, z-increment after each layer, powder mass flow rate and shielding, carrier, shrouding gas flow rates were kept constant at 600 W, 600 mm/min, 2.2 mm, 20 mm, 0.7 mm, 25 g/min, 5 l/min, 10 l/min, and 10 l/min, respectively. Table 1 shows the parameters used in the other case, where the attempt to minimize the effect of heat accumulation was
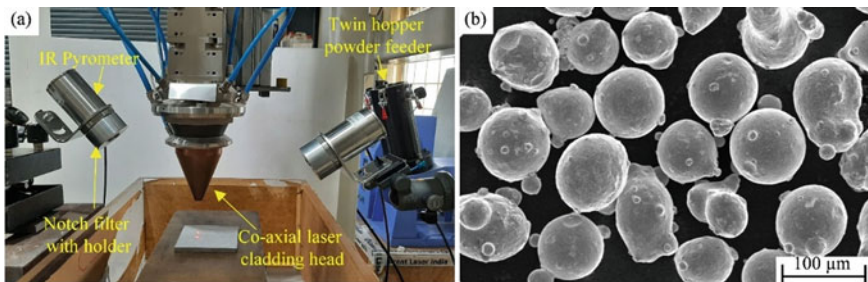

Fig. 1 **a** Experimental setup and **b** morphology of Inconel 718 powder

Table 1 Process parameters for wall deposition with variation in scanning speed, SOD, and interpass delay

Number of layers	10	20	30	40	50−80	90−150	160	170	180	190	200	212
Scanning speed (mm/min)	600	650	800	950	–	–	–	1100	–	–	–	–
SOD (mm)	–	–	–	20	–	–	16	15	15	18	18	18
Dwell time (s)	–	–	–	–	20	–	–	–	30	–	–	–

carried out. Based on the molten pool thermal history and waviness, laser scanning speed was varied with an increase in layer number.

To investigate the bead geometry, the single tracks were cross-sectioned using a wire-cut EDM (Electronica, model: Sprintcut WIN), mirror polished using P400–P2000 grade SiC papers, followed by 1 μm diamond paste and etched with 15 ml HCL, 10 ml acetic acid, and 10 ml HNO3 solution. A scanning electron microscope, SEM (Zeiss, EVO 18 Research), was used for imaging the bead geometry.

3   Results and Discussions

3.1   Effect of Heat Accumulation in Thin Wall Depositions

To investigate the effect of heat accumulation on the molten pool thermal history and thin wall geometry, 80 layers of 120 mm length were continuously deposited, i.e., without any interpass delay using the process parameters discussed in Sect. 2. Figure 2 shows the molten pool thermal cycles of the first 20 layers. It can be observed that the width of each thermal cycle increased with an increase in layer number, indicating slow cooling resulting from the heat accumulation. Further, it may be observed that after the 8th layer, the starting temperature of the layer is above the detectable temperature range of the pyrometer, i.e., above 400 °C. This pre-deposition temperature of each layer after the 8th can be seen continuously increasing. The effect of this heat accumulation on the surface quality or geometrical integrity of the thin wall can be clearly observed in Fig. 3. The top surface of the thin wall can be seen exhibiting waviness. Further deposition on this wall resulted in an increase in peak-to-valley distance, further deteriorating the quality of the wall.
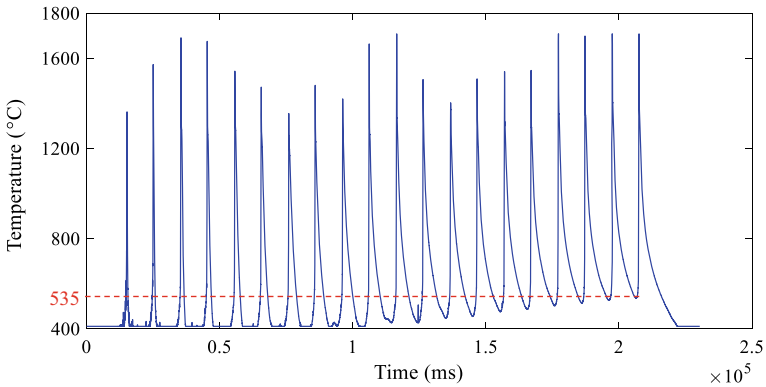
Fig. 2 Variation in molten pool thermal history with layer number (layer 1 to layer 20)
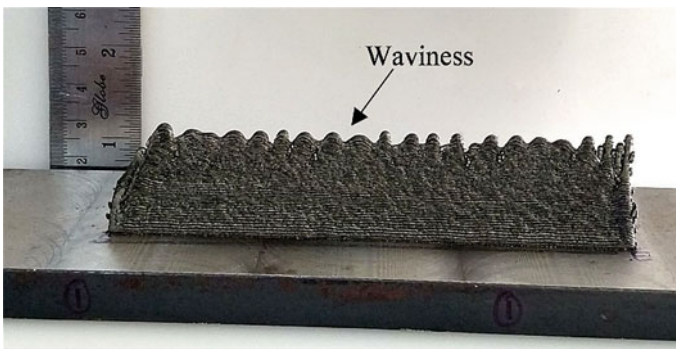
Fig. 3 Continuously deposited multi-layered Inconel 718 thin wall showing waviness (80 layers)

3.2 *Effect of Varying Laser Scan Speed and Introducing Dwell Time*

From Sect. 3.1, it can be observed that the molten pool thermal history measured using an IR pyrometer clearly depicts the heat accumulation in terms of the pre-deposition temperature of the layer. Therefore, based on these observations, the scanning speed was systematically varied for every 10 layers as shown in Table 1, to keep the pre-deposition temperature below the detectable range of the IR pyrometer. Unlike in the case of Fig. 2, it can be observed that the molten pool thermal cycles for the 11th to 20th layer as shown in Fig. 4a were found to reach below the detectable temperature of the pyrometer with a well-defined flat temperature curve before the next layer starts. In this course, the scanning speed was varied from 600 mm/min to 950 mm/min at four intervals from 1st to 40th layer as shown in Table 1. Figure 5 shows the morphology of the thin wall generated by the 40 layers. It can be observed that the wall is very uniform both in terms of uniformity on the top surface as well

as the quality of the side surface compared to Fig. 3. However, from Fig. 4b, it can be observed that the pre-deposition temperature in the case of the 31st to 40th layer was found to be above pyrometer detectable temperature, alarming the excess heat accumulation. Therefore, from the 41st layer, interpass delay was introduced apart from scaling up the speed to 1100 mm/min which thereafter was kept constant as the further increase in scanning speed may result in insufficient energy for fusion. From Fig. 4c and d, it can be clearly observed that with the interpass delay time, the molten pool thermal history for all the layers between 41 and 212 was almost similar, indicating the effectiveness of introducing the interpass delay time. However, in spite of the controlled molten pool thermal history, the deposited wall exhibited an on-set of waviness which is significantly visible after the 80th layer as shown in Fig. 6. The reasons for this could be a fluctuation in the powder mass flow rate, burning of the reused oxidized powder particles, oxidation of molten pool due to some random event, etc. These variables or otherwise called noise in the process cannot be eliminated completely but can be reduced by using an enclosed inert chamber, limiting the re-use of the powder, and using a powder feeder with precise control. However, this increases both the capital and operation costs. The subsequent section discusses the method to mitigate the generated waviness, yet this cannot be considered as a substitute or alternative to the previously discussed solutions.
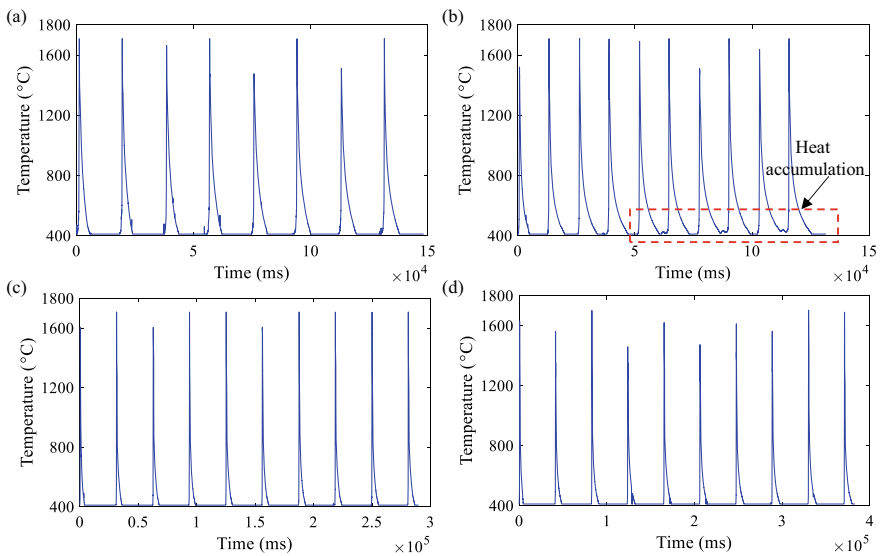

Fig. 4 Molten pool thermal cycles **a** 600 W, 650 mm/min, 11th to 20th layers, no interpass delay, **b** 600 W, 950 mm/min, 31st to 40th layer, no interpass delay, **c** 600 W, 1100 mm/min, 41st to 50th layer, 20 s interpass delay and **d** 600 W, 1100 mm/min, 200th to 212th 30 s interpass delay
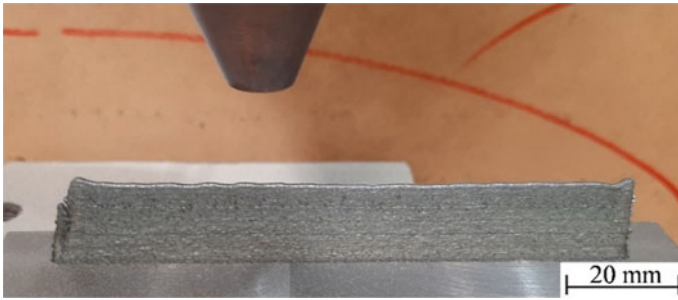
Fig. 5 Geometry of multi-layered Inconel 718 thin wall with varying speed and interpass delay (40 layers)
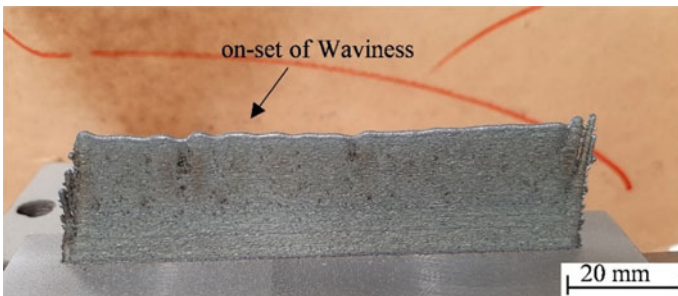
Fig. 6 On-set of waviness (80 layers)

3.3 Controlling Waviness Through Adjustment of Stand-Off Distance

One of the ways to mitigate the generated waviness in the case of thin wall deposition is to selectively deposit more material in the valley and less on the peaks. This can be achieved by a proper understanding of the powder flow characteristics of a given nozzle. Figure 7a shows the powder flow characteristics of the nozzle used in the present study, i.e., the location of the powder focusing distance from the nozzle tip and the powder footprint at that location for 25 g/min powder mass flow rate and 40 l/min carrier gas flow rate.

Further, Fig. 7b shows the laser-powder interaction zone (in pale pink color) without any substrate below the nozzle. The relative location of the substrate surface with respect to the powder focusing point or the laser-material interaction zone greatly affects the amount of material deposited or in other words the catchment efficiency. Figure 8 shows the effect of the relative position of the substrate with respect to the powder focusing point. In the case of 15-mm SOD, the powder focusing point is below the substrate, i.e., the powder is still not in focused condition, or the footprint of the powder is large relative to the spot diameter being used as well as the length
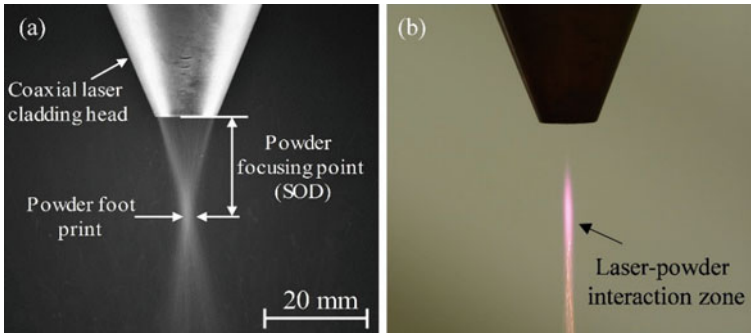
Fig. 7 **a** Powder stream and its characteristic parameters at powder mass flow rate and carrier gas flow rate of 25 gm/min and 40 l/min, respectively and **b** the laser-material interaction zone
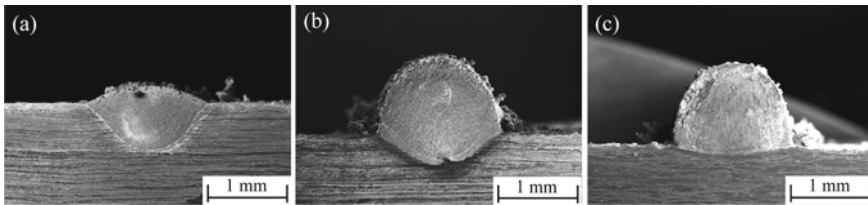
Fig. 8 Effect of stand-off distance on bead geometry **a** 15 mm, **b** 20 mm, and **c** 25 mm (600 W, 600 mm/min, 2.2-mm spot diameter, 25 g/min)

of laser-material (powder) interaction zone in such case is less, resulting in the lower deposition as shown in Fig. 8a.

In the case of 20-mm SOD, where the powder almost focuses on the substrate surface, the deposition or catchment efficiency has increased forming a proper clad track with the minimum amount of dilution or remelting of the substrate or previously deposited layer as shown in Fig. 8b. In the case of 25-mm SOD, the powder focusing point is 5 mm above the surface of the substrate, increasing the laser-powder material interaction length or time. This reduces the laser power reaching the surface while increasing the percentage of laser energy coupled with the powder material [16]. Therefore, as shown in Fig. 8c, a clad track with the minimum amount of substrate remelting will be formed compared to the other two cases discussed. Thus, from these results, it can be inferred that by adjusting the relative position of the powder focusing point with respect to waviness; one can mitigate the surface undulations. Therefore, from layer number 160, the SOD, i.e., the distance between the nozzle tip and the peak was maintained as shown in Table 1, such that deposition of the material was maximum in the valley while it was minimum in the peak resulting in the relatively uniform wall even after deposition 212 layers, as shown in Fig. 9. Thus, the proposed method can be effectively used for the mitigation of waviness generated in multi-layer thin wall deposition. One of the main drawbacks of the overall process described in this study is the continuous need for human/operator

Fig. 9 Wall with mitigated waviness (212 layers)

intervention. This can be reduced to the maximum extent through the use of various displacement sensors [17] along the pyrometers and feedback control systems which will be the future direction.

4 Conclusions

In the present study, the variation in the molten pool thermal history with the layer number in the case of laser-directed energy deposition of thin Inconel 718 wall was monitored in real time using an IR pyrometer. Based on the molten pool thermal history, the following conclusions, and the strategies for modification of process parameters from layer to layer was reported:

1. In the case of continuous deposition without interpass delay, the heat accumulation in the thin wall takes place significantly and can be clearly predicted from the molten pool thermal cycles.
2. Based on the molten pool thermal cycles, the scan speed can be varied up to a certain extent to keep the pre-deposited layer temperature below the threshold level.
3. Beyond the threshold level, introducing the interpass delay for maintaining the pre-deposited layer temperature within the permissible level will significantly help in controlling the waviness.
4. Further, the existing waviness can be effectively mitigated by adjusting the relative position of the powder focusing point with respect to the peak and valley, i.e., by keeping the powder focusing point on the valley.

References

1. Monzón, M., Ortega, Z., Martínez, A., Ortega, F.: Standardization in additive manufacturing: activities carried out by international organizations and project. Int. J. Adv. Manuf. Technol. **76**, 1111–1121 (2015)
2. Svetlizky, D., Das, M., Zheng, B., Vyatskikh, A.L., Bose, S., Bandyopadhyay, A., Schoenung, J.M., Lavernia, E.J., Eliaz, N.: Directed energy deposition (DED) additive manufacturing: physical characteristics, defects, challenges and applications. Mater. Today **49**, 271–295 (2021)
3. Zhu, L., Xue, P., Lan, Q., Meng, G., Ren, Y., Yang, Z., Xu, P., Liu, Z.: Recent research and development status of laser cladding: a review. Opt. Laser Technol. **138**, 106915 (2021)
4. Graf, B., Marko, A., Petrat, T., Gumenyuk, A., Rethmeier, M.: 3D laser metal deposition: process steps for additive manufacturing. Welding in the World **62**, 877–883 (2018)
5. Wu, B., Pan, Z., Ding, D., Cuiuri, D., Li, H.: Effects of heat accumulation on microstructure and mechanical properties of Ti6Al4V alloy deposited by wire arc additive manufacturing. Addit. Manuf. **23**, 151–160 (2018)
6. Liu, F.Q., Wei, L., Shi, S.Q., Wei, H.L.: On the varieties of build features during multi-layer laser directed energy deposition. Addit. Manuf. **36**, 101491 (2020)
7. Sadhu, A., Choudhary, A., Sarkar, S., Nair, A.M., Nayak, P., Pawar, S.D., Muvvala, G., Pal, S.K., Nath, A.K.: A study on the influence of substrate pre-heating on mitigation of cracks in direct metal laser deposition of NiCrSiBC-60%WC ceramic coating on Inconel 718. Surf. Coatings Technol. **389**, 125646 (2020)
8. Gudur, S., Nagallapati, V., Pawar, S., Muvvala, G., Simhambhatla, S.: A study on the effect of substrate heating and cooling on bead geometry in wire arc additive manufacturing and its correlation with cooling rate. Mater. Today: Proc. **41**, 431–436 (2021)
9. Trapp, J., Rubenchik, A.M., Guss, G., Matthews, M.J.: In situ absorptivity measurements of metallic powders during laser powder-bed fusion additive manufacturing. Appl. Mater. Today **9**, 341–349 (2017)
10. Chakraborty, A., Tangestani, R., Batmaz, R., Muhammad, W., Plamondon, P., Wessman, A., Yuan, L., Martin, É.: In-process failure analysis of thin-wall structures made by laser powder bed fusion additive manufacturing. J. Mater. Sci. Technol. **98**, 233–243 (2022)
11. Jinoop, A.N., Paul, C.P., Nayak, S.K., Ganesh Kumar, J., Bindra, K.S.: Effect of laser energy per unit powder feed on Hastelloy-X walls built by laser directed energy deposition based additive manufacturing. Opt. Laser Technol. **138**, 106845 (2021)
12. Kim, M.J., Saldana, C.: Thin wall deposition of IN625 using directed energy deposition. J. Manuf. Process **56**, 1366–1373 (2020)
13. Chua, B., Ahn, D.: Estimation method of interpass time for the control of temperature during a directed energy deposition process of a Ti–6Al–4V planar layer. Materials **13**(21), 4935 (2020)
14. Sridharan, N., Bunn, J., Kottman, M., Fancher, C.M., Payzant, A., Noakes, M., Nycz, A., Love, L., Narayanan, B., Babu, S.S.: Consumable development to tailor residual stress in parts fabricated using directed energy deposition processes. Addit. Manuf. **39**, 101837 (2021)
15. Muvvala, G., Karmakar, D.P., Nath, A.K.: In-process detection of microstructural changes in laser cladding ofin-situ Inconel 718/TiC metal matrix composite coating. J. Alloy Compd. **740**, 545–558 (2018)
16. Lia, F., Park, J., Tressler, J., Martukanitz, R.: Partitioning of laser energy during directed energy deposition. Addit. Manuf. **18**, 31–39 (2017)
17. Binega, E., Yang, L., Sohn, H., Cheng, J.C.P.: Online geometry monitoring during directed energy deposition additive manufacturing using laser line scanning. Precis. Eng. **73**, 104–114 (2022)

Development of a Clay 3D Printing Pen

Santosh Kumar ⓘ**, Meshram Himanshu Dheeraj** ⓘ**, Pankaj Kumar Singh** ⓘ**,
Ravi Prakash Singh** ⓘ**, Md. Meraz** ⓘ**, and Pramod Kumar Jain** ⓘ

1   Introduction

Additive manufacturing (3D Printing) is defined as a procedure in which a computer model object is formed by depositing the material in layered style on all surfaces of the sliced model (Fig. 1). A direct link to the machine is established a preparatory code for the CAD items to be printed from a CAD file, and no need for production planning is required. This generative-additive technology has evolved as a disruptive technology for producing complicated parts straight from a CAD model. It has altered the way items are designed, manufactured, distributed, and sold. In 2013, the market revenue of India's 3D printer was $17 million, and by 2021, it has reached $79 million, with applications in biomedical and education sectors growing at a faster rate than other areas [1].

The graphic standards use the digital model (CAD) once it has been obtained in the (.STL) format splitting the surfaces into a triangle element network (mesh) (as shown in Fig. 1b); as a result, triangular facets are used to simplify the representation of the object's internal and external surfaces. With the help of customized software, the model (say Fig. 1a) has been sliced into thin layers (as shown in Fig. 1b, c); the corresponding file is transmitted to the CNC 3D printer which prints (Fig. 1d) the original digital model by layering material on top of previous layers until it becomes a

S. Kumar · M. H. Dheeraj · P. K. Singh (✉) · R. P. Singh · Md. Meraz
Department of Mechanical Engineering, IIT (BHU), Varanasi 221005, India
e-mail: pankaj.krsingh.rs.mec18@itbhu.ac.in

S. Kumar
e-mail: santosh.kumar.mec@iitbhu.ac.in

R. P. Singh
e-mail: ravips.rs.mec16@itbhu.ac.in

P. K. Jain
Department of Mechanical and Industrial Engineering, IIT Roorkee, Roorkee, India
e-mail: pramod.jain@me.iitr.ac.in
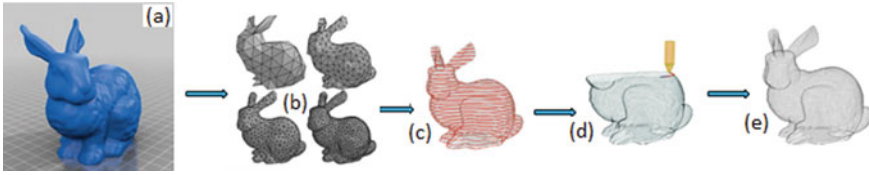
Fig. 1 **a** CAD model, **b** versions of triangulated models, **c** slicing of one model, **d** layer-wise deposition of the model, and **e** Final printed physical model

real object (Fig. 1e). Various steps like slicing, (Gcode) file export, and clay extrusion are involved.

Turner et al. [2] described traditional fused deposition modeling (FDM) as "melting a filament that solidifies as it is pushed out of the nozzle." The material options for FDM are limited to thermoplastics, with acrylonitrile butadiene styrene (ABS) and polylactic acid (PLA) being the most widely used [3]. The extrusion-based 3D printing adds pastes and gels like clay, hydrogel, and silicone to the list of printable inks [4]. 3D printing is possible if the ink can be extruded through a nozzle and preserved its shape after deposition. Because of its adaptability, 3D printing may be employed with various applications, together with cell scaffolds [5] and flexible electronics [6].

An extrusion-based 3D printer has two primary components: the printer, which controls the movement and location of the nozzle, and the extruder, which regulates the material flow. Mainly extrusion system is categorized into conveying screw (delivers material from the hopper to the nozzle) [7], piston operated by a stepper motor (i.e., physical contact between extrusion and material) [8], and pneumatic (utilizes compressed gas as a driving force for extrusion) [4, 9]. The major material utilized in this project is Terracotta clay, which is inexpensive and frequently used for constructing clay models. Clay is a natural material made up mostly of fine-grained minerals, most of which are aluminosilicate plastics [10]. It is considered an inorganic substance. It controls the atmosphere by storing heat in the winter and releasing it in the summer, as well as cleansing the air around it by buffering humidity by taking moisture from the air during high humidity and releasing it at low humidity [11]. Furthermore, clay is reusable, recyclable, and emits less carbon than other construction materials, all of which contribute to a reduction in pollution [10].

2 Experimentation

The experiment was completed through various innovative and challenging stages from conceptualization to actual fabrication and from material selection to printing the models. These stages are extensively explained below.

2.1 Fabrication of the Clay 3D Printing Attachment

The complete fabrication process of the clay 3D printing pen consists of an early prototype, modifications if needed, change in the initial prototype, and finally 3D printing with further changes.

2.1.1 Conceptualization and Early Prototype

The current clay 3D printing attachment was conceptualized initially by taking motivation from a 3D printing pen which works by extruding heated plastic (ABS, PLA) that cools almost instantly into a solid, stable structure, that allows for freehand production of 3D printed things. So, the idea was to fabricate a clay 3D printing pen, i.e., a mechanism capable of extruding clay, and then develop freehand 3D models using clay as the extruding material.

After assembling all the parts shown in Table 1, the first prototype fabricated can be seen in Fig. 2a.

But, owing to the problems in working and size of the motor, one more gear was included in between the existing gears connected to the motor and lead screw. Also, a bearing was installed on the U-bracket, just above the gear facilitating the movement of the lead screw, for smooth functioning of the lead screw.

The new design of the pen after changes can be seen in Fig. 2b. Subsequently, a DC motor controller along with a speed regulator and control switch has been used to change the direction of rotation of the motor as seen in Table 2 for the manual operation of the pen.

2.1.2 Recommendations to Modify the Design

Later, it was decided that rather than freehand printing the clay 3D printing pen should be mounted on a CNC machine and then perform automated 3D printing. So, to remove some limitations in the original design of the pen, a few modifications in the design of the pen were recommended.

In these modifications as shown in Fig. 3, it was suggested that the ram extrusion mechanism for clay extrusion be replaced by a continuous clay supply mechanism using an auger screw. This is because clay needs to be supplied after each outward stroke of the piston in the ram extrusion mechanism. Also, for continuous clay supply, there would be a tank mounted above the cylinder which can be filled with the desired amount of clay as required in the printing operation being performed.

But, implementing these recommended modifications meant the complete overhaul of the initial prototype with completely new parts. So, the recommendations were not implemented, and instead, it was decided to use the same prototype to carry out experiments with the necessary modifications required to make the pen rigid and correct the design flaws.

Table 1 Different parts used in fabricating this pen are as follows

S. No.	Part name	Specifications	Function	Figures
1	Piston cylinder	Aluminum material with external diameter 31 mm and internal diameter 28 mm	To store the clay and later be extruded through a nozzle	
2	Cylinder cap	Mild steel material with external diameter 40.5 mm and internal diameter 31 mm	Connected to the piston cylinder and facilitates smooth axial movement of the lead screw to which the piston is connected and also prevents the lateral vibrations of the lead screw	
3	Gears	Material—Al Two gears of the same module and same no. of teeth—21	Useful in motion transmission from motor to the lead screw	
4	Screw nut	Material—bronze internal diameter—8 mm	Used to convert rotational motion of gear to translational motion of lead screw to push the piston	
5	Lead screw	Material—stainless steel Diameter—8 mm	The piston is attached at one end of the lead screw. The translational motion of the lead screw causes the piston to move axially in the piston cylinder to extrude the clay	
6	Nozzle	Mild steel material with internal diameter 31 mm and extruding diameter 4 mm	Extruding the clay pushed by the piston	

Table 1 (continued)

S. No.	Part name	Specifications	Function	Figures
7	Piston (slotted with O-ring rubber)	Mild steel material	Extruding the clay axially in the cylinder. Two O-ring rubber is fitted to minimize the friction between cylinder and piston and avoids the leakage of clay in the upward direction	
8	Motor	200 rpm with DC supply	Supply power to the whole setup and also supplies the power to lead screw via connected gears	
9	Wooden base with U-bracket		The whole assembly is mounted on a wooden base. The cylinder and motor were fixed in the base	
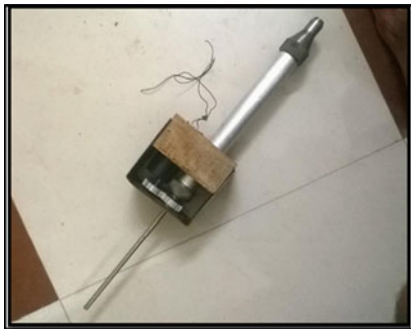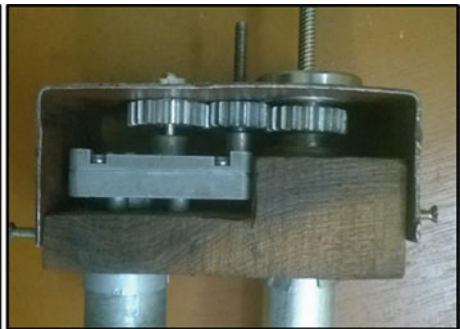
(a)   (b)

Fig. 2 **a** First prototype of clay 3D pen and **b** clay 3D pen with changes in the prototype

Table 2 Specifications of motor controller

Input voltage: DC 9–60 V Output voltage: Linear Output current: 0–20 A Speed regulation type: current Speed regulation range: 0–100% Size: approx. 92 × 52 × 36 mm	

Fig. 3 Assembly of recommended modifications
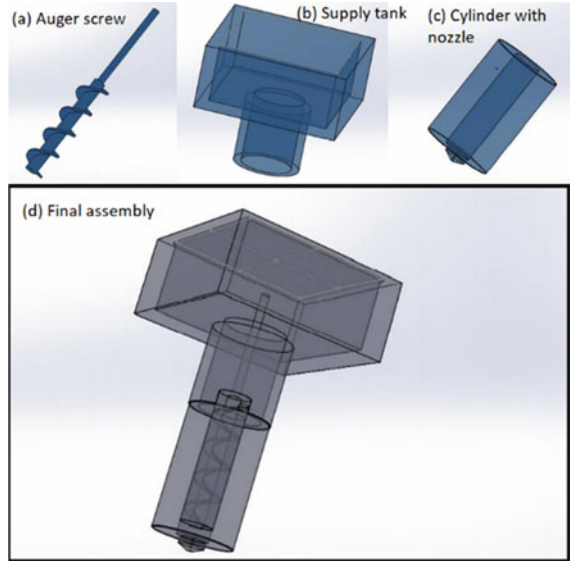
2.1.3 Modifications in the Initial Prototype

Thus, to correct the initial design flaws and to make the pen more rigid, some modifications were made. The metal plates were used to reduce the vibrations and eccentric movements of the gear shafts. Glues and metal wires were used to attach various sections of the pen, such as the motor controller, control switch, speed regulator, and piston cylinder, to the wooden base. This was done to stiffen the structure and reduce vibrations during operation as shown in Fig. 4.

After these modifications, the 3D printing attachment was sufficiently rigid and stable. But, controlling the speed of pistons via motor speed control remained a bigger concern. The torque generated by the motor at slow speeds was not sufficient to extrude the clay. It still could extrude the clay at higher speeds, but the clay flow was too high to print anything as the feed rate of CNC has its limitations.

2.1.4 Additional Adjustments to the 3D Printing Attachment

Thus, the better torque control for piston movement was the only solution, and to do so, the DC motor was replaced with a servo motor (specification shown in Table 3).

The torque control capacity of the servo motor is far better than that of the DC motor, and it can be easily controlled through the same software which runs the CNC machine; so, the concerns of syncing the speeds of CNC and clay extrusion easily got solved. The slotted pipe which was used to stop the lead screw from rotating got the better alternative of two vertical rods of steel.

Fig. 4 Holding and stabilizing arrangement for gears

Holdind and stabilizing arrangement for geras
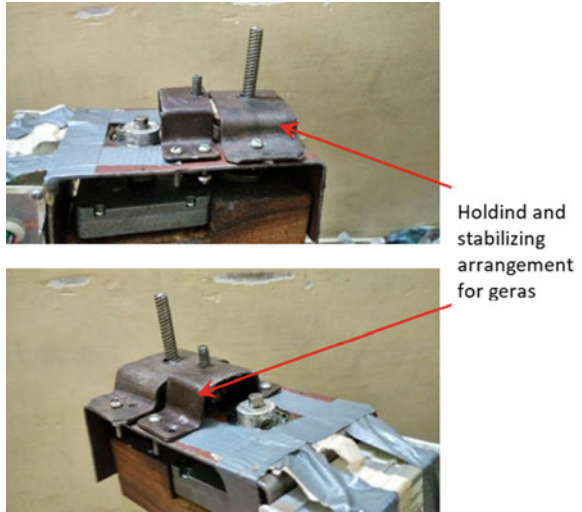
Table 3 Specifications of servo motor

Input 3φ AC 106 V 2.6 A	
Rated output 0.4 kW	
Rated revolution 3000 RPM	

This mechanism is more rigid, stable, and strong as compared to the pipe with the slot as shown in Fig. 5a. After making so many modifications to make the 3D printing attachment more rigid and with better control capability, it was ready in its final form as shown in Fig. 5b, c and ready to 3D print different models.

2.2 Slip Formation

All materials (terracotta clay, water, methylcellulose, and bentonite clay) are mixed well to have a homogeneous mixture. Normal tap water is added in the amount of 15–30% of the mass of clay taken. The water is added slowly in little amounts until the desired viscous mixture is obtained. A methylcellulose powder is added in the very small amounts of 2–4% of the mass of clay. It acts as a binder in the slip as the clay mixture must stay together while it is printed. Bentonite clay powder is also added in very small amounts of 2–5% of the mass of clay. Bentonite is added to increase plasticity and help in setting the extruded clay as early as possible. All of the ingredients are thoroughly combined to ensure that they are evenly distributed
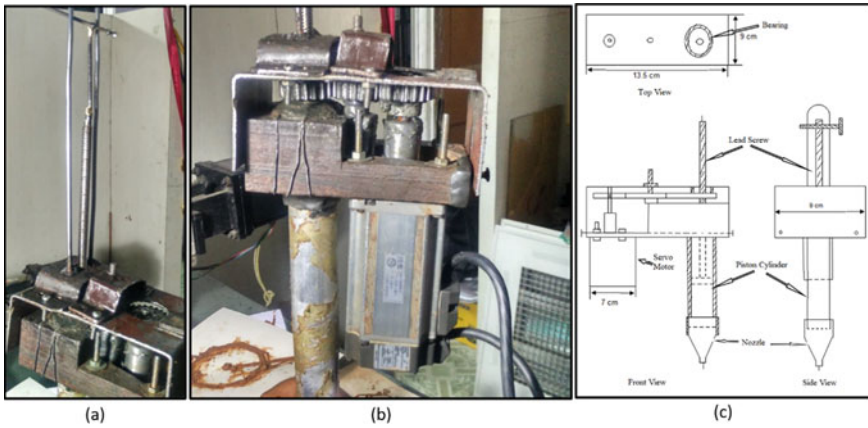
Fig. 5 **a** Two rods to prevent the leadscrew from rotating, **b** final assembly of clay 3D printing attachment, and **c** line diagram of 3D printer assembly

throughout the mixture. This slip is then poured into the piston cylinder and pressed down hard to prevent air from being trapped and causing discontinuous clay extrusion through the nozzle. The slip is then forced through the nozzle by a piston at the required speed to 3D print the desired model.

2.3 CNC Machines with Their Preparatory Codes

To 3D print, a model, the software (CAMSOFT) needs to be provided a CNC code for the model, which then interprets the code and guides the CNC machine through each step to generate the geometry of the object for which the code was written. The CNC machine can be programmed in two different ways: absolute coordinate programming and incremental coordinate programming.

The absolute coordinate system is employed by the CNC machine in this project. As a result, the programs were built to print various models. The specifications of the CNC machine are shown in Table 4.

2.4 3D Printing Parameters for Different Models

After all of the operations were finished, including attachment fabrication, CNC code writing, slip creation, and clay loading in cylinder arrangement, on the CNC machine, several 3D printing trials of diverse models were conducted as shown in Fig. 6a, b. The printing parameters like layer thickness, the width of each layer, and speed of

Table 4 CNC machine specifications

Machine type: CNC (6 axes) with 8-axis controller
Stepper motor—2.8 V, 4.5 A, 3000 rpm, 1.8°/step
Spindle speed: 3000 RPM
Maximum travel: X—49 cm, Y—49 cm, Z—60 cm
Size of table: 20 × 15 × 2 cm
Machine weight: 150 kg
Machine resolution:0.01 mm

the piston (in terms of rpm of the lead screw and axial increment of piston/length of the layer printed) were considered.

The experimented results, i.e., the different models printed and the effects of printing parameters on final parts are shown in the results and discussions section.

(a)　　　　　(b)
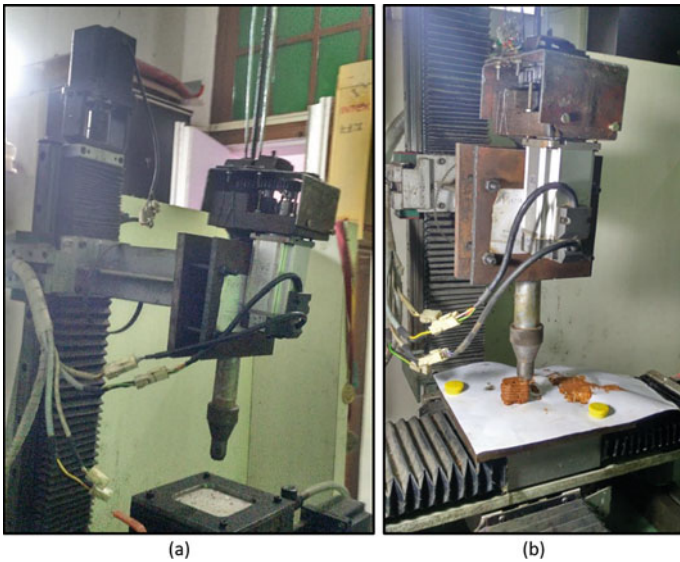
Fig. 6 **a** 3D printing attachment mounted on CNC machine, and **b** Clay 3D printing of a model

3   Results and Discussion

3.1   3D Printed Models
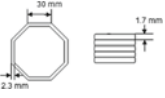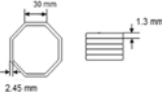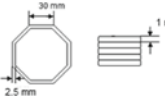
Different models were 3D printed using G-codes for each geometry with suitable dimensions as shown in Table 5.

Table 5   Line diagram, CAD model, printing parameters, and fabricated different models

Different models	Line diagram	CAD model	Printing parameters	Fabricated diagram
Model 1	6 mm, 40 mm, 2 mm, 40 mm		Layer thickness—2 mm, leadscrew—27 rpm, axial increment/length of the layer—1 mm/40 mm, road width—6 mm	
Model 2	6 mm, 40 mm, 3 mm, 40 mm		Layer thickness—3 mm, leadscrew—27 rpm, axial increment/length of the layer—1 mm/40 mm, road width—6 mm	
Model 3	5 mm, 40 mm, 3 mm, 40 mm		Layer thickness—3 mm, leadscrew—27 rpm, axial increment/length of the layer—1 mm/40 mm, road width—5 mm	
Model 4	30 mm, 2 mm, 3.4 mm		Layer thickness—2 mm, leadscrew—6 rpm, axial increment/length of the layer—0.2 mm/30 mm, road width—3.4 mm	
Model 5	30 mm, 2 mm, 2.2 mm		Layer thickness—2 mm, leadscrew—3 rpm, axial increment/length of the layer—0.1 mm/30 mm, road width—2.2 mm	

(continued)

Table 5 (continued)

Different models	Line diagram	CAD model	Printing parameters	Fabricated diagram
Model 6	30 mm / 1.7 mm / 2.3 mm		Layer thickness—1.7 mm, leadscrew—3 rpm, axial increment/length of the layer—0.1 mm/30 mm, road width—2.3 mm	
Model 7	30 mm / 1.3 mm / 2.45 mm		Layer thickness—1.3 mm, leadscrew—3 rpm, axial increment/length of the layer—0.1 mm/30 mm, road width—2.45 mm	
Model 8	30 mm / 1 mm / 2.5 mm		Layer thickness—1 mm, leadscrew—3 rpm, axial increment/length of the layer—0.1 mm/30 mm, road width—2.5 mm	

Model 1 was produced by extruding clay through a CNC machine's 3D printing attachment. Only three layers were printed to see if the pen could extrude the clay or not. The nozzle was 4 mm in diameter. As a result, the road was wider. The water content in this area was roughly 25–26%.

To avoid the problem of clay spreading more than desired, the nozzle diameter was lowered to 4 mm, and the water content was reduced to 20–22% for model 2. The attachment's ability to print diverse geometries with thick and broad layers with greater strength was demonstrated by the continuous printing of several layers.

When compared to the previous model, the nozzle diameter for model 3 was 2.5 mm, resulting in a reduction in road width. While printing this model, the road width appeared to be good at first, but as more layers were printed, the problem of water content varying throughout the mixture became apparent. The clay extruded in the top levels contained less water than the clay extruded in the first three layers. For this model, it was discovered that a homogeneous mixture is required, with all contents evenly distributed throughout the mixture, particularly water.

Model 4 had an octagonal with a 2.5-mm nozzle diameter and a 30 mm length on each side. The geometry of the models was kept the same from model 4 onward so that additional characteristics like road width, layer thickness, and piston speed could be compared. At a piston speed of '0.2 mm increment for the 30 mm length of layer printed,' clay extrusion was quick in this model, resulting in a wider road, which was not desired. As a result, the piston speed had to be reduced.

For model 5, the road width and piston speed were decreased to the previous model and realized that clay extrusion was too slow at low piston speed to continuously fill the layer height of 2 mm. In addition, the successive layers were unable to adhere adequately. The piston speed was low enough that the tiny layers of clay were extruded as required. However, because of the slow rate, the layer height had to be lowered.

During model 5, the height of the layer was too high, but piston speed was too low. So, for model 6, the layer height was reduced keeping the piston speed the same. A layer thickness of 1.7 mm produced superior results for the specified piston speed. The thickness of the layers can be lowered further, and eventually, optimum parameters can be determined.

For model 7, the layer thickness was further lowered while all other parameters remained unchanged. When compared to the prior model, this one had improved attributes in several areas. The layers seemed to be well connected, giving the product strength. Road width was also small enough, as required in every model.

For model 8, to test the characteristics at very low layer height, the layer thickness was further lowered. It was found in this experiment that the layers were nearly blending. The successive layers heavily compressed the prior layers, causing the material to leak out between them.

3.2 Optimization of Printing Parameters

As can be seen in the 3D printing of numerous models described above, little alterations in the value of individual parameters cause changes in remaining parameters that alter the final product's attributes such as strength. These modifications also affect the way clay is extruded layer by layer, as well as the ability of these layers to bind together.

As a result, by comparing the values of each model's parameters and observing the printed goods, we were able to quickly establish the optimal values for the parameters, resulting in a superior 3D printed product with better properties as shown in Table 6.

The flow of clay through the nozzle fluctuates when the nozzle diameter is changed, according to the law of continuity. To manage the speed of clay flowing through the nozzle, the piston speed should be adjusted in tandem with the nozzle diameter.

Table 6 Optimized printing parameters

Diameter of nozzle	2.5 mm
Content of water	18–20%
Height of layer	1.3 mm
Road width	2.45 mm
Piston speed	0.1 mm increment for the 30 mm length of layer printed

The optimal values of several parameters that might be picked for any other printing process were provided in Table 6 after researching and witnessing the 3D printing of the preceding models.

4 Conclusions

3D printing is a rapidly rising technology, and the same is true with the 3D printing industry. Thus, the theoretical investigation of numerous 3D printing technologies as well as the possibility of combining them with additional technologies and different materials is necessary, in addition to their practical, operational prototypes being fabricated and evaluated to check the theoretical results. The relevance of the theoretical results in a particular surrounding can only be verified by the practical results of the same type.

The goal of this research was to fabricate the clay 3D printing attachment which could be mounted on the CNC machine and then perform various experiments to generate a set of printing parameters that can give the best results for this combination of 3D printing attachment and the CNC machine. The results obtained are given below:

1. After numerous revisions to the original prototype, the 3D printing attachment was successfully constructed in its current form. The clay-filled attachment was then rigidly attached to the CNC machine to perform printing operations.
2. When the piston speed is modified, the amount of clay extruded through the nozzle changes, causing the road width to alter.
3. Changing the layer height modified the road width and, depending on the degree of compression generated by the nozzle, it also affected binding between consecutive layers.
4. The clay flow rate through the nozzle and the thickness of the layers were both modified by changing the nozzle diameter. As a result of the change in nozzle diameter, modifications in piston speed were required to keep printing at the optimal rate.
5. Following the analysis of the outcomes of numerous trials, a set of printing parameters was developed that can improve printing results.

References

1. 6Wresearch Homepage. https://www.6wresearch.com/press-release/india-3d-printer-market-2015-2021-share-news-forecasts-size.
2. Turner, B., Strong, R.A., Gold, S.: A review of melt extrusion additive manufacturing processes: I. Process design and modeling, Rapid Prototyp. J. **20**, 192–204 (2014)
3. Kuo, C.C., Liu, L.C., Teng, W.F., Chang, H.Y., Chien, F.M., Liao, S.J., Kuo, W.F., Chen, C.M.: Preparation of starch/acrylonitrile-butadiene-styrene copolymers (ABS) biomass alloys and their feasible evaluation for 3D printing applications. Compos. B Eng. **86**, 36–39 (2016)
4. Hölzl, K., Lin, S., Tytgat, L., Van Vlierberghe, S., Gu, L., Ovsianikov, A.: Bioink properties before, during and after 3D bioprinting. Biofabrication **8**, 32002 (2016)
5. Ouyang, L., Yao, R., Zhao, Y., Sun, W.: Effect of bioink properties on printability and cell viability for 3D bioplotting of embryonic stem cells. Biofabrication **8**, 35020 (2016)
6. Shin, S.R., Farzad, R., Tamayol, A., Manoharan, V., Mostafalu, P., Zhang, Y.S., Akbari, M., Jung, S.M., Kim, D., Comotto, M., Annabi, N., Al-Hazmi, F.E., Dokmeci, M.R., Khademhosseini, A.: A bioactive carbon nanotube-based ink for printing 2D and 3D flexible electronics. Adv. Mater. **28**, 3280–3289 (2016)
7. Wang, L., Zhang, M., Bhandari, B., Yang, C.: Investigation on fish surimi gel as promising food material for 3D printing. J. Food Eng. 1–8 (2017)
8. Li, W., Ghazanfari, A., Leu, M.C., Landers, R.G.: Methods of extrusion on demand for high solids loading ceramic paste in freeform extrusion fabrication. Int. Solid Freeform Fab. Symp. 332–345 (2015)
9. Hinton, T.J., Jallerat, Q., Palchesko, R.N., Park, J.H., Grodzicki, M.S., Shue, H.-J., Ramadan, M.H., Hudson, A.R., Feinberg, A.W.: Three-dimensional printing of complex biological structures by freeform reversible embedding of suspended hydrogels. Sci. Adv. 1 (2015)
10. Lourenco, P., Fernandes, F., Castro, F.: Handmade clay bricks: chemical, physical and mechanical properties. Int. J. Archit. Heritage (2010)
11. Ayadi, A.J., Soro, J., Kamoun, A., Baklouti, S.: Study of clay's mineralogy effect on rheological behavior of ceramic suspensions using an experimental design. Int. J. Recent Res. 374–385 (2013)

Modeling of Inconel Powder Flow and Thermal Distribution During the Direct Energy Deposition Process

Dharmendra Kumar ⬤**, Ojas Praveen Rahate** ⬤**, Murshid Imam** ⬤**, J. John Rozario Jegaraj** ⬤**, and Viswanath Chinthapenta** ⬤

1 Introduction

Additive manufacturing (AM) is layer-by-layer construction of the component. Of late, AM of metals and alloys is catching up. Recent manufacturing technologies such as electron beam melting, selective laser melting, and direct metal laser sintering have opened up enormous avenues for powder-based AM [1]. Further, different printing solutions for the powder bed fusion (PBF) are available from several OEMs such as 3D systems, AddUp, Arcam, Concept Laser, DMG Mori, EOS, Renishaw, Sisma, SLM Solutions, Trumpf, Aconity3D, Matsura, Velo3D, Aurora Labs, Sharebot, Xact Metal, OR Laser, among many others. However, the PBF-based component created for usage in the high-temperature application is still developing. Further, in the initial developmental stage, the AM is expensive due to challenges involved in atomization of the metal powders, laser control, heat treatment, powder re-usage, etc.

A brief review of the literature on solidification studies is discussed. Yao et al. [2] studied the control process parameters of DED-based additively manufactured components considering laser and powder properties. They used the DEM method

D. Kumar · O. P. Rahate · M. Imam
Mechanical Engineering, IIT Patna, Patna 801103, India
e-mail: dharmendra_2011me05@iitp.ac.in

O. P. Rahate
e-mail: ojas_1911me12@iitp.ac.in

M. Imam
e-mail: murshid@iitp.ac.in

J. John Rozario Jegaraj
Defence Research and Development Laboratory, Hyderabad 500058, India
e-mail: johnmfrg@drdl.drdo.in

V. Chinthapenta (✉)
Mechanical and Aerospace Engineering, IIT Hyderabad, Hyderabad 502284, India
e-mail: viswanath@mae.iith.ac.in

to generate the powder particles. They used a movable heat source model to capture the interaction between particles and laser. They simulated the solidification process of DED-AM using a combined phase-field and thermal model. Their experimental studies showed that finer side surface equiaxed grains are achieved with increased laser power due to the increment of the temperature gradient. Further, showed that increased temperature gradient during solidification can be achieved by decreasing the scanning speed.

Yu and Zhao [3] investigated a class of granular media involving thermal-induced phase changes by coupling DEM and computational fluid dynamics (CFD). Their experiments examined three key SLM input parameters: laser power, laser energy distribution, and hatch distance. Zhang and Liao [4] developed the phase-field solid-state sintering (SLS) model to predict the evolving microstructure during the process. Their model predicted the growth of the neck for various metallic materials. Panwisawas and Sovani [5] modeled the additive manufacturing of nickel-based super-alloys. They predicted features such as melting, sub-surface morphology, and porosity during the single pass of SLM.

The present work attempts to capture the influence of the particles' size on the powder flow using the simulation framework. Unlike conventional manufacturing, as discussed above, AM is multi-scale and multi-physics in nature [6]. Hence, it comes with several modeling challenges. Further, in the PBF method, powder particles are melted or sintered to achieve a continuum. However, there are limited studies in literature focusing on connecting the discrete particles to the continuum simulations. Hence it requires modeling the powder particles. In this effort, the discrete element method (DEM) is quite useful [7]. In this investigation, the role of the size of the particle, powder flow, and laser intensity in the printing of the metals is being explored at powder scale, later, the thermal simulations.

The outline of this paper is as follows: In Sect. 2, DEM methodology and modeling aspects are briefed. Section 3 presents brief results and discussions obtained from our preliminary investigations.

2 Simulation Methodology

In the early 1970s, discrete element modeling (DEM) is developed by Cundall [8, 9]. Unlike continuum, the DEM method uses few parameters in modeling a discontinuous system. Figure 1 shows each particle's force and moment computation due to the applied and contact forces. The individual particles' acceleration, velocity, and position are computed iteratively depending on the interactive forces.

The laser head model with four nozzles to disburse the powder particles was simulated using the DEM. The laser head dimensions were chosen similar to that of Yao et al. [2]. Figure 2 shows the CAD model of the laser head (all dimensions are in mm).
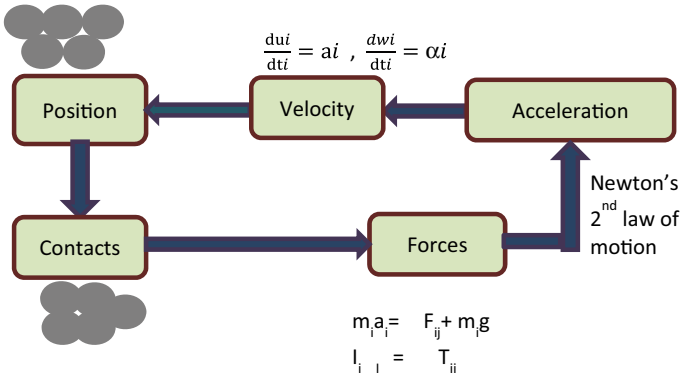
Fig. 1 Position, velocity, and acceleration of the particles [8, 9]
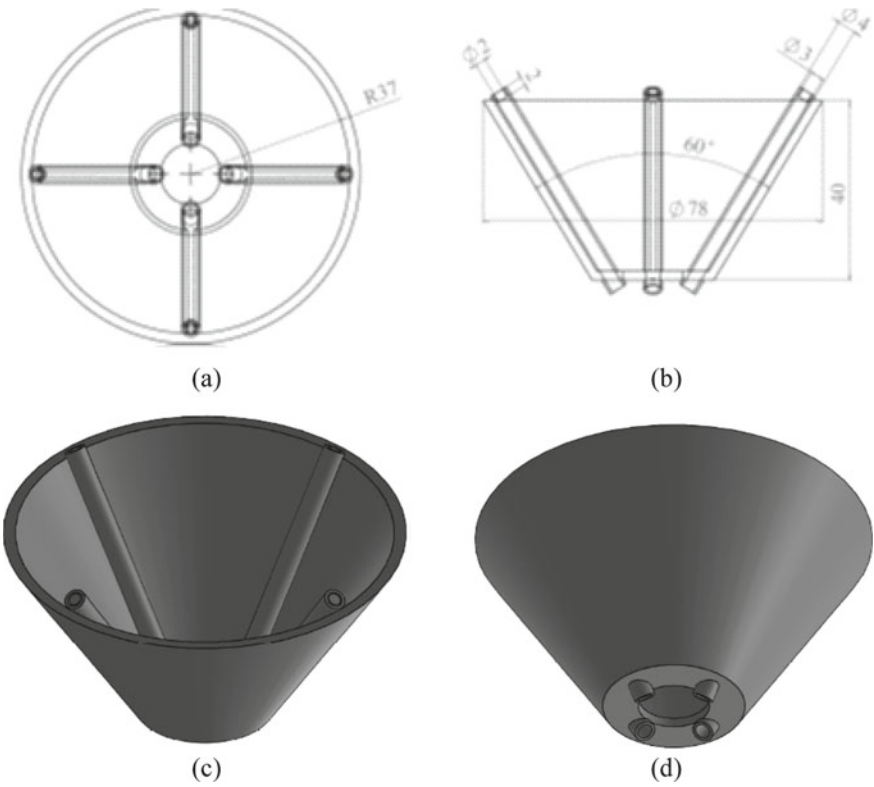
Fig. 2 Laser head with nozzle. **a** Top view. **b** Front view. **c–d** 3D view

3   Results and Discussions

The first phase of process modeling of SLM is to model the deposition of the particles from the laser head. In this study, the laser head was modeled, as shown in Fig. 2. A powder flow rate of 2 m/s in the vertical direction (206 g/s) with bi-particulate spherical powder of sizes 20 and 40 microns in diameter is used to simulate the particle deposition in a ratio of 3:7. In actual conditions, there would be a deviation from the spherical shape. However, the DEM of the arbitrary shape particles is still at the nascent stage [10].

Figure 3a shows the particulate distribution during the deposition captured through DEM simulations performed in the LIGGGHTS open-source software. The particles freely flow under gravity through the four nozzles of the laser head. Figure 3b illustrates the linear velocity distribution of the particles. The linear velocity magnitude varies between 0.15 and 2.7 m/s. Figure 3c illustrates the angular velocity magnitude varying from 4.2e3 to 8.4e4 rad/s. For the current simulation, the coefficient of restitution of 0.5 and coefficient of friction 0.5, Young modulus of 120 GPa, and poisons ratio of 0.41 are considered. The force on the particle is calculated as shown in Sect. 2. Figure 3d illustrates the force magnitude on the particles. Based on the force value, the position is updated iteratively.

(a) Particle distribution   (b) Linear velocity magnitude

(c) Angular velocity magnitude   (d) Force magnitude
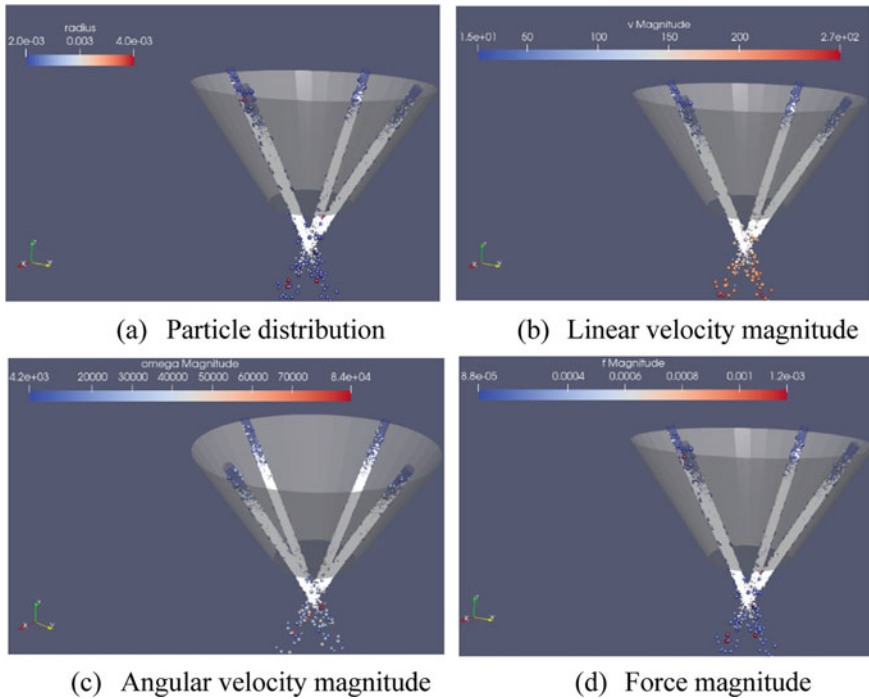
Fig. 3 In718 powder flow simulation from LIGGGHTS
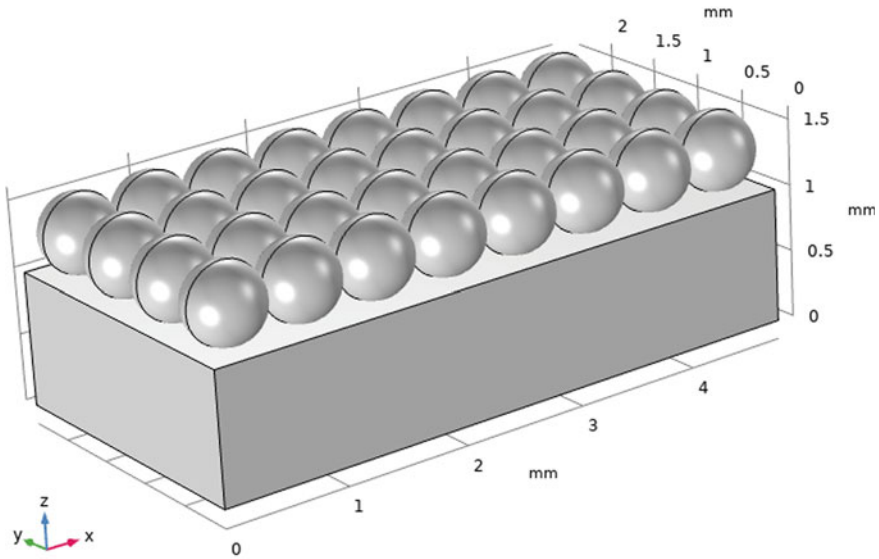
Fig. 4 Geometry of the particle for the thermal analysis

Thermal analysis of the particles sprayed over the baseplate simulation is carried out in the COMSOL. Figure 4 represents the base plate with equally spaced aluminum spherical particles. The particles of 0.6 mm diameter were spaced adjacent to each other. An array of 4 by 8 particles is considered for modeling purposes. Due to computational challenges, uniform and straightforward geometry is used. However, in the actual circumstance, the particle distribution is seldom not uniform [10]. Moreover, particle distribution also plays a role in thermal distribution.

The geometry considered in Fig. 4 was solved in COMSOL multi-physics. The mesh of the thermal model is illustrated in Fig. 5. A fine mesh was used to capture the temperature gradients. Hence, the total number of elements in the mesh used was 228,416. Here, both the base plate and the particles were meshed using tetrahedron elements.

The laser source was modeled as a moving line source of 0.6 mm width with a power of 50 J and an energy density of 7.3e3 GW/m^3. The velocity of the laser source considered in these simulations was 0.7 mm/min. The laser heat source was moved in a raster pattern over the particles.

Figure 6 demonstrates the surface temperature contour plot due to the moving laser source at time 5.9 s. It is observed that the temperature in the vicinity of the laser sources exceed is exceedingly high.

The temperature history of two-point A and B is shown in Fig. 6 is plotted in Fig. 7a. It can be seen that a gradual temperature rise is due to the approaching heat source. Once the heat source is within 1 mm, a steep increase in the temperature is observed. After the laser heat source moves past the point of observation, a steep decrease in temperature is observed, followed by a gradual decrease in temperature
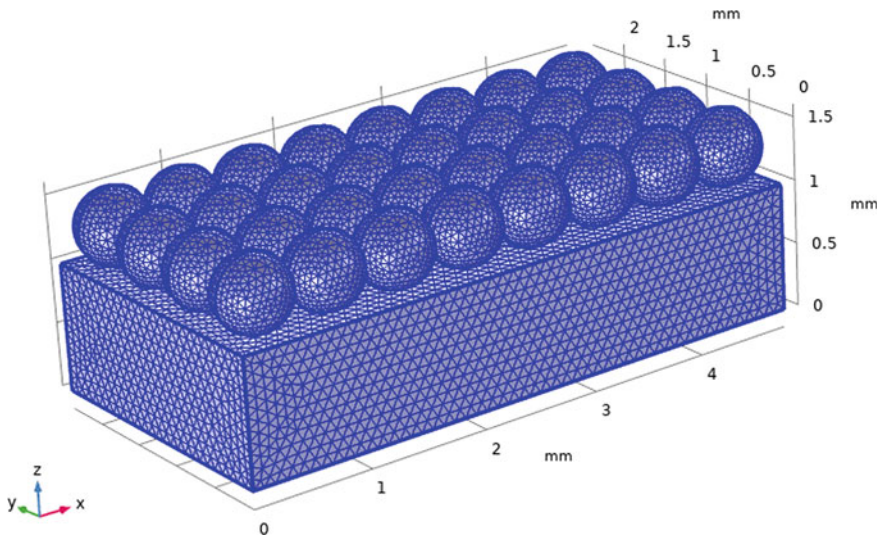
Fig. 5 Meshed thermal model
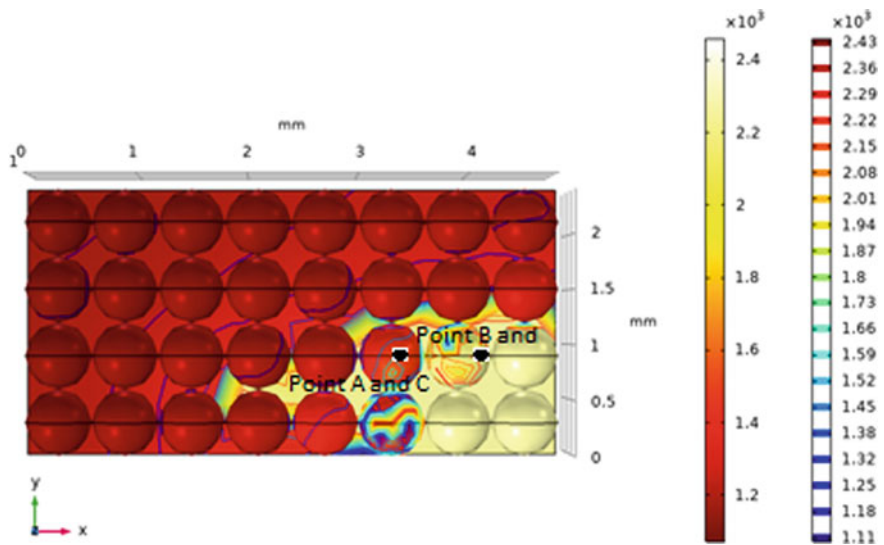
Fig. 6 Temperature contours at time of 5.9 s

due to the re-distribution of heat. It can be observed that the slope of the steep increase in heat source is much higher than the slope of the steep decrease in temperature. The temperature history of the different material points (C and D) in the deposition has a huge variation (see Fig. 7b). This variation depends on the location (depth),

(a) Location A (3.3, 0, 0.95) and B (4,0,0.95)

(b) Location C (3.3, 1, 0.95) and D (4,1,0.95)
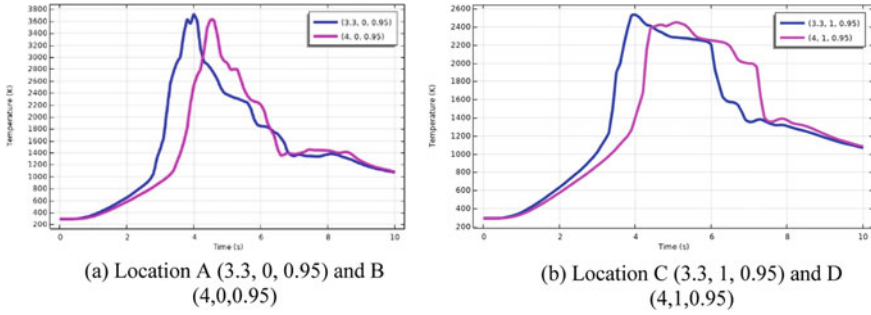
Fig. 7 Temperature history due to moving heat source

thermal properties, base plate conductivity, moving heat source pattern, and heat source velocity.

4 Conclusions

Using DEM, particle distribution through the four nozzles of the laser head is modeled using the open-source software LIGGGHTS. Further, the heat transfer model of uniformly spaced particles due to moving laser sources is modeled in COMSOL to obtain the thermal distribution in the particles and the base plate. It is observed that temperatures as high as 3600 K are observed. Later, the particle distribution, laser interaction, and laser heating will be extended to study the laser sintering between the discrete particles.

References

1. Samuel, H.H., Peng, L., Abhiram, M., Liang, H.: Additive Manufacturing and its societal impact. Int. J. Manuf. Technol. **67**(5–8), 1191–1203 (2013)
2. Yao, X.X., Ge, P., Li, J.Y., Wang, Y.F., Li, T., Liu, W.W., Zhang, Z.: Controlling the solidification process parameters of direct energy deposition additive manufacturing considering laser and powder properties. CMS **182**, 109788 (2020)
3. Yu, T., Zhao, J.: Semi-coupled resolved CFD–DEM simulation of powder-based selective laser melting for additive manufacturing. Comp. Met. App. Mech. Eng. **377**, 113707 (2021)
4. Zhang, X., Liao, Y.: A phase-field model for solid-state selective laser sintering of metallic materials. Pow. Tech. **339**, 677–685 (2018)
5. Panwisawas, C., Sovani, Y., Anderson, M.J., Turner, R., Palumbo, N.M., Saunders, B.C., Choquet, I., Brooks, J.W., Basoalto, H.C.: A multi-scale multi-physics approach to modeling

of additive manufacturing in nickel-based super-alloys. In: Super-alloys 2016: Proceedings of the 13th International Symposium of Superalloys, pp. 1021–1030 (2016)

6. John, G.M., Samuel, L., Athanasios, I.: Multi-physics challenges for controlling layered manufacturing process targeting thermomechanical performance. In: ASME 2014 International Design Engineering Technical Conferences & Computers and Information in Engineering Conference IDETC/CIE 2014, vol. I924DV, pp. 1–11 (2014)

7. John, C.S., Athanasios, P.I., John, G.M.: Discrete element modeling of particle-based additive manufacturing processes. Comp. Met. App. Mech. Eng. **305**, 537–561 (2016)

8. Cundall, P.A.: A computer model for simulating progressive large-scale movements in block rock systems. In: Proceedings of the Symposium of the International Society of Rock Mechanics, Nancy, France, Article 8 (1971)

9. Cundall, P.A.: A computer model for rock-mass behavior using interactive graphics for the input and output of geomechanical data. In: Report for Contract number DACW45-74-C-0066, for the Missouri River Division, U.S. Army Corps of Engineers, University of Minnesota, Minneapolis, Minnesota (1974)

10. Feng, Y.T.: An energy-conserving contact theory for discrete element modeling of arbitrarily shaped particles: Contact volume-based model and computational issues. Comp. Meth. App. Mech. Eng. **373**, 113493 (2021)

Experimental Study on Chemical Polishing of Laser Powder Bed Fusion-Based Inconel 718 Features

B. Srinivas [ID]**, M. M. Basha** [ID]**, and M. R. Sankar** [ID]

1 Introduction

In additive manufacturing (AM), the material is added layer by layer rather than removing it like most unconventional machining methods, and complex near net shape parts can be produced using AM technologies [1]. The additive manufactured parts surfaces are generally rough and need a post-processing process, i.e., finishing processes like shot peening, vibratory finishing, laser polishing, chemical polishing, electrolytic polishing, etc. [2, 3]. This study aims to study the chemical polishing of Inconel alloy manufactured by additive manufacturing technique of selective laser melting (SLM). SLM is a powder-based additive manufacturing process in which powder is used as raw material to produce metallic components usually under vacuum or inert atmosphere [2, 3]. Chemical polishing is applicable for both conventional as well as additive manufacturing. The most incurring problem of the additive manufacturing process is loose powder particles that are partially sintered particles that stick on the surface. This problem needs to be addressed by a feasible and acceptable post-processing technique. Here, chemical polishing is one of the techniques which serves the purpose [5]. Researchers tried different iterations to get the optimal chemical composition, chemical concentration, optimal polishing time, and corresponding dynamic action [6]. Due to surface irregularities, there is a chance to crack formation during functionality. If it is finished using chemical polishing, then cracks are closed,

B. Srinivas (✉) · M. M. Basha · M. R. Sankar
Department of Mechanical Engineering, Indian Institute of Technology Tirupati, Tirupati 517619, India
e-mail: me19m004@iittp.ac.in

M. M. Basha
e-mail: me19d505@iittp.ac.in

M. R. Sankar
e-mail: evmrs@iittp.ac.in

and fatigue strength is increased [3, 7]. The chemical polishing technique is a broad area for research at present and in near future.

Inconel 718 is a Ni-based superalloy that has excellent properties. It has to retain mechanical stability within the range of 253–650 °C, good fatigue strength, corrosion resistance, resistance to oxidation (chromium and molybdenum presence contributes to oxidation resistance), and creep resistance [8]. These are the properties useful in hostile environments or applications like aircraft engines, jet engines, and steam turbine power plants. If parts are manufactured by a conventional method such as casting, then the part needs to be post-processed for improvement of surface morphology and dimensional accuracy. It involves tool wear in conventional machining while finishing Ni-based superalloys. Due to Inconel 718 having good weldability, powder bed fusion could be the prospective candidate for making Inconel 718 parts. To date, no effective chemical polishing solution has been found for nickel-based superalloys. Semi-welded particles are formed in the heat-affected zone by sintering of the loose powder particles nearby melt pool which depends on the energy density of the laser scanning which is related to temperature [9].

2 Chemical Polishing

The mechanism involves in the chemical polishing process or bath is the formation of a passive layer on the surface of the part; generally, the formed layer dissolves in the chemical polishing solution [10]. If it does not dissolve in the solution, then a complexing agent is used to make it soluble in the polishing solution even with a small amount of agitation using an ultrasonic cleaner or magnetic stirrer to increase the polishing rate. The removal of material from the surface of the valleys is less as compared to peaks because of deficiency of water in the pits which was explained clearly in viscous film theory [11]. Figure 1 represents the overall chemical polishing process.

Fig. 1 Chemical polishing process [6]
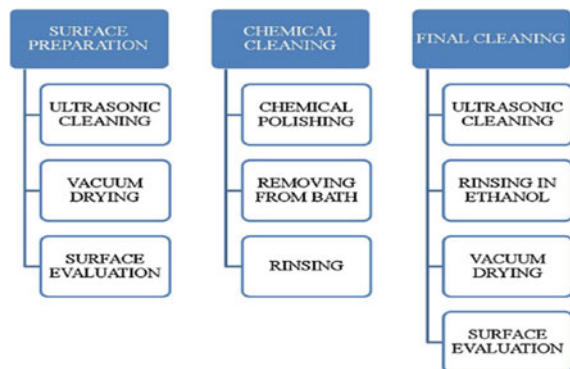
Before polishing, additive manufactured surface needs to be prepared on which loosely bond powder particles are removed using ultrasonic cleaner, and it needs to be dried using a vacuum drier, and then, surface morphology is evaluated. After that actual cleaning is done, i.e., surface is immersed in a chemical bath where polishing takes place removal of extra powder particles from the surface is done, then removal of the part from the bath and rinse it with clean water to ensure removal of any chemical residue. Finally, after the chemical bath, final cleaning is done, and surface evaluation is done [6, 12].

Generally, a chemical bath contains two agents. They are an oxidizing agent and complexing agent. After immersion of a part in the bath, the immediate reaction between bath and surface is the oxidization–reduction process. Oxidizing agent of the solution oxidizes the surface material. Oxidization product is usually not soluble in the polishing solution and adheres to the surface. If the oxidization product is not soluble in the polishing solution, then, the complexing agent reacts with the oxidization product and makes it soluble in the solution. Examples of an oxidizing agent are nitric acid (HNO_3), hydrogen peroxide (H_2O_2), and for a complexing agent for titanium, the sample is hydrofluoric acid (HF). Most often, water is used to dilute the solution [13].

Anodic reaction: where the surface of solid is dissolved in oxidizing solution and surface atom (A) becomes positive by losing an electron.

$$A \rightarrow A^+ + e^-$$
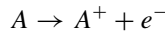
Cathodic reaction: where the oxidizing agent (X) diffuses to the surface and gains the electron.

$$X + e^- \rightarrow X^-$$
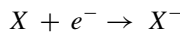
Therefore, the overall reaction would be

$$A + X \rightleftharpoons AX$$
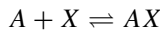
The surface atom can be removed if the compound AX is soluble in the chemical polishing solution otherwise complexing agent should be used to make compound AX soluble. In the chemical polishing of a semiconductor, the polishing constituents react with each other. Aqua regia (HNO_3 + 3HCl) is an example of it and forms chlorine which is not desirable since it contributes to ozone layer depletion. Neda Mohammadian et al. [9] worked on SLM built 3D printed Inconel 625 components to enhance the interior surface quality of tubular structure used in the aerospace industry by reducing the surface roughness, i.e., removing semi-welded particles adhered on powder-based additive manufactured Inconel 625 component surface and to fix the composition of chemical solution with abrasives such that machinery should not be damaged using hybrid mechanism, i.e., with chemical–abrasive flow polishing. The chemical solution consisting of 50% HF + 50% HNO_3 was used

as a chemical solution in chemical assisted abrasive flow finishing technique, since it reduced the surface roughness considerably compared with other solutions like 30% HNO_3 + 10% H_2SO_4 + 10% H_3PO_4 + 50% acetic acid, 64.5% acetic acid (ice cooled) + 35% HNO_3 + 0.5%HCl and 30% HF + 70% HNO_3. Finally, 40 vol.% HF + 40 vol.% HNO_3 + 20 vol.% H_2O (diluted) with abrasives alumina were selected to take care of the machinery. Various polishing techniques were compared in which static chemical polishing achieved R_a = 14.2 μm from 17.2 μm. Huang et al. [14] polished electrochemically Inconel 718 with rotating disk electrodes using $HClO_4$ and CH_3COOH solution with various concentrations. By using 10–20 vol.% $HClO_4$ observed leveled surface without brightening, 30–40 vol.% $HClO_4$ observed both leveled and brightened surface and with 50 vol.% or more $HClO_4$ got matt and gray surface by the mechanism of precipitation of salt film on the surface, and simultaneously, the corrosion resistance was enhanced.

3 Materials and Methods

The 3D printed EOS Inconel 718 sample having a density of 8.15 g/cc was used for experimentation. The sample was the rod of dimensions of 15 mm diameter and 150 mm length which were measured by Vernier Calipers. The powder particles and sample are shown in Fig. 2a, b respectively.

Enough samples were cut using WEDM for various experimentation like microstructural observation, on longitudinal cross-section (section along the longitudinal axis) and on transverse cross-section (a circular section which is perpendicular to the longitudinal axis) concerning building direction which is parallel to the longitudinal axis and for optimizing the constituents of chemical polishing solution, RPM of magnetic stirrer and polishing time thereby improving surface quality. The elemental composition of EOS Inconel 718 was known by scanning electron microscope by point EDS. And elemental composition is given in Table 1.
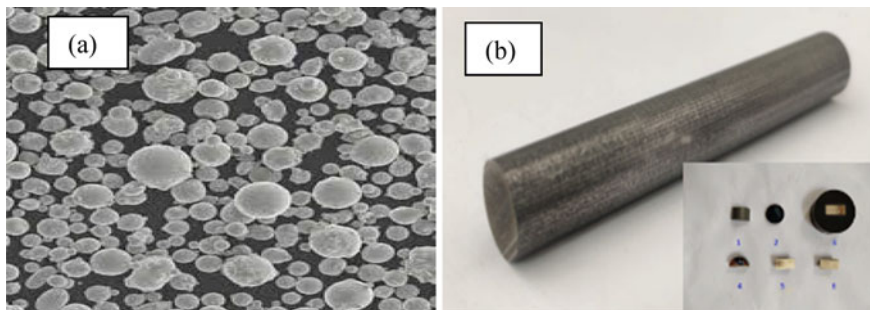
Fig. 2 **a** Inconel 718 particles used in laser powder bed fusion and **b** 3D printed Inconel 718 sample

Table 1 Elemental composition of 3D printed Inconel 718

Element	Ni	Cr	Fe	Ti	Mo	Mn	Al	Ta	Co	Cu
Wt. %	41.08	20.14	16.96	3.64	5.92	1.88	2.2	1.81	2.06	3.44

Microstructures are observed by using optical microscopy and secondary electron microscopy for both longitudinal and transverse cross-sections. Three different types of etchants H_2SO_4 + methanol, ethanol + HCl + $FeCl_3$, and HF + HCl + HNO_3 were tried to optimize the constituents of the bath. Here, a sequence of steps was followed; average surface roughness values were noted before chemical polishing followed by samples were cleaned properly using an ultrasonic cleaner, and then immersed in a chemical bath to allow for chemical polishing. After chemical polishing, samples were cleaned using ultrasonic cleaner, and surface roughness values were measured. For all the samples which are used for experimentation, weights were calculated before and after chemical polishing using digital weighing balance and weight loss % was calculated.

4 Results and Discussion

4.1 Microstructural Studies

The elemental composition of the sample before chemical polishing was known by scanning electron microscope (SEM) with point EDAX. The SEM image with focused point and corresponding SEM graph with a number of counts vs energy are shown in Fig. 3 are shown, respectively, and elemental composition was identified.

The WEDM cut samples longitudinal cross-section and transverse cross-section were subjected to manual polishing using emery papers of grit sizes in the sequence of 120, 240, 400, 600, 800, 1000 and velvet cloth polishing with colloidal silica solution on double disk manual polishing machine. Afterward, these samples were rinsed with distilled water and cleaned with CH_3OH using cotton and again rinsed
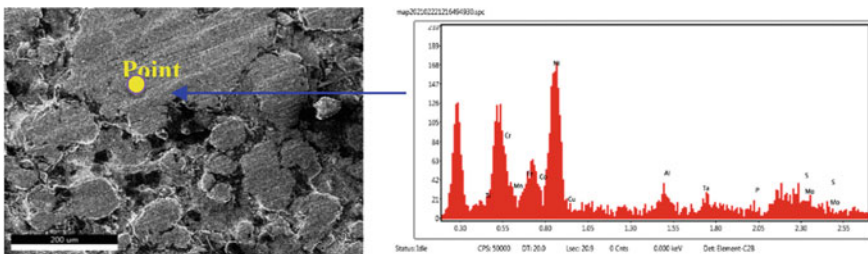
Fig. 3 Surface morphology of the 3D printed Inconel 718 surface before chemical polishing and its energy dispersive spectroscopy pattern
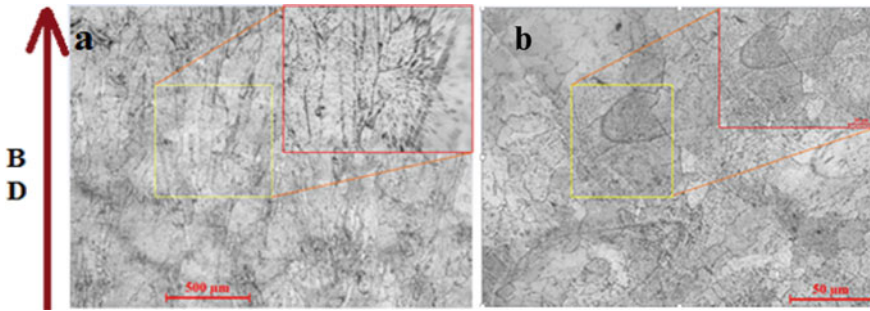
Fig. 4 Optical micrographs of **a** longitudinal and **b** transverse cross-sections. BD stands for build direction which was along the longitudinal axis of the rod

with distilled water, then dried the samples using a heating gun. The etchant prepared based on literature Apparao et al. [15] of 50% HCl, 10% HNO$_3$, 2% HF, and 38% of distilled water, in the same proportion of 5 ml HCl, 1 ml HNO$_3$, 0.2 ml HF, and 3.8 ml distilled water and allowed to react for 40 s then rinsed with distilled water and dried. The etched samples were sent to the optical microscope and therefore observed microstructures for both longitudinal and transverse cross-sections as shown in Fig. 4a, b respectively.

4.2 Chemical Polishing Experiments on Inconel 718

The average surface roughness (R$_a$) of the sample before chemical polishing was 5.786 μm. For chemical polishing, few trails with three different polishing solutions were performed. The selection of chemical polishing solution was taken based on a few factors like the constituent which controls etching and acts as solvent, i.e., methanol, etching and polishing constituent, i.e., H$_2$SO$_4$. The chemical polishing solution was 20 vol.% H$_2$SO$_4$ + methanol was tried with two different samples at different polishing times 60 and 90 min using dynamic action of magnetic stirrer at 250 RPM, and the average surface roughness values 7.1 and 7.452 μm, respectively, were observed after chemical polishing. A magnetic stirrer with 250 rpm was used for polishing, and it makes the surface an active site and leads to rigorous etching locally as shown in Fig. 5. However, there are no pits observed because the H$_2$SO$_4$ acts as a viscous layer over the surface and promotes the local etching. So, higher surface roughness values 7.1 and 7.452 μm were observed which is beyond the initial surface roughness (initial R$_a$ = 5.78 μm). Finally, no considerable results were obtained. Figure 6a, b shown are before and after chemical, polishing using 20 vol.% H$_2$SO$_4$ + methanol with 250 RPM and 90 min polishing time and the corresponding final surface roughness profile over the evaluation length with final R$_a$ = 7.452 μm as shown in Fig. 6c.
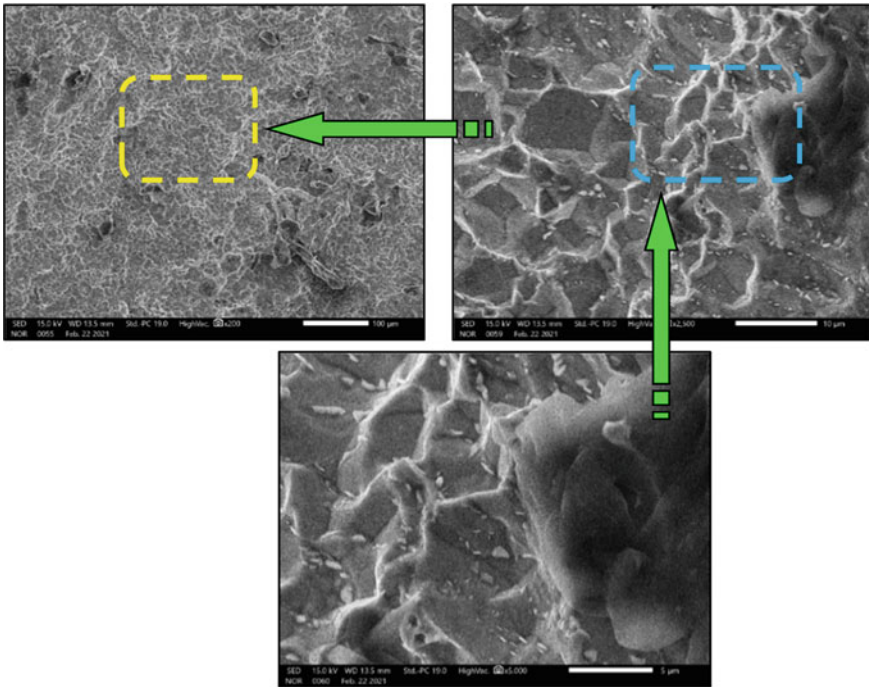
Fig. 5 Surface morphology after chemical polishing using 20 vol.% H_2SO_4 + methanol with 250 RPM and 90 min polishing time
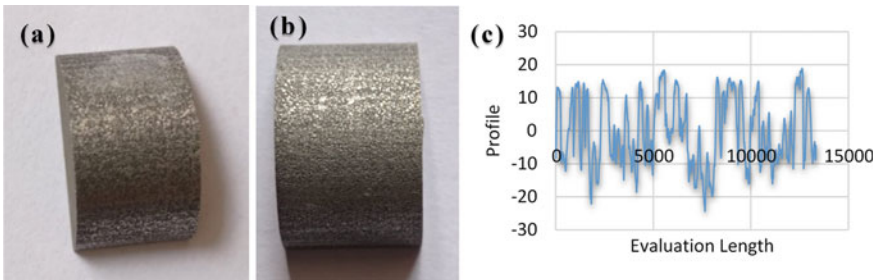
Fig. 6 **a** Before, **b** after chemical polishing, and **c** final surface roughness after chemical polishing

The solution consisting of ethanol (solvent and controls etching), HCl (etches), and $FeCl_3$ (brightening) was considered as another trial and tried to optimize the polishing bath under static conditions without a magnetic stirrer. By varying the ethanol from 10 to 18 ml (in volume) and keeping HCl (2.5 ml) and $FeCl_3$ (0.6 g) are constant and corresponding % weight loss also calculated as shown in Table 2.

While the increasing volume of ethanol to the polishing solution, more oxygen is generated and leads to localized pitting, so surface roughness values were increased.

Table 2 Variation of ethanol in the bath and time under static conditions

Ethanol (ml)	HCl (ml)	FeCl$_3$ (g)	Time (min)	R$_a$ (µm)	%wt. loss
18	2.5	0.6	90	6.39	0.749
10	2.5	0.6	90	5.756	0.399
12	2.5	0.6	90	4.194	0.439

HCl is not acting as viscous, so it can also indirectly influence the generating pits. More pits are generated without showing the difference between the strength of grain and grain boundary as shown in Fig. 7. The solution consists of 12 ml ethanol, 2.5 ml HCl, and 0.6 g with polishing time of 90 min under static conditions without magnetic stirrer gave the better results, i.e., R$_a$ from 5.786 to 4.194 µm, and the respective sample is shown in Fig. 8b, and corresponding final surface roughness profile over evaluation length is shown in Fig. 8c.

The polishing bath consists of HF, HCl, and HNO$_3$ were chosen based on HF acts as a complexing agent (which dissolves the oxide layer), HCl (which participates in etching), and HNO$_3$ acts as an oxidizing agent as well as participates in polishing. The polishing bath was optimized for better results by keeping HF (10 ml) and HCl
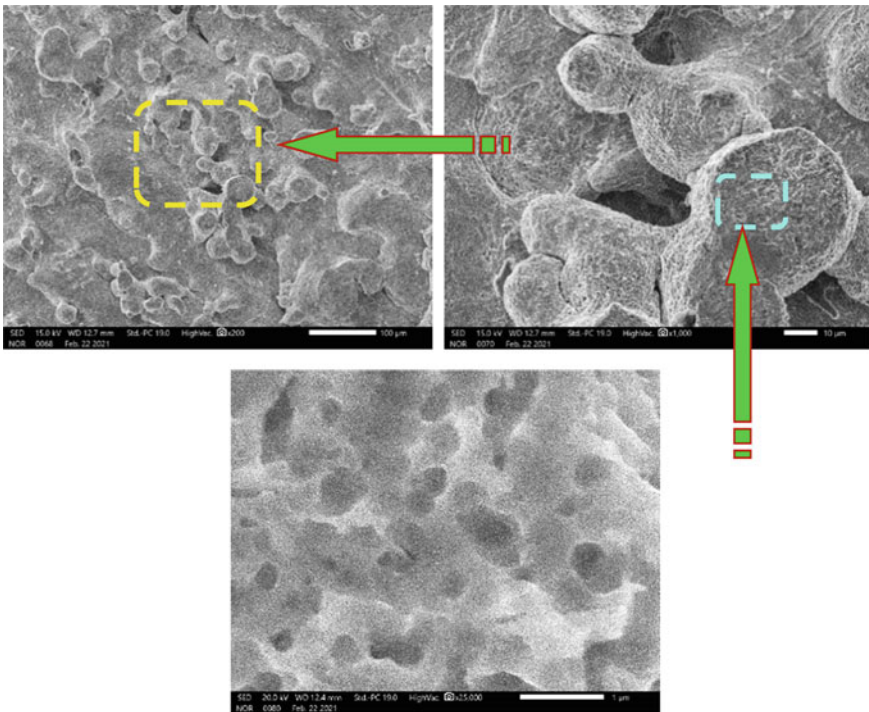
Fig. 7 SEM micrographs for polishing of sample under the static conditions 18 ml ethanol, 2.5 ml HCl, 0.6 FeCl$_3$ (g), 90 min time (R$_a$ = 6.39 µm)
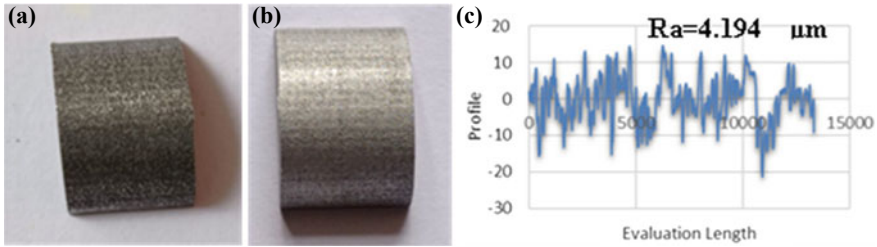
Fig. 8 a Before, b after chemical polishing, and c final surface roughness profile after polishing

Table 3 Variation of HNO$_3$ in the bath under static conditions

HF (ml)	HNO$_3$ (ml)	HCl (ml)	Time (min)	R$_a$ (μm)	%wt. loss
10	10	5	120	6.81	0.321
10	9.8	5	120	7.577	0.270
10	9.5	5	120	8.411	0.299
10	9	5	120	4.072	0.304
10	8.5	5	120	5.96	0.380
10	8	5	120	6.05	0.296

(5 ml) as constants throughout the experimentation and varying HNO$_3$ from 8 to 10 ml with polishing time 120 min under static conditions without magnetic stirrer, and corresponding % wt loss values were calculated as shown in Table 3. Before and after chemical polishing, samples were cleaned in an ultrasonic cleaner for 10 min after polishing bath followed by ultrasonic cleaning average surface roughness values were measured.

Initially, HNO$_3$ acts as an etching solution, so material removal is increasing along with whatever the shape of the surface; therefore, R$_a$ remained constant as shown in Fig. 9; then, it acts as an oxidizing agent, so material removal is decreasing up to a volume of 9.5 ml; consequently, good surface finish was observed. Afterward, pitting could be the reason for increasing the surface roughness values while keep on increasing the volume of HNO$_3$. The optical micrographs for final R$_a$ values 4.072 and 6.81 μm are shown in Fig. 10a, b, respectively.

By using 10 ml HF, 10 ml HNO$_3$, and 5 ml HCl, with a polishing time of 120 min under static conditions without magnetic stirrer, more pits were observed leading to non-homogeneous etching in which grain boundaries appeared which confirms Inconel 718 has stronger grain boundaries than grains as shown in Fig. 11 with R$_a$ = 6.81 μm. Similarly, for other cases in which surface roughness values were increased, this could be the reason.

By using 10 ml HF, 9 ml HNO$_3$, and 5 ml HCl, with a polishing time of 120 min under static conditions without magnetic stirrer, only a few pits were observed leading to homogeneous etching as shown in Fig. 12 with R$_a$ = 4.072 μm which is the better result among other baths. The samples which are shown in Fig. 13a, b are before

Fig. 9 Effect of HNO$_3$ in polishing solution at constant HF, HCl, and time
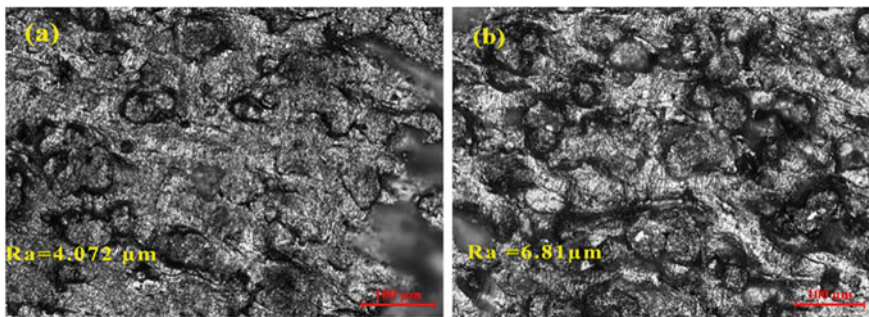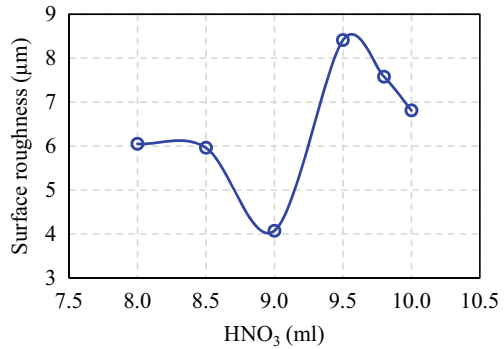
Fig. 10 Optical micrographs after chemical polishing at **a** 9 ml and **b** 10 ml HNO$_3$

polishing and after polishing using 10 ml HF, 9 ml HNO$_3$, and 5 ml HCl, with polishing time 120 min under static conditions, respectively, and Fig. 13c is the corresponding final surface roughness profile after chemical polishing with R_a = 4.072 μm.

5 Conclusions

In this paper, the conclusions are as follow:

- Etchant consisting of 50% HCl, 10% HNO$_3$, 2% HF, and 38% of distilled water was suitable etchant for microstructure observation.
- No remarkable results were observed using chemical polishing with dynamic action, i.e., with a magnetic stirrer at 250 rpm of bath consisting of 20 vol.% H$_2$SO$_4$ and methanol.
- The bath comprised of 12 ml ethanol + 2.5 ml HCl + 0.6 g FeCl$_3$ was the better polishing solution in trail 2 and reduction of surface roughness from R_a = 5.786 to 4.194 μm.
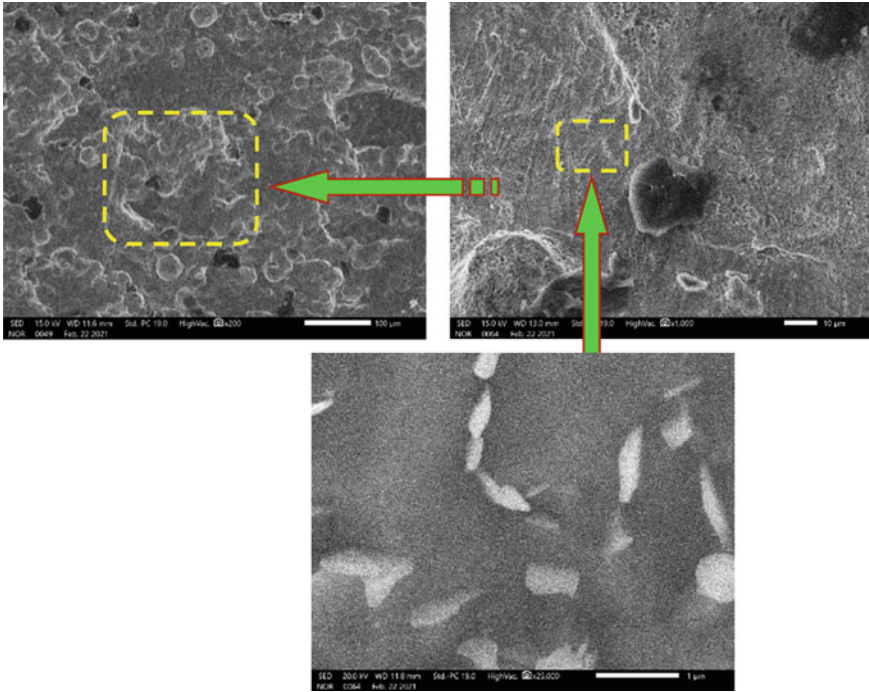
Fig. 11 Surface morphology after chemical polishing using 10 ml HF, 10 ml HNO$_3$, and 5 ml HCl, with polishing time 120 min under static conditions with more pits
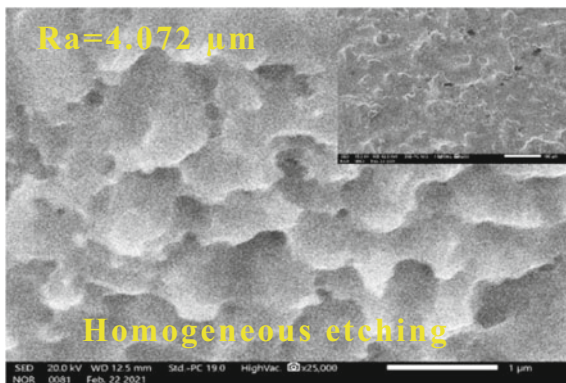
Fig. 12 Surface morphology after chemical polishing using 10 ml HF, 9 ml HNO$_3$, and 5 ml HCl, with polishing time 120 min under static conditions
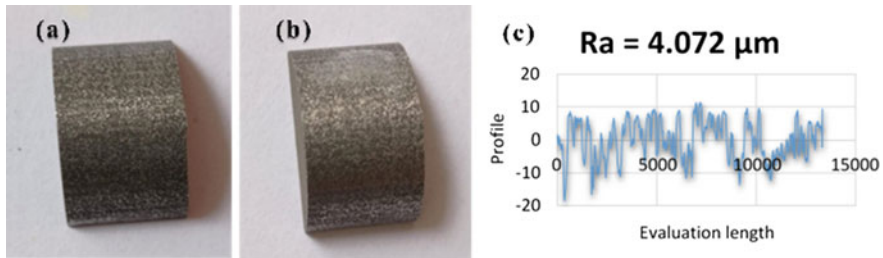
Fig. 13 **a** Before, **b** after chemical polishing, and **c** final roughness profile after chemical polishing

- The bath consists of 10 ml HF + 9 ml HNO_3 + 5 ml HCl was the better chemical polishing solution and reduction of surface roughness from $R_a = 5.786$ to $4.072\ \mu m$.

References

1. Spitaels, L., Ducobu, F., Demarbaix, A., Rivière-Lorphèvre, E., Dehombreux, P.: Influence of conventional machining on chemical finishing of Ti6Al4V electron beam melting parts. Procedia Manuf. **47**(2019), 1036–1042 (2020). https://doi.org/10.1016/j.promfg.2020.04.321
2. Dolimont, A., Demarbaix, A., Ducobu, F., Rivière-Lorphèvre, E.: Chemical etching as a finishing process for electron beam melting (EBM) parts. In: AIP Conference Proceedings, vol. 2113, no. July, p. 150020 (2019). https://doi.org/10.1063/1.5112696
3. Soro, N., Saintier, N., Attar, H., Dargusch, M.S.: Surface and morphological modification of selectively laser melted titanium lattices using a chemical post-treatment. Surf. Coat. Technol. **393**(December 2019), 125794 (2020). https://doi.org/10.1016/j.surfcoat.2020.125794
4. Dolimont, A., Rivière-Lorphèvre, E., Ducobu, F., Backaert, S.: Impact of chemical polishing on surface roughness and dimensional quality of electron beam melting process (EBM) parts. In AIP Conference Proceedings, vol. 1960, p. 140007 (2018). https://doi.org/10.1063/1.5034999
5. Scherillo, F.: Chemical surface finishing of AlSi10Mg components made by additive manufacturing. Manuf. Lett. **19**, 5–9 (2019). https://doi.org/10.1016/j.mfglet.2018.12.002
6. Lyczkowska, E., Szymczyk, P., Dybała, B., Chlebus, E.: Chemical polishing of scaffolds made of Ti-6Al-7Nb alloy by additive manufacturing. Arch. Civ. Mech. Eng. **14**(4), 586–594 (2014). https://doi.org/10.1016/j.acme.2014.03.001
7. 2019—The influence of chemical polishing of titanium scaffolds on their mechanical strength and in-vitro cell response. Elsevier Enhanced Reader.pdf
8. Yun Feng, K., Liu, P., Xue Li, H., Yu Sun, S., Bo Xu, S., Li, J.: Microstructure and phase transformation on the surface of Inconel 718 alloys fabricated by SLM under 1050°C solid solution + double ageing. Vacuum **145**, 112–115 (2017). https://doi.org/10.1016/j.vacuum.2017.08.044
9. Mohammadian, N., Turenne, S., Brailovski, V.: Surface finish control of additively-manufactured Inconel 625 components using combined chemical-abrasive flow polishing. J. Mater. Process. Technol. **252**, 728–738 (2018). https://doi.org/10.1016/j.jmatprotec.2017.10.020
10. Tyagi, P., et al.: Reducing the roughness of internal surface of an additive manufacturing produced 316 steel component by chempolishing and electropolishing. Addit. Manuf. **25**, 32–38 (2019). https://doi.org/10.1016/j.addma.2018.11.001

11. Keping, H., Jingli, F.: Study on chemical polishing for stainless steel. Trans. IMF **76**(1), 24–25 (1998). https://doi.org/10.1080/00202967.1998.11871186
12. Thenard, T., Catapano, A., Allena, R., El May, M., Saintier, N., Mesnard, M.: Topography and wettability characterization of surfaces manufactured by SLM and treated by chemical etching. Mech. Adv. Mater. Struct. (2020). https://doi.org/10.1080/15376494.2020.1836292
13. Bezuidenhout, M., Ter Haar, G., Becker, T., Rudolph, S., Damm, O., Sacks, N.: The effect of HF-HNO3 chemical polishing on the surface roughness and fatigue life of laser powder bed fusion produced Ti6Al4V. Mater. Today Commun. **25**(June), 101396 (2020). https://doi.org/10.1016/j.mtcomm.2020.101396
14. Huang, C.A., Chen, Y.C., Chang, J.H.: The electrochemical polishing behavior of the Inconel 718 alloy in perchloric–acetic mixed acids. Corros. Sci. **50**(2), 480–489 (2008). https://doi.org/10.1016/j.corsci.2007.07.005
15. Rao, G.A., Kumar, M., Srinivas, M., Sarma, D.S.: Effect of standard heat treatment on the microstructure and mechanical properties of hot isostatically pressed superalloy inconel 718. Mater. Sci. Eng. A **355**(1–2), 114–125 (2003). https://doi.org/10.1016/S0921-5093(03)00079-0

Effect of Input Parameters on Strength-to-Weight Ratio in Fused Deposition Modeling for ABS P430 Material

P. S. Thigle and D. V. Nehete

1 Introduction

Rapid prototyping emerges from the demand for shorter development time and reduced product life cycle. The manufacturing time and cost is also an important factor in the aerospace industries. Minimum manufacturing time leads to reducing its manufacturing cost. The optimization concerning higher strength at the lower weight of each component used in aerospace can be achieved broadly in three phases of design. The first one is a selection of the most suitable material considering all required properties along with its manufacturing method, the second one is testing its test experimentally, and the third one is to optimize its structure to reduce weight for higher strength. The use of design and analysis of computer software plays a vital role in such design and manufacturing stages [1]. The advantages of this technology are as follows: with the event of 3D printing, an outsized number of processes are developed that allow the utilization of a spread of materials and methods. Among these technologies, one of the most commonly used is fused deposition modeling (FDM), a layer-by-layer additive manufacturing technique, based on computer-aided design (CAD) and computer-aided manufacturing (CAM) [2]. And the manufacturers are generally used for demonstration [3]. This limits the utilization of FDM in industrial applications. Recently, many companies developed new materials for 3D printing like AB Plus P430 with base material as ABS and HIPS, which are some new materials introduced in recent years. These materials are required to be tested considering aerospace applications [4]. Different parameters are selected, and study of and the effect of those parameters on relative parameters is studied. Layer height is essential

P. S. Thigle (✉) · D. V. Nehete
Department of Mechanical Engineering, Marathwada Institute of Technology,
Aurangabad 431010, India
e-mail: pushkarthigale1988@gmail.com

D. V. Nehete
e-mail: dipak.nehete@mit.asia

out of all other parameters. Layer height 0.14 mm is best suitable for better dimensional accuracy [5]. The effect of layer thickness and rate of deposition on the tensile strength is studied. The maximum tensile strength is achieved at a lower layer thickness of 02 mm and a printing speed of 30 m/s [6]. Part orientation X0°Y0°demostrated the highest values for tensile strength and maximum fracture load, giving 29.36 MPa and 1409.09 N, respectively. To fabricate a model with the least manufacturing cost, part orientation X0°Y0°would be the best choice [7]. Acrylonitrile butadiene styrene (ABS) 400 material is also material used in different types of 3D printing applications. The model specimen is made, and different types of tests are carried out like tensile test, dimensional accuracy, and wear test. The Taguchi method is used to carry out the design of experiments [8]. Effect of raster angle and layer thickness both have marked effect on tensile strength for PEEK material. The strength of PEEK samples is higher than those of ABS samples. PLA is also a material used to produce fused deposition modeling (FDM) parts. Rep Rap 3D printers are introduced through standard tensile tests to determine different properties. 3D-printed components from Rp Rap are comparable in tensile strength and elastic modulus to the parts printed on commercial 3D printing systems [9].

2   Process Parameters

The selected process parameters are layer thickness, speed of deposition, and percentage infill with fixed flat build orientation. A detailed discussion about these parameters is explained in the section.

2.1   Build Orientation

Before the additive build-up, the part(s) is (are) oriented with the appropriate software. Today, the main target mostly is on an efficient build-up, which suggests that the part is oriented such a minimum of support material is required, and therefore, the part is built up in the shortest time possible. Concurrently, there is disregarded that additive manufactured parts are not isotropic thanks to the layered build-up and should have different behaviors than conventionally produced parts. Thus, the different persons have tried to work out how the mechanical properties of additive manufactured parts change thanks to orientation within the build-up volume. Therefore, tensile specimens can be produced as oriented flat, edgewise, and straight up. The layers are always parallel to the platform. Flat orientation is selected as being a higher strength component as per previous studies.

2.2 Layer Thickness

A more controversial parameter is layer thickness. Some researchers found that the optimal set of parameters for maximum performance of their model always includes the smallest layer thickness with an increase in the layer thickness tensile strength primarily increasing and decreasing. Figure 3 shows the concept of layer thickness. The possible layer thickness by Zortrax M200 is then 0.14, 0.19, and 0.29 mm. With the increase in the layer thickness, tensile strength primarily increases and then decreases.

2.3 Speed of Deposition

The speed of deposition is also an important parameter in 3D printing. The possible speed of deposition is 50 and 100 mm/s.

2.4 Percentage Infill

In any industry, amount of material used for any product affects its costs. In the optimization process, material saving can be possible with the help of infill percentage. The infill verification with the help of Zortrax M 200 type printer is possible as 80, 85, and 90% infill.

3 Experimentation

The experiment is conducted. The specimens were made as per ASTM standard D 638 Type-IV sample [10]. The dimensions are provided in Table 1.

The procedure to make the specimen is as follows:

(1) Study of selection of specimen dimension as per standard.
(2) Drawing the specimen using software Catia V5.
(3) Converting the drawing into STL format.
(4) Importing to a 3D printer to slice it.
(5) Setting the process parameters as per the design of experimentation.
(6) Printing specimen.
(7) Cleaning specimen.

The standard dimension of the specimen with thickness of specimen was 4 mm, width of 6 mm, and gauge length of 25 mm for testing purposes as shown in Fig. 1. Five specimens are taken for experimentation.

Table 1 Specimen dimensions as per ASTM standard D 638 Type IV

Dimensions	7 (0.28) or under		Over 7–14 (0.28–0.55)			Tolerances
	Type I	Type II	Type III	Type IV	Type V	
W-Width of narrow section	13 (0.5)	6 (0.25)	19 (0.75)	6 (0.25)	3.18 (0.125)	± 0.5
L-Length of narrow section	57 (2.25)	57 (2.25)	57 (2.25)	33 (1.30)	9.53 (0.375)	± 0.5
WO-Width overall, min	19 (0.75)	19 (0.75)	29 (1.13)	19 (0.75)	–	± 6.4
WO-Width overall, min	–	–	–	–	9.53(0.375)	± 3.18
LO-Length overall, min	165 (6.5)	183 (7.2)	246 (9.7)	115 (4.5)	63.5 (2.5)	No max
G-Gage length	50 (2.0)	50 (2.0)	50 (2.0)	–	7.62 (0.300)	± 0.25
G-Gage length	–	–	–	25 (1.0)	–	± 0.13
D-distance between grips	115 (4.5)	135 (5.3)	115 (4.5)	65 (2.5)	25.4 (1.0)	± 5
R-radius of filet	76 (3.0)	76 (3.0)	76 (3.0)	14 (0.56)	12.7 (0.5)	± 1
RO-outer radius (Type IV)	–	–	–	25 (1.0)		± 1

Fig. 1 Specimen as per ASTM standard D 638 Type IV

The material selected was an ABS-based advanced material, i.e., AB PLUS P430. This material was developed by the University of Science and Technology, Beijing, China. It is Acrylonitrile Butadiene Styrene Terpolymer-based thermoplastic. The strength and weight are output parameters. The strength of the specimen is measured on electromechanical universal testing machine model AUTOGRAPH, Shimadzu at CIPET, Aurangabad, as shown in Fig. 2.

Fig. 2 Experimental setup
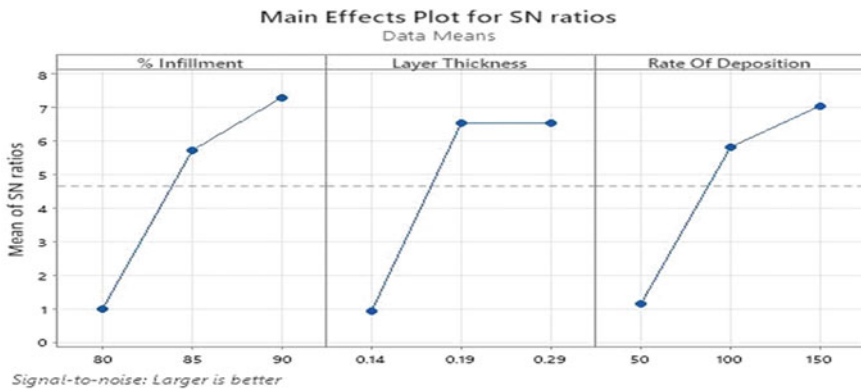
Fig. 3 Main effect plot for SN ratio

Robust design is an engineering methodology for improving productivity during research and development so that high-quality products can be produced quickly at a low cost.

4 Selection of Orthogonal Array for Experimentation

The selection of orthogonal array depends on the selection of numbers of factors and their operating levels. Based on the literature survey and machine constraints, the variables selected are layer thickness, speed of deposition of material, and percentage of infill. The levels are selected based on preliminary experimentation. The possible layer thicknesses produced by 3D printers are 0.09, 0.14, 0.19, 0.29, and 0.39 mm. Taguchi design of 019, 0.29, and 0.29 mm is selected. Only three speeds of depositions are possible 50, 100, and 150 mm/s. The possible infill percentage steps are selected as 80, 85, and 90%. Based on all the above parameters and levels, the Taguchi L9 orthogonal array design of experimentation is selected for flat orientation. The variables and their respective levels are shown in the table for flat orientation. Process parameters and levels during experimentation are shown in Table 2.

After testing using UTM machine, values for strength are shown in Table 3 for different percentage infillment. The average weights are found for each trial (Table 4).

Two trials are conducted, every trial is repeated three times, and average values are recorded. The measured average weights of the specimen and the values of strength-to-weight ratio are reported as shown in Tables 4 and 5.

Table 2 Process parameters and levels

Levels	Layer thickness in mm	Speed of deposition in mm/s	Infill percentage
1	0.14	50	80
2	0.19	100	85
3	0.29	150	90

Table 3 Experimental results

Trial No.	% Infill	Layer thickness (mm)	Rate of deposition (mm/s)	Tensile stress (N/mm^2)
1	80	0.14	50	1.46138
2	80	0.19	100	20.1063
3	80	0.29	150	28.0706
4	85	0.14	100	18.5067
5	85	0.19	150	26.7388
6	85	0.29	50	9.0665
7	90	0.14	150	22.0966
8	90	0.19	50	29.4704
9	90	0.29	100	22.3198

Table 4 Average weights of specimen

Trial No.	% Infillment	Layer thickness	Rate of deposition	Weights in gms
1	80	0.14	50	4.89
2	80	0.19	100	9.66
3	80	0.29	150	12.42
4	85	0.14	100	10.42
5	85	0.19	150	13.73
6	85	0.29	50	4.34
7	90	0.14	150	8.49
8	90	0.19	50	12.42
9	90	0.29	100	11.04

Table 5 Strength-to-weight ratio of specimen

Trial no	% Infillment	Layer thickness	Rate of deposition	Strength-to-weight ratio
1	80	0.14	50	0.29
2	80	0.19	100	2.08
3	80	0.29	150	2.26
4	85	0.14	100	1.77
5	85	0.19	150	1.94
6	85	0.29	50	2.08
7	90	0.14	150	2.60
8	90	0.19	50	2.37
9	90	0.29	100	2.02

5 Result and Discussion

From Table 5, the range of strength-to-weight ratio is highest in range for edgewise orientation followed by a flatwise straight-up orientation. It shows that the edgewise orientation component is most suitable for aerospace applications. The reason for getting the highest strength might be due to the type of structure generated, bonding, and position of load applied. Hence, modeling and optimization are done for edgewise orientation. Figure 3 shows the main effect of the plot for S/N ratios. Figure 4 shows the main effect for plots for means. The optimum strength-to-weight ratio is found at layer thickness as 0.19 mm, speed 150 mm/s, and 90% installments ratio for flatwise orientation.
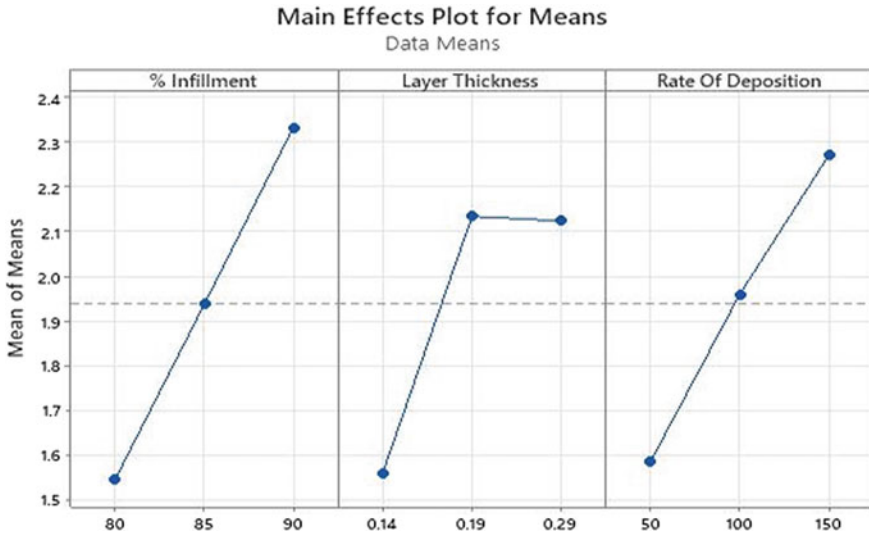
Fig. 4 Main effect plot for means

6 Conclusion

Experimental results show that values of strength built in different orientations are highest in range for edgewise orientation followed by flat and straight-up orientation for ABS PLUS P430 material. The semi-empirical models developed are validated with the experimental result and found within a 90% confidence level. The optimization values for a higher strength-to-weight ratio are found at 0.19-layer thickness, speed of deposition as 150 mm/s, and 90% installment in flatwise orientation. Material saving and machining cost-saving both are possible due to saving in weight and manufacturing products at higher speed.

References

1. Iliescu, M.: Applied finite element method simulation in 3D printing. Int. J. Math. Comput. Simul. **2**(4), 305–312 (2008)
2. Mohammad, V., Chee, K.: Effect of layer thickness and binder saturation level parameters on 3D printing process. Int. J. Adv. Manuf. Technol. **53**, 275–284 (2001)
3. Ivan, G., Jan, S.: Influence of printing conditions on structure in FDM prototypes. Tech. Ser. 231–236 (2013)
4. Tomislav, G.: Influence of processing factors on the tensile strength of 3D Printed models. Mater. Technol. **476**, 781–788 (2013)
5. Junhi, W.: Study on Optimization of 3D Printing Parameters. Department of Electrical and Mechanical Engineering, Jinangxi Water Resource Institute, Nanchang

6. Jaya, K.: A study on the influence of process parameters on the mechanical properties of 3D printed ABS composite. In: IOP Conference on Series Material Science and Engineering, vol. 114 (2016)
7. Ahmed, M.: Effect of part orientation on dimensional accuracy, part strength, and surface quality of three-dimensional printed part. In: IOP Conference on Series: Materials Science and Engineering, vol. 694, p. 012048 (2019)
8. Sood, A.K.: A Thesis Submitted in Fulfillment of the Required for the Award of the Degree of Doctor of Philosophy in Mechanical Engineering, National Institute of Technology, Rourkela, India
9. Tymark.: Mechanical Properties of Components Fabricated with Open-Source 3D Printers Under Realistic Environmental Condition, Materials & Design, vol. 58, pp. 242–246 (2014)
10. Wenzheng, W.: Influence of layer thickness and raster angle on the mechanical properties of 3D printing. Int. J. Aviat. Aeronaut. Aerosp. **2**(4), Article 2

Finishing of Laser Powder Bed Fusion-Based Turbine Blade Sample Using Polymer Rheological Abrasive Fluids

M. A. Manjunath , **Prakash Vinod** , **N. Balashanmugam** , **and M. R. Sankar**

1 Introduction

Critical components in most of the applications are associated with the requirement of improved surface finish once all other manufacturing processes are accomplished. The improvement in surface finish gets even more challenging when the initial surface roughness is very coarse, especially for additive manufactured parts. Additionally, automating the polishing process is desirable since the component's surface finish is achieved in the shortest possible time. The abrasive flow finishing technique is well known for finishing, deburring, radiusing, and recast layer removal for highly complex parts. The rheological media known as viscoelastic plays a predominant inference on the abrasive flow finishing process.

Surfaces finish plays a significant role in the service life of aerospace components. The higher surface finish in blade components results in higher friction loss with low efficiency. Through the velocity field measurement losses in the friction, coefficients are effective to the variable surface finish. The wake flow on the turbine blade component concerning its surface roughness is analyzed through image velocimetry [1]. The aerodynamic functions of the turbine blade are associated with its surface finish. Various surface finishes concerning boundary loss were estimated

M. A. Manjunath (✉) · P. Vinod · N. Balashanmugam
Central Manufacturing Technology Institute, Bangalore 560022, India
e-mail: manjunathma@cmti.res.in

P. Vinod
e-mail: prakashv@cmti.res.in

N. Balashanmugam
e-mail: balashanmugam@cmti.res.in

M. R. Sankar
Department of Mechanical Engineering, Indian Institute of Technology, Tirupati 517506, India
e-mail: evmrs@iittp.ac.in

through Reynolds numbers. Surface integrity directly influences the loss in aero-dynamics when it interacts with boundary layers. Addition of roughness results in a more pronounced velocity profile [2]. Experimental setups and sophisticated measurement techniques were used to test the heavy-duty gas turbines. The total pressure losses are recorded as higher pressure loss for coarser surface roughness [3]. Various approaches are reviewed for strengthening and improving the surface finish of impeller and blisk components. Comparative studies are done on manual finishing, belt grinding, Vibro tumbling, drag finishing, and abrasive flow finishing. Finishing processes with minimum steps are considered an effective and economical way to produce better surface finishes [4]. Experimental investigations for improving the surface finish of aluminum propeller through abrasive flow finishing relive the process capability for finishing complex geometry. For improving the surface rough-ness of propellers, abrasive grits in polymer media and machine parameters are exam-ined [5]. A theoretical simulation and experimental study are conducted on the blade surface of blisk, using an abrasive flow finishing process. The fixture design should predominate inference on achieving uniformity in surface finish [6]. Non-traditional machining and finishing methods are approached in the fabrication of turbine engine components. Abrasive flow finishing, ultrasonic machining, EDM, ECM, and laser-based drilling are explored for advanced materials with complex parts. Improved turbine engine design can be achieved by using non-traditional machining methods [7]. Abrasive flow finishing machine is associated with polymer and its rheological properties. The effect of apparent viscosity is analyzed concerning improvement for surface roughness on HSS die components [8]. A rheometer is used to examine the properties of silly putty in static and dynamic conditions. The silly putty material is applied for magneto-rheological finishing, and its mathematical modeling is gener-ated [9]. Using material testing machines, experiments are carried out to determine the properties of elastic and viscosity of silly putty. By loading mass onto a cylindrical scrap of silly putty material, deformations were recorded. The study on experimental and mathematical models provides the behavior of silly putty at room temperature [10]. The characteristics studies on the measurement of surface roughness of gas turbine blades are established. A surface profile captured randomly provides statis-tical computations. The distribution of surface roughness varies from point to point. The surface roughness of turbine engine blades can be very coarse [11].

The prototype samples of turbine blades with higher surface roughness are exposed to coarse grits (16, 60) of SiC abrasive polymer media in the current work. The work holding fixtures are designed accordingly for blade samples. The infer-ence of hydraulic pressure concerning cycle time is analyzed experimentally. The viscoelastic polymer material silly putty is analyzed to understand the rheological characterization through a rheometer. The surface topography is captured through stereo microscopy before and after AFFM; also, surface roughness profile parameters Ra, Rt, Rz are monitored by a contact-type surface roughness tester.

2 Experimentation

2.1 Viscoelastic Polymer Media

Silicon polymer (Silly putty) is a silicon-based polymer that is known for its unique rheological properties. This polymer has a wide range of applications in several fields, which is also an abrasive flow machining process as a carrier material. The silly putty viscoelastic polymer, as shown in Fig. 1, is used as the carrier material for abrasive particles in the abrasive flow finishing process. The material composition of silicon polymer material is as shown in Table 1. The rheological behavior of the viscoelastic material is analyzed through rheometer (DHR2-Waters).

The silly putty material of 10 g is placed over the Peltier plate of the rheometer. After the disk-type rheometer head is compressed with the polymer media, any excess polymer materials are removed. The viscosity is measured and recorded about the shear rate and temperature. During the characterization study, rheometer parameters with the step time of the 30 s and a temperature range from 22 to 70 °C were chosen.

Fig. 1 Viscoelastic polymer media analysis through rheometer (DHR2-waters)

Table 1 Material composition of silicon polymer (silly putty)

Elements	Percentage (%)
Dimethyl siloxane (PDMS)	65
Silica	17
Thixatrol	9
Boric acid	4
Glycerin	1
Titanium dioxide	1
Decamethyl cyclopentasiloxane	1

2.2 Blade Sample and Work Holding Fixture

Metal 3D printed blade sample is used for the initial experimental trials in AFFM (Fig. 2); the sample material is SS316L built through the DMLS process. The overall dimension of the blade sample is length 50 mm, width 25 mm, and thickness 2.5 mm. The constraining of a component in position during the abrasive flow finishing process is possible through fixtures. The fixture holds a component constraining 6 degrees of freedom and acts as a passage for extruded viscoelastic polymer media flow.

The fixture is designed for blade sample as shown in Fig. 3 for experimentation. The fixture consists of a cylindrical block with an internal hollow passage, in which the blade samples are placed horizontally. Materials used to fabricate the fixture include MS, and the rectangular slot is provided inside the cylinder passage to locate the sample in the horizontal direction. The washer ring on top and bottom locks the sample in position. The viscoelastic media containing abrasive particles comes into contact with the blade surface while passing through an internal hollow passage of fixture.
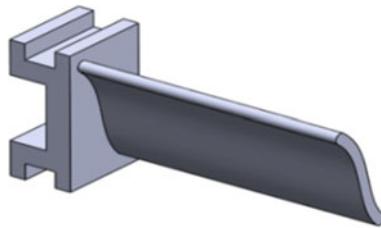
Fig. 2 Metal 3D printed blade sample
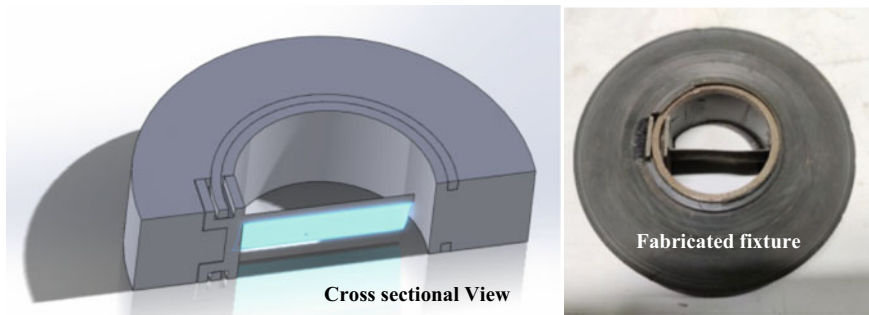
Fig. 3 AFFM fixture for blade sample

2.3 Abrasive Flow Finishing Machine

Abrasive flow finishing machine AFFM-150D (Fig. 4) is a two-way configured abrasive flow finishing setup developed at CMTI Bangalore. The machine consists of two media cylinders placed vertically to each other. The extrusion of a particular grade of viscoelastic abrasive polymer media starts from the bottom media to the top media cylinder. The AFFM unit cycle completes once the polymer media gets back to the bottom cylinder, passing through the fixture with component time. The fabricated fixture is assembled with a blade sample and hydraulically clamped in AFFM-150D. The chiller unit system maintains the temperature of 22 °C in the AFFM media cylinder. The silly putty and silicon carbide abrasives are mixed in a 1:1 weight ratio to form a viscoelastic abrasive polymer composition. The viscoelastic abrasive polymer grit of 16 and 60 has been used to improve the surface roughness. The abrasive particles SiC, grit size, and polymer media weight ratio have been selected based on the preliminary experiments conducted in AFFM-150D [5]. Table 2 represents the technical specification of AFFM-150D.
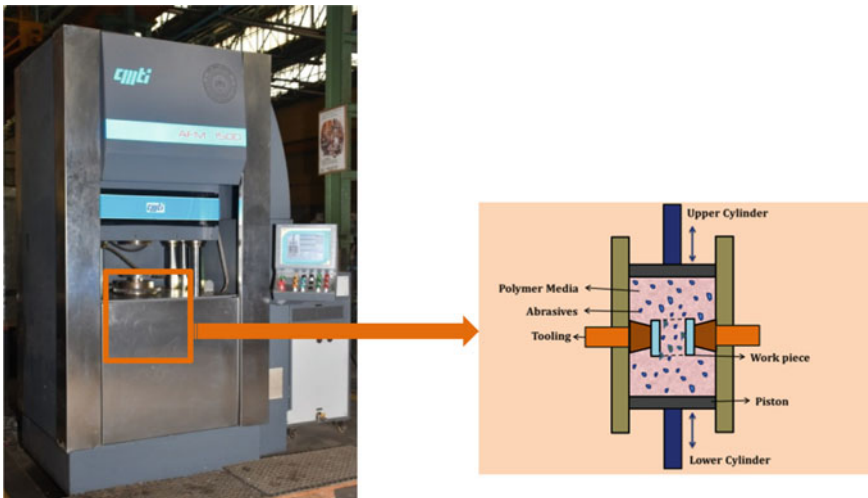
Fig. 4 Abrasive flow finishing machine (AFFM-150D)

Table 2 Technical specification of AFFM-150D

Parameter	Value
Clamping range (mm)	10–300
Hydraulic pressure range (Mpa)	0.5–100
Media cylinder bore diameter (mm)	150
Media piston stroke (mm)	250
Temperature control unit range (°C)	20–35

Table 3 Composition of polymer and abrasives

S. No.	Polymer media	Abrasives	Grit size	Composition of polymer and abrasives
1	Silicon polymer	SiC	16	1:1 weight ratio
2	Silicon polymer	SiC	60	1:1 weight ratio

AFFM hydraulic pressure ranges of 1–5 Mpa have been chosen with increments of 10 min in cycle time for each hydraulic pressure. The composition of a mixture of polymer media and abrasives is as shown in Table 3 is utilized for the current experimentation. The inference of input parameters of AFFM is hydraulic pressure, abrasive particles, and cycle time on surface roughness. To understand the effect of the abrasive flow process on peak and valley of the sample surface, roughness parameters Ra, Rt, Rz are monitored.

3   Results and Discussion

3.1   Rheological Analysis

The inference of variable shear rate, step time, and temperature in relation to stress and viscosity is analyzed through the rheometer. The rheological properties under AFFM operating circumstances can be realized through the plot obtained from the rheometer. The variable shear rate and stress on viscosity signify the viscoelastic behavior of the AFFM carrier material silly putty.

From the rheometer results (Figs. 5 and 6), polymer materials are affected by shear rate, the stress, and viscosity decrease gradually with an increase in shear rate. The effect of temperature with a gradual increase from 22 to 70 °C shows the predominant effect on shear rate and viscosity (Figs. 7 and 8). The gradual change in shear rate is observed up to 30 °C and keeps gradually constant, whereas viscosity drops continuously as the temperature is increased. The viscosity of 10,227 Pa-s is recorded at 22 °C with a stress of 15,915 Pa. The viscosity of the polymer media is temperature-dependent and varies with increasing temperature. Rheological results indicate a role for the thermal control unit in maintaining the temperature of polymer media during the AFFM process.

3.2   Surface Roughness Improvement

The experiment in AFFM utilizing the fabricated fixture investigates the effect of coarser abrasive on higher surface roughness. As an initial grit for experimentation, abrasive polymer media of 16 grits is used followed by 60 grits. The hydraulic pressure of 1, 2, 3, 4, 5 Mpa with a periodic interval of 10 min has been determined
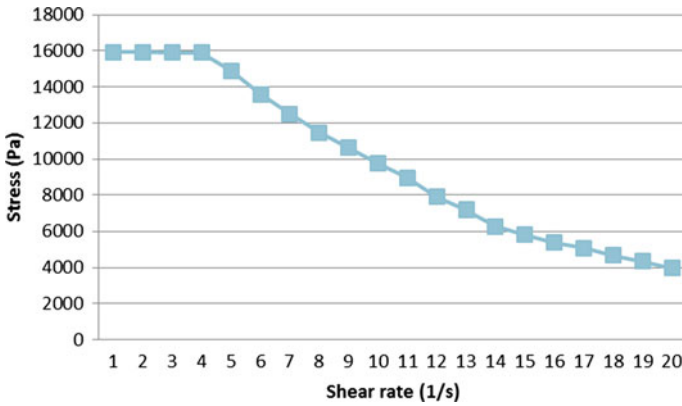
Fig. 5 Variation of stress with shear rate
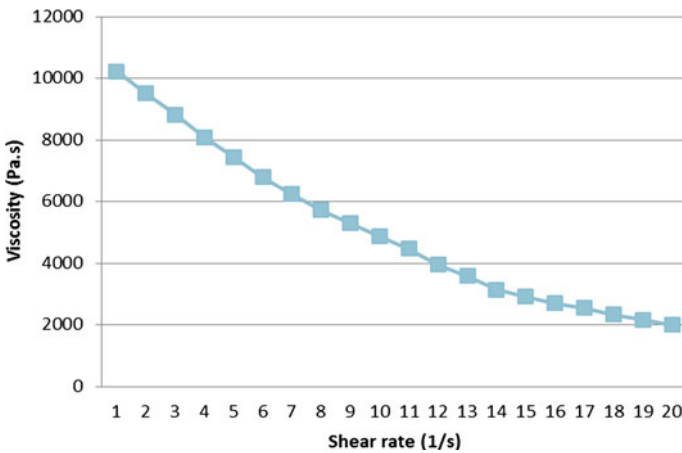
Fig. 6 Variation of viscosity with shear rate

for selected grits of abrasive media. The improvements in surface roughness Ra, Rt, Rz are recorded as a function of variable machine parameters hydraulic pressure, abrasive grits, and cycle time.

The initial surface roughness of the metal additive blade sample is observed to be very rough, that is, Ra 15.32 μm, Rt 87.32 μm, Rz 86.43 μm. The variation in surface roughness with hydraulic pressure is recorded for 16 grits as shown in Fig. 9. A variation in surface roughness with hydraulic pressure is recorded for 60 grits is recorded as shown in Fig. 10.

The result of surface roughness at regular intervals and increment in hydraulic pressure shows the gradual decrease of surface roughness Ra, Rt, Rz from the initial surface roughness. The hydraulic pressure after 2 Mpa for both 16 and 60 grits was
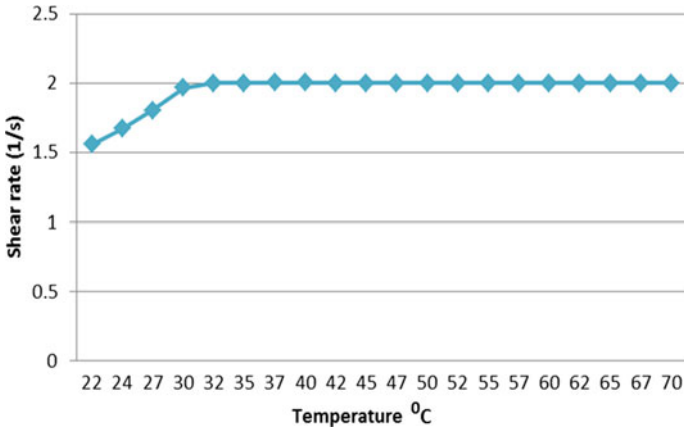
Fig. 7 Variation of shear rate with temperature
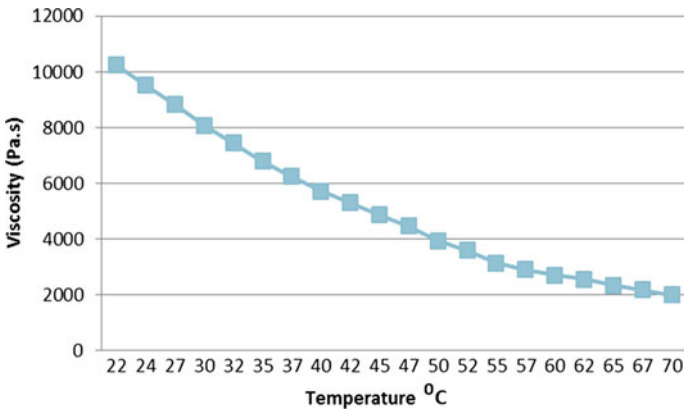
Fig. 8 Variation of viscosity with temperature

found to be more effective on the metal additive blade sample. The overall cycle time of 50 min each for the variable grits has been considered for the experiment.

The surface roughness before and after AFFM is analyzed through the Talysurf surface roughness tester for Ra, Rt, Rz parameters. The stereo microscopy images (Carl Zeiss Discovery V20) are captured at 1000X magnification to analyze the surface topography before and after AFFM.

The effect on the improvement of surface roughness before and after AFFM can be observed in Fig. 11 A1, B1. The initial rough surface turned out to be a slightly shiny surface from the stereo microscopy images shown in Fig. 11. A2, A3 represent the improvement in the surface finish. From the analysis of experimental results on blade samples, it is observed that the surface roughness has been improved from Ra
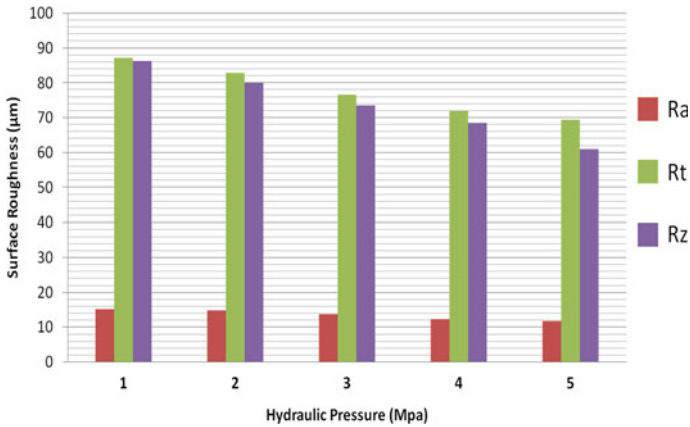
Fig. 9 Variations in surface roughness with hydraulic pressure at 16 grits
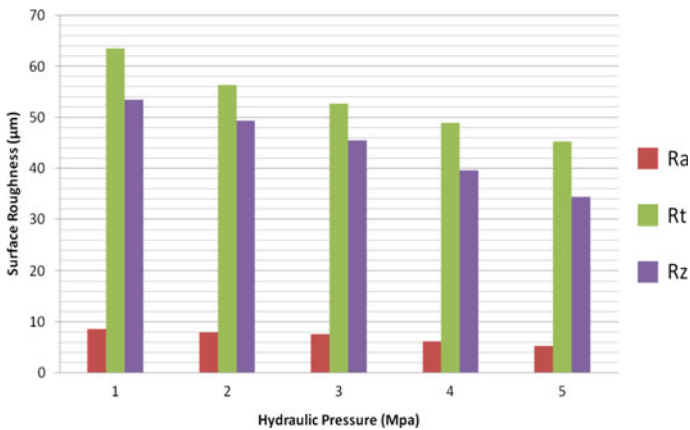
Fig. 10 Variations in surface roughness with hydraulic pressure at 60 grits

15.32 µm, Rt 87.32 µm, Rz 86.43 µm to Ra 5.33 µm, Rt 45.35 µm, Rz 34.47 µm (Fig. 11 A3, B3).

4 Conclusions

In this work, the prototype of a metal 3D printed blade sample with a rough initial surface is explored for abrasive flow finishing. The silicon carbide abrasive particle of coarser grit sizes has been selected for improving the rough surface of the blade sample. Improvement in the surface roughness with inferences of hydraulic pressure and cycle time is analyzed. The rheological characterization of silicon polymer and
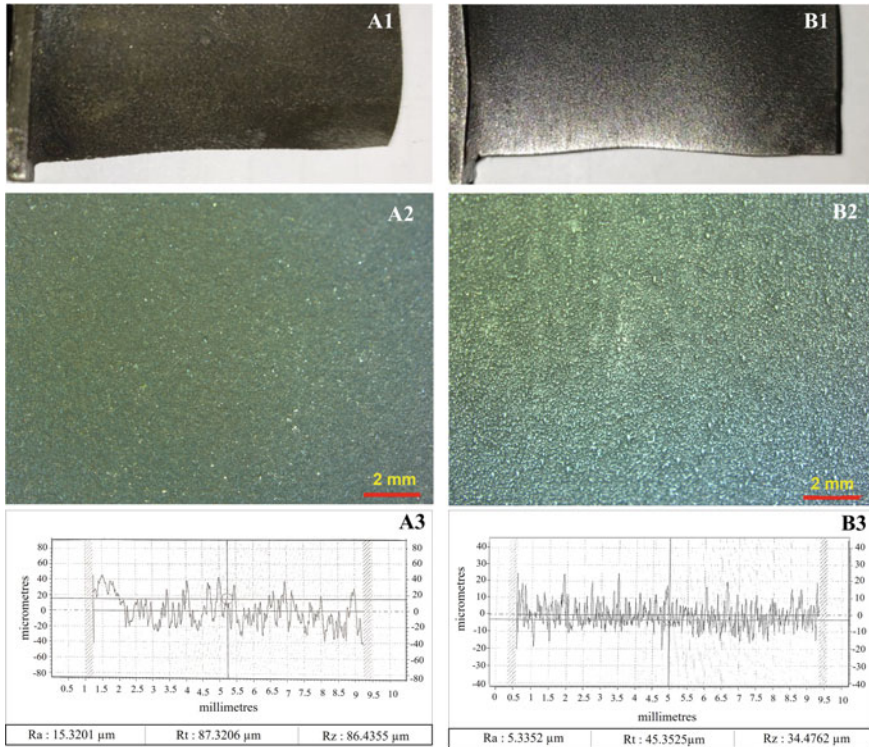
Fig. 11 **A1** before AFMM and **B2** after AFFM; **A2** surface topography in stereo microscopy before AFFM and **B2** surface topography in stereo microscopy after AFFM. **A3** surface roughness profile before AFFM and **B3** surface roughness profile after AFFM

analysis of blade sample before and after AFFM using surface roughness tester and stereo microscopy images following points can be concluded.

- The viscosity of 10,227 Pa s and stress of 15,915 Pa are recorded for silicon polymer material at temperature of 22 °C.
- The effect of shear rate and the temperature has the predominant influence on the viscosity of the silicon polymer material.
- The selected silicon carbide abrasives of 16 and 60 grits in viscoelastic abrasive media were found to be effective for rough surface finish.
- The AFFM hydraulic pressure above 3, 4, and 5 Mpa found to be more effective for improving the surface roughness.
- The surface roughness has been improved from Ra 15.32 μm, Rt 87.32 μm, Rz 86.43 μm to Ra 5.33 μm, Rt 45.35 μm, Rz 34.47 μm.
- The AFFM machine parameter and viscoelastic abrasive media parameters play a significant role in the improvement of surface roughness for metal additive parts.

References

1. Mulleners, K., Gilge, P., Hohenstein, S.: Impact of surface roughness on the turbulent wake flow of a turbine blade. J. Aerodyn. 9 (2014), Article ID 458757
2. Bain, T., Liu, J., Zhang, W., Zou, Z.: Effect of surface roughness on the aerodynamic performance of turbine blade cascade. Propul. Power Res. **3**(2), 82–89 (2014)
3. Hummel, F., Lötzerich, M., Cardamone, P., Fottner, L.: Surface roughness effects on turbine blade aerodynamics. J. Turbomach. **127**, 453 (2005)
4. Fu. Y., Gao, H., Wang, X., Guo, D.: Machining the integral impeller and Blisk of aero-engines: a review of surface finishing and strengthening technologies. Chin. Mechan. Eng. Soc. **30**, 528–543 (2017)
5. Manjunath, M.A., Vinod, P., Balashanmugam, N., Sankar, M.R.: Abrasive flow finishing for surface roughness improvement of aluminum propeller: a case study. Mater. Today Proc. **26**(Part 2), 1113–1118 (2020). https://doi.org/10.1016/j.matpr.2020.02.22
6. Fu, Y., Wang, X., Gao, H., Wei, H., Li, S.: Blade surface uniformity of Blisk finished by abrasive flow machining. Int. J. Adv. Manuf. Technol. (2015)
7. Rhoades, L.J.: Applying Nontraditional Machining Techniques for Improved Turbine Engine Designs. The American Society of Mechanical Engineers, Gas Turbine and Aeroengine Congress and Exposition (1989)
8. Mali, H.S., Kishan, J.: Developing alternative polymer abrasive gels for abrasive flow finishing process. In: 5th International & 26th All India Manufacturing Technology, Design and Research Conference (2014)
9. Guo, F., Du, C.-b., Yu, G.-j., Li, R.-p.: The static and dynamic mechanical properties of magnetorheological silly putty. Adv. Mater. Sci. Eng.11 (2016), Article ID 7079698
10. Cross, R.: Elastic and viscous properties of silly putty. Am. J. Phys. **80**, 870 (2012)
11. Agrawal, A., Jain, V.K., Muralidhar, K.: Experimental determination of viscosity of abrasive flow machining media. Int. J. Manuf. Technol. Manage. **7**(2/3/4) (2005)

Geometrical Form Deviation and Defect Analysis of SLM Processed Slender Parts Using Computer Vision Methodology

Brahmansh Kaushik ⓘ**, S. Anand Kumar** ⓘ**, and V. Rajkumar** ⓘ

1 Introduction

Additive manufacturing (AM) is a method that revolutionizes the way complex geometrical parts are being manufactured. AM provides high precision and customization capabilities even in complex-shaped intricate end-use parts. Selective laser melting (SLM) is widespread among AM technologies used in a wide range of industries. Sectors like aerospace, bio-medical, and the automobile are benefitting from AM technologies [1–3]. The main advantage of AM is the very high-dimensional accuracy with a shorter lead time while fabricating the components. However, defects are still present in-between the layers due to various possibilities like over-melting, under-melting, and metal shrinkage which is inevitable during the SLM process. The fabrication of features having a combination of thick and thin sections and slender dimensions is inevitable in a component having complex geometries. Further, SLM processing of the above-mentioned features results in dimensional distortions due to rapid solidification. Therefore, geometrical dimensional investigation of slender parts is important given practical applications.

Various defects are observed are gas-induced porosity, process-induced process, and deviated melting are some of the common defects in the SLM process [4–7]. Conventional inspection methods like X-ray topography, radio topography, and thermography are post-process inspection methods [8, 9]. Therefore, if the part is not up to the benchmark quality, it can be uneconomical due to complete waste.

B. Kaushik (✉) · S. Anand Kumar (✉) · V. Rajkumar
Additive Manufacturing Research Laboratory, Department of Mechanical Engineering, Indian Institute of Technology Jammu, Jammu and Kashmir 181221, India
e-mail: kaushik.brahmansh@gmail.com

S. Anand Kumar
e-mail: anand.subramaniyan@iitjammu.ac.in

V. Rajkumar
e-mail: rajkumar.v@iitjammu.ac.in

Hence, in situ monitoring techniques can be quite advantageous in these scenarios and decide whether the defects and deviation of the product are getting out of the permissible limit. Therefore, a waste reduction and a lesser carbon footprint for the environment can be a valuable addition for AM technology as a green manufacturing process.

The proposed method is motivated by the in situ monitoring of layers during the SLM process, which is anticipated for quality assurance throughout the manufacturing process. Several researchers contributed to computer vision-based inspection and quality control using the grayscale pixel value analysis [10–13]. In the recent years, in situ monitoring gained a lot of attention from researchers. Several in situ processes are proposed with the help of full-field infrared thermography, optical coherence tomography, and other complex monitoring devices [14–16]. This proposed method is simple and easy in the application. The proposed analysis is independent of layer count, making it more robust for the application in the industry environment. The analysis is limited to identify the defects having micrometer dimension, but it can extrapolate for sub-micro level if the image resolution is increased. When it comes to bulk manufacturing of a product, the proposed method is beneficial as it reduces the monitoring efforts and post-processing waste [17]. The defect assessment is assisted by new advancements like artificial intelligence and machine learning [18–20]. Algorithms of machine learning like support vector machines are capable of classifying the defected and non-defected layers [21].

The in situ monitoring analysis is performed on the layers prepared from the CAD model and image of simulated layer captured using a high-resolution camera. The proposed algorithms then analyze all the images captured for the comparable results from the CAD model and simulated layers. Further, an attempt is made to identify deviation present in the melted layer (simulated layer).

2 Experiment Design

Figure 1a shows the range of grayscale pixel values (GSPV). This scale starts from pixel value 0, which indicates the black color, and as the pixel values increase, it becomes light in color. This scale goes up to a pixel value of 255, which represents completely white color. Figure 1b shows the process flow for the analysis involved in the proposed method. This process has two different segments. The first segment starts with the CAD model. Then, CAD model is sliced into layers for the printing of the component. For the analysis, the CAD model is sliced into ten layers. These ten layers are reference layers for the calculation of error in the printed layers. Mean gray pixel value is calculated for these ten layers will behave as reference GSPV.

The second segment in the analysis algorithm involves capturing printed layer images. The next step is to get the value of each pixel, and in the subsequent step, it is converted to 255. This conversion is made to make the analysis uniform for each of the printed layers. After conversion, the mean GSPV is calculated. The mean
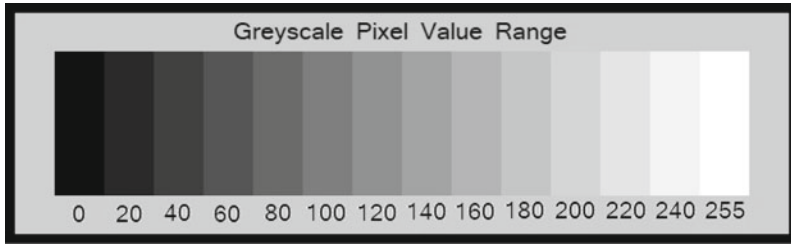
(a) Greyscale pixel value range chart
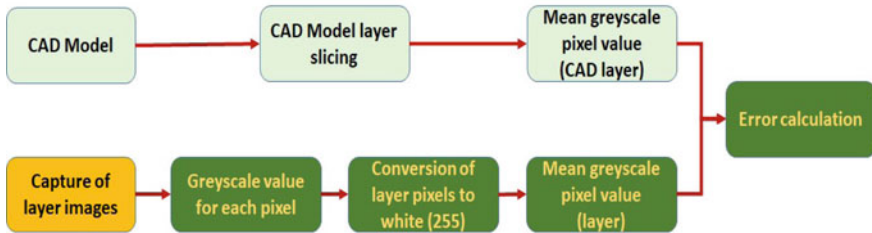
(b) Flowchart showing process of greyscale pixel value analysis

Fig. 1 Grayscale pixel value and flowchart of the process flow

GSPV from the CAD layer and printed layer is compared, and a calculation of error is performed.

2.1 CAD Model

The CAD model used in the analysis is shown in Fig. 2. Figure 2a shows the side view of the CAD model with an arrow showing the build direction. Figure 2b, c shows the top view and isometric view, respectively.

Figure 2d shows the dimensions of the CAD model used in the analysis. The thickness of the part is 10 mm

2.2 SLM Layer Simulation

The method proposed is analyzed with the replication of SLM process technology. The simulation for replication is performed with the help of wax. In the sectional geometry, wax is deposited on a black background surface. Possible defects are replicated in these layers to capture the imperfection in the layer. The thickness of the layer is equivalent in all the 10 layers, i.e., 0.5 mm. The dimension is used from

(a) Side view　　　　(b) Top view　　　　(c) Isometric view

(d) CAD model dimensions
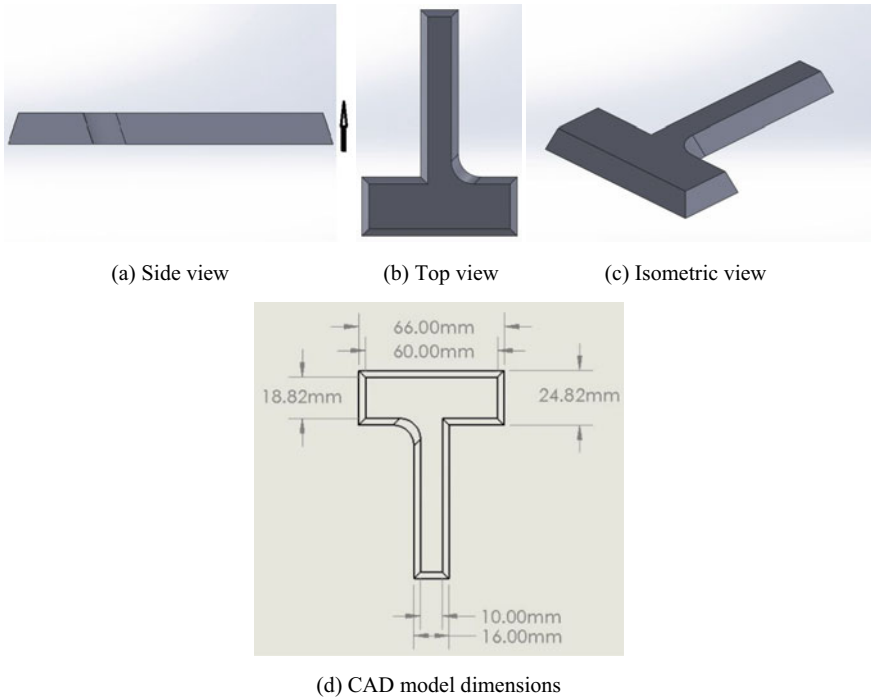
Fig. 2 CAD model projections

the CAD model. Table 1 gives the property of replicated layer with the defects in the layer.

After completion of the wax deposition process, a high-resolution image of each layer is captured. The images are captured using a 24.2-megapixel CMOS sensor at an f/5.6 aperture, 140 mm focal length, a shutter speed of 1/100 s, and ISO 11400. These images are analyzed with the proposed approach. Each layer image is captured in size 320px by 450px. This dimension of the image is constant for every image to make the analysis uniform.

The images captured for each layer are shown in Fig. 3. In these images, defects are visible. Some of these layers are perfect with no defect and, also melted according to the CAD model.

Table 1 Properties of layers

Layer No.	Properties of layer
Layer No. 1	Perfect layer
Layer No. 2	Imperfect layer due to over-melting at different places
Layer No. 3	Imperfect layer due to under-melting at different places
Layer No. 4	Layer with gas-induced porosity defect
Layer No. 5	Layer with process-induced porosity defect
Layer No. 6	Layer with power recoating is imperfect
Layer No. 7	Perfect layer
Layer No. 8	Imperfect layer due to over-melting at different places
Layer No. 9	Imperfect layer due to under-melting at different places
Layer No. 10	Perfect layer

(a) layer no. 1   (b) layer no. 2   (c) layer no. 3   (d) layer no. 4   (e) layer no. 5

(f) layer no. 6   (g) layer no. 7   (h) layer no. 8   (i) layer no. 9   (j) layer no. 10
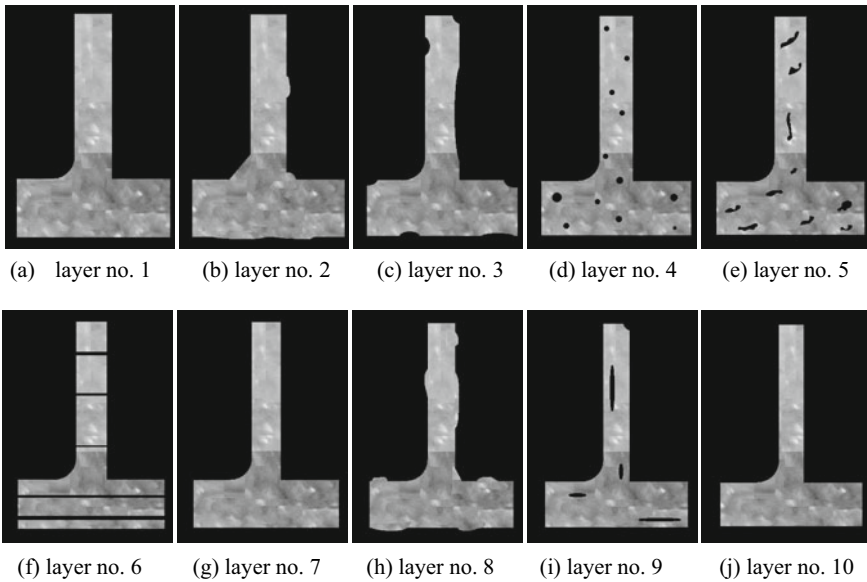
Fig. 3 Printed layers by simulation

3 Results and Discussions

3.1 *Grayscale Pixel Value Analysis*

CAD model is sliced into ten layers as shown in Fig. 4. These layers are modified for black background and conversion of CAD model part to 255-pixel value (white) for uniform analysis.

Table 2 gives the mean grayscale pixel value for CAD model layers. It is observed that the highest mean GSPV is from layer no. 1 as this layer is from the base of the CAD model. In subsequent layers, value of the mean GSPV is decreased as the laser melting area. This same is supported by the values which are decreasing in Table 2.

The subsequent analysis was performed for wax deposited layers. Images captured are processed, and to make the analysis uniform, the pixel value of the melted part is converted to a 225-pixel value (white) as shown in Fig. 5. In this, some of the layers are perfect, and others are with some possible defects. These modified layers are used in the calculation of mean GSPV. Several researchers and their results corroborate well with the patterns of defect analyzed in the present study. Similar trends of error values are observed related to the defects analyzed in the present study. This present work is found more realistic from the previously available analysis [22–24].

Table 3 gives the mean GSPV for simulated layers. These values are used for the comparison and calculation of error. Table 3 gives that the mean GSPV is almost

(a) CAD layer no. 1(b) CAD layer no. 2(c) CAD layer no. 3(d) CAD layer no. 4 (e) CAD layer no. 5

(f) CAD layer no. 6 (g) CAD layer no. 7(h) CAD layer no. 8 (i) CAD layer no. 9(j) CAD layer no. 10

Fig. 4 Layer slicing from CAD model for reference

Table 2 Mean GSPV for CAD model layers

Layer No.	Grayscale pixel value (Mean)
Layer No. 1	93.3406
Layer No. 2	90.3550
Layer No. 3	86.5122
Layer No. 4	83.7250
Layer No. 5	80.6172
Layer No. 6	77.5289
Layer No. 7	74.1466
Layer No. 8	71.1060
Layer No. 9	68.7260
Layer No. 10	64.7913

(a) CAD layer no. 1(b) CAD layer no. 2 (c) CAD layer no. 3(d) CAD layer no. 4 (e) CAD layer no. 5

(f) CAD layer no. 6(g) CAD layer no. 7 (h) CAD layer no. 8(i) CAD layer no. 9(j) CAD layer no. 10

Fig. 5 Modified printed layers by simulation

the same for some layers, which indicates these layers are as per the designed CAD model.

Figure 6 shows the plot for the mean GSPV from CAD model layers and simulated wax layers. A linear trend is observed in the values of CAD model layers as the symmetry is followed and surface area is decreasing in the build direction. The mean GSPV of layer no. 1st, 7th, and 10th is the same for both the CAD layer and wax layer. This demonstrates that the wax layer is perfect and as per the CAD model layers. The wax layer with a value below the CAD model layer indicates the probability of

Table 3 Mean GSPV for simulated layers

Layer No.	Grayscale pixel value (mean)
Layer No. 1	93.3406
Layer No. 2	92.9652
Layer No. 3	82.1796
Layer No. 4	81.4889
Layer No. 5	76.7679
Layer No. 6	69.7076
Layer No. 7	74.1466
Layer No. 8	74.7191
Layer No. 9	65.7250
Layer No. 10	64.7913

porosity and under-melting condition. Similarly, values of the wax layer above the line from the CAD model indicate the possibility of over-melting.

Table 4 gives the mean GSPV for both CAD layers and simulated layers with the error percentage. This error percentage helps in the quantification of defects present in the layer. The higher the value of error higher will be the defect, also the layer is not following the designed CAD model.

Table 4 is for the relative error value observed in the layer. The highest error value is in layer no. 6 which makes this layer highly defective. In layers no. 1, 7, and 10,
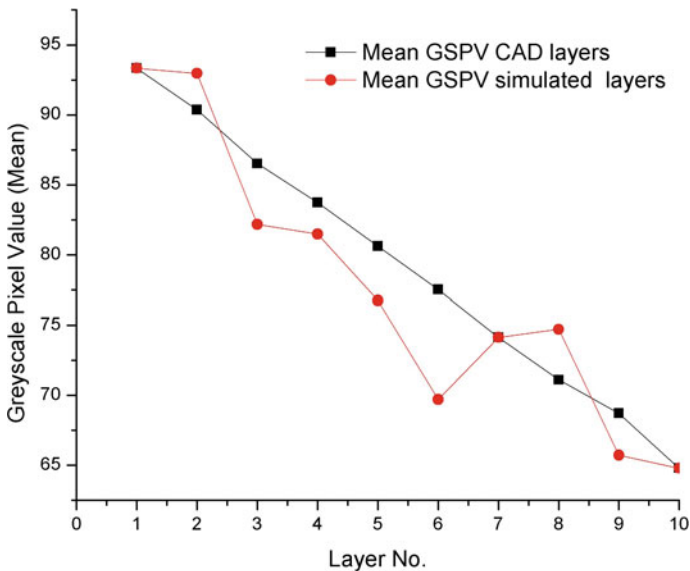
Fig. 6 Graph for mean grayscale pixel value versus layer number

Table 4 Calculations of error percentage

Layer No.	Mean GSPV for CAD layers	Mean GSPV for simulated layers	Error (%)
Layer No. 1	93.3406	93.3406	0.0000
Layer No. 2	90.3550	92.9652	2.8888
Layer No. 3	86.5122	82.1796	5.0080
Layer No. 4	83.7250	81.4889	2.6707
Layer No. 5	80.6172	76.7679	4.7747
Layer No. 6	77.5289	69.7076	10.0882
Layer No. 7	74.1466	74.1466	0.0000
Layer No. 8	71.1060	74.7191	5.0812
Layer No. 9	68.7260	65.7250	4.3667
Layer No. 10	64.7913	64.7913	0.0000

the error is coming as 0, which indicates these layers are entirely according to the
CAD model and perfect.

3.2 Deviation Analysis

The analysis is to capture any dimensional deviation in the SLM process with the
help of relative comparison between the CAD and melted layers. Figure 7a shows
the designed CAD layer. This CAD layer is divided into six sections, as shown in
Fig. 7b. The six-sectioned CAD layer is the reference layer for the analysis. Figure 7c
is the layer captured from the simulation. This layer is modified with conversion to
255-pixel value, and similar six sections are featured as in Fig. 7d. In the analysis,
a relative comparison is made between images from Fig. 8b, d. This comparison
results in the deviation image as shown in Fig. 8.

Figure 8 represents the deviation captured by comparing the reference CAD layer
and the modified melted layer. The deviation in different sections can be observed

(a) CAD Layer   (b) 6 section CAD layer   (c) Melted layer   (d) 6 section melted layer
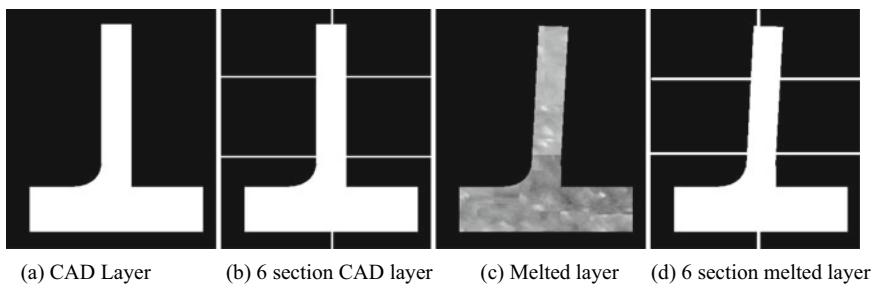
Fig. 7 Printed layer-6 by simulation
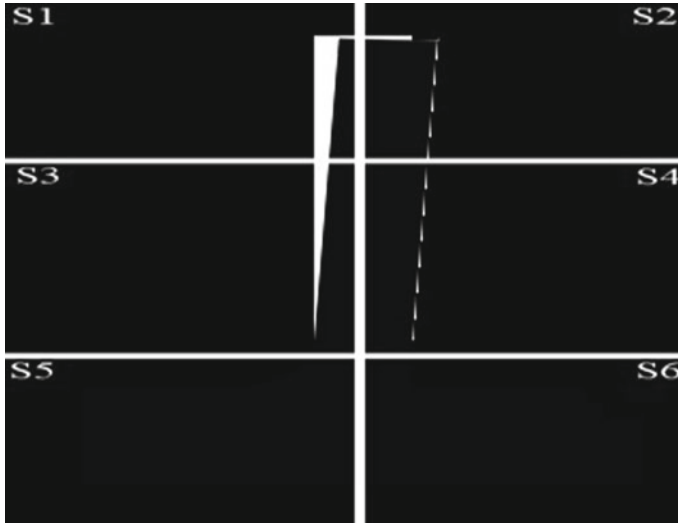
Fig. 8 Section-wise deviation

from Fig. 8. In Sections 1, 2, 3, and 4, the deviation is present, whereas Sections 5, 6 are complete as per the CAD model. This analysis is helpful to locate where the product is deviating from the designed CAD model.

Table 5 gives the section-wise analysis for detection of the deviation. Each section is analyzed separately as shown. Desired standard deviation pixel value should be zero if no deviation is observed in the section. The value is calculated for each section is given in Table 5. Sections 1–4 are having a nonzero value which indicates the presence of deviation in the section. This same is given in the result column in Table 5. Higher the value of standard deviation higher will be the deviation magnitude.

Table 5 Section-wise deviation results

Section No.	The desired standard deviation pixel value	Calculated standard deviation pixel value	Deviation result
Section 1	0.0	53.35	Deviation
Section 2	0.0	43.11	Deviation
Section 3	0.0	35.00	Deviation
Section 4	0.0	45.30	Deviation
Section 5	0.0	0.0	No-deviation
Section 6	0.0	0.0	No-deviation

4   Conclusions

The grayscale pixel value analysis allows the possibilities of in situ monitoring strategies for the manufacturing of high-quality parts. Results are obtained from the analysis of ten layers show the feasibility of deployment in an industrial environment. Geometrical form deviation analysis allows the decision regarding the termination or continuation of the product. If the deviation goes beyond the acceptable limit, real-time analysis and decisions are possible with the help of in situ monitoring. Integration of advanced algorithms from machine learning and artificial intelligence makes the proposed method more robust. Machine learning allows to categories the layer in perfect and imperfect automatically. AI will decide the identification of the defect type present in the layer. The maximum defected layer is identified in which improper powder recoating occurred with an error percentage of 10.08%. Several layers are perfect as per the CAD model, whereas different defects are easily quantified with the help of the proposed analysis algorithm. The section-wise deviation algorithm can identify the deviated section with the calculation of standard deviation in the greyscale pixel value throughout the section.

References

1. Uriondo, A., Esperon-Miguez, M., Perinpanayagam, S.: The present and future of additive manufacturing in the aerospace sector: a review of important aspects. Proc. Inst. Mechan. Eng. Part G: J. Aerosp. Eng. **229**(11), 2132–2147 (2015)
2. Ravi Kumar, Y.: Modeling and simulation of biomedical components by selective laser sintering. Int. J. Rapid Manuf. **2**(4), 234–257 (2011)
3. Anand Kumar, S., Rajkumar, V., Nagesha, B.K., Tigga, A.K., Barad, S., Suresh, T.N.: Single crystal metal deposition using laser additive manufacturing technology for repair of aero-engine components. Mater. Today: Proc. **45**, 5395–5399 (2021)
4. Taheri, H., Shoaib, M., Koester, L., Bigelow, T., Collins, P., Bond, L.: Powder-based additive manufacturing—a review of types of defects, generation mechanisms, detection, property evaluation, and metrology. Int. J. Addit. Subtractive Mater. Manuf. **1**, 172–209 (2017)
5. Bintao, W., Pan, Z., Ding, D., Cuiuri, D., Li, H., Jing, X., Norrish, J.: A review of the wire arc additive manufacturing of metals: properties, defects, and quality improvement. J Manuf Process **35**, 127–139 (2018)
6. Zhang, B., Li, Y., Bai, Q.: Defect formation mechanisms in selective laser melting: a review. Chin. J. Mechan. Eng. **30**, 515–527 (2017)
7. Sola, A., Nouri, A.: Microstructural porosity in additive manufacturing: the formation and detection of pores in metal parts fabricated by powder bed fusion. J. Adv. Manuf. Process. **1**, 06 (2019)
8. Carvalho, M.S., Martins, A.P., Santos, T.G.: Simulation and validation of thermography inspection for components produced by additive manufacturing. Appl Therm Eng **159**, 113872 (2019)
9. Thompson, A., Maskery, I., Leach, R.K.: X-ray computed tomography for additive manufacturing: a review. Meas Sci Technol **27**(7), 072001 (2016)
10. Jeyapoovan, T., Murugan, M., Clemend Bovas, B.: Statistical analysis of surface roughness measurements using laser speckle images. In: 2012 World Congress on Information and Communication Technologies, pp. 378–382 (2012)

11. Srivani, A., Anthony Xavior, M.: Investigation of surface texture using image processing techniques. Procedia Eng. **97**, 1943–1947 (2014)
12. Al-Kindi, G.A., Baul, R.M., Gill, K.F.: An application of machine vision in the automated inspection of engineering surfaces. Int. J. Prod. Res. **30**(2), 241–253 (1992)
13. Hussein, M., Diab, S.: New approaches for online visual inspection of products with multiple characteristics and known tolerances. Int. J. Rapid Manuf. **1**(3), 363–375 (2010)
14. Wu, B., Ji, X., Zhou, J. et al.: In situ monitoring methods for selective laser melting additive manufacturing process based on images—a review. China Foundry **18**, 265–285 (2021)
15. Gardner, M.R., Lewis, A., Park, J., McElroy, A.B., Estrada, A.D., Fish, S., Beaman Jr., J.J., Milner, T.E.: In situ process monitoring in selective laser sintering using optical coherence tomography. Opt. Eng. **57**(4), 041407 (2018)
16. Bartlett, J.L., Heim, F.M., Murty, Y.V., Li, X.: In situ defect detection in selective laser melting via full-field infrared thermography. Addit. Manuf. **24**, 595–605 (2018)
17. Pugalendhi, A., Ranganathan, R., Sreekanth, M.P.: Mass production strategy for additive manufacturing by stacking the product at the design phase. Int. J. Rapid Manuf. **9**, 12 (2018)
18. Caggiano, A., Zhang, J., Alfieri, V., Caiazzo, F., Gao, R., Teti, R.: Machine learning-based image processing for on-line defect recognition in additive manufacturing. CIRP Ann **68**, 04 (2019)
19. Heinl, M., Schmitt, F.K., Hausotte, T.: In-situ contour detection for additive manufactured workpieces. Procedia CIRP **74**, 664–668 (2018)
20. Scime, L., Beuth, J.: Anomaly detection and classification in a laser powder bed additive manufacturing process using a trained computer vision algorithm. Addit. Manuf. **19**, 114–126 (2018)
21. Zanaty, E., Aljahdali, S.H., Cripps, R.: Accurate support vector machines for data classification. Int. J. Rapid Manuf. **1**(1) (2009)
22. Craeghs, T., Clijsters, S., Yasa, E., Kruth, J.-P.: Online quality control of selective laser melting. In: 22nd Annual International Solid Freeform Fabrication Symposium—An Additive Manufacturing Conference, SFF (2011)
23. Kaushik, B., Anand Kumar, S.: Computer vision-based on-line monitoring technique part quality enhancement in selective laser melting process. Adv. Add. Manuf. Artif. Intell. Nat. Inspired Bio-manuf. (in press)
24. Kaushik, B., Subramaniyan, A.K.: Investigation on the greyscale pixel methodology for additive manufactured part: an in-situ quality assessment approach. Int. J. Rapid Manuf. **10**(1), 105–121 (2021)

Hybrid Additive Manufacturing of Knee Joint Implant: Possibilities and Challenges

Sayan Doloi [ID]**, Atul Singh Rajput** [ID]**, Sajan Kapil** [ID]**, and Manas Das** [ID]

1 Introduction

Hybrid manufacturing combines the various processes to manufacture the parts efficiently, faster, and productive. According to International Academy for Production Engineering (CIRP), the hybrid manufacturing process is defined as "the manufacturing process based on the simultaneous and controlled interaction of process mechanisms or energy sources/tools having a significant effect on the process performance. The 'simultaneous and controlled interaction' means that the process/energy sources should interact more or less in the same processing zone and at the same time" [1]. Hybrid manufacturing technology is becoming popular technology of modern manufacturing of difficult to process materials. It combines two or more manufacturing methods to obtain the benefits of individual manufacturing processes and overcome the manufacturing difficulties while these are applied separately. The hybrid manufacturing process can be concurrent hybrid manufacturing (operations cooccurring) and sequential hybrid manufacturing (processes occurring one after another).

Hybrid additive manufacturing (HAM) is a sequential combination of additive and subtractive manufacturing processes. The additive manufacturing process has some limitations like support structure removal, limited maximum build size, sufficient build speed, inadequate accuracy, and surface roughness. For overcoming these

S. Doloi (✉)
School of Mechanical Engineering, KIIT Deemed to be University, Bhubaneswar, Odisha, India
e-mail: sayandoloi123@gmail.com

A. S. Rajput · S. Kapil · M. Das
Mechanical Engineering Department, Indian Institute of Technology, Guwahati, India
e-mail: atulsingh@iitg.ac.in

S. Kapil
e-mail: sajan.kapil@iitg.ac.in

M. Das
e-mail: manasdas@iitg.ac.in

161

limitations, subtractive manufacturing, such as the material removal process, has been performed for finishing as well as support removal of the additively manufactured parts in a single machine. For biomedical implants, mostly metal additive manufacturing (AM) technologies such as powder bed fusion (PBF)-based AM and directed energy deposition (DED)-based AM are used. For finishing biomedical metal implants, a CNC milling operation is usually performed. The ready-to-use products are produced by combining additive and subtractive manufacturing in a single machine [2]. The hybrid manufacturing process has the ability for mass production of big and medium-sized products with high accuracy and geometrical complexity [3]. Digital manufacturing-assisted hybrid additive manufacturing (DM-HAM) is a promising and challenging activity of multi-operational, time-saving, and economical next-generation manufacturing under Industry 4.0 revolution. DM-HAM involves information technologies, artificial intelligence, computer-aided manufacturing, computer-aided process simulation, CNC, and robotic control in hybrid additive manufacturing [4].

The knee is the human body's most significant joint and a common site of athletic-related injuries. Knee joint replacement is a technique in which an artificial joint or prosthesis replaces a wounded or diseased knee. Metal alloys, plastics, and polymers are used to construct the prosthesis. It functions similarly to a knee. Knee replacement surgery is a prevalent procedure. The defective components of the knee joint are replaced with artificially made prosthetics during this surgical procedure to allow patients to move their knees more freely and reduce the sufferings caused by joint diseases, the most common of which are osteoarthritis and rheumatoid arthritis. Knee joint replacement may be advised for younger patients with the damaged knee joint or bone, as well as those who have advanced osteoarthritis. The femoral and tibial components around the knee joint and some portions of the patella are the primary knee joint parts replaced during knee replacement surgery [5]. Proper material selection is challenging for knee joint replacement; the material should have high biocompatibility, good corrosion resistance, high surface finish, and high fatigue strength. Ni–Ti alloys, Cu-Al-Ni, Cu- Zn-Al, polytetrafluoroethylene (PTFE), polyether ether ketone (PEEK), and stainless steel are examples of a few alloys that can be used efficiently in biomedical implants like the knee joint, hip joint, etc. [6].

According to the American Academy of orthopedic surgeons, more than 6 lakh knee replacements are performed in the United States each year [7]. There can be a need for different knee joint replacements based on age, weight, gender, activity level, and overall health. So manufacturing various types of knee joints is a demanding and challenging task in biomedical engineering.

Häfele et al. [8] discussed new challenges in process chain developments in the hybrid additive manufacturing process. For manufacturing the cost-effective and functional product, both additive and subtractive manufacturing methods were proposed to be combined efficiently to overcome the limitation of individual processes. The hybridization of additive manufacturing like selected laser melting (SLM), laser metal deposition (LMD), etc., and traditional/advanced subtractive manufacturing like electrochemical machining (ECM), turning and milling, etc., can be explored to meet the requirement of product formation. For post-processing

and required rework of semi-finished and complex products produced by additive manufacturing, conventional machining methods are included in the process chain of hybrid additive manufacturing.

2 Methods of Additive Manufacturing of Knee Joint Implant

Additive manufacturing is one of the methods of producing patient-specific biomedical metal knee joint implants directly from a 3D CAD model or computed digital tomography (CT) image by depositing/adding the material layer by layer. This layer information is obtained in STL file format by slicing the CAD model into a thin layer. The STL file is fed to AM machine for printing the parts. The commonly used software for generating the 3D CAD model and slicing it into STL files format for medical implant design is Mimics, 3-Matic, and Magics. For planning surgery, doctors require a prototype of patient-specific knee joint implants that can be rapidly manufactured from CT or MRI image data. However, for making a rapid prototype, a 3D CAD model is required to be created. The reverse engineering concept is applied to generate a 3D CAD model from existing physical parts using CT/ MRI image data. The additive manufacturing process chain for knee joint implant is shown in Fig. 1. The various metal additive manufacturing process mechanisms are represented in Fig. 2. The metal additive manufacturing processes are applied for making knee joint implant, but there are some limitations of AM such as geometrical accuracy and surface finish. In order to achieve the desired accuracy and surface finish for knee joint implant, the hybridization of AM and post-processing operations such as CNC machining is required. Different possibilities of hybrid AM process are shown in Fig. 3.

2.1 Powder-Based Fusion Techniques (PBF) of Additive Manufacturing

For metal biomedical implants of Fe-based alloys like stainless steel, commonly used PBF techniques are selective laser melting (SLM) and electron beam melting (EBM). SLM and EBM have the capability of producing parts with high geometrical complexity. SLM parts have higher accuracy compared to EBM parts. A schematic diagram of SLM is shown in Fig. 4. In EBM, the parts with less support and no residual stress, and no gas infusions are produced. EBM is a higher energy-efficient process, however, it requires a high vacuum environment and the process is limited to smaller parts. A schematic diagram of EBM is shown in Fig. 5.

The most suitable additive manufacturing technique for the metal medical implant is selective laser melting (SLM) and electron beam melting (EBM) based on metal
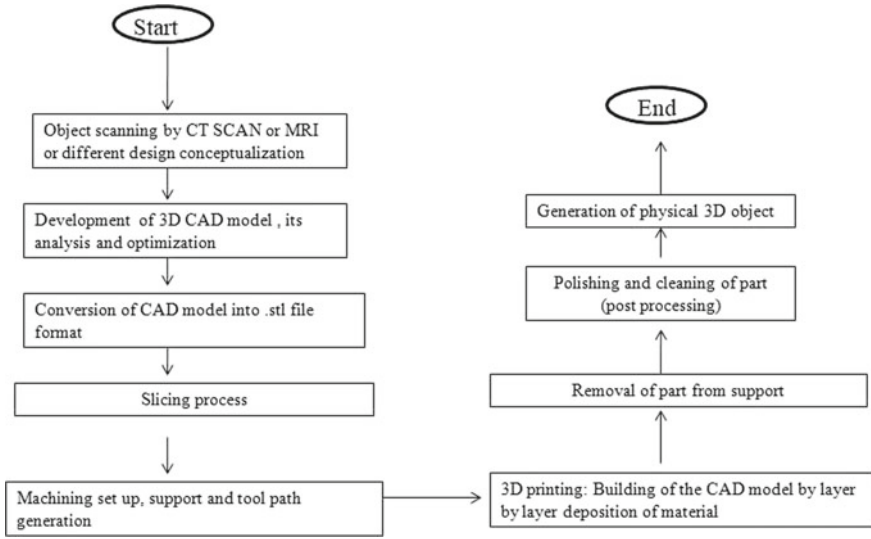
Fig. 1 Additive manufacturing process chain
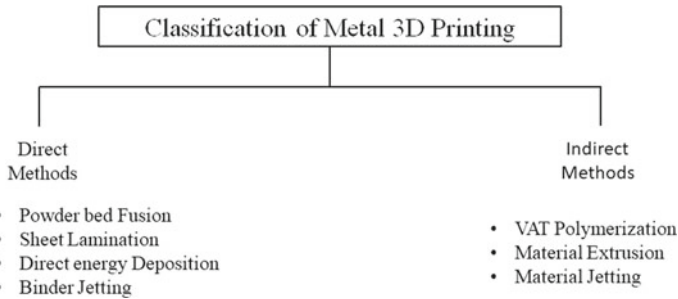
Fig. 2 Different metal 3D printing process
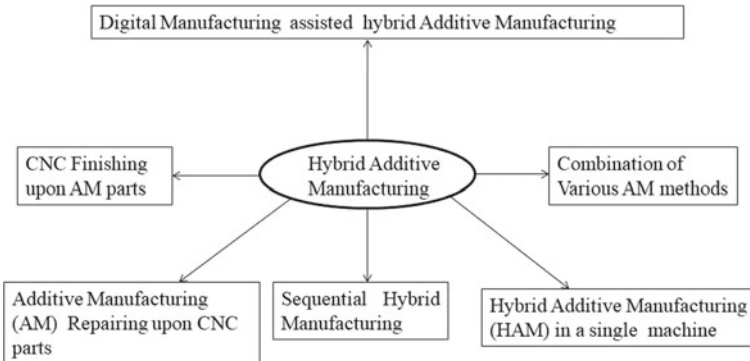
Fig. 3 Different types of hybrid additive manufacturing technique
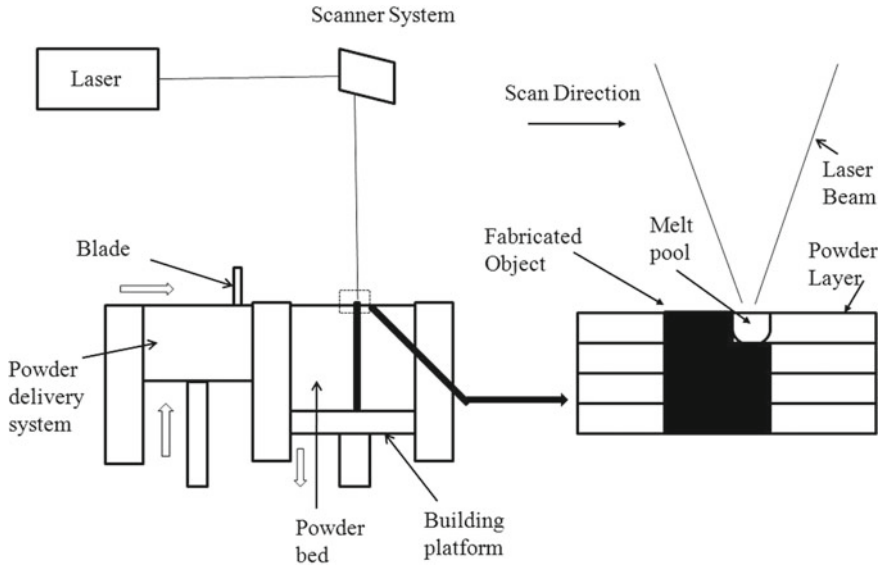
Fig. 4 Working mechanism of SLM process

Fig. 5 Schematic representation of EBM process
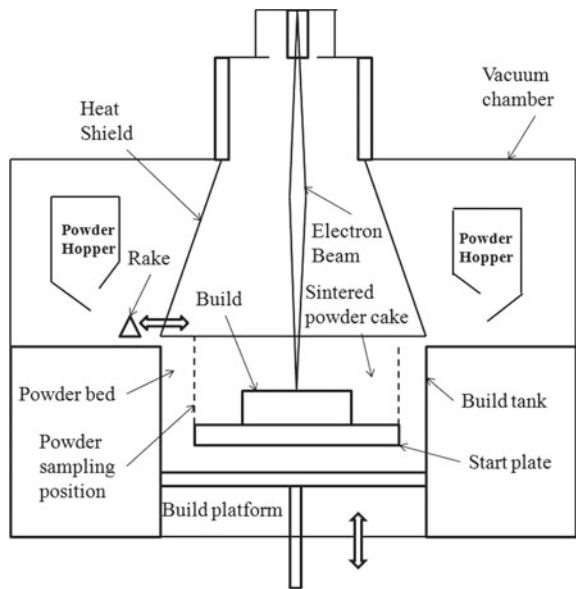
powder bed additive manufacturing (PB-AM) technology. For additive manufacturing, the first step is to develop a 3D CAD model. For creating a 3D CAD model of a medical implant, computed tomography (CT) scan image data are used. Various AM software such as Mimics, 3-Matic, and Magics are used to create a 3D CAD model of medical implants like knee joints [9].

The structural design optimization for selective laser melting of knee joint implants was performed by some researcher. Implant fixation, mechanical load, and geometry of implant were identified as design considerations. The size optimization, shape optimization, and topology optimization strategies were applied to fabricate lightweight implants with minimum stress shielding. The dimensions for width, height, and length of the stainless steel 316 L prototype of the implant were 62 mm, 152 mm, and 43 mm, respectively. For fabricating intramedullary tibia implant, an SLM system with CW fiber laser power of 170W, the spot diameter of 80 microns, the laser modulation frequency of 1 MHz, and laser scanning speed of 500 mm/s was utilized. The layer thickness of 50 µm was selected. The data preparation from CT scan data collection, customized design, structural optimization, prototype fabrication and evaluation, and future knee joint implant improvements were considered in this study. The structural design optimization achieved about 30% weight reduction of an implant. The surface roughness Ra value on the implant's surface fabricated by the SLM process was observed as 9.63 µm [10]. It needs finishing operation for final use. CNC machining can be performed for finishing the implant.

The selective laser melting (SLM) process was applied to produce stainless steel 316L parts of high density and low porosity faster. The laser power of 380 W was utilized. The micro-hardness of the building part was achieved between 213 and 220 HV, which is much higher than the annealing process. The scanning strategy was improved to use high laser power, and at the same time to enhance the build rate by 72% compared to the normal SLM process [11].

Selective laser melting (SLM) process was applied for metallic micro parts. Different research activities and commercial systems for the fabrication of micro-SLM were evaluated. Various issues with micro-SLM, such as powder recoating, laser optics, and powder particle size, were identified. Secondary finishing techniques for the post-processing of micro-AM components were discussed. The values of laser spot size, powder particle size, and layer thickness of micro-SLM are different from the conventional SLM process. Current µ SLM systems achieve a minimum feature resolution of 15 µm, minimum surface roughness of 1 µm, and maximum part density of 99.3%. The commercial micro-SLM system achieved a layer thickness of 1 µm and a minimum spot size of 20 µm. The surface finishing techniques for micro-SLM parts have been reviewed. Abrasive blasting and laser polishing are standard finishing techniques for miniature parts. An innovative approach in powder distribution and post-processing of the built parts for micro-SLM is very much needed to develop a new and hybrid micro-AM system. Micro-SLM will expand the scope of growing applications for metallic parts with micro features in various fields such as biomedical engineering and jewelry industries [12].

The rapid design with the help of computer-aided design method based on a patient's bone model has been made and a personalized total knee femoral component was made using CoCrMo-alloyed powder by selective laser melting (SLM). The mechanical properties, surface roughness, and biological corrosion resistance knee joint component were analyzed. The observed tensile strength, yield strength, hardness, and biological corrosion resistance of CoCrMo-alloyed personalized femoral component fulfill knee joint prosthesis standard. The research on SLM direct manufacturing gave a new direction for rapid manufacturing of personalized implanted prosthesis [13].

The knee and hip implant components containing porous structures of Ti-6Al-4 V and Co-29Cr-6Mo alloy were fabricated utilizing electron beam melting (EBM). Both solid and open-cellular prototypes were manufactured by additive manufacturing (AM) using EBM. The stiffness-compatible implants were fabricated for optimal stress shielding for bone regimes as well as bone cell in growth. The fabrication of patient-specific, monolithic, and multifunctional orthopedic implants using EBM was demonstrated [14].

2.2 Directed Energy Deposition (DED) Techniques of Additive Manufacturing

DED-based AM techniques for stainless steel implants are laser-engineered net shaping (LENS) and wire arc additive manufacturing (WAAM). LENS is applied for building complex and customized metallic parts and also for repairing any free-form surface. The LENS process can build parts of multi-materials. LENS can produce parts with higher accuracy and lower surface roughness than the WAAM process, but it is slower. The laser-engineered net shaping (LENS) process was applied for producing metallic parts made up of stainless steel, titanium alloy, etc. [15]. LENS process is utilized for fabricating and repairing parts of multi-materials. The higher solidification rate was achieved in LENS as compared to casting of metallic components. Controlling the significant process parameters such as powder feed rate, laser power, hatch distance, and scan speed, build rate in LENS can be improved. During the LENS process, powder feed rates of 5–10 g/min, a scan speed of 6–12 mm/min, and laser power of 150–400W were set for achieving better geometrical accuracy. Controlling the melt pool dimension to achieve the desired layer thickness in the LENS process is challenging. Laser-engineered net shaping (LENS) of Ti alloys was successfully made focusing on the microstructure and textural defect formation and their subsequent effect over mechanical properties. Additive manufacturing (AM) technique, LENS was used to fabricate near net shape 3D products from various materials including titanium (Ti) and Ti alloys[16]. A schematic diagram of LENS is shown in Fig. 6.

WAAM is mainly based on gas metal arc welding (GMAW), which has high build speed and less cost, but the surface finish of the produced part by WAAM is inferior,
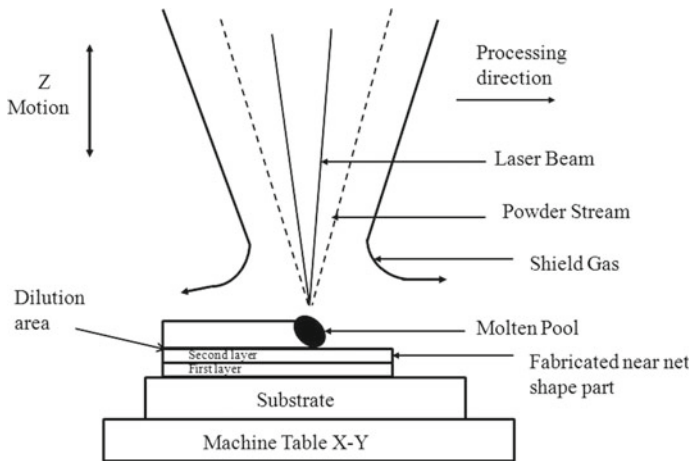
Fig. 6 Schematic representation of LENS

and it needs CNC machining for finishing. Wire arc additive manufacturing (WAAM) process in which more extensive parts were produced by depositing molten materials. The wire of different materials such as Ti, Ni, Al alloy, and steel can be welded using an electric arc as a heat source. Using WAAM technologies, near net shape large-scale components with high deposition rates at low production costs are achieved [17]. Gas metal arc welding such as MIG and TIG is used in the WAAM process. Due to high heat input, thermal stress development, and HAZ, poor surface quality is challenging in the WAAM process. The optimization of process parameters such as heat input and deposition time and speed is conducted to achieve uniform weld geometry during the fabrication of metallic parts. Combining the WAAM process with CNC machining can produce the desired part geometry with a better finish for the biomedical implant, which is one of the possible methods of hybrid additive manufacturing. A schematic diagram of WAAM is shown in Fig. 7.

3 Subtractive Manufacturing Methods of Knee Joint Implant

Combining additive manufacturing and subtractive manufacturing, such as material removal processes of machining and finishing in hybrid additive manufacturing in a single machine, can reduce the material handling activities. It can also improve the building speed and surface finish required for producing metal parts for biomedical implants like knee joint, hip joint, and dental implants.
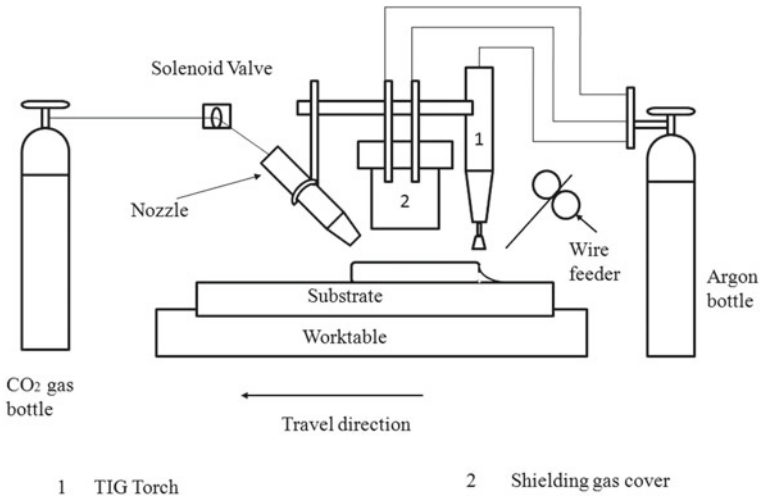
Fig. 7 Schematic representation of WAAM process

3.1 Research Studies on Implant Development

The research work in modeling, machining, analysis, and finishing of knee joint implants was carried out by different eminent scientists, which are discussed from now on. Lee. et al. [18] developed a CAD model of the femoral component of the knee joint and performed the rapid prototyping of the same. Lin. et al. [19] used the concept of reverse engineering to collect the data point of the physical model. A solid CAD model of the knee joint replacement was developed with the help of those data points by smooth fitting. The end product was fabricated using CNC machining. More accurate forms can be manufactured by increasing the number of control points and the degree of the curves. On the other hand, by lowering the value, more smooth shapes can be created. Different knee joint replacements are needed for different people. Hence, this method is advantageous to fulfill the needs of different patients; there is only a need to alter the data of the CAD model. As a result of reverse engineering, a database of various types of free-form prosthetic surfaces was developed, which establishes the basic theoretical foundation for prosthesis clinic application and significantly reduces the cost and production cycle.

Kumbhalkar et al. [5] carried out different biomedical studies for the replacement of the knee joint. The force distribution of knee joint replacement under different situations was analyzed with the help of finite element analysis. It was concluded that patellar tendon force, quadriceps force, and patellofemoral force are the main forces acting on the joint. The force distribution over the joint varies depending on the flexion angle and body weight. The patellofemoral and quadriceps forces are most significant at the maximal flexion angle, which is 110 degrees. Athlete's knee injuries are common because the force acting during jumping and running is greater

than steady-state or walking. According to the study, a knee joint replacement can function similarly to an original knee joint if the artificial tibia, femur, and patella dimensions are identical to those of the original joint.

Soni et al. [20] generated a computed topography data model with the help of reverse engineering. With the use of a medical image processing software (DeVide), the CT scan data were analyzed, and subsequently, a 3D CAD model was developed, and a subsequently, a stereolithography file format was generated, which was made error-free by MeshLab software and different finite element analysis had been carried out for different materials like CoCrMo alloy and stainless steel. It was concluded that CoCrMo alloys are a superior choice for implant materials since they have comparatively less deformation; the CoCrMo alloy has good biocompatibility and mechanical qualities, including high tensile and yield strength, stiffness, and wear resistance. Apart from that, it has great polishability, which is necessary for smooth surface interaction in knee and hip implants. All of these characteristics make CoCrMo an excellent orthopedic implant material.

Zavala et al. [21] carried out different researches for selecting the best material for manufacturing knee joint replacement. The paper focused on how the material properties, percentage composition of carbon nanotubes (CNTs), and manufacturing process conditions improve the properties and performances of bio- compatible nanocomposite materials. These studies will lead to the fabrication of biomedical replacements like knee joints, hip implants with better quality, mechanical properties, and functionalities. They concluded that 0.01 and 0.1 wt % concentration of single-walled carbon nanotubes reinforced composites of f-CNTs materials lead to better mechanical properties and biocompatibility for manufacturing unicompartmental knee joint replacements with approximately 12% increase in Young's modulus and 65% in UTS.

Markopoulos et al. [22] showed the different stages involved in manufacturing of a knee joint replacement and also analyzed the change in surface roughness with different parameters like feed rate and spindle speed, etc., in different stages. A difference between the change in measurements in the inner and upper surface of femoral components was noticed while analyzing the surface roughness, and it was found that the value of surface roughness was comparatively higher on the outer side than the inner side. Kumar et al. [23] performed the nanofinishing on the knee joint implant by different rotational magnetorheological abrasive flow machining processes in multiple steps. It was concluded that magnetic flux density, angle of incidence, and curvature of the workpiece were important parameters in the R-MRAFF process. An electromagnet instead of a permanent magnet would add more flexibility in varying the magnetic flux density. A uniform working gap was needed to maintain a steady MRR, and that could be made possible by using inverse and extended size of the workpiece.

Kumar et al. [24] proposed an abrasive-based finishing method for different biomedical components like the knee joint, hip joint, dental crown, elbow joint, heart valve, etc., for nanofinishing. The finishing of biomedical implants such as the knee joint and the hip joint is often better with the magnetorheological (MR) fluid-based finishing technique. Identifying which component will be polished should be

used to establish MRF's composition. The surface roughness of the material was improved by combining the suitable MRPF composition. Controlling the rotational and axial motion of the MR fluid allows for a flat, smooth mirror-like finish in the nm range was achieved. The rotating velocity of the magnet has the most significant impact on the surface roughness. With the R-MRAFF technique, the most effective attainable surface finish in stainless steel was 16 nm.

3.2 Modeling and Tool Path Generation for Multi-axis CNC Machining

The CAD model of knee joint implant has been developed, and a tool path has been generated for multi- axis CNC machining of the tibial component using the Mastercam® software. The procedure of tool path generation has been discussed. The machining data inputs required are also mentioned in this section.

Geometric modeling. Mastercam® is a computer-aided design/computer-aided manufacturing/computer-aided engineering software, which gives the user the platform for the most powerful, flexible, and innovative design and also enables the digital transformation of part manufacturing in CNC machine tools [25]. The visible tool path may be rapidly generated using the UG CNC machining module according to the defined machining procedure, and the CNC machining G code can be generated by determining the tool path using the post-processing module. After debugging, the CNC machining G codes are sent to the five-axis or three-axis CNC machine tool.

CAD Model Development. The knee joint mainly consists of three bones femur, patella, and tibia, which articulate relative to each other, allowing flexion and extension. The knee joint is the body's largest, and probably, most strained joint. The fulcrum of the joint is formed by the arrangement of the bones, which translates the activities of the knee's flexor and extensor muscles. For designing a knee joint, it is essential to study the different parts of it. The femur, also known as the thigh bone, is the strongest and largest, and heaviest bone. The main function of the femur is to bear the weight and enhance stability, and it also acts as a transmission surface to the tibia. Patella, also known as the knee cap, is a triangular-shaped bone that protects bones and tissues. Tibia, also known as shine bone, is a large bone of the lower extremity of a knee joint. The tibia's main job is to take in and distribute weight across the knee and to the ankle. The articulations of the tibia with the non-weight-bearing fibula serve to keep the tibia aligned. In the present study, a CAD model of knee joint replacement has been developed, which has mainly two components: the femoral component and the tibial component, shown in Fig. 8.

The femoral component is made of metal, and it curves around the femur's end (thighbone). It is grooved so that as the knee bends and straightens, the kneecap may easily slide up and down against the bone. The tibial component is usually a flat metal platform made up of typically stainless steel.
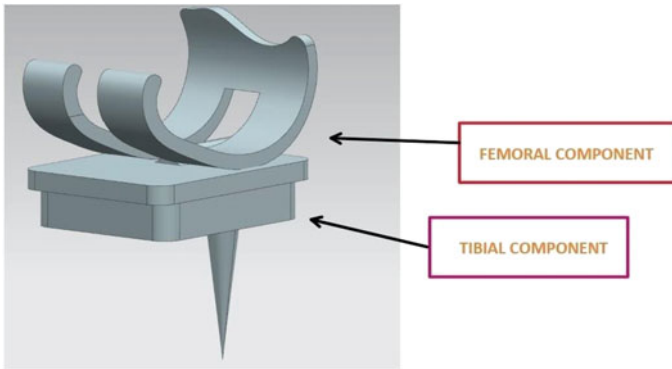
Fig. 8 Different parts of CAD model of knee joint replacement

Tool Path Generation in Mastercam®. The proper tool path generation is a vital need for multi-axis CNC machining. The different steps involved for the tool path generation of a CAD model in Mastercam® for multi-axis CNC finishing, roughing and semi-finishing, etc., are shown in Fig. 9. In the present study, the tool path has been generated to finish the tibial component of the developed CAD model. The different machining parameters chosen for generating the tool path for the finishing operation are shown in Fig. 10. The workpiece during and after the tool path generation is demonstrated in Fig. 11a and b, respectively. Thus, the Mastercam® software is used to analyze the structure and machining challenges of the tibial component of the knee joint replacement and planned the machining process, and also selected the tool, material, and the method accurately and compiled the tool path for finishing operation. The tool path generated for the knee joint replacement tibial component was usable, and the machining effect was excellent.

4 Challenges of Hybrid Additive Manufacturing of Knee Joint Implant

With the development of advanced materials for manufacturing of knee joint implant, there is a need of development of suitable additive manufacturing process to manufacture knee joint implant for specific materials. The selection of finishing process for knee joint implant is also very much important. To hybridize two or more processes in a single machining system is a challenging task during manufacturing of knee joint implant. The reduction of total time of manufacturing by integrating and selecting two or more processes with proper sequence is another challenge of hybrid manufacturing specifically for complex and patient-specific knee joint implant. The limitation of hybrid AM processes such as higher equipment cost and longer processing time can be overcome by carrying out economic analysis [26]. Hybrid AM processes

Start

CAD model development in AUTOCAD CATIA, SOLID WORKS,SIEMENS

Conversion of CAD model (if not in SIEMENS) to .igs or .step file format

Under Manufacturing section in NX selection of workpiece (Blank, part, material etc.)

Selection of desired tool (Type, Material , Shank, Tool Holder)

Selection of desired operation (milling, drilling, turning etc.)

Selection of desired operation method (Mill rough, Mill semi-finish, Mill finish ,Drill etc.)

Input given of required machining data (feed, depth of cut, spindle speed, step over etc.)

Generate tool path

Suitable post processor selection

Output programme creation

End

Fig. 9   Flowchart of a procedure of tool path generation in Mastercam®

Machining Data for finishing operation of the TIBIAI Component in NX 10

Work Piece

Material: Stainless Steel
Blank : Offset of 2 mm from part
Cut Area Specified: Single Face

Drive Method

Method : Area Milling
Non Step Cut pattern : Zig -zag
Direction: Climb Cut
Flat Diameter (%): 20
Step Over Applied :On Part
Cut Angle : Automatic
Z level Cut Levels: Constant
Z level Depth of Cut: 0.01 mm

Tool

Milling Tool : Ball Mill
Material: HSN End Mill
TIALN Coated
Ball diameter: 8 mm
Length : 75 mm
Flutes: 2
Medium Compressor holder
Feed : 250 RPM

Fig. 10   Machining data for the tool path generation for finishing operation of the tibial component

(a)   (b)
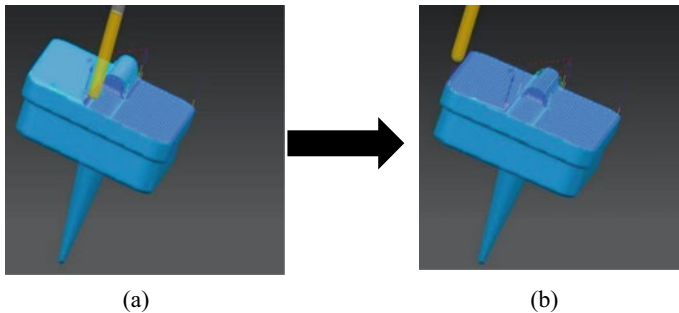
Fig. 11   a Tibial component during finishing operation and b generated tool path on the tibial component

can produce lightweight and high strength and defect free knee joint implant of multi-materials. There is a need of patient-specific knee joint repair using implant of biodegradable or bio-absorbable materials. Hybrid AM process can provide effective solution for manufacturing or repairing knee joint implant. Further research in the area of optimum selection of process parameters for the constituent manufacturing processes is needed for successful application of hybrid additive manufacturing of knee joint made up of bio-materials. There is a challenge of carrying out research on the process of residual stress relieving before finishing process of AM parts and also to achieve geometric dimensioning and tolerancing (GD&T), surface finish and desired mechanical properties of metal AM parts [27].

5   Conclusions

The hybrid additive manufacturing concept is applied recently to make medical implants where the additive manufacturing process is utilized to make the metal implant. There are a lot of developments in the area of hybrid manufacturing parts of knee joint implants. CNC machining operation is performed as post-processing of additive manufactured parts for finishing operation. The CNC machining process is used for rough machining, semi-finishing, and finishing different knee joint implant parts. Advanced machining processes can also be applied for finishing operations along with conventional CNC machining in the hybrid additive manufacturing process. To produce the free-form surfaces of knee joint implant, there is a need for 3D CAD modeling and tool path generation for multi-axis CNC machining for super finishing of 3D printed metal parts. There is also finishing requirement of a metal implant made up of absorbable or biodegradable bulk and porous metals such as iron, magnesium, and zinc which are initially produced by the metal additive manufacturing process. Sequentially, additive manufacturing and CNC machining are performed in a single setup or machine in the hybrid additive manufacturing process. The proper integration of research in both metal additive manufacturing and multi-axis CNC machining, especially CAD modeling and analysis, slicing, tool path generation strategy, etc., is essential for developing the efficient and faster process of just-in-time and rapid manufacturing of medical implants. For performing the repair work of medical implants such as knee joint implants or producing patient-specific medical implants, the development of modified CAD models is sometimes required for rapid and just-in-time production based on existing planned physical prototype or model utilizing the concept of reverse engineering approach.

References

1. Zhu, Z., Dhokia, V.G., Nassehi, A., Newman, S.T.: A review of hybrid manufacturing processes—state of the art and future perspectives. Int. J. Comput. Integer. Manuf. **26**(7), 596–615 (2013)
2. Merklein, M., Junker, D., Schaub, A., Neubauer, F.: Hybrid additive manufacturing technologies—an analysis regarding potentials and applications. Phys. Proc. **83**, 549–559 (2016)
3. Popov, V.V., Fleisher, A., Popov, V.V., Fleisher, A.: Hybrid additive manufacturing of steels and alloys. ManRv **7**, 6 (2020)
4. Chong, L., Ramakrishna, S., Singh, S.: A review of digital manufacturing-based hybrid additive manufacturing processes. Int. J. Adv. Manuf. Technol. 2017 955 **95**(5), 2281–2300 (2017)
5. Kumbhalkar, M.A., Rambhad, K.S., Jee Kanu, N.: An insight into biomechanical study for replacement of knee joint. Mater. Today Proc., May (2021)
6. Abitha, H., Kavitha, V., Gomathi, B., Ramachandran, B.: A recent investigation on shape memory alloys and polymers based materials on bio artificial implants-hip and knee joint. Mater. Today Proc. **33**, 4458–4466 (2020)
7. Total Knee Replacement—OrthoInfo—AAOS (2021). https://orthoinfo.aaos.org/en/treatment/total-knee-replacement
8. Häfele, T., Schneberger, J.H., Kaspar, J., Vielhaber, M., Griebsch, J.: Hybrid additive manufacturing—process chain correlations and impacts. Proc. CIRP **84**, 328–334 (2019)
9. Popov, V.V. et al.: Design and 3D-printing of titanium bone implants: brief review of approach and clinical cases. Biomed. Eng. Lett. **8**(4), 337–344 (2018)
10. Peto, M., Ramírez-Cedillo, E., Hernández, A., Siller, H.R.: Structural design optimization of knee replacement implants for additive manufacturing. **34**, 574–583 (2019)
11. Sun, Z., Tan, X., Tor, S.B., Yeong, W.Y.: Selective laser melting of stainless steel 316L with low porosity and high build rates. Mater. Des. **104**, 197–204 (2016)
12. Nagarajan, B., Hu, Z., Song, X., Zhai, W., Wei, J.: Development of micro selective laser melting: the state of the art and future perspectives. Engineering **5**(4), 702–720 (2019)
13. Song, C., Yang, Y., Wang, Y., Yu, J.K.: Personalized femoral component design and its direct manufacturing by selective laser melting. Rapid Prototyping J. **22**(2), 330–337 (2016)
14. Murr, L.E., Gaytan, S.M., Martinez, E., Medina, F., Wicker, R.B.: Next generation orthopaedic implants by additive manufacturing using electron beam melting. Int. J. Biomat. **2012**, Article ID 245727, 14 (2012)
15. Izadi, M., Farzaneh, A., Mohammed, M., Gibson, I., Rolfe, B.: A review of laser engineered net shaping (LENS) build and process parameters of metallic parts. Rapid Prototyp. J. **26**(6), 1059–1078 (2020)
16. Sahoo, S., Roy, SChapter 8 - Additive manufacturing of titanium alloys: microstructure and texture evolution, defect formation and mechanical response, Editor(s): M. Manjaiah, K. Raghavendra, N. Balashanmugam, J. Paulo Davim, In Woodhead Publishing Reviews: Mechanical Engineering Series, Additive Manufacturing, Woodhead Publishing (2021)
17. Karayel, E., Bozkurt, Y.: Additive manufacturing method and different welding applications. J. Mater. Res. Technol. **9**(5), 11424–11438 (2020)
18. Lee, J.N., Chen, H.S., Luo, C.W., Chang, K.Y.: Rapid prototyping and multi-axis NC machining for the femoral component of Knee prosthesis. Life Sci. J. **7**(1), 73–77 (2010)
19. Lin, Y.P., Wang, C.T., Dai, K.R.: Reverse engineering in CAD model reconstruction of customized artificial joint. Med. Eng. Phys. **27**(2), 189–193 (2005)
20. Soni, A., Kumar Modi, Y., Agrawal, S.: Computed tomography based 3D modeling and analysis of human knee joint. Mater. Today Proc. **5**(11), 24194–24201 (2018)
21. Diabb Zavala, J.M. et al.: Manufacture and mechanical properties of knee implants using SWCNTs/UHMWPE composites. J. Mech. Behav. Biomed. Mater. **120**, (2021)
22. Markopoulos, A.P., Galanis, N.I., Karkalos, N.E., Manolakos, D.E.: Precision CNC machining of femoral component of knee implant: a case study. Machines **6**(1) (2018)

23. Kumar, S., Jain, V.K., Sidpara, A.: Nanofinishing of freeform surfaces (knee joint implant) by rotational-magnetorheological abrasive flow finishing (R-MRAFF) process. Precis Eng **42**, 165–178 (2015)
24. Kumar, M., Kumar, A., Yzadav, H.N., Alok, A., Das, M.: Abrasive based finishing method applied on biomedical implants: a review. Mater. Today Proc. (2021)
25. NX|Siemens Digital Industries Software (2021). https://www.plm.automation.siemens.com/global/en/products/nx/
26. Altiparmak, S.C., Yardly, V.A., Shi, Z., Lin, J.: Challenges in additive manufacturing of high strength aluminium alloy and current developments in hybrid additive manufacturing. Int. J. Lightweight Mater. Manuf. **4**, 246–261 (2021)
27. Strong, D., Kay, M., Conner, B., Wakefield, T., Manogharan, G.: Hybrid manufacturing integrating traditional manufacturers with additive manufacturing (AM) supply chain. Addit. Manuf. **21**, 159–173 (2018)

Influence of Build Orientation on Tensile and Flexural Strength of FDM Fabricated ABS Component

Anubhav, **Rakesh Kumar**, **Shubhra Kamal Nandi**, and **Anupam Agrawal**

1   Introduction

Additive manufacturing is a rapidly growing manufacturing process having the enormous capability to make state-of-the-art products. It was developed in the 1980s, when Japan (Murutani), France (Andre et al.), and the USA (Masters and Hull) filed different patents on a similar concept describing fabrication of a 3D object by addition of material in a layer-by-layer manner. Further, different concepts of layer addition were developed and patented with time, which shows the potential and prospect of AM processes [1]. Initially, it was primarily used for prototyping because of the high initial cost of machinery and devices. FDM process is used to fabricate thermoplastic polymer parts through depositing heated molten material using extrusion process [2]. ABS is a lightweight thermoplastic with many applications in automotive hardware parts [3, 4], appliances, piping, etc. ABS is the most commonly used thermoplastic because of its high dimensional stability and low glass transition temperature [5]. Its peculiar property of having good adhesion to metal coating makes ABS a suitable candidate for various impact loading components [6].

Much research has already been carried out to investigate the FDM-printed polymer and plastic materials for different applications. Kristiawan et al. [7] have reviewed filament processing and printing parameters to fabricate PLA, ABS, and PP using the FDM process. The effect of different raster angles and infill density on strength and quality of FDM-printed ABS was studied [8] and concludes that the part fabricated at 55° raster angle with maximum infill density gives better mechanical strength. Hossain et al. [9] performed experimentation with different raster scan strategies to improve the mechanical properties of 3D-printed parts. Attempts to

Anubhav · R. Kumar · S. K. Nandi · A. Agrawal (✉)
Indian Institute of Technology Ropar, Rupnagar, Punjab 140001, India
e-mail: anupam@iitrpr.ac.in

R. Kumar
e-mail: 2017mez0023@iitrpr.ac.in

determine the anisotropic material properties with the effect of FDM build parameters for ABS show that the strength in a local area depends on the scanning direction [9]. Hatch orientation and hatch area also have an appreciable effect on 3D-printed plastics [11]. FDM-printed ABS and HIPS specimens were tested for tensile impact test and compression test to study the effect of layer thickness on fracture morphology [12, 13]. The presence of voids and bonds between deposited filaments has a more significant influence on the FDM-fabricated parts [14, 15].

Based upon the literature, it has been observed that it is very critical to correctly estimate the mechanical properties of FDM printed parts to make them suitable for various applications. Hence, the present work has been aimed to test 3D-printed ABS material with different orientations along with the horizontal and vertical directions. The FDM-fabricated ABS specimens have been tested for tensile and flexural (3-point bend test) to study its modulus, yield strength, and strain-energy absorption of ABS for its suitability in aerospace and automotive industries. Microscopic images have been used to study the type of failure in the fabricated parts and compared with the stress–strain behavior.

2 Materials and Methodology

2.1 Materials and Part Fabrication

Acrylonitrile butadiene styrene (ABS), a thermoplastic, has a lot of real-life applications. Natural color ABSplus- P430 with SR-30 as support material is used to fabricate the required specimens using FDM-based Stratasys makes Mojo 3D printer. The 3D printer used specimen fabrication has a built volume of 127*127*127 mm^3. The process parameters used for the fabrication of the test specimen are as shown in Table 1.

The specimens used for tensile testing and flexural test (3-point bend Test) are fabricated as per Type-III, confirming ASTM D638-14 and ASTM D790 standard, respectively. The specimens were modeled using SOLIDWORKS® with specified dimensions, as shown in Fig. 1. The CAD model is then converted to STL format

Table 1 FDM material's property and process parameters used for the fabrication of specimen

Properties	Values
Density of ABS	1.05 g/cm^3
Melting point of ABS	230 °C
Nozzle temperature	200 °C
Platform temperature	70 °C
Infill density	100%
Layer thickness	0.17 mm
Filament diameter	1.75 mm
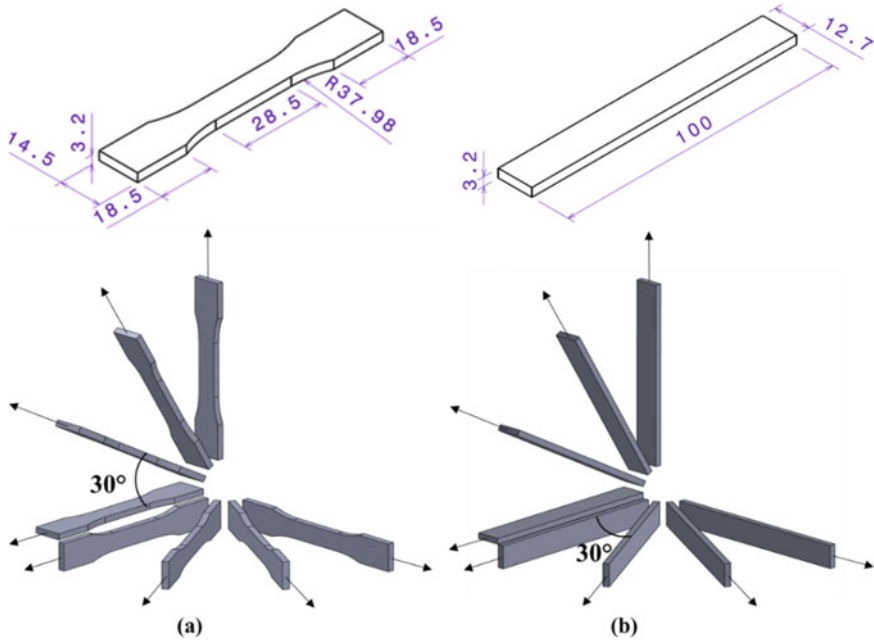
Fig. 1 Specimen with dimensions and CAD model of 0–90° at a step of 30° oriented specimen in the horizontal and vertical direction **a** Tensile testing, **b** Flexural test (3-point bend) (All dimensions are in mm)

and then sliced using open-source slicing software CURA with a minimum layer thickness of 0.178 mm (minimum layer thickness printed by Mojo 3D printer) with 100% infill density. The specimens were fabricated at different orientation angles to understand the mechanical behavior and bonding of material during the deposition in FDM process. The study of FDM-fabricated specimens with different orientations will enable the understanding of the characteristics of layer deposition, which will be helpful to analyze and optimize the design of any part with inclined features. Hence, in this work, tensile and flexural specimens were fabricated at varying angles ranging from 0–90 degrees with a step of 30 degrees (Fig. 1).

2.2 Mechanical Characterization

The specimens fabricated at different orientation angles were tested to study the tensile and flexural behavior. Universal testing machine (Make-Tinius Olsen, Model-H50KS) was used for the testing with 50kN load cell. A deformation rate of 1 mm/min was maintained for the tensile and flexural tests until fracture, which was then analyzed under the optical microscope. The fracture behavior was observed with

the help of optical microscopic image analysis. The required stress–strain values for FDM-fabricated ABS specimens were calculated for both the tests using the obtained force and displacement data from the UTM test by using respective formulae (Fig. 2);

$$\text{Tensile Stress } (\sigma_t) = \frac{\text{Force}(N)}{\text{Cross} - \text{Sectional Area}(\text{mm}^2)} \tag{1}$$

$$\text{Strain } (\varepsilon) = \frac{\delta l}{L} \tag{2}$$

$$\text{Flexural Stress}(\sigma_b) = \frac{3FL}{2bt^2} \tag{3}$$

$$\text{Flexural Strain } \left(\varepsilon_f\right) = \frac{6t\delta}{L^2} \tag{4}$$

$$\text{Modulus} = \frac{\text{Stress}}{\text{Strain}} \tag{5}$$

$$\text{Strain Energy Density } (u) = \int_0^\varepsilon \sigma_t d\varepsilon \tag{6}$$
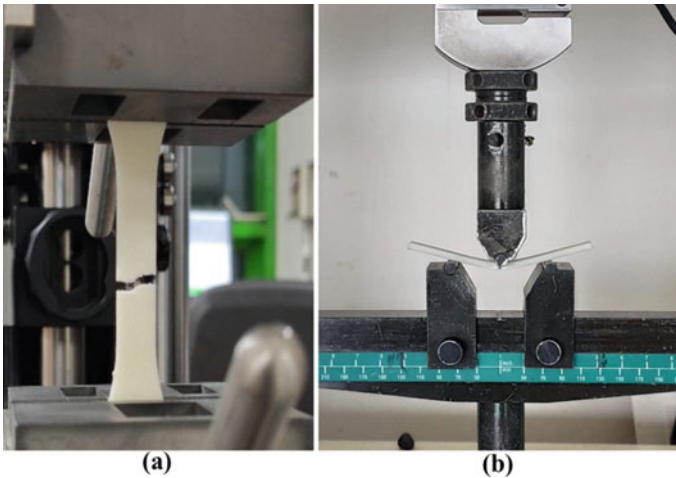
Fig. 2 Testing of FDM-fabricated specimen under different conditions **a** Uniaxial tensile test, **b** 3-point bend test

3 Results and Discussion

3.1 Uniaxial Testing

In total, three sets of ASTM standard tensile specimens of each category were 3D printed and tested to determine the mechanical properties. Deformation rate has a considerable effect in determining the stress–strain behavior; hence, a moderate rate of 1 mm/min was used to perform the tensile test experiment. Figure 3a shows the stress–strain plot for the vertically oriented specimens. The results indicate that the vertically printed parts have less plastic flow and are prone to brittle failure. The horizontally oriented specimens show better plastic flow as compared to vertically oriented specimens with the exception of H_30° (Fig. 3b). The horizontal specimens undergo 20–22% elongation before fracture, whereas the vertically aligned specimen is strained about 12–16% only. Hence, the horizontal specimen can withstand more stress as compared to vertically printed specimens.

Figure 4 represents the young's modulus and yield strength of the tested specimens, respectively. The young's modulus values were plotted and fitted with a second-order polynomial to correlate with the orientation angle (Fig. 4a). The modulus values increase with orientation angle for vertical specimens, whereas the horizontal specimen shows the highest modulus for 60° specimen. The yield strengths were calculated using 0.2% offset method for all the specimens. The yield strength of the vertical specimen represents a decreasing trend with an increase in orientation angle, while for horizontal specimen, it is maximum for a 90° oriented specimen (Fig. 4b). It indicates that the horizontally oriented specimens have better bond strength as well as they undergo more plastic deformation (more ductility) as compared to vertical specimens. As the deposition pattern for vertical and horizontal specimens are different hence the orientation of deposited filament has a more significant influence on part strength. In a horizontal specimen, the load is acting along the direction of deposited filament, whereas it is in the transverse direction for the vertical specimens (Fig. 5).
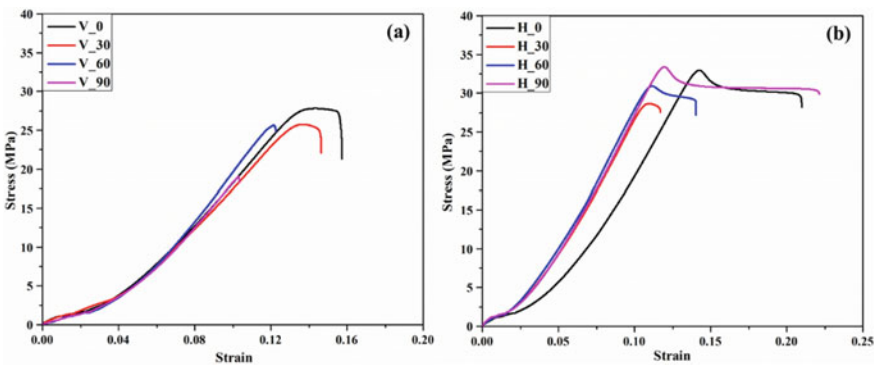
Fig. 3 Tensile stress versus strain plot for horizontal and vertical oriented FDM printed specimen

As the angle increases in the case of the vertical direction, the area of deposition for an instant also keeps on decreasing, which ceases the flow of material during UTM tensile testing. Hence, vertical oriented has less strength under tensile loading compared to horizontal specimens.

In Fig. 6, strain energy is computed and plotted against the respective strains up to the fracture using Eq. 6. When compared between vertical and horizontal results, the horizontal specimens are found to have more energy storage capacity than the vertical ones under the same loading conditions. The strain energy stored by horizontal specimens is more (almost twice) than that of vertically built specimens. Strain-energy absorbed till the yield point has been represented (in the inset image of Fig. 6) to understand the behavior of specimens in the elastic range.
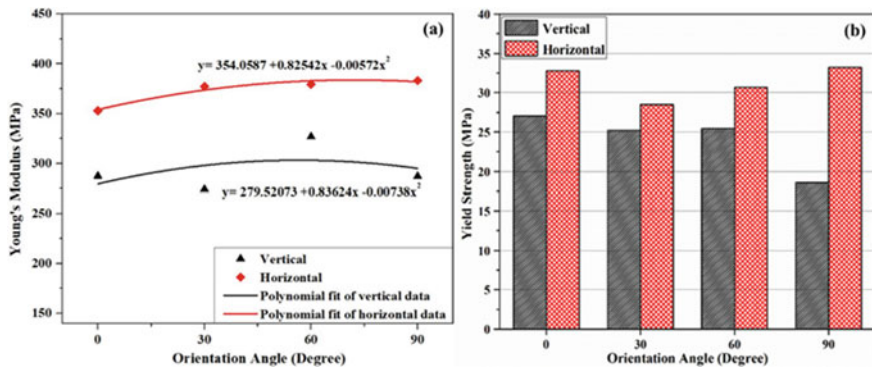
Fig. 4 Obtained results from stress–strain data for **a** Young's Modulus, **b** Yield Strength
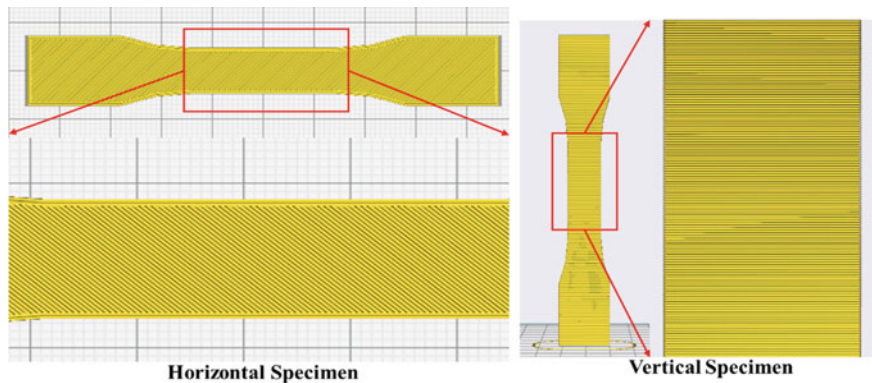
Fig. 5 Pattern of filament deposition in horizontal and vertical part printing
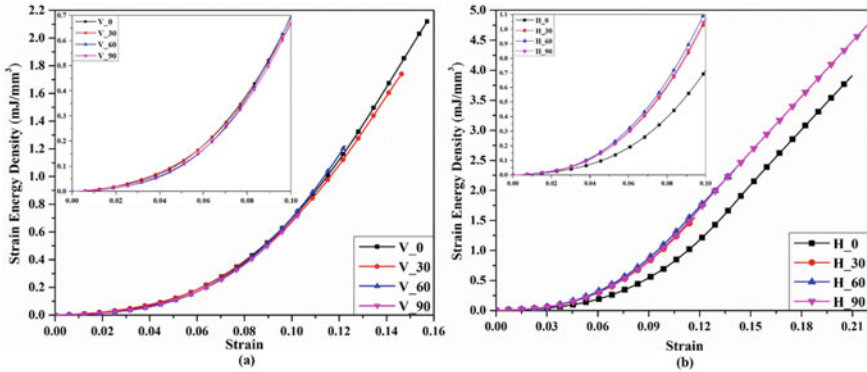
Fig. 6 Strain energy density obtained from tensile stress–strain data **a** Vertically oriented specimen, **b** Horizontally-oriented specimen

3.2 Flexural Testing

The 3-point bend test is the best method to measure the flexural properties under applied loading conditions. A set of 3-point bend test specimens were designed as per the ASTM D790 and 3D printed for further testing using ABS material. Like tensile test specimens, these specimens were fabricated in vertical and horizontal directions with a step of 30° angle. The specimens were tested at a velocity of 1 mm/min under 3-point load, and flexural modulus and flexural yield strength were calculated and compared (Fig. 8). The vertical specimen shows significantly less strain and flexural strength with increasing orientation angle (Fig. 7a), whereas in the horizontal specimen, the 0° and 90° specimen show approximately similar behavior.
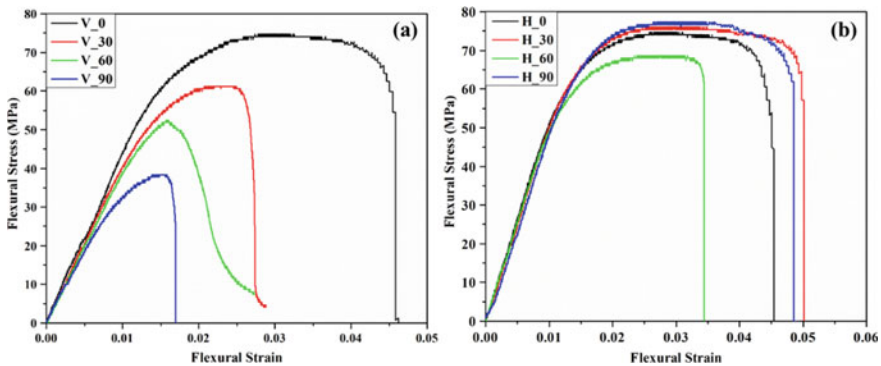
Fig. 7 Flexural stress–strain curve of vertically and horizontally oriented specimen
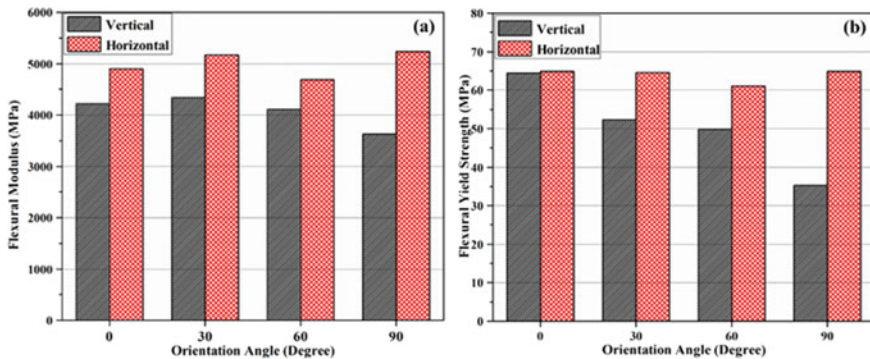
Fig. 8 Obtained results from Flexural stress–strain data for **a** Flexural Modulus, **b** Flexural Yield Strength

3.3 Fractography

Figure 9 represents the optical images of the fractured tensile specimens (for both vertical and horizontal orientations) to illustrate the type of failure that occurred in the specimen as it is clear that the outer peripheral layer for each specimen is fractured and tore off differently than the inner material. It happens due to the inherent fabrication constraint of the FDM process by printing the outer layer before filling the inner part in a defined scanning pattern. Fractographs of specimens of angle 0° and 30° with vertical show abrupt delamination of deposited filaments representing brittle failure. The 30° oriented horizontal specimen also shows a similar trend. Whereas in the case of 0°, 60° and 90° oriented horizontal specimens show material accumulation at the fractured zone, indicating ductile fracture. In a few cases (like V_60, H_0, H_60, and H_90), the accumulation of voids and crack formation is also visible, which explains the ductile fracture of the designed specimens.

4   Conclusion

The FDM process is the most versatile 3D printing process because of its ease to fabricate any customized part using thermoplastics for different applications. In the present work, it has been observed that the part orientation during printing plays a crucial role in its strength and behavior under different loading conditions. The obtained results show that the part orientation directly relates to material deposition and layering to bond the deposited material cohesively. Horizontally printed parts show qualitatively better tensile and flexural properties than the vertically printed specimens. For the horizontal specimens young's modulus and flexural modulus are about 350–385 MPa and 4.8–5.3 GPa, respectively, whereas for vertical specimen, it lies in the range of 275–325 MPa and 3.6–4.4 GPa, respectively. The obtained
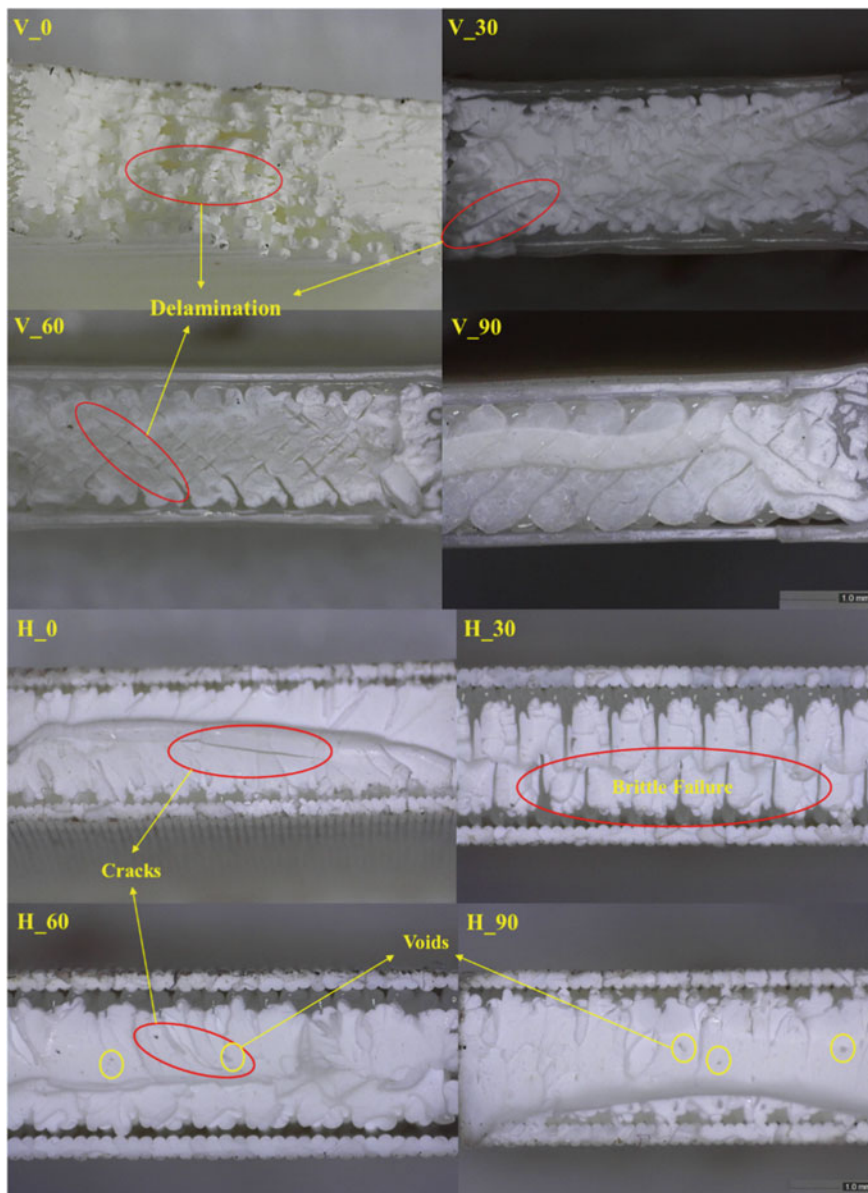
Fig. 9 Magnified optical images of the fractured surface of tensile specimens (scale bar −1.0 mm)

fractography indicates the modes of failure that occurred during tensile testing. This work will pave for future studies of complex geometries, metamaterial designing and optimal printing orientations.

References

1. Ngo, T.D., Kashani, A., Imbalzano, G., Nguyen, K.T.Q., Hui, D.: Additive manufacturing (3D printing): a review of materials, methods, applications and challenges. Compos. Part B Eng. **143**, 172–196 (2018). https://doi.org/10.1016/j.compositesb.2018.02.012
2. Singh, J., Chawla, K., Singh, R.: Applications of thermoplastic polymers in 3D printing. In: Reference Module Materials Science Materials Engineering, Elsevier, (2020). https://doi.org/10.1016/b978-0-12-820352-1.00010-9
3. Moore, J.D.: Acrylonitrile-butadiene-styrene (ABS)—a review. Composites **4**, 118–130 (1973). https://doi.org/10.1016/0010-4361(73)90585-5
4. Yadav, D.K., Srivastava, R., Dev, S.: Design and fabrication of ABS part by FDM for automobile application. Mater. In: Today Proceedings, vol. 26, pp. 2089–93. Elsevier, (2019). https://doi.org/10.1016/j.matpr.2020.02.451
5. Weng, Z., Wang, J., Senthil, T., Wu, L.: Mechanical and thermal properties of ABS/montmorillonite nanocomposites for fused deposition modeling 3D printing. Mater. Des. **102**, 276–283 (2016). https://doi.org/10.1016/J.MATDES.2016.04.045
6. Olivera, S., Muralidhara, H.B., Venkatesh, K., Gopalakrishna, K., Vivek, C.S.: Plating on acrylonitrile–butadiene–styrene (ABS) plastic: a review. J. Mater. Sci. **51**, 3657–3674 (2016). https://doi.org/10.1007/s10853-015-9668-7
7. Kristiawan, R.B., Imaduddin, F., Ariawan, D., Ubaidillah, Arifin, Z.: A review on the fused deposition modeling (FDM) 3D printing: Filament processing, materials, and printing parameters. Open Eng. **11**,639–49 (2021). https://doi.org/10.1515/eng-2021-0063
8. Selvamani, S.K., Samykano, M., Subramaniam, S.R., Ngui, W.K., Kadirgama, K., Sudhakar, K., et al.: Preliminary investigation of acrylonitrile butadiene styrene (ABS) properties. In: AIP Conference Proceedings, pp. 2059. (2019). https://doi.org/10.1063/1.5085983
9. Hossain, M.S., Espalin, D., Ramos, J., Perez, M., Wicker, R.: Improved mechanical properties of fused deposition modeling-manufactured parts through build parameter modifications. J. Manuf. Sci. Eng. Trans. ASME **136**, (2014). https://doi.org/10.1115/1.4028538
10. Ahn, S.H., Montero, M., Odell, D., Roundy, S., Wright, P.K.: Anisotropic material properties of fused deposition modeling ABS. Rapid Prototyp J. **8**, 248–257 (2002). https://doi.org/10.1108/13552540210441166
11. Koch, C., Van Hulle, L., Rudolph, N.: Investigation of mechanical anisotropy of the fused filament fabrication process via customized tool path generation. Addit. Manuf. **16**, 138–145 (2017). https://doi.org/10.1016/j.addma.2017.06.003
12. Uddin, M.S., Sidek, M.F.R., Faizal, M.A., Ghomashchi, R., Pramanik, A.: Evaluating mechanical properties and failure mechanisms of fused deposition modeling acrylonitrile butadiene styrene parts. J. Manuf. Sci. Eng. Trans. ASME **139**, (2017). https://doi.org/10.1115/1.4036713
13. Mizera, A., Bednarik, M., Mizera, M., Tomanova, K., Mohorko, M.: Tensile impact behaviour of 3D printed parts on FFF/FDM printer Zortrax M200. In: MATEC Web Conference 2018, vol. 210, pp. 2–6. (2018).https://doi.org/10.1051/matecconf/201821004049

14. Gurrala, P.K., Regalla, S.P.: Part strength evolution with bonding between filaments in fused deposition modelling: This paper studies how coalescence of filaments contributes to the strength of final FDM part. Virtual Phys. Prototyp. **9**, 141–149 (2014). https://doi.org/10.1080/17452759.2014.913400
15. Rodriguez, J.F., Thomas, J.P., Renaud, J.E.: Characterization of the mesostructure of fused-deposition acrylonitrile-butadiene-styrene materials. Rapid Prototyp J. **6**, 175–185 (2000). https://doi.org/10.1108/13552540010337056

Leaf Vein Structure in Additively Manufactured Aluminium Components for Stiffness

Jyothirmay Bhattacharjya, Meenakshi Devi Parre, and Vamsi Krishna Pasam

1 Introduction

Additive manufacturing (AM) is one of the emerging trends in the manufacturing sector. The complex part manufacturing capabilities as well as its ability to produce high-quality products with minimum loss of material makes it a versatile technique. A number of additive manufacturing techniques are commercially available nowadays for both polymer and metal 3D printing. Some of them are selective laser melting (SLM), fused deposition modelling (FDM) and electron beam melting (EBM). However, process parameters selection is a tedious task to obtain the products with desired quality. A good set of process parameters can reduce the errors of the production process to a great extent. A lot of process parameters were observed from the literature of AM technology, among which some are interdependent also. Fused deposition modelling (FDM) is a widely adopted process that works on this technology [1]. In this technology generally, the material is used in the form of solid and with the help of some heating source it is melted and then extruded through a nozzle, like in the case of icing. The popular heat source used is induction heating. This technology is more popular for polymers like thermoplastics. The raw material can be used in the form of a spool of wire or small pieces of wire. For continuous feeding of the material, spool of wire is preferable. With the help of some roller mechanism, the wire is pulled inside the heating chamber. If the material is used in

J. Bhattacharjya
Department of Mechanical Engineering, National Institute of Technology, Warangal, Telangana 506004, India

M. D. Parre (✉) · V. Krishna Pasam
Department of Mechanical Engineering, RGUKT, RK Valley, YSR Kadapa(Dt), Andhra Pradesh, Idupulapaya 516330, India
e-mail: pmeenakshidevi@gmail.com

V. Krishna Pasam
e-mail: vamsikrishna@nitw.ac.in

any form other than a spool of wire, then it has to feed inside the heating chamber manually. Within the heating chamber, the material will be melted and it will be extruded through the nozzle. The nozzle is allowed to move in XY axis, while the building platform is allowed to move in Z-axis. Each layer will be fabricated by the XY direction movement of the nozzle. After printing one layer, the platform lowers down by the thickness of one layer and then again extrusion started. The speed at which material is extruded is a very important parameter for obtaining a good quality product.

The influence of nozzle temperature and infill line orientations for parts made with short carbon fibre (CF)-reinforced polylactic acid (PLA) is studied [2]. They proved the influence of nozzle temperature on the mechanical properties, with an optimum temperature maximizing the tensile properties. The addition of a reinforcing agent such as CF in the polymer matrix also improves the tensile properties if the process parameters are well chosen. The influence of the raster angle and the moisture content percentages on the mechanical properties of 3D-printed polylactic acid (PLA) material is studied [3]. This research specifies that specimens with a 90° raster angle and 10% moisture content have the optimum strength and strain mechanical properties. Three different types of polymers, including polylactic acid (PLA), polyethylene terephthalate glycol (PETG) and acrylonitrile butadiene styrene (ABS), were used in fused deposition modelling (FDM) process to fabricate several parts results of statistical analysis indicated the temperature as the significant factor on tensile strength while the material change did not show a significant effect [4]. A methodology for optimizing both process efficiency, i.e. time and energy consumption, and part quality, i.e. surface roughness and dimensional accuracy, of polylactic acid (PLA) components produced by FDM and it is shown that, according to the context, different parameter settings pursue different goals in terms of part quality and process efficiency[5]. The proposed approach may effectively help designers determine process parameters' settings to optimize both part quality and process efficiency and can be applied to either prototype or part production. The impact of FDM fabricated parts made up of ABS and the influence of build direction on mechanical properties is studied [6]. The parts are made with and without a hole in the centre. The parts were built in C + 45 orientation, XY and XZ directions. It was concluded from the study that parts fabricated in XZ direction have higher fracture strength and C + 45 has a lower strength. Parts without a hole are significantly affected by build direction. The change in dimension of the hole both in diameter and in-depth affects the fracture strength of the parts. The effect of process parameters on mechanical properties on 3D-printed PLA parts is studied [7]. Layer thickness of 0.1, 0.12, 0.15, 0.18 and 0.2 mm and orientation of 00, 180, 450, 720 and 900 are considered. The study identified that the ultimate tensile strength of the part decreased as the infill orientation reaches 900. The strength of the parts increased with an in-layer thickness to the value of 0.18 mm.

The effect of the external perimeter on FDM fabricated parts is studied [8]. Contour number, layer thickness, raster width, part orientation, raster angle and air gape were the factors considered in the study. It was observed that as the external perimeter is increased, the strength of the parts also increased. This is attributed to the shift in stress

concentration towards the centre due to the addition of contours. The combination of contour number = 5, layer thickness = 0.330 mm, raster width = 0.4064 mm, part orientation = 00, raster angle = 00 and air gape = 0 mm is found to give best results.

The mechanical properties are studied and compared the same among the alloy manufactured by selective laser melting (SLM), laser direct deposition (LDD) and electron beam melting (EBM) [9]. The mechanical properties of AM Ti alloys manufactured by different techniques are identified [10]. The author also studied the surface roughness, wear properties of AM alloys in comparison with wrought alloys. The complex relationship between AM processes, microstructure and resulting properties for metals is described [11]. Special attention is paid to AM specific grain structures. Micromilling of Ti alloys manufactured by conventional as well as AM techniques is focussed [12]. The surface finish, cutting forces and burr formation were studied. The microstructural and mechanical properties variation among different AM techniques were highlighted [13]. It also highlights the manufacturers of AM equipment.

In this work to improve the mechanical properties, bionically inspired structures are introduced into the samples. The stiffness of different thermoplastics is relatively low and it can be improved by the introduction of carbon fibres into it [14]. Two thermoplastics polylactic acid (PLA) and acrylonitrile butadiene styrene (ABS) were studied. Parts were fabricated using 3D printing technology and subjected to three-point bending test. The sample was made up of PLA, ABS, PLA reinforced with carbon fibres and ABS reinforced with carbon fibres. PLA reinforced with carbon fibres had the highest stiffness value followed by the unreinforced PLA and unreinforced ABS had the least value of stiffness. PLA material has a higher value of stiffness than ABS. A bionically inspired topological optimization to improve the stiffness for the column of a grinding machine is used [15]. Earlier due to the manufacturing constraints generally '#' and 'x' shaped stiffener layouts are used to improve the stiffness. There are three levels in which analogical analysis should be considered, those are structure, i.e. topology or shape, loading and functional similarity. These bionic structures can be used to solve engineering problems only if it satisfies the analogy. A leaf can be assumed as a cantilever subjected to the loadings due to the environmental impact and dead weight. The leaf vein structures are generally classified into two categories depending upon the number of principal veins, which are pinnate venation and palmate venation. The pinnate venation system used to have only one principal vein, while the palmate venation system used to have two principal vein structures. Improvisation of the stiffness with the help of a sandwich structure containing two thin, stiff face sheets of carbon fibre reinforced polymer and a thick low density porous structure is done [16]. The stiffness was improved remarkably with this model. This model was inspired by biological tissue structures. One problem with this type of sandwich structure is it is subjected to local failure, which limited its mechanical properties. The local failure includes debonding between the face and the core, and the core may collapse sometime. But this type of limitation in mechanical properties can be avoided by the use of structures like veins inside the sandwich structure. In nature, both grass leaves and tree leaves have the sandwich kind of tissue structure but the tree leaves are stronger than the grass leaves due

to the presence of vein structures in them. An approach to improve the mechanical properties of the parts fabricated by fused deposition modelling is proposed [17]. Thermally expandable microspheres were used in the matrix during fabrication and later on exposed to temperature increase due to which the microsphere expanded and occupied the voids in the parts. Positive results were observed for tensile strength. The addition of 2 weight% microspheres and heating at a temperature of 1400 C for 120 s improves the tensile strength of the parts by 25.4% than the untreated samples. The prime material used for FDM machines is ABS and PLA which are having melting temperatures in the range of 1800 C to 2200 C and the microspheres need heating at a temperature of 1400 C; hence, these microspheres effectively can be used without distortion of the main part during heat treatment.

In this work, simulation of the sample made up of PLA is done in ANSYS Workbench and the simulation results are obtained. Then, sample with the same dimensions as per ASTM D790 and made of PLA is fabricated in FDM and simulation and experimental details are validated. After the validation of results to check material dependency of leaf vein structures, an attempt is made to simulate the effect of different leaf vein structures on the strength of aluminium 6061-T6 alloy. Three-point bending test is used in this work to determine the strength of the sample. This work also emphasizes the role of bionically inspired structures in improving the design and strengthening the existing components by reducing stress and deformation. In addition, the design and fabrication of bionic structure reinforced additive manufactured components provides a new method of improving the mechanical properties of components produced by the aforementioned technique.

2 Design and Simulation

2.1 Fabrication of Standard Sample

After slicing and generating the G-code in the Flash Print, parts were fed to a Flash Forge printer. The standard specimen was fabricated, i.e. the rectangular bar without any vein structure. The specimen is fabricated according to ASTM D790 standard [18] with 127 mm long, 12.7 mm wide and 3.2 mm thick as in Fig. 1. The material used during fabrication is white polylactic acid (PLA), which is a widely used thermoplastic material for 3D printing machines. Some of the important specifications of the Flash Forge printer used for fabrication are listed in Table 1 and is shown in Fig. 2.

2.1.1 Steps in the Design of Vein Structures

The step-by-step process of how the veins are designed is described for arcuate vein structure. The same process is used for designing the other vein structures.

Fig. 1 Test specimen
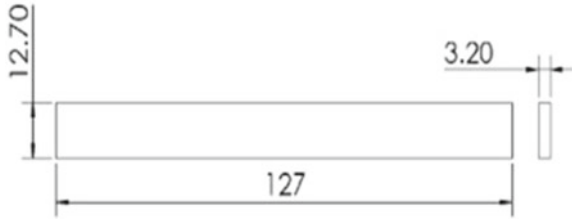
Table 1 Specification of the Flash Forge printer used

S. No	Specification	Details
1	Print speed	40–60 mm/s
2	Layer resolution	100–300 microns
3	Nozzle temperature	220 °C
4	Build volume	$140 \times 140 \times 140$ mm^3
5	Nozzle diameter	0.4 mm
6	Product dimension	$420 \times 420 \times 420$ mm^3
7	Extruder	Single
8	Filament diameter	1.75 mm
9	Supported filament	PLA
10	File type	.stl,.obj
11	Software	Flash print

Fig. 2 Line diagram of FDM
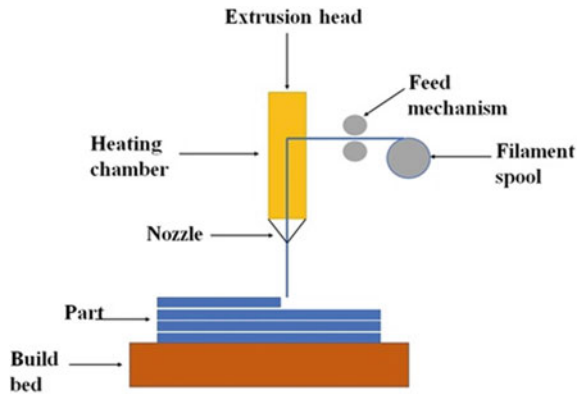
- At the start of the design, the type of modelling and unit for the dimensions has to select. The type of modelling selected was solid part and the unit selected was mmks.
- After setting the unit, the plane for drawing has to select. The front view was selected to draw the cross section of the rectangular bar.

- After selecting the plane, the sketch mode has to be selected where the primitive structures are present to draw the 2D profiles.
- For this model, the rectangular primitive was selected and the cross section was drawn in the front view. The dimension of the rectangle is 127 mm long and 12.7 mm wide.
- After obtaining the 2D cross section of the rectangular bar, it has to be extruded to get the 3D model. For this, the extrude command should be used. The cross section was extruded by 3.2 mm to get the rectangular bar of dimension 127 × 12.7 × 3.2 mm.
- After getting the rectangular bar, one of its faces has to be selected to draw the leaf veins on it using the spline command. Using spline command if veins are drawn, the advantage is that more control points are obtained on the vein to give it desired shape.
- After drawing all the primary, secondary and tertiary veins on the selected plane, the 3D shape was given to the drawn veins using swept blend command. This command helps in sweeping a cross section over an axis ununiformly.
- The cross section selected for the veins was circular with an initial diameter of 1.5 mm that converges to 1.2 mm for primary veins using the swept blend command. Similarly, for secondary veins, 0.8 mm converges to 0.6 mm and for tertiary veins; 0.6 mm converges to 0.4 mm.
- After sweeping the cross section of all the veins, the 3D model was ready for further use.

2.2 Three-Point Bending Test

In this work, three-point bending test was carried out to study the load vs. deformation behaviour of the standard sample, i.e. the one without any vein structure and with different vein structures. The schematic representation of three-point bending is shown in Fig. 3. Moreover, the data obtained from the experiment were used to find the flexural strength of the parts. The deflection of the sample was allowed until the rapture. It is used to get the modulus of elasticity in bending, flexural stress, flexural strain and flexural stress–strain response of the fabricated PLA sample. The elastic modulus in bending (E) can be extracted from a flexural test. The advantage of the flexural test comes from the ease of sample preparation and testing. However, the disadvantage comes from the fact that the results of the testing method are sensitive to specimen and loading geometry and strain rate. In the experiment, the sample was kept in the flat position on adjustable support. Then, the sample was loaded with the help of a moving crosshead located in between the support. The dimension of the test specimen is 127 mm long, 12.7 mm width and 3.2 mm thick and the support span length used here is 102 mm, according to ASTM D790. Total three samples were tested. The mechanical properties of the samples are given in Table 2.

Fig. 3 Three-point bending test
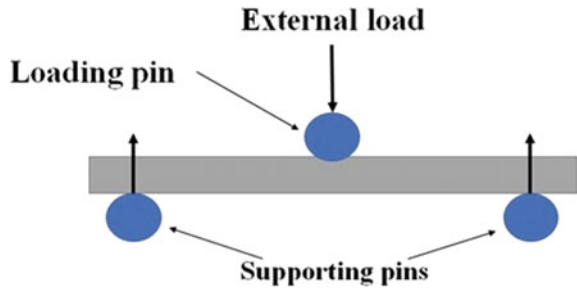
Table 2 Average mechanical properties of all the samples

S.No	Specimen type	Average maximum load (N)	Average deflection at the centre of the sample(mm)	Average flexural stress (MPa)	Average flexural strain (mm/mm)	Average flexural modulus (GPa)
1	Sample with dichotomous vein structure	52.630	24.36	61.92	0.0449	1.38

2.3 Mesh Independency Checking

Boundary conditions:

The boundary condition used in the analysis is, deflection at a beam length $x = 0$ is 0, i.e. $y(0) = 0$, deflection at a beam length $x = l$ is 0, i.e. $y(l) = 0$, load is applied at the centre of the beam, deflection at centre is allowed in y-direction only. The element size of 0.22 mm was used as it is observed that after the element size of 0.25 mm the deformation is identical to the second digit after the decimal. A fine mesh consisting of 5,02,860 elements was used.

Validation is the process of checking the degree to which a simulated model is accurate to use in a real-world problem. In this study, the standard sample was simulated to determine the stiffness. The design was validated by performing a 3-point bending test on the fabricated part. Both the simulation and experimental results are compared and checked the error % in the simulated results as shown in Table 3 and Fig. 4.

Table 3 Validation of model

Sample	Deflection obtained from simulation up to 30N load in 'mm'	Deflection obtained from experiment up to 30 N load in 'mm'	% Error
Standard sample	8.9915	9.1910	2.17
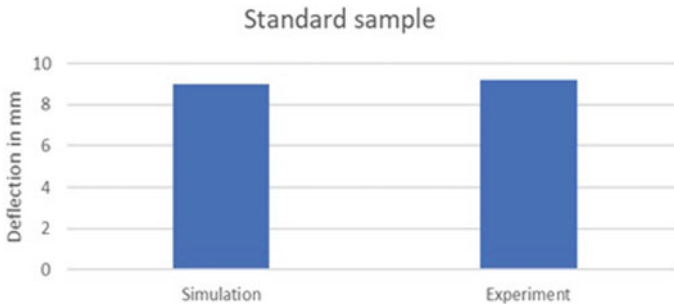
Fig. 4 Comparison between experimental results and simulation results for three-point bending test up to 30 N load

It can be observed that the error obtained in the case of the standard sample is 2.17%. The reason for obtaining this error may be due to

- The human errors involved during the experiment and due to the limitations of the fabrication, technology employed, i.e. additive manufacturing in this work.
- Moreover, the difference is also occurred due to the material definition in ANSYS, where the value of Young's modulus is assumed as 2.4 GPa, but in reality, it can be in the range of 2 to 3 GPa.
- During analysis, the element size for the fine node was taken as 0.22 mm, which was obtained from the mesh independency checking of parts without any vein structures. The same element size was used for the other two samples also. However, the samples with leaf vein structures are more complex and hence the element size of 0.22 mm may not be the finer one to get an accurate result.
- From this, the FE model developed is evaluated and found to give satisfactory results with minimum error.

3   Results and Discussion
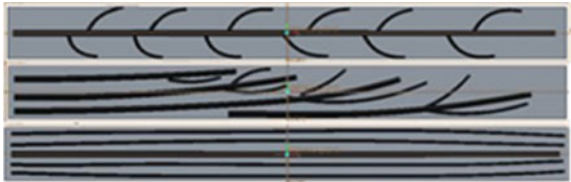
3.1   Simulation of Aluminium 6061-T6 Parts

The model developed earlier is used to simulate the effect of different leaf vein structures on the strength of the component made of aluminium 6061-T6 material. Table 4 represents the properties of aluminium 6061-T6 material. Three-point bending simulation was done on the rectangular bars consisting of the leaf vein structures. At the very first step, the material was defined, as it is not present in the material library of ANSYS Workbench. The material definition is done following the properties of aluminium 6061-T6 as given in Table 5. Four-leaf vein structures were evaluated, namely arcuate, dichotomous and parallel vein structure along with standard sample, i.e. without leaf vein structure as given in Table 5.

Table 4 Aluminium 6061—T6 material property

S. No	Properties	Magnitude
1	Young's modulus	6890 MPa
2	Tensile ultimate strength	310 MPa
3	Tensile yield strength	276 MPa
4	Density	2.7 g/cm^3
5	Poisson's ratio	0.33

Table 5 Specimen structures

S. No	Name of the structure	Structure
1	Arcuate	
2	Dichotomous	
3	Parallel	

Simulation results are shown in Figs. 5, 6, 7 and 8 and tabulated in Table 6 for a load range of 0—30 N to compare and find out the most suitable vein structures among all. In the Table 6, simulation results of three-point bending test for a range of loading from 0 to 30 N are shown. The corresponding deformation values are directly collected from the solution module of ANSYS Workbench. From Table 6, it can be seen that the parallel and dichotomous leaf vein structures have shown the least value of deflection for the range of loading. The standard specimens, i.e. the specimen without any leaf vein structures have shown a deflection value of 2.7427 mm for a load of 30 N. On the other hand, samples with parallel and dichotomous leaf vein structures have shown deflection values of 2.1075 mm and 2.0383 mm, respectively, as shown in Table 7 and also in Fig. 10.

This is an indication of the stiffer design due to the application of the leaf vein structures upon the samples. The leaf vein structure acts as a support to withstand the external load and hence increases the resistance of the part to bending under the application of an external load. Load vs. deflection curve up to 30 N load of the above results has shown in Fig. 9. From the graph, it can be seen that the slope of load vs. deflection curve is highest or dichotomousand parallel leaf vein structures and is least for standard sample, i.e. the sample without any leaf vein structures. Higher the slope of load vs. deflection curve more is the stiffness. From the above results, two conclusions can be made.

The use of leaf vein structure has improved the stiffness of the parts as the leaf veins act as a support structure to withstand the external load and hence increase the resistance of the part to bending under the application of an external load.
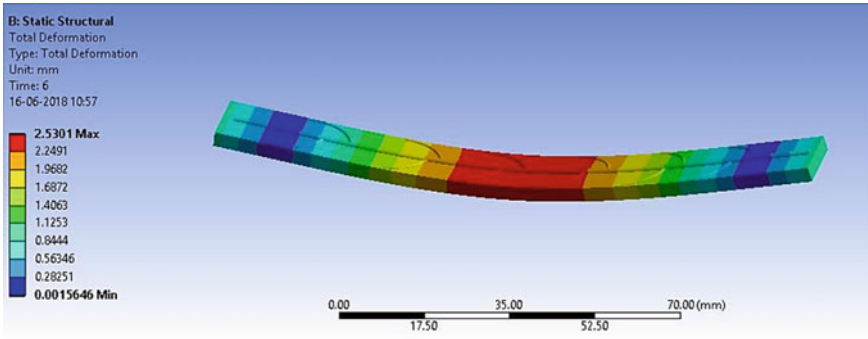
Fig. 5 Three-point bending simulation for Al 6061-T6 parts with arcuate vein structure
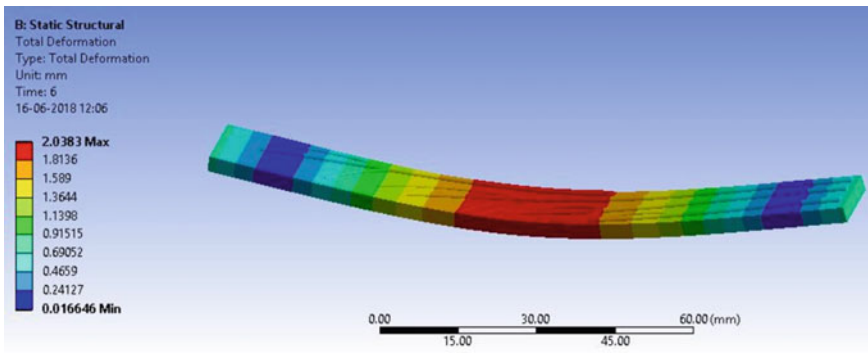
Fig. 6 Three-point bending simulation for Al 6061-T6 parts with dichotomous vein structure
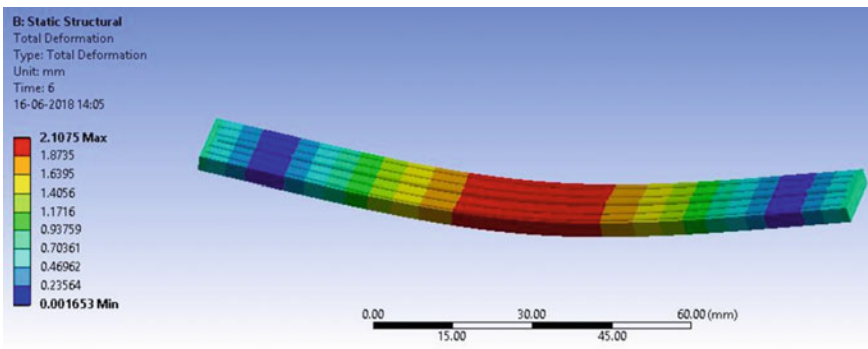
Fig.7 Three-point bending simulation for Al 6061-T6 parts with parallel vein structure
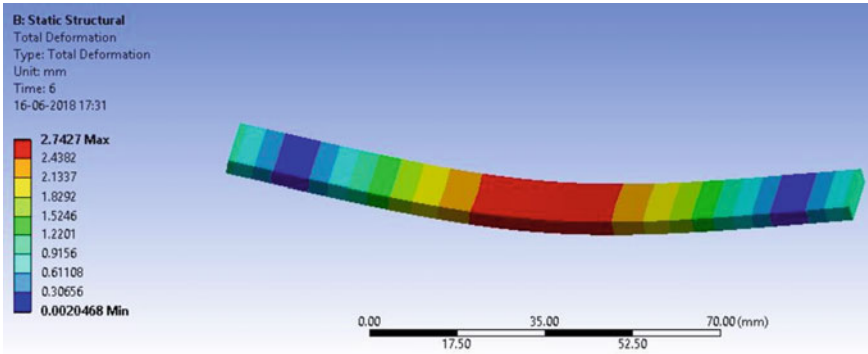
Fig. 8 Three-point bending simulation for Al 6061-T6 parts without any vein structure

Table 6 Summarized simulation results for Al 6061-T6 parts with different vein structures

S. No	Load	Arcuate	Dichotomous	Parallel	Standard
1	0	0	0	0	0
2	6	0.50602	0.40765	0.4215	0.54854
3	12	1.012	0.81531	0.843	1.0971
4	18	1.518	1.223	1.2645	1.6456
5	24	2.0241	1.6306	1.686	2.1942
6	30	2.5301	2.0383	2.1075	2.7427

Table 7 Summarized results for deflection

S. No	Samples with leaf vein structure	Aluminium 6061-T6 'mm'
1	Arcuate	2.5301
2	Dichotomous	2.0383
3	Parallel	2.1075
4	Samples without vein structure	2.7427

Among all the leaf vein structures, dichotomous and parallel structures are most suitable to improve the stiffness. The difference in the deflection value of the samples with the leaf vein structures under the application of the same amount of load is due to,

i. The distribution pattern of the leaf veins over the surface of the sample.
ii. Difference in the constituent veins present, i.e. in dichotomous structure, more than one primary veins are present which have more thickness than the secondary and tertiary veins; hence, it can provide more support to the applied load. Similarly, though in parallel vein structure, only one primary vein is present along
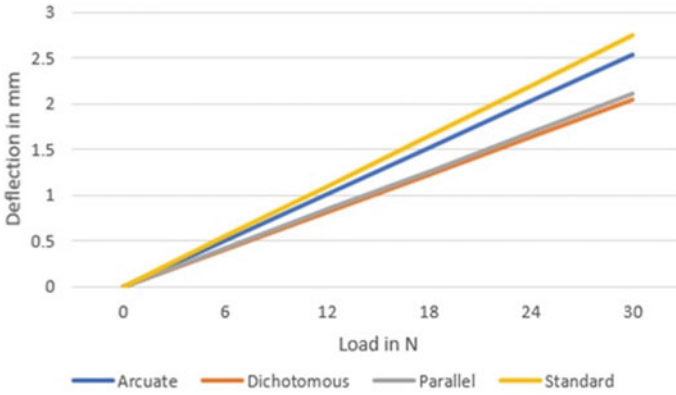
Fig. 9 Load versus deflection
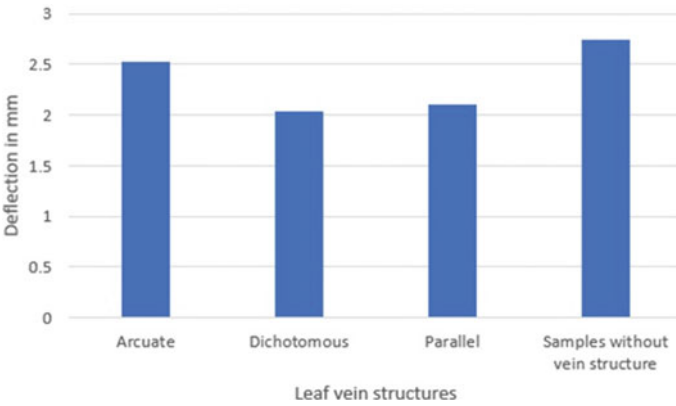
Fig. 10 Deformation of aluminium 6061-T6 samples

with other secondary veins they are symmetrically distributed and in parallel with the primary veins. More than one primary veins are also present in rotated vein structure but their distribution is not uniform over the surface of the sample.

4 Conclusions

In this work, with the help of leaf vein structure, an approach was followed to improve the stiffness of the skin of aircraft wings. For this different leaf vein, structures were designed in CREO and studied in ANSYS Workbench to compare them and find the most suitable one among all. Standard samples were fabricated using additive manufacturing technology. Fabricated samples were subjected to three-point bending

test in a universal testing machine to compare the simulated results with the experimental one. After validation, leaf vein structures were simulated for aluminium 6061-T6 material. These designs are evaluated and the influence of leaf vein structure is studied.

- It is observed that the stiffness of the parts increased when vein structures were used. Almost all the types of vein structure can improve the stiffness as proved by the simulation results. Among all, the vein structures two most preferable vein structures are dichotomous veins and parallel veins.
- Simulation results are almost similar to the experimental results. It implies that the simulation model adapted is correct.
- Due to the change of material from PLA for the standard specimen to aluminium 6061-T6 for the samples, though the deflection value for all the samples under the same loading condition has decreased, which is due to the higher Young's modulus of aluminium 6061-T6 than PLA, the preference order for all the eight vein structures is same in both cases. It implies the material independency of the design.
- From the study, the dichotomous leaf vein structures are found to be more effective with less deformation.

References

1. Gibson, I., Rosen, D., Stucker, B.: In: Additive Manufacturing Technologies, 2nd edn. Springer, (2015). https://doi.org/10.1007/978-1-4939-2113-3
2. Anouar El, M. et al.: Mechanical properties of CF-reinforced PLA parts manufactured by fused deposition modeling. J. Thermoplastic Composite Mater. **34**(5), 581–595 (2021)
3. Algarni, M.: The influence of raster angle and moisture content on the mechanical properties of PLA parts produced by fused deposition modeling. Polymers **13**(2), 237 (2021)
4. Sehhat, M., Mahdianikhotbesara, H.A., Yadegari, F.: Impact of temperature and material variation on mechanical properties of parts fabricated with fused deposition modelling (FDM) additive manufacturing (2021)
5. Maurizio, G., Verna, E., Genta, G.: Effect of process parameters on parts quality and process efficiency of fused deposition modeling. Comput. Indus. Eng. **156**, 107238 (2021)
6. Keles, O., Blevins, C.W., Bowman, K.J.: Effect of build orientation on the mechanical reliability of 3D printed ABS. Rapid Prototyping J. **23**(2) (2017). Retrieved from https://doi.org/10.1108/RPJ-09-2015-0122
7. Lanzotti, A., Grasso, M., Staiano, G., Martorelli.: The impact of process parameters on mechanical properties of parts fabricated in PLA with an opensource 3-D printer. Rapid Prototyping J. **21**(5) (2015). Retrieved from https://doi.org/10.1108/RPJ-09-2014-0135
8. Mishra, S., Malik, B., Mahapatra, R.S.: Effect of external perimeter on flexural strength of FDM build part. Res. Article–Mech. Eng. (2017). https://doi.org/10.1007/s13369-017-2598-8
9. Liu, S., Shin, Y.C.: Additive manufacturing of Ti6Al4V alloy : a review. Mater. Des. **164**, 107552 (2019)
10. Tong, J., Bowen, C.R., Persson, J., Plummer, A.: Mechanical proper-ties of titanium-based Ti–6Al–4V alloys manufactured by powder bed additive manufacture. Mater. Sci. Technol. **33**(2), 138–148 (2017)

11. Herzog, D., Seyda, V., Wycisk, E., Emmelmann, C.: Additive manufacturing of metals. Acta. Mater. **117**, 371–392 (2016)
12. Hojati, F., Daneshi, A., Soltani, B., Azarhoushang, B., Biermann, D.: Study on machinability of additively manufactured and conventional titanium alloys in micro-milling process. Prec. Eng. (2019)
13. Frazier, W.E.: Metal additive manufacturing: a review. J. Mater. Eng. Perform. **23**(6), 1917–1928 (2014)
14. Ahmed, M., Islam, M., Vanhoose, J., Hewavitharana, L., Stanich, A., Hossain, M.: Comparisions of bending stiffness of 3D printed samples of different materials, November 11–17, (2016)
15. Li, B., Hong, J., Liu, Z.: Stiffness design of machine tool structures by a biologically inspired topology optimization method. Int. J. Machine Tools Manuf. 33–44 (2014). Retrieved from https://doi.org/10.1016/j.ijmachtools.2014.03.005
16. Sun, Z., Li, D., Zhang, W., Shi, S., Guo, X.: Topological optimization of biomimetic sandwich structures with hybrid core and CFRP face sheets. Compos. Sci. Technol. 79–90 (2017). Retrieved from https://doi.org/10.1016/j.compscitech.2017.01.029
17. Wang, J., Xie, H., Weng, Z., Senthil, T., Wu, L.: A novel approach to improve mechanical properties of parts fabricated by fused deposition modeling. Mater. Design 152–159 (2016). Retrieved from https://doi.org/10.1016/j.matdes.2016.05.078
18. ASTM D790—17.: Standard test methods for flexural properties of unreinforced and reinforced plastics and electrical insulating materials. (n.d.). Retrieved from ASTM International. https://www.astm.org/Standards/D790.htm

Laser Induced Forward Transfer-Based Micro-3D Printing of NiTi Alloy

Anshu Sahu [ID]**, Pravin Karna** [ID]**, Vipul Singh** [ID]**, and I. A. Palani** [ID]

1 Introduction

Demand for microscale manufacturing processes has increased over the last two decades to reduce component size. The size reduction decreases material wastage, reduces power loss with the system, and enhances the performance of the devices. Hence, the micro- and nano-manufacturing processes play a major role in the performance of the device by fabricating components with high resolution and more precision. Various techniques have been used for the high-resolution features such as photolithography, an etching process, thin film deposition. These techniques have constraints on types of material, an aspect ratio of the micro devices, and a planar substrate [1, 2]. Laser-induced forward transfer-based micro-3D printing is an alternative fabrication technique that can be used for fabrication of micro as well as nanoscale devices. In this process, the material is coated on a transparent substrate by flash evaporation or sputtering techniques. The donor thin film is irradiated from the backside of the donor substrate by the laser beam to eject the material in the form of droplets/solid pixels. For solid-phase deposition, a sacrificial layer is deposited in between the substrate and donor film to avoid the direct heating of donor thin film. The sacrificial layer absorbs all laser energy and transfers the material in the form of solid pixels.

A. Sahu (✉) · P. Karna
Mechatronics and Instrumentation Lab, Discipline of Mechanical Engineering, Indian Institute of Technology Indore, Indore, India
e-mail: phd1901203002@iiti.ac.in

V. Singh · I. A. Palani
Molecular and Nanoelectronics Research Group, Discipline of Electrical Engineering, Indian Institute of Technology Indore, Indore, India
e-mail: vipul@iiti.ac.in

I. A. Palani
e-mail: palaniia@iiti.ac.in

It has shown its potential to fabricate solid as well as high viscous liquid with higher resolution [3]. Different metals have been deposited selectively on solid as well as a flexible substrate for the fabrication of micro-sensors, micro-actuators, micro-pillars for microelectromechanical systems devices [4–7]. There is insignificant literature available for the deposition of alloy structures using LIFT-based micro-3D printing. NiTi alloy is one of the better choices for micro-actuators and sensor applications because of having a high work density (~1 J/g) [8]. Hence in the work, an attempt is made to investigate the process parameter of micro-3D printing on NiTi alloy line pattern.

In this study, laser decal transfer is deployed for the micro-3D printing of NiTi line pattern using CO_2 laser at 10.6 μm wavelength. The NiTi line pattern is deposited at optimized laser fluence at three different stands of distance (distance from focusing lens) and 30%, 60%, and 90% laser spot overlap. The deposited line pattern is investigated with an optical microscope (Leica DMS1000) and the deposition is confirmed by scanning electron microscopy (SEM, JEOL J-7100) with EDS for X-ray spectroscopy.

2   Transfer Mechanism

Laser micro-3D printing is used to deposit metal thin film pixel by pixel to fabricate 3D structures. It consists of donor substrate, sacrificial layer, and donor thin film for the transfer of the material from one substrate to another. The donor substrate is transparent to the laser wavelength so that it passes its energy without any loss. As the beam passes through the silicon wafer, it reaches to sacrificial layer, i.e., PDMS layer. PDMS has a better absorption coefficient at 10.6 μm hence the beam gets absorbed and rises the temperature leading to melting and ablation of the sacrificial layer. Due to volumetric expansion, it tries to expand toward the free surface to release its energy and apply a thrust force over the coated donor thin film. Once the thrust force reaches the ultimate fracture strength of thin film the material gets ejected from its position and deposited on the acceptor substrate placed below as shown in Fig. 1. This causes the forward transfer of the NiTi thin film. The shape of the transferred material is governed by the laser spot, beam profile, spot overlap %, and ejection velocity pixel during the transfer process. The laser spot is varied by changing the distance from the focusing lens while the continuity of the line pattern is made by changing the overlap percentage.

3   Experimental Setup

The P-type silicon wafer used as donor substrate is transparent to the laser wavelength (10.6 μm). The silicon wafer is cleansed properly with acetone in a sonicator to remove any foreign particles over the surface and dried by placing it in a desiccator.
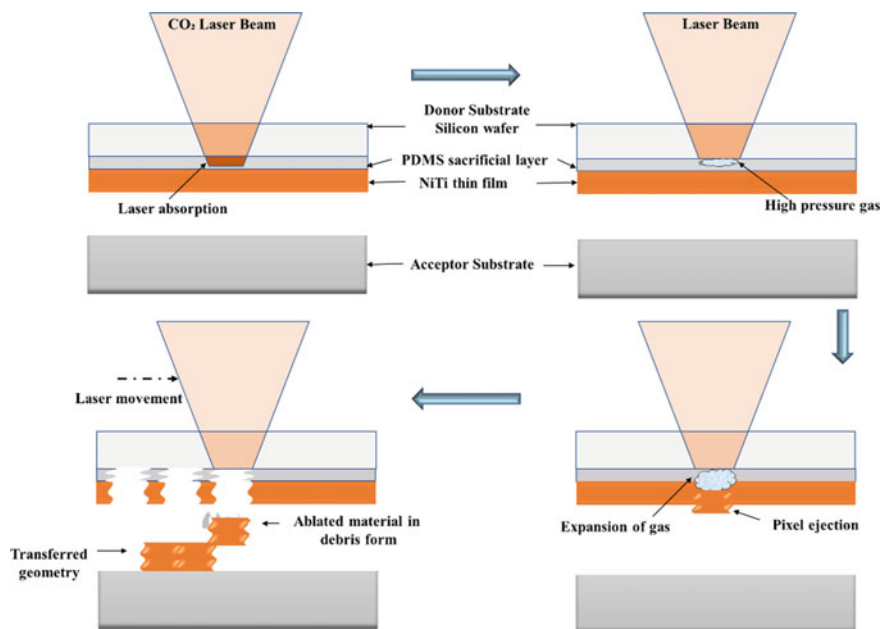
Fig. 1 Transfer mechanism during the micro-3D printing

PDMS (Sylgard 184 kit) is mixed with a curing agent in the volumetric ratio of 10:1 and steered for 10 min for proper mixing. The mixture is coated on the silicon wafer over a spin coater. The solidification of the PDMS mixture over the donor substrate is carried out by baking it at 60 °C for 90 min. NiTi thin film is coated over the PDMS coated silicon wafer using the DC sputtering process. The distance between the target and the acceptor substrate is maintained at 5 cm and sputtering is carried out for 20 min. Argon is purged at 20 sccm inside the chamber at a pressure of 980 mbar. The pressure inside the chamber during sputtering is around $2*10^{-3}$ mbar. The thickness of the NiTi thin film was measured using cross-sectional FESEM and was found to be around 200 nm. For micro-3D printing. A CO_2 laser of wavelength 10.6 μm is used to irradiate the donor substrate. The laser beam is focused with a lens (f = 100 mm) for a spot size of 300 μm. The donor and acceptor substrates are kept on an XYZ translation and maintain the spacing gap of 100 μm. The optimized laser fluence 1270 mJ/cm^2 is used for the deposition in a line pattern. The transfer pattern is studied by varying the distance of the donor–acceptor substrate system from the lens is varied from 100–160 mm while the overlap percentage of the laser spot varies from 30%, 60 and 90%. The schematic diagram and the experimental setup are shown in Fig. 2.
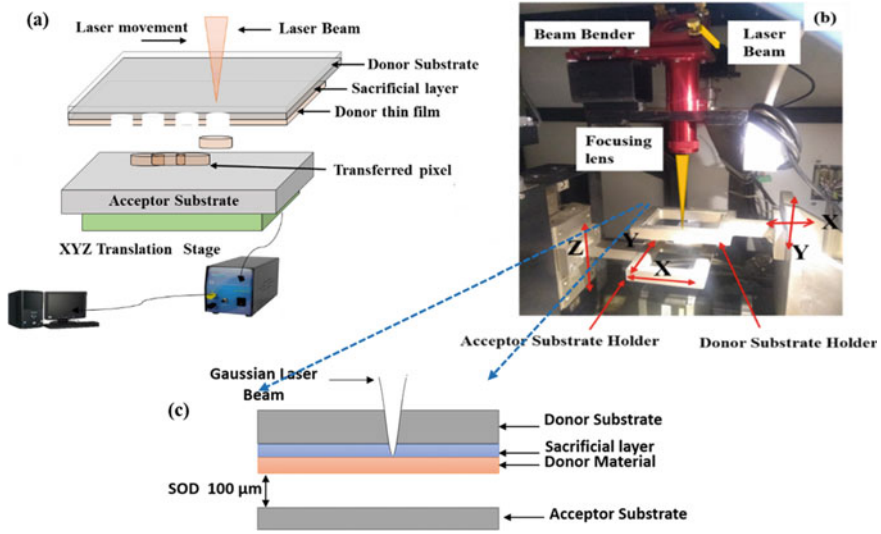
Fig. 2 **a** Schematic diagram of LIFT process and **b** Experimental setup for micro-3D printing

4 Results and Discussion

The variation in deposition pattern of the transferred material with variation in stand-off-distance is shown in Fig. 3. The laser beam has maximum intensity and thereby maximum fluence at the focal length of the lens. Any movement-upward or downward from the focal point causes a decrease in intensity thereby fluence of the beam. From Fig. 3, it can be seen that with an increase in the stand of distance, the deposited pattern becomes discontinuous. This is because the transfer of material occurs best at the threshold intensity of the laser. Increasing the laser intensity would cause burning of the donor material well as a spattering of the transferred material due to high vaporization pressure. The laser intensity lower than the threshold intensity would not be enough to create enough vaporization pressure to transfer the donor material hence discontinuous transfer occurs as seen in Fig. 3c.

The width of the deposited patterns was measured through an optical microscope and is represented in the bar graph in Fig. 4. It is seen that the width of the deposited line is maximum when the material is transferred at 130 mm from the focusing lens. As the distance from the focal point to the donor–acceptor system increases, the deposited pattern becomes less prominent highlighted by a decrease in width at the stand of the distance of 160 mm. When the stand of distance was increased to 180 mm, the deposition was not observed on the acceptor substrate.

The variation in the deposited pattern due to variation of overlap percentage of the laser beam is shown in Fig. 5. At the 90% overlap, the deposited pattern is continuous while at 60% overlap, the deposited pattern is discontinuous. The width of the deposited pattern at 90% overlap was measured to be approximately 0.481 mm.
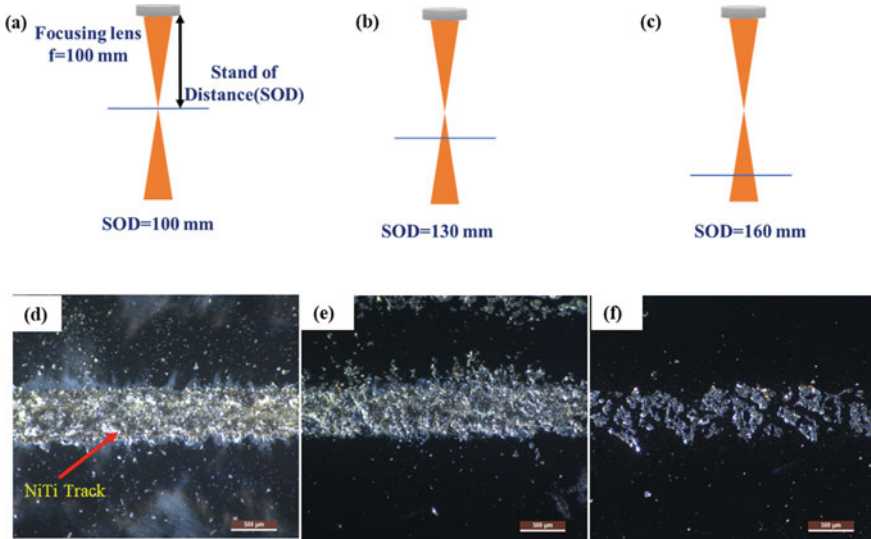
Fig. 3 **a-c** Schematic of the focusing condition and **d-f** shows the material deposited with respect SOD 100,130,160 mm, respectively

Fig. 4 Track width at the different stand of distance from focusing length at laser fluence 1240 mJ/cm^2
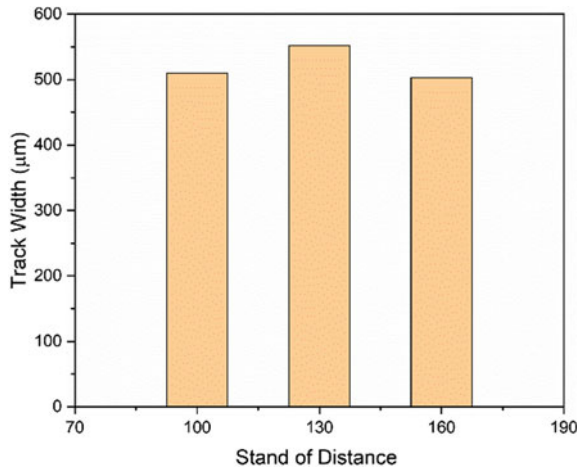
With an increase in overlap percentage, the amount of donor material is transferred to the proximity of each other increases thus increasing continuity of the transferred material. At 60% overlap, transferred material gets spattered and hence the decrease in continuity. With further reduction is overlap %, decreases the pixel density of the deposition.

Figure 6a shows the SEM images of the deposited pattern at 90% spot overlap at 130 mm from the focusing distance. The image shows that the deposited pattern
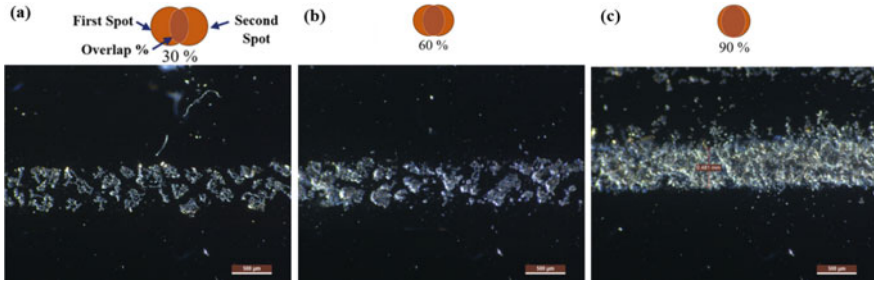
Fig. 5 Variation in deposited pattern at **a** 30% overlap **b** 60% overlap, and **c** 90%
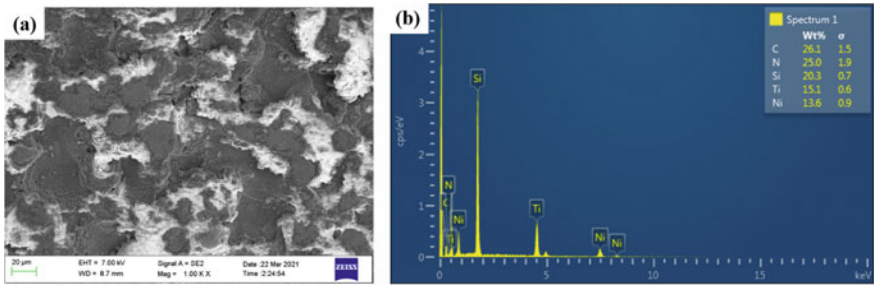
Fig. 6 **a** SEM image of the deposited pattern at a stand-off distance of 100 mm **b** EDS analysis of the deposited pattern

is fairly continuous with infiltration of some amount of PDMS layer. The presence of PDMS is further confirmed by the presence of carbon and silicon obtained in the EDS analysis. Although the Ni and Ti % are low, they are nearly equiatomic.

5 Conclusion

For the first time, laser-induced forward transfer has been deployed for the micro-3D printing of NiTi alloy using a pulsed CO_2 laser at 10.6 μm wavelength. For solid-phase transfer of NiTi pixels, a PDMS sacrificial layer was used and the line pattern is deposition pixel by pixel. The optimized laser fluences 1240 mJ/cm2 are used for the transfer at three different 100 mm, 130 mm, and 160 mm from the lens. It is observed that due to the high energy density of the laser beam at 100 mm distance, the pixel is getting ablated from the top surface while at 160 mm distance the energy is insufficient for the complete transfer. The spot overlap % is varied from 30, 60, and 90%, and overserved that with an increase in overlap % the pixel density increases leading to continuous line pattern. The deposited line pattern at 130 mm focusing distance and 90% spot overlap is analyzed with SEM and EDS to confirm the elemental composition of the deposition. It is observed that Ni and Ti are nearly

equal in wt. % with Si, and C due to the dissociation of the PDMS sacrificial layer. This study shows the feasibility of the micro-3D printing process to fabricate NiTi structures for mems devices.

References

1. Cohen, A., Efab, G.: Rapid, low cost dextop micromachining of high aspect ratio true 3d Mems. In: Twelfth IEEE International Conference on Micro Electro Mechanical Systems IEEE; pp. 244–51. (1999)
2. Ashley, J.F., Cramer, N.B., Davis, R.H., Bowman, C.N.: Soft-lithography fabrication of microfluidic features using thiol-ene formulations. Lab Chip **11**(16), 2772–2778 (2011)
3. Serra, P., Piqué, A.: Laser-induced forward transfer: fundamentals and applications. Adv. Mater. Technol. **4**(1800099), 1–33 (2019)
4. Fogel, O.: 3D printing of functional metallic microstructures and its implementation in electrothermal actuators. Addit. Manuf. 307–11 (2018)
5. Gorodesky, N.: Concurrent formation of metallic glass during laser forward transfer 3D printing. Adv Func. Mater. **30**(25), 1–6 (2020)
6. Shen, H., Wang, Y., Cao, L., Xie, Y., Wang, Y., Zhang, Q., et al.: Fabrication of periodical micro-stripe structure of polyimide by laser interference induced forward transfer technique. Appl. Surf. Sci. **541**, 148466 (2021)
7. Fogel, O: Mechanical properties of 3D metallic microstructures printed by laser induced forward transfer. In: 10th CIRP Conference on Photonic Technologies, p. 285–9. Elsevier (2018)
8. Knick, C.R.: Rapid and low power laser actuation of sputter deposited NiTi shape memory alloy (SMA) MEMS thermal bimorph actuators. Sens Actuators, A **291**, 48–57 (2019)

Machine Learning Module for Predicting Tensile Response of SLMed Ti-6Al-4V

M. Banerjee , **A. Banerjee** , **D. Mukherjee** , **A. K. Singla** , **and J. Singh**

1 Introduction

Additive manufacturing (AM), also known as rapid prototyping (RP), is a cost-effective and time-efficient single-shot manufacturing process for intricate customized shapes (preferably low volume) produced from a digital system (3D CAD, MRI, CT scans, etc.). In particular, among the powder-based AM processes, the powder bed fusion (PBF) is categorized into two, namely selective laser melting (SLM) and selective laser sintering (SLS). During the SLM process, the powder gets completely fused in an inert environment (e.g., argon) through near-infrared wavelength laser radiation, and overlapped melt tracks get solidified to produce desired parts [1]. At present, it has appeared to be the most globally accepted approach for metal AM [2].

Among the several SLM process parameters involved in laser PBF technology, the high-power beam parameters are found to be the most effective ones for the desired output performance. The four most influencing parameters are found from

M. Banerjee (✉)
Department of Mechanical Engineering, IIT Kharagpur, Kharagpur, West Bengal, India
e-mail: mainakb_mech20@kgpian.iitkgp.ac.in

A. Banerjee
Department of Electrical Engineering, NIT Rourkela, Rourkela, Orissa, India
e-mail: ankan.banerjee95@gmail.com

D. Mukherjee
Department of Engineering, University of Cambridge, Cambridge CB2 1PZ, UK
e-mail: dm914@cam.ac.uk

A. K. Singla · J. Singh
Department of Mechanical Engineering, SLIET, Longowal, Punjab, India
e-mail: anilsingla@sliet.ac.in

J. Singh
e-mail: jagtarsingh@sliet.ac.in

the prolonged experimental observations to be laser power (P), scan speed (v), hatch spacing (h), and layer thickness (t) [1]. In addition, two energy densities, namely, the volumetric (E_V) and the linear energy density (E_L) are defined in terms of the four aforementioned parameters [3]

$$E_V \left(J/mm^3 \right) = \frac{P(W)}{v(mm/sec) \cdot h(\mu m) \cdot t(\mu m)} \tag{1}$$

$$E_L(J/m) = \frac{P(W)}{v(mm/sec)}, \tag{2}$$

which are observed to play a pivotal role in controlling various properties (mechanical, thermal) of the fabricated material.

Due to its high strength-to-weight ratio and good biocompatibility, titanium Ti-6Al-4V and its ELI alloys fetch most of the attention in the recent past [4]. The very requirement of the specific design of prosthetic and orthopedic parts partly necessitates the introduction of present matured three-dimensional (3D) printing technology for this titanium alloy. Moreover, for fruitful utilization of the AMed parts as structural components, namely, aircraft structures, gas turbines, biomedical implants, etc., their tensile behavior is considered to be one of the most important mechanical properties. The aforementioned behavior can be quantified via yield strength (YS), ultimate tensile strength (UTS), percentage of total elongation (TE), and elastic modulus (E). From most of the researches (~81%), it has been observed that the values of elastic modulus lie in the range of 105–120 GPa [1], which is considerably higher than the requirement for human bones (~40 GPa) [5]. Achieving the same involves mostly porous structure formation, which is not intended to include in the ongoing study.

Achieving the mechanical properties in the as-fabricated AMed components comparable to the thermo-mechanically processed ones is still found to be challenging. In fact, for the AMed parts, it has also been observed that ductility enhancement is one of the most concerns to date [6]. The reason behind this is that the components manufactured by the AM typically exhibit lesser ductility than the desired as per the ASTM standards, e.g., [2, 7].

The tensile strength is observed to depend directly on the in-process parameters involved in the AM process. For example, the consequence of increasing scan speed on decreasing tendency of all the tensile properties of Ti-6Al-4V alloy (Grade 23) samples has been reported by Gong et al. for the SLM process [8].

Machine learning (ML), on the other hand, serves as an excellent tool to predict a number of output features in modern manufacturing science, especially in 3D printing. Being a subset of artificial intelligence, it is based on rigorous algorithms through which a machine can automatically learn and improve itself from experience rather than being programmed via pre-determined models. The learning techniques are classified as supervised learning, unsupervised learning, and reinforcement learning. Supervised learning algorithms are trained using the input and the desired labeled output data. In the case of support vector machines (SVM), a

sub-category of supervised learning algorithm, respective algorithms (i.e., linear, quadratic, cubic, fine Gaussian, medium Gaussian, and coarse Gaussian) make a contrasting separation between the classes by means of corresponding nature of kernel scale.

In this context, the authors briefly mention some recent works employing ML tools to aid manufacturing and control like Ng et al. highlighted deep learning, a branch of ML, as a promising advancement in the era of 3D bio-printing emphasizing the potential of this algorithm in every phase of the printing process [9].

Khorasani et al. have studied the impact of process parameters on the relative density and involved an artificial neural network (ANN) as a part of numerical analysis [10]. For the laser melting deposition (LMD) AM process, Velázquez et al. have used a fuzzy logic-based inference system (based on the Mamdani method) for predicting the volumetric energy input on single AISI316 SS beads deposition [11].

In a different study, an ensemble learning-based algorithm was declared as well capable for surface roughness prediction in extrusion-based additive manufacturing processes, after comparing the model output with the corresponding experimental values [12]. Interestingly, another ML-based fatigue life prediction approach for AM-printed SS316L has recently been carried out by Zhan and Li training the models with continuum damage mechanics (CDM)-based experimental data involving ANN, RF, and SVM algorithms [13].

In this context, no investigation regarding the prediction of the tensile strength in terms of the AM process parameters has been reported as per the best of the authors' knowledge. Evidently, it may be acknowledged to be a very fruitful effort to expedite the tensile properties prediction involving the ML module (specifically SVM). Here, it has been further considered to carry out material-specific modeling, typically for SLM-manufactured Ti-6Al-4V alloys. As mentioned, most influencing parameters have been considered in the present study, along with two well-established energy function relationships for predicting the YS, UTS, and yielding TE of the SLM as-built samples. In the beginning, the ML module training methodology has been briefly demonstrated. During analysis, a comparison of the accuracy of ML-based classifiers has been illustrated for different combinations of training data for all the considered tensile properties each. Along with that, the variation effect of cross-validation folds has been studied on model accuracy during the classifier model training. Finally, the developed models have been probed for using the set of validation data.

2 Methodology

The tools and methods used to develop three distinct trained models for YS, UTS, and TE prediction have been discussed in the following subsections.

Table 1 Scanning parameters used for printing different SLMed Ti6A4V samples and corresponding tensile properties

P (W)	v (mm/sec)	h (μm)	T (μm)	YS (MPa)	UTS (MPa)	TE (%)	Refs.
120	960	100	30	1098	1237	8.8	[8]
120	540	100	30	1150	1257	8	[8]
120	400	100	30	1066	1148	5.4	[8]
120	1260	100	30	932	1112	6.6	[8]
120	1500	100	30	813	978	3.7	[8]
375	1029	120	60	1106	NR	11.4	[14]
194	1000	70	20	1030	NR	NR	[15]
250	1600	60	30	1125	1216	6	[16]
*170	1250	100	30	1143	1219	4.89	[17]
*275	805	120	50	1200	1280	2.4	[7]

NR = Not Reported

2.1 Database Development

The analysis for the tensile properties prediction was done on a dataset that was collected from several reputed journals and proceedings' articles, a few among these are provided in Table 1. After a rigorous data collection (number of data points for YS: 107, UTS: 95, and TE: 102) from the literature, a number of MATLAB tools and applications have been used in the present work for the predictive model preparation and testing. Here, MATLAB R2015a (8.5.0.197613) academic licensed version has been used in a 4 GB RAM and Intel CORE™ i3 supporting system capable of smoothly handling the load of the database used.

Labeling of the output data is done for all the three models based on the suitable range of values as the authors contemplate and has shown with respective results (Sects. 3.1–3.3). Instead of using the exact values, the trained models predict the range of values in terms of labels, as initially have designated before data analysis.

The authors follow the typical route to ML-based modeling and divide the latter into three categories, namely training, testing, and validation dataset. Based on the types of model validation method (cross-validation) considered, in the present case, a set of about 15% of totally collected data (e.g., marked * in Table 1) was kept separately as validation dataset for model development.

2.2 ML Model Architecture

For each of the predictive models' development, subsequent operation sequences have been followed, adhering to their respective features. After trial-and-error with

various available classifiers, a handful among them is finalized based on the trained model accuracy. As the application for the specific data-driven classification can easily be tackled in the available MATLAB versions, the authors find it redundant to show and describe the intermediate processing steps in the ongoing discussion.

In the very first stage of classification, the data matrix is imported into the classification learner application. Thereafter, the minute selection of predictor(s) and response (only one) is executed as per the users' choice. For the present work, label (L) has always been selected as a response, and for each of three matrices, all the rest variable(s) has (have) fixed as the predictor(s). At this final phase, the validation method is applied depending on its typical effectiveness based on the size of the data-set it is going to handle. In the present work, it is noticed that the dataset is sparse (~100, specific number provided in Sect. 2.1). Hence, the cross-validation method appeared to be the best one for executing the complete work.

After all the above-mentioned choices, the data is imported. Then selecting each classifier, the model is trained, and the corresponding accuracy is displayed. Finally, a comparison is made to identify the relatively accurate one based on the number of folds and classifiers of the particular choice group. In particular, the accuracy of the trained predictive model is compared among the SVM classifiers, and accordingly, the best models have been identified for respective properties. Subsequently, the model is exported for a specific model that shows the highest accuracy to test its prediction capability with already experimentally known data (test dataset).

3   Results and Discussions

After carrying out several model training with the developed data, the outcomes and consequent comprehensive observations from the three tensile behavior representing models are highlighted in the following three subsections. The authors have executed training with all the categories, but unsatisfactory accuracy made us decide not to include the irrelevant results in the present manuscript. Hence, the main focus is given to the SVM analysis in detail, and the corresponding results are graphically presented. To obtain a suitable number of folds that maximizes the model's accuracy, the fold numbers from 2 up to 32 are analyzed. For each of the typical cases, the models have been trained ten times as it is based on statistical analysis. Consequently, the mean values are carefully considered in practice and will be discussed in subsection 3.5. Trained model accuracy accordingly portrays its real-world usefulness from its applicability traits.

3.1   *Yield Strength Predictive Model Training*

For the GR_I category (Fig. 1e) using the YS labeled dataset (Fig. 1d), maximum predictive model accuracy is obtained to be 84.5% using the fine Gaussian SVM

Fig. 1 3D plot for **a** GR_I, **b** GR_II and **c** GR_III YS predictive model accuracy; and **d** labeled data used during model development and **e** input variables

classifier bearing a fold number of 22 (Fig. 1a). Compared to the fine Gaussian, quadratic, and cubic, SVM classifiers show comparable model accuracy. Still, greater fluctuation in accuracy variation was observed in the latter two (~17–18%) compared to the former one (~14%); see Fig. 1a. Moreover, it is quite clear that linear and coarse Gaussian SVM is not suitable for classifying this kind of dataset. It is also observed that for smaller validation fold numbers, the trained models have shown a bit lesser accuracy compared to the higher numbers (Fig. 1a).

In the case of GR_II grouping (Fig. 1e), maximum accuracy for the trained YS predictive models is obtained for a fold number of 13 in the fine Gaussian SVM classifier as 85.7% (Fig. 1b). From the accuracy viewpoint, it has revealed an almost similar nature with the latest group of variables (GR_I). However, for the present group, the quadratic SVM classifier shows slightly better overall accuracy compared to the cubic (Fig. 1b). The changes may be interpreted as the involvement of numbers and a set of variables varied from the previous grouping (GR_I). Furthermore, throughout the change in fold numbers, quadratic shows a better fluctuation trend compared to the cubic after a few initials (Fig. 1b). The present instance also indicates the poor model behavior for training both with linear and coarse Gaussian SVM classifiers.

Finally, in the case of the GR_III combination (Fig. 1e) of the trained YS predictive model, the maximum accuracy is obtained for a fold number of 2 as 50% in both cubic and medium Gaussian SVM classifiers (Fig. 1c). In this case, an abrupt change (decrement) in the accuracy has been observed throughout, compared to the

percentage that appeared for the previous two variable groups (GR_I and GR_II). The reason behind this scenario is highly expected to be the involvement of only one labeled dataset. In this situation, overall accuracy throughout the folds was found stable in medium Gaussian SVM. Besides that, the quadratic and cubic classifiers show a similar extent of accuracy, but a fluctuation (~12–13%) is observed throughout the fold variation; see Fig. 1c.

From the three instances considered for YS model training, the overall accuracy of the model has been finally indicated as 85.7% using the GR_II variable set and fine Gaussian SVM classifier. The GR_I variable set has exhibited almost comparable utility through trained model performance. According to the validation method considered here, the model accuracy found may be deemed as moreover too satisfactory from its application viewpoint.

3.2   Ultimate Strength Predictive Model Training

In the case of GR_I combination using the UTS labeled dataset (Fig. 2d), maximum predictive accuracy is obtained as 80.4% for a fold number of 22 in the fine Gaussian SVM classifier (Fig. 2a). Moreover, it shows the accuracy of almost the same order throughout the fold variation. After fine Gaussian, the overall accuracy decreases consecutively for cubic and quadratic classifiers (Fig. 2a). Along with that, the variation in the accuracy due to cross-fold number alteration also fluctuates too much for the two aforesaid classifiers (about 28% and 21%, respectively). Notably, the linear and coarse Gaussian SVM classified the least accurate (~52%) trained models with marginally better performance (~62%) for medium Gaussian one.

For the GR_II category in the UTS predictive trained model, maximum accuracy for the model is obtained as 71.7% for the fine Gaussian SVM classifier bearing a fold number of 15 (Fig. 2b). A bit fluctuating nature has been observed throughout the fold variation for this particular case. Subsequently, models with accuracy lie in the near about ranges observed for the cubic and quadratic classifiers as depicted in the 3D plot (Fig. 2b).

Finally, the GR_III grouping for the UTS predictive model has displayed maximum accuracy for a fold number of 16 in the fine Gaussian SVM classifier as 52.2% (Fig. 2c). Also, for all the classifiers, inconsistent patterns in the model accuracy appeared as usual, like the YS model.

From the above-discussed three illustrations considered for training UTS predictive model, the overall accuracy of the model has been cumulatively indicated as 80.4% using fine Gaussian SVM classifier for GR_I variable set. From the model validation method selection aspect, the trained model's accuracy may be considered as overall satisfaction with respect to its reliable implementation viewpoint.
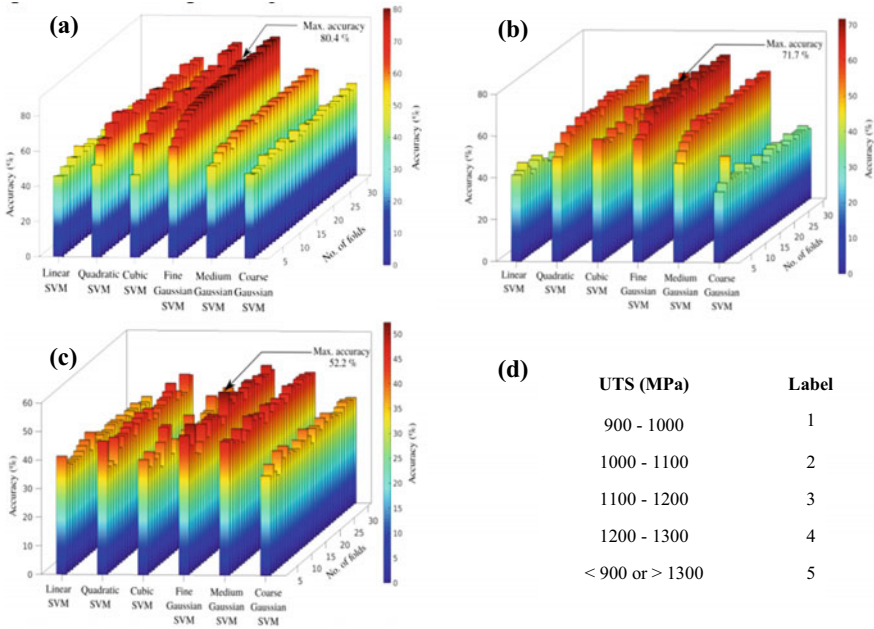
Fig. 2 3D plot for **a** GR_I, **b** GR_II and **c** GR_III UTS predictive model accuracy; and **d** labeled data used during model development

3.3 Ductility Predictive Model Training

In the case of training with the GR_I grouping using the TE labeled dataset (Fig. 3d), maximum accuracy for the predictive model is obtained for a fold number of 14 in the fine Gaussian SVM classifier as 91.7% (Fig. 3a). For a maximum of the fold variations apart from a few initials, the fluctuation in the accuracy is almost stable. After the best classifier, the overall second and third best appeared are cubic and quadratic, respectively. Linear and coarse Gaussian appeared as least effective (<50%) for the present case with a marginally better (~65%) for the medium Gaussian SVM classifier.

In the case of the GR_II variable set, the maximum accuracy for the trained model is attained for a fold number of 8 as 74% in the fine Gaussian SVM classifier (Fig. 3b). During the number of cross-fold variations, minor luctuations have been observed in the fine Gaussian except for a few initials; and it appears as prominent for the quadratic, cubic, and medium Gaussian (Fig. 3b). However, the quadratic and cubic SVM have classified the data with almost similar accuracy (~70%) comparable to the best one (fine Gaussian SVM).

Next, in the case of the GR_III category, the maximum accuracy for the model is obtained as 53.1% for the fine Gaussian SVM classifier bearing a fold number of 4 (Fig. 3c). As usual, accuracy is drastically low like the previous two modeling
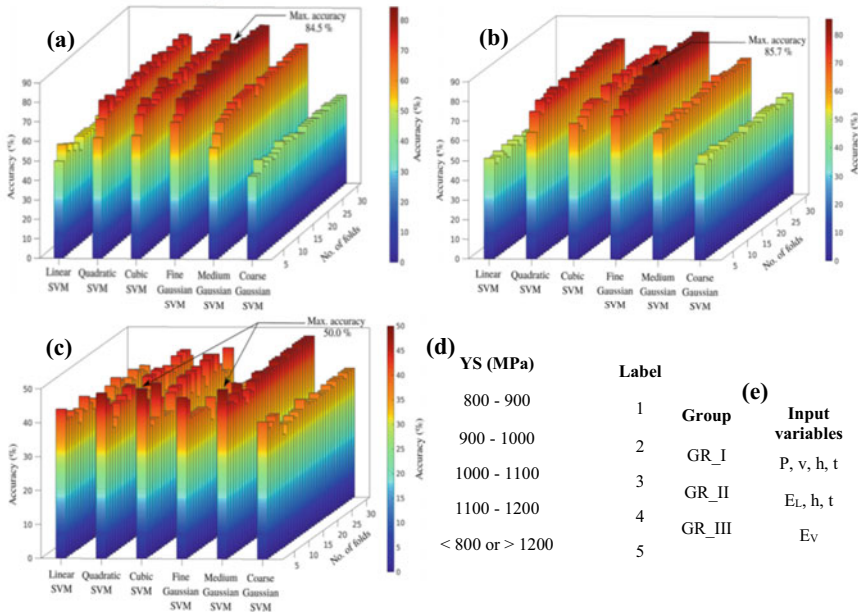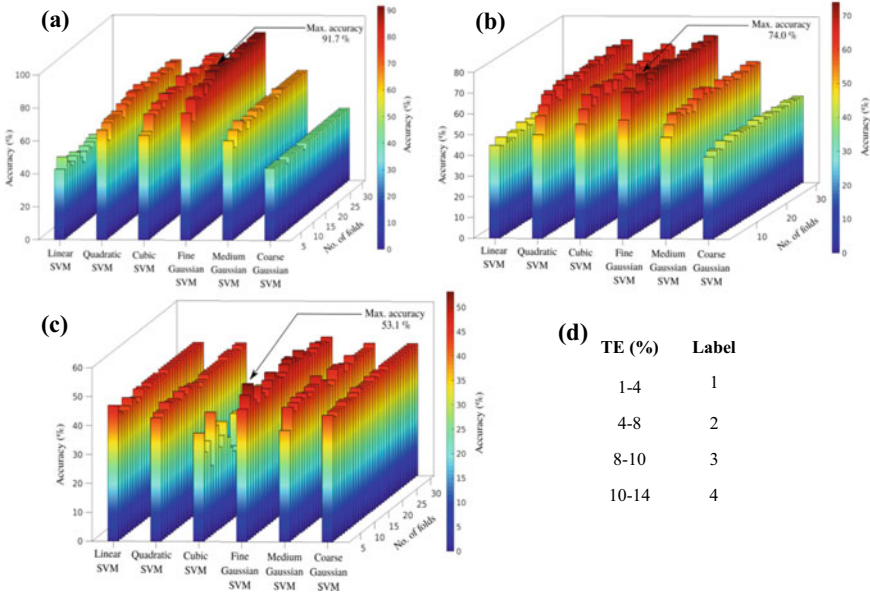
Fig. 3 3D plot for **a** GR_I, **b** GR_II, and **c** GR_III TE predictive model accuracy; and **d** labeled data used during model development

sections (Sects. 3.1 and 3.2). During the fold variations, except the cubic SVM, fine and medium Gaussian classifiers have shown comparatively remarkable fluctuations than the rest (Fig. 3c).

From the three instances discussed in the present subsection, the overall accuracy of the trained model has been finally pointed out as 91.7% using the fine Gaussian SVM classifier for the GR_I variable set. Also, it appeared to be the maximum among all the presently studied model categories. According to the currently considered validation method, the ductility predictive model accuracy, found after numerous training, may be regarded as highly satisfactory from its application perspective and expected to predict accurately in most of the future scenarios.

3.4 Validation of Trained Models

Next, the authors export the most accurate trained models for the YS, UTS, and ductility as indicated in the last three sections. For validation of each of the models, all the models of each group having the highest accuracy are now successfully authenticated with the validation dataset as already kept aside (for YS: 16, UTS: 14, and TE: 15). For a better presentation of the validation study, the results have been given in Table 2 with corresponding correctness during the trained model validation.

Table 2 Prediction correctness of trained models during validation

Variable group	YS model (%)	UTS model (%)	TE model (%)
GR_I	81.25	85.71	93.33
GR_II	87.50	71.43	80
GR_III	62.5	57.14	46.67

3.5 Discussions

From the whole model training outcomes, it can be inferred that it is hardly possible to achieve too much accurate predictive model through ML for such a specific model condition considered in the current work. There may exist plenty of reasons for this deviation of the trained model's output from real-life experimentation. According to the trailing discussion, four variables have been considered, in individual or the form of already traditional relations. Evidently, the rest of the huge printing parameter-family may act as a noise factor in different extents as per situations. Few of the relevant instances have been mentioned in the subsequent discussions, primarily focusing on the tensile properties considering specific material (Ti-6Al-4V) and printing process (SLM).

It has been highlighted by Agius et al. in their review work that the properties are affected due to different laser scanning strategies [18]. Pal et al. observed the significant effect of different building orientations on the tensile properties through building samples in four different directions [19]. As a consequence of minimizing the aforementioned influence, all the data considered for the current study are typically for vertically built (along z-direction) samples.

Furthermore, the influence of the variation of focal offset distance [3], inter-layer time [3, 20], and powder bed temperature [3, 21] has appeared as effective on the tensile properties of SLM as-built Ti-6Al-4V samples. From the broad observations, it may be said that different printing systems usually affect the mechanical properties to some extent.

Despite all the concerns regarding deviation in predictions, accuracy in all the three subdivisions was found well satisfactory (>80%) from an implementation viewpoint. Most interestingly, as a most concerned property among the SLM as-built structures, the ductile behavior predictive model achieved the highest (>90%) accuracy. As indicated at the very beginning of the current section regarding obvious consideration of the mean values, a glimpse of observed deviations in the accuracy has been marked in the bar chart (Fig. 4) just for providing the impression cumulatively.

4 Conclusions and Future Perspectives

Based on the behavior of trained models' accuracy, the following brief remarks may be provided in terms of its operative and consistent solicitation:
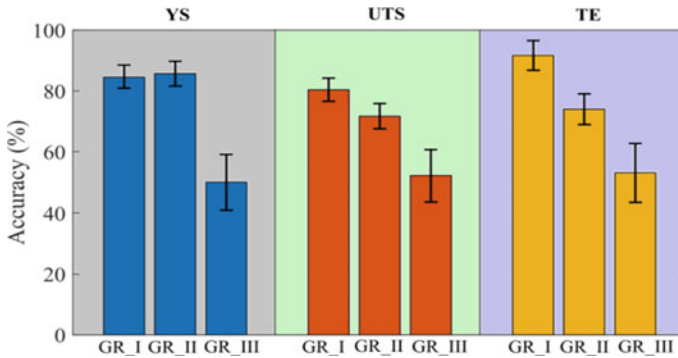
Fig. 4 Accuracy variations during model training

- Based on the tendency of the input dataset, the fruitful functionality of the classifier changes in terms of the model accuracy. For any particular classifier, a too abrupt shift in model accuracy has not been observed for all the instances, as desired. However, minor changes were found due to variations in the number of folds.
- The accuracy of the GR_III variable set is too low (~50%) on average in comparison with the other two groups (GR_I and GR_II). Hence, the GR_III group may be discarded any further to train the ML module for the AMed parts.
- For model development involving 3D printing parameters, the fine Gaussian SVM classifier is found to be most useful as a whole from the present training–testing trend through the ML algorithm. For YS, UTS, and TE predictive models, the maximum accuracy of the models is obtained as 85.7%, 80.4%, and 91.7%, respectively, using the fine Gaussian SVM classifier.

To gain further acceptance from the industry as well as in research and development, separate model development using ML modules can be expedited in AM for other mechanical properties like fatigue strength, tribological behavior, microhardness, impact strength, etc. ML algorithms also can be utilized to predict the properties of thermally and mechanically post-treated components at specified conditions. The authors expect that the present work would surely provide an adequate paradigm to future researchers in the advancement of time and cost-effective AM process.

References

1. AK Singla M Banerjee A Sharma J Singh A Bansal MK Gupta N Khanna AS Shahi DK Goyal 2021 Selective laser melting of Ti6Al4V alloy: process parameters, defects and post-treatments J. Manuf. Process 64 161 187
2. WSW Harun MSIN Kamariah N Muhamad SAC Ghani F Ahmad Z Mohamed 2018 A review of powder additive manufacturing processes for metallic biomaterials Powder Technol. 327 128 151

3. H Shipley D McDonnell M Culleton R Coull R Lupoi G O'Donnell D Trimble 2018 Optimisation of process parameters to address fundamental challenges during selective laser melting of Ti-6Al-4V: a review Int. J. Mach. Tools Manuf. 128 1 20

4. H Eskandari Sabzi 2019 Powder bed fusion additive layer manufacturing of titanium alloys Mater. Sci. Technol. (United Kingdom) 35 875 890

5. F Trevisan F Calignano A Aversa G Marchese M Lombardi S Biamino D Ugues D Manfredi 2018 Additive manufacturing of titanium alloys in the biomedical field: processes, properties and applications J. Appl. Biomater. Funct. Mater. 16 57 67

6. D Herzog V Seyda E Wycisk C Emmelmann 2016 Additive manufacturing of metals Acta. Mater. 117 371 392

7. A Popovich V Sufiiarov E Borisov I Polozov 2015 Microstructure and mechanical properties of Ti-6AL-4V manufactured by SLM Key Eng. Mater. 651–653 677 682

8. H Gong K Rafi H Gu GD Janaki Ram T Starr B Stucker 2015 Influence of defects on mechanical properties of Ti-6Al-4V components produced by selective laser melting and electron beam melting Mater. Des. 86 545 554

9. WL Ng A Chan YS Ong CK Chua 2020 Deep learning for fabrication and maturation of 3D bioprinted tissues and organs Virtual Phys. Prototyp. 15 340 358

10. AM Khorasani I Gibson AH Ghasemi A Ghaderi 2019 A comprehensive study on variability of relative density in selective laser melting of Ti-6Al-4V Virtual Phys. Prototyp. 14 349 359

11. Tasé Velázquez, D.R., Helleno, A.L., de Oliveira, M.C., Fals, H.C., Macias, E.J.: Fuzzy logic-based inference system for prediction of energy input in laser metal deposited Aisi316 single-beads. In: 32nd European modelling simulation symposium EMSS 2020. pp. 400–409. (2020)

12. Z Li Z Zhang J Shi D Wu 2019 Prediction of surface roughness in extrusion-based additive manufacturing with machine learning Robot. Comput. Integr. Manuf. 57 488 495

13. Zhan, Z., Li, H.: Machine learning based fatigue life prediction with effects of additive manufacturing process parameters for printed SS 316L. Int. J. Fatigue. **142**, 105941 (2021)

14. W Xu M Brandt S Sun J Elambasseril Q Liu K Latham K Xia M Qian 2015 Additive manufacturing of strong and ductile Ti-6Al-4V by selective laser melting via in situ martensite decomposition Acta Mater. 85 74 84

15. J Han J Yang H Yu J Yin M Gao Z Wang X Zeng 2017 Microstructure and mechanical property of selective laser melted Ti6Al4V dependence on laser energy density Rapid Prototyp. J. 23 217 226

16. V Cain L Thijs J Humbeeck Van B Hooreweder Van R Knutsen 2015 Crack propagation and fracture toughness of Ti6Al4V alloy produced by selective laser melting Addit. Manuf. 5 68 76

17. HK Rafi TL Starr BE Stucker 2013 A comparison of the tensile, fatigue, and fracture behavior of Ti-6Al-4V and 15–5 PH stainless steel parts made by selective laser melting Int. J. Adv. Manuf. Technol. 69 1299 1309

18. Agius D, Kourousis KI, Wallbrink C (2018) A review of the as-built SLM Ti-6Al-4V mechanical properties towards achieving fatigue resistant designs. Metals 8(1):75

19. Pal S, Gubeljak N, Hudak R, Lojen G, Rajtukova V, Predan J, Kokol V, Drstvensek I (2019). Tensile properties of selective laser melting products affected by building orientation and energy density. Mater Sci Eng A 743:637–647

20. Xu W, Lui EW, Pateras A, Qian M, Brandt MJ (2017) In situ tailoring microstructure in additively manufactured Ti-6Al-4V for superior mechanical performance. Acta Materialia 125:390–400

21. Ali H, Ma L, Ghadbeigi H, Mumtaz K (2017) In-situ residual stress reduction, martensitic decomposition and mechanical properties enhancement through high temperature powder bed pre-heating of Selective Laser Melted Ti6Al4V. Mater Sci Eng A 695:211–220

Multi-objective Optimization of Laser Beam Drilling in Carbon Fiber-Reinforced Plastics Using Nd: YAG Laser

Yadvendra Kumar Mishra ⬤**, Sanjay Mishra** ⬤**, S. C. Jayswal** ⬤**, and Ajay Suryavanshi** ⬤

1 Introduction

Carbon fiber-reinforced plastics (CFRPs) are normally used in engineering applications where strength-to-weight ratio is crucial factor. In aircraft manufacturing, the combination of carbon fiber composite materials with other advanced engineering material results in reduction of weight by 30%. The rapid adoption of this material by various industrial sectors has enhanced the requirement of machining technique which can conveniently create different features. Conventional machining methods do not find preference for machining of CFRP due problems like fiber breakage, delamination, fiber pull out, etc. Laser machining has been used by few authors to create features on various tailored made materials. The laser beam's inherent property helps obtain good lateral resolution during machining. The flexibility of laser beams in terms of precise control of pulse energy allows us to use laser beam for the machining of advanced engineering materials.

In recent years, the laser drilling method has evolved into an industrial option for drilling of small-sized holes. Fabrication of small holes in CFRP having consistent geometrical accuracy is a challenging task. In LBD, several physical processes like melting, vaporization, melt ejection, melt spatter, etc., disturb the geometrical accuracy of the drilled hole. Furthermore, the continuous reduction of laser intensity with depth and scattering of laser beam also deteriorates the hole quality. Figure 1 depicts a geometrical feature of a drilled hole by laser drilling. D_{top} and D_{bottom} represent the

Y. K. Mishra (✉) · S. Mishra · S. C. Jayswal
Mechanical Engineering Department, Madan Mohan Malaviya University of Technology, Gorakhpur 273001, India
e-mail: mr.yadu@gmail.com

A. Suryavanshi
Mechanical Engineering Department, Bundelkhand Institute of Engineering and Technology, Jhansi 284001, India
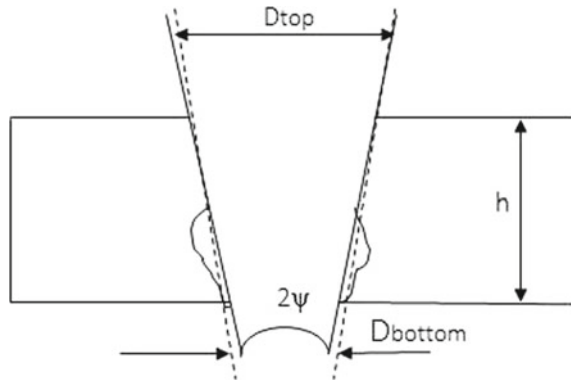
hole's top and bottom diameters; h represents workpiece thickness, and ψ represents the taper angle.

Laser percussion drilling and laser trepan drilling are the commonly used techniques to create hole using laser beam. Small holes with high productivity can be obtained by percussion drilling. The taper and circularity of a drilled hole are the two most important features of any drilled hole in the laser percussion drilling process. CFRPs mainly contain carbon fiber in epoxy matrix. The thermal properties of carbon and epoxy widely differ from each other. Since LBD process is based on the absorption of photon and its subsequent conversion into thermal energy, therefore, LBD in CFRP becomes difficult particularly with increase of thickness. Rodden et al. [2] investigated the effect of pulse energy and material thickness on the diameter of the hole using Nd: YAG laser drilling of a multi-layer CFRP in argon atmospheres and partial vacuum. Tom et al. [3] developed a MATLAB-based design model (DREAM) to forecast various drilling process outcomes. Anarghya et al. [4] investigated the heat accumulation zones during laser drilling in CFRP. Loumena. et al. [5] explored the effect of wavelengths in surface ablation. Ghoreishi et al. [6] investigated the effect of peak power, laser pulse width, pulse frequency, number of pulses, assist gas pressure, and focal plane position on hole taper and circularity.

The identification of critical input parameters and its optimum level will help to produce hole of consistent quality. Multi-objective optimization (MOO) helps to identify the optimum level of input parameters at which best trade-off between the hole quality can be achieved. The uncertainty associated with LBD process requires a robust optimization technique which can reduce the instability associated with the LBD process. Taguchi methodology is a well-established robust methodology used by various authors to identify the importance of input parameters. Therefore, in this study, MOO of LBD has been performed using the Taguchi methodology. Single objective optimization (SOO) and multi-objective optimization (MOO) have been compared to find the extent of improvement by MOO. Analysis of variance (ANOVA) was also used to analyze relative effect of the different factors.

2   Fabrication and Experimental Details

The experiment was conducted by Nd: YAG laser drilling system on a CNC work-bench. Compressed air is employed as an assist gas in the laser drilling operation. The process factors include pulse current, pulse width, gas pressure, and thickness of the workpiece material. The nozzle tip diameter (400 μm) and distance of nozzle tip from workpiece surface (1.0 mm) remained constant during the experiment. Work-piece material for this experiment included three different thicknesses such as 1, 3, and 5 mm of carbon fiber-reinforced plastic (CFRP). The hardener K-6 serves as a curing agent when mixed with epoxy resin (L-12) to form a thermoset polymer matrix with excellent thermal conductivity.

The fabricated CFRP laminates were allowed to cure for 48 h in the open air. After curing, the samples were trimmed to a final size of 200 mm × 200 mm at different thicknesses at 1, 3, and 5 mm. To ensure that the workpiece shows a flat surface, a digital Vernier caliper is used having a least count of 0.002 mm. Laser power of 250 W and 400 μm as a beam diameter was used to create these samples using an Nd: YAG laser. The dimensions of the holes on the top and bottom surfaces of the workpiece were measured at a magnification of 10 times using a Leica MC170 HD optical microscope. Hole circularity (HC) and hole taper (HT) are considered as response variable which is obtained by Eq. 1.

$$HC = \frac{D_{\min}}{D_{\max}} \text{ at top surface} \tag{1}$$

$$HT = (D_{\text{top}} - D_{\text{bottom}})/(2 \times h)$$

the $D_{\max}$ and $D_{\min}$ of the holes at the top and bottom surfaces of the workpiece were directly measured using the image analysis software tool in MATLAB-R2017a. The diameter at the top (D_{top}) and bottom (D_{bottom}) surfaces of the workpiece was obtained by averaging $D_{\max}$ and $D_{\min}$ for the respective surfaces.

3   Results and Discussion

3.1   Selection of Input Parameters, Their Levels, and Responses Factors

The input parameters range as pulse current (200–300 A), pulse width (2–6 ms), gas pressure (4–8 kg/cm^2), and workpiece thickness (1–5 mm). Numerical values at various levels based on an extensive pilot experiment carried out to determine the parameter range for drilling operation are shown in Table.1 The process parameters have been selected in such a way that the effect of both the laser and non-laser input

Table 1 Input parameter and their level

Input parameter	Unit	Level I	Level II	Level III
Pulse current (W)	A	200	250	300
Pulse width (X)	ms	2	4	6
Gas pressure (Y)	kg/cm^2	4	6	8
Thickness (Z)	mm	1	3	5

parameters on the geometrical accuracy of the hole can be analyzed. Following are the reasons for selecting the input process parameters.

(a) Pulse current (W): The peak power generated by the laser machining system during the actual experiment depends on the pulse current.
(b) Pulse width (X): The energy of each pulse is controlled by pulse width.
(c) Gas pressure (Y): The gas pressure protects the lens from the material ejected during drilling and minimizes the debris build-up around the hole.
(d) Thickness of workpiece (Z): It helps to analyze the effect of changes in the workpiece dimension.

The level of input parameters was decided based on the pilot experiment conducted using one factor at a time approach. Only those levels were selected which produced desired hole quality.

3.2 Orthogonal Array Selection Based on Balancing Property

The overall degree of freedom (*dof*) for all components is considered when selecting the orthogonal array (OA). In mathematical analysis, orthogonal arrays are a type of matrix in which each row represents a different condition, and the entries reflect different input parameters. Orthogonal arrays are those in which all possible combinations for each factor level for any pair of columns can be found and occur on an equal number of occasions for each variety [7].

$$dof = (\text{Total level count} - l) \text{ for each variable} + (\text{Total level count} - 1)$$
$$(\text{Total level count} - 1) \text{with regard to each interaction} + 1 \qquad (2)$$

The degree of freedom is determined as follows in the current situation of four parameters at three different levels, assuming there is no factor interaction:

$$\text{dof} = (3 - 1)4 + 1 = 9$$

As a result, a typical L$_9$ orthogonal array (OA), as suggested by Taguchi, shown in Table 2.

Table 2 Orthogonal array (OA) of the input variable

Experiment No.	Factors and their level			
	W	X	Y	Z
1	200	2	4	1
2	200	4	6	3
3	200	6	8	5
4	250	2	6	5
5	250	4	8	1
6	250	6	4	3
7	300	2	8	3
8	300	4	4	5
9	300	6	6	1

3.3 Calculation of Quality Losses for Every Quality Feature

The Taguchi technique computes the difference between experimental and desired values by means of quality loss, also known as the mean square deviation (MSD) function. The MSD varies depending on the type of problem, for example, in situations where the smaller the solution, the better.

$$\text{MSD} = \left(r_1^2 + r_2^2 + r_3^2 + ... \right) / n \tag{3}$$

And for problems of the higher-the-better variety,

$$\text{MSD} = \left(1/r_1^2 + 1/r_2^2 + 1/r_3^2 + ... \right) / n \tag{4}$$

where r_1, r_2, r_3, and r_n are the experimental results (responses), and n is the number of repetitions of r_i. In this case, the hole taper is off the smaller-is-better variety, whereas the HC is of the higher-is-better variety. The results of experiments for response hole taper (rad) and HC are shown in Table 3. The quality loss values for each quality characteristic are displayed when different experimental runs are compared in Table 4.

3.4 Normalized Quality Loss Calculation for Each Quality Characteristic

Use the symbol L_{ij} to express the quality loss for each ith quality characteristic at the jth trial condition or run in the experimental design matrix. Because each quality feature has its own unit of measurement, the quality metric must be standardized. The normalized quality loss is determined using this method.

Table 3 Experiment results with the L$_9$ orthogonal array (OA)

Exp. No.	HT (rad)	HC
1	0.0299	0.4294
2	0.0520	0.4536
3	0.0404	0.4403
4	0.0851	0.4840
5	0.0388	0.4386
6	0.0481	0.4500
7	0.0673	0.4677
8	0.0625	0.4624
9	0.0393	0.4389

Table 4 Values of quality loss for each quality characteristic

Exp. No.	Quality loss (dB)	
	HT (rad)	HC
1	0.0009	5.4235
2	0.0027	4.8602
3	0.0016	5.1583
4	0.0072	4.2688
5	0.0015	5.1983
6	0.0023	4.9383
7	0.0045	4.5716
8	0.0039	4.6770
9	0.0015	5.1912

$$r_{ij} = L_{ij} / L_{i*} \tag{5}$$

where r_{ij} = Normalized quality deterioration

The ith quality characteristic has the greatest quality loss. Overall experimental runs are denoted by $Li*$. As a result, the value of r_{ij} is between 0 and 1. The normalized quality loss for HT and HC is shown in Table 5.

3.5   Total Normalized Quality Loss Calculation (TNQL)

At first, a weighting factor is assigned to each quality feature considered during the optimization process in order to calculate the total normalized quality loss (X_i) for each trial condition. If extensive is the weighting factor for the ith quality characteristic, then q the number of quality characteristics, and r_{ij} the loss function associated with the ith quality characteristic at the jth trial condition, then X_i can be calculated by Eq. (5) which follows:

Table 5 Normalized quality loss for hole taper and HC

Exp. No.	Normalized quality deterioration	
	HT (rad)	HC
1	0.1234	1.0000
2	0.3734	0.8961
3	0.2254	0.9511
4	1.0000	0.7871
5	0.2079	0.9585
6	0.3195	0.9105
7	0.6254	0.8429
8	0.5394	0.8624
9	0.2133	0.9572

Table 6 Total loss of normalized quality (TLNQ) and multiple S/N ratios

Exp. No.	TLNQ	Multiple S/N ratios (dB)
1	0.2988	5.2468
2	0.4779	3.2064
3	0.3705	4.3119
4	0.9574	0.1890
5	0.3580	4.4612
6	0.4377	3.5884
7	0.6689	1.7463
8	0.6040	2.1898
9	0.3621	4.4123
Mean MSNR (η_m)		3.2612

$$X_j = \sum_{i=1}^{q} w_i r_{ij} \tag{6}$$

In laser drilling, material removal occurs of distinct CFRP sheets is thought to be unequal in this case with $q = 2$ and unequal weights, i.e., $w_i = 0.8$ for hole taper (HT) and $w_i = 0.2$ for (HC). The (HC) has been selected as a quality characteristic because it produces two different qualities (HC) of higher and lower hole taper (HT). Table 6 shows the total normalized quality loss for each experimental run.

3.6 Calculation of Multiple S/N Ratios (MSNR)

After determining the total normalized quality loss (X_i) for each trial condition, the multiple S/N ratios at each design point are complete. This data have been provided by:

$$\eta_j = -10\log_{10}(X_j) \tag{7}$$

Table 6 displays the different S/N ratios as well as the total normalized quality losses for each trial condition and trial condition and its combination. If you use Taguchi methodology to perform single quality optimization, instead of computing multiple S/N ratios, first calculate the different S/N ratios for every quality characteristic, where X_j denotes the quality loss values of various quality characteristics. The repetition of the steps is the same as in multi-objective optimization (MOO).

3.7 The Variance Analysis (ANOVA)

Analysis of variance (ANOVA), also known as regression analysis, helps to understand the relative importance of numerous aspects in a situation more effectively. It is a computational method for estimating each factor's relative importance (F-ratio) and percentage contribution (PC). Prior to calculating the F value, the sum of squares (SS) and mean sum of squares or variance (V) for each factor must be computed, as well as the error (EP) generated. For each factor, the degree of freedom (dof) determines in the manner

$$dof = \text{number of levels} - 1 \tag{8}$$

Using the ANOVA shown in Table 8. Following factor such as: pulse current (15.63%), pulse width (22.09%), gas pressure (3.20%), and workpiece thickness (55.22%) impact on the output variable.

3.8 Factor Effects and Optimal Settings Determination

In the following phases, initially calculate the average influence of each element on a variety of quality attributes at various levels. Essentially, this is calculated by dividing the sum of all S/N ratios associated with a certain level by the number of factor level repetitions. The best level of optimization was determined by the factor levels with the greatest average effect. Table 7 depicts the average factor effect of this experiment, and the response plot has been shown in Fig. 2. This is the optimal parameter settings: W1X3Y1 Z1.

3.9 Confirmatory Experiment

It is vibrant to complete the creation of a robust design by performing a verification experiment. This step is necessary to ensure that the optimal conditions suggested by

Table 7 ANOVA table for HC and HT

Source	DF	Seq SS	Contribution (%)	Adj SS	F-Value
W	2	3.2512	15.63	3.2512	3.32
X	2	4.3871	22.09	4.3871	4.47
Y	2	0.0426	3.20	0.0426	0.04
Z	2	9.2000	55.22	9.2000	9.38
Error	4	3.9223	3.85	3.9223	
Total	8	16.88	100.00		

Table 8 Effect of factor levels on MSNR

Factors	Mean MSNR (dB)		
	Level I	Level II	Level III
Pulse current (W)	4.2550[a]	2.7462	2.7828
Pulse width (X)	2.3940	3.2858	4.1042[a]
Gas pressure (Y)	3.6750[a]	2.6025	3.5064
Thickness (Z)	4.7068[a]	2.8470	2.2302

[a] Optimum parameter level

Fig. 2 Plot for MSNR
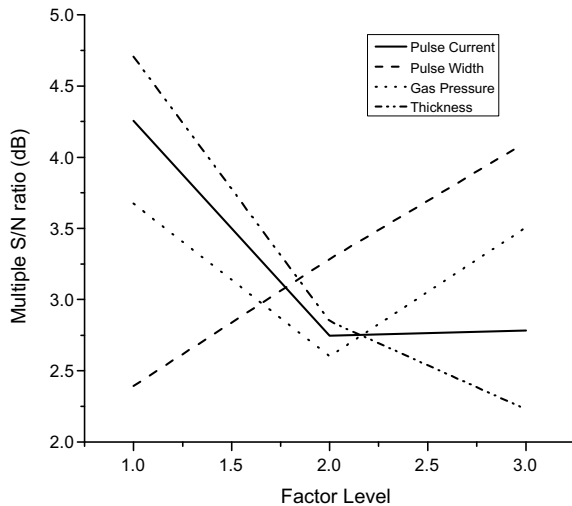
the matrix experiment produce the desired improvement. A confirmation experiment is carried out by running a test with the best settings for the previously investigated components and levels. Calculate the predicted value of multiple S/N ratios at the optimum level (o) using the following formula:

Table 9 Confirmation experiment results

	Initial setting	Optimum values	
		Prediction	Experiment
Level	$W_1X_1Y_1Z_1$	$W_1X_3Y_1Z_1$	$W_1X_3Y_1Z_1$
HT (rad)	0.0299		0.0234
HC	0.4294		0.5281
MSNR (dB)	5.2468	6.9574	7.4826

Improvement of MSNR = 2.2358

$$\varepsilon_o = \varepsilon m + \sum_{i=1}^{k}(\varepsilon i - \varepsilon_m) \tag{9}$$

where k denotes the number of factors and ε_m denotes the across all experimental runs, the average of multiple S/N ratios, and ε_i is the number of multiple S/N ratios associated with the best factor levels. Table 9 shows the expected value of the multiple S/N ratios as well as the confirmation test results. When operating at the optimal level, the increase in multiple S/N ratios is significant 2.2358 dB. The optimal value of hole taper (rad) and hole circularity values are 0.0234 rad and 0.5281 in comparison to initial parameter settings of 0.0299 rad and 0.4294.

4 A Comparison of the Outcomes of Multi-objective at the Initial Level

The conclusions of a single quality optimization for hole taper (HT) and hole circularity (HC) are summarized and is presented in Tables 10, 11, 12, 13, and 14 and the response graphs are shown in Figs. 3 and 4. Table 15 shows a comparison of the multi-objective optimization (MOO) with the initial level of the parameter. The results of MOO are primarily determined by the weights assigned to quality values; in this case, the most essential quality assumed was hole taper with a weight of 0.8 single objective optimizations (SOOs) and multi-objective optimization (MOO) are compared to the initial setting to find a better improvement. The aim is to maximize many quality features; simultaneously, there is still the chance of a quality loss occurring throughout the optimization process. Multi-objective optimization is beneficial because it allows one to obtain the optimum quality value of several quality characteristics simultaneously, rather than just a single ideal quality feature, by optimizing the same optimum parameter level.

Table10 S/N ratios of (HT) and (HC) in single qualify optimization

Exp. No.	S/N ratio (d B)	
	HT (rad)	HC
1	30.4866	− 7.3428
2	25.6799	− 6.8665
3	27.8724	− 7.1250
4	21.4014	− 6.3031
5	28.2234	− 7.1586
6	26.3571	− 6.9357
7	23.4397	− 6.6007
8	24.0824	− 6.6996
9	28.1121	− 7.1527
Overall mean (m)	26.1839	− 6.9094

Table 11 S/N ratio response table for hole taper (HT)

Factors	Mean MSNR (d B)		
	Level I	Level II	Level III
Pulse current (W)	28.0100[a]	25.3300	25.2100
Pulse width (X)	25.1100	26.0000	27.4500[a]
Gas pressure (Y)	26.4800	25.0600	26.5100[a]
Thickness (Z)	28.9400[a]	25.1600	24.4500

[a] Optimal level

Table 12 S/N response table for hole circularity (HC)

Factors	Mean MSNR (d B)		
	Level I	Level II	Level III
Pulse current (W)	− 7.1110	− 6.7990[a]	− 6.8180
Pulse width (X)	− 6.7490[a]	− 6.9080	− 7.0710
Gas pressure (Y)	− 6.9930	− 6.7740[a]	− 6.9610
Thickness (Z)	− 7.2180	− 6.8010	− 6.7090[a]

[a] Optimal level

Table 13 Experiment results for hole taper confirmation (HT)

	Initial setting	Optimum values	
		Prediction	Experiment
Level	$W_1X_1Y_1Z_1$	$W_1X_3Y_3Z_1$	$W_1X_3Y_3Z_1$
HT (rad)	0.0299		0.0210
MSNR (dB)	30.4866	32.3583	33.5556

Improvement of S/N ratio = 3.069

Table 14 Experiment results for hole circularity confirmation (HC)

	Initial setting	Optimum values	
		Prediction	Experiment
Level	$W_1X_1Y_1Z_1$	$W_2X_1Y_2Z_3$	$W_2X_1Y_2Z_3$
HC	0.4294		0.6380
MSNR (dB)	-7.3428	-5.0026	-3.9024

Improvement of S/N ratio $= 3.4404$

Fig. 3 Response graph for the hole taper (HT)
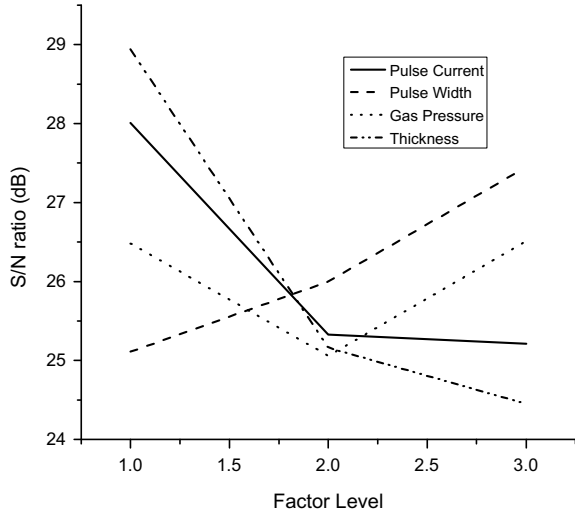
Fig. 4 Response plot for hole circularity at the top (HC)
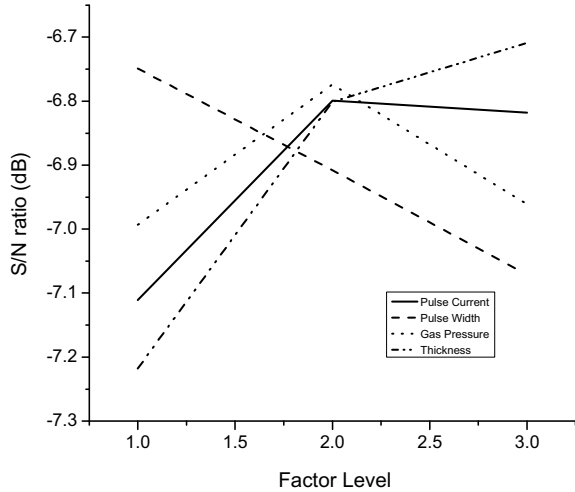
Table 15 Results of single and multiple objective optimizations are compared

	Initial setting		MOO results	(%) change
	HT	HC	HT and HC	
Level	$W_1X_3Y_3Z_1$	$W_2X_1Y_2Z_3$	$W_1X_3Y_1Z_1$	
HT (rad)	0.0299	–	0.0220	03.01(decrease)
HC	–	0.4294	0.5816	35.45(increase)

5 Conclusions

In this study, Taguchi methodology has been used for the simultaneous optimization of hole taper (HT) and hole circularity (HC) during laser beam drilling (LBD) of carbon fiber-reinforced plastics (CFRPs) of different thicknesses. Conclusions of this study are robust; Taguchi methodology can be used for the multi-objective optimization of LBD of CFRP. When the parameters were set to their optimum values, the signal-to-noise ratio has increased significantly (2.2358 dB) in the present study. The output parameters at an optimum level were compared with initial parameter settings, and significant improvement in quality characteristics has been obtained. According to the present operating conditions, the best parameter values are as follows: pulse current = 200 A, pulse width = 6 ms, pulse frequency = 4 kg/cm^2, and workpiece thickness = 1 mm. Gas pressure (03.20%), pulse current (15.63%), pulse width (22.09%), and workpiece thickness (55.22%) are the factors with the highest percentage contributions in increasing order. Comparing to input parameters at an initial value, the MOO increases the HC by 35.45% and decreases the HT by only 3.01%.

References

1. Kuar, A., Mitra, S.: Optimization of Nd: YAG laser parameters for microdrilling of alumina with multiquality characteristics via grey–Taguchi method. Mater. Manuf. Process. **27**(3), 329–336 (2012)
2. Rodden, W.S.O et al.: A comprehensive study of the long pulse Nd: YAG laser drilling of multi-layer carbon fiber composites. Opt. Commun. **210**(3–6), 319–328 (2002)
3. Eppes, T.A. et al.: Laser percussion drilling modeling utility. J. Laser Appl. **21**(2), 102–109 (2009)
4. Anarghya, A. et al.: Drill-ability studies of laser drilled micro holes on CFRP composites. In: New developments in biology, biomedical and chemical engineering and materials science. International conference proceedings, pp. 15–17. Vienna, Austria (2015)
5. Loumena, C. et al.: Potentials for lasers in CFRP production. In: International congress on applications of lasers and electro-optics, vol. 2012(1), pp. 1026–1034 (2012)

6. Ghoreishi M (2002) Comparative statistical analysis of hole taper and circularity in laser percussion drilling. Int J Mach Tools Manuf 42(9):985–995

7. Dubey et al.: Simultaneous optimization of multiple quality characteristics in laser beam cutting using Taguchi method. Int. J. Precis. Eng. Manuf. **8**(4), 10–15 (2007)

8. Gautam, G.D., Pandey, A.K.: Pulsed Nd: YAG laser beam drilling: a review. Opt. Laser Technol. **100**, 183–215 (2018)

9. Nandi, S., Kuar, A.S.: Parametric optimization of Nd: YAG laser microdrilling of alumina using NSGA II. Int. J. Mach. Mach. Mater. **17**(1), 1–21 (2015)

10. Arrizubieta et al.: Internal characterization and hole formation mechanism in the laser percussion drilling process. Int. J. Mach. Tools Manuf. **75**, 55–62 (2013)

11. Low et al.: The effects of process parameters on spatter deposition in laser percussion drilling. Opt. Laser Technol. **32**(5), 347–354 (2000)

On Surface Features of Canine Strategic Teeth by Metal Additive Manufacturing and Investment Casting—A Comparative Study

Smruti Ranjan Pradhan ⓘ**, Rupinder Singh** ⓘ**, Sukhwant Singh Banwait** ⓘ**, Satinder Singh** ⓘ**, Mehak Mahant** ⓘ**, and Arun Anand** ⓘ

1 Introduction

Digital manufacturing technology plays a pioneering role in the modern-day manufacturing process. The involvement of computer-aided design (CAD) in traditional manufacturing processes improve mass production with great tolerance, and reduced downtime [1]. So, computer-aided manufacturing (CAM), with the help of CAD techniques, brings the revolution in digital manufacturing with the use of data processing by optimizing different phases of design, process planning, component engineering, and market analysis [2]. Scanning techniques for generation of surface data, and further processing to generate three-dimensional (3D) virtual model/ CAD model with reverse engineering techniques helps in making perfect manufacturing strategy in the form of a selection of material, method, tooling, etc. Due to the digitization of manufacturing processes, scheduling, process planning, and control, procuring, inventory, and scrap management are feasible in a better-controlled way. Additive manufacturing, especially 3D printing is a comparative newer fabrication method where the designed part is fabricated by layer-wise consolidation of material in a controlled way as per computer instruction (using standard triangulation language

S. R. Pradhan (✉) · R. Singh · S. S. Banwait · S. Singh
National Institute of Technical Teachers Training and Research, Chandigarh, India
e-mail: smrutijana@gmail.com

R. Singh
e-mail: rupindersingh@nitttrchd.ac.in

S. S. Banwait
e-mail: ssb@nitttrchd.ac.in

S. Singh
Punjab Engineering College (Deemed to be University), Chandigarh, India

M. Mahant · A. Anand
Guru Angad Dev Veterinary and Animal Sciences University, Ludhiana, India

(.STL) file format) which minimize the scrap and maximize the production rate with simple to complex part geometry [3].

Different additive manufacturing processes like 3D metal printing (3DMP), lost thermoplastic/wax assisted IC, electroforming, metal forming process like swaging, and subtractive manufacturing processes like CAD-based carving in CNC milling are used for fabrication DC and other accessories associated in dental industries. Different metals and alloys like gold, palladium, nickel, cobalt, chromium, titanium, stainless steel, etc., are used as dental materials in the manufacturing of DC [4]. In 3D metal printing, laser melting and laser sintering techniques are used for the fabrication of DC directly from the CAD model. Different parameters like hatch spacing to control cooling rate, optimum laser power for selective curing, scan speed are used as input process parameters in DMLS for controlling output parameters necessary for functional product manufacturing. Here, a focussed high energy-dense laser selectively cures the contour of the CAD file in a controlled manner [5, 6]. In CAD-assisted IC, the thermoplastic/thermosetting resin base pattern is fabricated with the help of fused deposition modelling (FDM) machine or digital light processing (DLP) machine for IC. Different IC casting parameters like powder to water ratio, pH of water, use of surfactant, angle to pour investment slurry to the IC ring, velocity and pressure of the molten metal flow, rate and type of cooling, the material composition may affect the final casting [7].

The dental industry includes manufacturing inlay, on lay, bridge, implants, full and partial dentures of fixed and removed types, clasps, occlusal appliances, and veneers in periodontic and prosthodontic treatments [8]. The literature review reveals that significant work has been reported on prosthodontic therapies for humans, but hitherto little has been reported for VP. It has been reported that the adult dog has 42 teeth, out of which eight teeth are considered as strategic ST according to their function. Two molar (M1) and two canines in the lower mandibular arc and two fourth-premolar (PM4) and two canines in the upper maxillary are treated as ST [9]. The significant functions like tearing of food (flesh), self-protection against external attack by upper and lower canines, and shearing and crushing of food by the combined effect of M1 and PM4 are performed by ST. It should be noted that some unique breeds of dogs (sniffer dogs) are engaged in narcotics, police, and defence sectors after the successful training (involving high cost). If fully trained dogs lose ST (fully or partially), may die in a short time span of 15–30 days (subject to change in food habit and severity in traumatic condition), thus requiring special periodontic treatment. The proposed DC may act as a safeguard for a dog to avoid future prosthodontic treatments.

2   Selected Methodology

The methodology for DC fabrication is illustrated in Fig. 1.
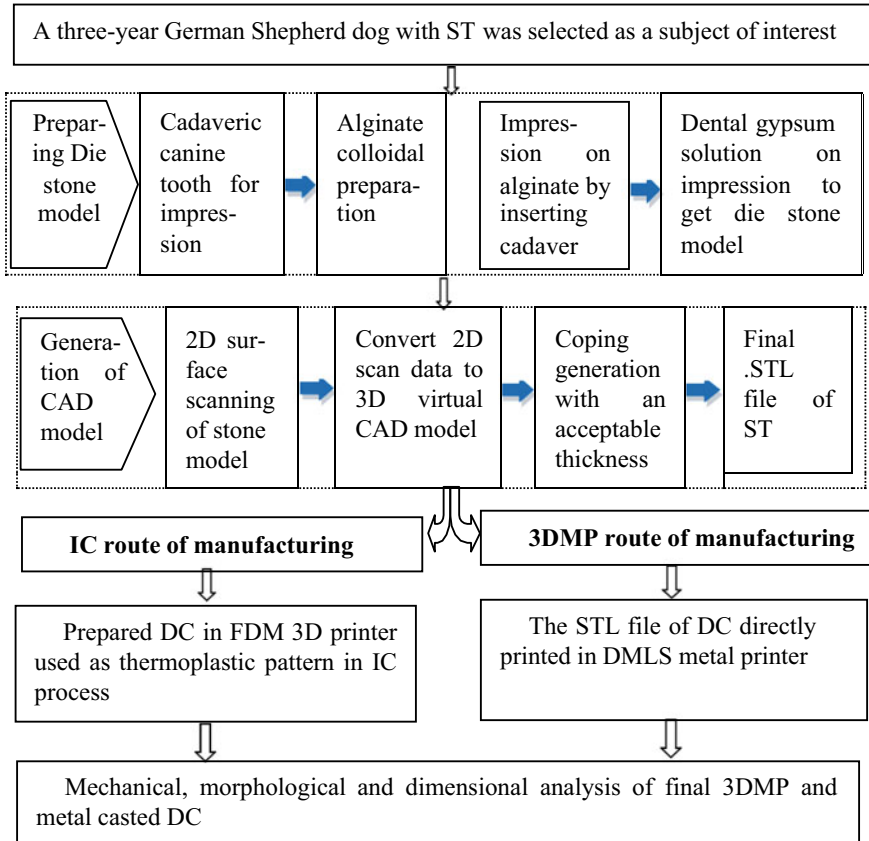
Fig. 1 Adopted methodology of present work

3   Experimentation

3.1   Development of Die Stone Model for 3D Scanning

Alginate is an elastic hydrocolloid used commercially for impression making. In the present work, the cadaveric tooth of a German Shepherd dog was used for developing a die stone model. A mixture of calcium sulphate and sodium alginate as hydrocolloid was placed over a stainless steel adjustable dental tray for impression making
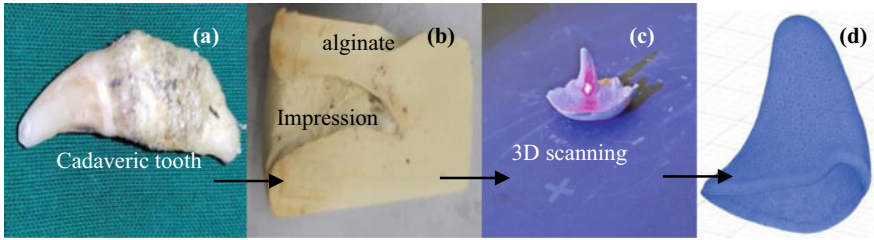
Fig. 2 **a** Cadaver of canine, **b** alginate with impression, **c** 3D scanning of die stone model, **d** .STL CAD file of DC

in this study. The negative cavity formed due to dog biting over the colloid was instantly filled by pouring dental gypsum/ die stone solution. After solidification and shrinking, the poured dental gypsum solidified, and the corresponding ST was replicated. The developed die stone model was tested under a profile projector and optical microscope for analysing the surface details. Digital Vernier calliper and micrometre were used on the die stone model to counter verify the dimensional stability, which further helped during the scanning and development of the virtual CAD model. The dental die stone model was then scanned under a rotary table comet 3D scanner for generating two-dimensional (2D) surface data. The different operating conditions like measuring field, the acceptable colour of part to scan, environmental factors like humidity, temperature, scan volume, scanner resolution, scanning speed were taken into account during 3D scanning of different die stone models. These 2D surface data were further processed in 3 shape dental software for generating 3D virtual CAD models of coping/ DC after selecting the region over the surface and giving 0.6 mm thickness for final coping. These 3D CAD models were saved as printable .STL file format. The process flow of printable .STL file from scanned data is given in Fig. 2.

3.2 FDM-Based Thermoplastic Printing of CAD Files

Sacrificial master pattern (MP) of DC of selected ST were fabricated with the help of FDM by using acrylonitrile butadiene styrene (ABS) as model base material and polycarbonate (PC) as support material in uPrint FDM 3D printer of Stratasys, USA. The DC of the left mandibular canine was printed at optimized settings of uPrint 3D printer (at sparse high density with 90° orientation angle). During this printing of ABS base DC, the material consumption (both model and support), built time estimation, and the number of layers consumed were recorded by CatalystEX dedicated software of uPrint. The printed DC were further processed for the thermodynamic heating–cooling cycle based on the glass transition temperature of ABS [10]. The thermoplastic DC was exposed to sensible heating of samples to 90 °C from room temperature (25 °C) in 10 min followed by keeping the samples at 90 °C for 10 min,
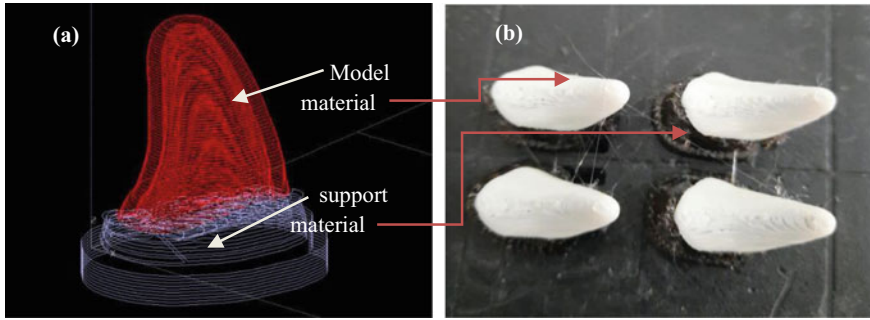
Fig. 3 **a** CAD file after imported into CatalystEX software, **b** 3D printed thermoplastic DC on the built plate of FDM printer

and by bringing the samples to room temperature in 10 min as per the designed algorithm in the heat treatment furnace. This heat treatment of thermoplastic DC showed improved surface hardness and dimensional stability. The imported CAD file inside the CatalystEx software and printed thermoplastic parts showing model and support material is shown in Fig. 3.

3.3 3D Printing Assisted IC of Metallic Crowns

The fabricated thermoplastic pattern of DC after corresponding heat treatment procedures was taken for IC. The runners of the appropriate size were connected to thermoplastic DC. One runner was used for a pattern of canine for uniform flowing of molten metal into cavities. Then the investment tree was formed by joining the different wax runners with thermoplastic patterns to sprue base well. The investment slurry was prepared by mixing investment powder with liquid at recommended proportion inside a rubber bowl with the help of a spatula. The investment tree was placed inside the metallic casting ring. The investment slurry was poured inside the casting ring at an angle of 110° with horizontal with a controlled manner in three stages to avoid dross and bubble formation by air entrapment. Then the slurry hardened inside the ring within 10–15 min after full pouring. Then this casting ring was kept vertically down inside a furnace at 1050 °C for about 100 min. During this tenure of heating inside the furnace, all wax and thermoplastic contents were melted and evaporated results the formation of cavities as the investment can withstand a temperature up to 1750° C. After that the casting ring was placed at the specified place in a spring-loaded centrifugal IC machine with the help of holding arrangements. The Ni-Cr-based molten metal was poured instantly to the sprue base well, and the spring load was released. Due to the release of spring load by changing the lever position, the molten metal centrifugally flew into the cavities of the investment ring in a faster way than gravity casting. Then it took around 30 min to solidify the molten metal as per the natural convection method. After this, the investment was
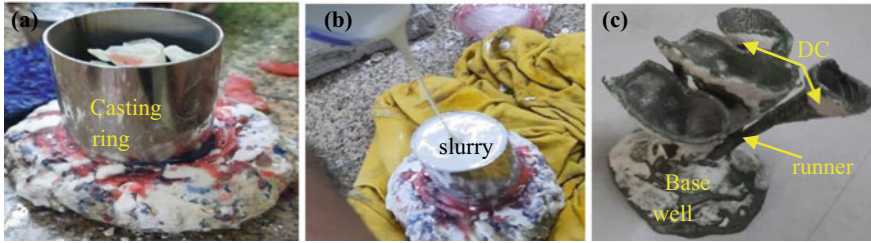
Fig. 4 **a** Thermoplastic pattern inside the casting ring, **b** Pouring of investment slurry into the casting ring, **c** Cast metallic DC after breaking investment

broken, and the final metal cast tree was replicated. The final metal cast DC was restored after cleaning and separated from the branches of runners and sprue base well [11]. The IC of metallic DC from the thermoplastic pattern is shown in Fig. 4.

3.4 Direct Metal Printing of DC

DMLS is one of the advanced 3D metal printing technology being used by most of the metal printing industries. The 3DXpert dedicated software of the 3D system was used for positioning, 3D printing analysis, support structure management, lattice finite element analysis (FEA), slice calculation, print estimation of the total number of .STL files to print after adding the virtual 3D components into it. Proper orientation (in the upside-down direction of virtual models so that the support structure first touches the closed side of the part (see Fig. 5a) and support honeycomb wall support were selected after virtual positioning the component body in 3DXPert software. The 3D printing analysis was done to check the effect of residual stress and overhang angle with respect to printing direction to avoid part failure. The lattice FEA was taken into consideration before printing of the DC for failure analysis. Then the slice was calculated for the number of layers required for printing. Print estimation option in software interface gave the volumes powder material (in cm^3) of part, support, lattice with corresponding estimated built time in an optimized way for easy calculation of cost and time. Copy array option in the interface is used for a number of the same components added to the building base. By using the scan path manager, the fab file was created and imported to the metal printer's PX Control software.

In this study, 17–4 PH stainless steel powder was processed for moisture removal where it was kept inside the oven at 80° C for 16-hour prior to the planning to run the printer one day. The Cu content in 17–4 PH stainless steel has enhanced the antibacterial property of the material, avoiding the colonization of bacteria after cementing DC over the affected tooth surroundings. Then the heated powder from the oven was sieved in a sieve shaker to remove any foreign material. After this, the required powder height in the supply piston of the metal printer was crosschecked in software, and the processed powder was filled as per the requirement for this
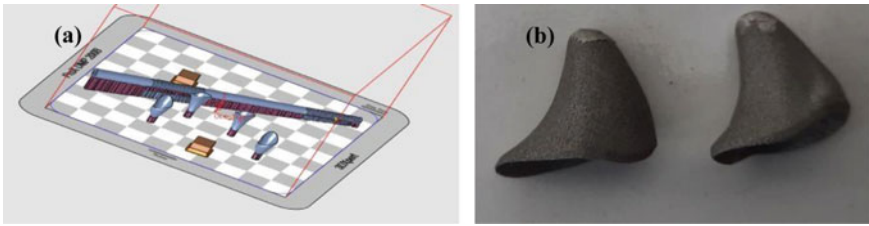
Fig. 5 **a** CAD files of DC in 3DXpert software, **b** Final printed DC after removed from the built plate

work. A new standard built plate was fitted on the sintering piston. Then the machine conditions like the movement of a roller, carriage scraper to its mean position, and maximum travel in side the machine were crosschecked. In order to maintain an inert printing chamber, the nitrogen gas at 0.5 bar pressure and air supply pressure at 3 bar was supplied to the process filter, and mixing was performed at 20–25 mbar pressure. This filtered mixture was supplied to build the chamber and purge valve condition crosschecked. The print command was given after reaching the oxygen level below 1000 ppm inside the chamber. The total time for printing and the number of layers consumed were recorded. The printing process automatically stopped after the building of part. The build plate with components was removed from the sintering piston after cutting the supply of nitrogen. After cleaning, the parts were removed from the build plate. A twin shut blaster was used to remove powder residues, and the final part was restored [12–18]. The DMLS printed crowns from .STL file is shown in

4 Result and Discussion

The results are analysed for surface morphology, dimensions irrespective of the material of teeth, die stone model, thermoplastic crown, and metal crowns fabricated in two different routes. The Ra, porosity, grain dimensions, ADF, PC, BRC, and 3D rendered images are analysed with the help of SEM-based computerized micrographs as per corresponding ASTM standards [18]. The observed values for comparison at different manufacturing stage from the micrograph-based analysis are discussed in Table 5. The idea here is to stabilize the development process regardless of the composition of the crown being prepared. The compositions of final fabricated parts compared with natural teeth through EDS data is given in Table 1.

Table 1 SEM and EDS of natural tooth compared with IC part and DMLS part

Natural tooth	IC part	DMLS part

4.1 Porosity and Grain Size Analysis at Each Stage of Fabrication

The porosity and grain size are compared at each step in Table 2.

4.2 Surface Roughness, Amplitude Distribution Function, Peak Count, and Bearing Ratio Curve
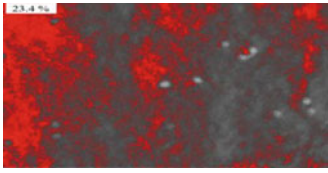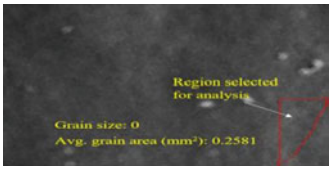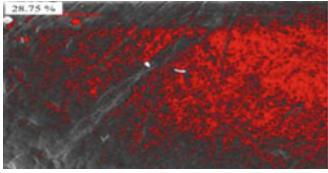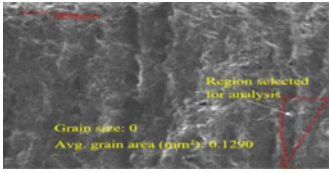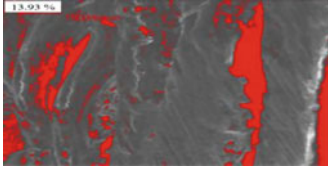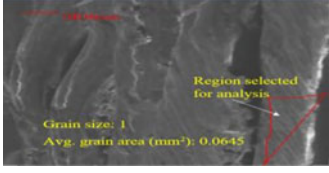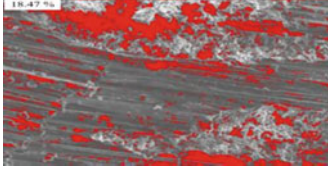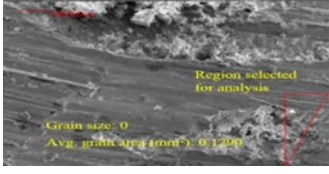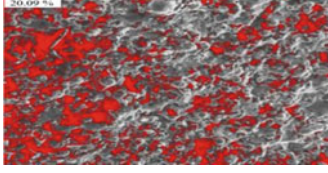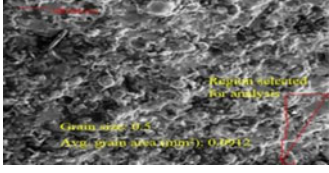
The Ra values in Table 3 and ADF, BRC, and PC are analysed in Table 4.

In ADF analysis, the bell-shaped curves with more distribution were found for fabricated metal parts. The distribution is more prominent in the case of DMLS-based 3D metal printed parts than metal cast parts manufactured for the same functional prototype. The porosity was better controlled in manufactured parts than the original cadaveric tooth. From the 3D rendered images, more uniformity is found in the metal matrix for 3D metal printed parts than cast parts. Table 5 shows the comparative result analysis of Ra, porosity, grain size, ADF, BRC, and PC values.

4.3 Verifying Dimensions as Per IT Grade

The height, major diameter, and minor diameter of DC fabricated by thermoplastic-based FDM parts, metal cast parts, and 3D metal printed parts were calculated with the help of a digital micrometre and Vernier height gauge and evaluated based on the international grade of tolerance (IT) [19]. It was observed that major diameter and height were in the acceptable range for every case. The height of metal printed DC shows an excellent result which may not require further processing. The diameters

Table 2 Porosity and grain size analysis at different stages in the fabrication
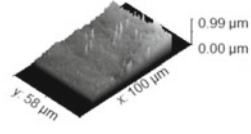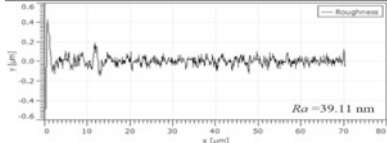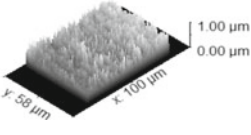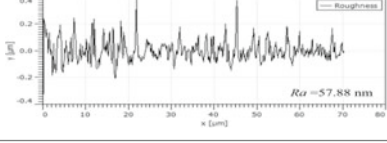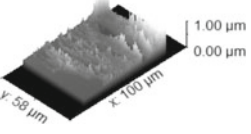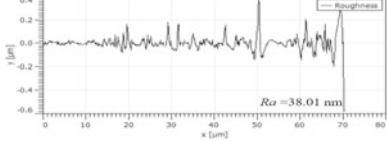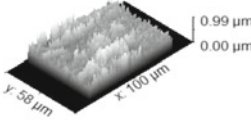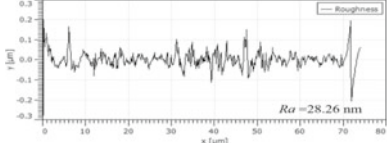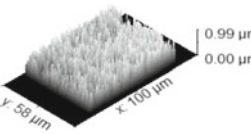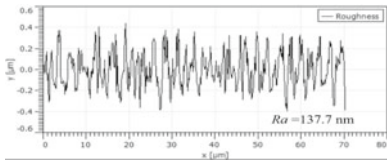
ST: Canine	Porosity (%) based on ASTM B 276 standard	Grain size number based on ASTM E 112 standard
STAGE-I: Cadaveric tooth	23.4 %	Grain size: 0 Avg. grain area (mm²): 0.2581
STAGE-II: Die stone model	28.75 %	Grain size: 0 Avg. grain area (mm²): 0.1290
STAGE-III: Thermoplastic DC	13.93 %	Grain size: 1 Avg. grain area (mm²): 0.0645
STAGE-IV: Metal cast DC	18.47 %	Grain size: 0 Avg. grain area (mm²): 0.1290
STAGE-V: 3D Metal printed DC	20.09 %	Grain size: 0.5 Avg. grain area (mm²): 0.0942

(major and minor), height, and thickness are calculated in dedicated CAD software (Solidworks 2020). The thickness of DC of thermoplastic, IC, and DMLS was calculated as 0.63 mm, 0.845 mm, and 0.61 mm. The calculated values of height, thickness, and diameter (major and minor) by CAD software (Refer Table 6; Fig. 6).

The calculations for height, major diameter, and minor diameter of fabricated DC in three different routes were given below: $i = 0.45 \times D^{1/3} \pm 0.001 \times D = 1.29$

$$n = 1000(DJN - DJM)/i$$

Table 3 3D rendered SEM images and relative surface roughness values at different stages in the fabrication of DC

ST: Canine	3D rendered SEM image	Relative Ra values at cut-off length at 0.05 mm
STAGE-I: Cadaveric tooth	0.99 μm / 0.00 μm; Y: 58 μm, X: 100 μm	$Ra = 39.11$ nm
STAGE-II: Die stone model	1.00 μm / 0.00 μm; Y: 58 μm, X: 100 μm	$Ra = 57.88$ nm
STAGE-III: Thermoplastic DC	1.00 μm / 0.00 μm; Y: 58 μm, X: 100 μm	$Ra = 38.01$ nm
STAGE-IV: Metal cast DC	0.99 μm / 0.00 μm; Y: 58 μm, X: 100 μm	$Ra = 28.26$ nm
STAGE-V: 3D Metal printed DC	0.99 μm / 0.00 μm; Y: 58 μm, X: 100 μm	$Ra = 137.7$ nm

$$\text{Geometric Mean} = D = (18 \times 30)^{1/2} = 23.23 \text{ mm}$$

Note:

$\rightarrow n = $ *tolerance unit*
$\rightarrow i = $ *standard tolerance factor*
$\rightarrow DJN = $ *nominal CAD dimension*
$\rightarrow DJM = $ *Physical measured dimension*

Table 4 ADF, BRC, and PC analysis
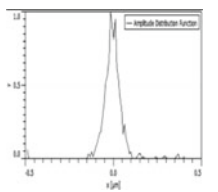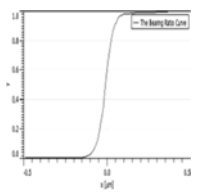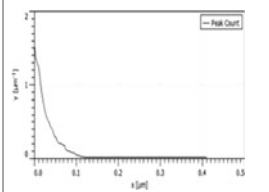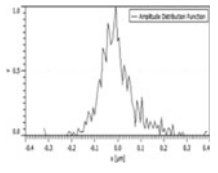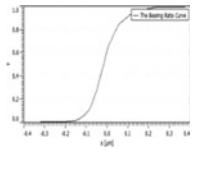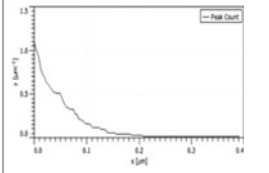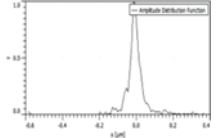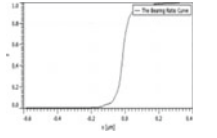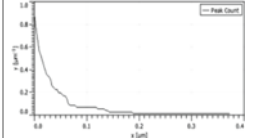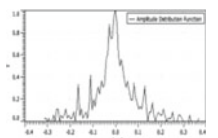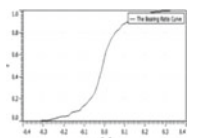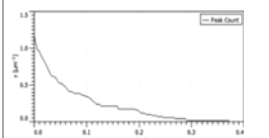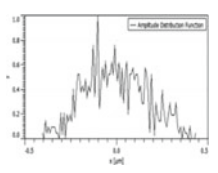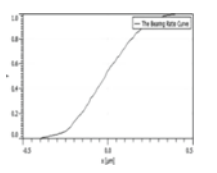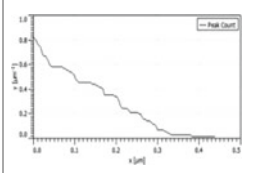
ST: Canine	Amplitude distribute function	Bearing ratio curve	Peak count
STAGE-I: Cadaveric tooth			
STAGE-II: Die stone model			
STAGE-III: Thermoplastic DC			
STAGE-IV: Metal cast DC			
STAGE-V: 3D Metal printed DC			

Table 5 Comparative analysis of results at different stages

Surface parameters	Stages				
	I	II	III	IV	V
Ra (in nm)	39.11	57.88	38.01	28.26	137.7
Porosity (%)	23.4	17.48	13.93	18.47	20.09
Grain area (mm^2)	0.2581	0.1290	0.0645	0.1290	0.0912
ADF (rank wise distribution)	5	3	4	2	1
BRC (distribution range)	7	7.5	3.5	7.5	9
PC	1.5 (stiffer)	1.1 (stiffer)	0.83 (stiffer)	1.3 (comparatively flatter)	0.82 (flatter)
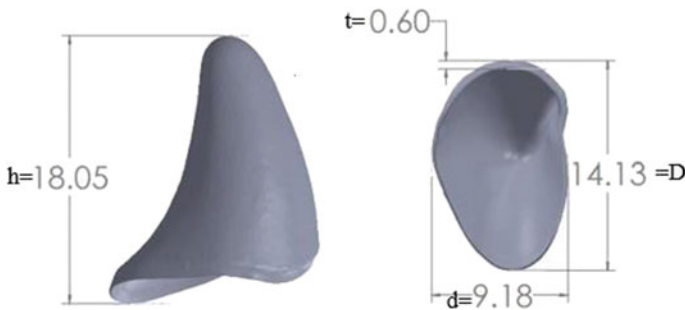
Fig. 6 Height (*h*), major diameter (*D*), and minor diameter (*d*) were calculated from the CAD file

Table 6 For height, major, and minor diameter wise examinations of IT grade of DC

DC stages		DJN in mm	DJ Min mm	(DJN-DJM) in mm	D	*i*	*n*	IT grade
Polymer DC	*h*	18.05	18.5	0.45	23.23	1.29	348.83	13–14
	D	14.13	15	0.87	13.41	1.07	813.08	15–16
	d	9.18	10	0.82	7.74	0.89	921.34	Over 16
IC metallic DC	*h*	18.05	20	1.95	23.23	1.29	1511.6	Over 16
	D	14.13	14.5	0.37	13.41	1.07	345.79	13–14
	d	9.18	10.5	1.32	13.41	1.07	1233.6	Over 16
Metal printed DC	*h*	18.05	18	0.05	13.41	1.07	46.72	8–9
	D	14.13	14.5	0.37	13.41	1.07	345.79	13 to 14
	d	9.18	10.5	1.32	13.41	1.07	1233.6	Over 16

5 Conclusions

The following conclusions are drawn in the morphological and dimensional analysis of the present study.

- The porosity and grain size show better results in case metallic crowns than cadaveric teeth.
- The ADF, BRC, and PC show extremely good results for DMLS parts as well as casted parts.
- The surface roughness of IC parts shows very good results in comparison to natural teeth; however, some powder density optimization may help to improve the density of DMLS parts.
- Dimension wise the DMLS parts show very good results with respect to fitting as per IT grades for the height of functional prototypes.

References

1. Bikas, H., Stavropoulos, P., Chryssolouris, G.: Additive manufacturing methods and modelling approaches: a critical review. Int. J. Adv. Manuf. Technol. **83**(1–4), 389–405 (2016)
2. Singh, N., Singh, R., Ahuja, I.P., Farina, I., Fraternali, F.: Metal matrix composites from recycled materials by additive manufacturing assisted investment casting. Compos. Struct. **207**, 129–135 (2019)
3. Zhang, Y., Bernard, A., Harik, R., Karunakaran, K.P.: Build orientation optimization for multi-part production in additive manufacturing. J. Intell. Manuf. **28**(6), 1393–1407 (2017)
4. Pradhan, S.R., Singh, R., Banwait, S.S.: A frame work on crown fabrication for veterinary patients using 3D thermoplastic and metal printing. Ref. Module Mater. Sci. Mater. Eng. (2020) (https://doi.org/10.1016/B978-0-12-820352-1.00063-8)
5. Komal, U.K., Kasaudhan, B.K., Singh, I.: Comparative performance analysis of polylactic acid parts fabricated by 3d printing and injection molding. J. Mater. Eng. Perform. **30**, 6522–6528 (2021)
6. Singh, G., Singh, R., Singh, S.: Partial denture by centrifugal casting assisted by additive manufacturing. Sadhana **44**(6), 1–11 (2019)
7. Pradhan, S.R., Singh, R., Banwait, S.S., Singh, S., Anand, A.: 3D printing assisted dental crowns for veterinary patients. Ref. Module Mater. Sci. Mater. Eng. (2021). (http://dx.doi.org/10.1016/B978-0-12-820352-1.00153-X)
8. Enlund, K.B., Brunius, C., Hanson, J., Hagman, R., Hoglund, O.V., Gustas, P., Pettersson, A.: Dental home care in dogs-A Questionnaire study among Swedish dog owners, veterinarians and veterinary nurses. BMC Vet. Res. **16**(1), 1–13 (2020)
9. Lemmons, M., Beebe, D.: Oral anatomy and physiology. Wiggs's Vet. Dent. Principles Pract. 1–24 (2019), Wiley

10. DiBenedetto, A.T.: Prediction of glass transition temperature of polymers: a model based on the principle of corresponding states. J. Polym. Sci. Part B: Polym. Phys. **25**(9), 1949–1969 (1987)
11. Singh, G., Singh, R., Singh, S., Bhardwaj, A.: On multi-factor optimisation of Ni-Cr- based partial dentures by centrifugal casting. Adv. Mater. Process. Technol. **7**(4), 630–646 (2020)
12. Wang, S., Yang, K., Shen, M., Yang, C.: Effect of Cu content on antibacterial activity of 17–4 PH stainless steel. Mater. Technol. **30**(sup6), B115–B119 (2015)
13. Yalman, O., Topuz, A.: Manufacturing of Metal Based Dental Brackets. IMMC (2018)
14. Marques, R.A., Saliba-Silva, A.M., Rogero, S.O., Montemor, M.D., Costa, I.: A comparative study of the corrosion resistance of stainless steels obtained by powder metallurgy techniques for application in dental prosthesis. Mater. Sci. (Trans Tech Publications Ltd.), **660**, 617–622 (2010)
15. Averyanova, M., Cicala, E., Bertrand, P., Grevey, D.: Experimental design approach to optimize selective laser melting of martensitic 17–4 PH powder: part I–single laser tracks and first layer. Rapid Prototyping J. **18**(1), 28–37 (2012)
16. https://support.3dsystems.com/s/prox-dmp-200?language=en_US, Last accessed 30 Jan 2021
17. Park, D.Y., Lee, G.M., Kwon, Y.S., Oh, Y.J., Lee, S., Jeong, M.S., Park, S.J.: Investigation of powder size effects on sintering of powder injection moulded 17–4PH stainless steel. Powder Metall. **60**(2), 139–148 (2017)
18. Singh, R., Sidhu, J.S., Pabla, B.S., Kumar, A.: Three-dimensional printing of innovative intramedullary pin profiles with direct metal laser sintering. J. Mater. Eng. Perform. **31**(1), 240–253 (2021)
19. Singh, J., Singh, R.: Investigations for statistically controlled rapid casting solution of low brass alloys using three dimensional printing. Int. J. Rapid Manuf. **1**(2), 208–221 (2008)

Part Quality Improvement of Fused Filament Fabrication-Based Additive Manufacturing by Means of Slicing Software Modifications

M. Anand Sankar ⓘ **, K. Deepak Lawrence** ⓘ **, and Jose Mathew** ⓘ

1 Introduction

One of the most widely used Additive Manufacturing (AM) technique is Fused Filament Fabrication (FFF) in which the physical parts are created directly from the virtual 3D model. In this process, the heated plastic filament is extruded through a nozzle and deposited in layer-by-layer fashion to form the geometry of the object. This technique is one of the earliest types of AM process and was commercialized in the name Fused Deposition Modeling (FDM) by Stratasys company in United States in 1992. Its capability to fabricate production-grade engineering thermoplastics parts at low cost in a safe and efficient operation with acceptable durability made this AM process one the most widely used AM processes in the industry for functional prototypes and production series parts.

The improvement of the part quality produced by FFF has gained attention of the researchers because of the inherent limitations in surface texture and dimensional accuracy of the parts due to the workflow and process mechanics aspects of fused filament fabrication process. These research efforts can be classified in to four main areas that are improvements in surface finish, enhancement in accuracy, build orientation and slicing strategies. Out of these, this work mainly concentrates on the slicing strategies that can be developed to improve the quality of the component.

Being a layer-based process, FFF has inherently characterized by stair-stepping artifacts, as reported by Hague et al. [1]. Apart from this point, the parameters like build orientation, layer thickness, orientation in which the part is placed for the build,

M. Anand Sankar (✉) · K. Deepak Lawrence · J. Mathew
Department of Mechanical Engineering, National Institute of Technology, Calicut 673 601, India
e-mail: anandsankar.manipuzha@gmail.com

K. Deepak Lawrence
e-mail: deepaklawrence@nitc.ac.in

J. Mathew
e-mail: josemat@nitc.ac.in

etc., will affect the quality of the final products. By keeping all other parameters, the same, build orientation alone can significantly impact the surface quality of the parts.

Different post-processing operations can be applied to the produced components to improve the part quality [2–4]. Modifying process parameters can also be an option to solve the issues in part quality, and the strategies like ironing and remelting can also be a solution [5, 6]. However, these operations will increase the cost of the component due to additional methods, labor, material and machining. Hence, the current research mainly focuses on exploring the preventive actions that can be done before the rise of surface quality issues.

An approach was proposed by Chakraborty et al. in which different Z heights are possible during the printing of a single layer based on the Curved Layer Fused Deposition Modeling (CLFDM) technique [7]. In that work, they successfully defined the three factors regarding the curved layer printability, namely orientation of extruder, adhesion between adjacent extruded layers and correct tool path G code generation. However, they did not demonstrate the approach by producing a real component. With the use of the parametric surfaces, Huang et al. created the first real physical parts using FFF [8]. Singamneni et al. [9] were introduced the parts with curved layers which are closer to the original geometry of the design. In their work the surface is discretized with special scripts and rasters are obtained so that the toolpaths are generated along the raster points. But every surface cannot do with nonplanar curved surface and Huang et al. [10] presented a combined approach of nonplanar layers over a set of planar layers. The printability conditions for curved layers are identified and checked so that all the printable regions are grouped in the surface mesh. Remaining parts of the surface are executed with planar slicing. But in the real scenario, while printing nonplanar layers there is a chance of collision within the toolpath, that is print head may collide with the previously printed layers. Also, while printing nonplanar layers with a common 3 axis gantry system the material is not extruded normal to the printing surface which is very unlikely to the planar printing technique. So, Jin et al. [11] introduced a dynamic compensating system while printing nonplanar layers with upward or downward slopes. Otherwise, the printing nozzle will be a bit high or low in accordance with the deposition directions. This dynamic compensation was done mainly based upon slope of printing surface and printing toolpath direction [12]. The mechanical properties of planar and nonplanar sliced parts were tested by Khurana et al. [13]. Parts with nonplanar slicing were both stiffer and stronger in comparison with normally printed counterparts [14].

Though researchers proposed various algorithms for nonplanar slicing, less attempts were done toward revealing the scope for practical and application-level components. So, in this work we tried to identify the suitable regions, check for possible collisions and automatically generate a combined tool path with mostly planar layers and nonplanar layers on the top surface by designing a hemisphere model and airfoil model whose surfaces suffer strongly from stair-stepping effect. The analysis proposed in this work helps FFF manufacturers to find suitable strategy to print the parts with nonplanar layers in order to minimize the stair-stepping artifact and thereby increasing the part quality.

2 Methodology

In this work, an attempt is made to modify "Slic3r" which is an open source software [15] for slicing to generate the G codes for nonplanar surfaces. So, all the implementations are done in the same Slic3r software. Overview of the methodology is shown in Fig. 1. The source codes are identified and manipulated using Visual studio and Gnu C Compiler (GCC). Slicing algorithm Graphical User Interface (GUI) is rendered in Open Graphics Library (GL) and the developed G codes will be nonplanar or active in Z-direction.

2.1 Collision Model of the Print Head

In order to avoid the collision of the nozzle, printing extruder body or cooling fans of the print head with previously deposited material, geometry of the print head is analyzed and a collision model of the printhead is made as shown in the Figs. 2 and 3. This collision model is essential for developing nonplanar toolpaths because in the case of nonplanar printing the print head or nozzle can trace curves in Z-axis too which can cause collision of parts of the printhead with previously deposited layers.
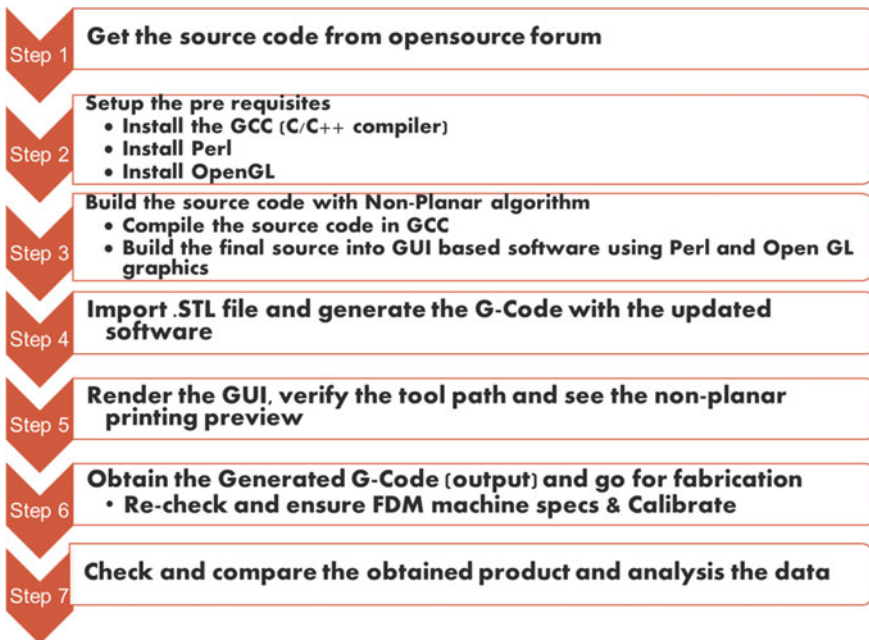
Fig. 1 Overview of methodology of our implementation

Whereas in planar printing there is no Z-axis movements of the printhead until a layer is completely deposited and no chance of printhead collisions.

Since nonplanar toolpath involves the travel of printhead down into regions with already deposited structures, the algorithm needs additional information about the printhead geometry to prevent the possible collisions between parts of the printhead and initially deposited structures. If we have more data about printhead, the slicer can predict more accurately whether a nonplanar layer can be deposited or not without any collisions. But if we include a full model of the printhead to check collisions, it will be more complex because of the more constraints like different shapes of the extruder and printhead parts. So, a simple parametric model of the printhead with mainly two parameters would be much easier. Also, these parameters can be measured and stored as configurations in the slicer.

From the geometrical dimensions measured from the print head maximum nonplanar angle (Θ_{np}) and maximum nonplanar height (h_{np}) that are printable without collisions are calculated (Table 1). These are the two parameters that define the collision model of the printhead. The maximum nonplanar angle (Θ_{np}) is the maximum angle that we can go for a given printing surface which will be collision free over the tip of the nozzle. The maximum possible height that we can print the surface with the corresponding angle without any collisions with the parts of the printhead is termed as the nonplanar height (h_{np}).

From the Fig. 2 taking only the nozzle into account with a Θ_{np} of 45° we can go for h_{np} of 3 mm only (Region 1) whereas with a Θ_{np} of 36° we can go for h_{np} of 7 mm (Region 2). Even though we can get Θ_{np} of 41° and h_{np} of 8 mm in region 3, we will not be considering it because for the safety of printhead we are limiting the

Fig. 2 Print head of
Raise3D FFF printer

Fig. 3 Collision model of Raise 3D printer–regions of printhead that can cause collision with preciously printed structures in case of nonplanar printing
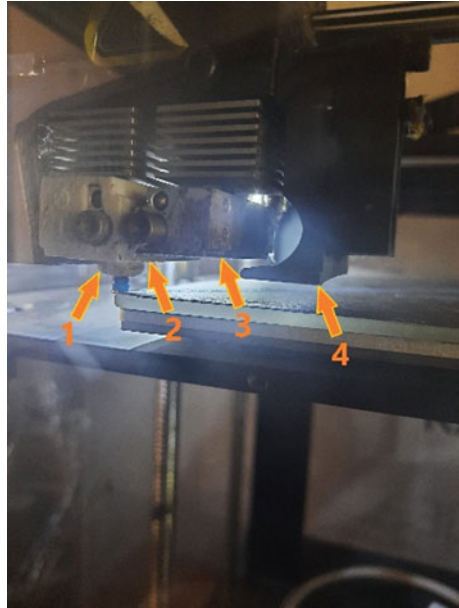
Table 1 Calculated parameters from the collision model

Case	Maximum nonplanar angle Θ_{np} ($^{\circ}$)	Maximum nonplanar height h_{np} (mm)
Region 1	45	3
Region 2	36	7
Region 3	41	8
Region 4	19	5

Θ_{np} as 36°. So, the safe maximum nonplanar printing angle we will be using in our model is 36° which can be printed at a maximum nonplanar height of 7 mm.

We can understand that, with these combinations, either small surfaces with a large Θ_{np} or large surfaces with a small Θ_{np} can be printed. Since, both parameters are different for different printing platform these can be considered as configuration parameters which must be provided by the user.

2.2 Surface Angle

In the case of nonplanar printing the quality of an inclined surface is affected by the surface angle. Unlike stair-stepping effect, here surfaces with low surface angle are printed with a very good quality. There are two factors that contribute to the surface roughness and these are the motion along the slope of the surface and perpendicular
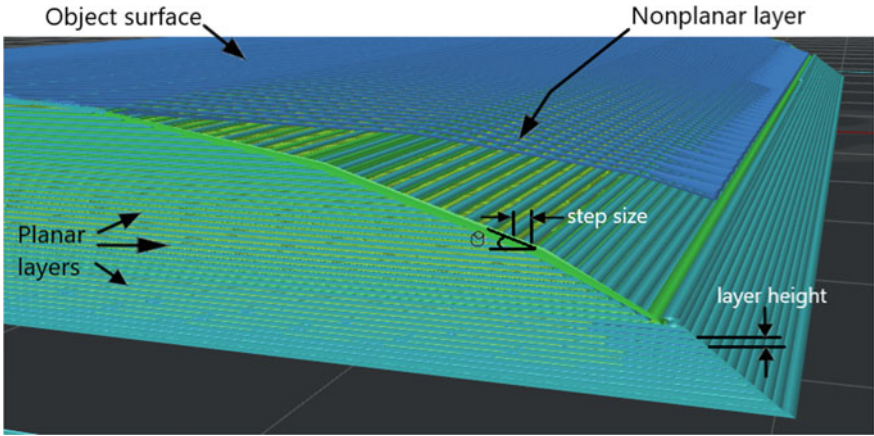
Fig. 4 Nonplanar extrusions (blue) on top of planarly deposited layers (green) considerably diminish the stair-stepping

to the slope of the surface. If we consider the first case, effect of uppermost planar layer is subsampled by the deposition of first nonplanar layer as shown in Fig. 4. So from this we can understand that if stair step size is higher than the width of extrusion then the resolution of the curved nonplanar layer will be more compared to the similar geometry formed with planar slicing layers. So, for a given layer height and extrusion width the threshold surface inclination can be computes as:

$$\theta_{th} = \tan^{-1}\left(\frac{\text{layer height}}{\text{extrusion width}}\right) \qquad (1)$$

Therefore, for a given region if the surface angle $\Theta < \Theta th$ then it could be printed using nonplanar layer. So, the angle for the region classification is limited as

$$\theta_m = \min(\theta_{th}, \theta_{np}) \qquad (2)$$

Coming to the second case, a surface deformation can occur due to the angle between nozzle orifice and the surface. That is the deposited filament is sheared off by the rim of the nozzle tip during a horizontal movement, which result a flat surface. But in the case of movements that are not horizontal in direction, the orifice of nozzle tip becomes increasingly "ellipsoid", which leaves either a convex profile or concave form of profile, depending on the upward motion or downward motion.

2.3 Toolpath Generation

The iterative checks for detecting surface with nonplanar slicing are performed initially. The possible surfaces are found out in the STL model library and these surfaces are checked for major collisions to generate the toolpaths for nonplanar layers. After this, the toolpaths are obtained by generating nonplanar surfaces within the layer structure. Then according to the nonplanar geometry these are projected. Finally, from the toolpaths, G code is obtained and started to generation. The visualization capability of toolpath of Slic3r software is enhanced so that it is able to display even 3D nonplanar toolpaths also along with planar toolpaths.

For generating the nonplanar toolpath, the nonplanar surfaces are found out from facet mesh of the given model. This step is executed once the layer generation for the normal planar slicing is completed. As described in the previous section there are two hardware limitations one is maximum printing angle and the other one is maximum height. All the facet of the given STL which refers to the nonplanar surface should be bound within these conditions. This is first condition. We can determine the orientation of the facets using its normal and the Z components can be used to determine the angle of the facet with reference to the Z-axis. If Θ is the threshold angle, every facet that meet the condition normal.z $\geq$ cos Θ, are stored as potentially printable facets. The components corresponding to X and Y-axis of the normal can be eliminated because the threshold angle should be valid in all the directions. So, nonplanar facets module stores the typical printable facets and here the computations for facet surface area is also done. A nonplanar facet are capable of rotate and scale functions that are required if it is needed to scale or rotate the model.

2.4 Collision Checks and Avoidance

Since the printing head never moves down to the level of present layer, there are no collisions in the case of planar printing. When printing nonplanar layers, the scenario is different. The printhead may pierce into previously deposited layers. It may lead to potential collisions with the parts of the printhead. To avoid this, the surface that may cause collision is not printed with nonplanar layers. It is possible to detect the collisions by checking the entire tool path when the deposition head would collide with the previously deposited structures or layers.

Strictly speaking 3D printing is not a printing in three-dimensions, since the each of the 2D layers are deposited and stacked we can call it is a 2.5D printing. But in the case of nonplanar printing, it becomes a real 3D printing and collisions may happen between the printhead and previously printed parts. To get the collisions on the whole toolpath every single layer can be checked for possible collisions. This idea will result a set of 2D collision check which are simple instead of a complex 3D collision. Table 2 gives a summary of algorithm for layer-by-layer collision check.

Table 2 Algorithm for layer-by-layer collision check

Algorithm: Layer-by-layer collision check
1.   function 2D_COLLISION_CHECK
2.   Collider polygon (empty)
3. $offset = \frac{layer\,height}{\tan\theta}$
4.   Nonplanar surface = HORIZONTAL_PROJECTION (nonplanar surface)
5.   for all layers between min_surf and max_surf
6.   do layer_colider = DIFFERENCE (colider, nonplnar_surface)
7.   if INTERSECTION (layer.surface, layer_colider) ≠ empty
8.   then return detected collision(s)
9.   else
10.   potential top = difference (layer.surface, upper layer.surface)
11.   new colider = intersection (nonplanar surface, potential top)
12.   collider = OFFSET(UNION (colider, new_colider), offset
13.   end if
14.   end for
15.   return not detected any collisions
16.   End

For checking the possible collisions that may occur, firstly, an empty collider polygon and a horizontal projection of the nonplanar surface is formed. After this the algorithm starts iterating through all layers that is between the highest and lowest nonplanar height. In other words, between the minimum nonplanar surface height and maximum nonplanar surface height. For every layer, intersection between collision polygon and surface polygon is calculated and ensured that collider polygon does not collide with anything from the surface. Since the projected nonplanar surface would generate a false positive it is excluded from the collision check. If the intersection is empty there is no collision, otherwise there is a collision; so, if intersection is empty then the step is continued. Even though intersection will be calculated against the collider polygon from the last iteration on each and every layer, in the case of first layer there can be no collisions because the nozzle is always above this layer. So, first layer is checked against the initially generated empty collider. Calculation of top potential surface are done by finding the difference between present and the subsequent layer. The intersection between top potential surface and nonplanar surface projection is calculated by using the polygon intersection operation. This value of intersection is further added to the collider. An offset is given to the collider by an amount which is the maximum value of radius that the collider can attain within the single layer. Suppose this radius is r units it can be calculated using Eq. (3) provided that h is the height of the layer and Θ will be the highest possible value of printing angle.

$$r = \frac{h}{\tan\theta} \tag{3}$$

3 Evaluation

To discuss the practical importance of suggested methodology, we fabricated a group of different models that could significantly affected from stair-stepping artifact and complex geometric surfaces. The slicing and printing speed for the designed components is evaluated. All the test objects are printed on a Raise 3D N series printer with a 0.4 mm nozzle. For the evaluation of test objects, we have kept print speed for perimeters as 60 mm/s, infill as 80 mm/s and bridges as 60 mm/s. The speed for non-print moves (travel) is 130 mm/s.

Figure 5 shows the tool path preview generated for planar and nonplanar sliced surfaces of a hemisphere. Figure 6 shows the printed results of the same. From these we can understand that it is also possible to use both planar and nonplanar slicing in a single object where the algorithm succeeds to detect automatically the regions suitable for nonplanar layer deposition. Here the implementation automatically detected which region of the hemisphere is worsened by stairstep effect and the required possible region is nonplanarly sliced. Even though both the objects are printed with same layer height, the region with nonplanar layer possess much smoother surface. Likewise in the case of planar layer deposition, the inner geometry of the underlying layers found to be disappearing upon the deposition of few top nonplanar layers. This is clearly illustrated in Fig. 7 where three set of nonplanar layers is printed on top of planar layers which are visualized in Slic3r.

Figure 8 shows a portion of G codes developed for the nonplanar sliced hemisphere. In this we can see that tool path for planar layers is completed in line number 57592 and from the 57601st line nonplanar toolpath is started, because afterwards the Z coordinate is started varying.

Figure 9 shows wing profiles printed with planar, nonplanar layers, where smooth surface is highly required due to aerodynamic considerations. Likewise in the previous case the surface finish is considerably improved for the nonplanar sliced wing profile. Furthermore, Table 4 indicates that there is no considerable increase in printing time for nonplanarly sliced object.
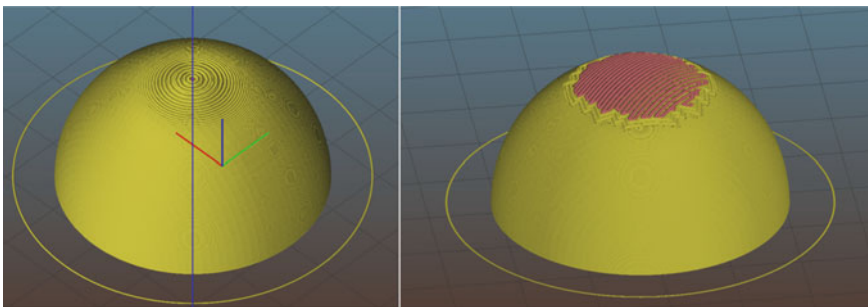
Fig. 5 Toolpath preview of hemisphere model with planar (left) and nonplanar layers (right)
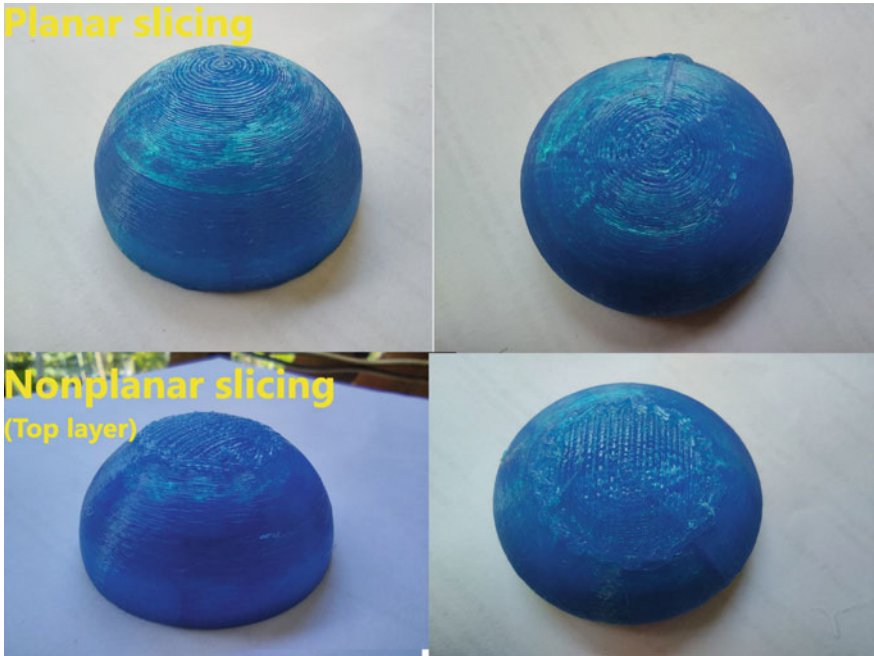
Fig. 6 Hemisphere model printed to showcase smooth surface on the top and the ability to combine planar and nonplanar layer in single shell. Planar slicing (top left and right) and nonplanar slicing (bottom left and right)
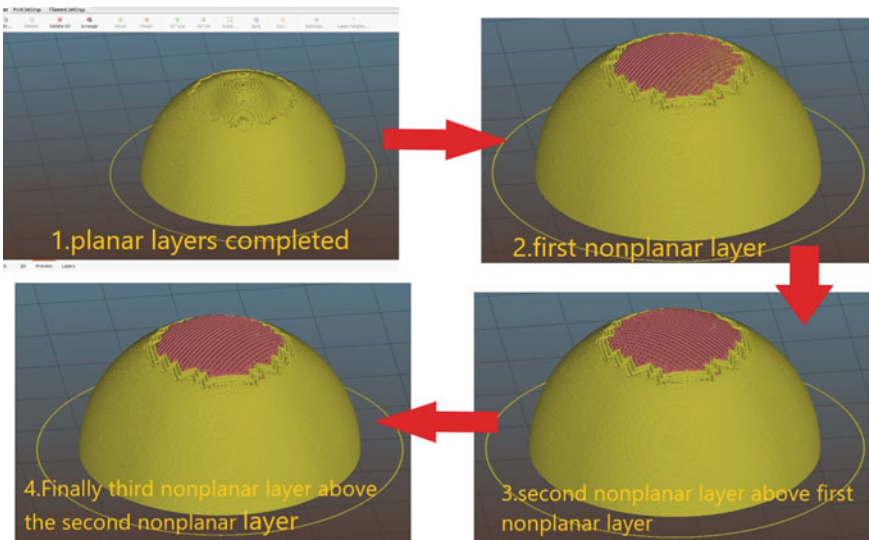
Fig. 7 Steps of the nonplanar toolpath generation in a typical three top nonplanar layer case

```
57580 G1 X100.024 Y101.300 Z20.200 F7800.000
57581 G1 F600
57582 G1 X100.617 Y100.707 Z20.200 E2.17070
57583 G1 X100.535 Y100.789 Z20.200 E2.17326
57584 G1 X99.188 Y101.021 Z20.200 F7800.000
57585 G1 F600
57586 G1 X101.022 Y99.187 Z20.200 E2.23111
57587 G1 X100.537 Y98.701 Z20.200 E2.24643
57588 G1 X100.392 Y98.701 Z20.200 E2.24964
57589 G1 X98.698 Y100.396 Z20.200 E2.30310
57590 G1 X98.698 Y99.979 Z20.200 E2.31239
57591 G1 X99.463 Y99.212 Z20.200 E2.33655
57592 G1 X99.881 Y99.212 Z20.200 E2.34588
57593 M106 S191.25
57594 G1 Z20.400 F7800.000
57595 G1 Z20.400 F7800.000
57596 G1 X96.346 Y110.235 F7800.000
57597 G1 Z17.374 F7800.000
57598 M106 S255
57599
57600 G1 F3600
57601 G1 X96.245 Y109.361 Z17.833 E2.37091
57602 G1 X96.215 Y109.096 Z17.951 E2.37842
57603 G1 X95.952 Y109.096 Z17.902 E2.38571
57604 G1 X95.089 Y109.096 Z17.685 E2.40973
57605 G1 X94.975 Y108.186 Z18.088 E2.43554
57606 G1 X94.941 Y107.921 Z18.185 E2.44301
57607 G1 X94.680 Y107.921 Z18.119 E2.45030
57608 G1 X93.538 Y107.921 Z17.756 E2.48213
57609 G1 X92.690 Y107.921 Z17.428 E2.50590
57610 G1 X92.548 Y106.979 Z17.763 E2.53251
57611 G1 X92.394 Y105.747 Z18.124 E2.56711
57612 G1 X92.361 Y105.482 Z18.183 E2.57454
57613 G1 X92.101 Y105.482 Z18.082 E2.58183
57614 G1 X91.234 Y105.482 Z17.683 E2.60629
57615 G1 X91.123 Y104.493 Z17.906 E2.63398
57616 G1 X91.016 Y103.221 Z18.118 E2.66943
57617 G1 X90.994 Y102.956 Z18.144 E2.67682
57618 G1 X90.736 Y102.956 Z18.025 E2.68411
57619 G1 X89.871 Y102.956 Z17.561 E2.70875
57620 G1 X89.803 Y102.012 Z17.657 E2.73506
57621 G1 X89.810 Y101.938 Z17.671 E2.73713
57622 G1 X89.761 Y100.728 Z17.730 E2.77077
57623 G1 X89.770 Y100.647 Z17.740 E2.77303
57624 G1 X89.758 Y99.353 Z17.734 E2.80896
57625 G1 X89.798 Y98.062 Z17.665 E2.84483
57626 G1 X89.861 Y97.044 Z17.556 E2.87319
```

planar G codes
(bottom layer g codes)

G codes of non-planar layers
(Top first nonplanar layer started)

Fig. 8 Transition of planar layer G codes to nonplanar layer G codes
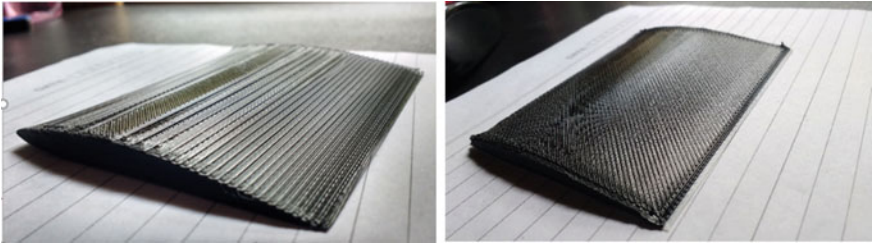
Fig. 9 Comparison of wing from the NACA 0024 airfoil profile printed with planar (left) and nonplanar layers (right)

To compare the slicing time or duration needed for the modified Slic3r to generate the toolpaths for a given model, all the models were sliced with planar and nonplanar layers. The layer thickness chosen for planar and nonplanar slicing is of 0.15 mm. Fabricated hemisphere surface is scanned using 3D optical profilometer (Alicona InfiniteFocus G5) for analyzing the surface roughness.

4   Results and Discussion

From the above evaluation, it is clear that it is possible to develop a general-purpose scheme to print nonplanar layers on top of planar layers in any practical and application-level components by introducing a modified slicing software. The generated toolpaths can be executed and printed on a common three axis 3D FFF-based printer without any significant modifications.

Table 3 shows the runtime of different slicing algorithm for various test parts. The slicing duration for nonplanar toolpaths is found to be more. Nonplanar slicing is always slower than planar algorithms because of the fact, it will make some extra steps to the tool path generation. However, the time take for slicing is not significant compared to the time taken for printing the entire object.

Table 4 shows the print time of evaluation models on Raise 3D N series 3D printer with a 0.4 mm nozzle. The planar and nonplanar sliced models shows a similar printing time and the increase in printing time for nonplanarly sliced objects is justifiable due to the quality in surface finish.

Figures 10 and 11 shows the surface scan images obtained using 3D optical profilometer (Alicona InfiniteFocus G5). From these we can understand material is deposited more evenly in nonplanar surfaces. There is a crater region formed in between raster scans of the print nozzle and in the case of surface with nonplanar layers, the size (both width and depth) of this crater region is less. So, in addition to the reduction of stair-stepping effect, this fact also contributes to the improvement of surface roughness. Table 5 gives an evidence for this deduction where R_a value is obtained from the constructed 3D image datapoints from the 3D profilometer.

Table 3 Time taken (Runtime) by the slicing algorithm for various test parts

	Hemisphere (s)	Wing profile (s)
Planar slicing	7	3
Nonplanar slicing	10	17

Table 4 Printing duration of different test parts

	Hemisphere (min)	Wing profile (min)
Planar slicing	26	41
Nonplanar slicing	28	46
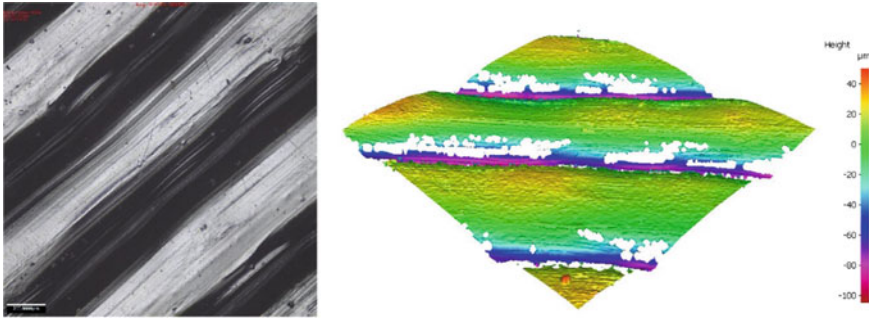
Fig. 10 Scan images of hemisphere surface with planar layers from 3D profilometer. 2D image (left) and constructed 3D graphical image (right) showing the crater region formed in between raster scans of the nozzle
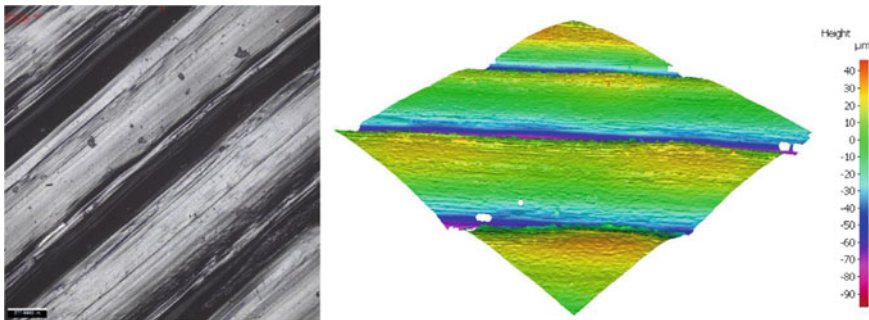
Fig. 11 Scan images of hemisphere surface with nonplanar layers from 3D profilometer. 2D image (left) and constructed 3D graphical image (right) showing the crater region formed in between raster scans of the nozzle

Table 5 Surface roughness data of hemisphere from Focus Variation Microscopy-based optical profilometer

	Planar slicing	Nonplanar slicing
Surface roughness R_a	1.5 µm	0.8 µm

5   Conclusions

In this paper, an attempt is made toward presenting the nonplanar slicing and 3D tool-path generation for the FFF process. The implemented slicer with modified algorithm can automatically suggest the best possible regions to undergo nonplanar slicing and groups and filters the regions to avoid the collision between parts of the printhead with already deposited layers. Another advantage is that the developed G codes can be fed to any three axis FFF printers and can be executed without any complexity.

Since the algorithm is embedded with the GUI of Slic3r, it is possible to preview the standard planar and generated nonplanar toolpaths.

It is observed that the printed objects visually presented much better which have smooth nonplanar surfaces rather than the surfaces with stair-stepping effects as result of planar slicing. The optical profilometer-based roughness comparison give clear indication of the improvement in surface quality with the suggested technique. The time taken for printing of a nonplanar sliced object does not increase considerably in comparison with that of a planar sliced object. Test results showed that for nonplanarly sliced objects the printing time increases only slightly. This is not only due to collision avoiding travel moves but also due to the fact that Z-axis of common 3D printers cannot move faster as X and Y-axis.

Post processing such as chemical treatment and heat treatment of fabricated parts may help to increase the tensile properties which is highly desirable. We plan to evaluate the mechanical properties of the objects after post processing as part of our future work which is expected to increase because of the increase in the interlayer bonding.

References

1. Hague, R., Campbell, L., Dickens, P.: Implications on design of rapid manufacturing. Proc. Inst. Mech. Eng. C J. Mech. Eng. Sci. **217**(1), 25–30 (2003)
2. Yasa, E., Demir, F., Akbulut, G., Cizioglu, N., Pilatin, S.: Benchmarking of different powder-bed metal fusion process for machine selection in additive manufacturing. In: Proceedings of International Solid Freeform Fabrication Symposium, pp. 390–403 (2014)
3. Gibson, I., Rosen, D.W., Stucker, B.: Post-Processing in Additive Manufacturing Technologies, pp. 415–435. Springer, New York (2010)
4. Fischer, M., Schoppner, V.: Finishing of ABS-M30 parts manufactured with fused deposition modeling with focus on dimensional accuracy. In: Proceedings of International Solid Freeform Fabrication Symposium, pp. 923–934 (2014)
5. Krol, M., Dobrzanski, L.A., Tanski, T.: Influence of technological parameters on additive manufacturing steel parts in Selective Laser Sintering. Arch. Mater. Sci. Eng. J. **67**(2), 84–92 (2014)
6. Taufik, M., Jain, P.K.: Role of build orientation in layered manufacturing: a review. Int. J. Manuf. Technol. Manage. **27**(1), 47–73 (2013)
7. Chakraborty, D., Aneesh Reddy, B., Roy Choudhury, A.: Extruder path generation for curved layer fused deposition modeling. Comput. Aided Des. **40**(2), 235–243, (2008).
8. Huang, B., Singamneni, S., Diegel, O.: Construction of a curved layer rapid prototyping system: integrating mechanical, electronic and software engineering. In: 15th International Conference on Mechatronics and Machine Vision in Practice, pp. 599–603. IEEE (2008)
9. Singamneni, S., Roychoudhury, A., Diegel, O., Huang, B.: Modeling and evaluation of curved layer fused deposition. J. Mater. Process Technol. **212**(1), 27–35 (2012)

10. Huang, B., Singamneni, S.: A mixed-layer approach combining both flat and curved layer slicing for fused deposition modelling. In: Proceeding of the Institution of Mechanical Engineers, Part B: Journal of Engineering Manufacture, vol. 229, no. 12, pp. 2238–2249 (2014)
11. Jin, Y., Du, J., He, Y., Fu, G.: Modeling and process planning for curved layer fused deposition. Int. J. Adv. Manuf. Technol. **91**(1–4), 273–285 (2017)
12. Daniel, A.: 3D Printing of Nonplanar Layers for Smooth Surface Generation, Technical Aspects of Multimodal Systems (TAMS). University of Hamburg, Germany (2018)
13. Khurana, J.B., Dinda, S., Simpson, T.W.: Active-z printing: a new approach to increasing 3D printed part strength. Solid Freeform Fabrication Symp. 1627–1644, (2017)
14. Khurana, J.B., Simpson, T.W., Frecker, M.: Structurally intelligent 3D layer generation for active Z-printing. In: Proceedings of the ISFFS 2018, pp. 2413–2426. Austin, US, Aug 13–15, 2018 (2020)
15. Slic3r Open source 3D printing toolbox. https://slic3r.org/, Last accessed 10 June 2021

Development and Characterization of Zn–Mg Biodegradable Materials Using Powder Metallurgy

Mahesh Choudhary [ORCID]**, Jinesh Kumar Jain** [ORCID]**, and Toshit Jain** [ORCID]

1 Introduction

To improve the healthcare and orthopedic sciences, zinc is considered an appropriate alloying ingredient for magnesium-based implants to enhance the material's corrosion resistance and mechanical characteristics [1–3]. Since zinc is considered a more noble metal than magnesium with more biocompatible in nature and considered as the better choice for implantations. It may be appropriate biodegradable material. Numerous Zinc-based materials [4] with improved mechanical and corrosion characteristics have been designed and investigated, but mere Zn is relatively cytotoxic (even in low doses) compared to Mg. An adult's daily zinc requirement is calculated to be 15 mg. Mg doses of up to 700 mg per day, on the other hand, can be tolerated. Zinc is an important nutritional element of the human body, with bone and muscle accounting for approximately 85% of Zn. It is a crucial component of macromolecules and enzymes, concerning for wider extent of enzymatic reactions. Owing to the rapid transport of ionic zinc in living tissue there should be no risk of systemic toxicity from metallic zinc. Furthermore, higher doses of zinc (≥ 100 mg/day) will be taken as non-toxic materials. In the future, more comprehensive cytotoxicity testing will be needed. In higher doses than zinc, magnesium triggers several enzyme reactions, protein synthesis co-regulation and muscle contraction, and the stabilization of DNA and RNA. Zinc is considered a good base material for the development of biodegradable implant materials due to its beneficial impact on the human body. Only a few studies have been done on zinc alloys in biomedical implant applications. According to the author's knowledge, there is only one article dealing with applying pure zinc as a bio-absorbable cardiac stent material. A four-wire series of samples were implanted inside the abdominal aorta of Sprague–Dawley rats for 1.5, 3, 4.5,

M. Choudhary · J. K. Jain (✉) · T. Jain
Deparment of Mechanical Engineering, Malaviya National Institute of Technology, Jaipur 302017, India
e-mail: jineshjain.mech@mnit.ac.in

and 6 months, respectively. The authors in [5] demonstrate the bio-corrosion activity of zinc. According to the findings, zinc-based alloys corrodes slower than magnesium and its alloys [6, 7]. For around four months, zinc implants are almost completely intact, during which time corrosion accelerates. Zinc oxide and zinc carbonate are the corroded outcomes of zinc. Since zinc corrodes slowly, there is enough time to filter out hydrogen produced under this process. That is both a major distinction and a distinct advantage over magnesium. This dissertation, however, did not provide any mechanical test results. Zinc has poor mechanical properties in general. Since the compressive stress–strain curve does not have a region of strict proportionality, the modulus of compressive elasticity of commercially pure zinc is not classified as an exact value. As a result, this value was calculated under the 75–145 GPa range. This material's Vickers hardness is 30 HV. Wrought pure zinc has a tensile strength of 120–150 MPa, according to its rolling direction. Pure casted zinc having a tensile strength of about 25 MPa, is very strong. Zinc alloying is a viable option due to the metal's weak mechanical properties. Magnesium, aluminum, and silver have also been tested as alloying elements. The mechanical characteristics of zinc alloys with aluminum constituents have significantly improved properties. This is attributable to containing Al–Zn solid solution and the volume fraction of the monotectoid reaction's lamellar micro-constituents serving as potential dislocation motion barriers. The tensile strength for the composition and alloy formed using hot rolling at 350 °C is 308 MPa appx. providing yield strength of 240 MPa, when 5.5 wt% aluminum is added. However, because of the uncertainty surrounding aluminum toxicity, the use of Zn–Al alloys in medicine is still limited [8]. Additionally, due to inter-granular corrosion, the corrosion resistance of Zn–Al alloys was lower than that of high purity zinc. Furthermore, implant cracking and fragmentation are caused by volume expansion associated with corrosion product formation. Silver is another alloying material that has a positive impact on its mechanical and biocompatible properties. The ultimate tensile strength of the cast zinc alloy improved to 287 MPa with the addition of 7.0 wt% Ag. Silver is also used in medicine to treat wounds and prevent bacteria from adhering to implant surfaces in nanoparticles. Secondary phase particles in Zn–Ag alloys, on the other hand, acted as anodes and caused micro-galvanic corrosion. As a result, when compared to pure Zn, Zn–Ag alloys degrade at a faster rate. Magnesium is perhaps the most talked-about alloying factor in zinc-based biodegradable materials [9]. Due to the presence of the hard Mg_2Zn_{11} intermetallic steps alloy structures, the hardness value enhances with increasing magnesium constituent, reaching 200 HV for cast alloy of 3% Mg. The hardness of cast alloys containing larger magnesium content (35–45 wt% Mg) can achieve values of 280–310 HV1 for 35 wt% of Mg (mainly depends upon the cooling rates for the casted product and their subsequent microstructure). Since another strengthening step exists in the alloy microstructure, the hardness increases ($MgZn_2$). The content of the $MgZn_2$ phase decreases as the alloy's magnesium content rises, while the content of the MgZn and Mg_7Zn_3 metal phase increases. The hardness of the alloy with 45 wt% magnesium drops again as the $MgZn_2$ content decreases to 255–280 HV1 [10, 11]. The presence of embrittlement in eutectic phases of alloys with a magnesium content greater than 1 wt%, on the other hand, hurts ultimate tensile strength. Ultimate tensile strength rises to

150 MPa (1 wt% Mg) before falling to 30 MPa (3 wt% of Mg). In addition, the alloy with 1 wt% magnesium has the highest elongation of any Zn–Mg alloy [12]. Another paper discusses how their hot extrusion processing can improve mechanical properties. The ultimate tensile strength of a hot extruded alloy containing 0.8 wt% magnesium is around 300 MPa, and the Vickers hardness is around 80 HV5. Hot extruded materials containing 1.6 wt% Mg have an U.T.S. of appx. 360 MPa and a Vickers hardness under the range of 97 HV5. The majority of the articles available deal with integrating alloying elements and their mechanical properties, corrosion resistance of zinc-based materials. Only a small amount of research has been done on the effect of the preparation process and its parameters on mechanical properties [13, 14].

This study examines how zinc materials are prepared using powder metallurgy: cold pressing and cold pressing later accompanied by sintering. To the author's knowledge, there is no published work on the preparation of zinc-based powder metallurgy biomaterials using these methods. This research looks over the influence of particle size of the powder materials applicable for investigating the resulting microstructure and their mechanical properties and the effect of the preparation process.

2 Materials and Methodology

2.1 Sample Preparation

Powder of pure zinc (98% purity) in the form of spherical particles size 45 μm, pure magnesium (99% purity) in the form of spherical particles size 63 μm, and pure manganese (99% purity) of particle size 45 μm provided by LOBA CHEMIE PVT LTD (INDIA) were used. For the first sample preparation, the zinc was taken as 99 wt% and magnesium as 1 wt% (i.e., Zn–1 Mg). For proper mixing and homogenization of zinc and magnesium, 16 h planetary ball milling process was used. Balls and vessels were clean with acetone to remove any impurities, to prevent oxidation the wet ball milling (toluene) manipulation of Zn–1 Mg was carried out in an inert atmosphere, i.e., argon gas atmosphere was used inside the glove box. Ball milling rotation speed was set at 350 RPM and the ball ratio was taken as 15:1. The process is carried out in 16 cycles each of one-hour cycles with 30 min rest in between each cycle. After ball milling, the powder samples of Zn–1 Mg were dried in a FUME-HOOD machine for 24 h. There were approx. 4 gm of powder wastage in the ball milling process and after 16 h of ball milling the size of powder was reduced to approximately 99% (397 nm) which was measured by the zeta-potential test. The reduced final size of Zn–1 Mg is shown in Fig. 1.

For the second sample, preparation zinc was taken as 98.2 wt%, magnesium at 1 wt%, and manganese at 0.8 wt% (i.e., Zn–1 Mg–0.8Mn). The process parameters were taken the same as that for the first sample preparation, i.e., 16 h ball milling
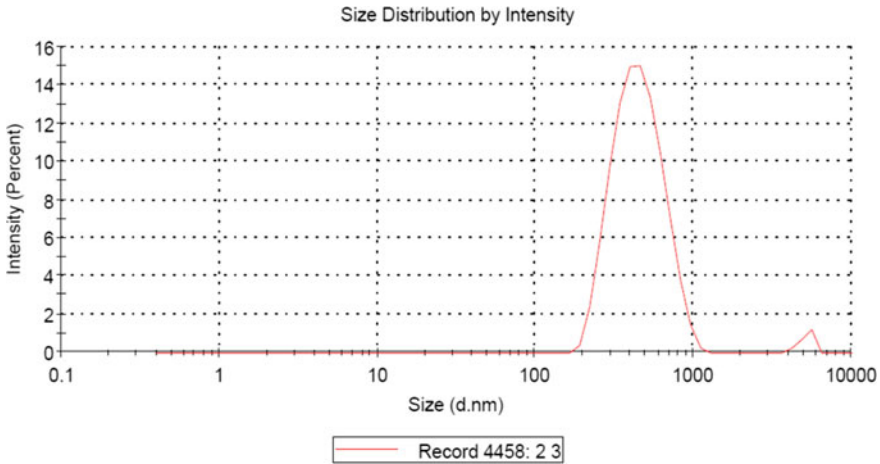
Fig. 1 Size distribution of Zn–1 Mg by Zeta potential test after 16 h ball milling process

at 350 RPM and 15: 1 ball ratio. The second sample (Zn–1 Mg–0.8Mn) wet ball milling with the inert atmosphere in argon gas atmosphere was carried out to prevent oxidation. The reduction in particle size was 99% (i.e., 387.9) after the ball milling process was tested by using the zeta-potential test for the reduced size of Zn–1 Mg–0.8Mn.

Experimental samples were processed on cold compaction manual hydraulic compaction machines. The compaction was carried out in hollow cylindrical steel die with 10 mm die and 70 mm height. Before the die was filled with powder it was cleaned with acetone and then graphite foil was used to prevent adhesion of sample powder on the die surface. Thus the graphite foil at as a barrier between the die surface and sample powder. Cold compaction was done manually on hydraulic compaction at 400 MPa pressure and held at this pressure for five minutes. In this way, we got a cylindrical billet of 30 mm height and 10 mm diameter. For sintering of cold compacted samples were done in a laboratory furnace. The sintering was carried out at 375 °C and held at that temperature for 2 h for uniform heating of the whole sample.

2.2 Density and Porosity Calculation

To calculate the density of the prepared billet samples Archimedes principle was used. According to the Archimedes principle, the volume of the object submerged in water equals the volume of the water displaced; through this concept, we will calculate the volume of the sample. We will first measure the weight of the sample, i.e., $W_1 = 8.6408$ gm for Zn–1 Mg, the initial volume of water $V_1 = 5.1$ ml, and calculated volume by Archimedes principle when the sample was inserted into water

$V_2 = 6.7$ ml. Thus, we calculate the volume of the sample, $v_1 = V_2 - V_1 = 6.7 - 5.1 = 1.6$ ml. Now we calculate the density of the sample, i.e., $\mu = W_1/(V_2 - V_1)$.

$$\mu = 8.6408/1.6 = 5.3775 \, \text{gm/cm}^3. (\text{for Zn} - 1\text{Mg}).$$

In the same way for Zn–1Mg−0.8Mn. $W_2 = 8.8203$ gm, $V_1 = 6$ ml, $V_2 = 7.5$ ml, sample volume $v_2 = 7.5 - 6 = 1.5$ ml.

$$\mu = 8.8203/1.5 = 5.8802 \, \text{gm/cm}^3. (\text{for Zn} - 1\text{Mg} - 0.8 \, \text{Mn}).$$

For porosity calculation, we required the particle size density and bulk density, i.e., density of the sample.

Porosity $=$ (particle density $-$ bulk density)/particle density

Particle density for $\text{Zn} - 1\text{Mg} = 7.07905 \text{gm/cm}^3$ and bulk density $= 5.3775 \, \text{gm/cm}^3$

Porosity$(\text{Zn} - 1\text{Mg}) = (7.07905 - 5.3775)/7.3775 = 0.2403 = 24.03\%$

Porosity$(\text{Zn} - 1\text{Mg} - 0.8 \, \text{Mn}) = (7.08032 - 5.8802)/7.08032 = 16.95\%$

2.3 Micro Hardness

Vickers micro harness HV.1 of Zn–1 Mg and Zn–1 Mg–0.8Mn was measured on cylindrical billet samples. Cross-sectional planes were perpendicular to the extrusion pressure direction. To measure the microhardness UHL VMHT Vickers microhardness testing machine was used and the applied load was only 100 g. Six readings were taken for each sample, i.e., five on the periphery and one at the center, to get an average result.

3 Results and Discussion

Here we use the powder metallurgical process to prepare bioresorbable zinc-based alloy to control the porosity of the prepared samples. Because Osseous tissue, also known as long bone, comprises two distinct components called cancellous and cortical bone. Cancellous is the innermost portion of the bone, spongy and has a volume porosity of 50–90%. Cortical bone is a dense outer layer of bone with less than 10% volume porosity. In this experiment, we try to make Zn–1 Mg (1 wt%) alloy prepared by powder metallurgy process with 24.03% porosity and Zn–1 Mg–0.8Mn alloy have 16.95% porosity. The density and porosity of the sintered zinc-based alloy sample with their alloy composition are shown in graph Fig. 2.
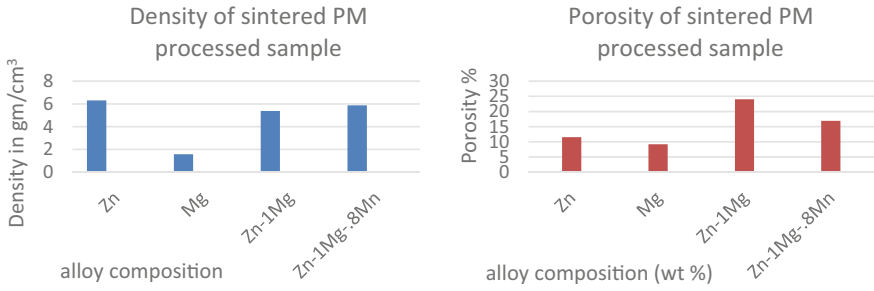
Fig. 2 Density and porosity of sintered PM processed sample with their alloy composition

The microhardness required for a cortical bone varies between 35 and 45 HV. In our experiment, we observed the microhardness value of Zn–1Mg equals 37 HV.1 and 39 HV.1 for Zn–1Mg–0.8Mn which is in the acceptable range required for an orthopedic implant. Also, while conducting the examination on Zn–1Mg–0.8Mn samples it is clearly seen that samples showed poorer corrosion rate and intermolecular bonding between the grains. The Vickers microhardness testing results are shown in Fig. 3.

The compressive strength needed for a cortical bone ranges from 90 to 250 MPa. According to the compressive testing, sintered pure zinc has a compressive strength of 96 MPa, pure magnesium has a compressive strength of 262 MPa, Zn–1 Mg has a compressive strength of 177 MPa, and Zn–1 Mg–0.8Mn has a compressive strength of 205 MPa comparatively lowered due to bonded with. Manganese was found to have the highest compressive strength. The compressive strength of pure zinc and the zinc-based sample is shown below in graph Fig. 4.
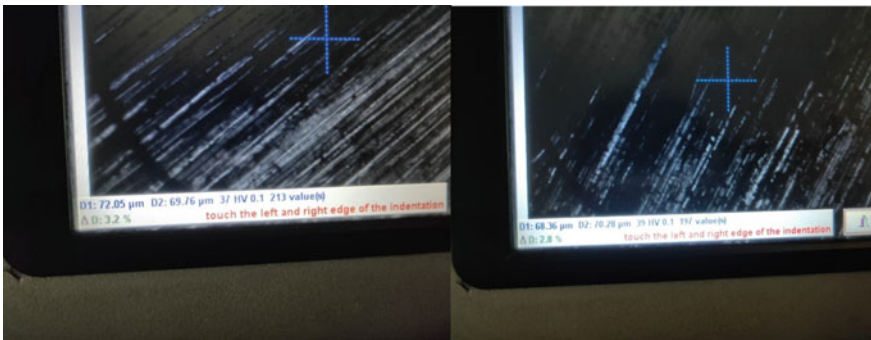
Fig. 3 Vickers microhardness testing result of Zn–1Mg and Zn–1Mg–0.8Mn, respectively
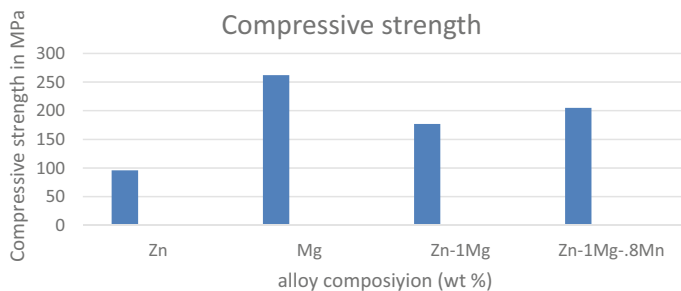
Fig. 4 Compressive strength of sintered zinc-based alloy sample

4   Conclusions

By varying the composition of alloying elements in weight percentages, a powder metallurgy procedure was utilized to manufacture zinc-based alloy samples, and it was concluded that:

- Any materials miscible or immiscible can be used to make composite alloy by using powder metallurgy techniques.
- After 16 h of ball milling, there was a 99% reduction of particle size and increased bonding strength during sintering.
- At reduced particle size, shrinkage volume increase by increasing pressure during compaction.
- After the sintering process component produces from PM routes gain sufficient strength.
- Compressive strength of pure zinc improved to 177 MPa by adding magnesium in 1 wt% composition.
- Enhancement in compressive strength to 205 MPa by adding manganese in zinc magnesium alloy composition.
- The sufficient compressive strength and uniform microhardness throughout the surface of zinc samples as required for cortical bone (35–45 HV) is obtained by alloying process using PM and homogenized sintering.
- MWCNT was successfully deposited on the zinc alloy sample using dip-coating method.

References

1. Abdulghani, S., Mitchell, G.R.: Biomaterials for in situ tissue regeneration: a review. Biomolecules **9**(11), 750 (2019)
2. Bae, B.H., Lee, J.W., Cha, J.M., Kim, I.W., Jung, H.D., Yoon, C.B.: Preliminary characterization of glass/alumina composite using laser powder bed fusion (L-PBF) additive manufacturing. Materials **13**(9), 2156 (2020)

3. Bains, P.S., Sidhu, S.S., Payal, H.S.: Fabrication and machining of metal matrix composites: a review. Mater Manuf Processes **31**(5), 553–573 (2016)

4. Bose, S., Robertson, S.F., Bandyopadhyay, A.: Surface modification of biomaterials and biomedical devices using additive manufacturing. Acta Biomater **66**, 6–22 (2018)

5. Brounstein, Z., Yeager, C.M., Labouriau, A.: Development of antimicrobial PLA composites for fused filament fabrication. Polymers **13**(4), 580 (2021)

6. Charbonnier, B., Hadida, M., Marchat, D.: Additive manufacturing pertaining to bone: hopes, reality and future challenges for clinical applications. Acta Biomater **121**, 1–28 (2021)

7. Chaudhary, M., Jain, T., Jain, J.: Advanced manufacturing techniques and advancements in biodegradable biomaterials. Mater. Today: Proc. (2021)

8. Deckers, J.P., Shahzad, K., Cardon, L., Rombouts, M., Vleugels, J., Kruth, J.P.: Shaping ceramics through indirect selective laser sintering. Rapid Prototyping J. **22**(3), 544–558 (2016)

9. Dosovitskiy, G.A., Karpyuk, P.V., Evdokimov, P.V., Kuznetsova, D.E., Mechinsky, V.A., Borisevich, A.E., Korjik, M. V.: First 3D-printed complex inorganic polycrystalline scintillator. Crystengcomm **19**(30) (2017)

10. Jain, T., Jain, J.K., Saxena, K.K.: Design and comprehensive study of biodegradable Zinc-based implants for bio-medical applications. Adv. Mater. Processing Technol. 1–18 (2021)

11. Ke, D.X., Bose, S.: Effects of pore distribution and chemistry on physical, mechanical, and biological properties of tricalcium phosphate scaffolds by binder-jet 3D printing. Addit Manuf **22**, 111–117 (2018)

12. Kumar, A., Kargozar, S., Baino, F., & Han, S. S.: Additive manufacturing methods for producing hydroxyapatite and hydroxyapatite-based composite scaffolds: a review. Front. Mater. **6** (2019). https://doi.org/10.3389/fmats.2019.00313

13. Lu, J.X., Dong, P., Zhao, Y.T., Zhao, Y., Zeng, Y.: 3D printing of TPMS structural ZnO ceramics with good mechanical properties. Ceram Int **47**(9), 12897–12905 (2021)

14. Parihar, R.S., Setti, S.G., Sahu, R.K.: Effect of sintering parameters on microstructure and mechanical properties of self-lubricating functionally graded cemented tungsten carbide. J Manuf Process **45**, 498–508 (2019)

Radial Slicing Methods for Rotary Substrate Wire Arc Additive Manufacturing

S. Saxena ⓘ**, H. Mishra** ⓘ**, A. U. Khan** ⓘ**, and Y. K. Madhukar** ⓘ

1 Introduction

Additive Manufacturing (AM) is defined as the process of layer-by-layer deposition of material on a set of 3D coordinates which are obtained from a 3D CAD model. There are different types of additive manufacturing processes developed in the last few decades for metals, such as Selective Laser Melting (SLM), Laser Engineered Net Shaping (LENS), Wire Arc Additive Manufacturing (WAAM). WAAM is based on an arc welding process that uses an electric arc to melt a metal wire and successful deposition of it on a substrate using a computer numerical control (CNC) workstation. The WAAM possesses many advantages in comparison with other metal-based AM processes, it includes ease of handling, higher catchment efficiency, higher deposition rate, and cost-effectiveness [2]. It makes this process applicable for the fabrication of large-scale metal parts with different geometries, an ideal choice for repair and maintenance operations. The reported material utilization in WAAM is about 90% and above [3]. However, the process suffers from a few challenges such as large heat accumulation due to a bigger melt pool which leads to thermal distortion and formation of residual stress. These are caused due to shrinkage and variation in cooling rates depending on the geometry [3]. The process parameters in the deposition process also pose challenges to surface quality, mechanical properties, controllability, and repeatability.

The AM process follows the path of the deposition generated using the 3D CAD model. Slicing of the CAD model is the process of splitting the model into a number

S. Saxena (✉) · H. Mishra · A. U. Khan · Y. K. Madhukar
Department of Mechanical Engineering, Indian Institute of Technology, Indore 452 020, India
e-mail: sajalsaxena09@gmail.com

A. U. Khan
e-mail: phd1801103005@iiti.ac.in

Y. K. Madhukar
e-mail: yuvrajmadhukar@iiti.ac.in

of layers. It determines the plane of the deposition and hence the toolpath/path planning. Therefore, path planning is an essential part of the process in order to enhance the geometrical accuracy of the process. In the case of WAAM, this path planning plays an important role in order to enhance accuracy and also minimize the use of support structures. Commercially available slicing platforms slice the CAD model horizontally along a particular axis only in the frame of reference. Though it serves the purpose to a great extent, the direction of the slicing may need to be changed depending on the complexity of part geometries in order to minimize the overhang deposition. Zhao et al. [4] proposed a radial slicing strategy for curved parts to print a fan made out of PLA using FDM. Radial slicing strategy for curved parts reduces the use of the support structures which are generally needed for overhanging parts. Their work used a decomposition-based slicing method in which a STEP (Standard for the Exchange of Product data) file of the fan model is cut into decomposed volumes in CATIAV5 to extract offset surfaces to generate five-axis toolpaths. MATLAB has also been utilized for radial slicing based on ray triangle intersections to generate five-axis toolpaths [5]. These techniques use five-axis control for toolpath generation and deposition, which come along with complicated machine dynamics for additive manufacturing. The presented experimental work proposes three different methods for WAAM using two linear axes and one rotatory axis, where two were based on volume decomposition implemented in SolidWorks, and one based on surface intersection implemented in MATLAB, for slicing the CAD model to keep the deposition head and deposition plane always perpendicular to each other. It would eliminate the use of the support structure for the deposition of the overhangs. The generated code has been used for the demonstration of deposition of the three-blade fixed-pitch ship propeller.

2   Experimental Details

The in-house developed WAAM setup was used for conducting the experiments. It consists of Gas Metal Arc Welding (GMAW) based WAAM integrated with a 4-axis CNC control system [1]. It consists of three linear axes (XYZ) and a rotating A-axis, Fig. 1. A GMAW welding power source (model: KEMPPI Fast MiG Pulse 450) was utilized as a deposition method with argon as the shielding gas. A Mach3 Control Board integrated with Mach3 CNC software was used for controlling the CNC setup. This platform typically takes 'G' and 'M' codes for the control.

The CAD model utilized for this study was a scaled version of a commercially available three-blade fixed-pitch propeller of diameter 144 mm. A hollow shaft, of outer diameter 25 mm and wall thickness 4 mm, was used for the deposition of three blades (Fig. 2). This shaft resembles the hub shaft of the propeller.

Three radial slicing methods were adopted for the slicing of all three blades. The primary objective was to generate the CNC readable 'G' and 'M' codes according to the radial slicing coordinates. The two methods developed in SolidWorks radially divide the model into smaller volumes and obtain radial coordinates by tracing the
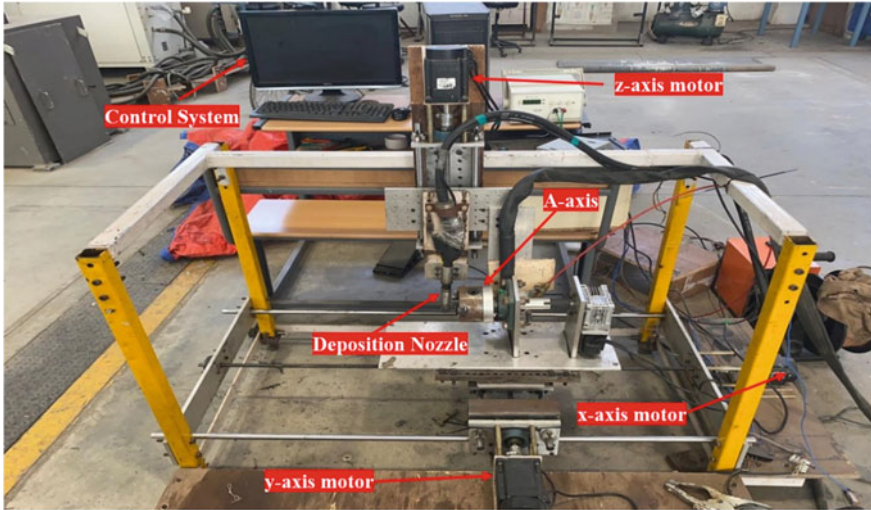
Fig. 1 Experimental setup
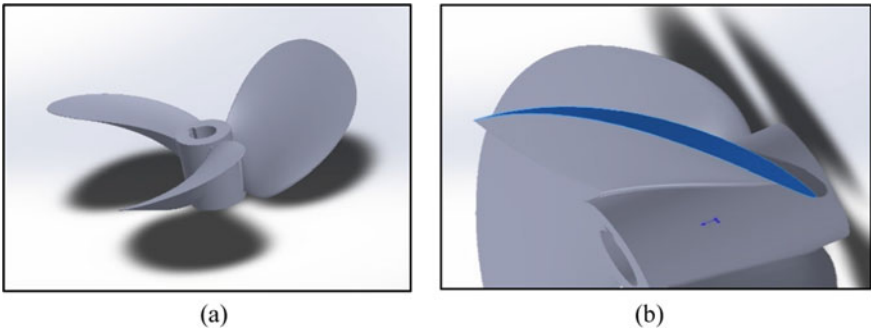
Fig. 2 a Fixed pitch propeller blade, **b** Radial cross-section of blade

contour line of the cross-section of each division. The method developed in MATLAB was based on finding intersection points between the STL model of the propeller blade and a set of cylindrical surfaces offset to each other.

3   Result and Discussion

3.1   Path Planning for the Deposition

The process of path planning consists of the selection of appropriate orientation of the part to minimize the overhang and accordingly slice the CAD model, i.e., obtaining coordinate points for each depositing layer in 3D space. These coordinate points were used further to generate the G-codes which were eventually responsible for providing the motion to the individual axes. The motion is in accordance with the building strategy used for the deposition including contour line deposition and contour area infill.

Slicing Using Solid Works. Two methods were developed using SolidWorks for the slicing which differed in the way they generated the coordinates representing the path planning.

Method 1. (a) Radial slicing: The propeller was radially sliced using cylindrical surfaces of different radii, offset to each other by the layer height of deposition. The sliced parts are saved as different part files which can be used for further processing (Fig. 3). (b) Tracing the boundary layer: In SolidWorks, plane boundaries could be traced only in 2D space, while the coordinates for the slicing were in 3D space. Therefore, the layer boundaries for each layer were obtained in two different planes (x–y and x–z). The boundary points were traced in the x–y plane first. A line was drawn from one endpoint of the layer in the vertical y-direction, then multiple parallel lines were drawn parallel to this line with a 1 mm offset till the other endpoint of the layer (Fig. 4). 2D (x–y) coordinates of the intersection between layer and lines were saved as an Initial Graphics Exchange Specification (IGES) file format in SolidWorks. A similar process was repeated for the x–z plane, as shown in Fig. 5. These x–z-coordinates need to be saved in a different IGES file. (c) Preprocessing and generating coordinates*: Both the obtained IGES files were converted into the text files and after preprocessing of the data, an independent excel file was generated containing the 3D Cartesian coordinates from slicing.

Method 2. (a) Radial slicing: The propeller was first sliced using cylindrical surfaces of different radii as similar to the *Method 1*. However, in this method the sliced surfaces were again sliced using a plane that passes from the center along the y–z plane. The cut parts were saved as different part files as shown in Fig. 6.

(b) Converting radial layer to planar layer: The radial layers were flattened from the sliced edge (Fig. 7). (c) Tracing the boundary layer: The tracing of the boundary layer was similar to the previous method. However, it was needed to be performed for the x–y plane only (Fig. 8). (d) Preprocessing and generating coordinates*: The obtained IGES file was used to generate the x–y coordinates.

Slicing Using MATLAB. The MATLAB program automates the radial slicing process which consists of four steps as follows: (a) Import an STL mesh: Importing
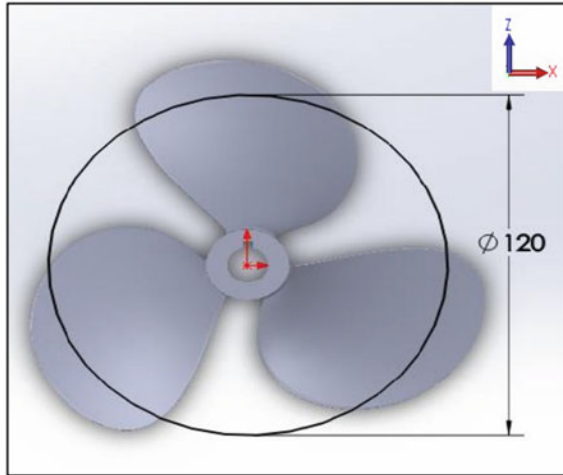
Fig. 3. Slicing for method 1
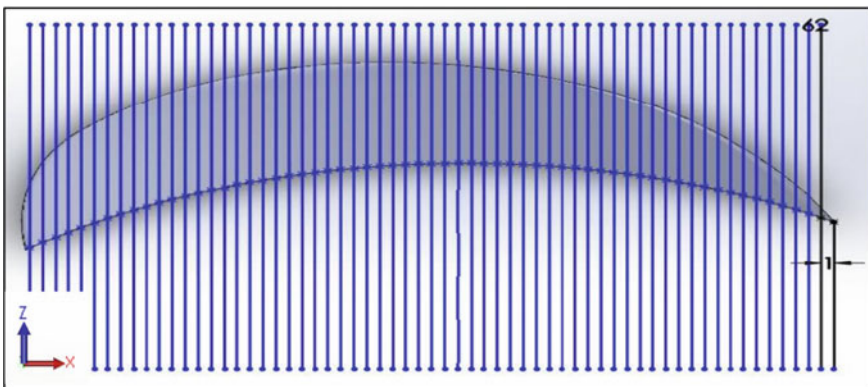
Fig. 4. Layer tracing in x-z plane

an STL file of the propeller model to return a face-vertex structure, i.e., triangulation of the STL file (Fig. 9).

(b) Generation of cylindrical surfaces: A set of N cylinders were created and triangulated to obtain a triangular mesh of cylindrical surfaces. N is calculated using the starting radius r_i, defined as the outer radius of the propeller hub, the end radius r_e, defined as the blade radius measured from the center of the hub, and the layer height h for the process as (Fig. 10):

$$N = (r_e - r_i)/h \tag{1}$$
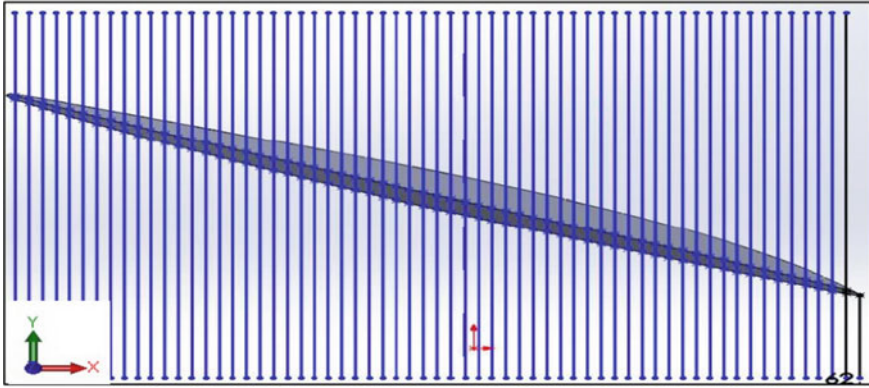
Fig. 5. Layer tracing in x-y plane
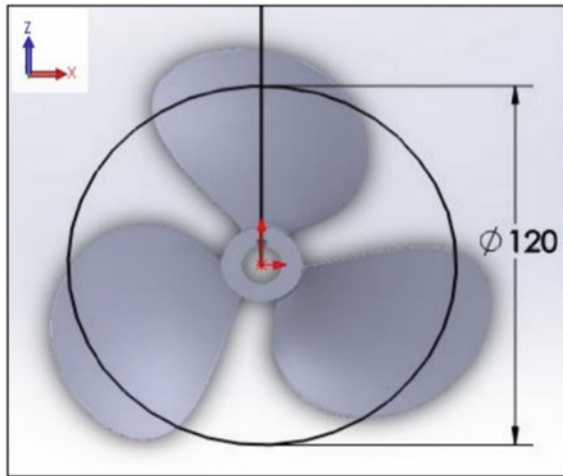
Fig. 6. Slicing for method 2
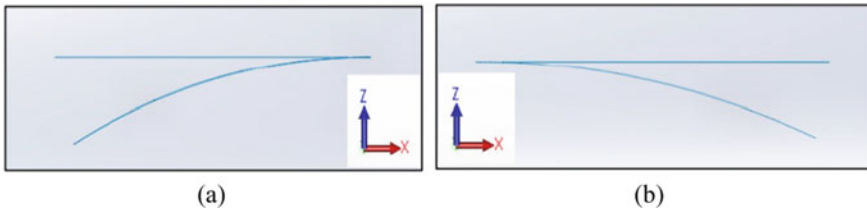
Fig. 7 **a** Flattened layer's left part, **b** Flattened layer's right part
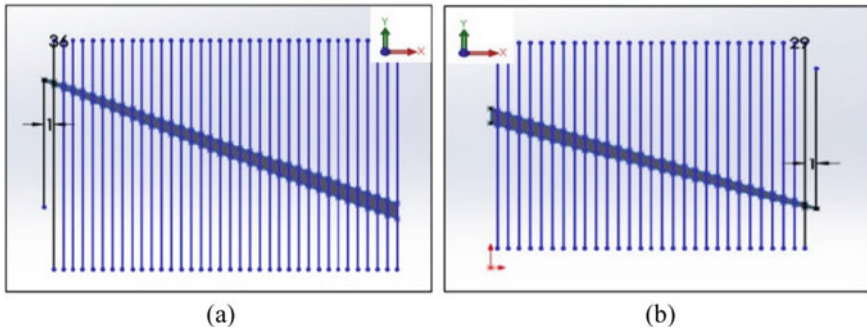
Fig. 8. a Layer tracing in *x*–*y* plane for left part, **b** Layer tracing in *x*–*y* plane for right part
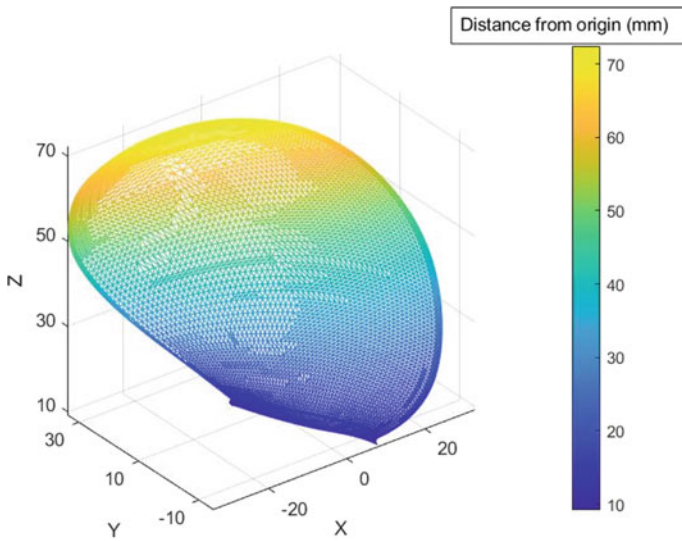
Fig. 9 Triangulated mesh from STL file of blade

(c) Find intersection with model: Intersection surface of each cylinder mesh with the blade mesh is found using a surface intersection function [6] based on the triangle/triangle intersection algorithm proposed by Tomas Möller (1997). Boundary points of the blade for intersection with each cylinder were obtained in this step (Fig. 11).

(e) Sorting the coordinates: Coordinates of each layer are sorted to control the torch motion starting from the leading edge to the trailing edge back to the leading edge of the aerofoil. The path was changed for every alternative layer; starting from the trailing edge to the leading edge back to the trailing edge.
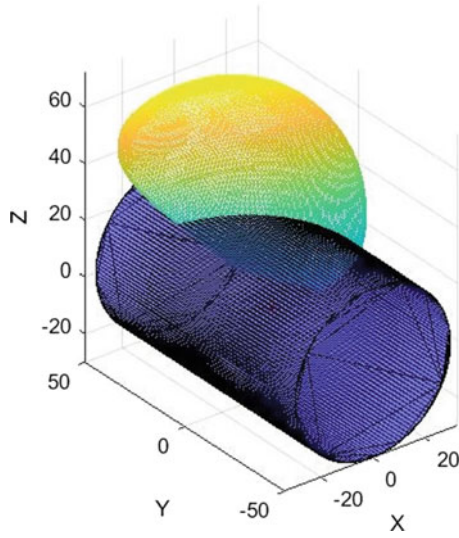
Fig. 10 Isometric view of the intersection of a single-cylinder with propeller blade (all dimensions are in mm)
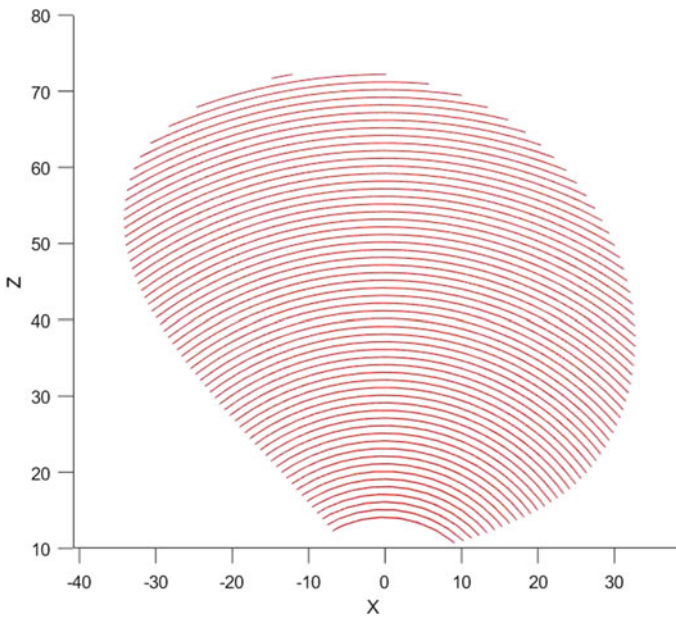
Fig. 11. Side view of sliced layers (all dimensions are in mm)

3.2 Validation of Code

STereoLithography (STL) file format has many disadvantages since it is only an approximation of the surface of the 3D model. An STL file is made of vertices of triangles that make up the surface of the 3D model, this causes issues like inaccuracy, redundancy of points, etc. Thus, it is important to validate the accuracy of the MATLAB program which uses the STL file format for slicing and generating data points. This was done by matching contour obtained from the radial slicing methods used in SolidWorks since it performs slicing on high fidelity files such as STEP and IGES, without converting to a mesh model. Sliced layers obtained from these methods are thus more accurate. From Fig. 12, it can be seen that the data points obtained from SolidWorks match well with the contour formed by the data points obtained from the MATLAB program.

To find the difference between the contour formed by MATLAB points and Solid-Works points, an image processing library *image compare* in Python was utilized [7].

The coordinates were compared in 2D planes–x–y and x–z (Fig. 13), and the resultant mismatch was found to be 0.1% and 0.06%, respectively, in the two planes, which are significantly low and thus, the slicing method based on MATLAB is validated.
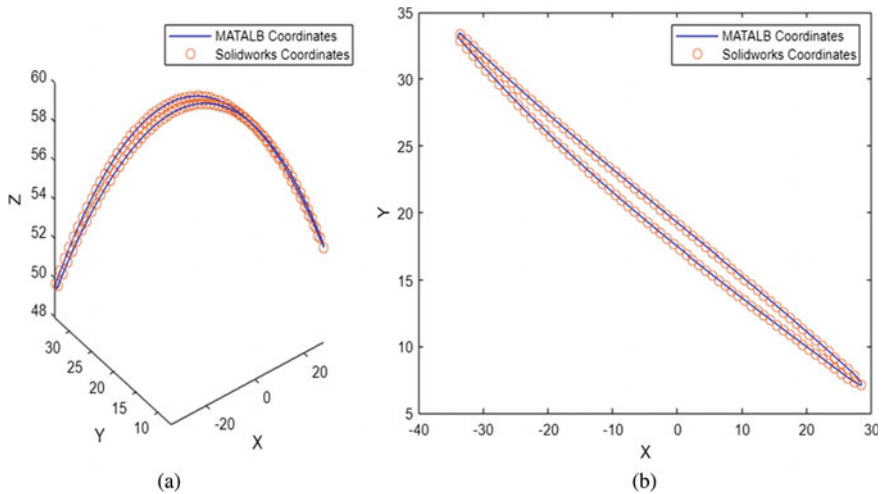
Fig. 12 **a** Isometric view of layer, **b** Top view of layer (all dimensions are in mm)
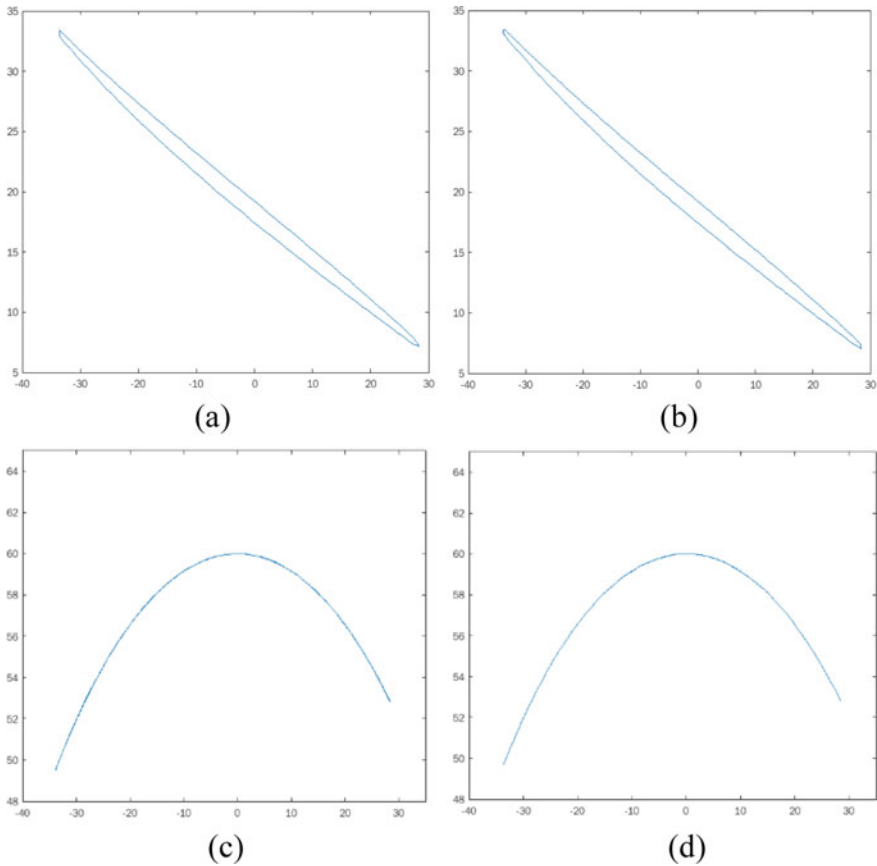
Fig. 13. a Contour formed by MATLAB points in the *x–y* plane, **b** Contour formed by SolidWorks points in the *x–y* plane, **c** Contour formed by MATLAB points in the *x–z* plane, **d** Contour formed by SolidWorks points in the *x–z* plane (all dimensions are in mm)

3.3 Part Deposition

A mild steel rod of a diameter of 25 mm was used as the substrate for part deposition. The substrate was selected to act as the propeller hub, as it is a common strategy to reduce post-processing time. The part was a Wageningen B series propeller whose deposition path was obtained from the radial slicing method in the form of *G*-codes. The *x*-, *y*-, and *z*-coordinates obtained from slicing were converted to polar coordinates to control the linear and rotational motion of the substrate. The linear motion of the substrate was controlled using *x*-coordinates, whereas the rotation was given using *y*- and *z*-coordinates. The GMAW torch motion in G-code was given in the z-axis by the average layer height for deposition. An operating range [8] was found out for stable and uniform deposition based on which the input parameters were chosen.

Table 1 Operation parameters for WAAM of propeller blades

Input parameters	Parameter value
Input voltage	19 V
Wire feed rate	3.5 m/min
Torch speed	300 mm/min
Shielding gas flow rate	10 L/min

The input parameters for deposition can be found in Table 1. The average height for each layer was measured as 1.2 mm, which was also incorporated in G-codes as layer height. It is usually observed in WAAM that the same start and endpoint for every layer may lead to dimensional inaccuracy in the form of non-uniform height. To avoid this limitation, the start point for deposition was changed between the two ends of a blade aerofoil for alternate layers.

The infill was not used in this deposition due to a small cross-section of blade/aerofoil. However, depending on the size of the model, a suitable infill strategy could be adopted to provide the necessary strength. All three blades were simultaneously deposited to avoid any thermal distortion and avoid collision of the torch with deposited blades. A total of 50 layers were deposited for each blade and the material of the wire used in the GMAW process was mild steel (ER70S) with a diameter of 0.8 mm. Also, an idle time of two minutes was provided between each layer for appropriate cooling. The final deposited propeller is shown in Fig. 14. The average propeller diameter obtained was ~144.1 mm and the design model had a diameter of 146 mm.

Fig. 14 Additive manufactured fixed-pitch ship propeller

4 Conclusions

This paper develops three methods for radial slicing using SolidWorks and MATLAB. In SolidWorks, the CAD model is sliced using a volume decomposition-based method, and coordinates for layer contour are obtained by tracing boundaries. The MATLAB script automates the slicing process to find the contour coordinates based on the intersection boundary of the STL model with triangulated cylindrical surfaces using a surface intersection algorithm. The slicing points obtained through the STL file are validated using a more reliable analytical model file type STEP.

The methods generate toolpath for three-axis Wire Arc Additive Manufacturing to keep the deposition tool normal to the deposition plane. The application of the methods was successfully demonstrated by manufacturing the prototype of a commercially available ship propeller using a Wire Arc Additive Manufacturing setup.

References

1. Patil, A., Lodhi, U.K., Madhukar, Y.K.: Design and development of wire arc additive manufacturing setup for fabrication of complex parts. Discipline Mech. Eng. IIT Indore (2019)
2. Cunningham, C.R., Flynn, J.M., Shokrani, A., Dhokia, V., Newman, S.T.: Invited review article: Strategies and processes for high quality wire arc additive manufacturing. Add. Manuf. **22**, 672–686 (2018)
3. Busachi, A., Erkoyuncu, J., Colegrove, P., Martina, F., Ding, J.: Designing a WAAM based manufacturing system for defence applications. Procedia Cirp **37**, 48–53 (2015)
4. Zhao, G., Ma, G., Feng, J., Xiao, W.: Nonplanar slicing and path generation methods for robotic additive manufacturing. Int. J. Adv. Manufact. Technol. **96**(9), 3149–3159 (2018)
5. Munasinghe, N., Paul, G.: Radial slicing for helical-shaped advanced manufacturing applications. Int J Adv Manuf Technol **112**(3), 1089–1100 (2021)
6. Tuszynski, J.: Surface intersection. MATLAB central file exchange, https://www.mathworks.com/matlabcentral/fileexchange/48613-surface-intersection, Last accessed 03 July 2021
7. Github: https://github.com/datenhahn/imgcompare. Last accessed 17 Oct 2021
8. Dahat, S., Hurtig, K., Andersson, J., Scotti, A.: A methodology to parameterize wire+ arc additive manufacturing: a case study for wall quality analysis. J. Manuf. Mater. Process. **4**(1), 14 (2020)

Topology Optimization as an Enabler of Additive Manufacturing: A Case Study

D. Praneashram ⓘ**, T. S. Balakrishna** ⓘ**, and S. Vinodh** ⓘ

1 Introduction

In the current state, applications of 3D printing have evolved from making prototypes to manufacturing spare parts and being used in small and medium scale manufacturing. Specifically, early adopters of this technology are the defense, medical, and aerospace industries which make high complex (or) high value/low volume products. For example, NASA operates a 3D printer in space to evaluate parts production where spare parts cannot be inventoried.

In subtractive manufacturing (SM), there is a tremendous increase in manufacturing cost and complexity in designs due to complicated tooling. In additive manufacturing (AM), the complicated designs cost the same as simplistic designs (assuming the same volume and material for both the components).

1.1 Topology Optimization

Topology optimization (TO) is a mathematical approach for optimizing material arrangement inside a given design space for particular load sets and boundary conditions so that the final layout achieves the desired performance goals. Through topology optimization, engineers can determine the optimal design that satisfies design requirements [1]. [2] and [3] provided the groundwork for today's topology optimization methods by establishing the notion of shape and topology optimization based on homogenization and density-based topology optimization, respectively. In most cases, the primary goal would be to reduce the mass of the component [4].

D. Praneashram (✉) · T. S. Balakrishna · S. Vinodh

Department of Production Engineering, National Institute of Technology, Tiruchirappalli 620015, India

e-mail: praneashram@gmail.com

For a long time, the manufacturability of topologically optimal structures has been questioned. In the early stages, applications of topology optimization were limited due to various manufacturing constraints [5] by conventional manufacturing techniques. The complexity of creating high-performance topologically optimized structures has also accelerated the development of additive manufacturing techniques [6]. With such a development, topology optimization has gained more importance due to AM's large design freedom and limited manufacturing constraints [7].

1.2 Literature Review

A comprehensive literature review is performed to review the studies performed on topology optimization for additive manufacturing. Tomlin and Jonathan [8] optimized a nacelle hinge bracket from Airbus A320 using Altair Optistruct. The bracket was made from Ti–6Al–4V. The loading conditions for the component were derived, optimization of the design was performed in two cycles, and a 64 percent weight reduction was achieved. The maximum stress in the component was also reduced by around 50 percent. Sudin [9] redesigned the brake pedal using topology optimization. The brake pedal was designed using CATIA V5 and optimized using Altair Optistruct software under linear static stress analysis. After optimization, there was a reduction of weight by 22%, and the factor of safety (FOS) decreased by 15.78%. Even though there was a decrease in the factor of safety, the study was considered successful since the factor of safety of the optimized model was under the permissible limits. Zhu et al. [5] gave an overview of various topology optimization methods such as Solid Isotropic Material with Penalty (SIMP) and Evolutionary Structural Optimization (ESO). The literature further explained various present topology optimization cases in aircraft and aerospace structures design and potential future applications. The study also focused on how additive manufacturing benefits topology optimization and increases design flexibility. Thompson et al. [7] provided an overview of macrostructure topology optimization. They pointed out that weight reduction can result in significant energy savings during a product's usable life, especially in the aerospace and automobile sectors.

Siva Rama Krishna et al. [10] optimized simply supported beam with mid-point loading using SIMP approach. Two approaches are followed where the first one considers the complete beam as the design area, whereas in the second approach, the elements in the boundary are excluded for optimization. After performing topology optimization, the beam is additively manufactured using the fused deposition modeling (FDM) technique. Liu and Shin [11] provided an overview of fabricating components manufactured by AM of Ti-6Al-4 V alloy. Mechanical properties of Ti-6Al-4 V such as tensile property and fatigue property were discussed, and advantages of producing it through AM instead of traditional techniques were highlighted. Tyflopoulos et al. [12] considered titanium and its alloys for the optimization process due to its high yield strength and conducted a case study on optimizing the brake caliper of a student race car. The classic compliance topology optimization

with SIMP as an interpolation approach was employed in this work, and optimization was conducted on ABAQUS CAE with the TOSCA optimization module. 41.6% weight reduction was achieved, and the maximum y-direction displacements of the calipers were also reduced by 50% and 17.5% for the front and rear calipers, respectively. Aliyi and Lemu [13] provided an overview of the formulation of topology optimized design. The case study involved performing topology optimization on a triangular bracket using ANSYS Workbench. The optimized bracket had a weight reduction of 72.86%. Moreover, by applying topology optimization, the factor of safety of the bracket increased from 1.11 to 2.17. Tanishk and Prithvi Reddy [14] performed a case study of topology optimization in a unidirectional helical gear using ANSYS Workbench. Defining exclusion regions and optimization parameters were explained thoroughly. The literature also contained the procedure for performing design and validation of the optimized component. The optimized component had a weight reduction of 23.75%, but its factor of safety decreased from 1.584 to 1.4262.

1.3 Problem Statement

From the literature review, the problem statement has been derived. The objective of the study is to perform topology optimization, to optimize a helical gear made of Ti–6Al–4V alloy, which can be manufactured by additive manufacturing processes like selective laser melting (SLM). The result is expected to lead to a design that is reduced by weight and enhanced mechanical properties compared to the previous studies.

1.4 Applications

Helical gear finds many applications in the real world. Helical gears can carry more load than a spur gear of the same size, and hence, helical gears are generally preferred for the transmission of heavy load applications. There is less wear and tear experienced by a helical gear when compared to spur gear of the same size and hence lasts longer.

The gears designed using Ti–6Al–4V alloy find multiple applications in the automotive industry, especially in drive trains [15]. A drivetrain is a system of components present in a motor vehicle that delivers power to the wheels for motion. It contains many components such as transmission, differential, and axles. The transmission in an automobile generally consists of a gearbox, which contains gears and gear trains. Helical gears can be used for power transmission in the gearbox. Reducing the mass of helical gears through topology optimization minimizes the fuel consumed compared to a typical helical gear. Further, it also enhances the gear's mechanical properties, which enables it to bear more load than it earlier could.

Section 2 presents methodological steps. Section 3 presents the case study and implementation of topology optimization for the case product, and the results and improvements are discussed. Section 4 presents the conclusions drawn from this study.

2   Research Methodology

The research methodology employed in this study is shown in Fig. 1:

The scientific articles that focused on topology optimization and additive manufacturing, and related case studies and their applications were considered in the scope

Fig. 1 Methodological steps

of the literature review. Google Scholar and Scopus databases were used to find the relevant research studies. A keyword search was employed, and keywords like "Additive Manufacturing", "Topology Optimization", "Case study", and "Aerospace", etc., were employed to identify the relevant articles.

The abstracts of the retrieved papers were examined to see whether the articles collected might be used in the study. Furthermore, the content of the selected publications is examined to ensure that they are consistent with our study. Helical gear, a common component used in the automobile and aerospace industries, is decided to be taken for this study. The gear is designed using SolidWorks and then imported to ANSYS. The material used for this study is Ti–6Al–V, whose properties are detailed in Sect. 4. Then, FEM analysis is performed to analyze existing stress and strain values.

Then topology optimization is performed, and material is removed from the areas that have the least stress. SIMP technique was used in the research methodology to conduct topology optimization. The material distribution through parameterization of the design domain was proposed by Bendsoe and Sigmund [16] around the 1990s. The SIMP approach, commonly known as the density method, employs a fixed finite element discretization [10].

The optimized model is then redesigned to ease manufacturability by smoothening the curves, standardizing the complicated shapes, etc., and FEM analysis is performed with the modified model. The pre-optimized and post-optimized stresses and displacement values are compared, and the results are then discussed.

3   Case Study

Topology optimization is performed on a helical gear using ANSYS Workbench 2021 academic version. ANSYS topology optimization tool eliminates elements where the stress levels are much lower than the permissible stress limits. If the factor of safety (FoS) falls below the minimum value, these elements are re-added to the model. This is the general working method in which topology optimization is performed using ANSYS Workbench.

The material used for the gear is Ti–6Al–V. It is a titanium alloy recognized for its high strength, low density, excellent corrosion resistance, high fracture toughness, and exceptional biocompatibility [11]. It was developed in the 1950s and is mainly used in aircraft structural applications. Due to its excellent mechanical properties, it finds applications such as aerospace, automobile, energy, marine, biomedical, chemical and marine industries. The properties of Ti–6Al–V are listed in Table 1.

Manufacturing Ti–6Al–V is challenging as it has poor thermal conductivity, is prone to strain hardening, and has ready chemical activity with oxygen. Conventional manufacturing of Ti–6Al–V using rolling, forging, and casting processes results in high manufacturing costs and large material waste. Additive manufacturing is a method that can be employed to overcome these difficulties. Using AM technologies,

Table 1 Ti–6Al–4V
properties

S. No	Property	Magnitude
1	Density, kg/m^3	4400
2	Young's modulus, GPa	107
3	Poisson ratio	0.323
4	Tensile yield strength, GPa	1.098
5	Ultimate tensile strength, GPa	1.15

near-net-shape structures could be produced directly from CAD models with minimal post-processing. Ti–6Al–4V can be produced using different AM processes such as DED, EBM, and SLM processes.

Helical gear (see Fig. 2) is designed using SolidWorks 2020 and is imported into ANSYS Workbench 2021 R1 as IGES file to perform static structural analysis and topology optimization. The material for the geometry is defined with isotropic elasticity and is also considered to be completely homogeneous. The helical gear designed has an outer radius of 77.5 mm and a thickness of 20 mm. It contains a keyhole with a radius of 22.5 mm and a helix angle of 15 degrees. The number of gear teeth = 80.

A tetra mesh is generated in ANSYS, with a resolution of 7, which is the maximum permissible value. 101,654 nodes and 57,881 elements are generated from the tetra mesh and are shown in Fig. 3.

Static structural analysis is performed on the gear. A remote force of 10,000 N is applied on one of the gear teeth and assigns fixed support to the shaft hole and keyways of the gear.

The optimization region is shown in Fig. 4. The region marked in red shows the exclusion region, and the region marked in blue shows the design region. Mass retention of 40% is kept, and the manufacturing constraint is assigned to have six and twelve sectors to obtain two different solutions. The edges produced using topology optimization are very rough, so the geometry has been remodeled using SolidWorks 2020. The optimized design for the six-sector (Fig. 5i) and twelve-sector model (Fig. 5ii) is shown below.

Fig. 2 Helical gear
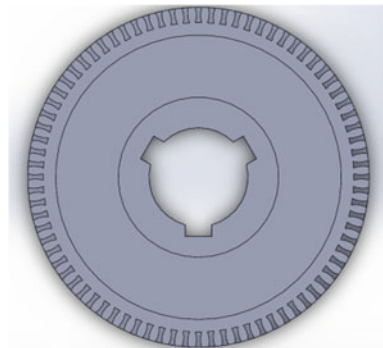
Fig. 3 Meshed finite element model of gear
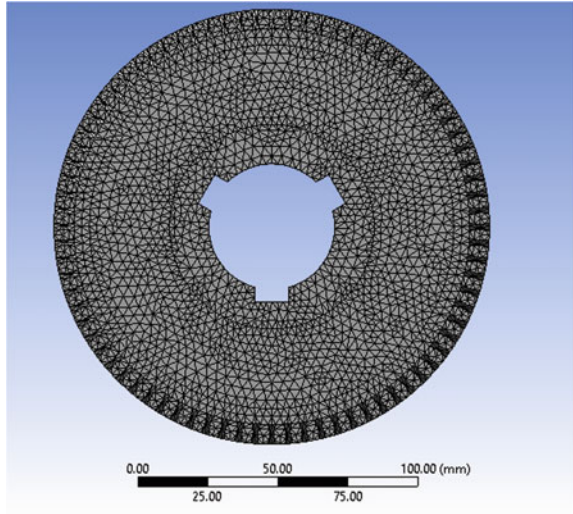
Fig. 4 Optimization region
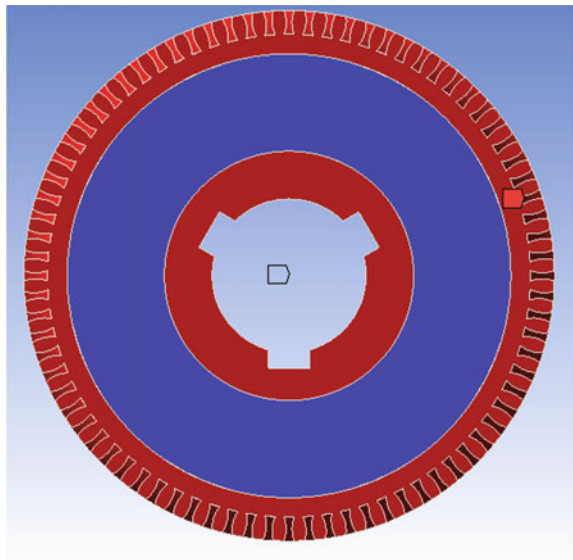
After the model is designed, it is necessary to perform design validation by applying the same parameters which were applied to the pre-optimized gear. Their factor of safety is to be checked for both equivalent stress and shear stress to make sure that the gear does not fail. A factor of safety of 3.0199 (Fig. 6i) is obtained in equivalent stress (maximum stress of 363.59 MPa) and a factor of safety of 2.6865 for shear stress (maximum stress of 204.36 MPa) for the six-sector model, whereas a factor of safety of 2.5373 (Fig. 6ii) is obtained in equivalent stress (maximum stress
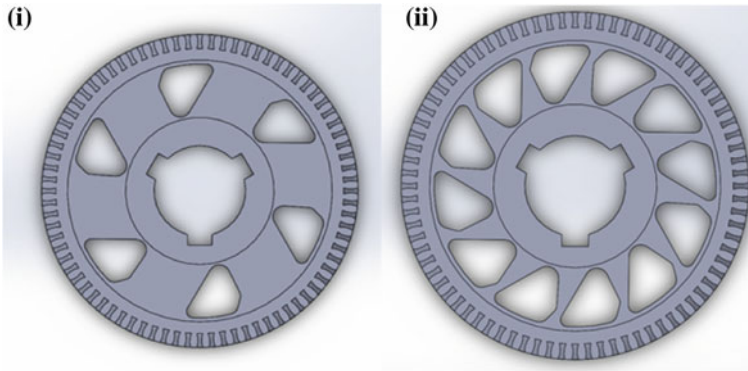
Fig. 5 i Case 1: Six-sector gear **ii** Case 2: Twelve-sector gear
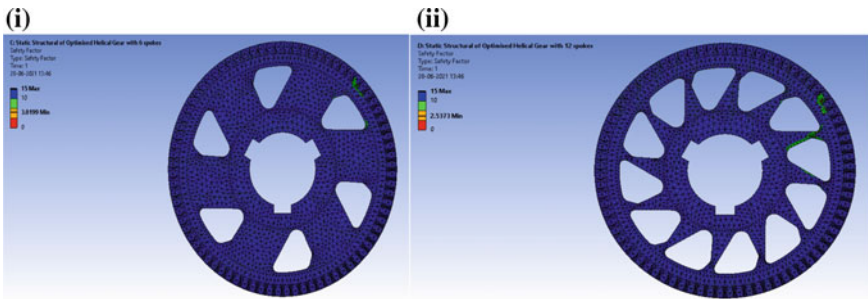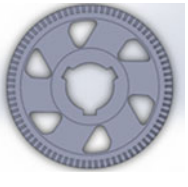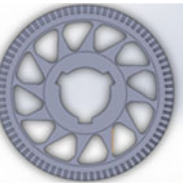
Fig. 6 i Factor of safety for Case 1 **ii** Factor of safety for Case 2

of 432.74 MPa) and a factor of safety of 2.3429 for shear stress (maximum stress of 234.33 MPa) in the twelve-sector model.

Then, the modal analysis is performed on the two models so that their natural frequencies can be calculated to identify which frequencies are risky and destructive to the structures. After performing modal analysis, the first natural frequency of the six-sector model is obtained to be 2642.7 and 2110.2 Hz for the twelve-sector model. Maximum deformation is obtained in the range of 85 mm to ensure that the gear does not operate in this frequency as it is highly critical and will damage the surrounding components (Table 2).

In the study performed by Tanishk and Prithvi Reddy [14] on a helical gear, the resultant model after topology optimization contained 12 spokes. Further, the optimized design in that study reduced mass by 23.75%. On the other hand, factor of safety is reduced by 9.94%. Therefore, in the present study, emphasis was made on optimizing the gear by reducing the mass as well as leading to better factor of safety. Trial and error method was adopted by varying parameters of the topology optimization tool in ANSYS 2020. The gear containing six spokes were obtained and found to improve its factor of safety by 6.90% with a weight reduction of 12.20%.

Table 2 Comparison of results

Results	Pre-optimized gear	Optimized gear with six spokes	Optimized gear with twelve spokes
Design			
Mass (kg)	1.0072	0.88435	0.75355
Max. equivalent stress (MPa)	388.69	363.59	432.74
Factor of safety (equivalent stress)	2.8249	3.0199	2.5373
Max. shear stress (MPa)	214.29	204.36	234.33
Factor of safety (shear stress)	2.5619	2.6865	2.3429
First natural frequency (Hz)	3131.6	2642.7	2110.2

Further, the gear with twelve spokes was also designed to validate the results of the aforementioned study. Both the results were coherent for the twelve spoke gear as it led to a similar percentage of decrease in weight and factor of safety.

4 Conclusion

In line with the industrial developments for generating lightweight structures, topology optimization enables the attainment of the same. This paper presented a case on enabling topology optimization for additive manufacturing. Topology optimization was performed on a helical gear by applying worst-case loading and assigning relevant response and manufacturing constraints.

- The original design of the helical gear has a mass of 1.0072 kg, maximum equivalent stress of 388.69 MPa (factor of safety 2.8249), and a first natural frequency of 3131.6 Hz.
- Case 1: Helical gear with six sectors: The optimized design of helical gear has a mass of 0.88435 kg (weight reduction of 12.2%), maximum equivalent stress of 363.59 MPa (factor of safety 3.0199), which is an increase of factor of safety by 6.90%, and first natural frequency of 2642.7 Hz (reduced by 15.61%).

- Case 2: Helical gear with twelve sectors: The optimized design has a mass of 0.75355 kg (weight reduction of 25.18%), maximum equivalent stress of 432.74 (factor of safety 2.5373), which is a decrease of factor of safety by 10.18%, and first natural frequency of 2110.2 Hz (reduced by 32.62%).

From the two designs, it can be concluded that Case 2 could be used in situations where reducing mass is an absolute necessity. In contrast, Case 1 could be used in situations where increasing factor of safety is a priority. The validation will be done by fabricating the helical gear with Ti–6Al–4V in the future regarding practical application.

References

1. Krog, L., Tucker, A., Rollema, G.: Application of topology, sizing and shape optimization methods to optimal design of aircraft components (2011)
2. Bendsoe, M.P., Kikuchi, N.: Generating optimal topologies in structural design using a homogenization method. Comput Methods Appl Mech Eng **71**, 197–224 (1988)
3. Sigmund, O.: A 99 line topology optimization code written in Matlab. Struct. Multi. Optimization **21**, 120–127 (2001)
4. Kolatsis, N.: Topology optimization for additive manufacturing (2020)
5. Zhu, J.H., Zhang, W.H., Xia, L.: Topology optimization in aircraft and aerospace structures design. Architect. Comput. Methods Eng. **23**, 595–622 (2016)
6. Meng, L., Zhang, W., Quan, D., Shi, G., Tang, L., Hou, Y., Breitkopf, P., Zhu, J., Gao, T.: From topology optimization design to additive manufacturing: today's success and tomorrow's roadmap. Arch. Comput. Methods Eng. **27**, 805–830 (2020)
7. Thompson, M.K., Moroni, G., Vaneker, T., Fadel, G., Campbell, R.I., Gibson, I., Bernard, A., Schulz, J., Graf, P., Ahuja, B., Martina, F.: Design for additive manufacturing: trends, opportunities, considerations, and constraints. CIRP Ann Manuf Technol **65**(2), 737–760 (2016)
8. Tomlin, M., Jonathan, M.: Topology optimization of an additive layer manufactured (ALM) aerospace part. In: Proceeding of the 7th Altair CAE Technology Conference, pp. 1–9 (2011)
9. Sudin, M.N.: Topology optimization in automotive brake pedal redesign. Int. J. Eng. Technol. (IJET) **6**(2), 398–402 (2014)
10. Siva Rama Krishna, L., Mahesh, N., Sateesh, N.: Topology optimization using solid isotropic material with penalization technique for additive manufacturing. Mater. Today Proc. ICMPC 2016 **4**(2A), 1414–1422 (2017)
11. Liu, S., Shin, Y.C.: Additive manufacturing of Ti6Al4V alloy: a review. Mater. Des. **164** (2019)
12. Tyflopoulos, E., Lien, M, Steinert, M.: Optimization of brake calipers using topology optimization for additive manufacturing. Appl. Sci. **11** (2021)
13. Aliyi, A.M., Lemu, H.G.: Case study on topology optimized design for additive manufacturing. In: IOP Conference Series: Materials Science and Engineering, IRMES 2019, vol. 659, Kragujevac, Serbia 659 (2019)
14. Tanishk, V., Prithvi Reddy, S.V.: Topology optimization of a unidirectional helical gear. Int. J. Sci. Eng. Technol. Res. (IJSETR) **9**(8), 140–144 (2020)
15. Ajayi, K., Malomo, B.O., Paul, S.D., Adeleye, A.A., Babalola, S.A.: Failure modeling for titanium alloy used in special-purpose connecting rods. Mater. Today Proc. **45**(6), 4390–4397 (2021)
16. Bendsoe, M.P., Sigmund, O.: Material interpolation schemes in topology optimization. Arch Appl Mech **69**(9–10), 635–654 (1999)

Metal Joining

A Study on Friction Stir Lap Welding of Dissimilar Al 6061 to Polycarbonate

Nisith Ku. Goswami and **Kamal Pal**

1 Introduction

In recent applications, the demand for joining dissimilar materials like aluminium alloy and magnesium alloy to thermoplastic polymer has been raised due to their low weight, high specific strength and reshaped properties [1]. Thermoplastics and aluminium alloys are widely used in the aerospace and automotive industries [2]. However, it is a highly challenging task for the dissimilar metal to polymer airtight joining using fusion welding processes due to drastic differences in their thermal properties. Adhesive bonding and mechanical fastening are two common methods are used [2]. In recent decades, new advanced joining techniques have been employed to overcome the limitation of conventional methods to join metal and polymer [3]. However, ultrasonic welding, friction stir welding have been used successfully in joining metal to the polymer. FSW is a solid-state welding method, in which a non-consumable tool rotates and traverses along the weld interface to produce a sound weld without melting the base materials [4].

In past few years, several metal to polymer work have been carried out using FSW. From many FSW studies, it has been observed that primary factors such as tool geometry [5–7] and tool materials [8–11] have a significant effect on joint strength and weld bead profiles. Friction stir butt welding [12, 13] and friction stir spot welding [14, 15] have been proposed by many researchers. The friction stir lap welding of AA5058 aluminium-magnesium alloy and polycarbonate (PC) was performed by using tungsten carbide tool [1]. Mechanical interlocking plays a vital role in friction stir lap welding of AA6061-T6 aluminium alloy to polyether ether ketone [2]. In joining of AA-5052-H34 aluminium alloy with PP-C305 polypropylene by friction

N. Ku. Goswami (✉) · K. Pal
Department of Production Engineering, Veer Surendra Sai University of Technology, Burla, Sambalpur, Odisha 768018, India
e-mail: nisithgoswami82@gmail.com

299

stir lap welding, the weld strength was achieved to be 5.1 MPa, i.e. 20% of polymer strength [8].

In recent years, metallic parts are being replaced by thermoplastic composites in aerospace and automobile industries to improve the strength-to-weight ratio which ultimately reduces the annual fuel consumption [2]. Thus, friction stirring processes are found to be useful for difficult to weld dissimilar metallic non-ferrous to thermoplastics such as aluminium alloy to polycarbonate which is not investigated in detail as per previous studies. It indicates the research gap which is the basis for the present investigation. In this work, the primary objective is to investigate the feasibility for the joining of Al 6061-T6 to PC sheets by FSW tool of H13 tool steel in partial overlap configuration. Though there are several works on dissimilar joining there is hardly any work on this metallic to polymer materials combination. The influence of tool position (plunge depth and tilt angle) for different tool rotational speeds on weld bead profile (extended to weld shear strength) has been examined which was not studied in detail in previous works. Lastly, the sensitivity analysis on the significance of parametric influence on process stability in terms of weld quality characteristics has also been processed using the experimental data.

2 Experimental Procedure

The experimental setup for friction stir lap welding is shown in Fig. 1a. The tests were done on a 3 Tonne; 3-axis NC controlled FSW machine (RV M/c Tool8, Coimbatore). The 6061-T6 aluminium alloy and polycarbonate specimens have been prepared with dimensions of $85 \times 75 \times 2$ mm and $85 \times 75 \times 3$ mm, respectively. These dissimilar base materials (Al 6061 and polycarbonate) combinations are now used in various parts in aerospace and automotive industries [1, 2]. The physical, thermal and mechanical properties of base materials are shown in Table.1. The 6061-T6 Al alloy sheet has been placed on the polycarbonate laminate with an overlapping length of 19 mm along the longitudinal direction as shown in Fig. 1a. The tool is made up of H13 steel with a taper pin profile having tool shoulder diameter of 18 mm, and outer and inner diameter of taper pin are 6 mm and 4 mm, respectively, with a pin length of 3.5 mm. The end view of the FSW tool having a taper pin is shown in Fig. 1b.

The design of experiments (L_8) was considered here as a full factorial design with two levels (low and high) of three process variables, namely tool revolving speed, tilt angle and plunge depth after going through the sufficient number of trial experiments (for the satisfactory welds) as shown in Table.2. Hence, a total of eight tests have been conducted in single-pass friction stir welding keeping tool traverse speed (75 mm/min) constant throughout the experiments. However, four randomly chosen additional experiments have also been performed to check the repeatability of the FSW machine.

The tensile test of the lap-welded samples has been conducted by a Universal testing machine (Model-UTE 20-HGFL, 200kN-FIA Private. Limited, Maharashtra). The welded samples have been cut as per ASTM standard (D1002-05) for the sheer
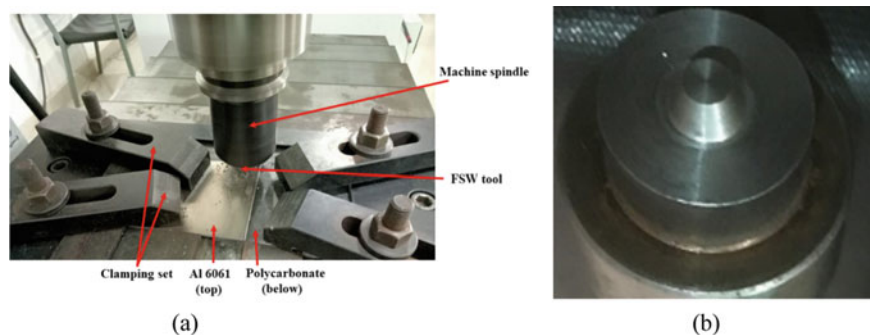
Fig. 1 **a** Friction stir lap welding set up. **b** H13 steel tool with taper pin profile

Table 1 The Physical, thermal and mechanical properties of weld base materials

Properties	Al 6061-T6	PC
Density (kg/m^3)	2700	1220
Ultimate tensile strength (MPa)	280.7	48
Thermal conductivity (W/mk)	151–202	0.25
Co-efficient of friction	0.60	0.25

Table 2 Process parameters with their levels

Process variables	Parametric settings
Traverse speed (mm/min)	75
Tool rotational speed (rpm)	1100, 1400
Tool tilt angle (degree)	0, 2
Plunge depth (mm)	0.1, 0.3

tensile test. The ultimate point of the load versus elongation diagram has been processed which indicated the ultimate stress (load divided by overlapped area in the tensile test sample). The base sheets have also been tensile tested as per ASTM standard.

3 Results and Discussions

The weld UTS for different parametric conditions in FSW is specified in Table.3. The lap shear strength was found to be maximum (joint strength efficiency 19.78 MPa, i.e. 41.2% of ultimate tensile strength of base polycarbonate) at N1400, tilt angle (0°) and plunge depth (0.1 mm).

Table 3 Parametric settings with corresponding process output

Expt. No.	Tool rotational speed (rpm)	Tool tilt angle (degree)	Plunge depth (mm)	Weld UTS (MPa)
1	1100	0	0.1	17.96
2	1100	0	0.3	18.19
3	1100	2	0.1	18.56
4	1100	2	0.3	17.19
5	1400	0	0.1	19.78
6	1400	0	0.3	16.05
7	1400	2	0.1	14.06
8	1400	2	0.3	15.22
9	1100	0	0.1	18.31
10	1100	2	0.3	17.70
11	1400	0	0.1	19.57
12	1400	2	0.3	15.82

3.1 Effect of Process Parameters on Weld Bead Profile

The parametric interaction effect on the weld bead profile is presented in Fig. 2. The top weld beads were found to be slightly blackish at greater plunge depth (0.3 mm), whereas it was whitish with expelled aluminium along tool advancing side (AS) at tool perpendicular condition (tilt angle = 0°) as shown. The soft polycarbonate (whitish) beneath the aluminium sheet was also expelled due to axial tool thrust at low plunge depth (0.1 mm) and zero tilt angle. However, this expelled material was marginally blackish substrate in whitish polycarbonate at high plunge depth (0.3 mm) without any tool tilting. The tool pin-assisted groove was wider without much depth at low tool plunging, whereas there was a deep narrow slot at higher tool plunge depth. Therefore, the degree of non-uniformity along the longitudinal groove was prominent at high tool plunging conditions as indicated. This weld profile non-uniformity was more pronounced with consecutive holes at high tool tilt angle (2°) and low plunge depth (0.3 mm). Thus, it specified unstable (i.e. non-uniform axial thrust and circumferential torque) conditions during the welding period. The weld profile was also found to have deviated initially when both plunge depth and tilt angle of the rotating tool were high (0.3 mm and 2°, respectively) at low tool revolving speed (1100 rpm) because of the same reason as shown. It was observed that the pin influenced weld groove was relatively narrower with scattered expelled or extruded metallic aluminium debris at a high tool tilt angle with high or low tool plunging conditions, respectively as shown. The weld bead contour was found to be non-uniform when both plunge depth and tilt angle of the rotating tool were high for both higher and lower tool rotational speed. However, at higher tool rotational speed, lower tilt angle and lower plunge depth, the weld bead contour was found to be uniform.
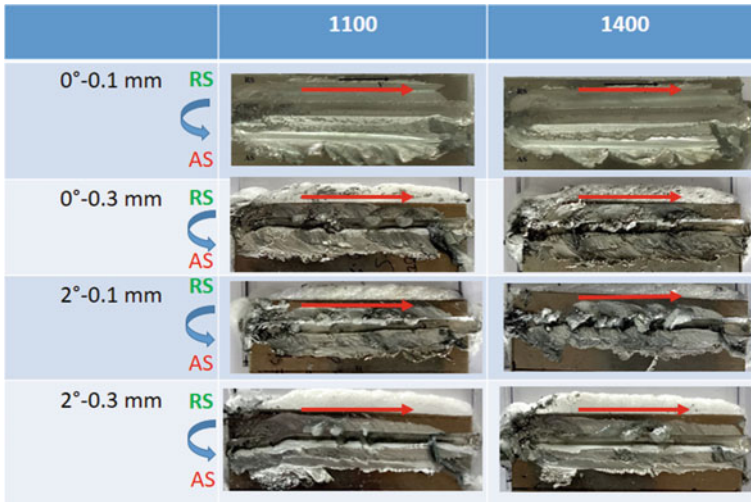
Fig. 2 Weld bead profiles at different parametric conditions

3.2 Effect of Process Parameters on Joint Strength

In the present work, the aluminium sheet has been positioned into the fixed-grip, and polycarbonate was placed in the moving grip during the tensile test of the lap welds [1]. The results of the tensile test of joints with different tool rotational speeds as shown in Fig. 3. According to the results, by increasing the tool rotational speed keeping constant low tilt angle and low plunge depth of 0° and 0.1 mm, respectively, the ultimate tensile strength was found to be significantly improved (17.96–19.78 MPa) probably due to more frictional heat generation leads to the upgraded bonding at the dissimilar weld base materials interface. Thus, weld bead profile was more uniform without any defect; a wider and deeper weld was found particularly at the final welding phases as presented in Fig. 2.

The joint strength efficiency was predominately reduced with either high tool plunging depth or high tilt angle shown in Fig. 3. Thus, tool position (plunge depth and tilt angle) was highly sensitive on weld strength at this high tool revolving speed (i.e. high frictional heart condition). The pin assisted longitudinal groove along the weld bead comprised of consecutive holes at high tool tilt angle (2°) though plunge depth was low (0.1 mm) at this condition which in turn resulted from the weakest weld (14.06 MPa i.e. joint efficiency of 29.2%) as shown in Fig. 2. However, non-uniformity in top weld bead profile was indicated poor joint strength when both tool tilt angle and plunge depth were high as indicated. On contrary, the tool position concerning base materials was not as sensitive (i.e. no significant variation of weld strength with different tool positioning) at low tool rotating speed as represented in Fig. 3. Thus, the mean, as well as individual weld strength at this low tool rotational speed, was also higher than high tool rotational speed except at low plunge depth
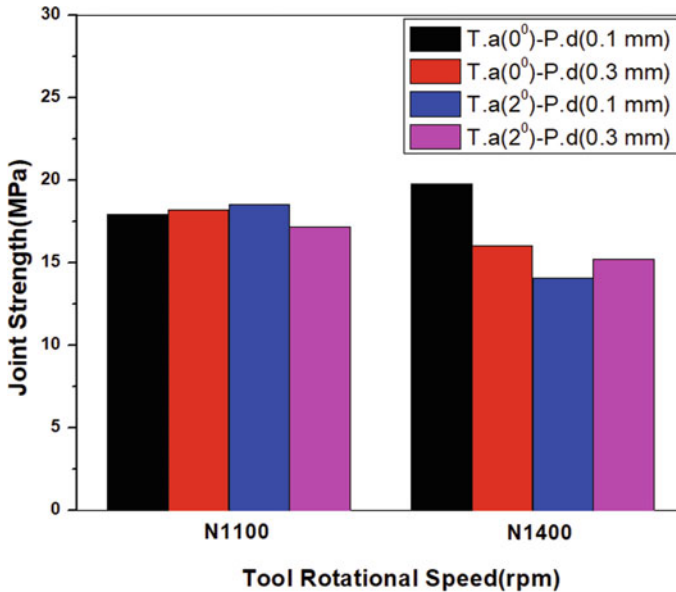
Fig. 3 Effect of process parameters on joint strength

with tool perpendicular condition as shown. The joint efficiency was found to be the highest (18.56 MPa) at a high tilt angle with low plunge depth when the tool rotational speed was low (1100 rpm). However, there was further improvement in shear tensile strength (18.56–19.78 MPa) was noticed at high tool rotational speed when both tool tilt angle and plunge depth were low (Expt #5). The repeatability of the FSW machine was achieved to be highly acceptable as the weld bead profile and joint strength as there was no significant variation (within ± 4% over mean) of each as indicated in Table 3.

3.3   Sensitivity Analysis

Sensitivity analysis is a statistical approach to identifying the most significant process parameter. Therefore, this analysis plays a vital role in determining which parameter of the process has to be modified to obtain the improved process output. In this study, the impact of process variables on joint strength has been analysed as presented in Table 4. Three statistical parameters, namely mean range and standard deviation of the welded shear strength have been determined considering one process variable (tool rotational speed, tilt angle and plunge depth) constant at a time. The variation of each statistical index for the respective changes of each input parameter has been calculated as shown. For example, when tool rotational speed was changed from 1100 to 1400 rpm, there was a corresponding drop in average weld strength of 1.24 MPa

as shown. Similarly, the range and standard deviation of joint strength were found to be varied as a hike of 4.35 MPa and 1.88 MPa, respectively, which indicated as an index of process stability due to this parametric variation.

Thus, it was observed that, when the tool rotational speed (rpm), tilt angle (deg) and plunge depth (mm) were increased, the average value of weld strength was found to be decreased by 1.24, 1.88 and 1.34 times, respectively. But when the tool rotational speed was increased, it was reported that the range and standard deviation of weld strength were increased by 4.35 and 1.88, respectively. However, the range and standard deviation were decreased by 2.75 and 0.9 times, when the plunge depth was increased. Therefore, there was a significant impact of tool rotational speed and plunge depth on the variation of weld strength (i.e. range, standard deviation) possibly due to variable heat generation and weld penetration, respectively. But, this variation was negligible by the variation of tool tilt angle on weld strength as compared to tool rotational speed and tool plunge depth. On the other hand, the effect of tool tilt angle on mean weld strength was highly predominant (a significant drop of 1.88 MPa), whereas this impact was found to be relatively less for plunge depth or tool rotational speed (1.34 MPa and 1.24 MPa, respectively). Therefore, it can be concluded that tool rotational speed and plunge depth should be minutely adjusted to achieve a sound weld as both parameters are highly sensitive, whereas the overall impact on average weld quality (strength) is primarily governed by tool tilt angle.

4 Concluding Remarks

It has been found that the 6061-T6 aluminium alloy and polycarbonate have successfully joined by friction stir lap welding in a partial overlap position. The weld strength increases with increasing tool rotational speed, possibly due to higher frictional heat along tool pin circumference to base materials interface at tool perpendicular alignment with low plunge depth (0.1 mm). The weld top bead contour was observed to be whitish at this tool position, whereas it was blackish at a higher tool plunge depth of 0.3 mm. The tool tilt angle is more predominant on mean joint strength. Therefore, the tool revolving speed is highly sensitive to weld shear strength as per parametric sensitivity analysis. The joint efficiency can be improved up to 41.2% of polycarbonate (19.7 MPa) at high tool rotational speed (1400 rpm) and zero tilt angle with low plunge depth (0.1 mm) due to uniformity of weld profile without much material expulsion along tool advancing side.

Table 4 Comparative assessment of parametric influence on weld strength

Process variables	Tool rotational speed (rpm)		Hike (*H*)/drop (*D*)	Tilt angle (deg)		Hike (*H*)/Drop (*D*)	Plunge depth (mm)		Hike (*H*)/Drop (*D*)
Parameter settings	1100	1400		0	2		0.1	0.3	
Weld strength (MPa)									
Mean	17.99	16.75	1.24 (*D*)	18.31	16.43	1.88 (*D*)	18.04	16.7	1.34 (*D*)
Range	1.37	5.72	4.35 (*H*)	3.73	4.5	0.77 (*H*)	5.72	2.97	2.75 (*D*)
Standard deviation	0.48	2.36	1.88 (*H*)	1.34	1.68	0.34 (*H*)	2.07	1.17	0.90 (*D*)

References

1. Derazkola, H., Elyasi, M.: The influence of process parameters in friction stir welding of Al-Mg alloy and polycarbonate. J. Manuf. Process. **35**, 88–98 (2018)
2. Huang, Y., Meng, X., Wang, Y., Xie, Y., Zhou, L.: Joining of aluminium alloy and polymer via friction stir lap welding. J. Mater. Process. Technol. **257**, 148–154 (2018)
3. Derazkola, H., Khodabakhshi, F., Simchi, A.: Friction-stir lap-joining of aluminium-magnesium/poly-methyl-methacrylate hybrid structures: thermo-mechanical modelling and experimental feasibility study. Sci. Technol. Weld Joining **23**(1), 35–49 (2018)
4. Nagatsuka, K., Onoda, T., Okada, T., Nakata, K.: Direct dissimilar joining of aluminium alloys and polyamide 6 by friction lap joining. Weld Int. **31**(1), 9–16 (2017)
5. Sahu, S.K., Mishra, D.: Friction stir welding of polypropylene sheet. Int. J. Eng. Sci. Technol. **21**, 245–254 (2018)
6. Buffa, G., Baffari, D., Campanella, D., Fratini, L.: An innovative friction stir welding based technique to produce dissimilar light alloys to thermoplastic matrix composite joints. Procedia Manuf. **5**, 319–331 (2016)
7. Liu, F., Liao, J., Nakata, K.: Joining of metal to plastic using friction lap welding. Mater. Des. **54**, 236–244 (2014)
8. Shahmiri, H., Movahedi, M., Kokabi, A.: Friction stir lap joining of aluminium alloy to polypropylene sheets. Sci. Technol. Weld Joining **22**(2), 120–126 (2017)
9. Ratanathavorn, W., Melander, A.: Dissimilar joining between aluminium alloy (AA 6111) and thermoplastics using friction stir welding. Sci. Technol. Weld Joining **20**(3), 222–228 (2015)
10. Yan, Y., Shen, Y., Lan, B., Gao, J.: Influences of friction stir welding parameters on morphology and tensile strength of high-density polyethylene lap joints produced by the double-pin tool. J. Manuf. Process **28**, 33–40 (2017)
11. Yusof, F., Miyashita, Y., Seo, N., Mutoh, Y., Moshwan, R.: Utilising friction spot joining for the dissimilar joint between aluminium alloy (A5052) and polyethene terephthalate. Sci. Technol. Weld Joining **17**(7), 544–549 (2012)
12. Rahmat, S., Hamdi, M., Yusof, F., Moshwan, R.: Preliminary study on the feasibility of friction stir welding in 7075 aluminium alloy and polycarbonate sheet. Mater. Res. Innov. **18**(6), 515–519 (2014)
13. Dalwadi, C., Patel, A., Kapopara, J., Kotadiya, D., Patel, N., Rana, H.: Examination of mechanical properties for dissimilar friction stir welded joint of al alloy (AA-6061) to PMMA (Acrylic). Mater. Today Proc. **5**, 4761–4765 (2018)
14. Ibrahim, I., Yapici, G.: Optimization of the intermediate layer friction stir spot welding process. Int. J. Adv. Manuf. Technol. **104**(1–4), 993–1004 (2019)
15. Lambiase, F., Paoletti, A., Grossi, V., DiIlio, A.: Friction assisted joining of aluminium and PVC sheets. J. Manuf. Process. **29**, 221–231 (2017)

Characterization of Dissimilar Welding of AISI 409 Ferritic to AISI 316l Austenitic Stainless Steel Using AISI 308 Filler Wire Under Different Temperature Conditions

K. Sripriyan , **M. Ramu** , and **P. R. Thyla**

1 Introduction

Stainless steel (SS) is used in various applications such as oil and gas industries, nuclear power plants, coal-fired boilers, and the automobile manufacturing industry [1]. The joining of two dissimilar materials may significantly reduce the weight of the product and minimize the cost of production, without compromising on the safety and structural requirements [2]. Also, sufficient tensile strength and ductility can be achieved, so that the joint will not fail [3]. Joining of ferritic steels and austenitic stainless steels (F/A) is used in many applications because ferritic steel is preferred to avoid the problem of nickel leaching by molten magnesium, while austenitic steel has good creep strength and oxidation resistance. These properties are required at higher temperature regions, in applications such as oil and gas industries, ship industries, nuclear plants, and automobiles [4]. F/A steel obtained through manual metal arc (MMA), metal inert gas arc (MIG), and tungsten inert gas arc (TIG) welding can provide adequate performance at a reasonable cost [5]. The joining of dissimilar materials is a challenging task, owing to the differences in their thermal properties, which might cause interface crack [6, 7].

Sanjay Kumar Gupta [8] formed a butt weld with base metals of AISI 409L ferritic stainless steel using two different filler wires, viz., Er304L and Er308. They obtained

K. Sripriyan (✉)
School of Mechanical Engineering, VIT Bhopal University, Bhopal-Indore Highway, Kothrikalan, Sehore Madhya Pradesh-466114, India
e-mail: sripriyan.k@vitbhopal.ac.in

M. Ramu
Amirta Vishwa Vidyapeetham University, Coimbatore Campus, Coimbatore-641112, India
e-mail: m_ramu@cb.amrita.edu

P. R. Thyla
Department of Mechanical Engineering, PSG College of Technology, Coimbatore-641004, India
e-mail: prt.mech@psgtech.ac.in

good mechanical properties by using 304L filler wire rather than 308L filler wire, irrespective of the input parameters. Iman Agha Ali [9] studied the correct behavior of repeated repair of 316L stainless steel. Microstructure investigations revealed that compared with other zones HAZ is more sensitive. Due to the increasing number of repairs, pitting corrosion was found to increase [10, 11]. Nabendu Ghosh [12] investigated the welding of dissimilar metals of SS409 and SS316L by considering input parameters of gas flow rate, current, and nozzle-to-plate distance. The input process parameters were optimized by using Taguchi-desirability analysis. The research work concluded that welding current and gas flow rate are significant parameters that influence weld quality. Kumar [13] performed studies on the output responses of tensile strength and hardness obtained in the welding of AISI 304 and low carbon steel using S/N ratio and analysis of variance (ANOVA).

In the year 2015, Kasuya [14] investigated the effect of ambient temperature on the weldability of steel. The experimental results revealed that the ambient temperature has a significant role in microcracking susceptibility. The cracks may increase at lower ambient temperatures. Lin Chen [15] performed numerical and experimental studies on the effect of the residual stress of multi-pass hybrid laser-arc welding and laser beam welding on 316L. The results of simulation and experimental measurements of residual stress are found to be in good agreement. The results indicated that due to the effect of residual stress, intermetallic zone slightly altered and also the grain size and orientation in the re-melting zone altered significantly.

From the literature review, it could be seen that residual stress is one of the major problems in the joining of F/A stainless steel. When two different parent metals are in the molten state, expansion is prevented by the relatively cooler parent metal with higher yield strength, which results in high-temperature plastic deformation in the weld metal.

Similarly, shrinkage in the weld zone and HAZ is restrained during cooling by the colder parent metal, causing tension in the HAZ and the weld metal. However, the weld zone and HAZ shrink as the temperature reduces after welding, but it is controlled by the cooled parent metals, consequently causing tension in the weld zone and HAZ. Net residual stress (tensile) in both the zones may be balanced by compressive residual stress in the parent metals.

During the past few decades, a variety of welding processes have been developed to perform the joining of F/A stainless steels for various industrial applications. Still, there is a gap that necessitates addressing the residual stress on the joining of F/A. This paper focuses on the investigations of residual stress and mechanical properties on dissimilar welding of AISI 409 ferritic steel to AISI 316L austenitic steel by using AISI 308 filler wire at different temperature conditions. In addition, the effect of process parameters is discussed in this paper.

The impact of input parameter on the response quality is always a consideration [16, 17]. The current work investigates the effects of input parameters on the ultimate tensile strength (UTS), hardness (HV), and grain distribution in GMA welding of dissimilar ferritic stainless steel AISI 409 and austenitic stainless steel AISI 316L materials to achieve the goals. Experiments were carried out using L_9 orthogonal

array. To optimize the process parameters, the S/N ratio was chosen based on the larger-is-better criterion.

The novelty of the work is the welding of dissimilar welding of AISI 409 ferritic to AISI 316L austenitic stainless steels by using AISI 308 filler wire at different temperature conditions, along with optimization of process parameters to understand the residual stress and mechanical properties.

2 Parameters and Experimental Apparatus

2.1 Process Parameters and Methods

In this study, MIG (FAST MIG MXF 65) welding was used for the joining of dissimilar stainless steel at different temperature conditions. The welding robot setup was employed to carry out automatic welding. The basic schematic of the dissimilar arrangement is shown in Fig. 1. Ferritic stainless steel (AISI 409) and austenitic stainless steel (AISI 316L) are used as the base metals and combinations used in petrochemical industries, ship industries, nuclear power plants, pulp, and paper industry, due to their better corrosion resistance and good weldability [18]. Furthermore, because of its lower thermal conductivity, which is one-third that of normal carbon steel [3], heat dissipation is rather poor. Because of its higher coefficient of thermal expansion, the deflection is greater than that of conventional carbon steel with the same heat input [19]. Therefore, MIG welding with a low heat input is more suitable for welding dissimilar stainless steels, i.e., AISI 409 and AISI 316L, by using AISI 308L austenitic filler wire. The chemical compositions of the stainless steel base metal and filler used in this work are listed in Table 1. Butt joints have been formed out as per the L_9 orthogonal array and welding process parameters selected, and their levels are shown in Table 2. Each butt-welded sample is made by joining two 3 mm thick sheets, each of dimensions 100 mm × 130 mm × 10 mm.

In any welding, mechanical properties including distortion, residual stress, tensile strength, fracture, and more have become more considered [20, 21]. In addition, due to the complex thermal effects in the welding process, the residual stress distribution in the components is complicated. Specifically, the study of dissimilar metals, not an easy task, may expiate different residual stress while welding due to the differences in thermal conductivities and thermal expansion which may cause crack formation interface [2]. However, many dissimilar materials can be joined successfully with minimal residual stress by adapting the appropriate joining process and specialized procedures, which possess sufficient tensile strength and ductility, Therefore, the weld joint will not fail [10]. Moreover, the residual stress of the components may exceed the yield strength of the alloy affecting corrosion resistance, fracture toughness, crack propagation behavior, and fatigue performance [20]. In this regard, influences of residual stress in joining of the dissimilar metals AISI 409 and AISI are considered at different temperature conditions in this study. The key parameters
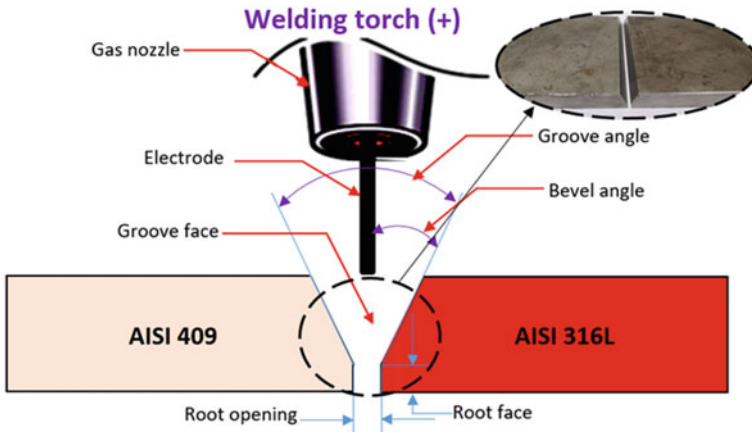
Fig. 1 Schematic illustration of the dissimilar metal weld joint

Table 1 Chemical composition of base metal and electrode used, % by wt

Base and filler metals	Composition wt %									
	C	Mn	Si	P	Cr	Ni	Mo	Cu	Al	S
AISI 409	0.08	1.00	1.00	0.45	11.75	0.5	–	–	0.02	0.45
AISI 316L	0.03	1.00	2.00	1.00	16.50	11.02	2.00	0.19	0.01	0.01
AISI 308L	0.03	2.00	1.00	0.045	20.01	10.08	0.116	0.082	0.01	0.03

Table 2 Welding input parameters and their levels

Parameters	Level 1	Level 2	Level 3
Welding input current (A)	90	110	130
Nozzle-to-plate distance (mm)	9	12	15
Gas flow rate (L/min)	8	10	12
Temperature (°C)	Pre-heating	Post-heat	Freezing

defined for this study are welding current, nozzle-to-plate distance, gas flow rate, and three different temperatures. The selected welding input process parameters and their levels are presented in Table 2.

Different welding results are obtained, depending on three different conditions (i) pre-heating, (ii) post-heating, and (iii) freezing condition, and detailed view of steps involved in the welding sequence is shown in Fig. 2. In pre-heating conditions, the welded plates are heated above 475 °C in the 60 s. The same temperature has been maintained after welding for post-heat conditions. Similarly, the base metals are immersed in ice cubes for a few hours. The temperature of the base metals is
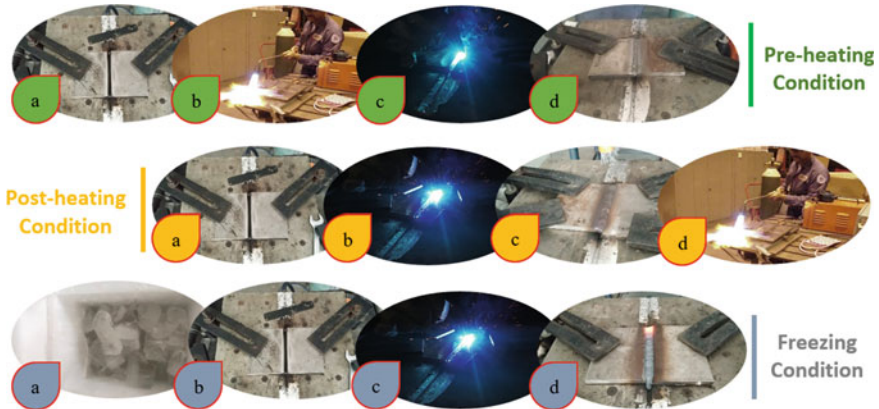
Fig. 2 Sequential arrangement of dissimilar welding at three different ambient conditions

measured by a thermistor, once the temperature reaches 10 °C, the base metals are taken for welding.

The experimental trial runs were conducted; with the edge, preparation maintained as 2 mm of root opening and face with 60-degree groove angle. After welding, the best quality of weld samples was obtained by sectioning and polishing for conducting tensile tests and hardness tests. The specimen is cut transversely from the weld joint, with the weld axis in the center of the specimen's parallel length. The mechanical or thermal techniques used to create the specimen must not affect the specimen's qualities. It is also crucial that the surface be devoid of notches or scratches, which might cause a fracture otherwise.

3 Result and Discussion

3.1 Visual Observations

All weld's surface is observed visually, no major defect found in any of the samples such as blowholes, uneven penetrations, excessive deposition, poor forming, oxidation blacking, burning-through, collapse, crack, and surface porosity. Very few welds surfaces are found in spatter, and this may be due to damp filler rod, arc blow/bubble of gas being entrapped in the molten metal, and projecting small drops of metal outside the arc seam [7, 19]. Also, some of the weld sample undercut defects are caused by base metal being ablated by arc, and weld pool metal is not backfilled due to its poor spreading property, typical weld bead top surface and cross-section are in Fig. 3.

Type	Weld bead top surface appearance	Cross section formation
Pre-heat (@475°C)	@ 90A 9mm-NPD 8 lpm-GFR — Spatter	FZ BZ HAZ HAZ
Post heat (@475°C)	@ 90A 12 mm-NPD 10 lpm-GFR — Undercut	FZ BZ HAZ HAZ
Freezing (@10°C)	@ 90A 15mm-NPD 15 lpm-GFR — Spatter	FZ BZ HAZ HAZ
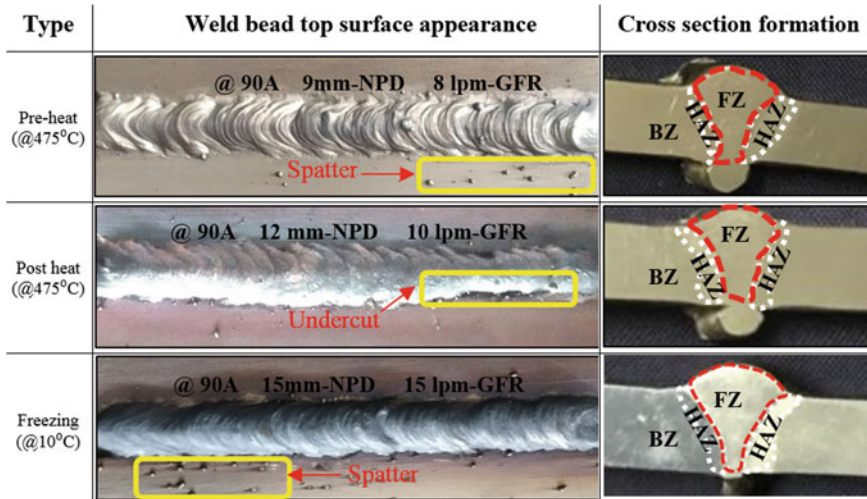
Fig. 3 Top surface weld bead appearances and cross-sections of weld joints

The depth of the fusion zone and the width of the weld beam have been measured. The figures show that the depth of the fusion zone slightly altered with the freezing condition, while the mean width of the fusion zone remains almost the same.

3.2 Tensile Tests

Tensile tests were carried out to determine the ultimate tensile strength of the welded section. The samples were prepared as per ASTM E8M-04 guidelines, and a typical sample is shown in Fig. 4. The results presented in Table 3 indicate that all the welded samples are satisfactory. The tensile strength was found to be in the range of 485.3 MPa to 412.2 MPa. The freezing condition weld sample was found to exhibit a lesser tensile strength (by 3% on an average) compared to pre- and post-heat conditions. After post-heating at 475 ºC for a few minutes, increase in the UTS by 0.6% for the pre-heating condition and 3.4% for freezing condition was observed. However, the average reduction in the cross-sectional area of weld bead under all three conditions is calculated; the reduction was found to be 1.1 times for pre-heating and 1.3 times for freezing as that of post-heat conditions. Further, the results indicated greater ductility of the weld bead under post-heating condition.

(a) Weld sample specimens   (b) Failure Location
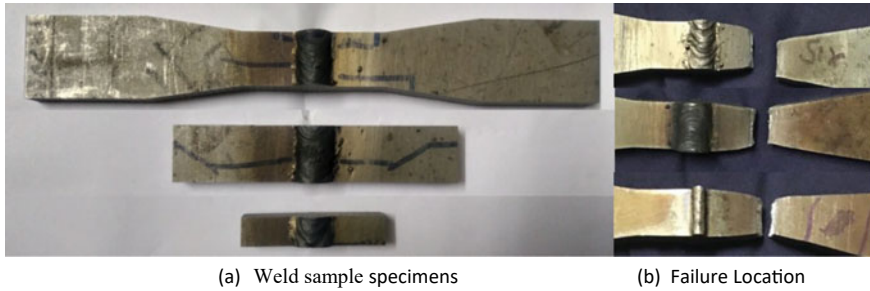
Fig. 4 Typical weld specimens and their failure location

3.3 Microhardness

"Vickers hardness tester" is used to find the microhardness of all welded samples in fusion zone (FZ) and heat-affected zone (HAZ) under a constant load of 10 kgf with a step size between each indentation is 0.4 mm as per ASTME384. The post-heat welding samples are reported that the maximum hardness value than that of pre-heating and freezing conditions, more details in Table 3. This is maybe accredited to the consequence of the grain coarsening phenomenon that arises due to after heating of welded samples. An increase in microhardness might be due to the development of martensite at the grain boundaries region, detailed in Fig. 3 (microstructure). The average microhardness of the weld zone of three conditions is measured, the range between 171.3 and 189.3 Hv.

3.4 Surface Residual Stress

Generally, residual stresses are developed because of the fluctuation of transient temperature gradient during the welding process [15]. The net effect is the development of tensile stress during and after welding; i.e., the residual stress in the weld metal and HAZ is tensile, which is balanced by compressive residual stress in the parent material.

The longitudinal residual stress is measured for all the samples. Typical X-ray diffraction is depicted in Fig. 5 for all three conditions with a collimator (Ø) of 1 mm. The variation of the longitudinal residual stress with respect to the distance from the centerline of the bead on either sides is depicted in Fig. 5. The figure reveals relatively low stresses in the AIS 316L base metal, in the range 26–220 MPa, and the measured stress rises about 220 MPa about 3 mm, 3 mm, and 5.5 mm, respectively, for all three temperature conditions from the centerline, whereas the difference in stress was found in the base metal of AISI409, in the range 36–257 MPa. The measured stress rises about 257 MPa (pre-heading), 225 MPa (post-heading), and 217 MPa (freezing) at the location about 3 mm, 3 mm, and 5.8 mm, respectively, from the weld

Table 3 Measured weld bead characteristics response

Experiments no	Welding parameter's				Observed and calculated value of weld bead characteristics							
	Welding current (A)	Nozzle-to-plate distance (mm)	Gas flow rate (L/min)	Temperature (°C)	Average micro-Vickers hardness (Hv)	Ultimate tensile strength property				Calculated grain size (μm)	Intercepts	Mean intercept length (um)
						Load at peak (kN)	UTS (N/mm²)	Reduction in cross-sectional area (%)	Failure location			
1	90	9	8	Pre-	170	83.0	469.5	24	Base metal zone @ AISI 316L	7.5	187	24.4
2	90	12	10	Post-	178	82.2	466.9	25			180	25.4
3	90	15	12	Freeze	182	72.0	412.2	26			199	23.1
4	110	9	10	Freeze	180	85.0	480.7	35			190	24.1
5	110	12	12	Pre-	168	85.8	483.4	32			186	24.6
6	110	15	8	Post-	188	85.1	482.4	25			189	24.2
7	130	9	12	Post-	202	84.1	477.6	25			180	25.4
8	130	12	8	Freeze	179	86.3	485.2	35			183	25.2
9	130	15	10	Pre-	176	82.6	467.6	29			184	24.8

Fig. 5 Residual stress profiles at welding of different ambient conditions
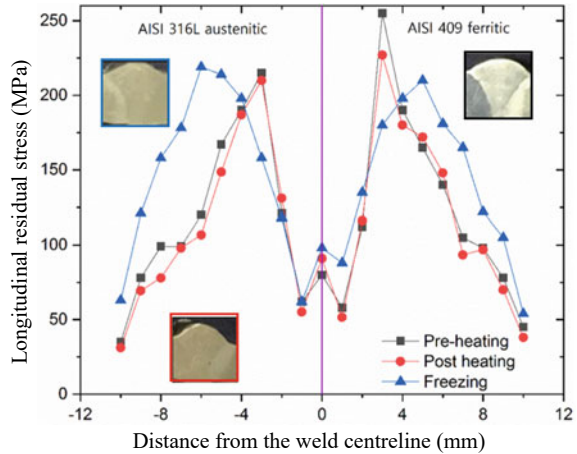
centerline. In addition, compressive stresses in the weld metal appear in the range 50–100 MPa in all three conditions, because of its different in thermal expansions of both materials and also welded under different temperature conditions. Overall results indicated that average residual stress developed in the post-heat condition is least in magnitude, it is about 3% and 20% lesser than that stress induced in the samples welded with pre-heating and freezing conditions.

3.5 Metallurgical Test

The weld bead geometry is shown in Fig. 4. The dimensions of the bead profile are measured; the bead width is found to be in the range 3.2–4.1 mm for the samples, while penetrations are in the range 6.5–8.9 mm. The bead profiles are observed to be consistent in all three conditions (pre-heating, post-heating, and freezing), with no significant difference. The average grain size was found to be 7.5 μm under the magnification of 100×.

All the zones are designated and the microstructure seems to contain a large amount of austenite and a small amount of ferrite, as detailed in Fig. 6 indicate. Moreover, the dimension of the HAZ in the freezing condition is lesser than that of pre- and post-heating conditions, due to less heat experienced during the welding, i.e., weld metal experiences higher cooling rates. Figure 6 also revealed the grain growth direction and the formation of the grains in different zones; the finest equiaxed dendrites exist as network morphology at the center of the fusion zone in freezing conditions. Generally, the primary dendrite arm spacing of the columnar structure is mainly affected by the cooling rate and the heat input [15]. It is also observed that the austenite and ferrite forms are disposed to grow along the weld seam. Very few
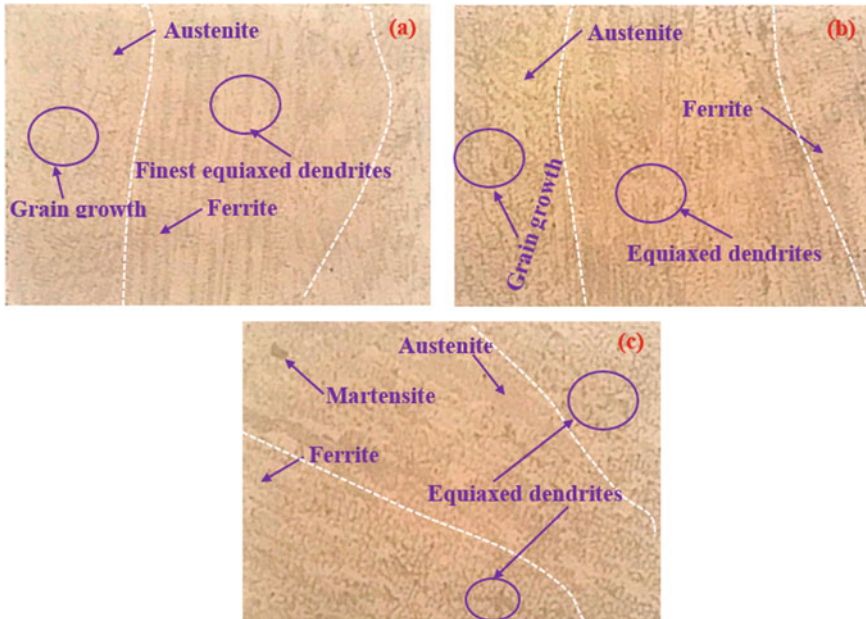
Fig. 6 Optical micrograph view of different boundaries of dissimilar F/A welded

weld defects are present, and the mechanical property of the weld is satisfactory, as detailed in Table 3.

4 Selection of Optimum Parameters

Taguchi orthogonal array analysis was carried out to identify the optimum process parameters. The "Larger the better" criterion is used to find the S/N ratio for tensile strength and hardness, and the response tables are presented in Tables 4 and 5. The maximum value of the S/N ratio confirms the optimum parametric combinations (current at 130 A, nozzle-to-plate distance of 12 mm, gas flow rate of 8 lpm, and temperature of 10 °C) that yield higher ultimate tensile strength (UTS = 485.2 MPa). The tensile strength is most influenced by welding current which has the maximum delta value of 0.62, followed by the nozzle-to-plate distance, gas flow rate with a delta value of 0.47, 0.42, and it is least influenced by temperature with the value of 0.33.

However, in respect of hardness, the maximum value of the S/N ratio confirms the optimum parametric combinations (current at 130 A, nozzle-to-plate distance of 9 mm, gas flow rate of 12 lpm, and post-heat temperature of 170 °C) that results in higher hardness (Hv = 202). The delta values indicate that hardness is most influenced by the temperature which has the maximum delta value of 0.86, followed

Table 4 Response table for signal-to-noise ratios for UTS

Level	Welding current (A)	Nozzle-to-plate distance (mm)	Gas flow rate(L/min)	Temperature (°C)
1	53.04	53.55	53.61	53.51
2	53.66	53.60	53.47	53.55
3	53.57	53.12	53.19	53.22
Delta	0.62	0.47	0.42	0.33
Rank	1	2	3	4

Table 5 Response table for signal-to-noise ratios for hardness

Level	Welding current (A)	Nozzle-to-plate distance (mm)	Gas flow rate (l/min)	Temperature (°C)
1	44.94	45.27	45.05	44.68
2	45.03	44.86	45.01	45.53
3	45.36	45.20	45.27	45.12
Delta	0.42	0.42	0.26	0.86
Rank	2	3	4	1

by welding current, nozzle-to-plate distance with a delta value of 0.42, 0.43, and it is least influenced by gas flow rate with a delta value of 0.26.

5 Conclusions

Characterization of the weld of dissimilar metals namely AISI 409 and AISI 316L by using AISI 308L filler wire has been carried out. From the experimental results, the following conclusions are drawn.

- The bead width and depth of penetration increase with increase in welding current as is evident from the microscopic image.
- The tensile test reveals that the weld joints are stronger than the base metal AISI 409 as the tensile failure is found to occur at the heat-affected zone of AISI 409.
- Welding current of 130 A, nozzle-to-plate distance of 12 mm, gas flow rate of 8 lpm, and temperature of 10 °C are found to result in high ultimate tensile strength (UTS = 485.246 MPa). Welding current has the most influence on tensile strength than nozzle-to-plate distance and gas flow rate, whereas the temperature has the least influence.
- By considering hardness, the combination of welding current of 130 A, nozzle-to-plate distance of 9 mm, gas flow rate of 12 l/min, and post-heat temperature of 170 °C yields higher hardness (Hv = 202). The post-heat temperature of 170 °C

has the greatest influence on hardness than welding current and nozzle-to-plate distance; gas flow rate has the least influence.

- The average grain size in all the specimens is the same, i.e., 7.5 μm. But difference in mechanical strength is observed in three different temperature conditions, which can be attributed to the difference in residual stress.

- In view of the results presented, dissimilar welding of AISI 409 ferritic to AISI 316L austenitic stainless steels under post-heating condition can be recommended as a potential alternate to reduce residual stress induced during welding.

References

1. Lee, H., Ji, C., Yu, J.: Effects of welding current and torch position parameters on bead geometry in cold metal transfer welding. J. Mech. Sci. Technol. **32**(9), 4335–4343 (2018)
2. Sripriyan, K., Ramu, M.: An experimental investigation of flat wire electrodes and their weld bead quality in the FCAW process. High Temp. Mater. Process. **21**(1), 65–79 (2017)
3. Wu, D., Hua, X., Ye, D., Ma, X., Li. F.: Understanding of the weld pool convection in twin-wire GMAW process. Int. J. Adv. Manuf. Technol. **88**(1–4), 219–227 (2017)
4. Sripriyan, K., Ramu, M.: Analysis of weld bead characteristics on GMAW by changing wire electrode geometry. J. Achieve. Mater. Manuf. Eng. **78**(2), 49–58 (2016)
5. Bayraktar, E., Kaplan, D., Devillers, L., Chevalier, J.P.: Grain growth mechanism during the welding of interstitial free (IF) steels. J. Mater. Process. Technol. **189**(1–3), 114–125 (2007)
6. Mattoo, S., Kumar, V., Ahmed, S.: Experimental analysis of effect of different filler rods on mild steel by shielded metal arc welding. Int. J. Eng. Res. **4**(10), 193–197 (2015)
7. Sripriyan, K., Ramu, M., Thyla, P.R., Anantharuban, K., karthigha, M.: Characteristic of weld bead using flat wire electrode in GMAW inline during the process: an experimental and numerical analysis. Int. J. Press. Vessels Pip. **196**, 104623 (2022)
8. Singh, S.K., Mishra, M., Jha, P.K.: Experimental investigations on thermo-hydraulic behavior of triple concentric-tube heat exchanger. Proc. Inst. Mech. Eng. Part E J. Process Mech. Eng. **229**(4), 299–308 (2015)
9. Agha Ali, I., Farzam, M., Golozar, M.A., Danaee, I.: The effect of repeated repair welding on mechanical and corrosion properties of stainless steel 316L. Mater. Des. **54**, 331–341 (2014)
10. Jaleel, A.: Grey-based Taguchi method for optimization of bead geometry in laser bead-on-plate welding. Prod. Eng. **5**, 225–234 (2010)
11. Sripriyan, K., Ramu, M., Thyla, P.R.: Effect of flat electrode and Fuzzy logic model for the prediction of weldment shape profile in GMAW. J. Mech. Sci. Technol. **71**(5), 2477–2486 (2017)
12. Ghosh, N., Pal, P.K., Nandi, G.: Parametric studies of dissimilar welding of AISI 409 ferritic stainless steel to AISI 316L austenitic stainless steel using Taguchi desirability analyses. J. Mech. Behav. Mater. **27**(1–2), 1–7 (2018)
13. Praveen Kumar, V.B.S.: Optimization of shielded metal arc welding parameters for welding of pipes by using Taguchi approach. Int. J. Eng. Sci. Technol. **4**, 2083–2088 (2012)
14. Kasuya, T., Yurioka, N.: Effects of ambient temperature on steel weldability. Weld Int. **6**(2), 145–150 (1992)
15. Chen, L., Mi, G., Zhang, X., Wang, C.: Numerical and experimental investigation on microstructure and residual stress of multi-pass hybrid laser-arc welded 316L steel. Mater. Des. **168** (2019)
16. Sripriyan, K., Ramu, M., Thyla, P.R., Anantharuban, K.: Weld bead characterization of flat wire electrode in GMAW process part II: a numerical study. J. Mech. Sci. Technol. **35**(5), 1–8 (2021)

17. Sripriyan, K., Ramu, M., Palani, P.K.: Study and analysis of the macrostructure characteristics in FCAW with the use of a flat wire electrode and by optimizing the process parameter using the Taguchi method and regression analysis. High Temp. Mater. Process. **20**(3), 197–224 (2016)
18. Nasiri, M.B., Enzinger, N.: An analytical solution for temperature distribution in fillet arc welding based on an adaptive function. Weld. World. **63**(2), 409–419 (2019)
19. Sripriyan, K., Ramu, M., Thyla, P.R., Prashant, M.: Analysis of molten pool characteristics on hybrid GMAW process. Asian J. Res. Soc. Sci. Humanit. **7**(10), 2249–7315 (2017)
20. Karthigha, M., Latha, L.: A comprehensive survey of routing attacks in wireless mobile ad hoc networks. In: 2020 International Conference on Inventive Computation Technologies (ICICT), IEEE, pp. 396–402
21. Sripriyan, K., Ramu, M., Thyla, PR., Anantharuban, K., karthigha, M.: Characteristic of weld bead using flat wire electrode in GMAW inline during the process: An experimental and numerical analysis. Int J Press Vessels Pip. 196:104623 (2022)

Experimental Investigation and Optimization to Maximize Ultimate Tensile Strength and Elongation of Weld Joint During GMAW of AISI 201LN

Vivek Singh, **M. Chandrasekaran**, **D. Devarasiddappa**, and **Bishub Choudhury**

1 Introduction

Austenitic stainless steel is demanding in industries due to its superior strength and corrosion resisting properties. The major applications of ASS 300-Series include cryogenic vessel, oil and gas application, power piping, chemical and process industries, pressure vessel, food industries, etc. [1, 2]. The price of ASS primarily depends on the nickel (Ni) composition which increases the production cost of conventional AISI 304 grade [3]. Nitrogen alloyed ASS considered as economical low Ni grade with addition of nitrogen as an alloying element which replaces AISI 304 in service failure components and in fabrication of cryogenic vessels [4]. AISI 201LN is becoming an alternative SS grade for the production of LNG tanks due to its superior strength and good toughness at low temperature. The addition of nitrogen tends to increase strength, solid solution strengthening, pitting corrosion resistance and stabilizes the austenitic phase in stainless steel [5].

The GMAW process is widely used in many industrial components due to its increased productivity, good weld quality, ease of mechanization and positional welding capability [6, 7]. The process has ability to reduce the heat input (HI) due to its controlled droplet transfer techniques [8]. The quality of weld is depends on the bead profile, mechanical properties of the weld which is greatly influenced by welding input parameters. Kamble and Rao [9] conducted experiments on structural steel AISI 321 with GMAW process. They developed mathematical models using central composite design matrix with 28 experimental set. The welding parameters

V. Singh
Department of Mechanical Engineering, AKGEC, Uttar Pradesh, Ghaziabad, India

M. Chandrasekaran (✉) · B. Choudhury
Department of Mechanical Engineering, NERIST, Nirjuli 791109, India
e-mail: mchse1@yahoo.com

D. Devarasiddappa
Department of Automobile Engineering, Rajiv Gandhi Polytechnic, Itanagar, India

viz., WFR, *V*, *S* and gas flow rate were considered to investigate bead width, penetration and bead height and hardness. Naik and Reddy [10] have performed welding optimization on duplex stainless steel 2205 using Taguchi method L9 experimental design by tungsten inert gas welding process. They considered input parameter viz., current, electrode diameter, time and oxide flux to investigate the strength, hardness and weld penetration. The authors applied Taguchi method and ANOVA coupled with neural network for optimizing the weld quality. Palanivel et al. [11] developed ANN model to predict ultimate tensile strength of titanium tubes during friction welding. The authors employed CCD experimental design matrix consisting 20 trials and observed ANN model to predict more accurately than RSM.

Xu et al. [12] performed statistical modeling of bead profile during narrow gap GMAW process. They conducted 50 set of experiments based on CCD design matrix by considering five input parameters viz., WFR, *S*, dwell time, oscillation and welding position. The adequacy and significance of model were checked by ANOVA. The result indicates that WFR has significant effect on weld bead profile. Weld height is reported to decrease with an increase in *S*. Oscillation and dwell time reported to have positive effect on bead profile and sidewall penetration. Son et al. [13] have investigated the bead profile during robotic GMAW process. The authors used multiple regression analysis and selected wire diameter, *V*, *S* and current as an input parameters. The result showed that the empirical models were able to predict the optimal weld parameter required to obtain the desired bead width. Saha and Waghmare [14] studied the laser welding of SS316 with the help of Yb-fiber laser in continuous mode. The UTS, bead width and micro hardness were obtained as output variables. The confirmatory experiment showed that the input variables were optimized to achieve the higher tensile strength and lower bead width. Conesa et al. [15] studied the bead profile during GMAW process using response surface methodology. They selected gas flow rate, WFR, *V* and torch angle as process parameters to investigate the responses viz., depth of weld, bead width and thickness. The result revealed good balance between maximum depth of weld and minimum bead width and thickness can be obtained at higher gas flow rate and at lower WFR and *V*. From the review of literature, welding investigation of AISI 201LN has not been carried out. Considering the potentiality of its use in many applications, the investigation on mechanical strength of the weld during GMAW is carried out in this work. The microstructural analysis of the weld also studied.

2 Materials and Methods

2.1 Experimental Work

AISI 201LN nitrogen alloyed austenitic stainless steel with dimension of $150 \times 130 \times 3$ mm thick was used as a base metal. A Fronius machine (Model: TPS 3200) was used to weld test coupon. The test coupons were prepared with butt joints having a
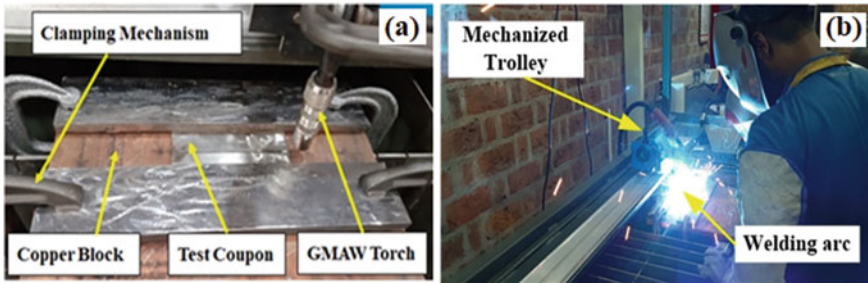
Fig. 1 Experimental set up **a** welding fixture and **b** welding process

root gap of 2 mm. ER308L wire spool having 1.2 mm electrode wire diameter was used as a filler metal in combination with shielding gas of 98%Ar and 2% CO_2. The WFR, V, S and NTD were varied as per design matrix. The welding of the test coupon was carried out with a mechanized set up holding a welding torch. The experimental set up showing welding fixture and welding process is shown in Fig. 1.

After visual inspection radiographic inspection was performed on the welded joint. The selected input parameter's levels are 4, 5, 6 m/min; 16, 17, 18 V; 220, 250, 280 mm/min and 10, 15 and 20 mm, respectively, for WFR, V, S and NTD.

2.2 Tensile Testing

The tensile test was conducted to determine the UTS and E of welded specimen using a universal testing machine (Model: WDM–200Y). The tensile testing of the sample was conducted at room temperature as per ASTM E08. The tensile specimen is mounted on UTM, and gradual loading condition is applied until the sample breaks. The fractured tensile specimen is depicted in Fig. 2. The experimental results obtained are summarized in Table 1.

2.3 Development of Predictive Modeling of Weld Strength

The influence of mechanical property during the welding of GMAW process was studied. Four welding parameters viz., WFR, V, NTD and S are considered as influencing factors for accessing the mechanical property of welded joint during GMAW process. The weld strength is evaluated using UTS and elongation (E) as performance measures of the weld joint. The range of each process parameter is decided by carrying out a number of trail experiments and examining weld bead appearance for acceptable weld joint. In the investigation of mechanical property of welded

Fig. 2 Tensile tested
samples

joint, response surface methodology (RSM)-based statistical modeling approach is
adopted for the model development.

2.4 RSM Modeling of UTS and **E**

RSM is one of the widely used mathematical and statistical techniques to model
and analyze engineering systems. It establishes quantifiable relationship between
numerous input variables and output responses [16]. This methodology aims to opti-
mize the output responses influenced by the controllable input factors. The experi-
ments are conducted as per Box-Behnken design matrix to develop the mathematical
models showing the relationship between the welding input parameter viz., WFR, *V*,
NTD and *S* and output responses viz., UTS and *E*. In general, the response measure
(*Y*) can be represented as a function of welding parameters as given in Eq. 1.

$$Y = \phi(\text{WFR, V, NTD, S}) \tag{1}$$

where the desired response is denoted *Y* and ϕ is response function.

Generalized response surface model for four welding input parameters is given
by Eq. (2).

$$Z = k_0 + \sum_{i=1}^{n} k_i x_i + \sum_{i=1}^{n} k_{ii} x_i^2 + \sum_{i=1}^{n} \sum_{j=1}^{n} k_{ij} x_i x_j + e, \tag{2}$$

Table 1 Experimental result

Std order	Test piece No.	Welding parameters				Mechanical property	
		WFR (m/min)	V (volt)	S (mm/min)	NTD (mm)	UTS (MPa)	E (%)
25	1	5	17	250	15	676	30.5
22	2	5	18	250	10	642	27.0
15	3	5	16	280	15	682	30.5
21	4	5	16	250	10	687	30.0
9	5	4	17	250	10	677	30.0
16	6	5	18	280	15	688	27.0
19	7	4	17	280	15	615	24.5
27	8	5	17	250	15	681	28.5
8	9	5	17	280	20	509	9.0
18	10	6	17	220	15	648	31.0
2	11	6	16	250	15	655	27.0
23	12	5	16	250	20	564	17.0
7	13	5	17	220	20	603	22.0
14	14	5	18	220	15	673	30.5
26	15	5	17	250	15	658	27.5
6	16	5	17	280	10	652	27.0
20	17	6	17	280	15	703	27.0
5	18	5	17	220	10	630	24.5
13	19	5	16	220	15	692	28.0
17	20	4	17	220	15	689	29.0
12	21	6	17	250	20	615	21.5
10	22	6	17	250	10	697	31.0
1	23	4	16	250	15	691	31.0
24	24	5	18	250	20	602	19.0
3	25	4	18	250	15	665	27.0
4	26	6	18	250	15	700	30.0
11	27	4	17	250	20	550	12.0

where x_i is the ith input parameter ($i = 1$–4), k_o is a free term, k_i, k_{ii} and k_{ij} correspond to the coefficients of linear, square and interaction terms, and e is error. The Minitab 18® was used for the analysis of computational work. The relationship of the model was obtained at a confidence level of 95%. The developed quadratic response surface models for UTS and E are given in Eqs. 3 and 4, respectively.

$$\text{UTS} = 6828 - 646\text{WFR} - 536\text{V} - 0.77\text{S} + 22.7\text{NTD}$$
$$+5.25\text{WFR} \times \text{WFR} + 9.75\text{V} - 0.01097\text{S} \times \text{S} - 2.175\text{NTD} \times \text{NTD}$$

$$+ 17.75\text{WFR} \times \text{V} + 1.075\text{WFR} \times \text{S} + 2.25\text{WFR} \times NTD + 0.208\text{V} \times \text{S}$$
$$+ 4.15\text{V} \times \text{NTD} - 0.1933\text{S} \times \text{NTD} \tag{3}$$

$R^2 = 93.21\%, \; R^2(\text{Adj}) = 85.28\%$

$E = 28 - 37.9\text{WFR} - 19.4\text{V} + 1.821\text{S} + 6.36\text{NTD} + 0.187\text{WFR} \times \text{WFR}$

$\quad 0.562\text{V} \times \text{V} - 0.00132\text{S} \times \text{S} - 2.475\text{NTD} \times \text{NTD} + 1.75\text{WFR} \times \text{V}$

$\quad 0.0042\text{WFR} \times \text{S} + 0.425\text{WFR} \times \text{NTD} - 0.0500\text{V} \times \text{S} + 0.250\text{V} \times \text{NTD}$

$\quad 0.02583\text{S} \times \text{NTD}$

$R^2 = 94.00\%, \; R^2(\text{Adj}) = 87.01\%$ $\hspace{4cm}$ (4)

The coefficient of determination (R^2) of response surface models developed for UTS and E is observed as 93.21% and 94.00%, while adjusted coefficient of determination ($R^2(\text{Adj})$) is obtained as 85.28% and 87.01%, respectively. Higher value of (R^2) and ($R^2(\text{Adj})$) indicates that the developed models adequately fit the experimental data and establish a strong relationship between input parameters and responses in GMAW process.

3 Results and Discussion

3.1 ANOVA Analysis

Analysis of variance (ANOVA) is used to check the model adequacy and significance of factors on response variable. In this study, ANOVA is performed at 95% confidence level. The p-value less than 0.05 for model and factor effects is considered as significant. The ANOVA result obtained for different models is summarized in Table 2. The NTD is found to have significant effect on UTS and E with contribution of 38.11% and 45.78%, respectively, while S, WFR and V are obtained as least influential factors.

3.2 Model Analysis

The relationship between the significant factors and responses of the GMAW process were analyzed by surface plots as depicted in Fig. 3a, b. The UTS value depends on HI of the weld and weld quality. Generally, the tensile strength of the weld joint has detrimental effect with increase in HI. At lower HI, sometimes the lower UTS is obtained due to the lack of fusion at the side wall of the welded joint, and as a result, the weld joint fails at that location. The higher NTD leads to decrease in welding current due to resistance of wire per unit length, which causes the reduction of HI

Table 2 ANOVA for responses for UTS and E

Response	Source	DOF	SS	MS	F-value	p-value	Contribution (%)
Ultimate tensile strength (UTS)	Model	14	59,876.2	4276.9	11.76	0.000	93.21
	WFR	1	1430.1	1430.1	3.93	0.071	2.23
	V	1	0.1	0.1	0.00	0.988	0.00
	S	1	616.3	616.3	1.69	0.217	0.96
	NTD	1	24,480.3	24,480.3	67.31	0.000	38.11
	NTD * NTD	1	15,768.7	15,768.7	43.36	0.000	24.55
	WFR * S	1	4160.3	4160.3	11.44	0.005	6.48
	V * NTD	1	1722.3	1722.3	4.74	0.050	2.68
	S * NTD	1	3364.0	3364.0	9.25	0.010	5.24
	Error	12	4364.4	363.7			6.79
	Total	26					
Elongation (E)	Model	14	814.708	58.193	13.44	0.000	94.00
	WFR	1	16.333	16.333	3.77	0.076	1.88
	V	1	0.750	0.750	0.17	0.685	0.09
	S	1	33.333	33.333	7.70	0.017	3.85
	NTD	1	396.750	396.750	91.63	0.000	45.78
	NTD * NTD	1	204.187	204.187	47.16	0.000	23.56
	S * NTD	1	60.062	60.062	13.87	0.003	6.93
	Error	12	51.958	4.330			6.00
	Total	26					

in the weld per unit length. From the Fig. 3a, b, it is observed that values of UTS and E increase with decreasing NTD. The increase in NTD decreases HI and causes the loss of metal in the form of spatters which results in the detrimental effects in weld quality. This reduction in weld quality reduces the UTS and E of the weld joint produced.

3.3　Parametric Optimization

In this work, desirability analysis (DA) is used for optimization of multiple responses viz., UTS and E to obtain the best settings of WFR, V, S and NTD during GMAW of AISI 201L-SS. Maximization of UTS and E using DA is implemented using response optimizer tool in Minitab 18 registered statistical software. In optimization using DA, individual desirability values calculated for each response are combined with weights assigned to obtain the composite or overall desirability for multi-response problem.

(a) UTS vs NTD, Speed   (b) Elongation vs NTD, Speed
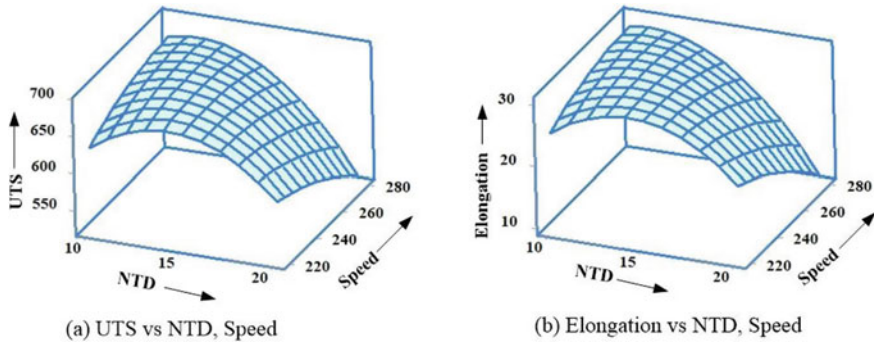
Fig. 3 a, b Surface plots

In this work, equal weightage (0.5) is assigned for both the responses. The parameter settings corresponding to the maximum composite desirability are considered as optimum. The optimization plot (also known as desirability plot) can be used to visualize the effect of change of parameter settings on the response variable. Desirability value (0–1) indicates how well the given parameter settings satisfies the defined optimization goal. Individual desirability is used to evaluate the effect of settings on a single response, whereas composite desirability is applied to assess impact of factor combinations on multiple responses. The desirability plot obtained in this present study for maximization of UTS and E is depicted in Fig. 4. The effect of weld parameters WFR, V, S and NTD on composite desirability and response variables is shown in the graph. The optimum factor settings yielding highest composite desirability are given. It can be seen that UTS and E can be maximized with weld parameter settings at WFR = 6 m/min, V = 18 V, S = 248.9 mm/min and NTD = 14.14 mm. The highest overall desirability is obtained as 1 at the optimum weld parameters settings. The maximum values of responses obtained at the optimum parameter settings are UTS = 714.68 MPa and E = 32.55%.

3.4 Microstructural Analysis

The microstructure examination of the base metal (AISI 201 LN) is carried out using microscope (Make: Leica). The surface of sample specimen was prepared by polishing with silicon carbide emery paper (grid size: 200–2400) followed by polishing by velvet cloth of 0.25 μm applying alumina paste to achieve a mirror-like finish. Figure 5a shows the microstructural image; it reveals the presence of austenitic twins in nitrogen alloyed ASS.

Figure 5b shows microstructural analysis of weld metal (test coupon 23). The etchant HNO_3, glycerol and HCl in 10:30:30 proportion were used to visualize weld profile. The weld strength (UTS and E) of test coupon 23 is 691 MPa and 31%. The corresponding weld parameters are 4 m/min, 16 V, 250 mm/min and 15 mm for WFR,
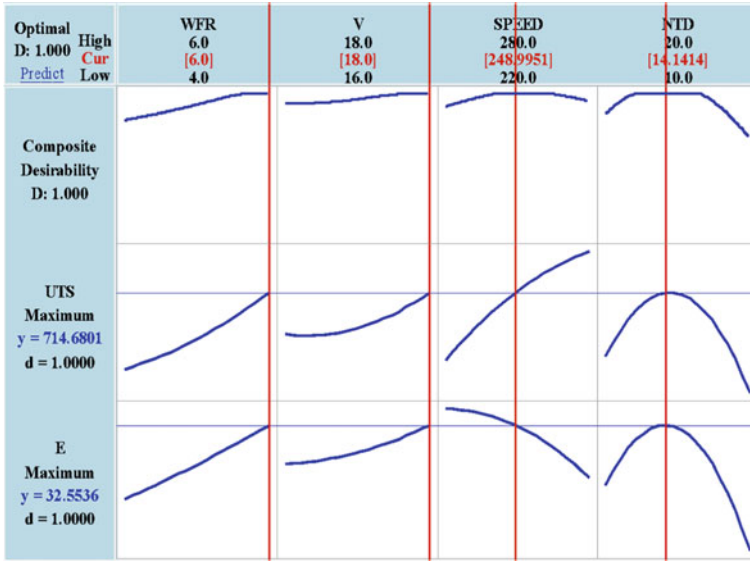
Fig. 4 Desirability plot for UTS and E

(a) Base metal   (b) Welded test coupon 23
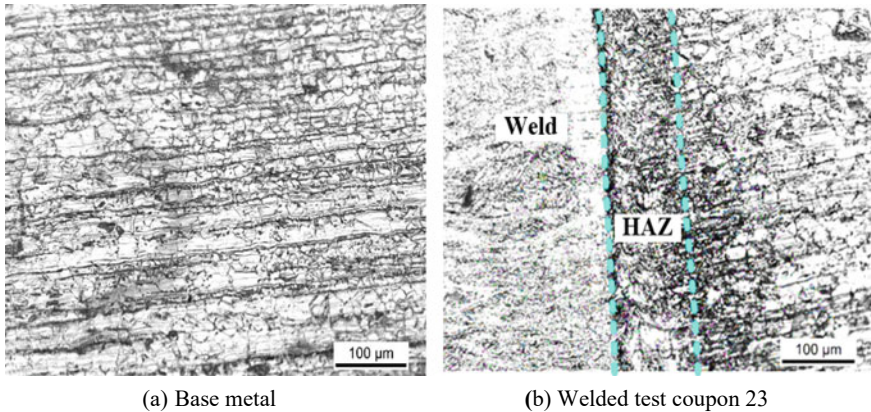
Fig. 5 Microstructural analysis

V, S and NTD, respectively. The NTD = 15 mm is found desirable for obtaining superior weld quality. However, the microstructural analysis of welds having significant impact on heat input (HI); low HI forms finer dendritic structure in the HAZ region of the weld joint due to higher cooling rate. The superior weld strength was obtained due to the presence of finer structure in the weld and HAZ region.

The scanning electron microscope (SEM) image of tensile tested specimen (test coupon 23) is shown in Fig. 6. The SEM (Make Zeiss EVO 18) was used for obtaining
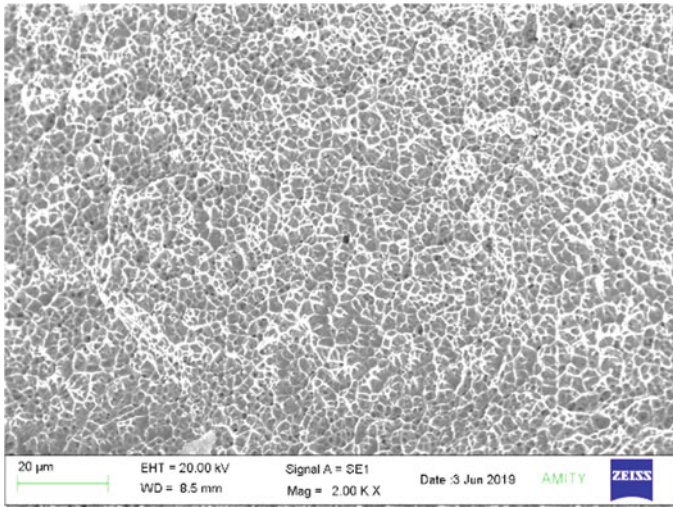
Fig. 6 SEM fractography of test coupon 23

fractured tensile surface morphology. The image confirms the presence of dimple structure in the fractured sample. The fine dimples are noticed in the image confirms higher UTS value and the elongation. The finer dimples formation is influenced by the faster cooling rate resulted from the weld.

4 Conclusions

In this study the strength of weld joint during GMAW of AISI 201LN-SS is investigated. Twenty-seven experiments were conducted by varying four weld parameters (i.e., WFR, V, NTD and S), and UTS and E of weld joint are evaluated. The following are important conclusions drawn.

- The developed full quadratic RSM predictive models showed good correlation between input and output variables with R^2 value of 93.21% and 94.00% for UTS and E, respectively.
- The input variable NTD is obtained as the most influencing parameter effecting both UTS and E. The increase in NTD decreases HI and causes the loss of metal in the form of spatters which results in the detrimental effects in weld quality.
- The ANOVA result showed significant contribution of NTD for UTS (38.11%) and E (45.78%), while S and V are obtained as the least influential factors.
- The optimum weld parameters for multi-response optimization (maximization of UTS and E) were obtained as WFR = 6 m/min, V = 18 V, S = 248.9 mm/min and NTD = 14.14 mm, respectively, with highest overall desirability of one (1).

The response variables at the optimum weld parameter settings were recorded as UTS = 714.68 MPa and $E = 32.55\%$.

- The microstructural analysis of welds shows finer dendritic structure in the HAZ region with low HI condition, which is resulted due to higher cooling rate. The fractured test sample image confirms the presence of dimple structure in the fractured sample.

References

1. Arutunow, A., Darowicki., K.: Impact of sensitization on dissolution process of AISI 304 stainless steel during intergranular corrosion evaluated using DEIS technique. J. Solid State Electrochem. 1687–1694 (2009). https://doi.org/10.1007/s10008-008-0642-z
2. Kumar, S., Shahi, A.S.: Effect of heat input on the microstructure and mechanical properties of gas tungsten arc welded AISI 304 stainless steel joints. Mater. Des. **32**, 3617–3623 (2011). https://doi.org/10.1016/j.matdes.2011.02.017
3. Vashishtha, H., Taiwade, R.V., Khatirkar, R.K., et al.: Welding behaviour of low nickel chrome-manganese stainless. ISIJ Int. **54**, 1361–1367 (2014)
4. Vashishtha, H., Taiwade, R.V., Sharma, S., Patil, A.P.: Effect of welding processes on microstructural and mechanical properties of dissimilar weldments between conventional austenitic and high nitrogen austenitic stainless steels. J. Manuf. Process. **25**, 49–59 (2017). https://doi.org/10.1016/j.jmapro.2016.10.008
5. Singh, V., Chandrasekaran, M., Samanta, S., Palanikumar, K.: Welding investigation on GMAW− cold metal transfer of AISI 201LN for superior weld quality. Int. J. Manuf. Mater. Mech. Eng. **10**, 1–12 (2020). https://doi.org/10.4018/IJMMME.2020100101
6. Cruz, J.G., Torres, E.M., Absi Alfaro, S.C. :Modelling and control of weld height reinforcement in the GMAW process. J. Braz. Soc. Mech. Sci. Eng. **40**, 1–9 (2018). https://doi.org/10.1007/s40430-018-1080-1
7. Kanti, K.M., Rao, P.S.: Prediction of bead geometry in pulsed GMA welding using back propagation neural network. J. Mater. Process. Technol. **200**(1–3), 300–305(2007). https://doi.org/10.1016/j.jmatprotec.2007.09.034
8. Zhang, Y., Wu, L. :Measurement and estimation of weld pool surface depth and weld penetration in pulsed gas metal arc welding. Weld J. 117s–126s (2010)
9. Kamble, A.G., Rao, R.V.: Experimental investigation on the effects of process parameters of GMAW and transient thermal analysis of AISI321 steel. Adv. Manuf. **1**, 362–377 (2013). https://doi.org/10.1007/s40436-013-0041-2
10. Naik, A.B., Reddy, A.C.:Optimization of tensile strength in TIG welding using the Taguchi method and analysis of variance (ANOVA). Therm. Sci. Eng. Prog. **8**, 327–339 (2018). https://doi.org/10.1016/j.tsep.2018.08.005
11. Palanivel, R., Dinaharan, I., Laubscher, R.F.: Application of an artificial neural network model to predict the ultimate tensile strength of friction-welded titanium tubes. J. Braz. Soc. Mech. Sci. Eng. **41** (2019). https://doi.org/10.1007/s40430-019-1613-2
12. Xu, W.H., Lin, S.B., Fan, C.L., et al.: Statistical modelling of weld bead geometry in oscillating arc narrow gap all-position GMA welding. Int. J. Adv. Manuf. Technol. **72**, 1705–1716 (2014). https://doi.org/10.1007/s00170-014-5799-2
13. Son, J.S., Kim, I.S., Kim, H.H., et al.: A study on the prediction of bead geometry in the robotic welding system. J. Mech. Sci. Technol. **21**, 1726–1731 (2007). https://doi.org/10.1007/BF03177401
14. Saha, P., Waghmare, D.: Parametric optimization for autogenous butt laser welding of sub-millimeter thick SS 316 sheets using central composite design. Opt. Laser Technol. **122**, 105833 (2020). https://doi.org/10.1016/j.optlastec.2019.105833

15. Conesa, M.E.J., Egea, J.A., Miguel, V., et al.: Optimization of geometric parameters in a welded joint through response surface methodology. Constr. Build. Mater. **154**, 105–114 (2017). https://doi.org/10.1016/j.conbuildmat.2017.07.163

16. Aslan, N., Cebeci, Y.: Application of Box-Behnken design and response surface methodology for modeling of some Turkish coals. Fuel **86**, 90–97 (2007). https://doi.org/10.1016/j.fuel.2006.06.010

Experimental Investigations of CO$_2$ Laser Beam Welded Joints of AISI 304 and AISI 4130 Steels

B. Narayana Reddy and **P. Hema**

1 Introduction

A variety of metals are being used for large scale manufacturing/production of products in the industrial sector to meet the global market demand with the possibility of improving the quality at lower costs. Such phenomenon has resulted in the investigation of modern technologies to weld dissimilar metals for large scale industrial applications. Amongst the present, existing welding techniques, LBW has received increased attention [1]. The behaviour of the laser beam helps to achieve high power density so as to focus onto a small spot. LBW has got more advantages compared to other processes of welding [2]. Small distortions and low residual stresses are developed in the narrow heat affected zone due to reduced energy transfer, while the high-intensity power leads to the production of keyholes. Improved mechanical properties are seen at a high cooling rate within fine microstructures in welding of dissimilar metals followed by the cost reduction while working with automobile components, aerospace, etc.

Dissimilar metals are generally utilized in power plants, chemical and oil plants, electronic and nuclear industries due to the reason of tailoring components with weight reduction [1]. Such dissimilar metal welds have been employed for welding steel pipe systems and alloy steel reactor pressure vessels used in water-based reactors and ships [3]. The development of certain metallurgical phases of joining of different metals like Austenitic AISI304 and AISI4130 steels results in a decrease in mechanical and useful properties of joints due to thermal conductivity, metallurgical defects and melting point, in addition to the solubility of alloying elements, leads to

B. Narayana Reddy (✉)

Department of Mechanical Engineering, Sai Rajeswari Institute of Technology, Proddatur, India
e-mail: nari.biju@gmail.com

P. Hema
SV University College of Engineering, Tirupati, India

cracking. Therefore, it is necessary to precisely manage not only the procedure but also input process parameters [4].

2 Literature Survey

Extensive research has been conducted on LBW including laser beam delivery systems and mechanical behaviour of welded joints. The weld joint protecting gas and gas flow rate has less influence on bead width and depth of penetration (DOP) [5]. Bead width and DOP increase with the increase in beam power, whereas bead width decreases as the welding speed rises [5]. The optimal welding conditions are identified in order to raise productivity and reduce total operating costs. Laser power between 1200 and 1230 W is needed to get better weld on AISI 304 steel joints [2]. The duty cycle of the LBW machine cannot exceed 98.38%, so as to obtain a good joint of dissimilar metals [6]. In the joining of AISI 304 and AISI4140 by EBW, GTAW and FRW, welding speed has a significant impact on fusion size, which is inversely related to UTS [3].

The welding of two metals like low carbon and austenitic steels by CO_2 laser by changing laser power, welding speed and focal point position requires detailed study [7]. Though various methods are available to design the experimental process, the DOE is at the forefront. Taguchi method with orthogonal array has been used to study the effects of process parameters on the weld bead geometry [8]. A numerical model was proposed to forecast the outcomes adequately within boundaries of the parameters of the welding that are used in the regression equations and to identify the welding optimum conditions for the desired geometric criteria of weld bead joints [9]. Though, low-cost welds help to obtain efficient numerical optimal welding conditions [1]. The extent to which the laser beam position has shifted from AISI420 steel to AISI304 steel leads to a gradual reduction in hardness along the weld zone cross-section during the parametric optimisation in welding of Inconel and stainless steel by fuzzy logic [10] and then compared with ANOVA [11]. Then, it is found that the thickness of fusion zone and HAZ in TIG welding is ten times larger than that of laser welding of alloy steel AISI 4130 [9]. It is also observed that there is a recovery in metal ductility particularly after laser welding [8]. More information can be obtained from laser weld technology—status and prospects [12] and the role of the laser beam in welding and assembly [13], a recent publication in this field.

2.1 Objective of the Research Paper

According to the literature review, it has been noticed that there are a limited number of studies relating to the effect of parameters like laser power (LP), welding speed (WS), beam angle (BA), focal point position (FPP) and focal length (FL) on mechanical properties and bead width of LBW weld joints. Therefore, the present study is

made with a solemn objective to conduct experiments and examine the influence of input parameters on the mechanical properties such as ultimate tensile strength (UTS), impact strength (IS), micro-hardness (MH) and bead width (BW) on the dissimilar metals joints obtained by LBW. The ANOVA carried outdoor to obtain influencing factors. The optimal combination of input parameters is identified by using whale optimisation algorithm, so as to validate the experimental results.

3 Experimental Process

3.1 Metals Selections

The first step starts with ith selection of metals for experimentation. AISI 304 stainless steel and AISI 4130 alloy steel plates are taken for the investigation. The dimensions of the plates consist of $140 \times 100 \times 2$ mm. Then, the specimen is prepared (cut) to require dimensions by wire in ordered to obtain smooth edges to achieve close and qualitative joints. Experiments relating to the welding of two different metals AISI 304 and AISI 4130 steel by CO$_2$ LBW machine are carried-out on Trumpf Lasercell-TLC1005. Specifications of the machine are shown in Table 1 followed by actual experimental setup in Fig. 1. The L$_{25}$ experiments are conduced based on process parameters, and their levels are shown in Table 2.

Specimen plates of two dissimilar metals, AISI 304 and AISI 4130 steel sheets are abutted together for joining by CO$_2$ laser beam. The plate edges are prepared after cleaning with acetone and then ensured that the contact gap is maintained along weld line of LBW. To avoid any distortion due to heat stress, the specimen plates are clamped rigidly. Based on the experimental design levels of process parameters (Table 3), experiments are repeated till 25 joints which are obtained. Few samples of the joints obtained by LBW are shown in Fig. 2.

Table 1 CO$_2$ LBW machine specifications

Parameter	Specification
Power range (W)	200–4000
Wave length (μm)	10.6
Flow pressure (bar)	15
Beam dia (mm)	2
Frequency (Hz)	20,000
Shielding gas	Argon (Ar)

Fig. 1 Experimental setup

Table 2 Process parameters with levels

Levels	LP (watts)	WS (m/min)	BA (degrees)	FPP (mm)	FL (mm)
1	1400	1.2	87	− 0.2	16
2	1600	1.4	89	− 0.1	17
3	1800	1.6	90	0	18
4	2000	1.8	91	0.1	19
5	2200	2.0	93	0.2	20

4 Weld Joint Testing

The weld joint strength is measuring by UTS, IS and MH. Those examination samples are processed as per standards of ASTM E8 (UTS) and ASTM E23-07(IS) wire cut EDM [13]. Tensile tests are conducted on FIE universal tensile machine, and tested UTS samples are shown in Fig. 3. Similarly, the impact strength is tested on FIE Charpy impact machine at room temperature and tested samples are shown in Fig. 4.

The samples for Vickers micro-hardness are encapsulated in plastic mould using hot mounting press and are shown in Fig. 5. The samples are tested for hardness on Wolpert micro-Vickers tester 402-MVD. The Struers welding expert system measures the weld geometry by measuring the bead width of the weld joint using macrographs acquired at 20X magnification (Fig. 6). Experimental test results of IS, UTM, MH and BW for each sample are presented in Table 3.

Table 3 Experimental results from laser beam welding

S. No.	Input process parameters					Output responses			
	LP (W)	WS (m/min)	BA (degrees)	FPP (mm)	FL (mm)	UTS (MPa)	IS (J)	MH (HV1)	BW (mm)
1	1400	1.2	87	− 0.2	16	656.8	15.2	452	1.3054
2	1400	1.4	89	− 0.1	17	645.6	14	548	1.2816
3	1400	1.6	90	0.0	18	645.6	14.8	530	1.1504
4	1400	1.8	91	0.1	19	542.4	13.6	525	1.1125
5	1400	2.0	93	0.2	20	296.8	12	621	1.0090
6	1600	1.2	89	0.0	19	344.8	12.8	636	1.1883
7	1600	1.4	90	0.1	20	644.8	14.8	484	1.1089
8	1600	1.6	91	0.2	16	525.6	18	539	1.1029
9	1600	1.8	93	− 0.2	17	545.6	16	528	1.1210
10	1600	2.0	87	− 0.1	18	232.8	18	531	1.1059
11	1800	1.2	90	0.2	17	584	18	482	1.1805
12	1800	1.4	91	− 0.2	18	524.8	16	541	1.2194
13	1800	1.6	93	− 0.1	19	668.8	18	459	1.3856
14	1800	1.8	87	0.0	20	646.4	16	548	1.1986
15	1800	2.0	89	0.1	16	639.2	16	536	1.1259
16	2000	1.2	91	− 0.1	20	672	18	474	1.2894
17	2000	1.4	93	0.0	16	671.2	16.8	438	1.3158
18	2000	1.6	87	0.1	17	650.4	19.2	454	1.3506
19	2000	1.8	89	0.2	18	645.6	12	529	1.3546
20	2000	2.0	90	− 0.2	19	336.8	12	518	1.2884

(continued)

Table 3 (continued)

S. No.	Input process parameters						Output responses				
	LP (W)	WS (m/min)	BA (degrees)	FPP (mm)	FL (mm)		UTS (MPa)	IS (J)	MH (HV1)	BW (mm)
21	2200	1.2	93	0.1	18		460	12.8	584	1.3594
22	2200	1.4	87	0.2	19		644.8	18	527	1.3982
23	2200	1.6	89	− 0.2	20		608	13.2	525	1.3775
24	2200	1.8	90	− 0.1	16		672.8	20	652	1.3561
25	2200	2.0	91	0.0	17		644.8	13.6	520	1.1849

Fig. 2 Samples of joints produced by CO$_2$ LBW experiments
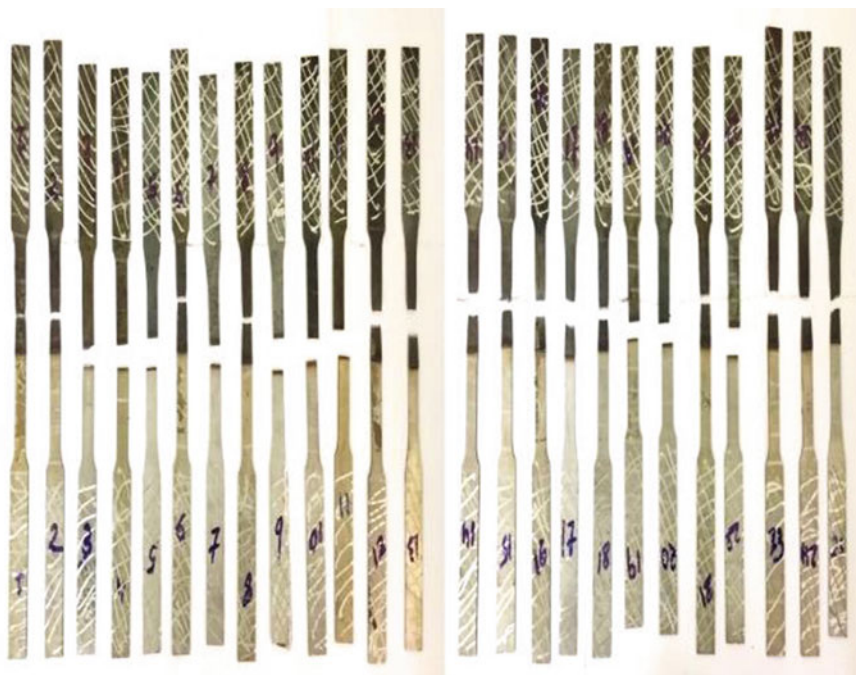
Fig. 3 UTS measured weld samples

5 Results and Discussions

Based on the experimental results, ANOVA test performed and performance curves are drawn and discussed in the following.

Fig. 4 IS measured weld samples

Fig. 5 Mounted weld samples
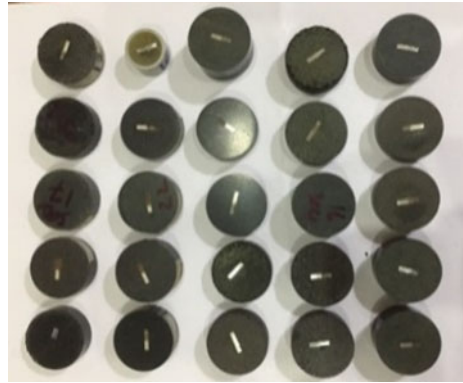
Fig. 6 Weld geometry measuring 20X macrographs
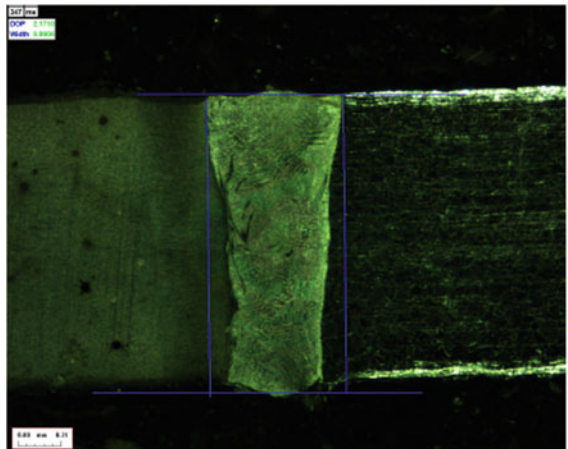
5.1 ANOVA Results and Discussions

ANOVA is carried-out on the input process parameters influence on the weld joints at 95% confidence level as shown in Tables 4, 5, 6 and 7. From the UTS ANOVA Table 4, it is clear from the experimentation that the percentage contribution of each parameter are LP—25.52%, WS—21.54%, BA—12.80%, FPP—30.06% and FL—8.73%. It is observed that the FPP has the most influence on UTS at R^2 = 98.7% of reliability of experiments. P values are smaller than 5%, based on the input process parameters have a substantial influence on the laser weld joints at 95% confidence level.

Similarly from IS (Table 5), MH (Table 6) and BW (Table 7) ANOVA tables, the LP has the most influence on IS at 32.52%, MH at 21.89% and BW at 26.92%. In the ANOVA tables, reliability of experiments R^2 values also above 90%. P values are smaller than 5%, based on the process parameters have a substantial influence on the weld joints at 95% confidence level.

Table 4 ANOVA results of UTS

S	DF	SS	F value	P value	% C
LP	4	57,835	19.31	0.007	25.52
WS	4	48,799	16.29	0.010	21.54
BA	4	28,999	9.68	0.025	12.80
FPP	4	68,120	22.74	0.005	**30.06**
FL	4	19,794	6.61	0.047	8.73
E	4	2996			
T	24	226,543	R-Sq = 98.7%		

Table 5 ANOVA results of IS

S	DF	SS	F value	P value	% C
LP	4	71.76	20.74	0.006	32.52
WS	4	24.06	6.95	0.043	10.90
BA	4	27.36	7.91	0.035	12.40
FPP	4	38.96	11.26	0.019	17.66
FL	4	55.06	15.91	0.010	24.95
E	4	3.46			
T	24	220.66	R-Sq = 98.4%		

Table 6 ANOVA results of MH

S	DF	SS	F value	P value	% C
LP	4	15,598	11.93	0.017	**21.89**
WS	4	15,158	11.59	0.018	21.27
BA	4	14,243	10.89	0.020	19.99
FPP	4	15,453	11.82	0.017	21.69
FL	4	9483	7.25	0.041	13.3
E	4	1308			
T	24	71,243	R-Sq $= 98.2\%$		

Table 7 ANOVA results of BW

S	DF	SS	F value	P value	% C
LP	4	0.0349	36.32	0.002	**26.92**
WS	4	0.0201	20.94	0.006	15.50
BA	4	0.0282	29.34	0.003	21.75
FPP	4	0.0278	28.91	0.003	21.45
FL	4	0.0177	18.38	0.008	13.65
E	4	0.0010			
T	24	0.1296	R-Sq $= 99.3\%$		

5.2 Effect of Process Parameters on Output Responses

The output responses for various strengths are used to build performance curves, as detailed below.

(a) **Laser Power (LP)**

The effect of LP on IS, UTS, MH and BW is depicted in Fig. 7 by performance plots.
From the graph in Fig. 7, it can be seen that as the LP increases from 1400 to 2000 W, the output characteristics are increasing. But when LP reaches 2000 W, the output of UTS, IS, MH and BW has reached maximum. This is due to the increase in heat input when beam power increases resulting in more melting of base material [14]. Increasing the laser mean power increases the penetration depth and the area of the fusion zone changing [15].

(b) **Welding Speed (WS)**

As illustrated in Fig. 8, performance curves for the influence of WS on UTS, IS, MH and BW are drawn. From the graph, it is observed that as the WS increases from 1.2 m/min to 2.0 m/min, the output characteristics UTS, IS, MH are also increasing up to 1.8 m/min. But when WS touches 1.8 m/min, the UTS, IS and MH have attained maximum and then falls after speed of 1.8 m/min, which shows the maximum output characteristic are attained at 1.8 m/min. The BW is decreasing, when welding speed
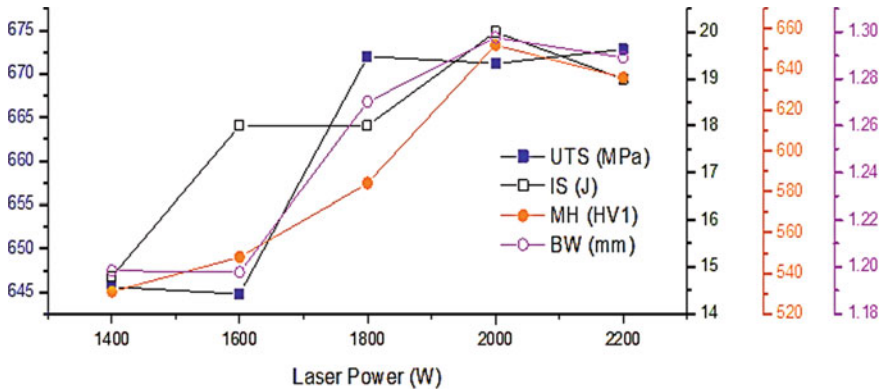
Fig. 7 Performance characteristic plots for LP

increasing. It is seen that as the WS increases depth of penetration, bead width and area of penetration decreases, because of time of exposure of laser energy on the workpiece decreases [7, 14].

(c) **Beam Angle (BA)**

As illustrated in Fig. 9, performance plots for the influence of BA on IS, UTS and MH are drawn.

From the graphs, Fig. 9, it can be seen that as the BA increases from 88° to 92°, the output characteristics UTS, IS, MH and BW are increases up to beam angle 91°. Since the beam is pointed in the direction of the welding, it preheats the edges of the joint, as the beam angle is changed in direction the join of laser beam to material decreases and hence, the responses are increased.
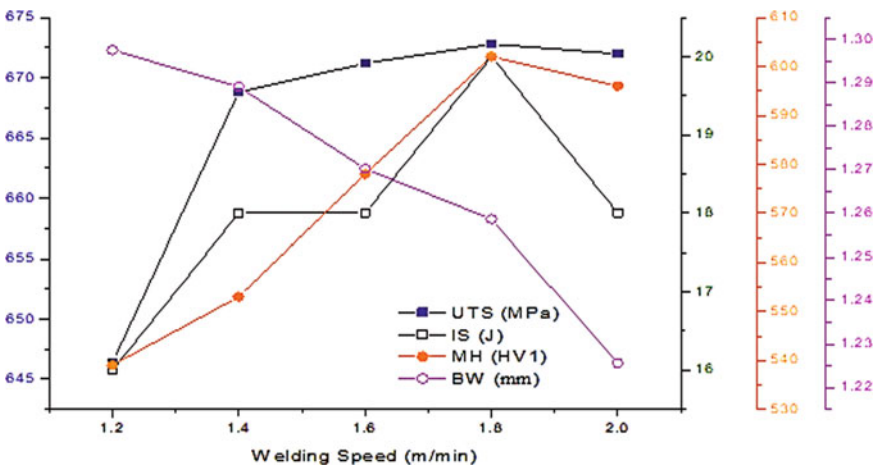
Fig. 8 Performance characteristic plots for WS
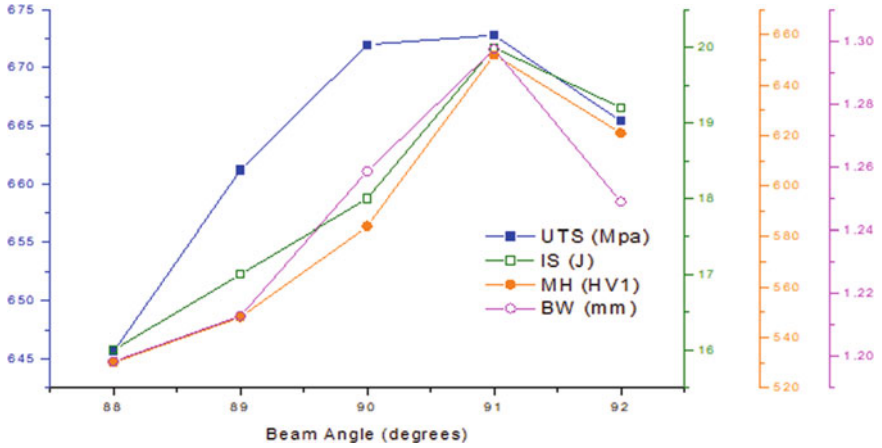
Fig. 9 Performance characteristic plots for BA

(d)   **Focal Point Position (FPP)**

Figure 10 shows performance plots for the influence of FPP on UTS, IS, MH and BW.

From the graph, Fig. 10, it can be observed that the FPP has a significant influence on UTS, IS, MH and BW. In addition, it can be observed that when FPP fluctuates from − 0.2 to 0.2 mm, UTS, IS, MH and BW are increase with an increase in FPP up to 0.1 mm. Further, increase in FPP leads to decrease in UTS, IS, MH and BW. From Fig. 10, it is also evident that the UTS, IS, MH and BW are maximum at the FPP
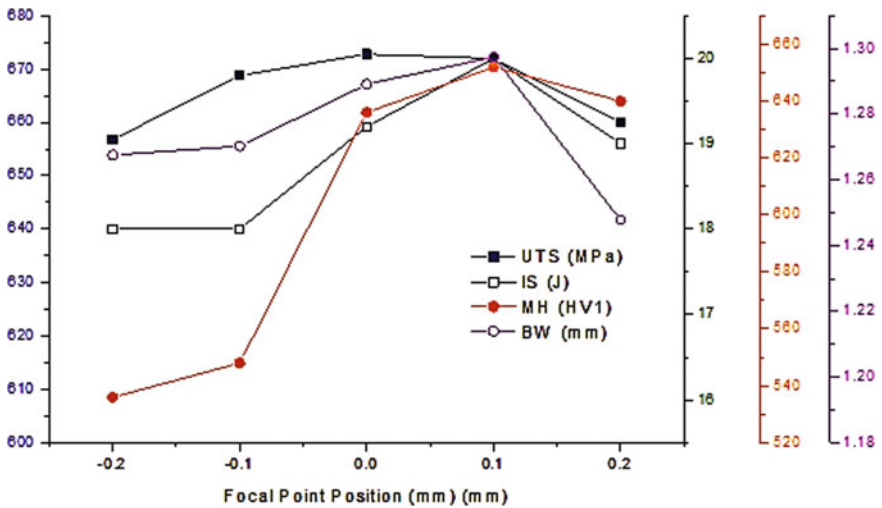
Fig. 10 Performance characteristic plots for FPP
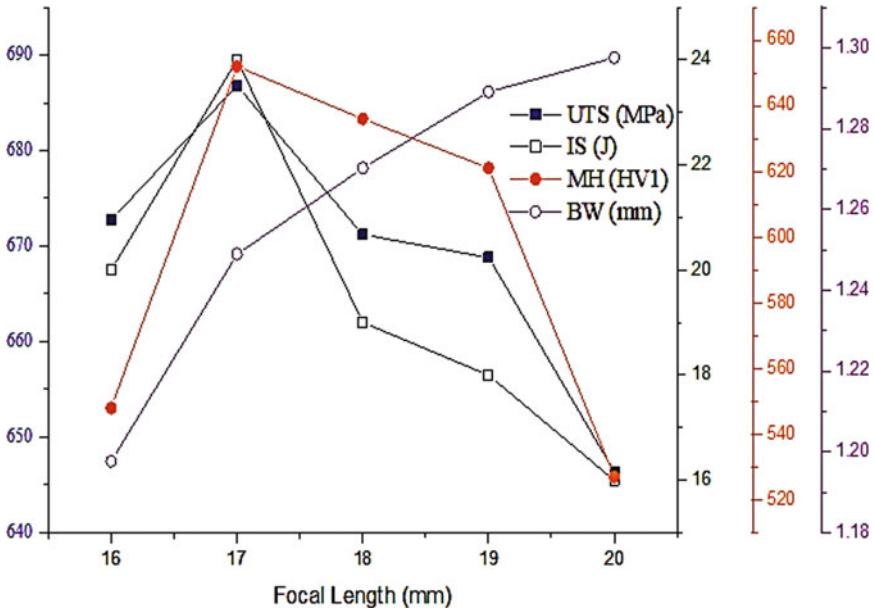
Fig. 11 Performance characteristic plots for FL

of − 0.1 mm. When the beam is focussed towards higher levels, a decreasing trend is observed in the three characteristics, which decrease up to 0 (zero) focal position. Later on, except the MH, the other two decrease as the FPP shifts towards higher point positions.

(e) **Focal Length (FL)**

As illustrated in Fig. 11, performance plots for the influence of FL on IS, UTS and MH are drawn.

From the graph, Fig. 11, it can be observed that as the FL varies from 16 to 20 mm, the output characteristics, IS, UTS and hardness slightly decrease with an increase in FL after 17 mm. But when FL increases from 16 to 20 mm, the BW increases with a fall in UTS, IS, MH. Subsequently, only the BW is increased with the laser intensity of light. The laser welding usually needs some FL, because too high power density of the beam centre at the laser focus is easy to vaporize. When the focus distance reduces to a certain value, the melting depth will suddenly change. So it has important influences to the melting depth and beam shapes. The FL is increases weld joint BW also increased, and the UTS, IS and MH are decreased [13].

6 Optimization

Based on the obtained experimental results, the input parameters are analysed to obtain optimum conditions using whale optimisation algorithm [4] as explained in the following sectors.

6.1 *Whale Optimization Algorithm*

An adult hump back whale is almost equivalent in size to that of school bus, and its favourite duty is to kill small fish's herds. Such behaviour is only investigated based on the observation from surface earlier to 2011. Later on, the investigations have revealed manoeuvres associated with bubble and named them 'upward-spirals' and 'double loops'. The bubble-net feeding is a unique and important behaviour that is observed in hump back whales. Accordingly, whale optimization algorithm is applied to find the best result to achieve the objective using regression equations and its boundaries. Such a spiral bubble-net feeding manoeuvre, in the present work, is mathematically modelled in order to achieve the optimization.

Nonlinear regression equations developed in Minitab for optimisation, for single objective function, are given in Eqs. (1), (2), (3) and (4).

$$
\begin{aligned}
\text{UTS} = {} & 133490 - (3.28 \times \text{LP}) + (630 \times \text{WS}) - (876 \times \text{BA}) \\
& + (755 \times \text{FPP}) + (22 \times \text{FL}) - \left(0.000074 \times \text{LP}^2\right) \\
& - \left(43 \times \text{WS}^2\right) + \left(15.4 \times \text{BA}^2\right) - \left(2241 \times \text{FPP}^2\right) \\
& - \left(4.6 \times \text{FL}^2\right) + (0.078 \times \text{LP} \times \text{WS}) + (0.0328 \times \text{LP} \times \text{BA}) \\
& - (0.960 \times \text{LP} \times \text{FPP}) + (0.0343 \times \text{LP} \times \text{FL}) + (539 \times \text{WS} \times \text{FPP}) \\
& - (43.2 \times \text{WS} \times \text{FL}) + (1.44 \times \text{BA} \times \text{FL})
\end{aligned}
\tag{1}
$$

$$
\begin{aligned}
\text{IS} = {} & 753 - (0.388 \times \text{LP}) + (136.3 \times \text{WS}) - (13.5 \times \text{BA}) \\
& - (2.8 \times \text{FPP}) + (13.4 \times \text{FL}) - \left(0.006 \times \text{LP}^2\right) \\
& - \left(9.38 \times \text{WS}^2\right) + \left(0.047 \times \text{BA}^2\right) + \left(93.2 \times \text{FPP}^2\right) \\
& + \left(0.84 \times \text{FL}^2\right) - (0.01759 \times \text{LP} \times \text{WS}) + (0.00585 \times \text{LP} \times \text{BA}) \\
& + (0.0120 \times \text{LP} \times \text{FPP}) - (0.00503 \times \text{LP} \times \text{FL}) - (16.7 \times \text{WS} \times \text{FPP}) \\
& - (4.17 \times \text{WSxFL}) - (0.313 \times \text{BA} \times \text{FL})
\end{aligned}
\tag{2}
$$

$$
\begin{aligned}
\text{MH} = {} & 31745 + (3.14 \times \text{LP}) - (228 \times \text{WS}) - (549 \times \text{BA}) + (433 \times \text{FPP}) \\
& - (1084 \times \text{FL}) + \left(0.000186 \times \text{LP}^2\right) - \left(121 \times \text{WS}^2\right) + \left(2.7 \times \text{BA}^2\right) \\
& + \left(617 \times \text{FPP}^2\right) + \left(8.89 \times \text{FL}^2\right) + (0.069 \times \text{LP} \times \text{WS})
\end{aligned}
$$

$$- (0.0423 \times LP \times BA) + (0.430 \times LP \times FPP) - (0.0107 \times LP \times FL)$$
$$- (762 \times WS \times FPP) + (29.9 \times WS \times FL) + (8.26 \times BA \times FL) \qquad (3)$$

$$BW = -94 + (0.0113 \times LP) + (3.2 \times WS) + (2.00 \times BA) + (3.3 \times FPP) -$$
$$(0.88 \times FL) + (0.000001 \times LP^2) + (0.251 \times WS^2) - (0.0097 \times BA^2)$$
$$- (0.16 \times FPP^2) + (0.0337 \times FL^2) - (0.00024 \times LP \times WS)$$
$$- (0.000093 \times LP \times BA) + (0.00403 \times LP \times FPP)$$
$$- (0.000313 \times LP \times FL) - (0.061 \times WS \times BA)$$
$$+ (0.28 \times WS \times FPP) + (0.106 \times WS \times FL)$$
$$- (0.041 \times BA \times FPP) + (0.0010 \times BA \times FL) - (0.442 \times FPP \times FL)$$
$$(4)$$

Multi-objective Functions

After generating the UTS, IS, MH and BW eq., the multi-objective mathematical model is constructed by using weighted method. The weighted coefficient considered as Wi without affecting the accuracy of the models.

$$Min.Z = (W_1Y_1) + (W_2Y_2) + (W_3Y_3) + (W_4Y_4)$$
$$Wi = 0.25, \; i = 1, 2, 3, 4. \qquad (5)$$

$$Y_1 = \text{Max. UTS}, \; Y_2 = \text{Max. IS}, \; Y_3 = \text{Max. MH and } Y_4 = \text{Min. BW}.$$
$$Min.\ Z = -(0.25 \text{ x UTS}) - (0.25 \times IS) - (0.25 \times MH) + (0.25 \times BW) \qquad (6)$$

The multi-objective is used in the present work to model and find the optimum welding parameters for comparison and validation of experimental results. The optimisation of search procedure in joining of two metals of AISI 4130 with AISI 304 weld joints by using Eq. 6. Equation 6 using to run the WOA programme is shown in Fig. 12. Table 8 shows the WOA optimum combination of process parameters for five sets. Confirmation test results at optimal condition based on those 5 experiments are conducted. The WOA values and confirmation test experimental values are shown in Table 9.

Validation

Validation is a process necessary in any research to show the trueness of the model results and experimental results. χ^2—test is conducted to validate the results at 5% of significance level. (95% confidence level) as9
described in the following.

$$\chi^2 = \sum \left[\frac{(f_o - fe)^2}{fe} \right] \qquad (7)$$
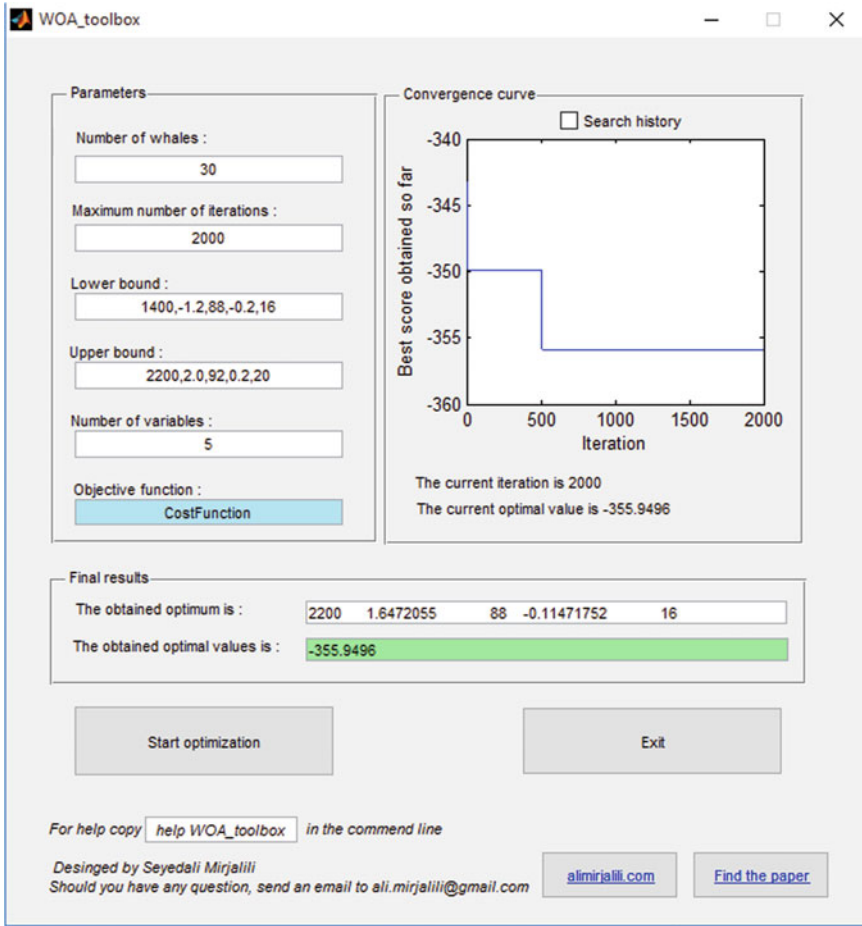
Fig. 12 Optimisation of AISI 4130 and AISI 304 weld joint

Table 8 WOA optimum results of AISI 4130 and AISI 304 weld joint

S. No.	LP(W)	WS(m/min)	BA	FPP(mm)	FL(mm)	UTS(MPa)	IS (J)	MH(HV1)	BW(mm)
1	2200	1.6472	88°	− 0.1147	16	634.30	17.664	624.15	1.3243
2	2200	1.6472	88°	− 0.1147	16	614.43	17.03	589.65	1.02
3	1400	1.2317	88°	0.0543	16	625.10	11.85	614.12	1.15
4	1400	1.2317	88°	0.0543	16	625.10	11.85	614.12	1.15
5	2200	1.6472	88°	− 0.1147	16	634.30	17.66	624.15	1.02

Table 9 χ^2—test for optimum results of AISI 4130 weld joints

S. No.	UTS (MPa)			IS (J)			MH (HV1)			BW (mm)		
	f_o	f_e	χ^2	f_o	f_e	χ^2	f_o	f_e	χ^2	f_o	f_e	χ^2
1	634.31	672	2.11	17.66	18	0.01	524.15	504	0.8	1.32	1.29	0.00
2	614.43	671.2	4.80	17.04	16.8	0.00	489.66	518	1.55	1.03	1.32	0.06
3	625.11	650.4	0.98	11.85	19.2	2.81	514.12	554	2.87	1.16	1.35	0.03
4	625.11	645.6	0.65	11.85	12	0.00	514.12	529	0.42	1.16	1.35	0.03
5	634.31	536.8	0.01	17.66	12	2.67	524.15	518	0.07	1.02	1.29	0.05
	$\chi^2_{calculate} =$		8.55	$\chi^2_{calculate} =$		5.49	$\chi^2_{calculate} =$		5.71	$\chi^2_{calculate} =$		0.17

where f_o—model observed values and f_e—expected values (experimental values).

From Table 9, the χ^2 calculate = 8.5589 and χ^2-Table = 9.488 at 5% of significant level. Since, the χ^2 calculate value is less than the table value, the null hypothesis is accepted. Thus, the validation is carried-out to show the trueness of the WOA output values in joining of two metals AISI 4130 and AISI 304. Therefore, WOA optimum results and experimental values are accepted. Similarly, the χ^2—test is conducted on the IS, MH and BW.

Table 10 shows the % of error value observe vs experimental values and form all the date as '–ve' error. It cleans stages that the experimental values are higher than the actuals for majorly of experimental levels.

It is observed that the maximum UTS 634.3087 MPa, IS 17.6613 J and MH 624.1529 HV1 followed by minimum bead width 1.0243 mm with input parameters of LP 2200 W, WS 1.6472 m/min, BA 88º, FPP − 0.1147 mm and FL16 mm. Therefore, optimal combination of the AISI 4130 and AISI 304 weld joint process parameters identified from the WOA is shown in Table 8.

Table 10 Error table

S No	UTS (MPa)			IS (J)			MH (HV1)			BW (mm)		
	f_o	f_e	Error	f_o	f_e	Error	f_o	f_e	Error	f_o	f_e	Error
1	634.31	672	− 5.61	17.66	18	− 1.89	524.15	504	4.00	1.32	1.29	2.33
2	614.43	671.2	− 8.46	17.04	16.8	1.43	489.66	518	− 5.47	1.03	1.32	− 21.97
3	625.11	650.4	− 3.89	11.85	19.2	− 38.28	514.12	554	− 7.20	1.16	1.35	− 14.07
4	625.11	645.6	− 3.17	11.85	12	− 1.25	514.12	529	− 2.81	1.16	1.35	− 14.07
5	634.31	536.8	18.17	17.66	15	17.73	524.15	518	1.19	1.02	1.29	− 20.93

7 Conclusions

The following are the conclusions gained from the experimental and optimization outputs:

- ANOVA tables show that the LP is the major influencing process parameter on impact strength, micro-hardness and bead width, whereas FPP influences UTS of AISI 4130 and AISI 304 weld joint.
- The BW is proportional to LP, WS, BA, FPP and FL, according to performance characteristics plots. Bead width, on the other hand, reduces when welding speed increases.
- The multi-optimal combination of processes parameters obtained by the application of WOA is LP 2200 W, WS 1.6472 m/min, BA 88º, FPP − 0.1147 mm, FL 16 for the dissimilar weld joint AISI 4130 and AISI 304 to obtain minimum BW 1.02 mm and maximum UTS 634.3087 MPa, IS 17.6613 J, MH 624.1529HV1.
- Confirmation experiment conducted for the optimal combination of process parameters. The χ^2 test is conducted for validation of model and experimental values.

References

1. Jose Roberto, B., De Rossi, W., Maurıcio David, M.D.N., de Almeida, I.A., Nilson Dias, V.J.: Pulsed Nd:YAG laser welding of AISI 304 to AISI 420 SS. Opt. Lasers Eng. **45**, 960–966 (2007)
2. Benyounis, K.Y., Olabi, A.G., Hashmi, M.S.J.: Multi-response optimization of CO_2 Laser welding process of austenitic SS. Opt. Laser Tech. **40**, 76–87 (2008)
3. Arivazhagan, N., Surendra, S., Prakash, S., Reddy, G.M.: Investigation on AISI 304 austenitic stainless steel to AISI 4140 Low Alloy steel dissimilar joints by gas tungsten arc, Electron beam and friction welding. Mater. Des. **32**, 3036–3050 (2011)
4. Seyedali, M., Lewis, A.: The Whale optimization algorithm. Adv. Eng. Softw. **95**, 51–67 (2016)
5. Balasubramanian, K.R., Siva, S., Buvansekharan, G.: Numerical and experimental investigation of AISI304 SS sheet. Adv. Prod. Eng. Manag. **32**, 93–105 (2008)
6. Kanaujia, K.K., Rout, M.P., Behera, B.C., Sahoo, S.K., Maharana, B.K.: Optimization of tensile strength of AISI 304 stainless steel and copper using Nd:YAG laser welding. In: Proceedings of the 5th ICAME, pp. 6–8 (2011)
7. Narayana Reddy, B., Hema, P., Vishnu Vardhan, G., Padmanabhan, G.: Experimental study of laser beam welding process parameters on AISI 4130–309 Joint strength. Mater. Today: Proc. **22**, 2741–2750 (2020)
8. Madadian, A.H., Najafi, H., Safarkhanian, M.A., Nategh, S., Mechanical properties of dissimilar welds between AISI 4130 and GOST09ch16N4B. Int. J. Iron & Steel Soc. Iran **13**, 1–7 (2016)

9. Souza Neto, F., Neves, D., Silva O.M.M., Lima, M.S.F., Abdalla, A.J.: An analysis of the mechanical behaviour of AISI 4130 steel after TIG and LBW. Procedia Eng. **114**, 181–188 (2015)
10. Vijay, D., Ashok, B., Tadamalle, P.: Optimization of laser welding process by fuzzy logic technique. Int. J. Eng. Sci. Innov. Tech. **2** (2013)
11. Kannetey, A.: Principles of Laser Material Processing. Jhonwiley and Sons Inc. (2008)
12. Christopher Dawes, C.: Laser Welding: A Practical Guide. Abington Publishing, Cambridge, England (1994)
13. Narayana Reddy, B., Hema, P., Eswara Reddy, C.: Role of Laser Beam in Welding and Assembly: A Status Review, pp. 1056–1060. COPEN, IIT Madras (2017)
14. Tadamalle, A.P., Reddy, Y.P., Ramjee, E.: Influence of laser welding process parameters on weld pool geometry and duty cycle. Adv. Prod. Eng. Manag. **8**, 52–60 (2013)
15. Ruggiero, A., Tricarico, L., Olabi, A.G., Benyounis, K.Y.: Weld-bead profile and costs optimization of the CO$_2$ dissimilar laser welding process of low carbon steel and austenitic steel AISI316. Opt. Laser Technol. **43**, 82–90 (2011)
16. Anawa, E.M., Olabi, A.G.: Optimization of tensile strength of ferrites/austenitic laser-welded components. Opt. Lasers Eng. **46**, 571–577 (2008)

Identification of Optimized Process Parameters for Solid State Joining of AA6063 with AISI 4130 Using Friction Welding Technique

Yashwant Chapke and **Dinesh Kamble**

1 Introduction

Material can be joined with help of friction welding is a solid-state joining process. Joining dissimilar materials having different melting points can be done using the friction welding process. Weld produced using friction welding has good strength at the weld joint. Applications of friction welding are in the aerospace, automotive, and shipping industry. In the joining of engine valves, suspension rods, shafts friction, welding process is used. Joining different materials may result in cost-saving as well as the use of the material of desired properties and result in a remarkable weight reduction of parts. Different joining combinations can give flexibility to the designer for selecting lightweight material as per the required characteristics and properties of the material. Aluminum alloy is a premier material known for its lightweight and corrosion resistance property. Pure aluminum has less strength by adding an alloying element such as Mg, Si, and other alloying elements; strength of aluminum can be increased, and corrosion resistance property also improved.

Aluminum alloy is used as the primary material in the frame of aircraft structures. Most of the designers from the aerospace industry are familiar with designing various aerospace parts and structures with aluminum alloy material. Ample of design data available with the designer with aluminum alloy as a primary material. Properties of aluminum can be enhanced by alloying it with different alloying materials like silicon, magnesium, copper, zinc, etc. Because of these improved properties of aluminum alloy due to alloying, it becomes a very important material for aerospace as well the automotive industry. Bimetallic parts can be fabricated using friction welding, and friction welded joints exhibit good results in terms of good tensile strength. The aerospace and automobile industry has challenges for weight reduction. This weight reduction can be achieved through this friction welding process as bimetallic parts

Y. Chapke (✉) · D. Kamble
Vishwakarma Institute of Information Technology, Savitribai Phule Pune University, Pune, India
e-mail: yashchapke@gmail.com

can be produced. Weldable high strength aluminum magnesium and silicon alloy can be used commercially due to their high strength and corrosion resistance property. Aluminum alloy has less density than steel, and some portion of the complete steel part can be replaced by aluminum alloy as it is lightweight, low-density material which can be introduced in the same part using bimetallic joining by friction welding.

2 Literature Survey

As per geometry and application of welding part, welding process type is selected and studied by various researchers. Researcher worked on joining of similar as well dissimilar material using friction welding, and the following observations were made by them. They also studied the microstructure of welded joints and testing of welded joints done to find out Ultimate Tensile Strength (UTS) of joint. Researchers have identified dominant process parameters of Friction Welding Process and effect of variation of this process parameters on weld joint strength stated by reserchers. The researcher defined the relationship of geometry width of the work piece on the UTS of the welded joint. More the width of the joint will result in reduced UTS of the joint. The hardness of friction welded joints was also studied by researchers, and they have found no change in hardness in the longitudinal joint from the center toward the periphery of the joint. But hardness will be decreasing when considered from the center toward the transverse direction from the joint along its horizontal axis. c et al. also wrote a computer algorithm for simulation of the effect of diameter of the work piece on tensile strength of welded joint Through this research, researcher has suggested that with the increase in diameter of workpiece tensile strength of welded joint decreases [1].

Radosław had joined lightweight expensive material titanium with copper. They have stated tensile strength of the joint is directly proportional to upset pressure up to a certain limit. Also, they stated that the width of recrystallization has a major impact on upset pressure. These researchers have identified upset pressure as a major influential process parameter on tensile strength and recrystallization zone of friction welded joint. Also, they have identified optimum process parameters value for friction pressure, friction time, upset pressure, and upset time for attainment of good quality friction welded joint with high tensile strength [2].

Sathiya et al. in their research work studied Effect of Process parameters such as Upset Time, Upset Pressure and burn of length on Friction Welded joint strength [3]. Eder et al. found that during welding of dissimilar metals AA 1050 with AISI 304 using friction welding maximum heat is dissipated during the friction of both metals. 374 °C Temperature was recorded by them at welding zone during friction welding because of heat generated at joining surfaces [4]. Shanjeevi On joining of steel 304 with copper, it has been found that tensile strength of joint increased by 2.5% as compared to its parent material copper [5]. Sathyanarayana worked on joining austenite steel with ferrite steel using electron beam welding process and friction welding process. Further, they did a comparison of weld joint strength

obtained by both electron beam welding and friction welding process for austenite and ferrite steel. In comparison with the welding joint obtained by both processes, it was found that welding joint obtained from electron beam welding has higher tensile strength [6]. Various researchers have worked on the joining of similar and dissimilar materials using friction welding. While investigating on joining of metals friction welding, researchers primarily focused on the investigation of the microstructure of joints and finding mechanical properties of the weld joint [7, 8]. As per the literature studied to the best of knowledge, no work has been reported in weld joint predication specifically for joining aluminum alloy 6063 with AISI 4130. This project work aims at finding optimized process parameters for joining dissimilar material AA6063 with AISI 4130 for joining the particular class of dissimilar material using the rotary friction welding process.

3 Material Selection

3.1 Aluminum Alloy

In Aluminium Alloy, Aluminium is used as base metal and alloying of other elements done in it. The purpose of this mixing other material with aluminum is to improve strength, corrosion resistance, conductivity ductility, and other properties of aluminum. Alloying of other material in aluminum is done in liquid form for homogeneous mixing of alloying element in aluminum. In aluminum alloy, alloying is done of other materials up to 15% [9].

3.2 Aluminum Alloy Series

In the designation of aluminum alloy, first digit indicates principle alloying element exception which is AA1XXX series as its pure aluminum. Second digit denotes changes to the impurity limit. Potential use of aluminum alloy 6XXX series: Pure aluminum is soft and ductile hence to improve its strength alloying is done with alloying elements like silicon, manganese, zinc, copper, lithium, and its processing alloys. AA6XXX series carries a good weight to strength ratio making; this series alloy has good workability, weldability, and corrosion resistance properties. AA6XXXseries is the most popular material for various industrial applications as lightweight material and AA6063 possessing corrosion resistance and weldability and good mechanical properties make this alloy a hot favorite for structural applications in the aerospace, automotive, and space industry. AA6063 is generally known as architectural alloy and is used in the window door frame, structural bodies, and for various other applications. AA 6000 series has Al–Mg–Si alloying. AA 6XXX

alloys strength can be improved through heat treatment major automotive industries used AA6xxx alloy and made vehicles lightweight [9, 10].

3.3 Steel Dissimilar Metal for Joining with Aluminum Alloy

Different grades of steel were studied and compared for the selection of dissimilar material to join with aluminum alloy using the friction welding process. AISI 4130 steel has been selected as a dissimilar material for joining with aluminum alloy due to its favorable mechanical properties, good weldability, and machinability resulting from its low carbon content. This AISI 4130 material is very popular and used in the fabrication of sections of the aircraft, automobile industry, oil, and gas pipe industry also [11, 12].

4 Process Parameters Selection

Process parameters considered for optimization are selected based on various friction welding processes studied and compared, and then the rotary friction welding process is further selected for study and experimentation. Friction pressure and upset pressure has dominant effect on tensile strength of friction welded joint [12].

4.1 Levels of Process Parameters and DOE

The influence of variation of process parameters on tensile strength and hardness has to be observed for the development of empirical relation between process parameters and tensile strength and hardness [13]. RSM is grounded on the use of factorial design. In RSM, the key influence of factors is well defined as the deviation in response initiated by a variation in a level of the factor considered like friction pressure, friction time, rotation speed, and upset pressure.

Levels for process parameters are identified based upon literature survey [1, 2, 5, 7, 8, 11] and pilot experimentation as per given in Table 1. By using Design of Experiemt and RSM 09 Trials Runs obtained.

As per the CCD, the approach suggested in RSM trial runs for experimentation identified. In DOE, four parameters are considered: friction pressure FP denoted by P, friction time FT denoted by Q, upset pressure UP denoted by R, and spindle rotation speed SS denoted by R. Three levels for each parameter considered and with this total 30 trial runs obtained.

Table 1 Level of process parameters

Process parameter	Level 1 (− 1)	Level 2 (0)	Level 3 (1)
Friction pressure (MPa)	48	73	97
Friction time (s)	2	4	6
Upset pressure (MPa)	38	68	97

5 Experimental Setup

For joining samples of AA6063 with AISI 4130, continuous drive friction welding machine was used. This was a computerized controlled machine, and process parameters friction pressure, friction time, upset pressure and spindle rotation speed can be controlled (Figs. 1 and 2).

5.1 *Joining of AA6063 with AISI 4130*

In this research work, aluminum alloy AA6063 was joined with AISI 4130 by rotary friction welding process. Material AA6063 and AISI 4130 were first machined to diameter 16 mm each and length 104 mm for both material workpieces (Figs. 3 and 4).

Joining surfaces of both workpiece AA6063 and AISI 4130 are claened using Acetone Chemical before joining. AA6063 loaded in rotating chuck and AISI 4130 loaded in the fixture from the dead stock end and work piece are joined.
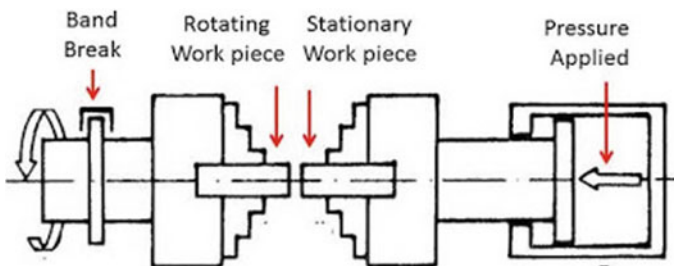
Fig. 1 Schematic of experimental setup

Fig. 2 Experimental setup. *Image Courtesy* Friction Welding Institute, Pune
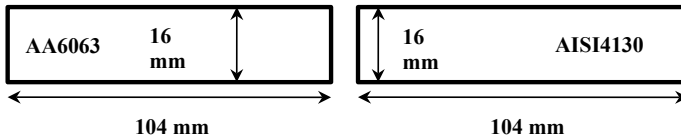
Fig. 3 Workpiece of AA6063 and AISI 4130

6 Tensile Testing of Specimen

For tensile testing specimen prepared by machining, friction welded samples according to ASTM standards E8 M 04 are shown in Fig. 5.

All dimensions shown in Fig. 5 are in mm.

Tensile testing performed on tensile test was conducted on this specimen on UTM as shown in Fig. 6.

On the universal testing machine as shown in Fig. 6, tensile testing of all specimens joined as per experimental design was done. (Courtesy: Friction Welding Institute).

Fig. 4 Friction welded samples

Fig. 5 Tensile test specimen
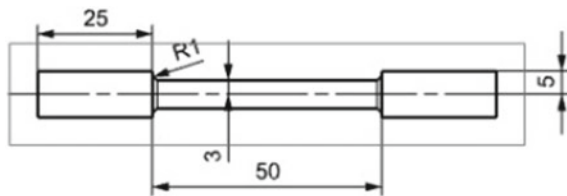
7 Result and Discussion

Tensile strength results obtained are mentioned in Table 2.

From experimentation feasibility of joining AA6063 alloy with AISI 4130 was examined, and it is found that friction pressure plays a vital role in joining aluminum alloy with dissimilar material and minimum 48 MPa required for plastically deformation and joining of dissimilar material using rotary friction welding process. Parameters required for successful joining of AA alloy with dissimilar material identified and their level are decided at −1 level. From the above Table 2, tensile strength is achieved at the various process; parameter combinations can be found.

8 Conclusions

Optimized process parameters for joining of AA6063 with dissimilar metal AISI4130 are identified through experimentation. For friction pressure 71 MPa, upset pressure

Fig. 6 Computerized universal testing machine

Table 2 Tensile strength of friction welded joints

S. No.	Friction pressure (MPa)	Friction time (s)	Upset pressure (MPa)	Spindle rotation speed (RPM)	Tensile strength (MPa)
1	71	6	68	1500	226
2	93	2	38	1200	248
3	**71**	**4**	**68**	**1500**	**305**
4	93	2	38	1200	245
5	71	4	97	1500	232
6	48	2	38	1800	246
7	48	6	97	1200	256
8	71	4	68	1200	246
9	48	2	97	1500	212

68 MPa, and friction time of 4 s joint obtained have maximum tensile strength of 305 MPa. Threshold value of process parameters like friction pressure (FP), friction time (FT), and upset pressure (UP) for joining AA6063 with dissimilar material AISI 4130 is identified. It is also observed from experimentation that friction pressure, upset pressure and friction time has a dominant effect on Tensile Strength of Friction welded joints. Observations made for flash are produced in the form of curls if the value of upset pressure is greater than friction pressure. When friction pressure (FP) is greater than upset pressure (UP) and more friction time is taken, then flash produced will come in a straight line out of joint instead of producing curl at friction welded joint.

References

1. Sahin, M.: Joining of Aluminium and copper materials with friction welding. The Int. J. Adv. Manuf. Technol. **49**, 527–534 (2010)
2. Winiczenkoa, R., Gorochb, O., Krzynska, A., Kaczorowski, M.: Friction welding of tungsten heavy alloy with aluminium alloy. J. Mater. Process. Technol. **246**, 42–55 (2017)
3. Sathiya, P., Aravindan, S., NoorulHaq, A.: Mechanical and metallurgical properties of friction welded AISI 304 austenitic stainless steel. Int. J. Adv. Manuf. Technol. **26**, 505–511 (2005)
4. Alves, E.P., An, C.Y., Neto, F.P., dos Santos, E. F.: Experimental determination of temperature during rotary friction welding of dissimilar materials. Front. Aerosp. Eng. **1**(1) (2012)
5. Shanjeevi, C., Satish Kumar, S., Sathiya, P.: Multi-objective optimization of friction welding parameters in AISI 304L austenitic stainless steel and copper joints. Proc. Inst. Mech. Eng. Part B: J. Eng. Manuf. **230**(3), 449–457 (2016)
6. Sathyanarayana, V.V., Madhusudhan Reddy, G., Mohandas, T.: Dissimilar metal friction welding of austenitic–ferritic stainless steels. J. Mater. Process. Technol. **160**, 128–137 (2005)
7. Murali Mohan, C., Haribabu, S., Reddy, Y., Muthupandi, V., Sivaprasad, K.: Joining of AISI 1040 Steel to 6082-T6 aluminium alloy by friction welding. J. Adv. Mech. Eng. Sci. (JAMES) **1**, 57–64 (2015)
8. Meengam, C., Chainarong, S., Muangjunburee, P.: Friction welding of semi-solid metal 7075 aluminum alloy. Mater. Today: Proc. **4**, 1303–1311 (2017)
9. TolgaDursun, C.S.: Recent developments in advanced aircraft aluminium alloys. Mater. Des. **56**, 862–871 (2014)
10. Shailesh Singh, K., Chattopadhyay, K., Phanikumar, G., Dutta, P.: Experimental and numerical studies on friction welding of thixocast A356 aluminum alloy. Acta Mater. **73**, 177–185 (2014)
11. Uzkut, M., ÜNLÜ, B.S., YILMAZ, S.S., AKDAĞ, M.: Friction welding and its applications in today's world. IBU Repository, Mater. Sci. 710–724 (2010)
12. Paventhan, R., Lakshminarayanan, P.R., Balasubramanian, V.: Optimization of friction welding process parameters for joining carbon steel and stainless steel. Sci. Dir. J. Iron Steel Res. Int. **19**(1), 66–71 (2012)
13. Meisnar, M., Baker, S., J.M. Bennett, A. Bernad, A. Mostafa, S. Rescha, N. Fernandes, A. Norman: microstructural characterization of rotary friction welded AA6082 and Ti-6Al-4V dissimilar joints. Mater. Des. **132**, 188–197 (2017)

Investigation and Optimization of Weld Bead Geometry of AISI 1023 with Varying Plate Width Using Taguchi and Multiple Regression Analysis

Vinod Kumar Aswal , **Jinesh Kumar Jain** , **Manoj Kumar** ,
Tejendra Singh Singhal , **and Tapas Bajpai**

1 Introduction

Steel is the material that is mostly used in structural components of bridges, buildings, and many other types of machine parts. It is generally used in turbine disks, shaft coupling, and gear blanks of ships. Among all kinds of steel, plain carbon steel (PCS) is most common as it is inexpensive, strong despite being low carbon content, and easily formable to mold in any desired shape. It shows excellent weldability because of its low carbon content. Though low carbon steel shows good weldability is also dependent on welding process parameters.

Welding is the process in which localized joints can be produced for the joining of material. Welding has helped many industries and products by increasing productivity and lifetime, respectively. SAW is the most used arc welding process in industries as it produces high heat which enables metal deposition at a higher rate, also it provides deeper penetration [1]. In the SAW process, the arc is being generated between granular flux and continually feed wire. A granular flux was used to submerge the

V. K. Aswal · J. K. Jain · T. S. Singhal (✉) · T. Bajpai
Department of Mechanical Engineering, Malaviya National Institute of Technology, Jaipur, Rajasthan, India
e-mail: 2019RME9043@mnit.ac.in

V. K. Aswal
e-mail: 2019PPE5286@mnit.ac.in

J. K. Jain
e-mail: Jineshjain.mech@mnit.ac.in

T. Bajpai
e-mail: Tapas.mech@mnit.ac.in

M. Kumar
Department of Mechanical-Mechatronics Engineering, The LNM Institute of Information Technology, Jaipur, Rajasthan, India
e-mail: Manojkumar@lnmiit.ac.in

weld bead and wire tip region to enhance the weld bead quality, and this flux is used to increase the properties of the weld pool region by shifting the alloying element to the weld pool [2]. Thus, to produce a quality bead profile, the selection of these chemical compounds also plays a key role [3]. SAW process has some benefits such as a more stable arc and higher productivity, no contact with environmental contaminants. SAW provides a higher welding current which is around four times of other processes like GMAW, SMAW results in higher heat input [4].

The study on the effect of various input variables on weld bead profile has been reported by many investigators. The effect of process parameters on weld bead width and height on stainless steel plates was investigated and observed that current increases bead height and voltage increases bead width [5]. The effect of heat input as well as SAW process parameters on the weld pool were explained in accordance with weld bead geometry and shape relationship [6]. A large weld deposited area has been generated using high welding speed and low voltage on DCEN polarity. The impact of SAW input variables on mechanical properties and microstructure was studied and observed that in multi-pass welding, due to the presence of differential rate of heating and cooling fully conversion of δ ferrite to γ is not possible. SAW weld joints develop better weld beads, show higher hardness and tensile properties but with increments in voltage and current their tensile properties deteriorate [7]. The effects of wire preheating and nozzle cooling on plain carbon steel were studied and optimized the parameters with AHP and TOPSIS [8]. Agglomerated flux grain size and viscosity behavior were investigated, and observation shows viscosity reduction with rising in temperature [9]. Studies show that more ferrite and lesser graphite were observed at lower heat input in multi-pass SAW, by which hardness of HAZ increases and weld metal hardness decreases [10]. Studies on the impact of input variables on penetration by flux-cored arc welding show that penetration increases with voltage [11]. Researchers examined similar responses with robotic gas metal arc welding (GMAW) and observed that penetration increases with current and welding speed while it decreases with voltage [12].Various studies have explained the cladding process through welding with different approaches and explained the advantages of various processes [13]. In some studies various sustainability measures including the various form of welding with different process parameters and limits and about how these processes could become sustainable and can produce benefits to the society [14]. The impact of varying plate thickness observed and explained that increment in plate thickness decreases penetration because heat conduction loss in thickness direction becomes predominate for thick plates, while little increment in bead width is observed due to heat sinking in the thickness direction [15].

Very few works were done on the impact of varying plate width on weld bead geometry till now. Although it is a very important aspect as it will result in variation of cooling rate of the weldments and that will affect the microstructure and finally quality of weld bead. This paper focused on the impact of varying plate width on weld bead profile through the Taguchi method and multiple regression analysis.

2   Materials and Methods

In this experiment, Plain Carbon Steel (AISI 1023) is used as a workpiece plate. Plain Carbon Steel (AISI 1023) provided good weldability because of its lower carbon contents. The experiment was conducted with varying the plate width (50, 75, and 100 mm), 200 mm length, and 12 mm plate thickness. The experiment was carried out using Cu coated wire, having 4 mm diameter. The composition of the workpiece plate and wire is given in Table 1. The head-on-plate method is used to deposit metal on the workpiece surface along the centerline in the longitudinal direction. Experiments were conducted with direct current reverse polarity and the nozzle to plate distance (NTPD) was kept as constant 30 mm. For experimental setup, ESAB CPRA 800(S) SAW Welding Machine is used. The setup is shown in Fig. 1.

The input process variables such as voltage, WFR, speed, and plate width were selected to find their impact on weld bead profile. The input variable levels and

Table 1 Chemical composition of workpiece plate and welding wire

	Composition (wt%)						
	Carbon	Silicon	Sulfur	Manganese	Phosphorus	Copper	Chromium
Workpiece plate	0.22	0.30	0.043	0.45	0.042	0.15	0.082
Wire electrode	0.10	0.07	0.020	0.60	0.018	0.28	–
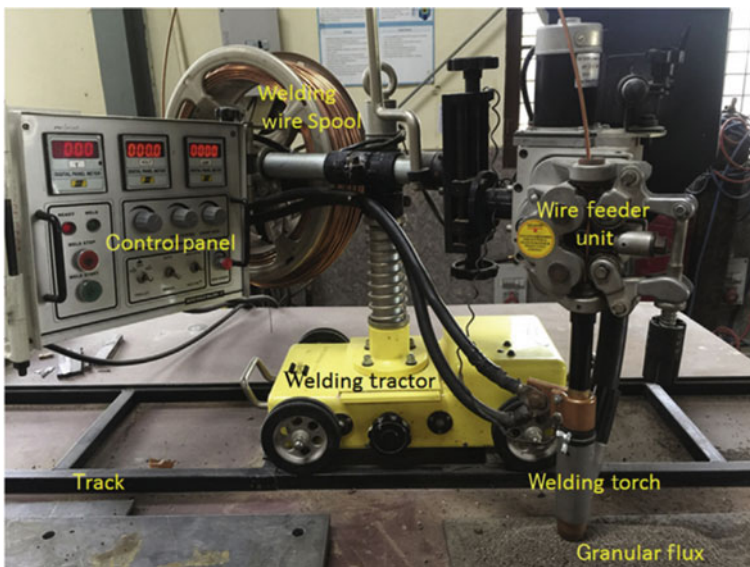
Fig. 1 Experiment setup for SAW

their respective values are selected based on previous research as given in Table 2. Experiments were conducted by using Taguchi L_9 orthogonal array in which three levels and four variables were selected. [16–18]. The experimental design using the L9 orthogonal array is given in Table 3. Total nine experiments were conducted using various combinations of process parameters as per design matrix. Plates were cut into desired size by plasma arc cutting and cleaned with hand grinder to remove dust and any small scratches from workpiece plate. Flux is heated up to 200 °C for 1 h to remove moisture contents. Place the workpiece plate on fixture at SAW setup and used two backup plate at both sides to eliminate arc blow, measured the NTPD as 30 mm, mark the end point of plate, and submerged the plate by flux. Perform the operations one by one, after welding operation kept the weld plate at dry place to cool. After that with help of abrasive cutter cut the uniform section of sample from the plate, take three samples from each plate, with use of grinding machine clean the samples, remove burrs. Then each sample polished with different emery papers starting from 120 up to 2000 through belt grinder and rotary polishing machine. These samples etched with 2% nital solution. After etching with help of high-resolution scanner, weld bead parameters were measured.

Table 2 SAW input variable values

Process parameter	Units	Symbols	Levels		
			− 1	0	+ 1
Welding voltage	volts	V	36	40	44
Wire feed rate	mm/min	F	21	23	25
Welding speed	mm/s	C	7	8	9
Plate width	mm	D	50	75	100

Table 3 Design of experiment

S. No.	Voltage	Wire feed rate	Welding speed	Plate width
10	36	21	7	50
11	36	23	8	75
12	36	25	9	100
13	40	21	8	100
14	40	23	9	50
15	40	25	7	75
16	44	21	9	75
17	44	23	7	100
18	44	25	8	50

2.1 Taguchi

Taguchi's quality engineering method, which employs the design of experiment (DOE), is the most used statically tool for developing a high productivity process at a low cost. This method is a systematic and effective method for optimizing designs for performance, cost, and quality. The fundamental stage in Taguchi's strategy for achieving high productivity economically is to optimize input variables. Traditional process parameter design is difficult and time-consuming. Formalized paraphrase to accomplish this work, the Taguchi method employs a unique design of orthogonal arrays to investigate the entire process parameter space with a small number of experiments. Depending on the characteristic, there are several S/N ratios. Lower is better (LB), nominal is better (NB), and higher is better (HB). By examining the amount of variation present as a response, control factors that may contribute to reduced variation (improved quality) can be quickly identified. The higher the bead width, depth of penetration, and weld reinforcement of the weld bead geometries, the better the quality [19].

The loss function of the higher-quality characteristic is written as HB,

$$L_f = \frac{1}{N} \sum_{i=1}^{n} \frac{1}{Y_i^2} \tag{1}$$

$$\text{LB}, L_f = \sum_{i=1}^{n} \frac{Y_i^2}{N_i} \tag{2}$$

where L_f is the overall loss function and Y_i is the experimental value at ith test and N are no. of tests at the same level. The S/N ratio is derived from the overall loss function. The S/N ratio is used in the Taguchi method to calculate the deviation of the quality characteristic from the desired value.

The S/N ratio (dB) can be written as follows:

$$\eta = -10 \log L_f \tag{3}$$

In the SAW process, the Taguchi method is used for optimization procedures to determine the optimal input variables. Researchers have experimented on shrinkage reduction using polypropylene and optimized the results using Taguchi and ANOVA. The paper shows the optimization of the effects of various process parameters in the reduction of shrinkage in plastic components manufacturing [20].

2.2 Multiple Regression Analysis

To determine the relationships between variables, multiple regression analysis techniques are used. Linear equations are the most commonly used method among social

scientists. The multiple linear regression formula is as follows:

$$R = A + B_1 x_1 + B_2 x_2 + \cdots + B_k x_k \tag{4}$$

where R is the dependent variable to be determined, $x_1, x_2, \ldots, x_k$ are the known variables on which predictions are to be made, and $A, B_1, B_2, \ldots, B_k$ are the coefficients with values determined by the method of least squares.

The relationship between the dependent variables of bead geometry with input variables is determined using MR analysis. The regression analysis was done using Minitab 15 version.

3   Results and Discussion

In this study, experiments were conducted accurately and their responses were measured, then critical process parameters were identified by analyzing their effects on weld bead geometry. The output parameters considered in this work are penetration, bead width, % dilution, reinforcement height, and HAZ. These output parameters were measured through Adobe Acrobat® software. The weld bead geometry obtained on AISI 1023 plate is shown in Fig. 2. The results obtained for each response are described in detail below, along with their analysis.

3.1   Effect of Input Variables on Penetration

Weld penetration was measured through the weld joint's cross section. By machining and polishing, good surface finish was obtained on weld joint area. Table 4 shows the experiment design and S/N ratio for SAW process. The optimum input variable value is A_2–B_3–C_1–D_2, arc voltage 40 V, wire feed rate 25 mm/min, speed 7 mm/sec, and plate width 75 mm (as given in Table 5).

It is shown that for SAW wire feed rate having maximum impact on penetration followed by plate width, welding speed, and welding voltage, respectively (Fig. 3).

Fig. 2 Scanned images of bead geometry

Table 4 Experiment design and S/N ratio for weld penetration

S. No.	Voltage	Wire feed rate	Welding speed	Plate width	Penetration (mm)	S/N ratio of penetration
1	36	21	7	50	6.9	16.7770
2	36	23	8	75	8.1	18.1697
3	36	25	9	100	7.94	17.9964
4	40	21	8	100	6.6	16.3909
5	40	23	9	50	7.21	17.1587
6	40	25	7	75	10.28	20.2399
7	44	21	9	75	7.48	17.4780
8	44	23	7	100	7.33	17.3021
9	44	25	8	50	8.44	18.5268

Table 5 Mean values of S/N ratio for input variables

Level	Welding voltage (V)	Wire feed rate (F)	Welding speed (c)	Plate Width (D)
1	17.65	16.88	18.11	17.49
2	17.93	17.54	17.70	18.63
3	17.77	18.92	17.54	17.23
Delta	0.28	2.04	0.56	1.4
Rank	4	1	3	2
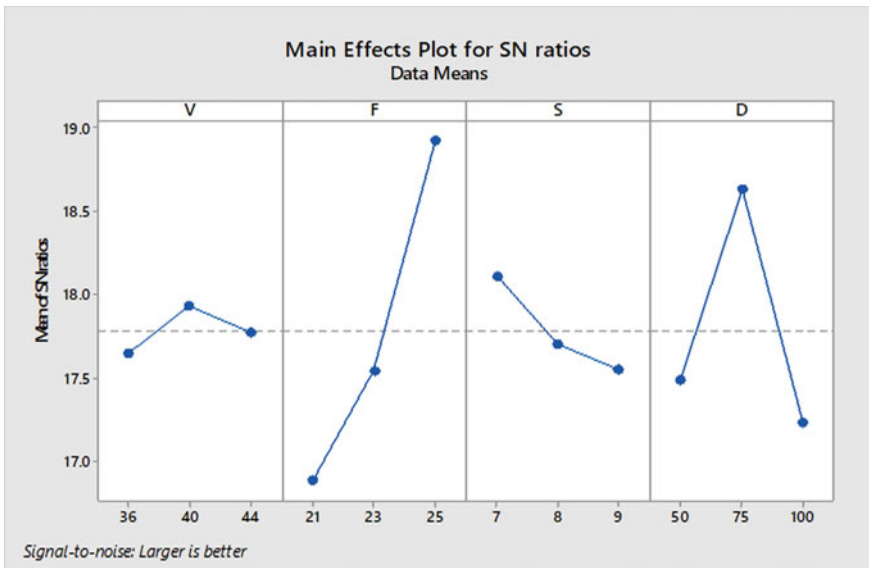
Fig. 3 Effect of input variables on mean S/N ratio for weld penetration

The relationship between penetration and input variables is determined using multiple regression (MR) analysis.

The linear equation of predicted weld penetration for SAW

$$P = -0.75 + 0.0129\ V + 0.473\ F - 0.313\ S - 0.0045\ D \qquad (5)$$

The coefficient of determination ($R2$) obtained for the model is 63.18%.

3.2 Effect of Input Variables on Weld Bead Width

Measurement of weld bead width was observed from each experiment to analyze the influence of each input variable. Table 6 shows the experiment design, and S/N ratio was found with help of above equation. The values of average S/N ratios for bead width and optimum input variables value for SAW are A_3–B_1–C_1–D_1, arc voltage 44 V, wire feed rate 21 mm/min, speed 7 mm/s, plate width 50 mm as given in Table 7.

Table 6 Experiment design and S/N ratio for weld bead width

S. No	Voltage	Wire feed rate	Welding speed	Plate width	Bead width (mm) SAW	S/N ratio of bead width SAW
1	36	21	7	50	13.93	− 22.879
2	36	23	8	75	13.33	− 22.496
3	36	25	9	100	12.59	− 22.000
4	40	21	8	100	14.46	− 23.203
5	40	23	9	50	15.07	− 23.562
6	40	25	7	75	14.69	− 23.340
7	44	21	9	75	17.59	− 24.905
8	44	23	7	100	17.31	− 24.765
9	44	25	8	50	17.83	− 25.023

Table 7 Mean values of S/N ratio for input variables

Level	Welding voltage (V)	Wire feed rate (F)	Welding speed (c)	Plate width (D)
1	− 22.46	− 23.66	− 23.66	− 23.82
2	− 23.37	− 23.61	− 23.57	− 23.58
3	− 24.90	− 23.45	− 23.49	− 23.32
Delta	2.44	0.21	0.17	0.50
Rank	1	3	4	2
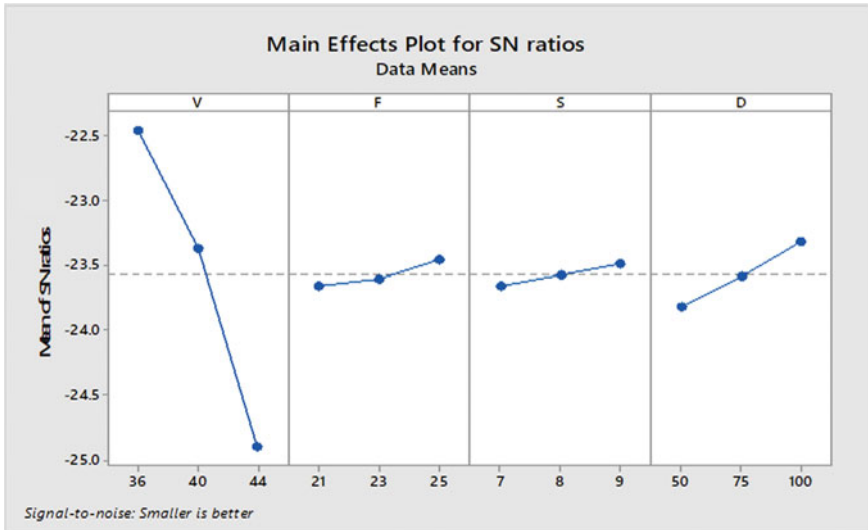
Fig. 4 Effect of input variables on mean S/N ratio for weld bead width

It is shown that for SAW welding voltage having maximum impact on weld bead width followed by plate width, wire feed rate, and welding speed.

For SAW,

$$W = -2.46 + 0.5367\,V - 0.0725\,F - 0.113\,S - 0.01647\,D. \tag{6}$$

The coefficient of determination ($R2$) obtained for the model is 96.79% (Fig. 4).

3.3 Effect of Input Variables on Reinforcement Height

Measurement of reinforcement height was observed from each experiment to analyze the influence of each input variable. Table 8 shows the experiment design, and S/N ratio was found with help of above equation. The values of average S/N ratios for reinforcement height and optimum input variables value for reinforcement height for SAW process are A_2–B_3–C_2–D_3, arc voltage 40 V, wire feed rate 25 mm/min, speed 8 mm/s, and plate width 100 mm as given in Table 9.

It is shown that for SAW wire feed rate having maximum impact on reinforcement height followed by welding voltage, plate width, and welding speed, respectively.

The relationship between reinforcement height and input variables is determined using MR analysis. The linear equation of predicted reinforcement height is observed from regression analysis for SAW.

$$R = -0.85 + 0.0483\,V + 0.1058\,F - 0.1567\,S + 0.00800\,D \tag{7}$$

Table 8 Experiment design and S/N ratio for reinforcement height

S. No.	Voltage	Wire feed rate	Welding speed	Plate width	Reinforcement (mm)	S/N ratio of reinforcement
1	36	21	7	50	2.27	− 7.1205
2	36	23	8	75	2.74	− 8.7550
3	36	25	9	100	2.78	− 8.8809
4	40	21	8	100	3.17	− 8.8809
5	40	23	9	50	2.6	− 8.2995
6	40	25	7	75	3.31	− 10.3966
7	44	21	9	75	2.53	− 8.0624
8	44	23	7	100	3.27	− 10.2910
9	44	25	8	50	3.15	− 9.9662

Table 9 Mean values of S/N ratio for input variables

Level	Welding voltage (V)	Wire feed rate (F)	Welding speed (c)	Plate width (D)
1	− 8.252	− 8.401	− 9.269	− 8.462
2	− 9.572	− 9.115	− 9.581	− 9.071
3	− 9.440	− 9.748	− 8.414	− 9.731
Delta	1.320	1.347	1.167	1.269
Rank	2	1	4	3

The coefficient of determination ($R2$) obtained for the model is 80.36 (Fig. 5).

3.4 Effect of Input Variables on Percentage Dilution

Measurement of % dilution was observed from each experiment to analyze the influence of each input variable. Table 10 shows the experiment design, and S/N ratio was found with help of above equation. The values for average S/N ratios for % dilution and optimum input variables value for % dilution for SAW are A_2 − B_3–C_3–D_1, arc voltage 40 V, wire feed rate 25 mm/min, speed 9 mm/sec, and plate width 50 mm as given in Table 11.

It is shown that for SAW wire feed rate having maximum impact on % dilution and further followed by welding voltage, welding speed, and plate width.

The relationship between % D and input variables is determined using MR analysis. The linear equation of predicted % D is observed from regression analysis for SAW.

$$\%D = 0.565 + 0.00140 \text{ V} + 0.00121 \text{ F} + 0.00597 \text{ S} - 0.000237 \text{ D} \qquad (8)$$
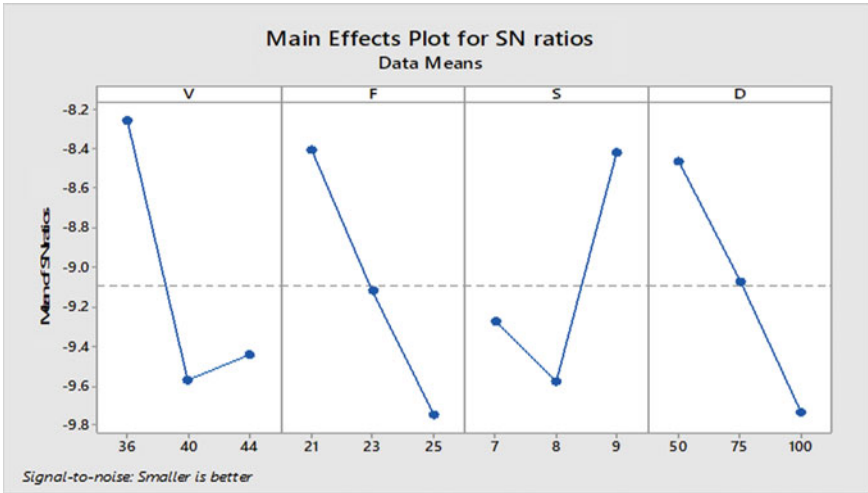
Fig. 5 Effect of input variables on mean S/N ratio for reinforcement height

The coefficient of determination ($R2$) obtained for SAW for the model is 33.12% (Fig. 6).
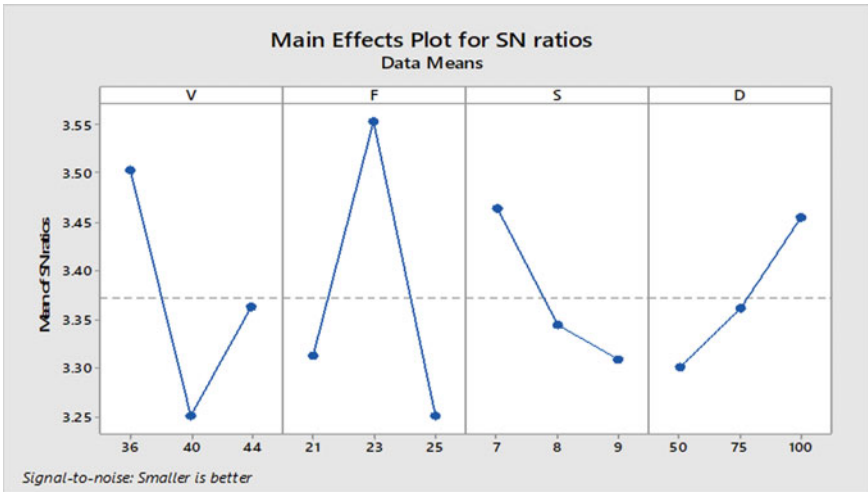
Fig. 6 Effect of input variables on mean S/N ratio for % dilution

Table 10 Experiment design and S/N ratio for % dilution

S. No	Voltage	Wire feed rate	Welding speed	Plate width	% dilution (mm)	S/N ratio of % dilution
1	36	21	7	50	67.10704	3.46464
2	36	23	8	75	65.7173	3.64641
3	36	25	9	100	67.59646	3.40152
4	40	21	8	100	68.82648	3.24489
5	40	23	9	50	68.4153	3.29694
6	40	25	7	75	69.10098	3.21032
7	44	21	9	75	68.95744	3.22838
8	44	23	7	100	65.18138	3.71753
9	44	25	8	50	69.64202	3.14257

Table 11 Mean values of S/N ratio for input variables

Level	Welding voltage (V)	Wire feed rate (F)	Welding speed (c)	Plate width (D)
1	3.504	3.3132	3.464	3.301
2	3.251	3.554	3.345	3.362
3	3.363	3.251	3.309	3.455
Delta	0.253	0.302	0.155	0.153
Rank	2	1	3	4

3.5 Effect of Input Variables on HAZ

Measurement of HAZ was observed from each experiment to analyze the influence of each input variable. Table 12 shows the experiment design, and S/N ratio was found with help of above equation. For SAW, the values of average S/N ratios for HAZ and optimum input variables value are A_2–B_1–C_1–D_1, arc voltage 40 V, wire feed rate 21 mm/min, speed 7 mm/sec, and plate width 50 mm as given in Table 13.

It is shown that for SAW plate width will have maximum impact on HAZ followed by welding voltage, speed, and wire feed rate, respectively.

The relationship between HAZ and input variables is determined using MR analysis. The linear equation of predicted HAZ is observed from regression analysis for SAW.

$$\text{HAZ} = 70.2 + 0.049\,\text{V} - 0.518\,\text{F} - 1.14\,\text{S} - 0.1632\,\text{D} \qquad (9)$$

The coefficient of determination ($R2$) obtained for the model for SAW is 54.41% (Fig. 7).

Table 12 Experiment design and S/N ratio for HAZ

S. No	Voltage	Wire feed rate	Welding speed	Plate width	HAZ (mm)	S/N ratio of HAZ
1	36	21	7	50	42.65	− 32.5984
2	36	23	8	75	36.46	− 31.2363
3	36	25	9	100	30.14	− 29.5829
4	40	21	8	100	39.9	− 32.0195
5	40	23	9	50	47.4	− 33.5156
6	40	25	7	75	36.13	− 31.1574
7	44	21	9	75	36.13	− 31.1574
8	44	23	7	100	34.91	− 30.8590
9	44	25	8	50	39.38	− 31.9055

Table 13 Mean values of S/N ratio for input variables

Level	Welding voltage (V)	Wire feed rate (F)	Welding speed (c)	Plate width (D)
1	− 31.14	− 31.93	− 32.04	− 32.67
2	− 32.73	− 31.87	− 31.72	− 31.68
3	− 31.31	− 31.38	− 31.42	− 30.82
Delta	1.59	0.54	0.62	1.85
Rank	2	4	3	1
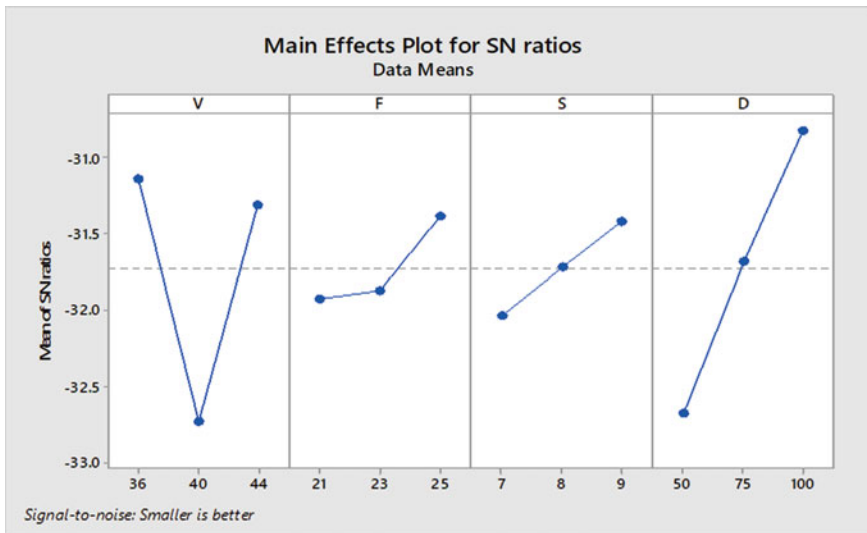
Fig. 7 Effect of input variables on mean S/N ratio for HAZ

4 Conclusion

In this paper, the following investigation and outcomes have been made in the following points:

In this experiment, the Taguchi technique and MR analysis were used to predict the optimum values of various responses on varying width plate of AISI 1023. By experimenting with the Taguchi method, optimum values of weld penetration, bead width, the height of reinforcement, % D, HAZ area can be achieved as A2–B3–C1–D2, A3–B1–C1–D1, A2–B3–C2–D3, A2–B3–C3–D1, A2–B1–C1–D1 for SAW process. Weld bead is the most significant factor found, as the coefficient of determination is above the required value. Voltage increases arc length which spread over more areas of the workpiece. Hence, weld bead width increases. Welding current increases wire feed rate which produces more heat and the rate of metal deposition results in penetration increases. Welding speed increases torch travel speed which produces narrow penetration and higher weld bead width. As plate width decreases, a lesser area of heat conduction results in an increase in HAZ area.

References

1. Aswal, V.A., Jain, J.K., Sonia, P.: Review on the behavior of various parameters on heat distribution in the SAW process. Mater. Today: Proc. **47**(1), 6734–6739 (2021)
2. Choudhary, A., Kumar, M., Unane, D.: Experimental investigation and optimization of weld bead characteristics during submerged arc welding of AISI 1023 steel. Defence Technol. **15**(1), 72–82 (2019)
3. Viano, D.M., Ahmed, N.U., Schumann, G.O.: Influence of heat input and travel speed on microstructure and mechanical properties of double tandem submerged arc high strength low alloy steel weldments. Sci. Technol. Weld. Joining **5**(1), 26–34 (2000)
4. Sonia, P.: Review on heat and mass transfer in submerged arc welding (SAW) and gas metal arc welding (GMAW). Int. J. Eng. Adv. Technol. **8**(1), 503–512 (2019)
5. Vedrtnam, A., Singh, G., Kumar, A.: Optimizing submerged arc welding using response surface methodology, regression analysis, and genetic algorithm. Defence Technol. **14**(3), 204–212 (2018)
6. Yang, L.J., Chandel, R.S., Bibby, M.J.: The effects of process variables on the weld deposit area of submerged arc welds. Weld. J. **72**, 11–16 (1993)
7. Sharma, H., Rajput, B., Singh, R.: A review paper on effect of input welding process parameters on structure and properties of weld in submerged arc welding process. Mater. Today: Proc. **26**(2), 1931–1935 (2020)
8. Karuthapandi, S., Ramu, M., Thyla, P.R.: Effect of flat electrode and Fuzzy logic model for the prediction of weldment shape profile in GMAW. J. Mech. Sci. Technol. **71**(5), 2477–2486 (2017)
9. Kumar, A., Ghosal, A., Kumar, S., Dwivedi, S.: Grain size and viscosity behaviour of developed agglomerated fluxes during submerged arc welding. Mater. Today: Proc. **34**(3), 829–831 (2021)
10. Jaiswal, D.: Analysing the effect of parameters in multipass submerged arc welding process. Int. J. Theor. Appl. Res. Mech. Eng. **2**, 60–70 (2013)
11. Mostafa, N.B., Khajavi, M.N.: Optimization of welding parameters for weld penetration in FCAW. J. Achievements Mater. Manuf. Eng. **16**(1), 132–138 (2006)
12. Karadeniz, E., Ozsarac, U., Yildiz, C.: The effect of process parameters on penetration in gas metal arc welding processes. Mater. Des. **28**(2), 649–656 (2007)

13. Singhal, T.S., Jain, J.K.: GMAW cladding on metals to impart anti-corrosiveness: machine, processes and materials. Mater. Today: Proc. **26**(2), 2432–2441 (2020)
14. Singh, T., Jain, J.K.: A quantitative and qualitative review of sustainable manufacturing. Recent Adv. Mech. Eng. 941–960 (2021)
15. Arya, H.K.: Effects of welding speed, welding current and plate thickness on temperature variation and angular distortion in butt joint welding. In: International Conference on Materials Science, pp. 131–136 (2011)
16. Chandel, R.S., Seow, H.P., Cheong, F.L.: Effect of increasing deposition rate on the bead geometry of submerged arc welds. J. Mater. Process. Technol. **72**(1), 124–128 (1997)
17. Kumanan, S., Dhas, R., Edwin, J., Gothman, K.: Determination of submerged arc welding process parameters using Taguchi method and regression analysis. Indian J. Eng. Mater. Sci. 177–183 (2007)
18. Yang L.J.; Chandel R.S.; Bibby M.J.: The effects of process variables on the weld deposit area of submerged arc welds. Weld. J. **72**(11) (1993)
19. Tarng, Y.S., Juang S.C., Chang C.H.: The use of grey-based Taguchi methods to determine submerged arc welding process parameters in hardfacing. J. Mater. Process. Technol. **128**(1–3), 1–6 (2002)
20. Singh, T., Singh, M.P., Alam, M.M.: Taguchi and ANOVA analysis of shrinkage of injection moulded polypropylene component. Int. J. Sci. Eng. Res. **5**(7), 750–756 (2014)

Joining of Dissimilar Galvanized Steel Sheets by Resistance Spot Welding and Self-piercing Riveting

Suraj Gupta , **R. Ganesh Narayanan** , **Sukanta Das** ,
and Brajesh Asati

1 Introduction

Spot welding technologies are considered to be the most reliable joining technology in the manufacturing and automotive industries. Friction stir spot welding [1], resistance spot welding (RSW) [2], clinching [3], and self-pierce riveting (SPR) [4] are the common spot joining processes. RSW is predominantly used in the fabrication and assembly of parts in cars, truck cabins, and other vehicles. Less cycle time, low cost, easy maintenance of the RSW setup, and easy automation are the common effective advantages over other joining processes. RSW process belongs to the resistance welding family, in which the faying surfaces are joined using the heat produced from the resistance to the electric current and the application of pressure [5].

On the other hand, SPR is a cold-forming technique used to join two or more similar or dissimilar sheet materials. A semi-tubular rivet is driven through the top sheet in this process, penetrating it, spreading the rivet leg with the help of a die along with plastic deformation of the lower sheet. The process is named 'self-piercing' because there is no requirement to have predrilled holes for the joining of sheets. SPR is widely used for the joining of a variety of materials. Heavy zinc-coated, organic coated, or pre-painted steels, steel-to-aluminum alloy combinations, and various polymers to metals are examples of materials joined by the SPR process [6–9]. Galvanized coating is the most common coating applied to steel sheets used in the automotive sector because of its superior corrosion resistance. Coated steel

S. Gupta · R. Ganesh Narayanan (✉) · S. Das
Department of Mechanical Engineering, IIT Guwahati, Guwahati 781 039, India
e-mail: ganu@iitg.ac.in

S. Das
e-mail: sukan176103114@iitg.ac.in

B. Asati
Tata Steel R&D, Jamshedpur, India
e-mail: brajesh.asati@tatasteel.com

sheets showed different behavior compared to uncoated steel. Upon welding of the coated sample, the coating of the sheet melted first by creating contact resistance between the interface. In the available literature, several articles deal with RSW of galvanized steel sheets, and few on SPR. Hence, the present work aims to compare the spot joints made on dissimilar galvanized steel sheets by RSW and SPR through lap shear tests.

2 RSW and SPR of Thin Sheets

2.1 Methodology of RSW

As depicted in Fig. 1, after placing the two thin sheets between the two copper electrodes, a suitable amount of pressure is applied so that the workpiece is properly clamped. After the workpiece is properly clamped, an electric current is passed through the workpieces for a short time. Due to the resistance of the thin sheets towards the flow of electric current, a suitable amount of heat is generated at the interface leading to the formation of a molten nugget. The pressure through the electrodes is applied throughout the process to maintain proper current flow and pressure required to form a weld nugget. At the end of the third stage, the flow of the current is stopped while maintaining the electrode pressure, the molten nugget starts to solidify [10–12]. In the end, the upper electrode is retracted, leaving behind a successful joint.

The shape and size of the nugget dictate the quality and strength of the joint. Good-quality joints are achieved with the help of a proper combination of processing parameters. Electrode force, welding time, and input current are the important process parameters of RSW [13]. The formation of the joint depends upon the contact resistance between the sheets and Joule's law of heating [14]. Joule's law of heating is expressed as follows:
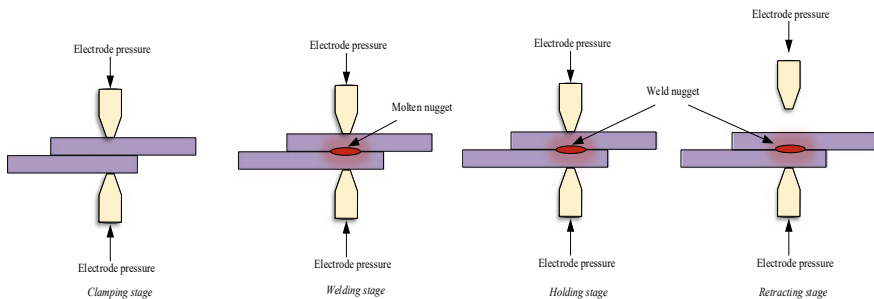
Fig. 1 Different stages of the RSW process

$$Q = I^2 Rt \tag{1}$$

where Q is heat input in joules, I is input current in amperes, R is resistance in ohm, and t is time in seconds [15, 16].

2.2 Methodology of SPR

The mechanism of the SPR process is shown in Fig. 2. Initially, in the clamping stage, the rivet is positioned directly above the sheets to be joined. The nose piece is lowered against the die underneath to contact with the workpiece and a force is applied to lock the workpiece below the blank holder. In the 2nd stage, the rivet is driven by the punch, and the rivet penetrates the upper sheet. In this flaring stage, the upper sheet is split into two sections, and then the rivet penetrates the lower sheet and begins flaring to produce a mechanical interlock. In the releasing stage, after the rivet has been pierced into the sheet and the joining has been formed, the punch and nose pieces will return to their initial positions.
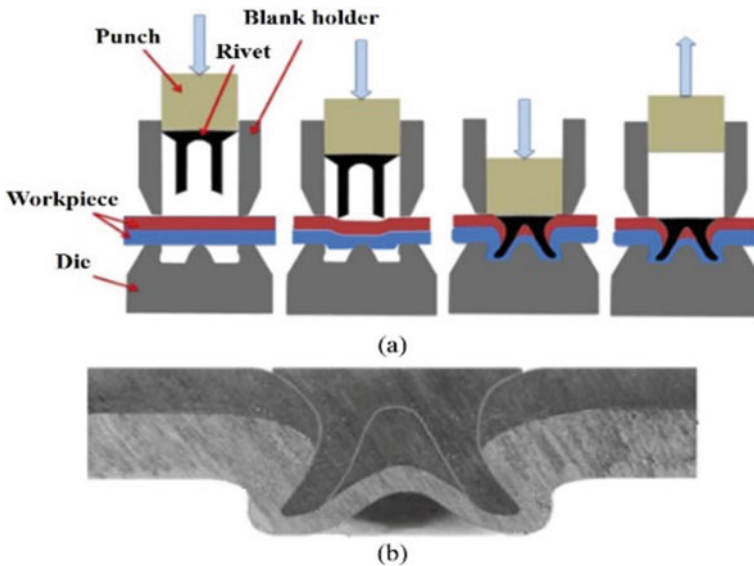
Fig. 2 Mechanism of the SPR process **a** schematic, **b** fabricated joint (used with permission from Rao et al. [17], copyright Elsevier)

2.3 Material Properties

Tensile test on dissimilar galvanized steel sheets of 0.8 and 1.2 mm thickness with a coating weight of 100 gsm each was carried out in a universal testing system (INSTRON, Model 5985) at a cross-head speed of 1 mm/min to obtain load–displacement data. The tensile samples were prepared as per the ASTM E8 standard. Engineering stress–strain data were evaluated as per the usual procedure (Fig. 3).

The chemical composition of the base materials is shown in Table 1. The mechanical properties of the base materials along with the average plastic strain ratio are listed in Table 2. The average plastic strain ratio of the base materials is measured according to ASTM E517-19 standards.

Fig. 3 Engineering stress–strain curve of the base materials
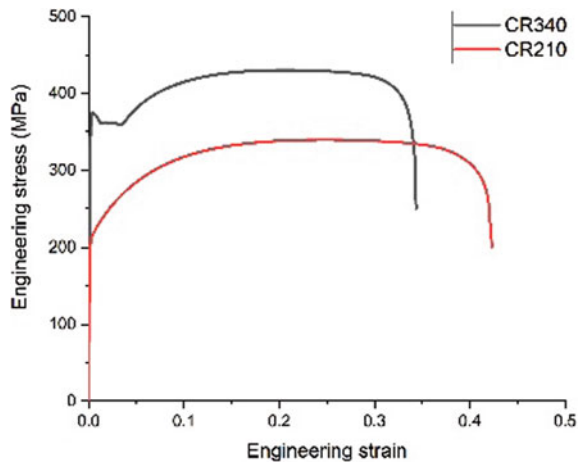
Table 1 Chemical composition of base materials

Base materials	C (%)	Mn (%)	Al (%)	Ti (%)	Nb (%)	Si (%)	S (%)	P (%)	N (ppm)
CR210	0.0019	0.55	0.04	0.053	–	0.003	0.009	0.047	18
CR340	0.045	0.86	0.048	–	0.035	0.008	0.006	0.019	27

Table 2 Mechanical properties and average plastic strain ratio of base materials

Base materials	Yield strength (MPa)	Tensile strength (MPa)	Elongation (%)	Strain hardening exponent	R_{avg}
CR210	234	344	41	0.21	1.94
CR340	395	443	27	0.15	0.91

3 Welding and Characterization

3.1 RSW

The base materials used in this study are CR210 and CR340 steels, which are galvanized steel sheets of 0.8 mm and 1.2 mm thicknesses, respectively. The arrangement of the experimental setup is shown in Fig. 4. RSW is carried out in an RSW machine with specifications provided in Table 3.
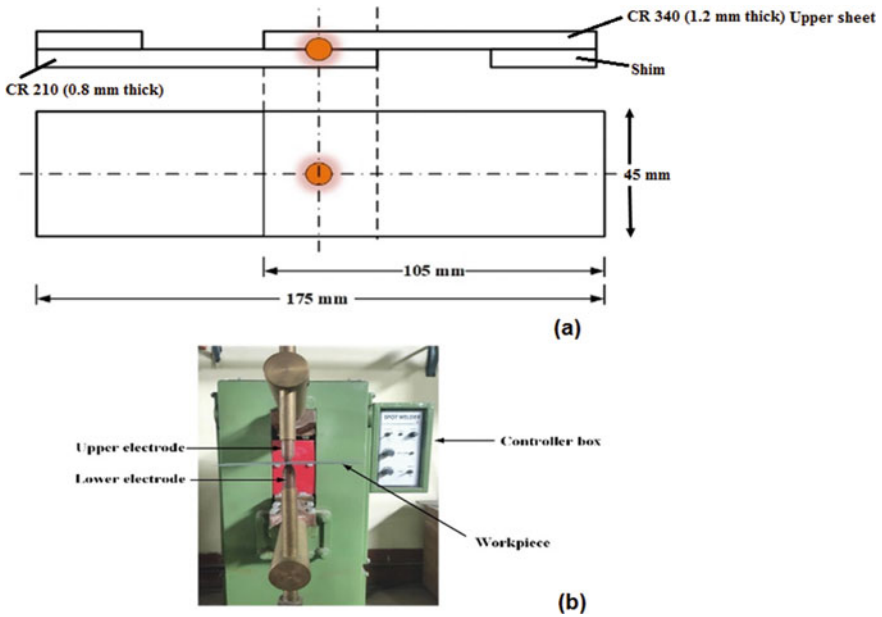
Fig. 4 a Workpiece dimension **b** RSW experimental setup

Table 3 RSW machine details

Product No	LX 30
Rated supply	2 Phase, 415 V
Frequency	50 Hz
Load	30 kVA
Throat depth	360 mm
Throat clearance	250 mm
Output current	5600 Amps
Clamping force	128 kgf
Electrode diameter	6.5 mm

Table 4 Combination of welding parameters for RSW

	Heat (kVA)	Time (ms)
Case 1	15	600
Case 2	18	750
Case 3	21	900

Table 5 SPR rivet and die geometry

Rivet	Die	Penetration
3.35 mm × 4.5 mm; 480 Hv	D 070 120 000	− 0.8 mm

The base materials are cut according to the AWS D8.9-97 standard. Once the samples are cut, they are polished with 400 grit size emery paper and cleaned with acetone solution. After the sample preparation, these are overlapped with an overlap length of 35 mm and welded. Since the thickness of the base materials is not identical, shims were provided during the lap shear test to maintain the uniform uniaxial loading.

During RSW, three different combinations of input parameters were used to determine the joint quality and strength (Table 4). The variable input parameters are heat and time.

3.2 SPR

Joint preparation in SPR is crucial as the quality of the joint is greatly affected by the selection of rivet-die combination and rivet penetration. It is important to achieve leakproof joint (no gap between the rivet head and the top sheet), good mechanical interlocking, and remaining thickness ($T_{min.}$) values to produce sound joints with improved mechanical performance. Optimized riveting parameters were used to produce the riveting joints post cross-sectional examination of joint quality.

Tucker ERT 80 machine having a maximum capacity of 80 kN was used to obtain SPR joint. The rivet was made of boron steel with a countersunk head and Zn/Sn coating. Rivet and die geometries are shown in Table 5 and Fig. 5. Rivet leg thickness is about 0.5 mm.

3.3 Macrostructure and Hardness Evaluation

To study the RSW joint macrostructure, the joint was sectioned along the center of the sample. After sectioning the joint, rough finishing was done with emery paper up to a grit size of 2000 to have a smooth surface finish. For the steel grades, the section is polished with alumina powder on a velvet cloth for a shiny surface. Further, the
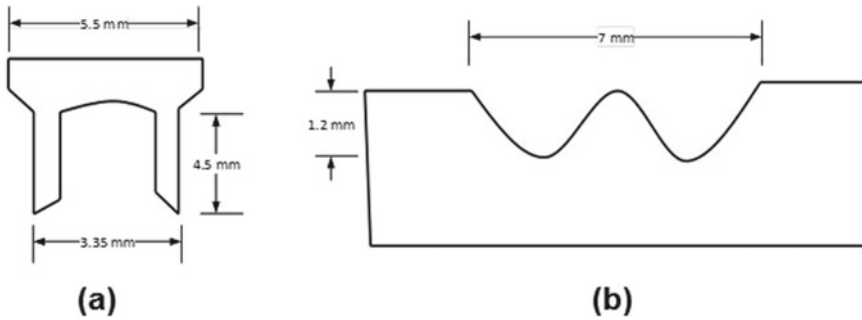
Fig. 5 Schematic of **a** SPR rivet **b** SPR die

microstructure of the RSW joint was also investigated. The polished samples were mildly etched with Nital reagent (20 ml ethanol and 0.5 ml HNO_3) for 10 s for the grains to be visible. The microstructural images were captured using Carl Zeiss Axiocam MR3 Microscope at 50X magnification.

Vickers hardness was measured across the joint cross-section at two levels. The top sheet is CR340, and the bottom sheet is CR210. Hardness was measured at the mid thickness of both sheets. Measurement was done on both sides of the fusion zone. Indentation was done by applying a load of 200 gf for 10 s. Hardness was evaluated as per established procedures.

3.4 Lap Shear Test

The lap shear test is one of the most extensive procedures to experimentally characterize the mechanical performance of joints under shear loading. The sample to be tested is kept in the position as shown in Fig. 6a. Each end of the specimen is clamped in the tensile grip of UTM (Make: SHIMADZU) having a capacity of 100 kN. Lap shear tensile tests are carried out at 1 mm/min crosshead speed to evaluate the maximum load and displacement at failure.

4 Results and Discussion

4.1 Lap Shear Test Results

The tensile shear load increases with the increase of welding heat and time as shown in Fig. 6b. The maximum load obtained in the 15 kVA-600 ms case is lower than that of the maximum load obtained in the 18 kVA-750 ms case. However, in the third case, 21 kVA-900 ms, the maximum load is almost the same as in the first
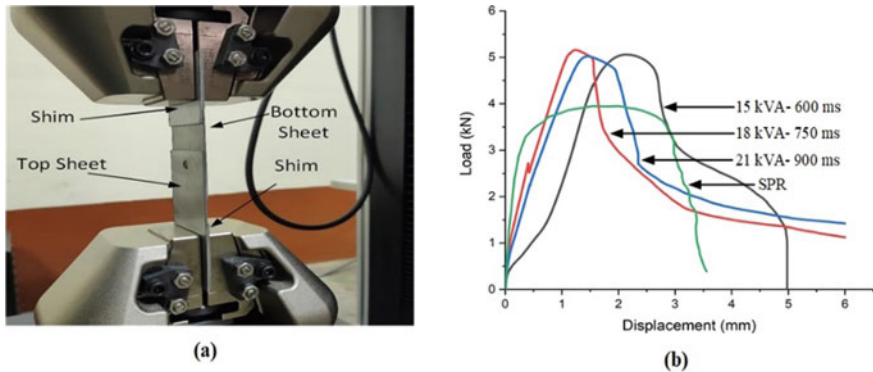
Fig. 6 **a** Experimental setup of lap shear test. **b** Load evolution in lap shear test

case. Application of lower heat results in smaller nugget size diameter and hence the tensile shear load. Weld nugget size diameter increases with the increase in heat and time. However, on increasing the heat and time beyond 18 kVA-750 ms due to the huge quantity of heat, the joint quality is affected reducing the load-bearing ability.

Two types of failure modes are observed during the lap shear test of RSW joints. These are pull-out failure (PF) mode and pull-out failure with tearing (PF-T) mode as shown in Fig. 7a–c respectively. As the heat input and time are increased, a larger and strong nugget is formed and the failure mode shifts from PF to PF-T. When the welding heat is 15 kVA-600 ms, the load-bearing capacity dropped slightly indicating poor weld. PF is characterized by larger displacement at failure in the case of 15 kVA-600 ms sample. PF-T is characterized by a reduction in displacement at failure by about 1–2 mm in 18 kVA-750 ms and 21 kVA-900 ms cases. Similar findings are reported by Wan et al. [18] and Pouranvari [19]. In Pouranvari's work, RSW of DP steel and low carbon steel is attempted to evaluate the lap shear test and cross-tension test performances. However, both interface failure and PF failures are observed in the work. As suggested, the driving force for PF mode is the tensile stress at the nugget circumference, i.e., tensile bending stresses play a crucial role in PF mode. Stiffer samples result in IF mode. As the CR210 sheet is weaker (lower strength) than the CR340 sheet, PF mode is witnessed. For the same reason, tearing occurred in the CR210 side for 18 kVA-750 ms and 21 kVA-900 ms cases (Fig. 7b and c).

4.2 Macrostructure and Microstructure

The typical macrostructure of the RSW joint between CR210 and CR340 steel sheets is shown in Fig. 8. The region shown within the white boundary is the fusion zone (FZ). From the figure, it is observed that the columnar grains make up the majority of FZ. The microstructures of the weldment are shown in Fig. 9. It is observed that all three cases have significant coarse and elongated grains in the FZ, and the grain size
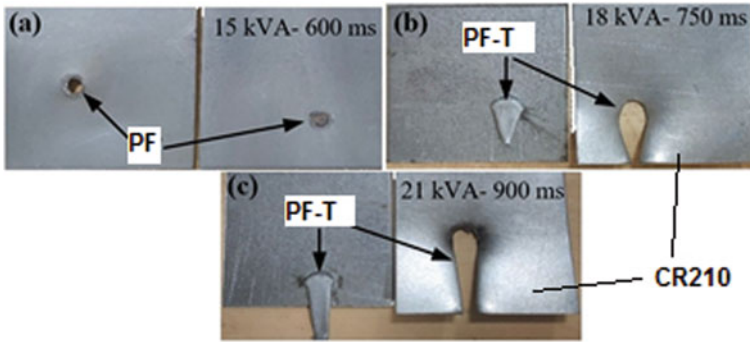
Fig. 7 Failure modes of RSW joints during lap shear test **a** pull out failure for 15 kVA-600 ms, **b** and **c** pull out failure with sheet tearing for 18 kVA-750 ms and 21 kVA-900 ms respectively
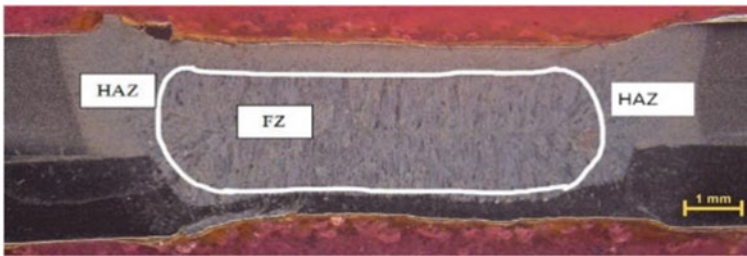
Fig. 8 Typical macrostructure of RSW joint

variances are minor. The region near the FZ, i.e., HAZ, experiences a temperature less than that of FZ. It is observed from Fig. 9a–c that grains of smaller size are present in the HAZ and evenly distributed in the given area.

4.3 Microhardness

Figures 10a and b show the hardness distribution in the CR210 sheet and CR340 sheet, respectively, in the RS welds. Hardness characteristics of RS welds affect the failure characteristics of the joint. A decrease in the hardness value is observed from FZ to the base material. The highest value of hardness is found in FZ followed by HAZ, and then the base material. RSW parameters have a negligible effect on hardness distribution. Figure 10c shows the hardness distribution in the joint for the optimized case, i.e., 18 kVA heat and 750 ms time. The maximum value of hardness is 315 $\pm$ 15 VHN belongs to FZ, which is due to the rapid melting and cooling. Also, as the heat input and time are increased, the nugget size increases. Due to the electrode force throughout the holding period of the joint, deformation hardening
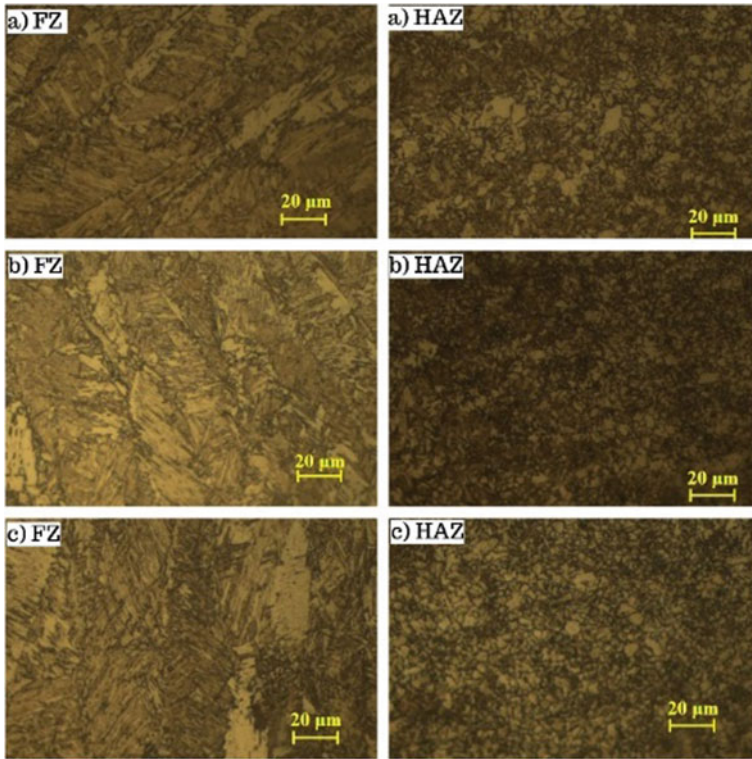
Fig. 9 FZ and HAZ microstructures **a** welding heat $=$ 21 kVA-900 ms, **b** welding heat $=$ 18 kVA-750 ms, **c** welding heat $=$ 15 kV-600 ms

occurs at the nugget zone, which causes an increase in the hardness value at the nugget as compared to HAZ and base material.

4.4 Comparison of Lap Shear Test Performance of RSW and SPR Joints

SPR is a spot joining technique with the use of rivet as consumable. In this process, mechanical interlocking is responsible for joint formation. On the other hand, melting and fusion are responsible for joint formation in RSW. Figure 6b compares the performance of RSW and SPR joints. For the RSW joint, the average FZ diameter measured was 3.3 mm, 3.9 mm, and 4.2 mm for 15 kVA, 18 kVA, and 21 kVA heat, respectively. For SPR, a rivet of shaft diameter 3.35 mm was used to make the comparison with RSW. The joint strength in SPR is determined by the amount of interlock, i.e., the greater the interlock, the higher is the joint strength. The maximum
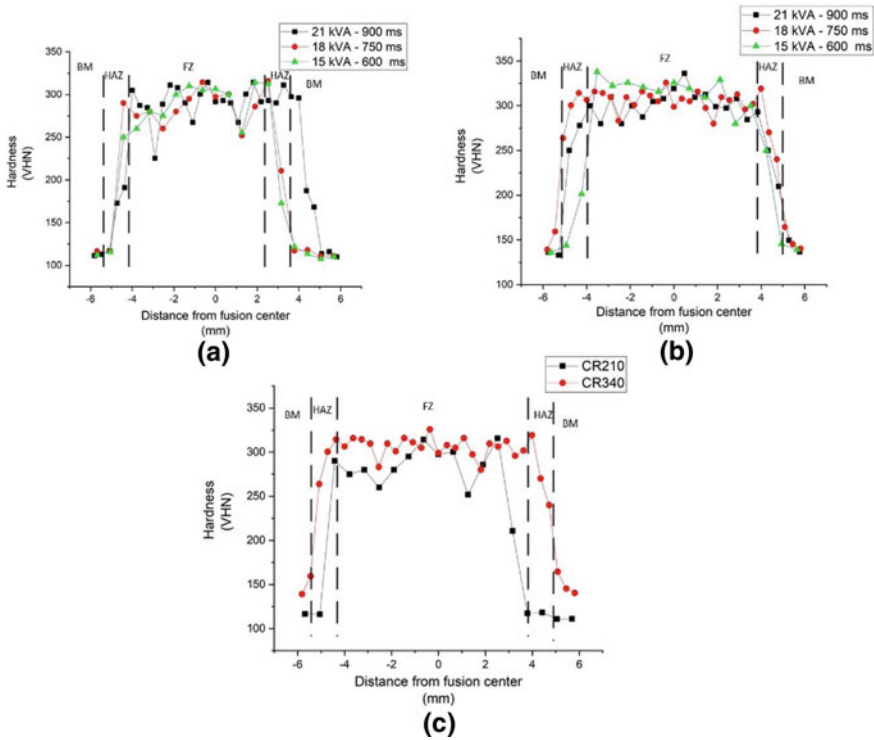
Fig. 10 Hardness distribution in RS welds **a** CR210 sheet at various cases, **b** CR340 sheet at various cases, **c** for 18 kVA-750 ms in CR210 and CR340 sheets

shear load obtained for 15 kVA, 18 kVA, and 21 kVA heat are 5.06 kN, 5.15 kN, and 5.02 kN, respectively. SPR exhibited a maximum shear load of 4.5 kN, which is lower compared to RSW.

Large variation in the maximum load-bearing capacity can be attributed to the difference in the nugget diameter. An increase in the rivet head diameter creates a larger stress concentration in SPR, which leads to a decrease in the maximum load-bearing ability. The energy absorbed in the failure of the SPR joint under static shear loading conditions is significantly lesser than the RSW joint indicating that metallurgical bonding in RSW is responsible for improved load-bearing ability. After 3 mm displacement in SPR, the maximum load decreases rapidly in the SPR joint and is characterized by shearing across the joint with less sheet deformation.

5 Conclusions

The following conclusion is drawn from the preliminary results obtained.

- In RSW, with the increase in heat, the maximum load increases up to the optimum case, and after that, it decreased. In the current work, 18 kVA-750 ms case is the optimum one, and the maximum force is highest in this case. As weld current and weld time are increased, nugget diameter increases, and after a point, expulsion occurs.
- Displacement at failure is directly proportional to the maximum load capacity. Thus, as maximum load increases, displacement at failure also increases.
- All the RSW cases show significant coarse grains in the FZ. Hardness is higher in FZ and relatively lower in HAZ due to HAZ softening.
- Load bearing ability of RSW joints is better than that of SPR joints when tested through lap shear mode indicating good static strength. About 14% improvement is seen in RSW as compared to SPR. The displacement at the failure of the RSW joint is higher than SPR showing greater stiffness and energy-absorbing capacity of the joint.

References

1. Rana, P.K., Narayanan, R.G., Kailas, S.V.: Friction stir spot welding of AA5052-H32/HDPE/AA5052-H32 sandwich sheets at varying plunge speeds. Thin-Walled Struct. **138**, 415–429 (2019). https://doi.org/10.1016/j.tws.2019.02.016
2. Briskham, P., Blundell, N., Han, L., Hewitt, R., Young, K., Boomer, D.: Comparison of self-pierce riveting, resistance spot welding and spot friction joining for aluminium automotive sheet. SAE Technical paper, 2006-01-0774 (2006). https://doi.org/10.4271/2006-01-0774
3. Eshtayeh, M.M., Hrairi, M., Mohiuddin, A.K.M.: Clinching process for joining dissimilar materials: state of the art. Int. J. Adv. Manuf. Technol. **82**(1–4), 179–195 (2016). https://doi.org/10.1007/s00170-015-7363-0
4. He, X., Xing, B., Zeng, K., Gu, F., Ball, A.: Numerical and experimental investigations of self-piercing riveting. Int. J. Adv. Manuf. Technol. **69**(1–4), 715–721 (2013). https://doi.org/10.1007/s00170-013-5072-0
5. Manladan, S.M., Yusof, F., Ramesh, S., Fadzil, M., Luo, Z., Ao, S.: A review on resistance spot welding of aluminum alloys. Int. J. Adv. Manuf. Technol. **90**(1–4), 605–634 (2017). https://doi.org/10.1007/s00170-016-9225-9
6. Liu, Y., Li, H., Zhao, H., Liu, X.: Effects of the die parameters on the self-piercing riveting process. Int. J. Adv. Manuf. Technol. **105**(7–8), 3353–3368 (2019). https://doi.org/10.1007/s00170-019-04567-4
7. Du, G., Xing, Y., Li, X.: Fatigue properties of self-piercing riveted multi-rivet joints in steel and aluminum sheets. Mater. Werkst. **50**(12), 1495–1502 (2019). https://doi.org/10.1002/mawe.201800114

8. Deng, J.-H., Lyu, F., Chen, R.-M., Fan, Z.-S.: Influence of die geometry on self-piercing riveting of aluminum alloy AA6061-T6 to mild steel SPFC340 sheets. Adv. Manuf. **7**(2), 209–220 (2019). https://doi.org/10.1007/s40436-019-00250-9

9. Li, D.: Influence of local surface texture by tool impression on the self-piercing riveting process and the static lap shear strength. J. Manuf. Process. **29**, 298–309 (2017). https://doi.org/10.1016/j.jmapro.2017.08.003

10. Saha, D.C., Park, Y.-D.: A review on Al-Al/Al-steel resistance spot welding technologies for light weight vehicles. J. Weld. Join. **29**(4), 35–40 (2011). https://doi.org/10.5781/KWJS.2011.29.4.397

11. Summerville, C., Adams, D., Compston, P., Doolan, M.: Nugget diameter in resistance spot welding: a comparison between a dynamic resistance based approach and ultrasound C-scan. Proc. Eng. **183**, 257–263 (2017). https://doi.org/10.1016/j.proeng.2017.04.033

12. Aslanlar, S., Ogur, A., Ozsarac, U., Ilhan, E.: Welding time effect on mechanical properties of automotive sheets in electrical resistance spot welding. Mater. Des. **29**(7), 1427–1431 (2008). https://doi.org/10.1016/j.matdes.2007.09.004

13. Aslanlar, S.: The effect of nucleus size on mechanical properties in electrical resistance spot welding of sheets used in automotive industry. Mater. Des. **27**(2), 125–131 (2006). https://doi.org/10.1016/j.matdes.2004.09.025

14. Eisazadeh, H., Hamedi, M., Halvaee, A.: New parametric study of nugget size in resistance spot welding process using finite element method. Mater. Des. **31**(1), 149–157 (2010). https://doi.org/10.1016/j.matdes.2009.06.042

15. Manladan, S.M., Abdullahi, I., Hamza, M.F.: A review on the application of resistance spot welding of automotive sheets. J. Eng. Technol. **10**, 20 (2015)

16. Hayat, F.: The effects of the welding current on heat input, nugget geometry, and the mechanical and fractural properties of resistance spot welding on Mg/Al dissimilar materials. Mater. Des. **32**(4), 2476–2484 (2011). https://doi.org/10.1016/j.matdes.2010.11.015

17. Rao, Z., Ou, L., Wang, Y., Wang, P.C., A self-piercing-through riveting method for joining of discontinuous carbon fiber reinforced nylon 6 composite. Compos. Struct. **237**, 111841 (2020). https://doi.org/10.1016/j.compstruct.2019.111841

18. Wan, X., Wang, Y., Zhang, P.: Modelling the effect of welding current on resistance spot welding of DP600 steel. J. Mater. Process. Technol. **214**(11), 2723–2729 (2014). https://doi.org/10.1016/j.jmatprotec.2014.06.009

19. Pouranvari, M.: Susceptibility to interfacial failure mode in similar and dissimilar resistance spot welds of DP600 dual phase steel and low carbon steel during cross-tension and tensile-shear loading conditions. Mater. Sci. Eng. A **546**, 129–138 (2012)

Optimization of Weld Parameters on Bead Characteristics During EBW of Inconel 825

Bishub Choudhury , **M. Chandrasekaran** , **Vivek Singh** ,
and **R. Ramesh**

1 Introduction

Electron beam welding (EBW) is a popular fusion welding technology in which the weld joint is produced by using an intense heat source in the form of an electron beam. When compared to arc welding processes, this energy-intensive beam welding technique provides better overall metallurgical and mechanical properties. This makes EBW an appealing choice for welding a variety of aerospace alloys, particularly nickel-based superalloys. However, weldability-related difficulties such as poor penetration, lack of strength in the heat-affected zone (HAZ), and fusion zone (FZ), susceptibility to surplus phases, cracking and welding defects are witnessed when welding various nickel-based alloys [1]. Choudhury and Chandrasekaran conducted a thorough study in the welding investigation of aerospace alloys focusing primarily on nickel-based aerospace alloys [2]. Superior weld quality is observed when employing laser beam welding (LBW) and EBW processes. Peng et al. studied the mechanical and metallurgical properties of Inconel 718 weldments welded with the EBW process. The HAZ and FZ grain sizes decrease from top to bottom [3]. Mei et al. studied the effect of welding speed on the microstructure and HAZ hot cracking susceptibility of Inconel 718 specimens welded with EBW. Higher welding speed is found effective in terms of lowering the likelihood of hot cracking [4]. Arulmurugan et al. investigated the mechanical and metallurgical properties of Inconel 686

B. Choudhury · M. Chandrasekaran (✉)
North Eastern Regional Institute of Science and Technology (NERIST), Nirjuli, Itanagar,
Arunachal Pradesh 791109,, India
e-mail: mchse1@yahoo.com

V. Singh
Department of Mechanical Engineering, AKGEC, Ghaziabad, Uttar Pradesh, India

R. Ramesh
Department of Mechanical Engineering, PSG College of Technology Coimbatore, Coimbatore,
Tamil Nadu, India

welded using the EBW process. Reduction of ductility and toughness in the welded joins is observed due to the segregation of Mo and *W* from the grain boundary [5]. The effect of EBW parameters on the microstructure, fracture, and fatigue properties of Nimonic 80A weldments was investigated by Zhang et al. Higher fatigue crack propagation is observed in the weld metal than the base metal [6]. These findings indicate that welding Ni-based alloys are feasible if correct procedures are followed. The importance of mathematical tools in welding practice is also emphasized in the studied literature.

The modern welding industry necessitates highly automated computer-assisted machines capable of producing high-quality components in the shortest amount of time and at the lowest possible cost. To satisfy this demand, the welding process settings need to be optimized in the best possible way. Optimization of welding parameters is considered to be a difficult task due to the involvement of various process variables and uncertainties. Over the years, many statistical and soft computing-based optimization approaches were developed to optimize various welding process parameters to produce components of optimal weld shape and mechanical properties. Moradi et al. optimize the process parameters of high-power diode laser surface hardening using a desirability and response surface methodology (RSM) approach while hardening AISI 410 [7]. Prabaharan et al. used a factorial design approach to study and optimize the gas tungsten arc welding (GTAW) process variables for optimum bead area [8]. Kumar and Kumar implemented Taguchi-grey relational analysis (GRA) to optimize friction stir welding (FSW) process parameters [9]. Sarkar et al. applied an analytical hierarchy approach based on the Taguchi method to optimize SMAW process parameters for optimal bead width, penetration, and bead reinforcement [10]. Chaudhury et al. proposed an integrated artificial neural network (ANN)-TLBO approach to optimize the GTAW parameters for optimal weld strength [11]. Nagesh and Dutta proposed an ANN-GA approach to predict and optimize the GTAW process parameters for optimal bead geometry [12]. Sathiya et al. conducted comparative research on three meta-heuristic soft computing-based optimization techniques, namely, GA, simulated annealing (SA), and particle swarm optimization (PSO), to optimize FSW variables for an optimum weld strength [13]. Babu et al. implemented an integrated ANN-GA algorithm to anticipate and optimize FSW variables for optimal mechanical and corrosion resistance properties of AA2219 weldments [14].

This study investigates the influences of EBW process parameters on two weld bead characteristics, namely, weld penetration (*P*) and weldment area (WA) during welding of a prominent Ni–Fe–Cr-based superalloy Inconel 825 known for its application in industries including aerospace, marine, nuclear, automotive, chemical processing, etc. Parametric optimization was performed employing two distinct approaches, namely, GA and desirability approach to optimize the EBW process parameter. The weld characteristics are simultaneously optimized to maximize weld penetration and minimize the weldment area. The optimization result will also provide important information to the manufacturing industry while EBW of Inconel 825.

2   Experimental Investigation

In this work, EBW investigation was carried out on a solid-solution strengthened nickel-base superalloy Inconel 825 having dimensions 100 mm × 75 mm × 2.2 mm. The chemical composition of Inconel 825 consists of Ni (41.2%), Fe (30.4%), Cr (21.32%), Mo (3.36%), Cu (1.67%) and balance (2.05%). Four EBW parameters namely beam current (I), accelerating voltage (V), welding speed (S), and beam oscillation (O) are varied through a series of pilot experiments to obtain the working ranges of each parameter. A design of experiments (DoE) named central composite design (CCD) having 30 experimental runs is considered to reduce the cost and time of conducting experiments. The EBW experiments were conducted in an 80 kV, 12 kW EBW facility, indigenously developed by Bhabha Atomic Research Center (BARC), available in IIT Kharagpur. The experimental procedure in carrying out welding investigation is presented in [15], and Fig. 1 shows the experimental setup used.

This work aims to investigate two weld bead characteristics, namely, weld penetration (P) and weldment area (WA). A weld bead of lower weldment area (WA) with higher weld penetration is considered economic in the welding industry. To obtain the P and WA of the weldments, a standard metallographic procedure is followed which includes a polishing in emery paper and aluminum slurry followed by etching. The final dimensions of P and WA of the weldments are recorded using a NIKON SMZ 25 Microscope. The results observed are stated in Table 1.
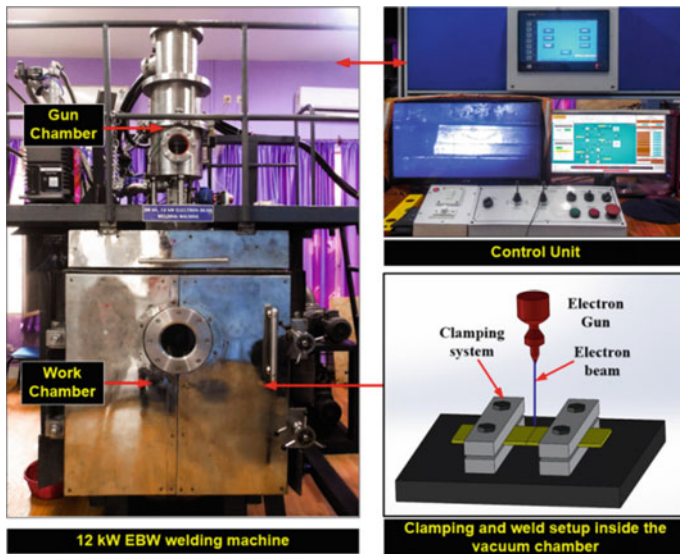
Fig. 1   EBW experimental setup

Table 1 Experimental results

S. No.	I (mA)	V (kV)	S (mm/min)	O (Hz)	P (mm)	WA (mm^2)
1	38	48	900	200	1.44	4.86
2	46	60	1200	600	2.40	5.99
3	42	54	1050	400	2.38	5.39
4	38	48	1200	600	1.56	3.93
5	38	48	1200	200	1.40	3.24
6	38	60	1200	600	2.34	5.06
7	38	60	1200	200	2.37	5.12
8	38	48	900	600	1.72	4.81
9	46	48	900	600	2.28	6.06
10	46	48	1200	600	2.00	4.92
11	42	54	1050	400	2.28	5.33
12	38	60	900	600	2.40	5.69
13	46	60	900	600	2.35	6.07
14	46	48	900	200	2.23	6.15
15	42	54	1050	400	2.37	5.54
16	42	54	1050	400	2.34	5.38
17	46	48	1200	200	1.76	4.52
18	38	60	900	200	2.42	5.89
19	46	60	1200	200	2.35	5.42
20	46	60	900	200	2.38	5.53
21	46	54	1050	400	2.54	6.02
22	42	54	1200	400	2.31	4.93
23	42	54	1050	400	2.31	5.38
24	42	54	1050	600	2.49	5.32
25	38	54	1050	400	2.46	5.33
26	42	54	900	400	2.54	5.64
27	42	54	1050	200	2.37	5.56
28	42	48	1050	400	1.66	4.89
29	42	54	1050	400	2.27	5.63
30	42	60	1050	400	2.28	5.67

3 Response Surface Modeling (RSM)

RSM is a popular and efficient statistical methodology that gives crucial informa-
tion about a process by developing a regression-based mathematical model between
process variables and response. RSM is commonly utilized in various industrial appli-
cations for solving various complicated nonlinear problems due to the advantages
such as less complexity in model development, strong accuracy and predictability

for both extrapolation and interpolation data, time and cost-effectiveness, and so on [16, 17]. This investigation establishes and investigates the predictive models of the weld penetration (P), and weldment area (WA), against the electron beam welding process variables. The general representation of an RSM model is presented in Eq. 1.

$$Y = f(I, V, O, S) \tag{1}$$

where Y denotes the response variable which is a function of the EBW process variables. The same equation can be represented as a second-order polynomial equation which includes all first-order terms, all square terms, and the interaction terms as mentioned in the Eq. 2.

$$Y = \rho + \sum_{b=1}^{4} \rho_b x_b + \sum_{b=1}^{4} \rho_{bb} x_b^2 + \sum_{b=1, c<b}^{4} \rho_{bc} x_b x_c + \varepsilon \tag{2}$$

where ρ = constant term; ρ_b, ρ_{bb}, ρ_{bc} are the coefficients of linear, square, and interaction terms, respectively; ε is error terms.

In this investigation, RSM-based predictive models for P and WA are developed considering the 30 datasets (Table 1) against four independent EBW process variables, i.e., V, S, I, O. The modeling of dependent variables is done by considering the quadratic effect of all the independent variables. Initially, the coefficients of the quadratic models were evaluated at a 95% confidence interval. Based on the evaluated results, the insignificant model terms were eliminated using the backward elimination method to adjust the fitted quadratic models. The predictive models developed for P and WA are as follows (Eqs. 3 and 4):

$$
\begin{aligned}
P = & -30.52 + 1.456V - 0.00370S - 0.319I + 0.002365O - 0.01124V^2 \\
& + 0.00784I^2 - 0.005729V * I - 0.000040V * O + 0.000060V * S \\
& \left(R^2 = 96.41\%, \quad R^2_{\text{Adj}} = 94.79\% \right)
\end{aligned} \tag{3}
$$

$$
\begin{aligned}
\text{WA} = & -25.20 + 0.912V + 0.594I - 0.01660S - 0.00672V * V \\
& - 0.00927V * I + 0.000256V * S \\
& \left(R^2 = 90.39\%, \quad R^2_{\text{Adj}} = 87.89\% \right)
\end{aligned} \tag{4}
$$

3.1 Predictive Performance of the RSM Models

The predictive performance of the developed model is evaluated using ANOVA analysis. The coefficient of determination (R^2), adjusted coefficient of determination

(R^2_{adj}), average percentage error (APE), lack-of-fit test, and p-test were also carried out to find the adequacy of the model developed [16]. To evaluate the APE, the following equation is used:

$$\text{APE} = \frac{1}{n} \sum_{i=0}^{n} \left(\frac{\text{abs}(Y_i - \overline{Y})}{Y_i} \times 100 \right) \tag{5}$$

where Y_i indicates experimental values, $\ddot{Y}$ is the mean value, and $\overline{Y}$ is the predicted value. For the P model, the ANOVA results obtained are stated in Table 2. From the result, it is observed that the p-value for the model is 0.000 which is less than an acceptable level of significance ($\alpha = 0.05$). Again, the p-value for lack-of-fit of the model is observed as 0.098 which is insignificant as it is more than 0.05 as desired. This indicates that the model developed is adequate at a 95% confidence interval. The APE of the predictive model is calculated as 2.295%, while the R^2 and R^2_{adj} are found as 96.41% and 94.79%, respectively. This lower value of APE and higher value of R^2 and R^2_{adj} indicate that the predictive model developed for P is highly adequate.

The ANOVA result for WA is presented in Table 3. The p-value for the developed model was found as 0.000, and is less than the level of significance ($\alpha = 0.05$), as required. Again, the p-value for lack-of-fit of the model is observed as 0.057 which is insignificant as it is more than 0.05 as desired. This implies that the model developed for WA is adequate at a 95% confidence interval. The R^2 and R^2_{adj} values for the predictive model are observed as 90.39% and 87.89%, respectively. The average percentage error (APE) is observed as 3.161%. This higher R^2 and R^2_{adj}, and lower

Table 2 ANOVA results for P

Source	DF	SS$_{\text{Adj}}$	MS$_{\text{Adj}}$	F-value	p-value	Adequacy and significance (%)
Model	9	3.06486	0.34054	59.67	0.000	Adequate
V	1	1.52542	1.52542	267.28	0.000	50.29
I	1	0.26402	0.26402	46.26	0.000	8.70
S	1	0.08961	0.08961	15.70	0.001	2.95
O	1	0.03736	0.03736	6.55	0.019	1.23
V^2	1	0.56363	0.56363	98.76	0.000	18.58
I^2	1	0.05424	0.05424	9.50	0.006	1.79
$V * I$	1	0.30250	0.30250	53.00	0.000	9.97
$V * S$	1	0.04623	0.04623	8.10	0.010	1.52
$V * O$	1	0.03610	0.03610	6.33	0.021	1.19
Lack-of-fit	15	0.10359	0.00691	3.27	0.098	Insignificant
Pure error	5	0.01055	0.00211			0.35
Total	29	3.03325				

Table 3 ANOVA for WA

Source	DF	SS_{Adj}	MS_{Adj}	F-value	p-value	Adequacy and significance (%)
Model	6	10.5439	1.75732	36.08	0.000	Adequate
V	1	2.7691	2.76909	56.85	0.000	23.74
I	1	2.5313	2.53125	51.96	0.000	21.70
S	1	3.1836	3.18361	65.36	0.000	27.29
V^2	1	0.4215	0.42147	8.65	0.007	3.61
$V * I$	1	0.7921	0.79210	16.26	0.001	6.79
$V * S$	1	0.8464	0.84640	17.38	0.000	7.26
Lack-of-fit	18	1.0525	0.05847	4.31	0.057	Insignificant
Pure error	5	0.0679	0.01358			0.58
Total	29	11.6643				

APE demonstrate higher accuracy and predictability while predicting *WA* of the Inconel 825 weldments.

4 Parametric Study

Three-dimensional surface plots were plotted between the significant parameters to identify the influence of process parameters on the weld bead characteristics *P* and WA. The ANOVA analysis for *P* (Table 2) identifies *V* as the dominating factor with a percentage contribution of 50.29%. The second-order effect of *V* and the interacting effect of *V* and *I* tend to have the next significance with 18.57% and 9.97%, respectively. The surface plots for *P* are depicted in Fig. 2a–c. It is observed that *P* increases with an increase in *V* and *I* and decreases with an increase in *S*. Higher *I*, lower *S*, and intermediate value of *V* (54–56 kV) is found favorable for higher weld penetration [15].

The ANOVA analysis for WA (Table 3) demonstrates, *S* as the dominating factor followed by *V* and *I*, with a percentage contribution of 27.29%, 23.74%, and 21.29%, respectively. The influence of *O* is found negligible on the resultant WA. The surface plot for WA is illustrated in Fig. 3a and b. Higher WA is observed when *V* is in level (54–60 kV), *I* is at the highest level (46 mA), and *S* is at the lowest level (900 mm/min). This observation for both *P* and WA is a result of higher heat input with a higher value of *I* and a lower value of *S*. This higher heat input results in higher temperature in the weld pool which subsequently increases the molten metal in the weld pool. The presence of more molten metal in the weld pool increases the *P* and WA of the weldments [15, 16].
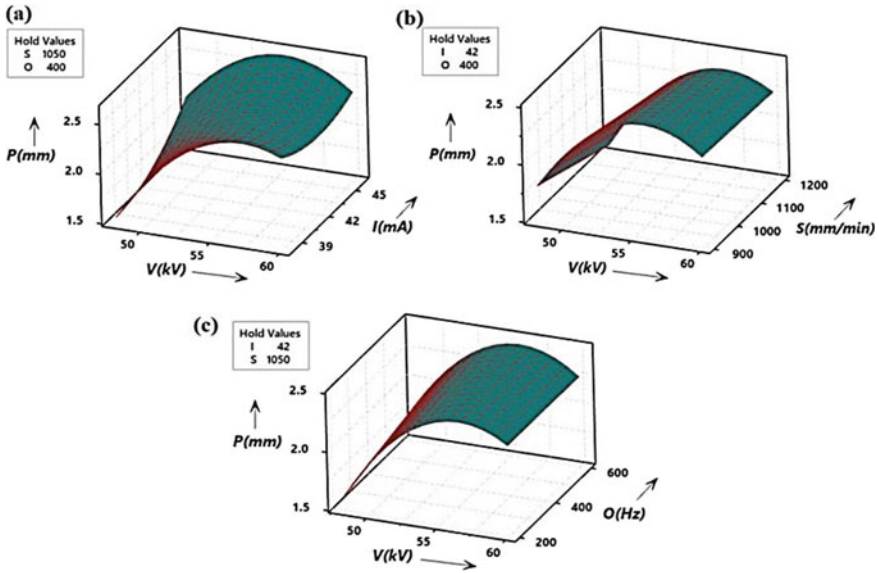
Fig. 2 Surface plot for *P* versus **a** *V* and *I*, **b** *V* and *S*, **c** *V* and *O*
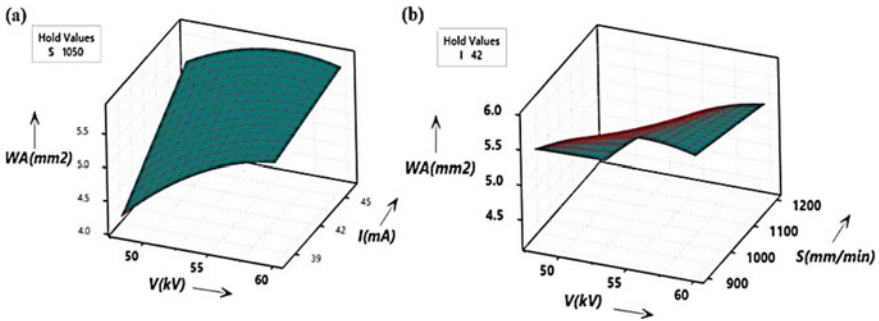
Fig. 3 Surface plot for WA versus **a** *V* and *I*, **b** *V* and *S*

5 Optimization of EBW Parameters

5.1 Indufstry Need-Based Multi Optimization Using GA

Genetic algorithm (GA) is a well-known optimization approach that handles many complicated nonlinear problems and has a wide variety of applications in diverse sectors. This algorithm works based on the mechanics of natural genetics and natural selection comprising selection, crossover, mutation, etc. The algorithm is begun with a set of solutions known as the population. The solution for one population is taken

and applied to the formation of a new population in the hope that the new population would outperform the previous one. The solutions are chosen based on their fitness to generate a new population (offspring). When either a maximum number of iterations have been generated or a suitable fitness level for the population has been reached [17].

In this work, EBW process parameters were optimized for optimum weld bead geometry. The two predictive models developed for P and WA are found adequate and acceptable, and hence are considered as an objective function for optimization. In general, a weld bead having higher weld penetration (P) while maintaining a smaller weldment area (WA) is considered economical. To satisfy both these objectives simultaneously, a multi-objective function is formulated as stated in Eq. 6.

$$\text{Minimize } Z = (w_{\text{WA}} \times f_{\text{WA}} - w_P \times f_P), \tag{6}$$

Subjected to: $38 \leq V \leq 46; 48 \leq I \leq 60; 900 \leq S \leq 1200; 200 \leq O \leq 400$ (7)

where f_{WA} is normalized function for WA, and f_P is normalized function for P. The w_{WA}, and w_P are the weightage assigned to WA and P, respectively, so that $w_{\text{WA}} + w_P = 1$. In this work, equal weightage i.e. $w_{\text{WA}} = w_P = 0.5$ is provided for both the characteristics. The optimization was performed in GA tool box in MATLAB version R2016a. The GA parameters considered for this investigation are as follows: (i) population size $= 100$, (ii) number of iterations $= 300$, (iii) selection operator $=$ tournament operator, (iv) crossover probability $= 0.95$, (v) crossover operator $=$ single point operator, and (vi) mutation probability $= 0.01$.

The multi-objective optimization using the GA approach provides a minimum composite function value of -0.1536 at parameter setting $V = 54$ kV, $I = 38$ mA, $S = 1179.48$ mm/min, and $O = 600$ Hz. The corresponding optimum values for P and WA are noted as 2.6517 mm and 4.728 mm^2, respectively. To obtain the Pareto optimal solution which provides all solutions to the problem, the code is rewritten considering both the objective functions, i.e., maximization of P and minimization of WA. As shown in Table 4, the method yields a total of 35 Pareto optimal solutions. The Pareto optimal front obtained is displayed in Fig. 4. In the present case, the desired penetration is 2.3 mm for the lowest value of WA. For such a case, the optimum $P = 2.316$ mm and WA $= 4.628$ mm^2 are obtained at Sl. No. 20 at parameter setting $V = 53.696$ kV, $I = 38.002$ mA, $S = 1200$ mm/min, and $O = 587.408$ Hz. Thus, a design engineer can easily pick one combination of the optimum parameter from Table 4 based on the design requirement for different values of P ranging from 2.721 mm to 1.501 mm.

Table 4 Pareto optimal solution

S. No.	I (mA)	V (kV)	S (mm/min)	O (Hz)	P (mm)	WA (mm^2)
1	38.002	48.014	1200.000	587.479	1.501	3.586
2	38.024	48.014	1181.624	587.537	1.516	3.668
3	38.002	48.493	1200.000	587.523	1.597	3.690
4	38.002	48.493	1181.624	587.515	1.612	3.767
5	38.002	48.921	1181.624	587.537	1.694	3.856
6	38.002	49.373	1200.000	587.479	1.762	3.874
7	38.009	49.373	1181.624	587.506	1.775	3.948
8	38.002	49.761	1181.624	587.537	1.842	4.023
9	38.002	50.297	1200.000	587.523	1.916	4.056
10	38.006	50.312	1181.639	587.521	1.931	4.128
11	38.002	50.797	1200.000	587.541	1.991	4.150
12	38.002	50.797	1181.624	587.538	2.003	4.216
13	38.002	51.325	1200.000	587.541	2.064	4.246
14	38.024	51.331	1181.624	587.537	2.076	4.313
15	38.002	52.021	1200.000	587.479	2.151	4.366
16	38.002	52.021	1181.624	587.537	2.162	4.426
17	38.002	52.571	1200.000	587.444	2.212	4.456
18	38.002	52.571	1181.624	587.537	2.223	4.514
19	38.002	53.071	1200.000	587.479	2.262	4.534
20	38.002	53.696	1200.000	587.408	2.316	4.628
21	38.002	53.696	1181.624	587.515	2.325	4.680
22	38.009	53.696	1157.125	587.479	2.337	4.751
23	38.008	54.937	1157.125	587.506	2.415	4.907
24	38.009	56.025	1157.125	587.515	2.455	5.027
25	38.009	55.838	1085.474	587.537	2.475	5.173
26	45.996	52.021	1200.000	587.479	2.483	5.259
27	45.996	52.021	1181.624	587.537	2.494	5.320
28	45.996	53.696	1200.000	587.537	2.572	5.397
29	45.998	54.937	1157.125	587.537	2.614	5.584
30	45.996	53.696	1085.478	587.538	2.626	5.724
31	45.998	54.937	1077.299	587.538	2.646	5.786
32	45.787	56.025	958.818	587.537	2.655	6.055
33	46.000	54.388	958.818	587.537	2.695	6.089
34	45.787	54.937	900.030	587.537	2.699	6.218
35	46.000	54.388	900.030	587.537	2.721	6.247

Fig. 4 Pareto optimal front
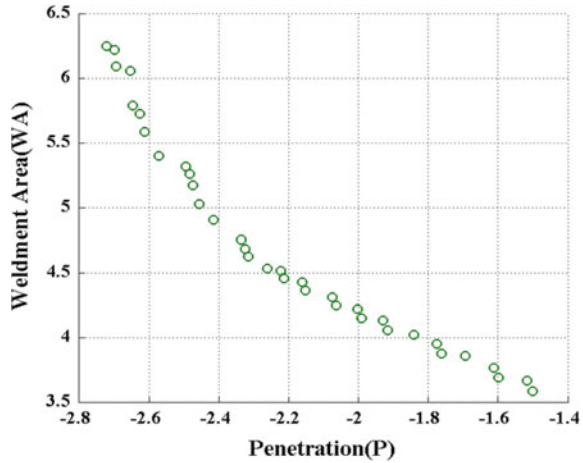
5.2 Desirability Optimization Approach

Harrington introduced the theory of desirability in 1965. Since then, this process has become an integral part of the fabrication industry for the optimization of different multiple response characteristics. Desirability function (DF) allows comparing responses with different scales of quality criteria and mapping them in $[0 - 1]$ scale [18]. In this work, desirability-based multi-objective optimization is carried out to optimize EBW process parameters that satisfy both the objectives, i.e., maximization of P and minimization of WA, simultaneously. The optimization was performed in Minitab 19, providing equal weightage (0.5) to each objective. Based on the objectives, the desirability approach will provide an optimal composite desirability value in the range [0–1].

The optimization result provides composite desirability of 0.6541 at optimum parameter setting $V = 53.45$ kV, $I = 38$ mA, $S = 1200$ mm/min, and $O = 600$ Hz. The maximum P was observed as 2.3039 mm which is higher than the desirable penetration, i.e., 2.3 mm. The desirability approach provides a minimum WA of 4.5798 mm^2. Figure 5 shows the desirability graph obtained.

5.3 Comparison of Results

A detailed comparison of the optimal results obtained using the GA and desirability approach is presented in Table 5. In both approaches, an equal weightage is provided to both the response characteristics. The optimal result obtained using both the approaches is found robust which provides a weld penetration above 2.3 mm as desired. The GA approach provides a superior weld penetration of 2.3517 mm compared to 2.3039 mm in the desirability approach. However, the WA observed in
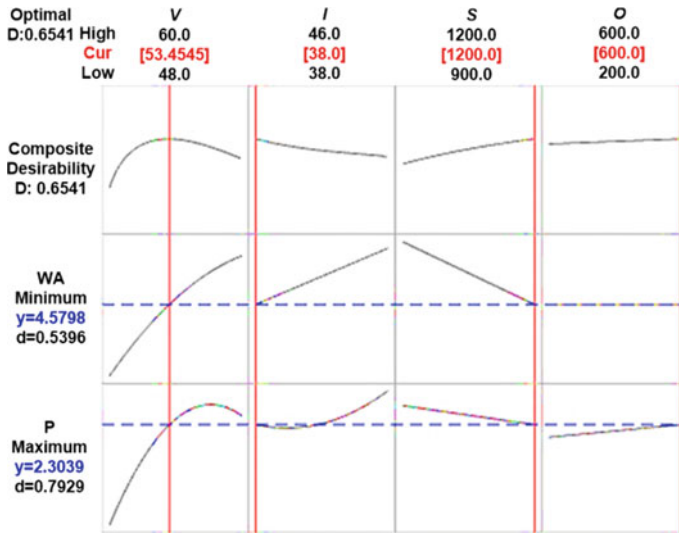
Fig. 5 Result of desirability optimization approach

Table 5 Comparison of optimal solutions

Methods	Optimal parameter setting				Optimum response	
	I (mA)	V (kV)	S (mm/min)	O (Hz)	P (mm)	WA (mm^2)
GA	38	54.00	1179.48	600	2.3517	4.7295
Desirability	38	53.45	1200	600	2.3039	4.5798

the desirability approach is found slightly superior and lower than the GA approach. This implies that both methods are adequate to locate the optimal solution within the search dimension during EBW of Inconel 825.

6   Conclusions

This work investigates the influences of EBW process parameters on two weld bead characteristics, namely, weld penetration (P) and weldment area (WA) during welding of Inconel 825. The conclusions drawn from this investigation are as follows:

1. The developed RSM predictive model for P and WA shows higher accuracy and predictability with R^2 of 96.41% for P and 90.39% for WA. The average percentage error (APE) for the P and WA models is noted as 2.295% and 3.161%, respectively.
2. The parametric study shows V and S as the most dominating factor for predicting P and WA, respectively, with a percentage contribution of 50.29% and 27.29%.

A diminutive influence of O is observed on both the characteristics. A higher I combined with a lower S for a specific value of V tends to increase the P and WA of the weldments.

3. The multi-objective optimization using GA results P of 2.3039 mm and WA of 4.7295 mm^2 at parameter setting $V = 54$ kV, $I = 38$ mA, $S = 1179.48$ mm/min, and $O = 600$ Hz. Again, the desirability approach results in a maximum P of 2.3039 mm and minimum WA of 4.5798 mm^2 at parameter setting $V = 53.45$ kV, $I = 38$ mA, $S = 1200$ mm/min, and $O = 600$ Hz.

4. Both the proposed approaches are found adequate in locating the optimal solution within the search dimension during EBW of Inconel 825. GA approach is found preferable as it provides a superior P, while the desirability approach provides the minimum WA of the Inconel 825 weldments.

References

1. Caron, J.L., Sowards, J.W.: Weldability of Nickel-based alloys. Elsevier Ltd (2014)
2. Choudhury, B., Chandrasekaran, M.: Investigation on welding characteristics of aerospace materials—a review. Mater. Today Proc. **4**, 7519–7526 (2017)
3. Peng, G., Kaifeng, Z., Bing-gang, Z., Shao-song, J., Bao-Wei, Z.: Microstructures and high-temperature mechanical properties of electron beam welded Inconel 718 superalloy thick plate. Trans. Nonferrous Met. Soc. China. **21**, S315–S322 (2011)
4. Mei, Y., Liu, Y., Liu, C., Li, C., Yu, L., Guo, Q., Li, H.: Effect of base metal and welding speed on fusion zone microstructure and HAZ hot-cracking of electron-beam welded Inconel 718. Mater. Des. **89**, 964–977 (2016)
5. Arulmurugan, B., Agilan, M., Jerome, S., Arivarasu, M., Manikandan, M., Srikanth, A., Arivazhagan, N.: Investigation of metallurgical and mechanical properties of 21st-century nickel-based superalloy 686 by electron beam welding technique. Sådhanå **43**, 117 (2018)
6. Karuthapandi, S., Ramu, M.: An experimental investigation of flat wire electrodes and their weld bead quality in the FCAW process. High Temp. Mater. Process. **21**(1), 65–79 (2017)
7. Moradi, M., Arabi, H., Shamsborhan, M.: Multi-objective optimization of high power diode laser surface hardening process of AISI 410 by means of RSM and desirability approach. Optik **202**, 163619 (2019)
8. Prabaharan, C., Venkatachalam, P., Kumar, S.K., Lenin, K.: Parametric optimization of gas tungsten arc welding processes by using factorial design approach. J. Scient. Ind. Res. **73**, 415–420 (2014)
9. Kumar, S., Kumar, S.: Multi-response optimization of process parameters for FSW of joining dissimilar Al alloys by grey relational analysis and Taguchi method. J. Braz. Soc. Mech. Sci. Eng. **37**(2), 665–674 (2014)
10. Sarkar, A., Roy, J., Majumder, A., Saha, S.C.: Optimization of welding parameters of submerged arc welding using analytic hierarchy process (AHP) based on Taguchi technique. J. Inst. Eng. (India) C. **95**(2), 159–168 (2014)
11. Choudhury, B., Chandrasekaran, M., Devarasiddappa, D.: Development of ANN modeling for estimation of weld strength and integrated optimization for GTAW of Inconel 825 sheets used in aero-engine components. J. Braz. Soc. Mech. Sci. Eng. **42**, 308 (2020)
12. Nagesh, D.S., Datta, G.L.: Genetic algorithm for optimization of welding variables for height to width ratio and application of ANN for prediction of bead geometry for TIG welding process. Appl. Soft Comput. **10**, 897–907 (2010)

13. Sathiya, P., Aravindan, S., Haq, A.N., Paneerselvam, K.: Optimization of friction welding parameters using evolutionary computational techniques. J. Mater. Process. Technol. **209**, 2576–2584 (2009)
14. Babu, K.K., Panneerselvam, K., Sathiya, P., Haq, A.N., Sundarrajan, S., Mastanaiah, P., Murthy, C.V.S.: Parameter optimization of friction stir welding of cryorolled AA2219 alloy using artificial neural network modeling with genetic algorithm. Int. J. Adv. Manuf. Technol. **94**, 3117 (2018)
15. Choudhury, B., Chandrasekaran, M.: Microstructural investigation and Integrated optimization of weld bead characteristics in electron beam welding of Inconel 825. Trans. Indian Inst. Met. **74**, 2681–2701 (2021)
16. Choudhury, B., Chandrasekaran, M.: Electron beam welding of aerospace alloy (Inconel 825): a comparative study of RSM and ANN modeling to predict weld bead area. Optik **219**, 165206 (2020)
17. Rao, R.V.: Advanced Modeling and Optimization of Manufacturing Processes. Springer, London Dordrecht Heidelberg, New York (2011)
18. Trautmann, H., Weihs, C.: Pareto-Optimality and Desirability Indices. University of Dortmund, SFB 475 Tech (2004)

Fuzzy Logic-Based Prediction of Mechanical Characteristics of Friction Welded AISI 430 Joint

G. Senthilkumar (ID)**, G. Rathinasabapathi** (ID)**, and T. Mayavan** (ID)

1 Introduction

Ferritic stainless steel (AISI 430) possesses brilliant mechanical properties and corrosion resistance. This material finds many applications in the field of boiler accessories and nuclear power plant equipment. The joining of ferrite stainless steel by friction welding yields the best joint characteristics compared with other joining techniques. The joint characteristics purely depend upon a selection of process variables and their values. Ultrasonic welding of two different materials has been modeled and optimized by fuzzy logic and genetic algorithm by which fuzzy logic yields good optimum results compared with a genetic algorithm [1]. The fuzzy logic technique has been applied to the combustion process in the boiler to predict heat dissipation coefficient which provides accurate results and good agreement with the preferred data [2]. A fuzzy regression equation is formulated to characterize weld bead dimension based on process parameters current, electrode diameter, arc voltage, and electrode movement speed [3]. The ultimate tensile stress of aluminum joined by friction stir welding modeled by ANFIS using process parameters and found that tool rotational speed is influencing the tensile strength [4]. The method of fuzzy analytical hierarchy process finds high-pressure vessels like boiler, and heat exchanger parts are welded by TIG welding and PAW techniques are most appropriate functionality [5]. TIG welding equipped with fuzzy controller and CCD system to produce good quality weld in terms of weld bead size and depth of penetration [6]. The fuzzy logic system is applied to the machining process to predict surface roughness of the component by coated tool and uncoated tool [7]. Fuzzy logic optimization technique applied to submerged arc welding to predict the best process parameter to produce sound weld [8]. Multiple

G. Senthilkumar (✉)
Department of Mechanical Engineering, Panimalar Institute of Technology, Chennai, India
e-mail: Senthilngt1978@gmail.com

G. Rathinasabapathi · T. Mayavan
Department of Mechanical Engineering, Panimalar Engineering College, Chennai, India

response performance indexes predicted for electrical discharge machining system by Taguchi method of optimization and fuzzy reasoning [9]. Fuzzy-2 logic systems create the best model predicting capacity by merging the initial ruleset with optimized new rules [10]. A micro-hole electrical discharge drilling machine equipped with a gain scheduling controller was not efficient as a fuzzy logic controller for reduced drilling time [11]. The complicated multi-response analysis is easily done by single grey fuzzy logic analysis [12]. Residual stress in the welded joint is predicted and validated by a fuzzy support vector regression model, and this is very accurate in terms of accuracy and computing speed [13]. Weld defects recognition and weld design implementation by different input vectors using ANFIS achieved excellent results [14]. ANN model is used instead of regression model for getting more accurate results, and fuzzy logic system controls the parameters effectively the welding of stainless steel [15]. The fuzzy-genetic algorithm is incorporated in wire tension control which is a very important phenomenon for electrical discharge machines is produces near-optimal responses [16]. The fuzzy-based approach for modeling of parameters in TIG welding gives better performance and is compared with radial basis function and multilayer perceptron of neural network techniques [17]. In pulsed MIG welding, short-circuiting is one of the biggest drawbacks to producing satisfactory weld. To avoid short-circuiting, control of process parameters is playing a vital role. Fuzzy-based models are exact alternatives for these situations [18]. The robust data analysis model is selecting the best process parameters combination from neural network tool and Taguchi analysis to prevent improper decision making from either of the method [19]. Response surface methodology-based model for milling of austenitic stainless steel is highly agreed with experimental data [20]. A model developed based on Buckingham's pi theorem using dimensions of process parameters is closely mapped with experimental results [21]. The fuzzy logic analysis yields the best results in the comparative study carried out for modeling of friction welding parameters using regression analysis, finite element analysis, and fuzzy logic analysis [22]. The literature review shows that most of the researchers used ANN and regression analysis for friction welding process parameters modeling, but very few works are available based on fuzzy logic. Therefore in this study, modeling of friction welding process parameters using fuzzy logic is developed, and it is used to forecast output response like ultimate tensile strength, impact toughness, and axial shortening.

2   Materials and Methods

In this work, experiments were conducted by a continuous drive friction welding machine. The material employed in this work is AISI430 Ferritic stainless steel and their composition is available in Table 1. L_{27} Orthogonal array is used as an experimental plan for this work to get uniformly distributed results for the given range of input parameters. FW specimen was cylindrical in the shape of diameter 12 mm and length 100 mm.

Table 1 Base metal chemical composition

Element	C	Cr	Ni	Mn	Si	S	P	Mo	Fe
%	0.12	16.39	0.45	1.59	0.42	Nil	0.028	0.22	Balance

Fig. 1 Friction welding machine

In this work, the welding operations performed out on an RV MACHINE TOOL-Friction welding machine are shown in Fig. 1. The process parameters used for friction welding, experimental plan, and experimental results are given in Table 2. Tensile test specimens and Impact Test Specimens were prepared by ASTM E8M and ASTM A370, respectively.

3 Fuzzy Modeling of Parameters

Figure 2 shows the input factors such as friction pressure, forging pressure, upset time, and rotational speed to output factors like tensile strength, axial shortening, and impact toughness embedded using fuzzy logic toolbox in MATLAB R2013(a). A fuzzy inference system creates and correlates a given input to an output using fuzzy logic which includes membership functions, IF–THEN rules, and logical operations. Membership function based on triangular, trapezoidal, Gaussian, generalized Gaussian, and sigmoid is available. In this paper, membership function based on the triangle is used due to its simplicity. Equation 1 and Figs. 2 and 3 show a mathematical representation of the Triangular membership function. Let x, y, and z represent the 'a' coordinate of these variables of $\mu_p(a)$ in a fuzzy set.

$$\mu_p(a) = \begin{cases} 0, & \text{if } a \leq x \\ \frac{a-x}{y-x}, & \text{if } x \leq a \leq y \\ \frac{z-a}{z-y}, & \text{if } y \leq a \leq z \\ 0, & \text{if } a \geq z \end{cases} \tag{1}$$

Table 2 Process parameters and experimental results

Welding parameters				Experimental results		
S. No.	Friction pressure (MPa)	Forging pressure (MPa)	Upset time (s)	Speed (rpm)	Ultimate tensile strength (MPa)	Axial shortening (mm)	Impact toughness (J)
1	20	50	3	800	518	10.933	14
2	20	50	3	800	514	10.88	16
3	20	50	3	800	519	10.533	20
4	20	55	5	1000	508	5.757	18
5	20	55	5	1000	515	5.98	21
6	20	55	5	1000	507	6.306	18
7	20	60	7	1200	518	17.781	23
8	20	60	7	1200	517	17.206	15
9	20	60	7	1200	519	17.51	19
10	30	50	7	1200	507	35.501	16
11	30	50	7	1200	510	34.306	18
12	30	50	7	1200	515	33.876	19
13	30	55	3	800	530	14.536	23
14	30	55	3	800	523	12.675	15
15	30	55	3	800	521	13.310	19
16	30	60	5	1000	523	16.656	16
17	30	60	5	1000	525	15.431	20
18	30	60	5	1000	521	16.123	18
19	40	50	5	1000	507	17.781	18
20	40	50	5	1000	510	17.585	23
21	40	50	5	1000	514	17.606	15
22	40	55	7	1200	523	18.08	20
23	40	55	7	1200	521	17.95	18
24	40	55	7	1200	518	18.31	21
25	40	60	3	800	534	8.89	18
26	40	60	3	800	532	8.68	19
27	40	60	3	800	536	9.53	15

In the membership function, friction pressure is a minimum of 20 MPa to a maximum of 40 MPa, forging pressure is a minimum of 50 MPa to a maximum of 60 MPa, upset time is a minimum of 3 s to a maximum of 7 s, and rotatioal speed minimum of 800 rpm to a maximum of 1200 rpm fed into fuzzy systems as an input variable.

Tensile strength in the range of 507–536 MPa, axial shortening in the range of 5.98–35.5 mm, and impact toughness in the range of 14–23 J are fed into the fuzzy
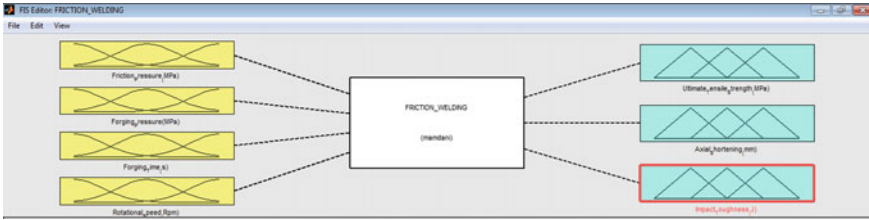
Fig. 2 Model for ultimate tensile strength, impact toughness, and axial shortening

Fig. 3 Triangular membership function
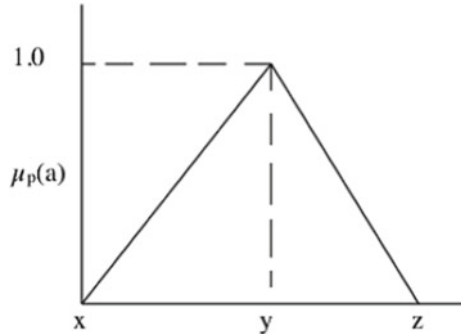
systems as an output variable. Figure 4 shows the membership function for friction welding as an input factor. Linguistic parameters such as low, medium, and high are used for friction pressure, forging pressure, upset time, and rotational speed to represent as input value similarly output values are represented.

The fuzzy rule set based on input parameters and experimental results created for 27 variations by taking minimum, maximum, and average of their values are listed in Table 3. The defuzzification output is shown in Fig. 5. The relationship between the fuzzy predicted value and experimental values is plotted in Figs. 6, 7 and 8. The figures show a very close correlation between fuzzy output values and experimental result values. This is confirmed that fuzzy-based mathematical modeling can be the best method used for predicting ultimate tensile strength, burn-off length, and impact toughness in friction welding of ferrite stainless steel.

4   Results and Discussion

The mechanical characteristics such as ultimate tensile strength, axial shortening, and impact toughness of friction welded joint are predicted from the fuzzy logic model. It is clear that high intensity of friction pressure, friction time, forging pressure, and low value of rotational speed give maximum tensile strength because higher friction pressure and friction time generate more heat at the interface, high-level plasticity, and
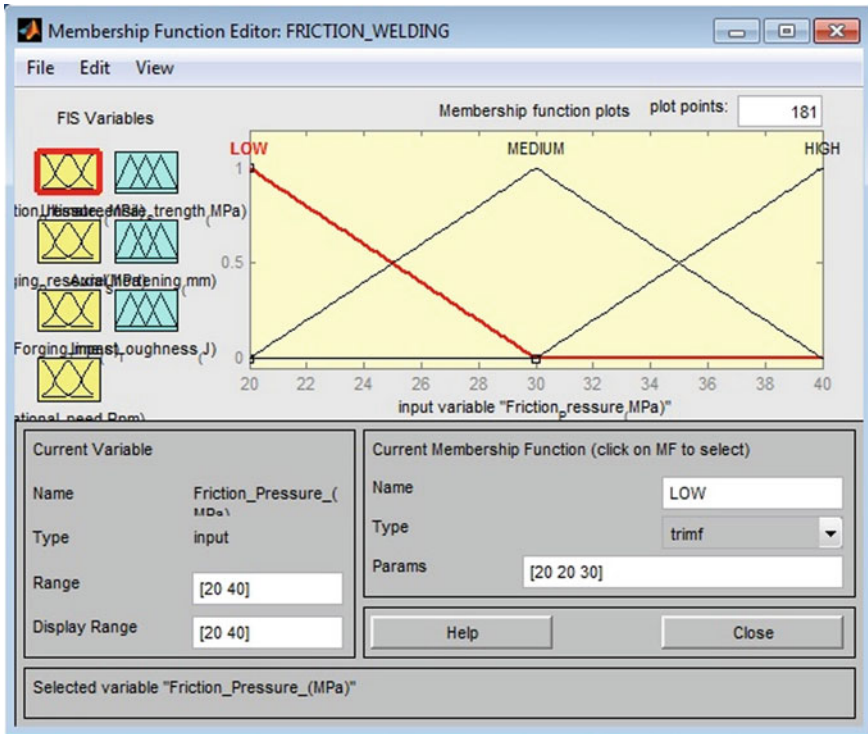
Fig. 4 Implementation of triangular membership function in fuzzy logic

fine grains at the HAZ region. High friction pressure and upset time tend to produce more axial shortening due to more softening of the weld interface. The reason to get high impact toughness is the increase in forging pressure which develops high cohesiveness in the interface. Friction welding input and output parameters were 3D surfaces modeled using a rule set in MATLAB R2013a software. Figures 9, 10 and 11 show the 3D surfaces model developed by fuzzy logic. The relationship between two input parameters and one output parameter is shown in the 3D surfaces model. The influence of input parameters on output parameters is directly observed through this 3D surface model. Input parameter 'friction pressure' which is shown in Figs. 9, 10 and 11 is scaled under numerical values of 20 MPa, 30 MPa, 40 MPa are considered low, medium, and high, respectively.

Similarly, forging pressure numerical values of 50 MPa, 55 MPa, and 60 MPa are considered low, medium, and high, respectively. Output response ultimate tensile strength shown in Fig. 9 that is scaled under numerical values below 510 MPa, between 514 and 525 MPa and above 530 MPa is considered low, medium, and high, respectively.

Figure 10 shows that the axial shortening values below 10.5 mm, between 10.9 and 18.3 mm, and above 33.8 mm are considered low, medium, and high, respectively.

Table 3 Fuzzy rules of input and output parameters

Rules	IF								THEN		
	FP		UP		UT		Speed		UTS	ΔL	IT
1	Low	And	Low	And	Low	And	Low		Medium	Medium	Low
2	Low	And	Low	And	Low	And	Low		Medium	Medium	Medium
3	Low	And	Low	And	Low	And	Low		Medium	Medium	Medium
4	Low	And	Medium	And	Medium	And	Medium		Low	Low	Medium
5	Low	And	Medium	And	Medium	And	Medium		Medium	Low	High
6	Low	And	Medium	And	Medium	And	Medium		Low	Low	Medium
7	Low	And	High	And	High	And	High		Medium	Medium	High
8	Low	And	High	And	High	And	High		Medium	Medium	Low
9	Low	And	High	And	High	And	High		Medium	Medium	Medium
10	Medium	And	Low	And	Medium	And	High		Low	High	Low
11	Medium	And	Low	And	Medium	And	High		Low	High	Medium
12	Medium	And	Low	And	Medium	And	High		Medium	High	Medium
13	Medium	And	Medium	And	High	And	Low		High	Medium	High
14	Medium	And	Medium	And	High	And	Low		Medium	Medium	Low
15	Medium	And	Medium	And	High	And	Low		Medium	Medium	Medium
16	Medium	And	High	And	Low	And	Medium		Medium	Medium	Low
17	Medium	And	High	And	Low	And	Medium		Medium	Medium	Medium
18	Medium	And	High	And	Low	And	Medium		Medium	Medium	Medium
19	High	And	Low	And	High	And	Medium		Low	Medium	Medium
20	High	And	Low	And	High	And	Medium		Low	Medium	High
21	High	And	Low	And	High	And	Medium		Medium	Medium	Low
22	High	And	Medium	And	Low	And	High		Medium	Medium	Medium
23	High	And	Medium	And	Low	And	High		Medium	Medium	Medium
24	High	And	Medium	And	Low	And	High		Medium	Medium	High
25	High	And	High	And	Medium	And	Low		High	Low	Medium
26	High	And	High	And	Medium	And	Low		High	Low	Medium
27	High	And	High	And	Medium	And	Low		High	Low	Low

Output parameter impact toughness shown in Fig. 11 shows that numerical values less than 15 J, between 16 and 20 J, and greater than 21 J are considered low, medium, and high, respectively.
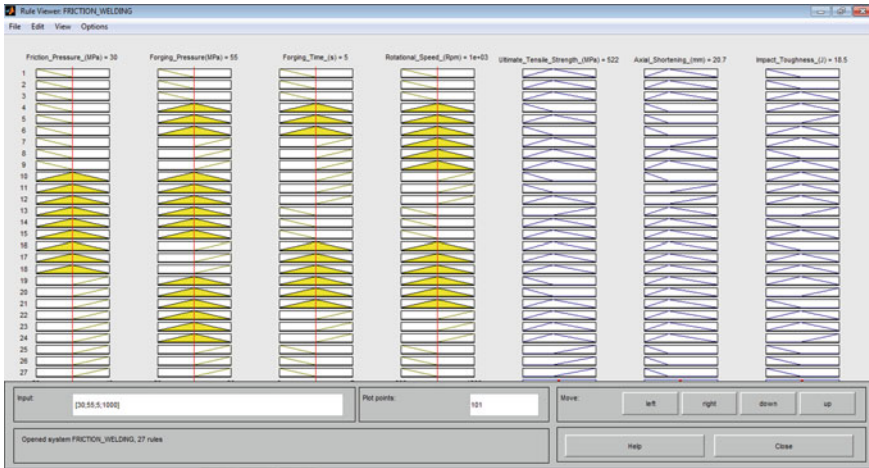
Fig. 5 MATLAB output of fuzzy rule set
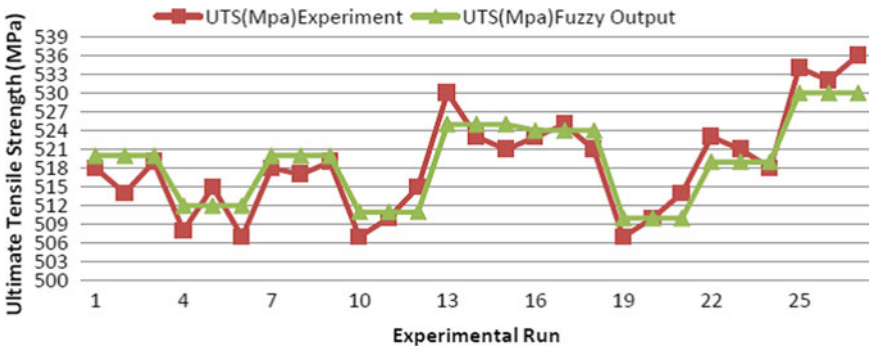
Fig. 6 Comparison of fuzzy logic output with experimental result for ultimate tensile strength of friction welded ferrite stainless steel joint

5 Confirmation Test

Fuzzy model validity is verified with the experimental result of ultimate tensile strength, burn-off length, and impact toughness using test numbers 1, 4, and 7. Figure 12a–c shows a comparison of experimental results with predicted results of the fuzzy model. It can be understood from the graph that fuzzy predicted values were close to the experimental results, which confirms the accuracy of the fuzzy model for friction welding of AISI 430 Ferritic stainless steel.
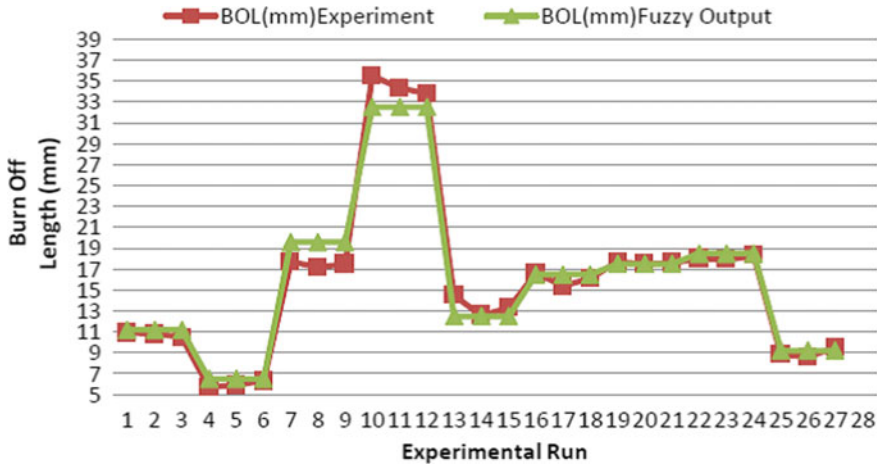
Fig. 7 Comparison of fuzzy logic output with experimental result for the burn-off length of friction welded ferrite stainless steel joint
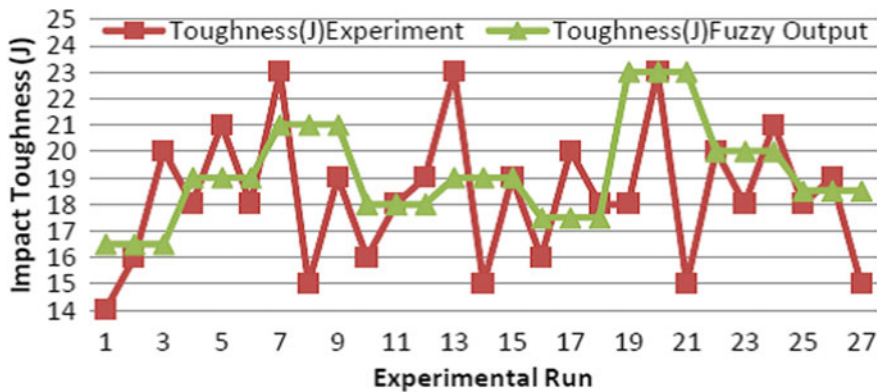
Fig. 8 Comparison of fuzzy logic output with experimental result for impact toughness of friction welded ferrite stainless steel joint

6 Conclusions

In this work, an artificial intelligence tool fuzzy logic-based model was developed and presented for predicting the mechanical characteristics of friction welded ferrite stainless steel. The conclusions are listed here.

1. Friction welding input parameters such as friction pressure, forging pressure, forging time, and rotational speed influence the output characteristics of tensile strength, axial shortening, and impact toughness of the friction welded ferrite stainless steel joint.
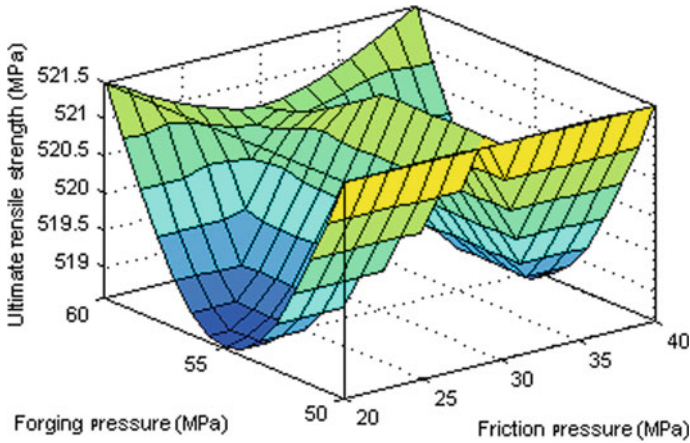
Fig. 9. 3D surface model for ultimate tensile strength with forging pressure and friction pressure
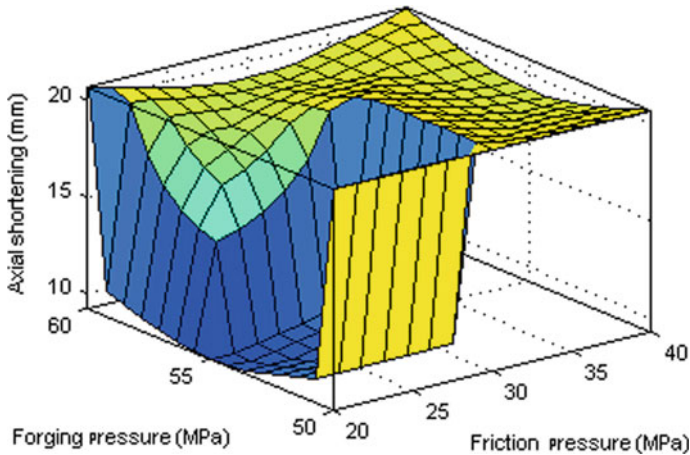
Fig. 10. 3D surface model for axial shortening with forging pressure and friction pressure

2. Predicting the mechanical characteristics of friction welded ferrite stainless steel joint is successfully created by an AI tool fuzzy logic.
3. Material loss can be minimized by predicting the axial shortening while friction welding by using this tool results in reduced material cost.
4. In this work, 3D surfaces developed are can be used as a fantastic tool for fixing the process parameter values.
5. The fuzzy-based output values are closely agreed with experimental values. Therefore, this technique can be applied to other welding techniques and machining processes to predict the system behavior.

Fig. 11. 3D surface model for impact toughness with forging pressure and friction pressure

Fig. 12 Confirmation trial of fuzzy modeling for **a** ultimate tensile strength, **b** burn-off length, and **c** impact toughness

References

1. Satpathy, M.P., Moharana, B.R., Dewangan, S., Sahoo, S.K.: Modeling and optimization of ultrasonic metal welding on dissimilar sheets using fuzzy-based genetic algorithm approach. Eng. Sci. Technol. Int. J. **4**, 634–647 (2015)
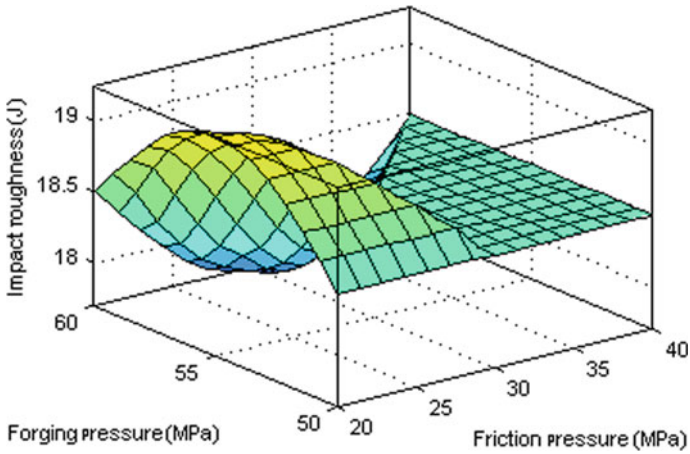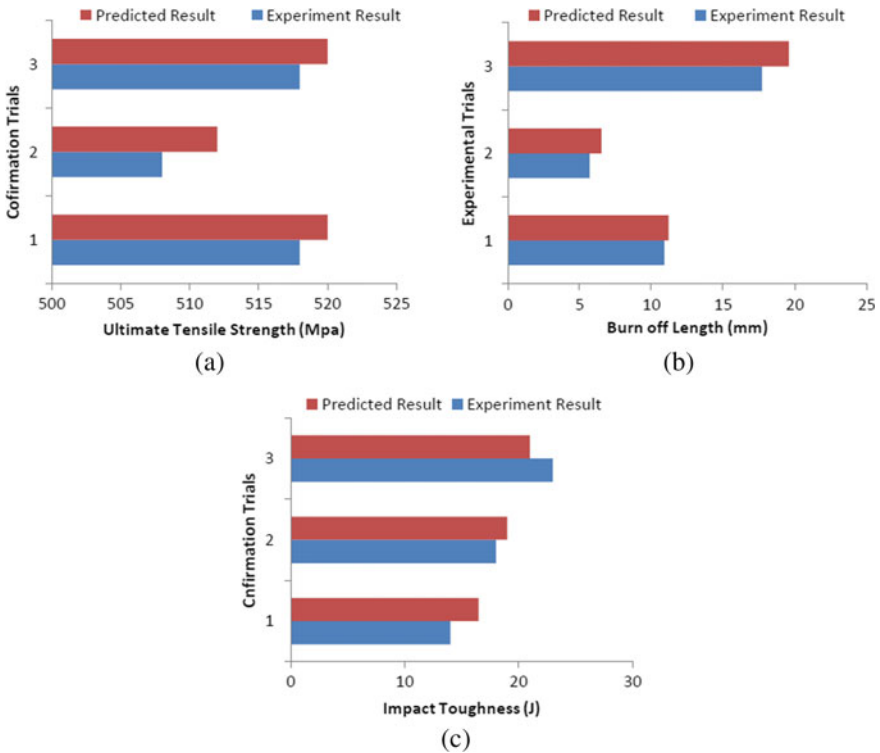2. Krzywanski, J., Nowak, W.: Modeling of bed-to-wall heat transfer coefficient in a large-scale CFBC by fuzzy logic approach. Int. J. Heat Mass Transf. **1**(94), 327–334 (2016)
3. Xue, Y., Kim, I.S., Son, J.S., Park, C.E., Kim, H.H., Sung, B.S., Kim, I.J., Kim, H.J., Kang, B.Y.: Fuzzy regression method for prediction and control the bead width in the robotic arc-welding process. J. Mater. Process. Technol. **164**, 1134–1139 (2005)
4. Shehabeldeen, T.A., Elaziz, M.A., Elsheikh, A.H., Zhou, J.: Modeling of friction stir welding process using adaptive neuro-fuzzy inference system integrated with Harris Hawks optimizer. J. Mater. Res. Technol. (2019)
5. Jafarian, M., Vahdat, S.E.: A fuzzy multi-attribute approach to select the welding process at high pressure vessel manufacturing. J. Manuf. Process. **14**(3), 250–256 (2012)
6. Tsai, C.H., Hou, K.H., Chuang, H.T.: Fuzzy control of pulsed GTA welds by using real-time root bead image feedback. J. Mater. Process. Technol. **176**(1–3), 158–167 (2006)
7. Thakur, A., Dewangan, S., Patnaik, Y., Gangopadhyay, S.: Prediction of work hardening during machining Inconel 825 using fuzzy logic method. Proc. Mater. Sci. **1**(5), 2046–2053 (2014)
8. Kumar, A., Maheshwari, S., Sharma, S.K.: Fuzzy logic optimization of weld properties for SAW using silica based agglomerated flux. Proc. Comput. Sci. **1**(57), 1140–1148 (2015)
9. Lin, J.L., Wang, K.S., Yan, B.H., Tarng, Y.S.: Optimization of the electrical discharge machining process based on the Taguchi method with fuzzy logics. J. Mater. Process. Technol. **102**(1–3), 48–55 (2000)
10. Baraka, A., Panoutsos, G.: Long-term learning for type-2 neural-fuzzy systems. Fuzzy Sets Syst. **1**(368), 59–81 (2019)
11. Kao, C.C., Shih, A.J.: Design and tuning of a fuzzy logic controller for micro-hole electrical discharge machining. J. Manuf. Process. **10**(2), 61–73 (2008)
12. Chiang, K.T., Chang, F.P.: Application of grey-fuzzy logic on the optimal process design of an injection-molded part with a thin shell feature. Int. Commun. Heat Mass Transf. **33**(1), 94–101 (2006)
13. Dhas, J.E., Kumanan, S.: Evolutionary fuzzy SVR modeling of weld residual stress. Appl. Soft Comput. **1**(42), 423–430 (2016)
14. Zapata, J., Vilar, R., Ruiz, R.: An adaptive-network-based fuzzy inference system for classification of welding defects. NDT e Int. **43**(3), 191–199 (2010)
15. Vasudevan, M.: Soft computing techniques in stainless steel welding. Mater. Manuf. Process. **24**(2), 209–218 (2009)
16. Yan, M.T., Fang, C.C.: Application of genetic algorithm-based fuzzy logic control in wire transport system of wire-EDM machine. J. Mater. Process. Technol. **205**(1–3), 128–37 (2008)
17. Ghanty, P., Paul, S., Roy, A., Mukherjee, D.P., Pal, N.R., Vasudevan, M., Kumar, H., Bhaduri, A.K.: Fuzzy rule based approach for predicting weld bead geometry in gas tungsten arc welding. Sci. Technol. Weld. Join. **13**(2), 167–75 (2008)
18. Madasu, V.K., Praveen, P., Yarlagadda, P.K.: Fuzzy modelling based estimation of short circuit severity in pulse gas metal arc welding. Aust. J. Mech. Eng. **7**(1), 9–17 (2009)
19. Krishnamoorthy, A., Boopathy, S.R., Palanikumar, K., Davim, J.P.: Application of grey fuzzy logic for the optimization of drilling parameters for CFRP composites with multiple performance characteristics. Measurement **45**(5), 1286–1296 (2012)
20. Majumder, H., Maity, K.: Prediction and optimization of surface roughness and micro-hardness using GRNN and MOORA-fuzzy-a MCDM approach for nitinol in WEDM. Measurement **118**, 1–3 (2018)

21. Senthilkumar, G., Ramakrishnan, R.: Influence of mechanical characteristics of friction welded ferrite stainless steel joint through novel mathematical model using Buckingham's Pi theorem. Int. J. Mech. Prod. Eng. Res. Dev. 185–198 (2020)
22. Senthilkumar, G., Ramakrishnan, R.: A comparative study of predicting burn off length in continuous drive solid state friction welding for ASTM A516 Steel by regression analysis, fuzzy logic analysis and finite element analysis. J. Appl. Sci. Eng. **24**(3), 359–366 (2021)

Productivity Benefits in Employing SiO₂ Flux-Based Activated TIG Welding for Joining Thicker Components

Bashab Chandra Paul[ID]**, Suman Saha**[ID]**, and Santanu Das**[ID]

1 Introduction

Welding is one of the joining processes where two or more materials are permanently joined together by weld bead formation with or without the supply of external filler material, pressure, and/or heat. Arc welding is a sub-group of welding processes, where an electric arc is employed for supplying heat for fusing the faying surfaces for coalescence (weld bead) formation. There are several arc welding processes; each one has distinct procedure, capability, and application. Tungsten Inert Gas (TIG) welding, also known as Gas Tungsten Arc Welding (GTAW), is one such arc welding process where a non-consumable tungsten electrode is employed for establishing the electric arc with the parent components that are to be joined. Since the TIG welding electrode is non-consumable type, it is not meant for melting down and subsequently depositing onto the weld bead in the form of filler. Accordingly, TIG welding inherently offers autogenous welding mode (i.e., joining without additional filler metal). However, filler metal that usually comes in the form of a small diameter rod can also be supplied separately during homogeneous welding (sometimes heterogeneous too) [1]. If carried out properly with the optimum set of parameters, TIG welding can offer defect-free reliable joint with good appearance requiring minimum effort.

Despite its multifarious advantages, TIG welding lacks economic benefit owing to low productivity, particularly in joining thicker plates [2]. Conventional TIG welding is capable of fetching typically up to 3.5-mm penetration depth in a single pass. Accordingly, edge preparation and multiple welding passes are indispensably required while joining thicker plates (thickness typically higher than 3.5 mm).

B. C. Paul (✉)
Department of Mechanical Engineering, Kalyani Government Engineering College, Kalyani, West Bengal, India
e-mail: bashabpaul.me@gmail.com

S. Saha · S. Das
Department of Mechanical Engineering, IIT Kharagpur, Kharagpur, West Bengal, India

These time-consuming steps not only increase overall welding time but also severely affect the metallurgical properties of the weld bead and surrounding region owing to repeated heat cycles. Consumption of higher volume of costly filler metal is also economically squandering. To get rid of its limited penetration capability while embracing its benefits, several new variants of conventional TIG welding process have been developed over the last few years. As highlighted by Saha et al., some of these variants include keyhole TIG, activated TIG, flux-bound TIG, strengthening activated TIG, advanced activated TIG, laser-assisted TIG, etc. [3].

Activated Tungsten Inert Gas (A-TIG) welding is a popular variant of conventional TIG welding process where a thin layer of suitable activating flux is deposited on the base plates prior to striking the arc [4]. The procedure of A-TIG welding is similar to the conventional TIG welding, except the additional step of flux deposition associated with the former one. A-TIG welding also employs a non-consumable electrode made of tungsten (with minor alloying elements like oxides of thorium, lanthanum, zirconium, cerium, etc.). Shielding gas (usually, inert gas like argon) is also supplied to protect the weld bead from atmospheric air. Several inorganic ingredients, mostly halides and oxides, were used as activating flux during A-TIG welding [5].

The most important benefit of A-TIG is its capability in enhancing penetration by a considerable margin, even up to four times as compared to conventional TIG welding [4]. Accordingly, it can eliminate the requirement of multiple passes during joining of thicker components. Reduction in welding passes, once again, helps reducing width of the heat-affected zone, distortion, inter-layer defects, etc. Elimination of time-consuming edge preparation step is added benefit. Usage of appropriate activated flux during A-TIG welding also reduces weld bead width. Less heat wastage together with power saving also makes the process more sustainable [6]. Although several experimental works are available in literature, quantitative assessment of the benefits of A-TIG welding is not carried out thoroughly. In an earlier work, the authors attempted to assess productivity benefits of T-TIG welding and it was observed that up to 70% reduction in actual welding time can be obtained by employing A-TIG for joining thicker components [7].

Objective of this article is to quantitatively assess the benefits of employing SiO_2-based A-TIG welding for joining 8 mm thick stainless steel plates. Benefits with regard to productivity and heating cycles are assessed in detail.

2   Experimental Details

Square-edged stainless steel (grade 316) plates of size $80 \times 60 \times 8$ mm^3 are used as base metal in this work. Such plates are first cleaned successively by wire brushing and acetone swabbing. Single component activating flux silica (SiO_2) is studied in this investigation. Conventional TIG welding is also carried out for comparison purpose. The flux ingredient is procured in the form of dry powder, and the as-received flux power is mixed with acetone to prepare a semi-solid paste. The flux
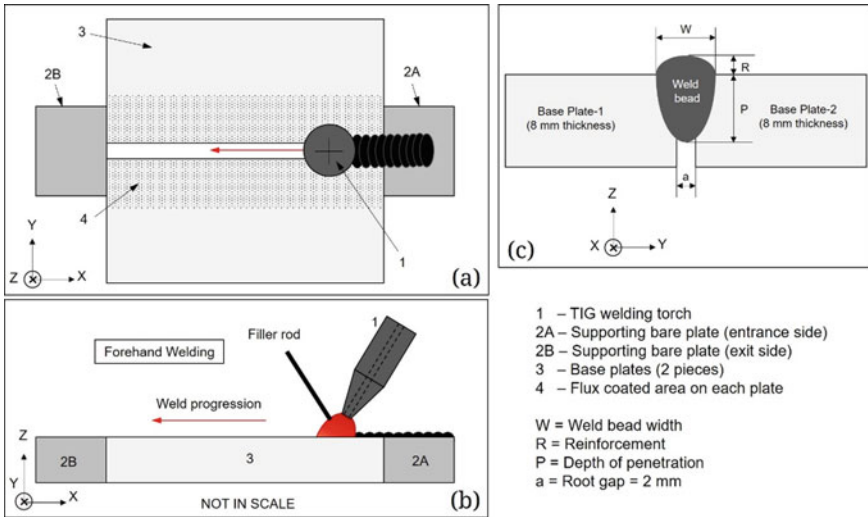
Fig. 1 Schematic representation of the forehand A-TIG welding setup in **a** top view, **b** side view, and **c** cross-sectional view [7]

paste is manually deposited on the faying surfaces as well as surrounding regions of both plates. Measured average thickness of the deposited flux layer is observed to be 43 μm. Flux-coated plates are then carefully gripped on a fixture maintaining about 2-mm root gap between two plates. Two bare scrap plates are also placed each at the entrance and exit side for initiating and terminating the arc (Fig. 1). About 10-mm approach and similar overrun are considered. Welding torch is then placed over the entrance side supporting plate maintaining about 3-mm arc length.

Butt joining is then carried out at a speed of 60 mm/min following the forehand welding technique [8]. An automatic vehicle is employed for moving the torch at a constant speed. Commercially, pure argon is supplied at a flow rate of 15 L/min for shielding purpose. For the non-consumable electrode, direct current electrode negative (DCEN) that is also known as direct current straight polarity (DCSP) is selected. Based on few trial experiments, welding current is set at 160 A in order to achieve proper fusion. The closed-circuit voltage, however, changes independently. KEMPPI Master TIG (MLS 3003ACDC, Finland) machine is used for carrying out entire set of TIG and A-TIG welding experiments. Filler metal of same composition is also supplied at a constant rate for homogeneous welding.

After completion of welding, the joined plates are allowed to cool in normal temperature. Finally, such joined specimens are dissected in a transverse direction, and the exposed weld bead is finished successively through belt grinding, disk grinding, and buffing polishing. Weld bead geometrical properties, namely, penetration, width, and reinforcement (Fig. 1c) are measured from such polished

Table 1 Details of the parameters and relevant features for experimentation

Base metal	Stainless steel (316) of 8 mm thick
Electrode metal	2% thoriated tungsten of 2.4 mm diameter
Filler metal	Stainless steel (316) of 2 mm diameter
Torch orientation	Downhand at 60° with horizontal
Shielding gas	Argon at 15 L/min flow rate
Welding speed	1.0 mm/s
Edge preparation	None (square-edge joining)
Root gap	2 mm
Arc length	3 mm approximately
Welding current	160 A (DCEN polarity)
A-TIG-activated flux	SiO_2

cross-sectional view of the samples using a Tool Maker's microscope (TM510 Mitutoyo, Japan). Table 1 summarizes the relevant parameters and features used for the experimentation.

3 Results and Discussion

In every arc welding process, an electric arc is constituted by allowing flow of a large number of electrons through a narrow gap. The closed-circuit voltage during an arc welding process indicates the minimum potential difference required between the electrode and the base plates for sustaining the electric arc without collapsing. This potential difference primarily depends on the activation energy of the electron-emitting and electron-receiving surfaces, but also varies with arc column length, geometry of the concerned surfaces, medium of arc formation, etc.

$$HI = \frac{\eta \times V \times I}{S}.$$ (1)

When comparison is made between conventional TIG welding and activated TIG welding, the presence of activated flux layer over the base plate surfaces can considerably change the activation potential [7]. This flux layer acts as the barrier for receiving electrons emitted by the electrode (for DCEN polarity) and thereby increases the closed-circuit voltage. However, in this investigation, the average closed-circuit voltage is found to remain more-or-less same for both TIG and A-TIG (Table 2). This can be attributed to the arc constriction phenomenon with A-TIG welding that actually reduces the area of the electron-receiving surface leading to a reduction in

Table 2 Measured values of the voltage and weld bead morphological parameters

	I (A)	V (V)	HI (kJ/mm)	P (mm)	W (mm)	R (mm)	Aspect ratio
TIG	160	15.56	1.86	3.59	9.26	1.78	0.38
A-TIG	160	15.35	1.84	6.86	9.12	0.00	0.75

potential for stable arc formation. The rate of heat input per unit length (HI) is calculated from the set current (*I*), closed-circuit voltage (*V*), and welding speed (*S*), as given in Eq. (1). An arc efficiency (*η*) of 75% is considered [9].

As shown in Fig. 2, welding at 160 A current fetches proper fusion, good appearance, and sound welding with negligible distortion. The same is true for both TIG and SiO$_2$-based A-TIGs. As given in Table 2, conventional TIG welding can give a depth of penetration of about 3.59 mm per pass, while SiO$_2$-based activated TIG welding can fetch about 6.86-mm penetration per pass under the same set of parameters. Aspect ratio of the weld bead (*P/W*) can also be improved by 97% (from 0.38 to 0.75) using SiO$_2$ flux-based A-TIG. Therefore, for joining two components of thickness typically more than 7 mm, multiple passes and/or edge preparation are required. A comparative productivity assessment between TIG and A-TIG for butt joining of thicker plates is presented here. For demonstration, 8 mm thickness of the parent components is considered.
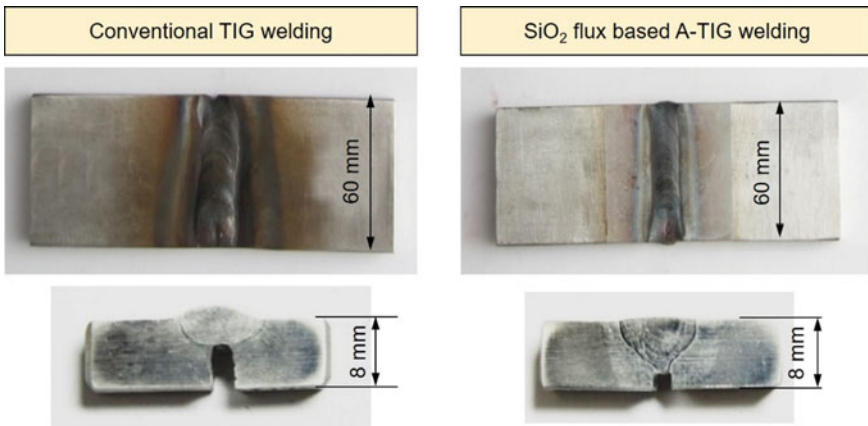
Fig. 2 Top view and cross-sectional view of the welded plates obtained through TIG and A-TIG welding (indicative dimensions are also given)

4 Productivity Assessment in Employing A-TIG Welding

During the application of TIG welding in civil or industrial sector, two distinct scenarios in terms of feasibility of accessing both faces of the components can occur in the simplest scenario, both faces of the components can be accessed, and thus, joining of the thicker plates can be carried out from both faces. In the other possible scenario, any one face of the components can be structurally restricted, and thus, the same face cannot be accessed for welding. In such restricted scenario, joining must be completed from the other accessible face only. Both these scenarios are separately discussed in the subsequent sections. For efficient analytical assessment of the welding productivity, an equivalent time concept is introduced here. It is assumed that one pass (or lap) of welding for the entire length of the plate along the joint takes a time, $T\left(t_{single-pass} = T\right)$. Time required for all other relevant operations is approximately transformed to a function of T (Fig. 3).

4.1 Productivity Assessment When Welding from Both Faces is Allowed

When only conventional TIG welding is permitted for butt joining of 8 mm thick plates with no restricted face, edge preparation is required because a maximum of about 6–7 mm penetration can be achieved if one pass is performed from both faces at square edge. A V-groove of about 5 mm depth can be cut on the faying surfaces of both the components (Fig. 4). Such grooving operation takes considerable time due to fitting individual components on a separate machine and further carrying out shaping, filing, or grinding operation. Thus, it can be approximately assumed that this unproductive edge preparation step for both the plates takes a total equivalent

Fig. 3 Penetration, bead width, and reinforcement obtained in TIG and A-TIG welding

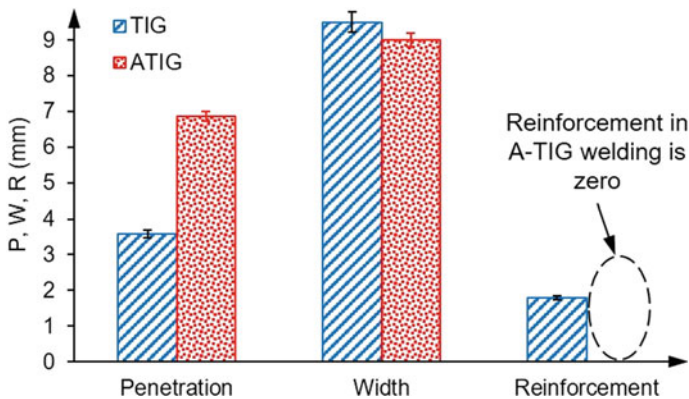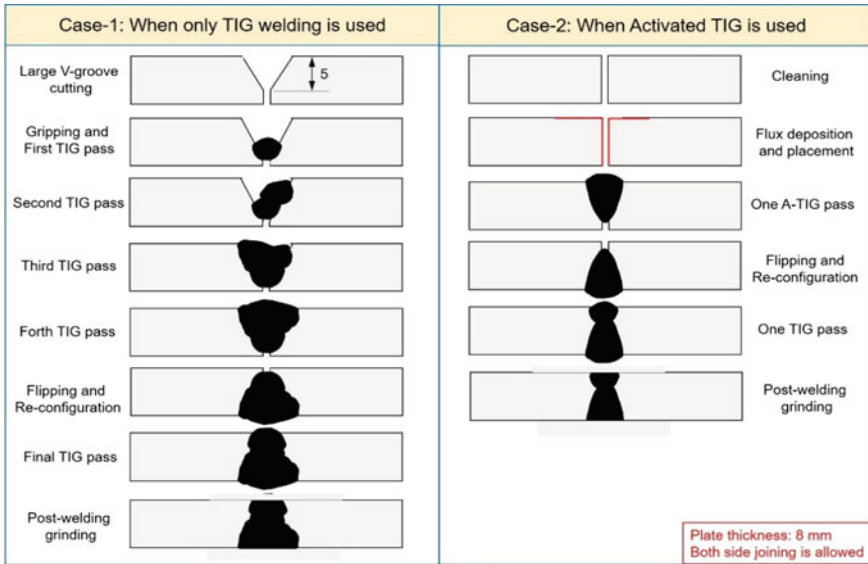| Case-1: When only TIG welding is used		Case-2: When Activated TIG is used	
Large V-groove cutting			Cleaning
Gripping and First TIG pass			Flux deposition and placement
Second TIG pass			One A-TIG pass
Third TIG pass			Flipping and Re-configuration
Forth TIG pass			One TIG pass
Flipping and Re-configuration			Post-welding grinding
Final TIG pass			
Post-welding grinding			Plate thickness: 8 mm. Both side joining is allowed

Fig. 4 Schematic of the welding steps when joining from both sides is allowed [7]

time of $3T$ when carried out in a large scale $(t_{\text{grooving}} = 3T)$. Such plates are further required to place under the welding torch and also tightly grip with the fixtures of the table. While placing the samples, it is also necessary to ensure that the root gap and arc length are in accordance with the predetermined limit. Placement of supporting plates at the entrance and exit ends of the root gap is also required to obtain a consistent weld bead. The entire placement and gripping time is assumed to take an equivalent time of T $(t_{\text{gripping}} = T)$.

First welding pass can thereafter be executed at the bottom of the V-shaped valley (Fig. 4). Each welding pass takes a time, T, as assumed earlier. TIG welding does not produce any slag layer at the top of the weld bead (due to absence of flux-based shielding). Thus, a second weld pass can be readily executed after the first pass without requiring a separate time-consuming slag removal operation (such as filing and/or chemical treatment). Accordingly, four welding passes can be consecutively carried out to fill the entire groove with filler metal from one face of the components.

Thereafter, the partially welded components can be flipped to bring the unfilled root gap beneath the welding torch. This reconfiguration (including declamping, flipping, accurate placement, and reclamping) is assumed to take an average time of $2T$, $(t_{\text{reconfig}} = 2T)$. Afterward, one conventional TIG welding pass can finally complete the joining process. Completely joined samples can be further grounded to remove reinforcement (weld metal situating above the component surface) from both faces. The girding and finishing take a total time of $2T$ for both faces $(t_{\text{finishing}} = 2T)$. Usually, TIG welding does not produce spatter, and thus, spatter removal step can be ruled out. Therefore, total joining time of 8 mm thick plates using only TIG welding when both faces are accessible can be expressed as follows:

$$t_{\text{OnlyTIG}}^{\text{Both faces}} = t_{\text{grooving}} + t_{\text{gripping}} + \left(4 \times t_{\text{pass}}\right) + t_{\text{reconfig}} + t_{\text{pass}} + t_{\text{finishing}}$$
$$= 3T + T + 4T + 2T + T + 2T$$
$$= 13T.$$

When SiO_2-based A-TIG welding is employed for the same purpose, the relevant steps change, and thus, time required for completing the same task also changes considerably. With A-TIG welding, edge preparation is not desired as about 6.86-mm penetration can be obtained in one pass. As shown in Fig. 4, the very step in this regard is the cleaning of the faying surfaces and surrounding areas for removing dirt, oil, grease, oxides, etc. Presence of such undesired deposits can significantly hamper the arc characterize leading to defective weld bead formation. Similar cleaning step is not incorporated in the earlier discussion with conventional TIG welding as the grooving step itself can inherently clean the faying surfaces. However, an equivalent time of T can be considered as cleaning time associated with A-TIG $\left(t_{\text{cleaning}} = T\right)$.

Another additional step associated with A-TIG welding is the preparation and application of activated flux layer on the parent components. For preparation of flux paste, the granulated flux powders are first mixed with a suitable liquid solvent (such as acetone, ethanol) to prepare a semi-solid mixture. Usually, the mixing ratio is not strictly followed as the solvent is highly volatile, even at room temperature. However, a sufficiently fluidic paste is prepared such that the same can be uniformly and efficiently applied over the parent components using a soft brush. This paste is usually applied over the faying surfaces as well as on the surrounding top surfaces extending up to 15–20 mm on each plate in transverse direction of the root gap. Maintaining homogeneity in terms of coating layer thickness is also crucial aspect to consider. After deposition of flux, the coated plates are also dried. This flux preparation and application step together is assumed to take an equivalent time of $2T$ when carried out in large scale $(t_{\text{flux}} = 2T)$. It is worth mentioning that this flux application time can be significantly reduced by employing an automatic spray-type dispenser [10].

As usual, the coated plates are carefully placed on the welding table beneath the torch maintaining the root gap and arc length to the predetermined level. Supporting uncoated plates is also required to place at the entrance and exit ends to initiate and terminate the arc on a bare plate. Similar to the conventional TIG welding, the entire placement and gripping time is assumed to take an equivalent time of $T \left(t_{\text{gripping}} = T\right)$. Thereafter, one A-TIG welding pass can be executed that can fetch a depth of penetration of about 7.0 mm. As shown in Fig. 4, only about 2.0-mm gap at the bottom remains to be filled with filler metal after first A-TIG pass. This gap can be easily filled through one conventional TIG pass. However, for the same, the plates must be flipped and reclamped in the similar way discussed in the previous scenario. Post-welding finishing can also be carried out through grinding, and the corresponding time remains same with previous scenario. Therefore, total time required to join 8.0 mm thick plates with both faces accessible using A-TIG welding can be expressed in the following manner:

$$t_{A-\text{TIG}}^{\text{Bothfaces}} = t_{\text{cleaning}} + t_{\text{flux}} + t_{\text{gripping}} + t_{\text{pass}} + t_{\text{reconfig}} + t_{\text{pass}} + t_{\text{finishing}}$$
$$= T + 2T + T + T + 2T + T + 2T$$
$$= 10T.$$

4.2 Productivity Assessment When Welding from Only One Face is Allowed

In several civil and industrial circumstances, one face of the components remains structurally inaccessible, and thus, joining from only one face is permitted. As conventional TIG welding can fetch a penetration of about 3.5 mm in a single pass (Table 2), edge preparation is indispensably necessary to fill the entire root depth of 8.0 mm. As shown in Fig. 5, a V-groove can be cut in the similar way using shaping, filing, or grinding operation as discussed in the earlier section. However, the depth of the groove should be 6–7 mm in this case. The corresponding grooving time for both the plates can be assumed to take a total equivalent time of $3T$ when carried out in a large scale $(t_{\text{grooving}} = 3T)$. The prepared plates can thereafter be placed and gripped maintaining the orientation and alignment, and the associated time can be assumed as $T (t_{\text{gripping}} = T)$. Five TIG welding passes can thereafter be executed one after another to fill the entire depth of the root, as shown in Fig. 5. In this case, no further flipping and reconfiguration are required. However, grinding or finishing can be carried out at the final step to remove protruded weld metal (reinforcement) and improve esthetic value. Here, finishing is required for only one face that can be assumed to take a time of $T (t_{\text{finishing}} = T)$. Therefore, total equivalent time for joining of 8 mm thick plates using only TIG welding when only one face is accessible can be expressed in the following way:

$$t_{\text{Only TIG}}^{\text{One face}} = t_{\text{grooving}} + t_{\text{gripping}} + (5 \times t_{\text{pass}}) + t_{\text{finishing}}$$
$$= 3T + T + 5T + T$$
$$= 10T.$$

Under the similar circumstances, if A-TIG welding is used, then also edge preparation is desired to ensure complete filling of the root gap from one face. A V-groove of depth about 3 mm can be prepared, and thereafter, one A-TIG welding pass can be given (Fig. 5). After this A-TIG pass, the weld metal is likely to reach the bottom of the plates; however, a small deviation at the top surface may exist (note that, reinforcement with A-TIG welding is zero, Table 2). Thus, a conventional TIG welding pass can be given after this A-TIG pass to fill the top portion. Considering the relevant steps, the overall equivalent time for joining 8 mm thick plates using A-TIG welding
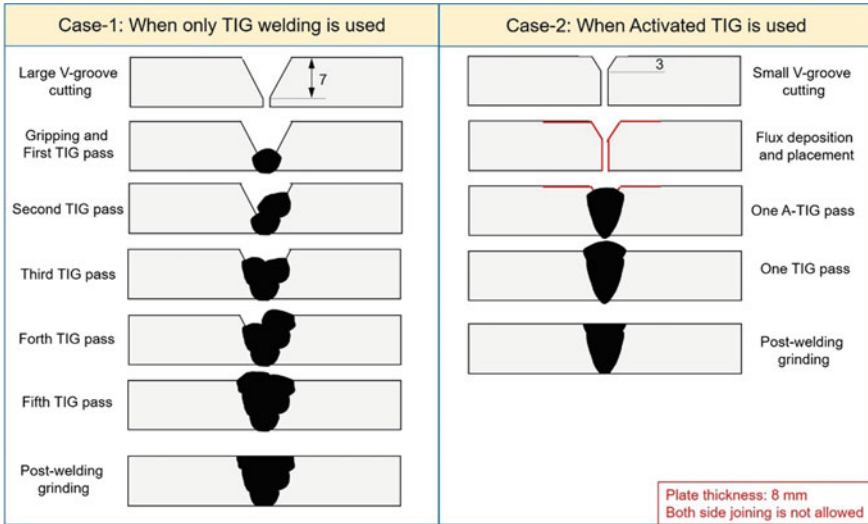
Fig. 5 Schematic of the welding steps when joining from only one side is allowed [7]

from one allowable face can be expressed as follows:

$$
\begin{aligned}
t_{A-\mathrm{TIG}}^{\mathrm{Oneface}} &= t_{\mathrm{grooving}} + t_{\mathrm{flux}} + t_{\mathrm{gripping}} + t_{\mathrm{pass}} + t_{\mathrm{pass}} + t_{\mathrm{finishing}} \\
&= 3T + 2T + T + T + T + T \\
&= 9T.
\end{aligned}
$$

4.3 Comparison with Respect to Time and Heating Cycles

During joining components having lower thickness, typically up to 3–3.5 mm, A-TIG welding is not required. Only conventional TIG welding can serve this purpose. Accordingly, time associated with flux preparation and application can be saved. When component thickness is relatively more, typically within 3.5–6.5 mm, one A-TIG welding pass can completely join the components. In such case, although flux deposition-related steps are additionally required, edge preparation and multiple passes are not desired. When plate thickness exceeds about 6.5 mm, then multiple passes and/or edge preparation are essential. While joining thicker plates, application of A-TIG welding by replacing TIG can save significant time. A comparison between TIG welding and A-TIG welding with respect to equivalent welding time for joining 8.0 mm thick plates is shown through the bar chart in Fig. 6a. In both the structurally restricted conditions, A-TIG welding requires lower time. In a simple case, when joining through both faces is permissible, A-TIG requires as much as 23% lower

Fig. 6 Comparison between TIG and A-TIG with regard to **a** equivalent welding time and **b** heating cycles for two distinct structurally restricted scenarios
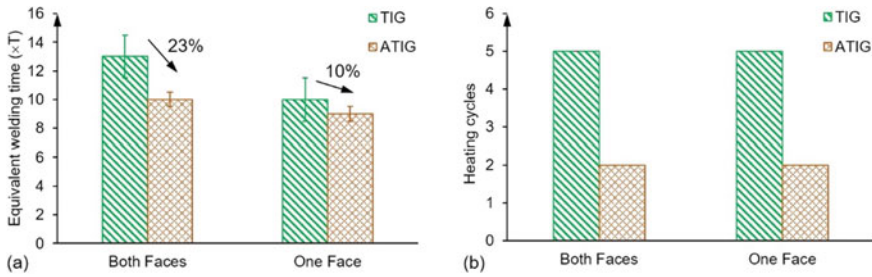
time as compared to the TIG welding. In the other scenario, when only one face is accessible for welding, A-TIG requires 10% lower time as compared to the TIG welding.

The key benefit in employing A-TIG welding while joining thicker plates is the considerable reduction of heating cycles. Similar to other arc welding processes, TIG welding also leads to the generation of heat-affected zone (HAZ). HAZ is the region within the base metals surrounding the weld bead that does not change its phase (melting) but gets metallurgically affected owing to the intense arc heating and post-welding cooling [7, 11]. When multiple welding passes are given for joining a particular pair, undesirably wider HAZ develops. Apart from the wider HAZ, multiple heating cycle leads to increase heat loss that deviates the process from energy-efficient and sustainable one [6, 12–14]. The more is the number of heating cycles, the more is the heat loss. Cost of energy is also one considerable factor. Components also tend to distort more with the increase in heating cycles. Thus, in every arc welding process, reduction in welding passes (or heating cycles) is one common requirement. As shown in Fig. 6b, joining of 8 mm thick plates using only TIG welding requires as much as five heating cycles. Application of A-TIG welding can complete the same task within just two heating cycles. Therefore, A-TIG welding can not only improve productivity but also favorably reduce the heating cycles required for joining of thicker components.

5　Conclusion

- For homogeneous welding of 8 mm thick stainless steel plates using 160 A current, conventional TIG welding can fetch 3.59-mm penetration with 9.26-mm weld bead width. Under same circumstances, SiO$_2$ flux-based A-TIG welding can give as much as 6.86-mm penetration with 9.12-mm bead width. Aspect ratio of the weld bead can also be improved by 97% using SiO$_2$ flux-based A-TIG.
- Joining 8 mm thick plates with both faces accessible, A-TIG requires as much as 23% lower time as compared to the TIG welding. For the same plate thickness

but with only one accessible face, A-TIG requires 10% lower time as compared to the TIG welding.

- Joining 8 mm thick plates using only TIG welding requires five heating cycles that can disadvantageously affect the welded components. Application of A-TIG for completing the same task can reduce the heating cycles to only two.
- A-TIG welding is not only one productive process for joining thicker plates but also a sustainable and energy-efficient technique.

References

1. Pandey, C.: Dissimilar joining of CSEF steels using autogenous tungsten-inert gas welding and gas tungsten arc welding and their effect on δ-ferrite evolution and mechanical properties. J. Manuf. Process. **31**, 247–259 (2018)
2. Sakthivel, T.: Comparison of creep rupture behavior of type 316L austenitic stainless steel joints welded by TIG and activated TIG welding processes. Mater. Sci. Eng. A **528**(22–23), 6971–6980 (2011)
3. Saha, S.: Effect of polarity and oxide fluxes on weld-bead geometry in activated tungsten inert gas (A-TIG) welding. J. Weld. Joining **38**(4), 380–388 (2020)
4. Pandya, D.: A novel perception toward welding of stainless steel by activated TIG welding: a review. Mater. Manuf. Process. **36**(8), 877–903 (2020)
5. Tathgir, S.: Activated-TIG welding of different steels: influence of various flux and shielding gas. Mater. Manuf. Process. **31**(3), 335–342 (2015)
6. Jamal, J.: A study on sustainability assessment of welding processes. Proc. Inst. Mech. Eng. Part B J. Eng. Manuf. **234**(3), 501–512 (2019)
7. Saha, S.: Productivity improvement in butt joining of thick stainless steel plates through the usage of activated TIG welding. SN Appl. Sci. **3**(4), 416 (2021)
8. Karuthapandi, K., Ramu, M.: An experimental investigation of flat wire electrodes and their weld bead quality in the FCAW process. High Temp. Mater. Process. **21**(1), 65–79 (2017)
9. Berthier, A.: TIG and A-TIG welding experimental investigations and comparison to simulation. Sci. Technol. Weld. Joining **17**(8), 609–615 (2012)
10. Rodrigues, A.: Effect of shielding gas and activating flux on weld bead geometry in tungsten inert gas welding of austenitic stainless steels. Sci. Technol. Weld. Joining **10**(6), 760–765 (2005)
11. Saha, S.: Investigation on the effect of activating flux on tungsten inert gas welding of austenitic stainless steel using AC polarity. Indian Weld. J. **51**(2), 84–92 (2018)
12. Saha, S.: An analytical approach to assess the variation of lubricant supply to the cutting tool during MQL assisted high speed micromilling. J. Mater. Process. Technol. **285**, 116783 (2020)
13. Saha, S.: Progressive wear based tool failure analysis during dry and MQL assisted sustainable micro-milling. Int. J. Mech. Sci. **212**, 106844 (2021)
14. Saha, S.: Shadow zone in MQL application and its influence on lubricant deficiency and machinability during micro-milling. Int. J. Mech. Sci. **220**, 107181 (2022)

Experimental Investigation on Joining of DP590–DP980 Automotive Steels by Resistance Spot Welding

S. U. Ghunage and **B. B. Ahuja**

1 Introduction

With the advent of newer and newer materials, the automotive industry has shifted its focus on the reduction of the vehicle weight and increment in the mileage without compromising the safety of passengers. For modern vehicular construction, a wide variety and grades of materials are needed to join together. Therefore, dissimilar metal welding is gaining momentum in the welding industry. For structural applications, it is required to join sheets of materials with different mechanical, metallurgical, and electrical properties. The difference in the properties of dissimilar metals results in challenges in obtaining the sound welds.

In recent years, Dual-Phase (DP) Steels have been practiced in the fabrication of vehicular components such as chassis, bumpers, vehicle frames, and wheel rims. Advanced High-Strength Steels (AHSSs) are a type of steel that combines high strength and ductility in one composition. These characteristics make them useful in automotive applications where higher values of strength and crash resistance are required while using thinner gauge parts. Higher fracture strain indicates good formability. The microstructure of DP steel consists of ferrite and martensite, which offers superior strength and excellent formability.

For the welding of dissimilar metals using the spot welding technique, the effect of welding time has been carried out by Bina et al. They have studied the weldability of austenitic stainless steel (AISI304) with ferritic stainless steel using Resistance Spot Welding. Optimum welding time for welding was obtained considering weld force and weld current constant [1]. Pouranvari et al. have presented a detailed review

S. U. Ghunage (✉) · B. B. Ahuja
Department of Manufacturing Engineering and Industrial Management, College of Engineering, Pune 411 005, India
e-mail: sug.mfg@coep.ac.in

B. B. Ahuja
e-mail: bba.mfg@coep.ac.in

of spot welding of automotive steels. The authors have reviewed metallurgical characterizations of the welded joints [2]. Aydin investigated the mechanical and metallurgical characteristics of dissimilar metal joints of DP600 and DP1000 steels. He has observed that better mechanical and metallurgical properties were obtained at a welding current of 10 kA [3]. Valera used Resistance Spot Welding for welding sheets of micro-alloyed steels (TRIP) and found optimal electrical parameter values for obtaining sound weld strength of the specimen [4]. Khan et al. have carried out a comparative study of welding of DP600 sheets using Resistance Spot Welding and Friction Stir Spot Welding [5]. Muhammad et al. have used the multi-objective Taguchi technique and response surface methodology to evaluate performance and to improve quality in Resistance Spot Welding [6]. Hwang et al. have investigated the weldability of DP780 steels. Experiments were carried out using AC-type and DC-type resistance spot machines [7]. Further researchers explored the combinations of different materials for dissimilar metal joining using Resistance Spot Welding and further investigated the affectability of variation in input process parameters on weld strength and failure modes effectively [8–10].

As per the literature review, researchers have welded DP steels with similar DP steels and different grades of DP steels. Major work has been reported for laser welding of DP780 and DP980 high-strength steel joints, Friction Stir Welding of DP590 steel, and Resistance Spot Welding of DP590 steels. However, no significant work has been reported using Resistance Spot Welding for joining of DP590 and DP980 steels. Therefore, the objective of the research work was to examine the weld characteristics of DP590 and DP980 steels and also to evaluate relation of input process parameters for greater weld strength of these joints.

2   Materials and Experimental Procedure

In this work, dissimilar metals (DP980 and DP590) have been joined using Resistance Spot Welding. Sheets of Dual-Phase Steels DP980 and DP590 having thickness 1.2 mm have been used for the experimental work. As per ASTM E8 standards, the sample size of the weld specimen was chosen as 80×20 mm and the overlap was kept equal to the width of the specimen, i.e., 20 mm.

The specimen required for the welding operation was cut in the direction of the rolling of the plates. Before welding operation, to eliminate dirt, surface scale, oxide layer, the specimen was carefully cleaned using ethanol. As the joint is of overlap type, for the weld combination, the DP980 plate is kept on the upper side and the DP590 plate is kept on the lower side. The welding process was carried out by using an RSW machine (KEJE make) having 25 kVA capacity as shown in Fig. 1. The machine was equipped with a controller (AMADA make) which controls the welding, squeezing, and holding cycles during the welding process. To ensure correct alignment of the overlapping plates and its stability during the welding process, a welding fixture has been used. The electrodes used for the RSW process are Cu–Cr alloy electrodes. These electrodes were water-cooled and had a tip diameter of 7 mm.

Fig. 1 Spot welding machine (KEJE make) used for experimentation

The chemical composition of DP590 and DP980 steels is indicated in Table 1. The mechanical properties of DP590 and DP980 steels are indicated in Table 2. From the screening experiments, three factors and three levels of welding current, electrode force, welding time are chosen for the study as indicated in Table 3. The experiments are conducted using Taguchi's L_{27} orthogonal array.

Table 1 Chemical composition of DP580 and DP980 steels

Steel	C	Mn	Si	Cu + Cr + Ni	Cr	Fe
DP590	0.12	1.6	0.4	1.3	–	Balance
DP980	0.177	1.38	1.42	–	0.44	Balance

Table 2 Mechanical properties of DP580 and DP980 steels

Steel	Yield strength (MPa)	Tensile strength (MPa)	% Elongation
DP590	360	610	23
DP980	650	1010	13.5

Table 3 Process parameters with their levels

Parameter	Levels		
Electrode force (kN)	2	3	4
Weld time (cycles)	8	12	16
Welding current (kA)	6	7	8

3   Design of Experiments

To determine the governing parameters inherent with any process, the Design of Experiments (DOE) methodology is effectively used by researchers. It helps in finding the optimal settings for these process parameters. With optimized parameters, the process yields higher performance and ensures better capability [11].

In this work, for the joining of DP590 and DP980 steels, the process parameters electrode force, weld cycles, and welding current are considered. Its effect on mechanical properties like tensile shear strength and indentation depth of weld metal has been evaluated. The three-level Full Factorial (3^n) method is adopted to design the experimental work. The total number of the experiments (27) is carried out. For the different levels, different values of the input parameters used in the experiment are tabulated in Table 3.

As per the design matrix, the 27 sets of trials are carried out. The samples for the tensile test are prepared as per the ASTM E8 standard. The data are used then to develop a mathematical model using the Design of Experiments (DOE) method [12]. The result of failure load and indentation of the electrode are shown in Table 4.

From Table 4, it is observed that for the higher values of current and weld cycles, the values of failure load were on higher side. The highest value of failure load was observed at 8 kA of current, 16 cycles of weld time, and 2 kN electrode force. A similar higher value of failure load was also observed at 8 kA of current, 16 cycles of weld time, and 4 kN electrode force, however, occurrence of splashing and arcing between the adjoin plates of the workpiece Fig. 2.

To investigate joint strength of the welded specimen, the tensile shear test was carried out. It was observed that the occurrence of fracture in the region of the base metal of DP590 than the heat-affected zone (HAZ) region. Failure modes for these welded samples were of mixed type, i.e., few samples where current and weld cycles were at the lowest level, and the interfacial mode of failure was observed as indicated in Fig. 3a and b respectively. On the contrary, for the higher value of weld current and weld cycles, the weld nugget was on the higher side and the failure mode was pullout type as indicated in Fig. 4a and b respectively.

The weld strength/failure load and indentation depth have been considered as response parameters. The output responses were analyzed using Minitab V17 and the main effect plots are shown in Figs. 5 and 6, respectively.

From the Design of Experiments, among the chosen factors for the study, it was inferred that welding current is the most dominating factor controlling the failure load or weld strength followed by weld cycles. The study also reveals that the weld force is the least influencing factor.

The depth of electrode penetration on the sheets governs the mechanical characteristics of the welded specimen. The contributing factors of the depth of penetration by electrodes on the sheets were the electrode pressure and temperature of the electrode–sheet interface. As the heat input increases, the temperature of the electrode–sheet interface also increases, causing higher degree of plastic deformation. In case of severe electrode indentation, the occurrence of expulsion was observed. It was

Table 4 Failure load and indentation of electrode

Weld schedule	Force (kN)	Weld time (cycles)	Welding current (kA)	Indentation (mm)	Failure load (N)
1	2	8	6	0.175	8440
2	2	8	7	0.238	9300
3	2	8	8	0.266	9900
4	2	12	6	0.203	9640
5	2	12	7	0.371	10,000
6	2	12	8	0.298	10,713
7	2	16	6	0.204	9760
8	2	16	7	0.349	10,438
9	2	16	8	0.332	11,050
10	3	8	6	0.192	8400
11	3	8	7	0.161	9100
12	3	8	8	0.226	9690
13	3	12	6	0.242	9280
14	3	12	7	0.266	9950
15	3	12	8	0.241	10,413
16	3	16	6	0.239	9590
17	3	16	7	0.297	9700
18	3	16	8	0.350	10,838
19	4	8	6	0.114	8120
20	4	8	7	0.157	8640
21	4	8	8	0.212	9690
22	4	12	6	0.201	9100
23	4	12	7	0.304	9920
24	4	12	8	0.287	9910
25	4	16	6	0.227	9540
26	4	16	7	0.307	10,288
27	4	16	8	0.377	11,050

ascertained that the welding current affects the electrode indentation comparatively more than that of the welding time.

The amount of indentation depth is deciding factor for mechanical properties and nugget size of the welded specimen. Therefore, the depth of electrode penetration is considered as the second response parameter. The output response is analyzed using Minitab V17 and the main effect plot is shown in Fig. 6.
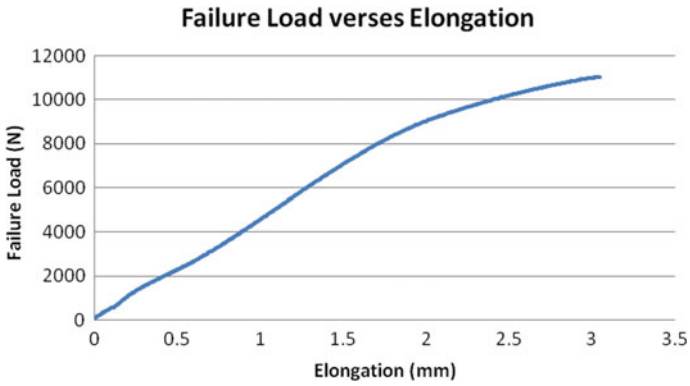
Fig. 2 Failure load versus elongation curve for DP590–DP980 welded specimen

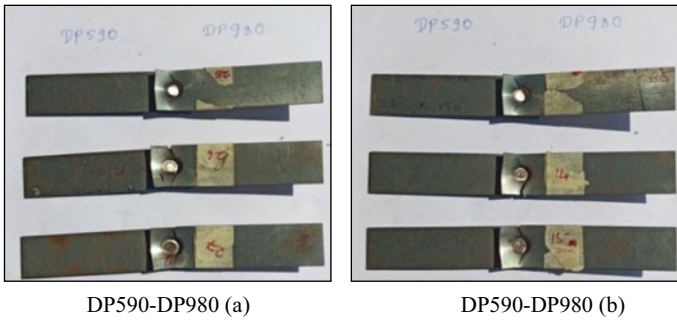DP590-DP980 (a)   DP590-DP980 (b)

Fig. 3 Interfacial failure mode of the welded specimen (**a** and **b**)

DP590-DP980 (a)   DP590-DP980 (b)
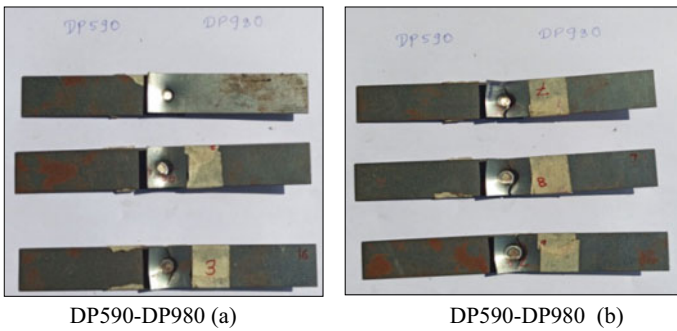
Fig. 4 Pullout failure mode of the welded specimen (**a** and **b**)

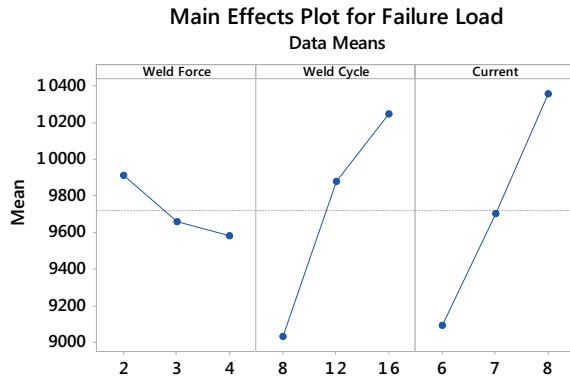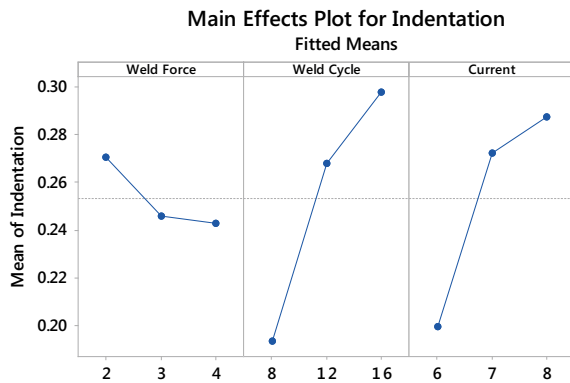**Fig. 5** Mean of S/N ratios for failure load

Fig. 6 Mean of S/N ratios for indentation

4   Analysis of Variance

For the Resistance Spot Welding of dissimilar materials, the quality characteristics of tensile shear strength of the welded specimens indicate the larger-the-better type. The result of ANOVA for the welding responses is presented in Table 5. The larger the F-value indicates major changes in the rank of the welding parameters. From Table 5, it can be concluded that welding current and weld cycles were the most influencing parameters affecting the responses, whereas the electrode force was comparatively less influencing.

For the higher values of welding current (8 and 9 kA) and weld cycles (12 and 16 cycles), the tensile shear strength of the weld specimen was higher. However, the values of tensile shear strength decrease as the electrode force increases from 2 to 4 kN. For Resistance Spot Welding (RSW) process, from the analysis, it was revealed that the governing parameter that influences the tensile shear strength was welding current with 46.07% contribution. The second important parameter that influences the tensile shear strength was weld cycles with a 44.99% contribution. The weld force was with marginal contribution (3.46%) in deciding the tensile strength.

Table 5 ANOVA for the tensile shear load of DP590–DP980

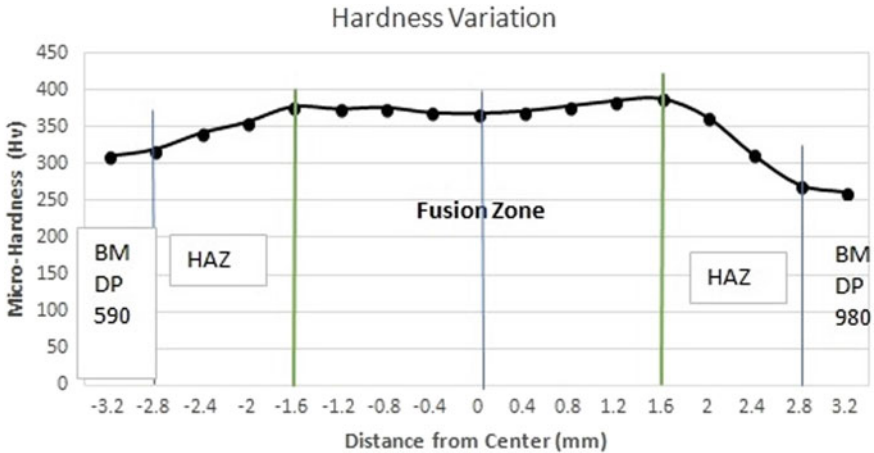| Source	DF	Seq SS	Contribution (%)	F-value	P-value
Weld force	2	540,404	3.46	6.44	0.022
Weld cycles	2	7,035,762	44.99	83.88	0.000
Current	2	7,203,531	46.07	85.88	0.000
Error	8	335,515	2.15		

Fig. 7 Microhardness of dissimilar weld nugget (DP590–DP980)

The measurement of microhardness was carried out using Future-Tech FM700 Hardness Testing Machine. Figure 7 represents the microhardness measurement of the joint obtained by Resistance Spot Welding for the weld specimen which was obtained for weld schedule 9 (Force 2 kN, weld cycles 16, and current 8 kA). The load applied was 100 gm and dual time was 10 s.

The cross-section of dissimilar weld joints (DP590–DP980) revealed three main microstructural zones like base metal (BM), heat-affected zone (HAZ), and fusion zone (FZ). A fusion zone or weld nugget is a zone that undergoes melting during the welding process. In addition to this, the DP980 side of the joint was with a transition zone which lies between the heat-affected zone and the base metal. It has been also observed that softening of the zone has occurred to higher levels. A similar soft transition zone was not observed on the DP590 side. Higher hardness values were observed in the fusion zone of the nugget, followed by heat-affected zones, and lesser values were found in the base metal as indicated in Fig. 7.

5 Conclusions

In the present study, the mechanical characteristics of dissimilar DP590–DP980 steel joints were experimentally investigated using Resistance Spot Welding. To investigate the optimal values of process parameters, Taguchi DOE has been effectively employed. From the analysis, it is inferred that by increasing the welding current from 6 to 8 kA, the tensile shear strength of the welded joints increased linearly. The peak values of tensile shear strength are observed at welding current 8 kA and weld cycles 16. The failure locations of the joints were at heat-affected zones (HAZ). The joints failed at DP980 side when the welding currents are increased to an 8 kA value, while the failure was on the DP590 side for a higher current range. The contribution of welding current, weld cycles, and electrode force toward tensile strength is 46.07%, 44.99%, and 3.46%, respectively. From the ANOVA analysis, it can be observed that the P-value for experimented variables, welding current, and weld cycles are not higher than 0.05. Therefore, these terms are significant on the sensitivity of the process. Using the Taguchi method, it is inferred as optimal values for welding of DP980 and DP580 sheets are welding current 8 kA, weld cycles as 16, and electrode force as 2 kN.

From the experimental work carried out for DP590–DP980 steels, the conclusions can be summarized as below.

1. For the welded joints of DP590–DP980 steels, the weld cross-section shows three distinct zones as base metals, heat-affected zones of both the steels, and fusion zone. On the DP980 side, a transition zone was also visible in between BM and HAZ.
2. Mechanical and metallographic characterization of welded joints was carried out using tensile testing and hardness mapping.
3. To achieve the mechanically sound welds, the welding current was the most influencing parameter followed by weld cycles.
4. As the values of welding current and weld cycles increase, the tensile properties of the welded joints have increased significantly.
5. Pullout failure mode was observed for most of the tested samples and fracture has occurred at base metal indicating good weld strength.
6. The highest values of microhardness are observed in the fusion zone of the welded specimen. However, for the DP980 side, the lowest values were obtained in the transition zone.

References

1. Bina, M.H., Jamali, M., Shamanian, M., Sabet, H.: Effect of welding time in the resistance spot welded dissimilar stainless steels. Trans. Indian Inst. Met. **68**, 247–255 (2015)
2. Pouranvari, M., Marashi, S.P.H.: Critical review of automotive steels spot welding: process, structure and properties. Sci. Technol. Weld. Join. **18**, 361–403 (2013)
3. Aydin, H.: The mechanical properties of dissimilar resistance spot-welded DP600-DP1000 steel joints for automotive applications. Proc. Inst. Mech. Eng. Part D J. Automob. Eng. **229**, 599–610 (2015)
4. Valera, J., Miguel, V., Martínez, A., Naranjo, J., Cañas, M.: Optimization of electrical parameters in resistance spot welding of dissimilar joints of micro-alloyed steels TRIP sheets. Proc. Manuf. **13**, 291–298 (2017)
5. Khan, M.I., Kuntz, M.L., Su, P., Gerlich, A., North, T., Zhou, Y.: Resistance and friction stir spot welding of DP600: a comparative study. Sci. Technol. Weld. Join. **12**, 175–182 (2007)
6. Muhammad, N., Manurung, Y.H., Hafidzi, M., Abas, S.K., Tham, G., Rahim, M.R.A.: A quality improvement approach for resistance spot welding using multi-objective Taguchi method and response surface methodology. Int. J. Adv. Sci. Eng. Inf. Technol. **2**, 215 (2012)
7. Hwang, I., Kim, D., Kang, M., Kwak, J.H., Kim, Y.M.: Resistance spot weldability of lightweight steel with a high Al content. Met. Mater. Int. **23**, 341–349 (2017)
8. Vignesh, K., Perumal, A.E., Velmurugan, P.: Resistance spot welding of AISI-316L SS and 2205 DSS for predicting parametric influences on weld strength—experimental and FEM approach. Arch. Civ. Mech. Eng. **19**, 1029–1042 (2019)
9. Zhang, H., Qiu, X., Xing, F., Bai, J., Chen, J.: Failure analysis of dissimilar thickness resistance spot welded joints in dual-phase steels during tensile shear test. Mater. Des. **55**, 366–372 (2014)
10. Karuthapandi, K, Ramu, M., Thyla, P.R., Anantharuban, K.: Weld bead characterization of flat wire electrode in GMAW process part II: a numerical study. **35**(5), 1–8 (2021)
11. Thakur, A.G., Nandedkar, V.M.: Application of Taguchi method to determine resistance spot welding conditions of austenitic stainless steel AISI 304. J. Sci. Ind. Res. (India) **69**, 680–683 (2010)
12. ASTM E8: ASTM E8/E8M standard test methods for tension testing of metallic materials 1. Annu. B. ASTM Stand. **4**, 1–27 (2010)

Review on Friction Stir Welding of Titanium Alloys—A Fracture Mechanics Perspective

Ramprasad Ganesan and **Hema Pothur**

1 Introduction

Welding of materials is a key step in the manufacturing of integrated systems with cost-efficient methods. Most of the welding mechanisms involve local melting along the weld line and successive solidification leading to the formation of a permanent joint. Out of the many conventional methods, FSW is a unique process where the deformation takes place with the help of a rotating tool advancing along the joint line leading to an excellent weld joint with minimum distortion and with better weld strength. This solid-state welding technique was invented (1991) and patented (1995) by Thomas et al. assigned to The Welding Institute, UK, and was originally referred to as "friction plunge welding" [1]. In this process, the weld is produced by forcing the rotating tool at a fixed travel speed and pressured against two metal plates butted together and causing a rotation of a viscous mass of the liquefied material of the workpiece, which is pushed against its cold walls by the pin rotation at the tip of the tool and forged by the shoulder. The heat for welding is produced by the friction generated by the rotating tool in contact with the workpiece, and the metal from the front of the probe/pin is swooped around the plasticized area to the rear, thus forming a strong weld joint. In general, FSW is used for joining many lightweight materials like aluminum and copper alloys and stainless-steel alloys. Recently, the domain of this process is getting increased applications in difficult to weld materials like titanium and magnesium alloys. This has been the main reason for its success in numerous automotive, shipbuilding, and aerospace applications. The FSW process setup has a cylindrical tool having a shoulder and pin profile that rotates in the counterclockwise direction and advances along the weld joint line. The advancing side can be considered on the right side of the probe, where the trajectory of the tool

R. Ganesan (✉) · H. Pothur

Department of Mechanical Engineering, Sri Venkateswara University, Tirupati, Andhra Pradesh 517502, India

e-mail: ramprasadofficial16@gmail.com

445

rotation is similar to the welding direction, whereas the retreating side is represented when the trajectory of the tool rotation is opposite to the direction of tool travel on the left side of the probe [2].

2 Objectives of the Present Paper

This paper focuses on the various researches conducted on FSW of Ti alloys by many scientists and researchers across the globe focusing mainly on the material characteristics; selection of tool materials, pin profiles, and process parameters; microstructural evolution and characterization of the mechanical properties; and finally, on the fracture mechanics aspects of the friction stir welded joints.

3 Processed Material Characteristics

Ti is a copious metal that is extracted from the mineral sources like ilmenite and rutile and is present at a level of about 0.6% in the earth's lithosphere. High specific strength, superior corrosion resistance, and minimal density are the main properties of this material and make it applicable for a variety of applications. Applicable areas include aeroengines and aircraft components, biomedical devices, and components in chemical processing equipment. The basic classifications for Ti alloys are:

- α alloys,
- near-α alloys,
- $\alpha + \beta$ alloys,
- near-β alloys, and
- β alloys.

In Ti alloys, the alloying elements are usually categorized into α and β stabilizing additions depending on the increase or decrease of the α/β transformation temperature (882 °C for pure Ti). The substitutional element (like aluminum) and the interstitial elements (like nitrogen and oxygen) are all strong α stabilizers, and when there is an increase in the solute elements, the transus temperature also increases. The β stabilizers are classified into β isomorphous elements (like vanadium, molybdenum, and niobium) and β eutectoid-forming elements, depending on the details of the resulting binary phase diagrams. The β eutectoid-forming elements like silicon, chromium, and iron are used frequently, whereas nickel, copper, manganese, tungsten, palladium, and bismuth have only very limited usage. These materials are used for aerospace, chemical, general engineering, and biomedical applications because they show an astonishing range of physical and mechanical properties like high melting point, minimal thermal conductivity, high strength, and high corrosion resistance. Apart from these properties, it was introduced in the aerospace applications (like rocket engine parts, landing-gear beams, hydraulic tubings, wing boxes, spacers, bolts, and

fuel tanks) due to its unique features like better fatigue resistance, easy formability, and high specific strengths. The low creep rates and better metallurgical stability at high temperatures of the material make it favorable for military and aerospace engine components like fan blades and disks in the low and intermediate sections of compressors.

4　Selection of Tool Materials, Pin Profiles, and Process Parameters

Joining Ti alloys by FSW requires tool materials having excellent wear resistance and should withstand high temperatures as the temperatures generated in the stir zone/nugget zone are very high and should have considerable tool life properties. This made many researchers develop new tool materials like tungsten, tungsten-based alloys, titanium carbide alloys, cobalt alloys, molybdenum-based alloys, and ceramic materials. Also, depending on the thickness of the workpieces needed to join, different tool probes are being designed [3]. Table 1 presents a list of some published tool materials with their respective geometries and various process parameters used in the joining of Ti alloys under various conditions, and from these observations, the following inferences have been deducted.

One of the many reasons reported for tool degradation mechanics was connected to the hot adhesion phenomenon. In an experiment conducted in 2013 [17], the workpiece materials like Ti, Al, V got adhered to the tool pin and the shoulder areas. This adhesion of the workpiece elements to the tool depends mainly on the hot adhesion and can be further addressed to reduce this phenomenon. In another experiment [19], a W–1%La$_2$O$_3$ material with an interior cooling system tool head was used and also [8] a tool having a convex shoulder with a tapered pin having a step-spiral pattern on the shoulder surface to intensify the stirring effect. Apart from those tool materials reported for joining workpieces with high melting points, the pcBN tool was used and it produced defect-free weld joints in steels and nickel-based alloys. In a research conducted in 2008 [9], a commercially pure Ti was welded using a pcBN tool and obtained better welds without cracks and porosities in the stir zones produced at the investigated welding parameters. Post-welding, the probe diameter was smaller as the tip got severely worn during the process. Further [13], a peculiar tool system was designed by using a liquid cooling holder and a shielding gas covering. The tool shank was fabricated from a nickel alloy and connected with the tungsten alloy pin. The primary reason for this tool system design was to reduce the influence of welding temperature on the rotation shaft of the FSW machine as the temperature reaches above 1000 °C. After the implementations, the tool maintained an optimum shape and the amount of wear was minimal. Even though different tool materials have been used to weld Ti alloys, the tool evaluations and wear mechanisms are a major concern that has to be investigated because the tools should withstand high loads during FSW and it should have minimal chemical interactions with the workpiece

Table 1 List of published tool materials and process parameters

Authors	Processed material	Tool material	Process parameters	Tool geometry (mm)
Ramirez and Juhas [4]	Ti–4Al–4 V (M-A and β-A) (6 mm)	Commercially pure W	Rotation speed—275 rpm; welding speed—1.6 mm/s; plunge depth—0.13 mm; Tilt—3.5°	Not specified
Lee et al. [5]	Pure Ti (5.6 mm)	Sintered TiC	Rotation speed—1100 rpm; welding speed—500 mm/min	Not specified
Reynolds et al. [6]	Ti metal 21S (1.59 mm)	W alloy	Welding speed—0.85–5.08 mm/s	Not specified
Pilchak et al. [7]	Ti–6Al–4 V	W–25 pct Re	Rotation speed—100 r/min; welding speed—1.7 cm/s; downward force—38.7 KN	Not specified
Zhang et al. [8]	Ti–6Al–4 V (3 mm)	Mo-based alloy	Rotation speed—300 and 600 rpm; welding speed—1 mm/s; plunge depth—2 mm	Convex Sh. D-15; Tapered Pin L-2, D-5.1–3
Zhang et al. [9]	cp-Ti (3 mm)	pcBN	Rotation speed—200 rpm; welding speed—50 mm/min; plunge depth—2 mm	Convex Sh. D-15; Tapered Pin L-1.7, D-5.1–3
Pasta and Reynolds [10]	Ti–6Al–4 V (2 mm)	W–25% Re alloy	Rotation speed—150 rpm; welding speed—100 mm/min	Flat Sh. D-15; Cylindrical Pin D-5;
Zhou et al. [11]	Ti–6Al–4 V (M-A) (2 mm)	W–Re alloy	Rotation speed—400 rpm; welding speed—50 mm/min, plunge depth—0.2 mm; tilt—2.5°	Sh. D-11; Pin L-1.8, D-6–4
Liu et al. [12]	Ti–6Al–4 V (M-A) (2 mm)	W–Re alloy	Rotation speed—400 rpm; welding speed—100 mm/min	Sh. D-11; Taper Pin L-1.8, D-6–4

Table 1 (continued)

Authors	Processed material	Tool material	Process parameters	Tool geometry (mm)
Liu et al. [13]	Ti–6Al–4 V (2 mm)	W–Re alloy	Rotation speed—300–600 rpm; welding speed—25–125 mm/min; tilt angle—2.5°	Not specified
Edwards and Ramulu [14]	Ti–6Al–4 V (3 mm, 6 mm, 9 mm, 12 mm)	W–La alloy	Rotation speed—140–300 rpm; feed rate—40–130 mm/min	Sh. D-19–32; Pin L-2.8–13.3
Pilchak et al. [15]	Ti–6Al–4 V (M-A) (10.3 mm)	W–1 pct La2O3	Rotation speed—120–800 rpm; welding speed—50.8–203.2	Sh. D-25; Pin L-9.9, D-15
Pilchak and Williams [16]	Ti–6Al–4 V (1.5 cm)	Not specified	Rotation speed—100, 150 rpm; welding speed—5.1, 10.2 cm/min; downward force—14.7–38.7 kN	Sh. D-19.05; Pin L-1.27, D-5.08
Farias et al. [17]	Ti–6Al–4 V (2 mm)	WC	Rotation speed—1000–1200 rpm; feed—40–60 mm/min; plunge depth—1.60, 1.65 mm	Sh. D-20; 30° Tapered Pin D-5
Wang et al. [18]	Ti–6Al–4 V (2.5 mm)	W–La, CY16, and WC411	Rotation speed—900–1100 rpm; welding speed—25 and 50 mm/min	Sh. D-9.5; Tapered Pin L-1.8, D-4.5–2.5
Mashinini et al. [19]	Ti–6Al–4 V (M-A) (3 mm)	W–1%La$_2$O$_3$	Rotation speed—500 rpm; welding speed—40–200 mm/min; tilt—1.5°	Sh. D-14; Tapered Pin L-2.9, D-7–5
Liu et al. [20]	Ti-6Al-4 V (2 mm)	Tungsten-rhenium alloy	Rotation speed—150 r/min; welding speed—50 mm/min; tilt—2.5°	Sh. D-12; Tapered Pin L-1.8, D-6–4
Ma et al. [21]	Ti–6Al–4 V (2 mm)	Not specified	Rotation speed—120 rpm; welding speed—30 mm/min	Not specified
Van der Merwe et al. [22]	Grade 23 6Al-4 V	Not specified	Rotation speed—2500 rpm; upset distance—1.5 mm; axial force—4 kN; upset forging force—6 kN	Not specified

Table 1 (continued)

Authors	Processed material	Tool material	Process parameters	Tool geometry (mm)
Nakai et al. [23]	Ti531C (2 mm)	Tungsten carbide-based alloy	Rotation speed—200 rpm; welding speed—25 mm/min	Sh. D-15; Pin L-1.8, D-6
Su et al. [24]	Ti–4Al–0.005B (4.2 mm)	Not specified	Rotation speed—450–850 rpm; welding speed—50 mm/min; plunge depth—0.2 mm; tilt—2.5°	Sh. D-16; Pin L-4, D-9–4
Gao et al. [25]	TA5 alloy (4 mm)	Co-based alloy	Rotation speed—400 r/min; welding speed—40 mm/min; tilt—2.5°	Concave Sh. D-18; Conical Pin L-3.8

materials. In the year 2014, researchers welded [18] Ti alloy by a tool material of three types made of W-La, CY16, and WC411. From Fig. 1, it can be noticed that the three tools have similar initial dimensions and experienced different patterns of degradation after the welding process. For evaluating the tool wear characterization, pin profile photography and tool weight loss measurement were implemented. From these, it was examined that deformation took place for the $W–La_2O_3$ tool having a small conical pin. It was then corrected by changing the pin profile to a larger cylindrical pin. The other tool material caused adhesive wear due to the chemical affinities between the WC-Co tool and the workpiece.

After the selection of the tool materials along with their respective geometries, then comes the process parameter identification. An experimental study [14] to establish a process window for welding a Ti alloy of varying thickness (3 mm–2 mm) by keeping the tool designs constant by having W–La alloy as the tool material with a small shoulder and a large tapered pin has been conducted. The primary process parameters investigated are spindle speed and feed rate. Here, a tungsten-based material was used as a backing anvil for all the experimental trials, and it was observed that the anvil material had high thermal conductivity and it extracted the heat from the weld zone and thus producing a cold joint. To curb this mechanism between the anvil and the workpiece, other materials like steel and ceramics (low thermal conductive materials) were used as the backing anvil to achieve full penetration welds and thus finally broadening the process window. In another study, a process window has been developed for joining 2 mm thick Ti sheets using a tungsten-based alloy to produce defect-free joints and it was stated that the microstructures of the welds affected the tensile properties. This can be mainly controlled by the processing parameters like reducing the tool rotational rate and/or increasing the traverse speed, thus leading to the improvement in the tensile strengths.
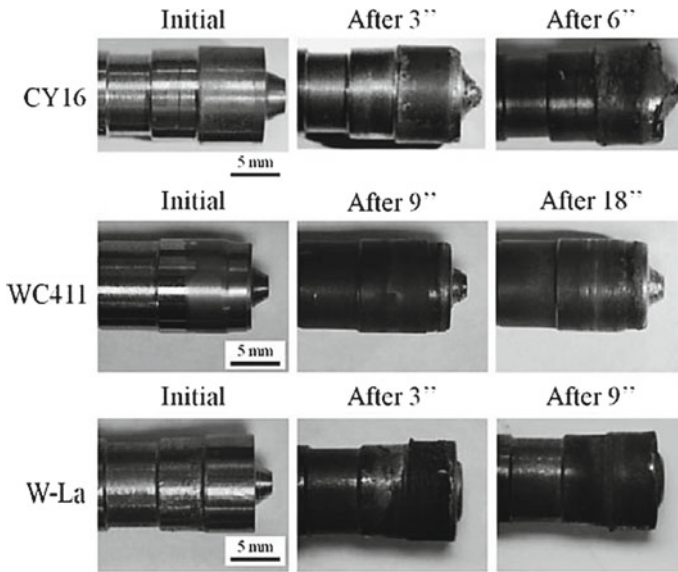
Fig. 1 Tool degradations after different welding lengths for three different tools [18]

5 Microstructural Evolution and Characterization of the Mechanical Properties

The study of microstructural examinations and the mechanical properties of the friction-stir welded joints is becoming a predominant approach as the changes in temperatures and deformation mechanics are taking place eventually during the welding of Ti alloys. The early researches on these areas were studied in the year 2004 [26], by welding three types of Ti alloys and discussing the stir zone (SZ) and heat-affected zone (HAZ) microstructures that occurred during the phase transformations. After the welding of the materials, tensile tests revealed that the β-Ti alloy exhibited higher tensile strength and a lower percentage elongation than that of the base metal (BM), whereas the other two alloys had lower strengths than the parent materials. This was mainly due to the strain localization and lack of penetration defect in the welds. Apart from these, Fatigue Crack Growth (FCG) rates were calculated on the weld specimens and found that it is higher at the weld nugget than at the base metal. The FCG rates were measured by machining center cracked tension specimens $M(T)$, as the compact tension (CT) geometry specimens produced severe out-of-plane cracking due to the residual stresses. The Ti–6Al–4V alloy generally consists of a bimodal microstructure containing α grains with colonies of β grains. Welding of this material (mill-annealed and β-annealed states) has been carried out [4] and found that the SZ microstructure is controlled by the severe deformation and exceeding the β-transus temperatures resulting in transformed β grains with fine grain boundary α. In the thermomechanically affected zone (TMAZ), small equiaxed

α (1 μm) was observed, but the temperature was below the β-transus temperature. This was due to the Dynamic Recrystallization (DRX) mechanism, which is also known as α globalization. In other cases, this mechanism was also observed in SZ microstructures as depicted in Fig. 2.

The SZ and HAZ had heterogeneous microstructures concerning the changing rotational speeds. At 400 rpm, the workpiece microstructures were examined at five regions using Scanning Electron Microscope (SEM). The SZ β grains' size was smaller than the BM due to the DRX mechanism. A sharp boundary (Fig. 3) having a phase transformation was found (instead of a TMAZ) between the SZ and the HAZ due to the thermal cycles during the process.

The effect of rotational speeds on the grain sizes, as with increasing speeds the peak temperatures in the stir zones will be increased resulting in coarser grains (Figs. 4 and 5). The Vickers hardness was measured and found that the SZ has a higher hardness value and the lowest hardness is present in the HAZ, and from Fig. 6, it is clear that the hardness values of the welds were inversely proportional to the tool rotation speeds.

With the increase in tool rotation speeds, the peak temperature in the SZ increases resulting in the increase of prior β grain sizes due to the larger driving forces. The
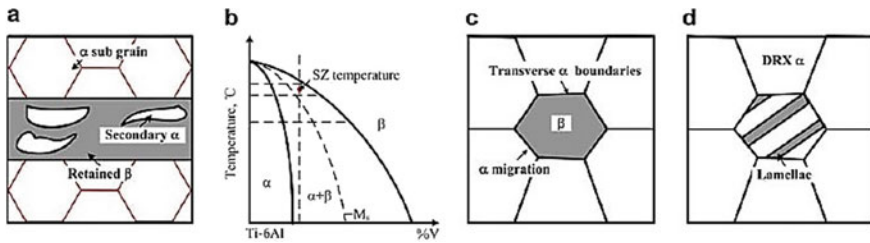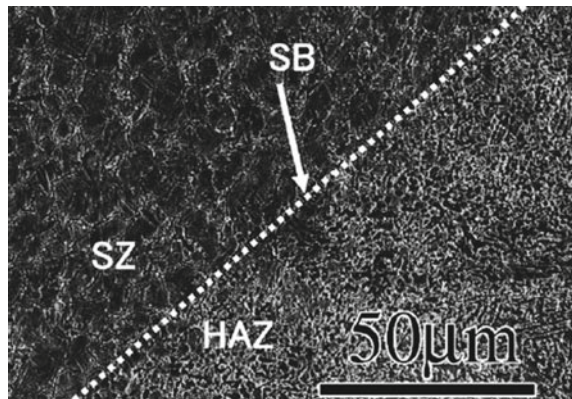

Fig. 2 Formation mechanism of SZ microstructure: **a** BM microstructure, **b** location of stir zone temperature in the phase diagram, **c** DRX and phase transformation, and **d** bimodal microstructure formation [11]

Fig. 3 Sharp boundary (SB) formed between the SZ and HAZ in the 400 rpm weld [8]
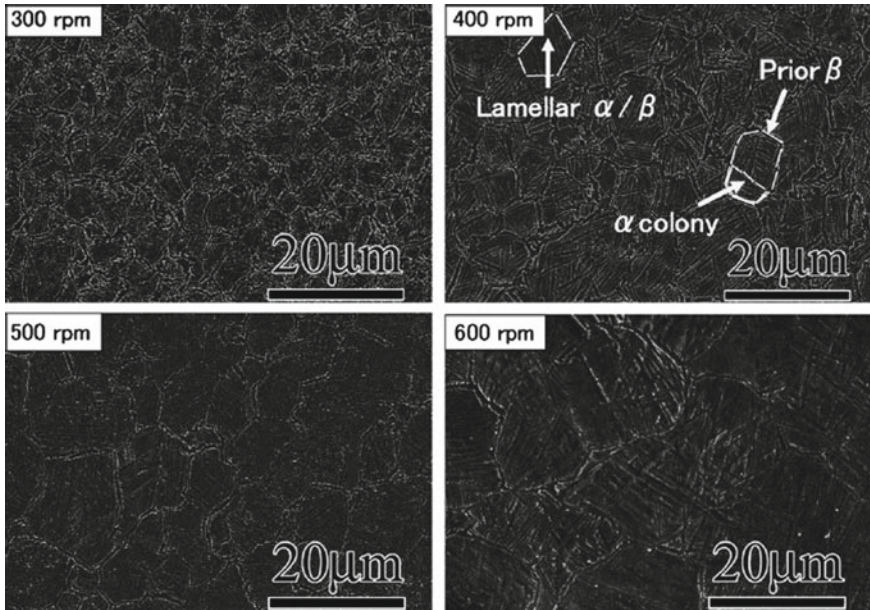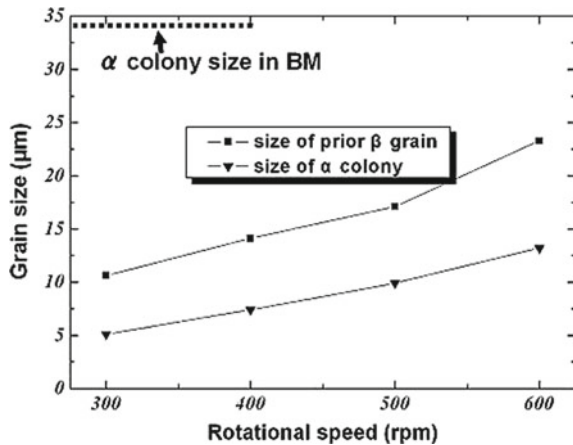
Fig. 4 Lamellar α/β, prior β, and α colonies are shown by arrows in the 400 rpm weld [8]

Fig. 5 Effect of rotational speed on grain size in the SZ [8]

cooling rates were controlled by increasing the speed of the tool travel and obtaining an equiaxed primary α phase [27]. Further for different thicknesses of the workpieces, the grain distributions and surface roughness profiles were examined [28] and the microhardness for varying thicknesses was measured. In a preliminary study conducted in the year 2014 [29], tensile testing was performed both at room temperature and higher temperatures with varying strain rates. True stress versus true strain

Fig. 6 Vickers hardness profiles over stir zone [8]
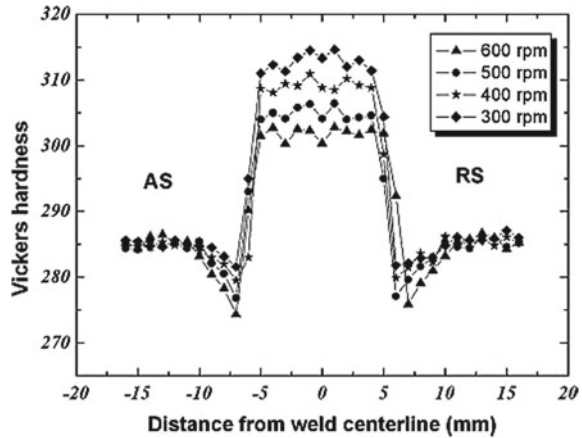
curves were plotted for both the conditions, and the microstructural evolution was correlated with the strain rates. Apart from the butt joints, nine different case studies (with varying feed rates and tool rotation speeds) were experimentally investigated [30], and the microhardness values of the lap joints along the transverse sections were measured. In another study, they also numerically simulated the welding process (FEM-based approach) for predicting the phase transformations and also plotted temperature and strain history models for different case studies. These model results were consistent with the experimental analysis (qualitative point of view) and need further developments in quantitative measurements. A friction stir lap welding was performed on an $\alpha + \beta$ Ti alloy by using different tool rotation speeds [31]. The weld cross-sections at varying speeds were examined and achieved a defect-free joint at the lowest rotating speed. When joining at higher speeds, hook defects and cold lap morphologies with plenty of small voids were detected as confirmed by the SEM analysis. At the HAZ and top regions of the SZ (at 200 rpm), $\beta \rightarrow \alpha + \beta$ transformations have occurred. The experiment was concluded by investigating the fracture morphologies by finding many dimples due to the mixing of the tool materials at the fracture surfaces and found that the mechanism of fracture followed a ductile fracture mode. To reduce the hook and tearing defects, a threaded pin tool was used for efficient vertical material flow along the joint and by slightly penetrating the lower sheet. From another research [32], it is believed that the material flow is not the reason for these defects and can be stated that, when the welding tensile stress exceeds the material tensile stress due to peak temperatures, the material will be shredded resulting in the tearing defect. Hence, lower rotating speeds seem an optimum solution to reduce the welding tensile stresses which comply with the results of experiments conducted in the year 2015 [33]. The peak temperatures can be considerably reduced by applying liquid nitrogen as an intense cooling mechanism. This leads to the formation of homogeneous grains at the SZ (butt joint configuration) resulting in higher tensile strengths and better microhardness when compared to the air-cooled joints. However, the concave shoulder of the tool was

flattened resulting in tool wear. This causes the adhesion of tool particles along with the weld microstructure. In FSW of pure Ti having hexagonal close-packed crystal structures, the SZ microstructure possessed a considerable number of twin structures and thick dislocations and with the absence of elongated grains in the TMAZ. The hardness at the weld nuggets was slightly higher than the BM. The fracture emerged at the retreating side of HAZ as the average tensile strength of the joints is lower than the BM [5]. In welding of this material, the formation of TMAZ was not found between the SZ and the HAZ, and only a linear boundary was found [9]. Here, the twin boundaries were formed in minimum proportions from the Electron Backscattered Diffraction (EBSD) results. The peak temperature during stirring exceeded the allotropic transformation temperature (885 °C) resulting in the formation of serrate grain boundaries along with pits and blocky particles in the top region of the SZ. The grain structure development using EBSD analysis in the BM was investigated and on the weld joints for examining the distributions of High-Angle Boundaries (HABs) and Low-Angle Boundaries (LABs) by plotting misorientation distribution histograms and pole figures [34]. A particular area in the weld material is taken into consideration for understanding the transition of the original grain structure to SZ microstructures. For this, the area was divided into three regions, and each region has been further magnified for knowing the deformation behaviors. In Region 1, the reorientation of grains takes place concerning the direction of tool rotation following the prism slip-mode mechanism. From Region 2, it was concluded that the transition has started and fine grains have developed without any substructures resulting in discontinuous recrystallization. At Region 3, the plastic deformation produced an asymmetrical mixture of HABs and LABs in the SZ. This further led to the texture examinations of the SZ, and the texture–microstructure relationships have been successfully established in this study. The Schmid factor ($\cos\phi \cos\lambda$) was calculated in the SZ and on the BM based on the EBSD results and found that it is higher in the SZ than BM. After the tensile deformation, the grain size became more significant, finally causing tensile failure in the BM [35]. In another experiment by implementing three types of backward cooling techniques, SZ microstructure with enhanced tensile strength and ductility than the BM was successfully obtained [36]. Apart from using high-pressure air and ice-water mixture, liquid nitrogen produced the finest grains through the geometric dynamic recrystallization mechanism. In the year 2009 [37], the friction stir welding of Ti-5111, a near α-Ti alloy were investigated and the texture developments in the SZ were examined. There was a sudden change of microstructure between the BM and the SZ, due to high temperatures resulting in the formation of β grains with fine α laths. In another study [38], they also observed a TMAZ between the HAZ and SZ. The TMAZ consisted of two regions, that are Outer TMAZ (near HAZ) and Inner TMAZ (near SZ). In the year 2013, the mechanical properties both in the longitudinal and transverse directions at a specific location in the weld zone were measured [39] and found that strengths were higher in the longitudinal direction than the transverse direction in the SZ. Finally, apart from the butt and lap joints, friction stir welding of α-Ti alloy by producing specially designed T joints was also performed and conducted microhardness and tensile tests [24]. In addition to that, a numerical model was developed for analyzing thermal distribution

in the joints and correlated with the experiments. As a result of these findings, the metallurgy of the weldment is divided into zones such as the stir zone, thermome-chanically affected zone, heat-affected zone, and base metal microstructure. For all titanium alloys, the metallurgical features of the weldment vary depending on the composition of the base material and the temperature changes that occur during the process.

6 Fracture Mechanics

In this section, the study of fatigue properties, fracture propagations, crack initiation, crack propagations, and fracture failures that occurred during friction stir welding of various types of Ti alloys was discussed in detail. The effect of residual stresses on crack propagation was studied by conducting Fatigue Crack Propagation (FCP) tests by preparing the CT specimens [10]. The cut compliance technique was used to find the weld residual stress and crack length in the microstructure. Numerical simulations were performed for crack growth rate and crack length prediction, and they were consistent with the actual experimental results. Thus, the inclusion of the residual stress factors in the simulation improves the prediction of the fatigue life of the welds. From the fractographic analysis, it was observed that the striations at the welded surface were smeared due to compressive residual stress generated as the cracks were initiated from the advancing side. FCG kinetics phenomenon was measured in two conditions (as-welded and residual stress-relieved plates) for the Ti-5111 material [40], and it was observed that the residual stress is favorable as the FCG rates were minimal. In another research [41], the fatigue life of α+β Ti alloy joints in two conditions (as-welded and finished welds) was measured. From the fatigue tests, it was observed that the fracture emerged at the SZ and the boundary between SZ and TMAZ. The finished welds obtained higher fatigue strengths than the as-welded specimens. This was further examined in the year 2014 based on the heat input [42]. A significant improvement in the fatigue strength concerning higher heat inputs in the polished specimens was observed. The fatigue strength is compared with the weld heat input and achieved a nonlinear relationship; moreover, multiple cracks and surface voids were seen at higher temperatures. The cracks were initiated at the RS of the fatigue specimens as the heat generated at this region was minimum. The fatigue performance based on various post-weld heat treatments was also investigated in the year 2015 [43]. The welds were heat-treated at four different temperatures, the highest fatigue strength was achieved at a maximum heat treatment temperature (927 °C), and the fracture emerged at the weld region. At this temperature, the average hardness values produced softer welds. Also from the tensile tests, it was observed that the mid-heat treatment conditions produced higher strengths and the highest % elongation was obtained at 927 °C. Hence, these softness and ductile properties were directly influenced by the post-weld heat treatment conditions and were also beneficial for the fatigue strength improvement. They also investigated the fatigue strengths for corner and T-joints' configurations and compared these with a wrought

square bar and L-shaped extrusions [44]. In another study, they also measured the fracture toughness and FCG rates in both transverse and longitudinal directions of the stress-relieved weld joints [45, 46]. Finally, in the year 2015, the FCP behavior based on the microstructural evolution was examined and the residual stresses did not affect FCP rates [47]. The crack propagations were measured, and it was found that a zigzag crack pattern was followed (at the SZ and Interfacial Zone) and majorly influenced by the crack tip microstructure. The fracture surface was classified into three regions based on crack initiation, propagation, and failure [20]. In another study, the crack initiation was mainly influenced by the size of the contaminations present in the weld material [21]. The high-cycle fatigue strengths were measured and found that the joints were significantly improved by the annealing process [23] and also reported that a small portion in the β phase of the SZ and at the boundary between SZ and BM was the reasons for high-cycle fatigue failures. Finally, the fatigue properties and the fracture toughness for TA5 Ti alloy were successfully measured in the year 2020 [25] and reported that the crack propagation paths were straight, and the microstructure and textures in the SZ directly influenced the reduction of fracture toughness.

7   Conclusions and Future Outlook

After the detailed study and thorough review of various research works on FSW of Ti alloys, consequential progress in the perception and development of this process was achieved. Nevertheless, the following conclusions along with some important issues that have to be redressed in future research are discussed below:

1. The tool material selection plays a major role, as still in some processes, the tool debris is getting adhered to the workpiece materials which affects the service properties of the finished joints. The pin profile design has to be carefully selected concerning the varying thickness of the workpiece materials.
2. The post-weld characteristics like mechanical properties, like tensile strengths, hardness, residual stresses, and fracture mechanics properties like fatigue strength and fracture toughness were examined in detail based on crack initiation, crack propagations, and fracture failure obtained from various testing methods which were reviewed thoroughly. From this, it can be presumed that more studies are necessary for evaluating the thermal gradient aspects during the joining process. For this, various numerical simulations were to be conducted by using FEM-based software for the prediction of the above-mentioned mechanical properties and can be used for the process optimization.
3. The microstructural evolution revealed that for each allotropic type of Ti alloys, the deformation characteristics were examined, and it is worth noting that α-Ti alloy, β-Ti alloy, and $\alpha + \beta$ Ti alloys have undergone different phase transformation mechanics yielding further complications. This metallurgical phenomenon has to be studied at a fundamental level for a better comprehension of the process dynamics.

4. The fracture mechanics aspect in the friction stir welding of Ti alloys reveal that the material flow undergoing different thermal cycles during the joining process has a critical footprint on the fracture properties and fatigue strengths of the processed material. But still, more work on the measurement of creep characteristics and the crack growth patterns has to be carefully examined in future studies.

References

1. Allen, R., Thomson, T.: Friction welding (1995)
2. Mishra, R., Mahoney, M.W., Sato, Y., Hovanski, Y., Verma, R.: Friction stir welding and processing VII (2016)
3. Zhang, Y., Cao, X., Larose, S., Wanjara, P.: Review of tools for friction stir welding and processing. Can. Metall. Q. (2012).
4. Ramirez, A., Juhas, M.: Microstructural evolution in Ti-6Al-4V friction stir welds. Mater. Sci. Forum **426**, 2999–3004 (2003)
5. Lee, W., Lee, C.-Y., Chang, W.-S., Yeon, Y.-M., Jung, S.-B.: Microstructural investigation of friction stir welded pure titanium. Mater. Lett. (2005)
6. Reynolds, A.P., Hood, E., Tang, W.: Texture in friction stir welds of Timetal 21S. Scripta Mater. **52**, 491–494 (2005)
7. Pilchak, A., Juhas, M., Williams, J.: Observations of tool-workpiece interactions during friction stir processing of Ti6Al4V. Metall. Mater. Trans. A Phys. Metall. Mater. Sci. **38**, 435–437 (2007)
8. Zhang, Y., Sato, Y., Kokawa, H., Park, S., Hirano, S.: Microstructural characteristics and mechanical properties of Ti-6Al-4V friction stir welds. Mater. Sci. Eng. A Struct. Mater. Properties Microstruct. Process. (2008)
9. Zhang, Y., Sato, Y., Kokawa, H., Park, S., Hirano, S.: Stir zone microstructure of commercial purity titanium friction stir welded using pcBN tool. Mater. Sci. Eng. A. (2008)
10. Pasta, S., Reynolds, A.P.: Residual stress effects on fatigue crack growth in a Ti–6Al–4V friction stir weld. Fatigue Fract. Eng. Mater. Struct. **31**, 569–580 (2008)
11. Zhou, L., Liu, H., Liu, P., Liu, Q.: The stir zone microstructure and its formation mechanism in Ti–6Al–4V friction stir welds. Scripta Mater. **61** (2009)
12. Liu, H., Zhou, L., Liu, Q.: Microstructural evolution mechanism of hydrogenated Ti–6Al–4V in the friction stir welding and post-weld dehydrogenation process. Scripta Mater. **61** (2009)
13. Liu, H., Zhou, L., Liu, Q.: Study of the key issues of friction stir welding of titanium alloy. Mater. Sci. Forum 638–642 (2010)
14. Edwards, P., Ramulu, M.: Identification of process parameters for friction stir welding Ti–6Al–4V. J. Eng. Mater. Technol.-Trans. ASME **132** (2010)
15. Pilchak, A., Tang, W., Sahiner, H., Reynolds, A.P., Williams, J.: Microstructure evolution during friction stir welding of mill-annealed Ti-6Al-4V. Metall. Mater. Trans. A **42**, 745–762 (2011)
16. Pilchak, A., Williams, J.: Microstructure and texture evolution during friction stir processing of fully lamellar Ti6Al4V. Metall. Mater. Trans. A Phys. Metall. Mater. Sci. **42**, 773–794 (2011)
17. Farias, A., Prados, E., Magnabosco, R., Delijaicov, S.: Tool wear evaluations in friction stir processing of commercial titanium Ti–6Al–4V. Wear **302**, 1327–1333 (2013)
18. Wang, J., Su, J., Mishra, R., Xu, R., Baumann, J.: Tool wear mechanisms in friction stir welding of Ti–6Al–4V alloy. Wear **321**, 25–32 (2014)
19. Mashinini, P.M., Dinaharan, I., Selvam, J., Hattingh, D.G.: Microstructure evolution and mechanical characterization of friction stir welded titanium alloy Ti–6Al–4V using lanthanated tungsten tool. Mater. Character. **139** (2018)
20. Liu, Z., Wang, Y., Ji, S., Yan, D.: Fatigue properties of Ti–6Al–4V titanium alloy friction stir welding joint. J. Mater. Eng. Perform. **27** (2018)

21. Ma, Z., Wang, Y., Ji, S., Xiong, L.: Fatigue properties of Ti–6Al–4V alloy friction stir welding joint obtained under rapid cooling condition. J. Manuf. Process. **36**, 238–247 (2018)
22. van der Merwe, H., James, M.N., Hattingh, D.G., Rall, W.: Fatigue life prediction for rotary friction welded Ti–6Al–4V under variable amplitude fatigue loading. Theor. Appl. Fract. Mech. **104**, 102321 (2019)
23. Nakai M, Niinomi M, Komine K, Liu H, Morisada Y, Fujii H (2019) High-cycle fatigue properties of an easily hot-workable (α+β)-type titanium alloy butt joint prepared by friction stir welding below β transus temperature. Mater Sci Eng A 742:553–563
24. Su, Y., Li, W., Liu, X., Gao, F., Yu, Y., Vairis, A.: Strengthening mechanism of friction stir welded alpha titanium alloy specially designed T-joints. J. Manuf. Process. **55** (2020)
25. Gao, F., Guo, Y., Yang, S., Yu, Y., Yu, W.: Fatigue properties of friction stir welded joint of titanium alloy. Mater. Sci. Eng. A **793**, 139819 (2020)
26. Jata, K., Reynolds, A.P.: Microstructure and mechanical behavior of friction stir welded titanium alloys (2004)
27. Kitamura, K., Iwata, Y., Sun, Y.S., Morisada, Y.: Flexible control of the microstructure and mechanical properties of friction stir welded Ti–6Al–4V joints. Mater. Des. **46**, 348–354 (2013)
28. Edwards, P., Ramulu, M.: Investigation of microstructure, surface and subsurface characteristics in titanium alloy friction stir welds of varied thicknesses. Sci. Technol. Weld. Join. **14** (2009)
29. Wang, J., Su, J., Mishra, R., Xu, R., Baumann, J.: A preliminary study of deformation behavior of friction stir welded Ti–6Al–4V. J. Mater. Eng. Perform. **23**, 3027–3033 (2014)
30. Buffa, G., Fratini, L., Schneider, M., Merklein, M.: Micro and macro mechanical characterization of friction stir welded Ti–6Al–4V lap joints through experiments and numerical simulation. J. Mater. Process. Technol. **213**, 2312–2322 (2013)
31. Xu, Z., Li, Z., Lv, Z., Zhang, L.: Effect of tool rotating speed on microstructure and mechanical properties of friction stir lap welded Ti–6Al–4V alloy. Int. J. Adv. Manuf. Technol. **90** (2017)
32. Ji, S., Li, Z.: Reducing the hook defect of friction stir lap welded Ti–6Al–4V alloy by slightly penetrating into the lower sheet. J. Mater. Eng. Perform. **26** (2017)
33. Edwards P, Ramulu M (2015) Material flow during friction stir welding of Ti–6Al–4V. J Mater Process Technol 218:107–115
34. Mironov, S., Sato, Y.S., Kokawa, H.: Development of grain structure during friction stir welding of pure titanium. Acta Mater. **57**, 4519–4528 (2009)
35. Liu, F., Liao, J., Gao, Y., Nakata, K.: Influence of texture on strain localization in stir zone of friction stir welded titanium. J. Alloys Compds **626** (2015)
36. Xu, N., Qining, S., Bao, Y.-F., Jiang, Y., Shen, J., Cao, X.: Twinning-induced mechanical properties modification of CP–Ti by friction stir welding associated with simultaneous backward cooling. Sci. Technol. Weld. Join. **22**, 1–7 (2017)
37. Knipling, K., Fonda, R.: Texture development in the stir zone of near-α titanium friction stir welds. Scripta Mater. **60**, 1097–1100 (2009)
38. Karuthapandi S, Ramu M (2017) An experimental investigation of flat wire electrodes and their weld bead quality in the FCAW process. High Temp Mater Process 21(1):65–79
39. Nimer, S., Wolk, J., Zupan, M.: Local property characterization of friction stir welded Ti-5111: transverse orientation measurements. Acta Mater. **61**, 3050–3059 (2013)
40. Pao, P., Fonda, R., Jones, H., Feng, C., Moon, D.: Fatigue crack growth in friction stir welded Ti–5111. **11** (2009)
41. Lertora, E., Mandolfino, C., Gambaro, C.: Ti–6Al–4V FSW weldability: mechanical characterization and fatigue life analysis. Key Eng. Mater. **611–612**, 1476–1483 (2014)
42. Mashinini, P.M., Hattingh, D.G., Lombard, H.: Influence of process heat input on static and dynamic properties of friction stir welded 3 mm Ti–6Al–4V alloy. Adv. Mater. Res. **1019**, 287–293 (2014)
43. Edwards, P., Ramulu, M.: Fatigue performance of friction stir welded Ti–6Al–4V subjected to various post weld heat treatment temperatures. Int. J. Fatigue **75**, 19 (2015)
44. Edwards P, Ramulu M (2015) Fatigue performance of friction stir welded titanium structural joints. Int J Fatigue 70:171–177

45. Edwards P, Ramulu M (2015) Fracture toughness and fatigue crack growth in Ti–6Al–4V friction stir welds. Fatigue Fract Eng Mater Struct 38:970–982
46. Sanders, D., Edwards, P., Cantrell, A., Gangwar, K., Ramulu, M.: Friction stir-welded titanium alloy Ti–6Al–4V: microstructure, mechanical and fracture properties. JOM J. Minerals Metals Mater. Soc. **67** (2015)
47. Muzvidziwa, M., Okazaki, M., Suzuki, K., Hirano, S.: Role of microstructure on the fatigue crack propagation behavior of a friction stir welded Ti–6Al–4V. Mater. Sci. Eng. A. **652** (2015)